Nanotextured surfaces: platform for tailored light-matter interaction and optical sensing

A theses submitted for the degree of
Doctor of Philosophy

by

Armandas Balčytis

Supervisor Prof. Saulius Juodkazis

Centre for Micro-Photonics

Faculty of Science, Engineering and Technology

Swinburne University of Technology

Melbourne, Australia

2018

Declaration

I, Armandas Balčytis, declare that this thesis entitled:

"Nanotextured surfaces: platform for tailored light-matter interaction and optical sensing"

is my own work and has not been submitted previously, in whole or in part, in respect of any other academic award.

Armandas Balčytis

Centre for Micro-Photonics
Faculty of Science, Engineering and Technology
Swinburne University of Technology
Melbourne, Australia

Dated this day, 28th of September, 2018

Abstract

Texturation of material interfaces provides a purely topological mechanism for altering or controlling the way a given object interacts with a range of physical phenomena, defined by the relative lengthscales of surface features to those of the relevant effects. For electromagnetic radiation, scattering and interference represent the two main points of leverage that can be employed to alter its propagation behavior at an interface. Visible or near-infrared light, of primary interest here, tends to possess wavelengths on the nanometer range, hence, necessitating nanotexturation to exert control over its interaction with mater.

This work is primarily geared towards development of methods and techniques for the creation of effective and affordable nanotextured surfaces exhibiting a range of optical functionalities. It is divided into three parts, based on the class of materials onto which nanotexturing is applied, and deals with solid-state semiconductors/dielectrics like silicon, polymers of natural origin with the primary focus on silk, and plasmonic noble metals such as gold.

The problem of matching the impedances of radiation propagating in free space and within high refractive index materials is of primary relevance to technological fields pertaining to photovoltaics, photodetectors as well as solid state light sources. Increasing the efficiency of such devices involves creating effective methods for suppressing reflectance-related loss. Here, after overviewing the major ways for the realization of anti-reflectance, we focus on black silicon, a specific type of stochastic nanotextured surface, created on different types of substrate materials by way of a self-masking reactive ion etching process. The relationship between topology and optical behavior of black silicon is investigated *via* experimental and numerical experiments, and methods of extending its anti-reflectance towards the infrared spectral region by changing the scale of structural features or by creating a hierarchical texture, are proposed. Lastly, ways of inducing absorbance in the black silicon transparency region by way of metal nanoparticle decoration and infrared absorber layer creation are sought out, and new prototype photothermovoltaic as well as hybrid photovoltaic and thermoelectric full solar spectrum energy harvesting devices are proposed.

Nanotexturation was first pioneered in the natural world, however, so it is unsurprising that for most of the contemporary artificial functional interfaces an equivalent in both form and function can be found among various organisms. Following a short summary of notable examples of nanotexturing in the biosphere, an in-depth investigation of the behavior of nanotextures overlaying the wings of cicadas, similar in appearance and behavior to the aforementioned black silicon, is presented. Furthermore, biopolymers represent an important class of materials in their own right, since they tend to be inherently compatible with human physiology, hence, suitable to a wide range of important biomedical uses. Here the focus is primarily on silk – a protein-based material with a range of exceptional properties. First, optical and electromagnetic absorbance of natural silk fibers is probed throughout an unprecedentedly wide spectral region, ranging from the ultraviolet down to terahertz frequencies. Also, preliminary results of silk film patterning by using laser as well as electron beams are reported, and represent important steps towards the top-down creation of arbitrary planar biopolymer textures.

Surface-augmented optical sensing is another set of applications where interface nanotexturing provides an important mechanism to attain optical energy confinement, particularly when light is coupled into plasmon-polariton oscillations. The oldest and most well developed is the surface-enhanced Raman scattering technique, which, nevertheless, struggles to be accepted as a full-fledged analytical method in large part due to a lack of effective, reproducible and affordable plasmonic substrates. In this work, after an overview of key aspects of surface-enhanced Raman scattering and plasmonics, new ever more straightforward, affordable and scalable approaches for creating high-performance stochastic noble metal coated substrates are proposed. First, close-packed gold nanopillar array substrates, prepared on a silicon template reminiscent of the aforementioned cicada wing surfaces, are outlined and discussed as potentially applicable to fields were good reproducibility is particularly important. Next, highly enhancing electrochemically roughened copper(II) oxide template-based nanotextured plasmonic surfaces are described and appear promising for sensing applications in the field. Lastly, extremely simple and low-cost nanotexturing methods based on thermal rescaling of commodity-grade pre-stretched plastic sheets are presented as a viable path to creating truly disposable substrates for surface-enhanced Raman scattering in everyday sensing.

Acknowledgment

This work could never have come to fruition were it not for the good examples, or good advice and counsel of many people. First of all, I wish to thank my supervisor Prof. Saulius Juodkazis for granting me the chance to become part of his research group, for demonstrating what it takes to excel in academia, and for sparing no expense or effort in creating opportunities for my professional development.

I am grateful to my good friend Dr. Gediminas Seniutinas for teaching me virtually everything I now consider important when it comes to nanofabrication, and for always being most helpful and steadfast. I am thankful to our frequent and always very welcome guest Assoc. Prof. Yoshiaki Nishijima for being an invaluable source of inspiration and ideas, which drove much of the work described herein. I wish to express my gratitude also to Prof. Junko Morikawa for the many fruitful collaborative research efforts and for being a wonderful host during my visit to Tokyo Institute of Technology. My thanks also go to Meguya Ryu, for always being a most capable and reliable partner through many a challenging experiment.

Great appreciation is due to the supervisor of my research endeavors at the Center for Physical Sciences and Technology in Lithuania, Dr. Raimondas Petruškevičius, for helping me set out to study at Swinburne University of Technology as well as for his continuous support and patience demonstrated throughout my dual-track study program.

Over the course of my studies I was allowed the opportunity to join many intriguing projects headed by, in no particular order, Prof. Elena Ivanova, Dr. Mangirdas Malinauskas, Prof. Yasuyuki Tsuboi, Assoc. Prof. Koji Hatanaka, Prof. Etienne Brasselet, Dr. Sivashankar Krishnamoorthy and Prof. Peter Hannaford, to all of whom I am ever grateful.

I thank Pierrette Michaux for showing me the ropes of, and the discipline needed for, working in a cleanroom environment, the latter of which was extremely valuable throughout my PhD studies. Also, important portions of this research were performed on the Soft X-ray Spectroscopy, Infrared Microspectroscopy, as well as THz/Far-IR beamlines at the Australian Synchrotron, part of ANSTO. Special thanks go out to beamline scientists Dr. Dominique Appadoo, Dr. Pimm Vongsvivut and Dr. Mark Tobin, for going above and beyond the call of duty in their help and guidance over the course of numerous hectic experiments. Similarly, parts of this work were conducted at the Melbourne Centre for Nanofabrication (MCN) in the Victorian Node of the Australian National Fabrication Facility (ANFF).

Lastly, I thank my love, Aurina, for following me all the way to Australia and for letting me be the benefactor of her invaluable help, support, understanding and sense of humor. Most of all I owe an immeasurable debt of gratitude to my mother, Nijolė, not only for the great care and effort spent in raising me, but also for bravely weathering any and all hardships that came up over the course of my long time away.

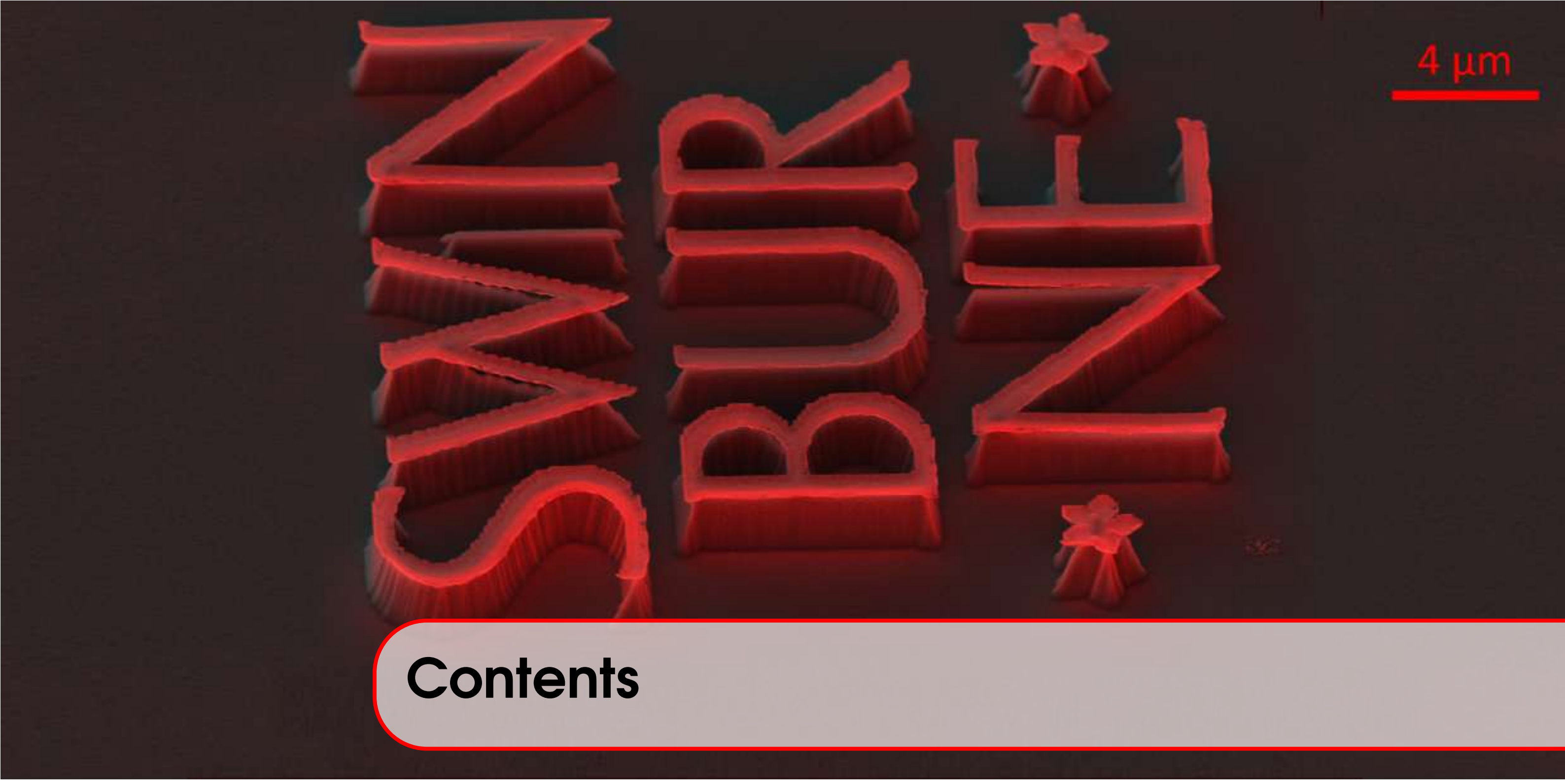

Contents

List of Figures

Preface

Science and application of nanotextured surfaces

The unrelenting drive to probe and harness new physical phenomena is at the core of the burgeoning field of nanotechnology. At the nanoscale, by convention understood to span from 1 to 100 nanometers, materials can exhibit properties absent in either their bulk or molecular counterparts. For instance, as dimensions of structural features approach the characteristic wavelengths associated with electrons, quantum confinement related alterations in the density of states and oscillator strengths induce new optoelectronic effects. Conversely, when electromagnetic waves propagate through structures with sizes far below the wavelength, effective medium approximations [1] can be employed to predicatively describe new materials with tailored optical properties. Novel chemical phenomena can likewise be uncovered at the nanoscale, such as catalytic action on nanoparticles of the usually chemically inert gold [2]. Furthermore, the expansive specific surface area of nanoparticles and nanostructures interfacing with reactants facilitates a significant increase in the rate of catalytic chemical transitions [3].

Nanotextured surfaces are interface layers of bulk materials with nanoscale structures formed or applied onto them. Such nanomaterials can endow surfaces with additional useful properties like hydrophobicity/hydrophilicity, bactericidal and anti-biofouling activity, as well as numerous modifications of optical response. While in the past few decades nanoscience has experienced rapid growth, it is still eclipsed by the wealth of self-optimized solutions present in nature, which had a head start amounting to hundreds of millions of years. Especially for nanoscale modification of surfaces, examples from the the biological realm - such as the bactericidal activity of insect wings [4], hydrophobicity of lotus leaves [5], structural colors of the wings of butterflies [6] - offer guidance for creating their synthetic functional counterparts.

Interaction of matter and light offers a particularly broad field where nanotextured surfaces as well as nanomaterials can be fruitfully harnessed. Observation of optical phenomena relies on the interactions between electromagnetic oscillations and the multitude of charged particles that comprise matter. At any heterogeneous interface between propagation media, energy re-radiated as a result of collective charge oscillations, together with interference of the superposing waves, underlie effects like reflectance and refractance. Therefore, provided feature dimensions can be at or below the wavelength scale, nanostructured surfaces can be used to control the coupling of light solely by changing interface topology. This effect is put to great use in creating anti-glare coatings for screens [7], enhancing radiance of light emitting diodes [8], and anti-reflectance layers for solar cells [9]. However, man-made solutions have been far preceded by developments in the natural domain, specifically, the subwavelength conical structures on moth eyes [10], on which this phenomenon was first observed and subsequently explained.

Biomimetics led to the discovery of numerous nature-inspired solutions and their realization by means of inorganic materials. However, in light of recent trends in closer interfacing between technology and the human body, organic nanomaterials become increasingly relevant due to their inherent bio-compatibility and mechanical plasticity. Among them, silk fibroin stands out as an especially prospective platform for creating sensor skins [11, 12] or implantable neural interfaces [13, 14]. The complex hierarchical nanoscale structure of silk underlies its extraordinary mechanical characteristics [15]. Similarly, the inherent complexity of protein based polymeric materials defines their equally complex optical properties, with spectral bands arising due to electronic transitions and intramolecular as well as collective vibrational modes.

In addition to light-matter interactions resulting from polarizability of atoms and molecules, coupling between electromagnetic waves and collective electron oscillations in conductors gives rise to a different branch of optical phenomena, jointly referred under the blanket term of plasmonics. When induced on nanoparticles or localized in nano-gaps, plasmonic oscillations can confine optical energy in spatial dimensions well bellow the diffraction limit. This gives rise to strong electromagnetic field enhancements that can be harnessed as transducers for refractive index sensing, either in localized surface plasmon (LSP) [16] or surface plasmon resonance (SPR) [17] geometries. For label-free spectroscopic chemical sensing methods, where molecules themselves are the optical signal sources, nanotextured plasmonic substrates enable low-threshold detection via surface-enhanced Raman scattering (SERS) [18, 19], or surface-enhanced infrared absorption (SEIRA) [20, 21].

The unifying goal of surface nanotexturing in the context of light-matter interaction is to shape the incoming electromagnetic wavefront towards specific desirable field distributions and propagation behaviors. Of course, what is ultimately achievable, and what applications can benefit, is dictated by the choice of substrate material (*i.e.* the nature of available optical oscillators). Thus, for example, functions of nanotextures on optoelectronically active semiconductor or passive dielectric layers will primarily involve shaping directional and spectral properties of reflectance and transmittance at the interface. On the other hand, whereas metals are opaque, their weakly bound electrons enable spatial confinement of optical energy in plasmons, which can be further exaggerated on surface topologies with high density of nanoscale gaps.

Regardless whether a solid state, soft-matter or plasmonic nanostructured surface platform is chosen for a given type of photonic function, in most cases either usage or cost considerations demand for fabrication methods capable of producing nanoscale features over macroscale areas. In practice this entails employing processing methods which exhibit significant degrees of parallelism. Mask projection or nanoimprint lithography, laser processing, physical vapor deposition as well as plasma etching are all examples of such techniques. However, in many cases, increases in manufacturing throughput come at a cost of loss in control over the shape and position of individual nanostructures. Yet, for functional nanotextured surfaces to be commercially viable, costly fabrication machinery should ideally be relinquished in favor of more straightforward paths of chemical etching or self assembly, well trodden in the biological realm. As in nature, such nanotextured optical surfaces will provide numerous additive improvements to light harvesting, optical sensing and imaging.

Outline of the thesis

This thesis describes the fabrication of nanotextured surfaces designed for photonic applications ranging from reflectance suppression to surface-enhanced sensing. Material platforms with different structure and nanotexturing potential, such as crystalline silicon, plasmonic metal particles and coatings as well as polymeric and bio-polymeric materials, were used. The properties of resultant surfaces were appraised by means of optical characterization and numerical simulations.

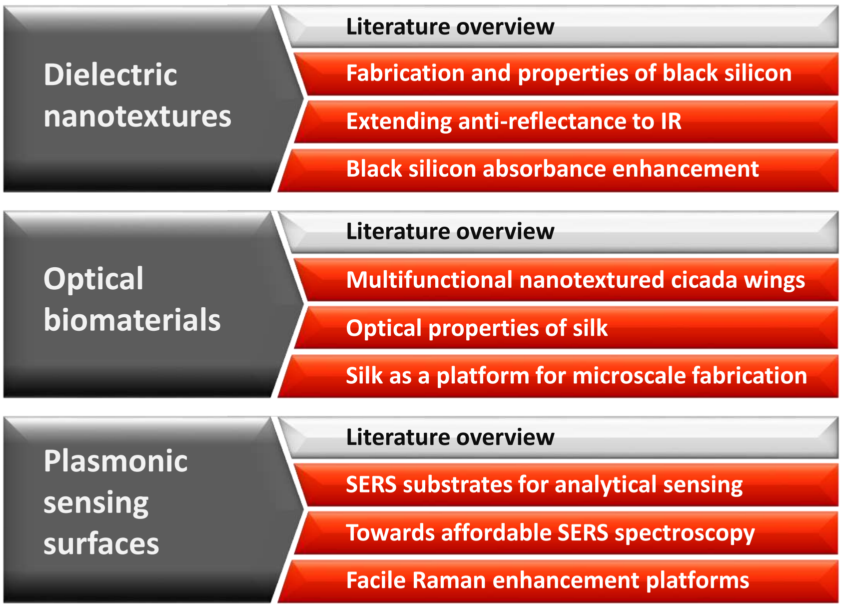

Figure A: Schematic outline of this thesis. Sections detailing original research contributions are highlighted in red.

The overarching structure of this thesis is summarized in Figure A. Individual chapters will detail the research performed along the three main directions. While topically all of the chapters are interlinked, each of them is structured to be self contained with separate introductory literature overview sections. Descriptions of relevant manufacturing, experimental characterization and numerical simulation techniques and methods are given as needed. Work described here is the result of several collaborative research initiatives and research projects. In every case, collaborators on any given project are acknowledged in the introductory part of the relevant section. Similarly, data and figures obtained without direct primary involvement of the author are denoted as such in every respective caption. The contents of the thesis can be summarized as follows:

- **Chapter 1 – Dielectric nanotextures** is devoted to various structures formed on surfaces in order to suppress their reflectance. After an overview of the conceptual principles of anti-reflectance and the current state of the art, work on a class of such surfaces covered with randomly arranged silicon needles is presented. The main focus of this direction was extending the anti-reflectance and absorbance of black silicon towards infrared wavelengths. In pursuit of this goal methods involving modification of morphology, hierarchical nanotexturing as well as plasmonic nanoparticle augmentation are investigated.

- **Chapter 2 – Optical biomaterials** describes applications of nanotextured surfaces in the biological realm as well as the recent progress on biocompatible, biodegradable and flexible functional materials geared towards closer integration between technology and the human body. Investigation of the influence of nanotexturing on the optical transmittance and other properties of a cicada wing serves as a case in point of the wealth of biomimetic solutions to technological challenges. However, the complex chemical and structural composition of biological materials necessitates understanding their effects on optical properties. To this end silk is studied as a particularly promising material by spectroscopically methods. Finally, research on techniques for creating nanoscale silk surface patterns is presented.
- **Chapter 3 – Plasmonic sensing surfaces** is focused on metal-coated substrates suitable for surface-enhanced Raman scattering sensing. Advances towards both single-molecular sensitivity as well as affordable Raman sensing solutions will be summarized in the introductory section. Work performed as part of this thesis centers mainly on high enhancement factor random plasmonic surfaces geared towards cost-effectiveness. Noble metal coated substrates based on chemically oxidized copper as well as thermally shrunk plastic are discussed. The problem of reproducibility of SERS performance is also tackled by means of area averaging.

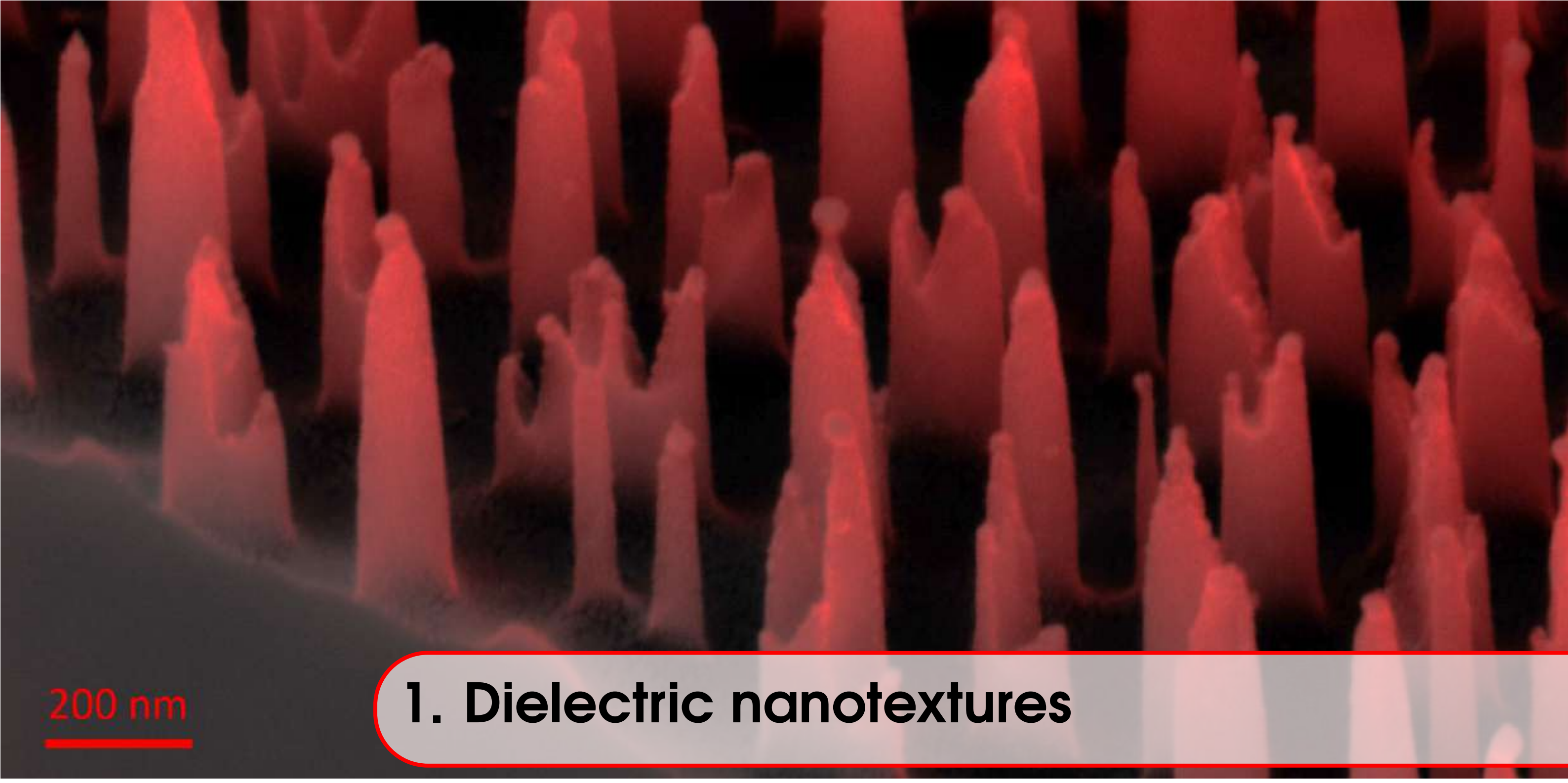

1. Dielectric nanotextures

Effects of electromagnetic radiation are made apparent and purposeful through interactions with various forms of matter. In general, the goal is to maximize the number of photons, hence energy, harnessed for liberating charge carriers, generating excitons or phonons. However, since materials are composed of charged particles that can be driven to oscillate by external fields, reflectance, *i.e.* elastic re-radiation at the material interface, limits the efficiency at which electromagnetic energy can be exploited. This effect is especially strong in materials with high densities of quasi-free charge carriers, such as metals or plasmas. Yet, even in dielectrics and semiconductors, where carriers are mostly in bound states, reflectance amounts to substantive losses before any other dissipation mechanisms can come into effect. The first formal solution to this problem is attributed to Lord Rayleigh, who showed how gradual transitions between materials aid in suppressing reflectance [22], which led to a subsequent demonstration that, counter-intuitively, tarnished glass exhibits an increased transmittance. Following these findings, a multitude methods involving the coating and patterning of surfaces to suppress their reflectivity have been developed. Currently, the anti-reflectance of dielectrics in general, and semiconductors in particular is of immense technological relevance for applications at visible and infrared wavelengths, such as solar cells, thermoelectric absorbers and photodetectors. This increasing demand and rapid advances in nanotechnology stimulate a vigorous race for novel methods of texturing surfaces to ever more efficiently capture and trap light.

This chapter focuses on nanostructured semiconductor surfaces tailored for suppressing the reflectance of visible and infrared radiation. It begins with a brief overview of the main concepts and mechanisms underlying anti-reflectance as well as a discussion of select examples published in the literature. The original research contributions outlined herein focus on black silicon - a particular variety of nanostructured surface exhibiting strong, broadband, omnidirectional and polarization-agnostic anti-reflectance (pictured in the title figure). Following a description of the fabrication method and properties of black silicon, further work aiming to extend the anti-reflectance of black silicon to the infrared wavelength region is presented. Three main strategies of achieving this, namely controlling the morphology of the nanotextured surface, implementing hierarchical textures, and using augmentation with plasmonic particles, are outlined.

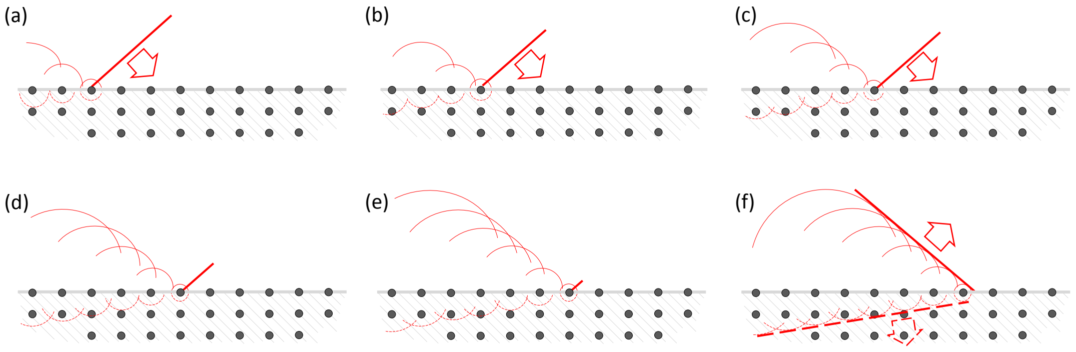

Figure 1.1: A sequence of sketches (a)-(f) depicting the formation of reflected and refracted wave-fronts when a plane wave gets scattered by atoms across an interface.

1.1 Light control at dielectric interfaces

This section provides a general overview of the concepts and mechanisms of reflectance suppression. For the sake of completeness it starts with a concise description of the phenomenon of reflectance, which directly feeds into the formulation of key problems of anti-reflectance. Two concepts ubiquitous in the fields of light capture and trapping, namely, the Effective Medium Theory and the Lambertian limit as discussed by Yablonovitch will be described in more detail. Finally, the major strategies for creating anti-reflective surfaces at optical wavelengths will be discussed and notable examples will be provided.

1.1.1 Fundamentals of reflectance and its suppression

The optical phenomenon of reflectance arises as a result of the constructive interference of wavelets emitted by oscillations of electric charges, driven by the incident optical field. Since dielectrics and semiconductors are a tightly packed agglomerations of atoms ($\sim 10^{10}$ per λ^3 cube), there is an overwhelming abundance of bound electrons capable of acting as re-radiators of such spherical wavelets. Electromagnetic waves emitted from sources so close together cannot reasonably be assumed to have uncorrelated phases, hence the aforementioned interference becomes crucial. When light is propagating through an optically dense medium the scattered wavelets experience destructive interference in all directions except forwards. Therefore, the more homogeneous, dense and ordered a material is, the less lateral and backwards scattering will be observed due to the more complete interference. This in turn allows radiation in non-absorbing condensed matter to propagate forwards in accordance with Fermat's Principle with little to no attenuation.

An interface between two media, on the other hand, presents a sharp break in symmetry. Wavelets emitted by atoms within a $\sim \lambda/2$ distance from the interface have no destructive counterparts and become free to interfere constructively to form a reflected wavefront, as sketched in Figure 1.1 (a)-(f). The either specularly or diffusely reflected wave can carry away an appreciable portion of energy, thereby presenting an impediment to the efficiency of many optoelectronic device types. It is critical to stress that interference is the underlying cause of reflectance, and therefore it is the central concept in most methods of attaining its suppression.

The amount of disturbance a given material presents to electromagnetic radiation propagating through it is characterized by the refractive index n [23]. In classical electromagnetic theory reflectance, *i.e.* the ratio between incident and reflected power, is expressed using the

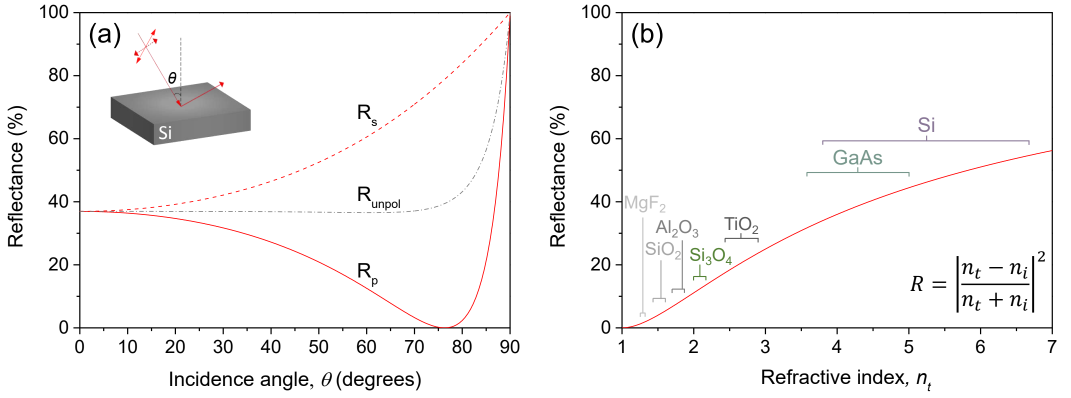

Figure 1.2: (a) Dependence of reflectance on incidence angle for s- and p-polarized light, as well as their average $R_{unpol} = (R_s + R_p)/2$, which represents the unpolarized case, calculated according to Equations 1.1. Refractive indices are assumed to be $n_i = 1.0$ and $n_t = 4.1$, which approximately correspond to values in air and Si for $\lambda = 532$ nm wavelength. (b) Dependence of reflectance on refractive index at normal incidence. Brackets show typical refractive index ranges for popular optoelectronic materials in the visible wavelength region.

familiar Fresnel equations [24]:

$$R_p = \left(\frac{E_{0r}}{E_{0i}}\right)_p^2 = \left(\frac{n_t\cos\theta_i - n_i\cos\theta_t}{n_t\cos\theta_i + n_i\cos\theta_t}\right)^2, \quad R_s = \left(\frac{E_{0r}}{E_{0i}}\right)_s^2 = \left(\frac{n_t\cos\theta_t - n_i\cos\theta_i}{n_t\cos\theta_t + n_i\cos\theta_i}\right)^2. \quad (1.1)$$

Here R_p and R_s correspondingly represent reflectance of p- and s-polarized light (*i.e.* parallel and perpendicular to the plane of incidence), E_{0r} and E_{0i} are the electric field amplitudes for reflected and incident waves, whereas n_i and n_t are the respective refractive indices of the media of incidence and from which the reflectance occurs. Of course, the angle of incidence θ_i is related to the angle of refraction θ_t via Snell's law $\sin(\theta_t) = (n_i/n_t)\cdot\sin(\theta_i)$. As a consequence of the conservation of energy, the transmittances can be expressed as $T = 1 - R$. While the propagation direction of a reflected wavefront is set by constructive interference, its amplitude is related to the angular dependence of power emitted by the induced dipoles.

Reflectance values calculated using the Fresnel equations and graphically depicted in Figure 1.2 illustrate the main issues related to interaction of light with the interfacial layer of a material. As mentioned previously, the most obvious result are the losses due to the failure to couple electromagnetic energy into the material. As shown in Figure 1.2 (a), reflectance related losses for silicon can amount up to $\approx 35\%$ at visible wavelengths. According to the normal incidence example given in Figure 1.2 (b), reflective losses scale with the refractive index mismatch between the material and the surrounding medium. This dependence is especially acute for optoelectronic materials, since their absorptive and dispersive properties are related through the Kramers-Kronig relations, *i.e.* changes in absorbance will induce variations in the real part of the refractive index, hence, can result in stronger reflections. Next, reflectance is also dependent on the angle of incidence, and overall tends to escalate as it increases. Lastly, polarization of light with respect to the plane of incidence significantly affects reflectance at oblique angles. In particular, reflection of light polarized along the plane of incidence is in stark contrast to its perpendicularly polarized counterpart, as in the former case reflectance drops to zero at a particular θ_i, called the Brewster's angle, due to the induced dipole moments being oriented along the direction of specular reflectance.

The aforementioned considerations give rise to a set of requirements that an anti-reflective modification of an interface is expected to fulfill, which can be summarized as follows:

- **Minimal reflectance.** The most straightforward aspect is reducing the fraction of reflected radiation, hence, maximizing the amount of energy coupled past the interface into the bulk of the material. Hence, the efficiency of reflectance suppression is directly related to the efficiency of solar energy harvesting devices and photodetectors.
- **Broadband performance.** While wavelength dependence of reflectance is not explicitly stated in the Fresnel equations, a certain amount of variability is introduced due to the refractive index dispersion of a given material. More importantly, since most anti-reflective layers operate based on interference or scattering, dimensions of their structural components have to be comparable to the relevant wavelengths. Obviously this precludes creating anti-reflective coatings for arbitrarily broad bandwidths. However, for many applications, such as those related to solar energy harvesting, anti-reflective coatings are expected to be consistent whilst operating in a spectral range spanning from UV to near-IR.
- **Ominidirectional anti-reflectivity.** As shown in Figure 1.2 (a), reflectance is heavily dependent on the illumination angle and tends to increase dramatically at glancing incidence. In most practical cases the angle of incidence for light can be arbitrary with respect to the surface normal, therefore an anti-reflectance layer should ideally suppress reflectance of beams incoming from the widest range directions. This is a particular concern in creating anti-glare screens as well as in photovoltaics, where solutions to orient panels to face the sun throughout the day come at a significant cost of implementation and are a continuous drain of energy.
- **Polarization insensitivity.** Reflectance of light incoming at oblique angles of incidence is strongly affected by polarization state. In particular, reflectance of the s-polarized component is substantially more challenging to suppress. It is therefore desirable that an anti-reflectance layer would efficiently couple light into the material regardless of polarization state. Polarization independence is relevant for anti-glare applications as well as in photovolataics, as atmosphere-scattered sunlight exhibits an appreciable degree of polarization.

In addition to these purely optical considerations, anti-reflective layers should be mechanically and chemically resilient, thermally compatible with the active substrate and exhibit good adhesion. Furthermore, properties such as hydrophobicity, self cleaning and anti-biofouling would likewise be beneficial. A realization of all this in a single nanostructured surface, along with the ever-present demand for attainability using scalable and low cost fabrication methods, is yet to be achieved.

A sketch of main principles employed for minimization of reflective losses is given in Figure 1.3 [25]. Anti-reflective coatings represent the most technologically straightforward, hence, widely used approach (Figure 1.3 (a)). It is based around introducing other interfaces that produce additional phase-shifted reflections, which superimpose to interfere destructively. Surface topology based methods (Figure 1.3 (b-c)) are morphologically more complex and their effect on reflectance depends on the ratio between the dimensions of constituent structural features and the wavelength of light. When structural features become significantly smaller then the wavelength, light perceives them as an effective refractive index medium. Therefore, by progressively changing the material fill-factor of an interfacial layer a gradual refractive index transition which minimizes reflectance can be achieved (Figure 1.3 (b)). As feature sizes approach the wavelength scale, light can be coupled into the substrate through forward-scattering either into a well defined set of diffraction orders [26] (when structures are strictly

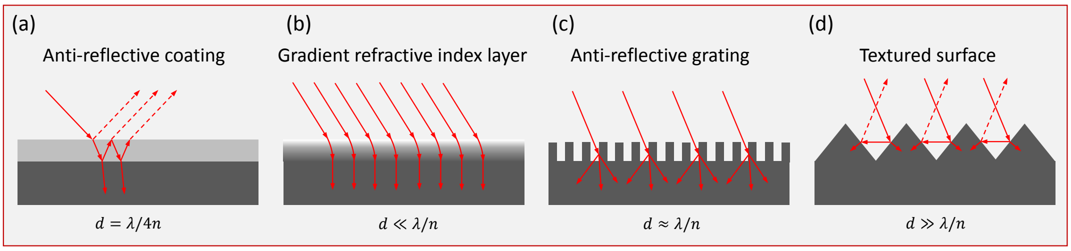

Figure 1.3: Sketches of the primary surface modification methods used for reflectance suppression. (a) Interference-based anti-reflection coating, (b) gradient effective refractive index layer in the subwavelength regime, (c) resonant anti-reflection structures which preferentially forward-scatter light into a certain set diffraction orders, (d) textured surface for light trapping, operating in the geometrical optics regime.

periodic as in Figure 1.3 (c)), or into a more broad region of k-space [27] (when structures are quasi-random). Lastly, principles of geometrical optics can be applied when feature sizes far exceed the wavelength. In this case mitigation of reflectance is realized through maximizing the number of external and internal reflections (Figure 1.3 (d)).

Of course, all of the aforementioned reflectance suppression methods are not mutually exclusive. Practical anti-reflectance surfaces can simultaneously harness multiple reflectance suppression mechanisms for maximum efficiency. For example, resonant anti-reflective structures are often conical in order to capitalize on the gradient effective refractive index effect [26]. Likewise, in all four of the aforementioned cases a functionally equivalent result can be achieved either through the control of composition or topology of the surface layer. In the next sections these main methods of achieving anti-reflectance along with representative examples will be discussed in greater depth.

1.1.2 Anti-reflective interference coatings

Traditional layered anti-reflective coatings rely on inducing additional reflecting interfaces and on precise control over the optical path of these reflected wavefronts so that they would eliminate each other through destructive interference. While the realization of such coatings does not necessitate nanotexturing, widespread use makes them a baseline against which more complex surfaces are compared. The simplest example of an anti-reflective coating is a single homogeneous layer of material with a refractive index representing a geometric mean of the air and substrate values. Assuming that only a single reflection is produced at each interface and that all other optical losses can be disregarded, Fresnel reflectance amplitudes from the two interfaces in the simplest case of normal incidence (*i.e.* angles of incidence and refraction $\theta = \theta' = 0$) can be expressed as:

$$r_{0,1} = \frac{n_1 - n_0}{n_1 + n_0}, \quad r_{1,s} = \frac{n_s - n_1}{n_s + n_1} \mathrm{e}^{-2i\delta}. \tag{1.2}$$

where n_0, n_1 and n_s denote the refractive indices of the different media as illustrated in Figure 1.4 (a), and $\delta = 2\pi d n_1 \cos\theta'/\lambda$ represents the phase thickness. Assuming total destructive interference between the reflected waves, *i.e.* that the amplitudes of both reflected waves are equal and that they exhibit a π radian phase difference, two conditions for minimum reflectance can be extracted [28]:

$$\frac{n_1 - n_0}{n_1 + n_0} = \frac{n_s - n_1}{n_s + n_1} \quad \longrightarrow \quad n_1 = \sqrt{n_0 n_s}; \tag{1.3}$$

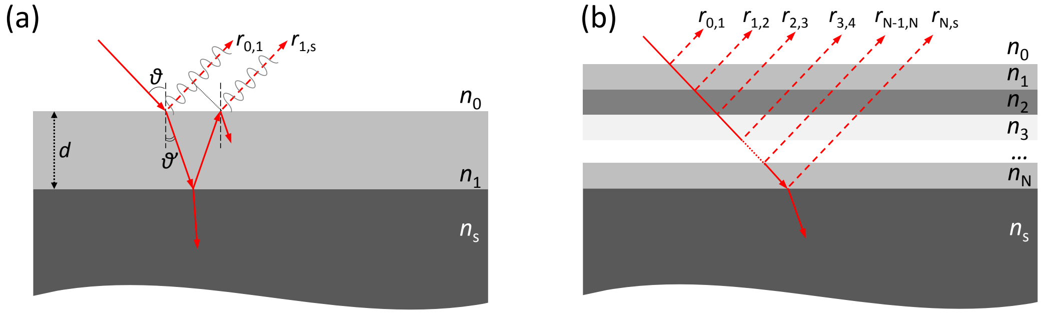

Figure 1.4: (a) Sketch depicting the propagation of electromagnetic radiation through a single homogeneous thin film deposited on a substrate. (b) Simplified illustration of light propagating through a multilayer coating stack. Variability of refractance angles due to different refractive indices is disregarded for simplicity.

$$\frac{4\pi n_1 d}{\lambda} = \pi \quad \longrightarrow \quad d = \frac{\lambda}{4n_1}. \tag{1.4}$$

Equation 1.4 is the reason why such layers are colloquially called quarter-wavelength coatings, although in general the coating can have thicknesses that are an odd multiple of $\lambda/4$ at the cost of degraded performance due to a more complex angular and spectral response.

At oblique incidence angles the full complexity of Fourier equations has to be considered, therefore anti-reflectance can be assured only for a single propagation direction and becomes strongly polarization dependent. Furthermore, dispersion limits the bandwidth in which conditions 1.3 and 1.4 are fulfilled. To compensate for these limitations more complex multilayer stacks are used. The aforementioned mathematical model can be generalized for an indefinite amount of layers, as sketched in Figure 1.4 (b). The total reflectance amplitude r_{tot} is expressed as the superposition of wavefronts reflected from all of the interfaces [28]:

$$r_{tot} = \sum_{j=1}^{N} \frac{n_j - n_{j-1}}{n_j + n_{j-1}} \mathrm{e}^{-2i\sum_{k=1}^{j}\delta_k}. \tag{1.5}$$

Here n_j and δ_j represent the refractive index and phase thickness of each individual layer. Optimal anti-reflectance can be attained by minimizing Equation 1.5 through iterative adjustments to refractive indices and thicknesses of each layer.

Despite its simplicity, a single quarter-wavelength coatings can decrease the reflectance in the visible spectral region from $\approx 35\%$ down to $\approx 5\%$ for Si [29], and from $\approx 4\%$ down to $\approx 1\%$ for SiO_2 [30] over a moderate bandwidth, say, spanning the visible 400–700 nm range, as can be seen in Figure 1.5. The materials relevant in the production of homogeneous quarter-wavelength coatings of Si surfaces are SiO_x (where $1.46 \leqslant n \leqslant 1.85$ for $1 \leqslant x \leqslant 2$), CeO_2 ($n \approx 2.2$), ZnS ($n \approx 2.3$) and TiO_2 ($n \approx 2.65$), just to name a few. Presently, plasma-enhanced chemical vapor deposited Si_3N_4 is the most widely embraced material [31], in part due to the broad tunability of its refractive index ($1.9 \leqslant n \leqslant 2.7$) throughout the region optimal for Si [32], but also because such coatings are scratch-resistant and furthermore provide surface passivation [33]. On the other hand, if substrate materials have low refractive indices to begin with (as is the case with BK7 glass $n \approx 1.51$), according to Equation 1.3 the optical density of

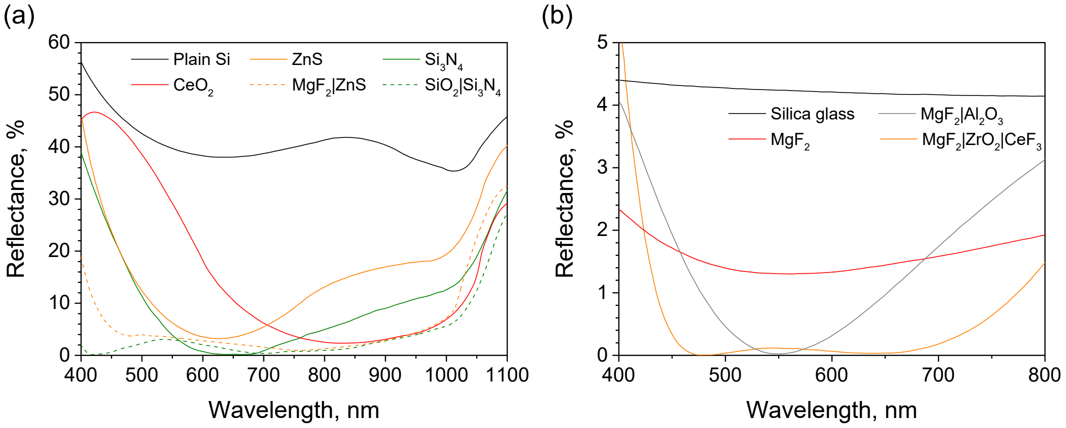

Figure 1.5: Wavelength dependent performance of different anti-reflection coatings. (a) Reflectance of Si substrates with single layer quarter-wavelength, or double layer quarter-quarter coatings. Si_3N_4 related data is plotted according to [31], all other data is based on [29]. (b) Reflectance of silica glass substrates with different anti-reflectance coatings: single layer quarter-wavelength MgF_2, quarter-quarter MgF_2/Al_2O_3 coating, three layer 0.25λ-MgF_2/0.25λ-ZrO_2/0.25λ-CeF_3 coating [30].

an optimal anti-reflective coating material should be still lower (correspondingly $n = 1.22$). Such suitable solid-state quarter-wavelength coating materials are not readily forthcoming, with MgF_2 and its $n \approx 1.38$ coming closest. However, high porosity columnar thin films of SiO_2 and TiO_2 can be created through glancing angle physical vapor deposition, which can have refractive indices as low as $n = 1.05$ [34, 35] at the cost of lower robustness.

One of the key drawbacks of single layer homogeneous anti-reflection coatings is a lack of technological flexibility as a result of the limited number of adjustable design parameters. Therefore, a natural extension of the method involves using additional layers. Double layer coatings can be applied when superior suppression of reflectance is required at a particular narrow wavelength range, or when a more broadband spectrum with two minima and a subdued central maximum is sufficient, with some examples provided in Figure 1.5. When both layers of such coatings have equal $\lambda/4$ optical thicknesses they are called quarter-quarter coatings, or simply V-coatings due to their characteristic spectral reflectance signature. The trade-off between minimization of reflectance and broadband performance is a recurring problem of interference based anti-reflection solutions, which forces the use of an ever-larger number of layers. Typically the properties of such multi-layer stacks can be modeled and optimized by computational means trough minimization of Equation 1.5.

Thin-film interference based homogeneous anti-reflectance coatings are mechanically robust, conceptually and technologically straightforward to implement and can offer reflectance suppression down to a few percent over a moderate bandwidth. Such properties make them well suited for laser optics. On the other hand, anti-reflection coatings can have adhesion issues and are liable to damage due to thermal expansion coefficient mismatch. However, their main drawbacks are the degradation of performance as the incidence angle of deviates from the value for which the coating was optimized, as well as the sensitivity to polarization at oblique incidence angles. When omnidirectionality and polarization insensitivity are key concerns in addition to high reflectance suppression, gradient refractive index layers offer a superior alternative.

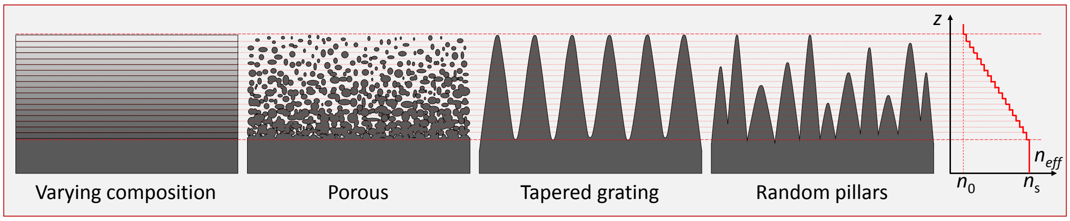

Figure 1.6: Schematic illustration of possible methods to implement gradient refractive index anti-reflective surfaces. The same linear gradient can be attained either by altering material composition or through creating subwavelength features ranging from pores to either periodically or stochastically arranged pillars.

1.1.3 Gradient refractive index layers

As was theoretically shown in the influential work by Lord Rayleigh in 1879, reflections of vibrations are suppressed when transition between two media is sufficiently gradual [22]. In such a case no abrupt junction is present from which scattered wavelets can interfere constructively, hence, no pronounced reflections are produced. This principle is valid not only for optics, as discussed here, but is likewise applicable for acoustic and other types of waves. Furthermore, as the wavefront propagates towards incrementally higher optical density regions it is progressively refracted towards the surface normal, thereby yielding good anti-reflectance at oblique incidence angles. Lastly, provided the refractive index transition from ambient n_0 to substrate n_s values occurs over a length-span similar to the maximum wavelength, such layers can provide optical impedance matching over an arbitrarily broad bandwidth.

The most obvious method of creating a gradient refractive index layer is either to prepare an inhomogeneous film with gradually shifting composition, or to deposit a stack of thin-films, each with stepwise incrementally smaller refractive indices, as illustrated in the first panel of Figure 1.6. However, for optimum performance the layer refractive index in the vicinity of the interface with air should be close to unity, which is not possible for available solid state materials. Fortunately, gradual refractive index transitions from values close to ambient to those of the substrate can be attained through changing the packing density of the film through inducing porosity or nanotexturing on a subwavelength scale (as shown in panels 2–4 of Figure 1.6) [30].

When light interacts with subwavelength-scale topography of a surface it propagates as if through a medium with properties averaged in some way between those of the mutually interspersed phases. Mathematical models used to estimate such averages and to establish relationships between microscopic properties (*e.g.* surface topology) and aggregate macroscopic ones (*e.g.* refractive index) are called Effective Medium theories [36]. Indeed, even the concept of a dielectric constant, and by extension the refractive index, is the result of an effective medium approximation - the Clausius–Mossotti relation, which ties the aforementioned electromagnetic properties to the individual atomic or molecular polarizibility values. The two main effective medium approximations used for estimating the optical properties of a mixture of phases are the Maxwell-Garnett model [37, 38], and the Bruggeman model [39].

The Maxwell-Garnett formula is obtained as an extension of the Clausius–Mossotti relation, by assuming that the composite material is made up of spherical inclusions with a refractive index of n_1 embedded in a host matrix n_0. Since at optical frequencies the polarization of atoms is mainly electronic, the Clausius–Mossotti relationship can be expressed through refractive indices (instead of the more common formulation using dielectric constants) as:

$$\frac{n^2 - n_0^2}{n^2 + 2n_0^2} = \frac{4\pi}{3} N\alpha. \tag{1.6}$$

Where α denotes the molecular polarizability and N is the number of molecules per unit volume. The Maxwell-Garnett model assumes, that inclusions are spherical with a radius a and a refractive index n_1. Elementary electrostatics yields the polarizability of such an inclusion [40]:

$$\alpha = \frac{n_1^2 - n_0^2}{n_1^2 + 2n_0^2} a^3. \tag{1.7}$$

Then, upon substitution of Equation 1.7 into Equation 1.6 we obtain the Maxwell-Garnett formula [36]:

$$\frac{n^2 - n_0^2}{n^2 + 2n_0^2} = \eta_1 \frac{n_1^2 - n_0^2}{n_1^2 + 2n_0^2}, \tag{1.8}$$

which relates the effective refractive index n of the composite material that consists of η_1 volume fraction of spherical refractive index n_1 inclusions in a surrounding matrix of n_0. Despite its convenience, the Maxwell-Garnett approximation has significant shortcomings related to the asymmetric way the host and inclusion materials are treated. If Equation 1.8 were to be restated as giving the effective medium approximation for $\eta_0 = 1 - \eta_1$ volume fraction inclusions of n_0 into a matrix of n_1 the result would not be the same. This is because validity of the spherical approximation hinges on a shell of the host material surrounding the inclusion. This asymmetry is particularly strong when disparity between the refractive indexes is large. Furthermore, when trying to generalize Equation 1.8 to account for inclusions of more than one type (*i.e.* a η_1 fraction of n_1 material and a η_2 fraction of n_2 material in a host matrix $\eta_0 = 1 - \eta_1 - \eta_2$ with n_0), the resultant effective refractive index n depends on the refractive index of the matrix n_0 even when it is completely replaced ($\eta_0 = 1 - \eta_1 - \eta_2 = 0$). Hence, the Maxwell-Garnett approximation holds only when the total volume fraction of inclusions is small.

On the other hand, this is not the case with the Bruggeman approximation, as it can be applied to arbitrary mixtures with no obvious contradictions. The assumptions in this method have some similarities to the Maxwell-Garnett case - a set of N different inclusions, each with their own volume fractions η_i and refractive indices n_i, are embedded in an infinite homogeneous medium n. However, the key hypothesis is that the Bruggeman effective refractive index n should be such, that the total dipole moment of the system is zero, or, in other words, the average flux deviations must be zero:

$$\sum_{i=1}^{N} \eta_i \Delta\Phi_i = 0. \tag{1.9}$$

Without retracing the relevant algebra [36], the Bruggeman effective medium formula is:

$$\sum_{i=1}^{N} \eta_i \frac{n_i^2 - n^2}{n_i^2 + 2n^2} = 0. \tag{1.10}$$

The inherent symmetry of the Bruggeman approach makes it very convenient in many practical cases for approximating nanostructured gradient refractive index surfaces. However, as it

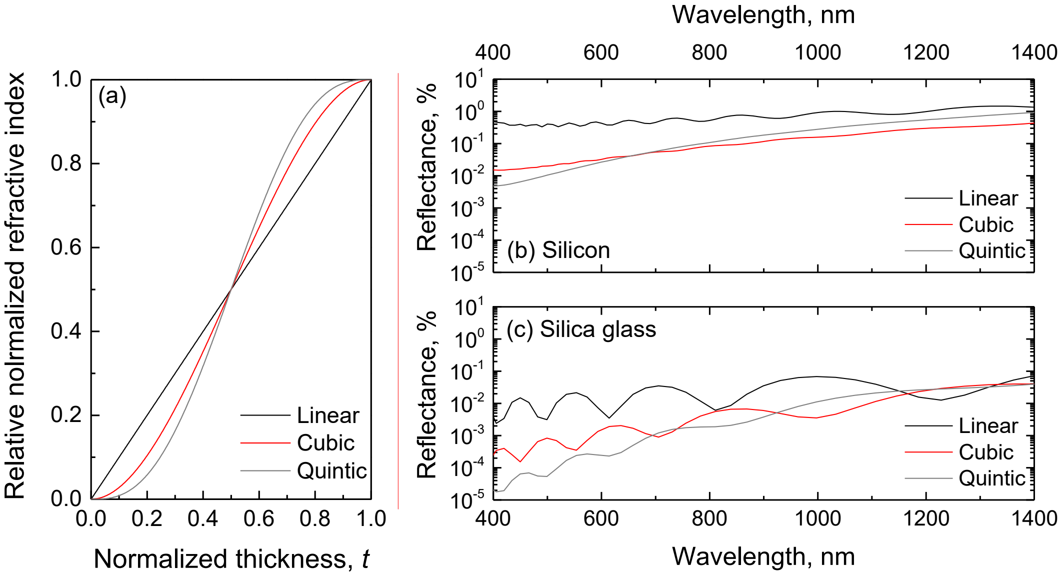

Figure 1.7: (a) Different effective refractive index profile types as a function of the normalized thickness of the impedance matching layer. (b) and (c) show reflectance at normal incidence of a 1 µm thickness gradient effective refractive index layer, corresponding to linear, cubic and quintic profiles depicted in panel (a), on crystalline silicon and silica glass respectively. Calculations were performed according to Equation 1.5 over 500 layers. Wavelength dependent refractive index values reported in the literature for Si [41] and SiO_2 [42] were used.

disregards geometric considerations, in some cases care must be taken. For example, in defiance of physical reality, insulating inclusions in a conductor would be treated the same, hence produce the same effective permittivity, as conducting inclusions in an insulator.

Provided the structure is sufficiently subwavelength to justify using an effective medium approximation, a nanotextured surface can be treated as a set of multiple layers, each with its own effective refractive index deduced based on the volume fraction, as shown in Figure 1.6. However, when optimizing the anti-reflectance of a gradient refractive index layer, the transition profile along the surface normal is of critical importance. The refractive index profile, varying from an ambient value of n_0 to substrate value n_s, can be described as a polynomial expansion to some specific order of a dimensionless thickness parameter t [43]:

$$\begin{aligned} &\text{Linear}: && n = n_0 + (n_s - n_0)t, \\ &\text{Cubic}: && n = n_0 + (n_s - n_0)(3t^2 - 2t^3), \qquad\qquad 0 \leqslant t \leqslant 1 \qquad\qquad (1.11) \\ &\text{Quintic}: && n = n_0 + (n_s - n_0)(10t^3 - 15t^4 + 6t^5). \end{aligned}$$

The effective refractive index profiles denoted by Equations 1.11 are illustrated in Figure 1.7 (a). The optical transition from ambient to substrate medium should ideally be as continuous and gradual as possible, with a linear relationship being a viable example. However, a cubic profile preserves continuity of both the value as well as the first derivative of the effective refractive index, and a quintic transition extends continuity to the second derivative. As shown in Figures 1.7 (b) and (c), increasing the polynomial order results in improved anti-reflectance at normal incidence, and this advantage tends to increase dramatically as the thickness of transition layer is increased in relation to the maximum wavelength. On the other hand,

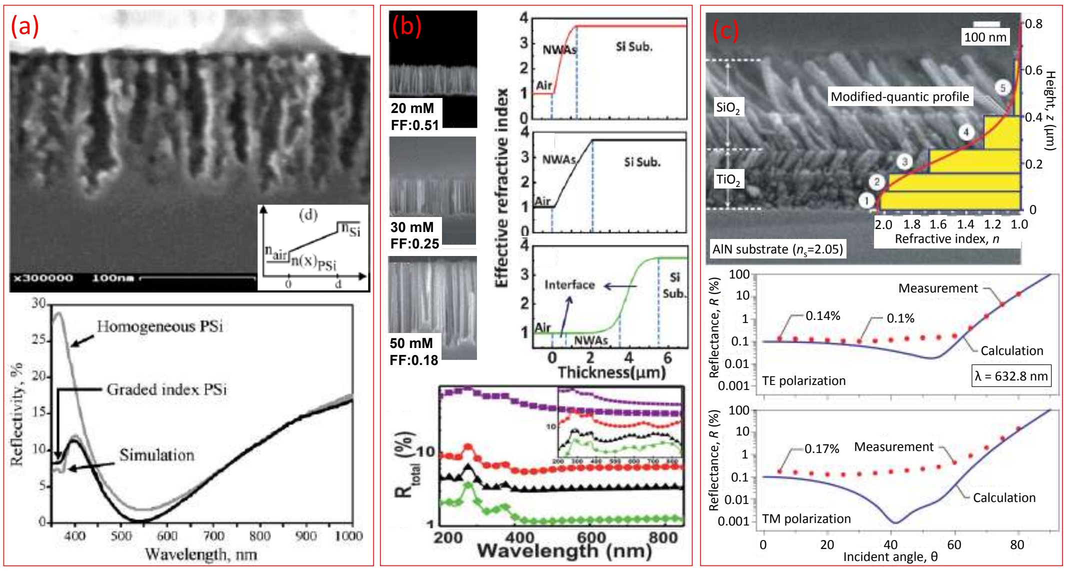

Figure 1.8: Gradient effective refractive index nanostructured surfaces reported in literature. (a) Graded index porous silicon created by electrochemical etching [45]. The refractive index profile is presumed to be discontinuous at layer boundaries. Reflectance spectra are given in the lower panel. (b) Silicon nanowire arrays with heights up to 5 μm fabricated using metal-assisted etching at different $AgNO_3$ catalyst precursor concentrations [46]. Refractive index profile curves are color-matched to respective total reflectance spectra. (c) Modified quintic effective refractive index profile coating on AlN prepared using sequential steps of physical vapor deposition of TiO_2 and SiO_2 at different oblique angles [35]. Spectral and angular dependencies of reflectance are in bottom panels.

further increasing the polynomial order can be detrimental, as it results in a sharper transition at the midpoint of the layer [43]. Furthermore, simpler linear profiles tend to excel when wavelengths are substantially larger than the thickness of the gradient index layer.

When light is incident at a normal to the surface, for acceptable reflectance suppression impedance matching layer thickness d should be above $\lambda_u/2$, where λ_u is the highest wavelength of the target bandwidth, and when $d \gg 2\lambda_u$ performance improvement becomes marginal [44]. Conversely, if the aim is broadband anti-reflectance at glancing incidence angles up to 89°, very high thickness ($d \sim 50\lambda_u$) layers of a particular extended quintic profile, with a more gradual transition from the low-index interface, have been proposed [44].

Notable fabrication methods for gradient effective refractive index nanostructured surfaces include physical vapor deposition, electrochemical or plasma etching, as well as lithographic patterning. Low refractive index anti-reflecting metal-oxide layers can be also fabricated using affordable and scalable sol-gel methods [47]. In this case the oxide film can be deposited using simple spin or dip coating methods, and an effective refractive index gradient can be imparted by a subsequent wet etching step [48]. Porous layers on silicon can be created through electrochemical etching in an aqueous HF solution [49]. Size of the etched subwavelength pores, hence the Si volume fraction and effective refractive index, can be controlled through adjusting the etching current. An example of a resultant structure, its index profile and reflectance spectra is given in Figure 1.8 (a). Since the etched layer amounts to a fairly small thickness of $d \sim 100$ nm, the reflectance is not particularly broadband, however, a moderate average reflectivity of 3.7 % over the solar spectrum has been achieved regardless [45].

One of the key drawbacks of thin gradient layers is that the effective refractive index profiles are discontinuous at both the ambient and substrate interfaces. More gradual high aspect-ratio structures can be achieved using metal-assisted chemical etching [50]. In this case removal of material in HF proceeds through the catalytic action of surface-deposited noble metal nanoparticles, with those composed of Ag or Au being the most widely used. Metal ions galvanically displace silicon and induce local oxidation, and this newly created SiO or SiO_2 gets dissolved by HF. Gradually, metal particles sink down into Si creating an anti-reflecting surface packed with large aspect ratio vertical nanowires up to 10 μm in height [51]. An example of such a nanotextured surface is given in Figure 1.8 (b), where changes in the concentration of the catalyst precursor $AgNO_3$ resulted in variations of the nanowire height [46]. Due to the variability of vertical etch rates as a result of the stochastic distribution of nanoparticle sizes the resultant effective refractive index profile for 5 μm wires becomes similar to the modified quintic profile well suited for omnidirectional anti-reflectance [44]. Overall, higher nanowire heights correspond to lower reflectance, however, even fairly shallow $d \sim 340$ nm metal assisted etching derived porous Si surface after passivation was successfully used to create an 18.2 % efficient solar cell [52].

In addition to the aforementioned subtractive fabrication methods, porous films can be created using additive physical vapor deposition at oblique angles [53]. When a substrate is oriented at an angle to the deposition source a shadowing effect is observed, whereby deposition behind initially formed nuclei is blocked. This in turn means that material is deposited not as a tightly packed film, but as a porous arrangement of inclined nanocolumns, as shown in Figure 1.8 (c). The key advantage of this method is that it affords a significant degree of control over the porosity, hence over effective refractive index of the resulting layers. Solely by changing the substrate tilt angle the refractive index of TiO_2 can be varied from 2.7 to 1.3, and that of SiO_2 from 1.46 to 1.05 (which is the lowest achieved value to date) [35]. The porous film deposited on AlN ($n = 2.05$) and shown in Figure 1.8 (c) likewise was tailored to have extended quintic profile and exhibits under 1 % reflectance over most of the visible wavelength range.

In many cases it is desirable that the anti-reflectance surface would not merely be a passive optical impedance matching layer, but would serve an optoelectronic function along with the rest of the substrate. This is particularly relevant for solar energy harvesting and photodetection. When the gradient effective refractive index layer is excessively porous the large surface area can result in substantial recombination losses. Furthermore, the robustness of such a layer often leaves much to be desired, as the delicate nanostructures can often collapse even under the effects of capillary forces. Figure 1.9 gives examples of more resilient nanotip structures on (a) silicon [54], and (b) fused silica [55], both fabricated using reactive ion etching. The geometry of these structures is inspired by the nipple-array structures first observed on the anti-reflective eyes of night-active moths [10]. Quasi-random silicon nanotips depicted in Figure 1.9 (a) were prepared using spontaneous self-masked etching using an electron cyclotron resonance plasma chamber with a silane (SiH_4), methane (CH_4), hydrogen (H_2) and argon (Ar) atmosphere. Total hemispherical reflectance was suppressed to values below 1 % over the entire visible wavelength region, and, for the longer 5.5 μm and 16 μm nanotip decorated substrates, throughout the near-infrared range [54]. Similarly, Figure 1.9 (b) shows an ordered array of fused silica nanotips, patterned using interference lithography and multi-step plasma etching in CHF_3, O_2 and HBr gasses [55]. This structure likewise exhibits significant suppression of reflectance over a broad range of incidence angles. In addition, nanotip array nanotextured surfaces exhibit other useful properties, such as hydrophobicity,

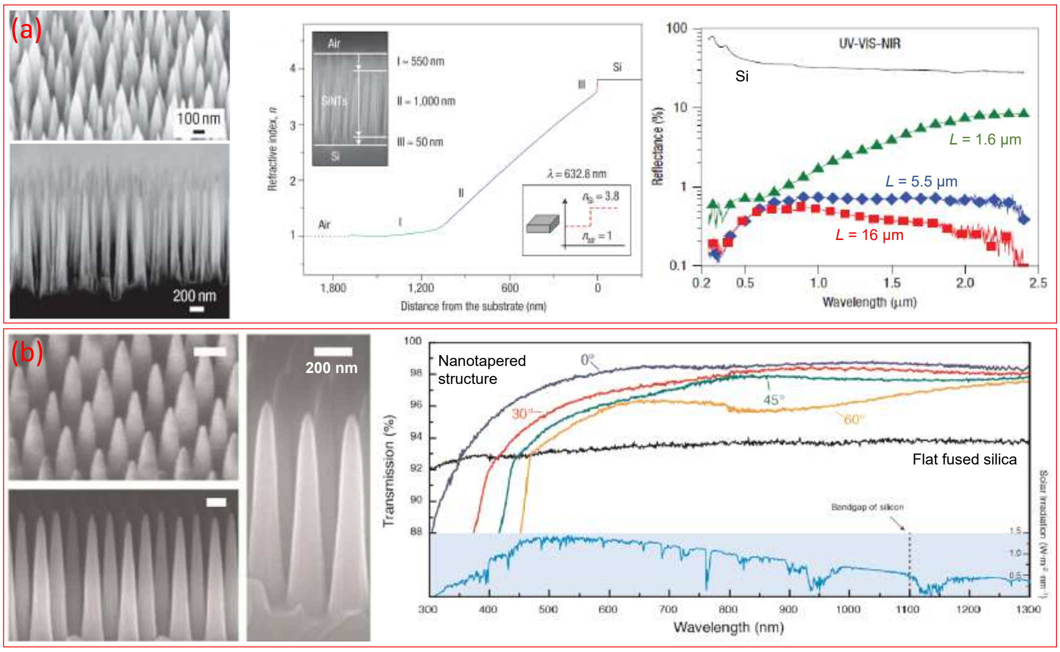

Figure 1.9: Plasma etched nanotip based gradient effective refractive index nanostructured surfaces reported in literature. (a) Scanning electron micrographs of silicon quasi-random nanotip decorated surface, estimated effective refractive index profile, as well as hemispherical reflectance spectra spanning ultraviolet to near-infrared regions for different spike heights [54]. (b) Lithographically defined fused silica nanotip decorated surface and its transmittance spectra at different light incidence angles [55].

anti-fogging [55] as well bactericidal activity [56]. Since nanotip spacing can be of similar order as the relevant wavelength, correlation length-dependent forward-scattering into the substrate propagation modes provides an additional light-trapping contribution, which will be discussed in more detail in the next section on resonant photon management approaches.

Gradient effective refractive index structures offer extremely high reflectance suppression, are not particularly sensitive to polarization, and can be made both omnidirectional and broadband. Furthermore, when graded layers are formed by etching the substrate, adhesion is not a significant issue. On the other hand, high aspect ratio porous or nanotextured surfaces can be quite fragile. Also, while impedance matching between air and substrate is an important issue, often further control over the propagation of coupled light is required. For such tasks deterministic scattering *via* grating or other resonant structures can be employed. However, adiabatic light coupling is a general principle, therefore gradient effective refractive index approaches for are often used to further augment other anti-reflectance methods.

1.1.4 Resonant anti-reflective structures

The anti-reflectance methods described up to this point rely on modifications of the surface layer along the direction of its normal, all of which are not in an essential way dependent on the lateral morphology used for their realization. This may be valid when both the size of constituent components as well as length-scales of any translational order in their arrangements are well below the wavelength of operation. Conversely, as the aforementioned parameters start to approach and exceed the wavelengths of incoming light, new scattering and interference

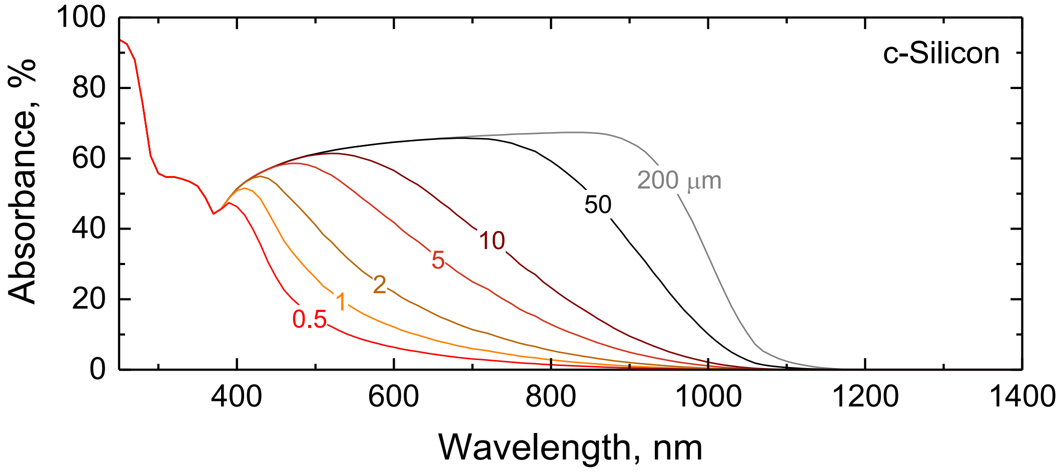

Figure 1.10: Numerically calculated absorbance ($A = 100\% - R - T$) spectra of different thickness planar crystalline silicon slabs assuming normal incidence. The indirect band gap of silicon gives rise to a small absorption coefficient throughout the visible spectrum, hence, hence total absorbance is strongly dependent on optical path length. Calculations were performed using silicon complex refractive index values reported in the literature [41].

effects come into play and in turn can be gainfully harnessed to control the propagation of light at dielectric interfaces.

Provided there is sufficient mode overlap, the optical excitation of a Mie resonance will result in preferential scattering into a high refractive index dielectric due to its higher local density of optical states [57]. This is one example of light trapping structures which can potentially exceed the ray optic limit, conceptually generalized in wave optics as the combination of a medium with maximum attainable local density of optical states and an appropriately matched incoupling mechanism [58]. Here the main focus will be on nanostructured surfaces, such as gratings, photonic crystals as well as periodic or quasi-random scatterers, all of which can offer anti-reflectance through efficient coupling of light [59].

In addition to providing a way to minimize inefficiencies related to reflective losses at interfaces, resonant nanotextured surfaces can also be harnessed to exert control over the refractive behavior of a dielectric boundary. An especially pertinent case for managing light propagation beyond the initial coupling into the bulk semiconductor arose as a result of the cost management related developments towards thin-film photovoltaics [60]. Beyond minimizing the requisite quantities of absorber materials, demands on their purity can likewise be relaxed in thin-film devices. This is because low recombination rates which give rise to minority carrier diffusion lengths in excess of active layer thicknesses provide only marginal performance benefits, hence materials remain viable at substantially higher dopant and defect density levels than would be possible for bulk devices [61, 62]. On the other hand, while carrier collection is more efficient at lower active layer thicknesses, photogeneration is rapidly diminished, particularly in the spectral region just above the band gap energy, as can be seen particularly for silicon in Figure 1.10. Therefore, various photon trapping schemes aimed at maximizing the cumulative light-matter interaction are indispensable in ensuring adequate efficiency of thin-film photovoltaic devices.

The most basic case in point of a resonant structure for efficient incoupling of light is the anti-reflection grating [59]. For instance, a planar 2D grating, shown in Figure 1.11 (a),

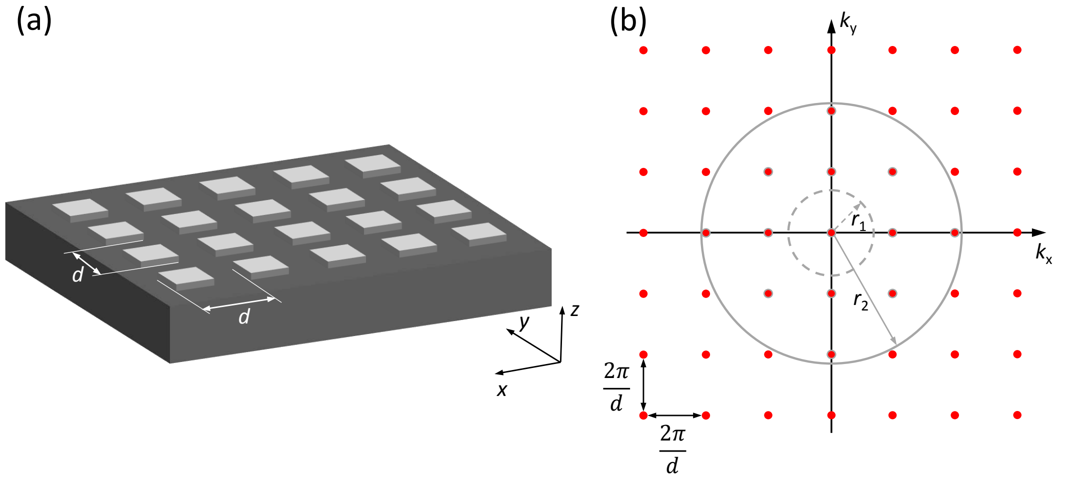

Figure 1.11: (a) Schematic representation of a hypothetical 2D grating with a period d. (b) k-space plot showing the diffraction modes allowed according to Equation 1.12. The reciprocal space radii $r_1 = 2\pi n_1/\lambda$ and $r_2 = 2\pi n_2/\lambda$ bound the possible propagating modes in surrounding medium and the substrate respectively. Here it is assumed that $d \leq \lambda$ and that the refractive indices $n_1 < n_2$.

exhibits periodicity which imposes interference-based constraints on possible directions for propagation of electromagnetic radiation. This results in the suppression of all plane waves, with the exception of those with wave vectors **k** that satisfy the familiar relationship:

$$\mathbf{k} = k_0 + \mathbf{G}_{m_1,m_2} = \mathbf{k}_0 + m_1\frac{2\pi}{d}\mathbf{x} + m_2\frac{2\pi}{d}\mathbf{y}, \tag{1.12}$$

where $\mathbf{k}_0$ is the in-plane wave vector component of incident light, $\mathbf{G}_{m_1,m_2}$ is the grating vector for diffraction orders m_1 and m_2, and d represents the grating period (both dimensions are assumed to have the same period for simplicity). The k vector values which satisfy Equation 1.12 are depicted in Figure 1.11 (b), were allowed diffraction modes are shown as red dots with equidistant $2\pi/d$ separation.

When grating periods are in the subwavelength region $d \ll \lambda$ all of the diffraction orders except the 0th are beyond the coupling range in both the substrate and the surrounding medium. This means that the grating can no longer substantially change the propagation direction of light and acts as an effective refractive index medium described in Section 1.1.3. On the other hand, when grating structures and their arrangement periods are large, $d > 100\lambda$, the total sum intensity of all he diffraction orders equals the transmittance and reflectance values given by the Fresnel Equations 1.1. Therefore, while large scale grating structures are not inherently anti-reflective, they can be used to redirect electromagnetic energy flow for light trapping purposes.

Resonant anti-reflectance can be achieved in the Bragg regime approximately when $2\pi/\lambda \leq 2\pi/d \leq 2\pi n/\lambda$, meaning that there is an asymmetry in accessible propagation modes with the incident light having multiple modes to couple to in the substrate (*i.e.* those inside the radius r_2), however, only a single 0th order mode in the surrounding environment. Thereby for a specific wavelength, angle of incidence and polarization state Fresnel reflections can be made to vanish almost completely [26]. This wavelength, polarization and incidence angle sensitivity represents the main drawback for such anti-reflective grating structures. However,

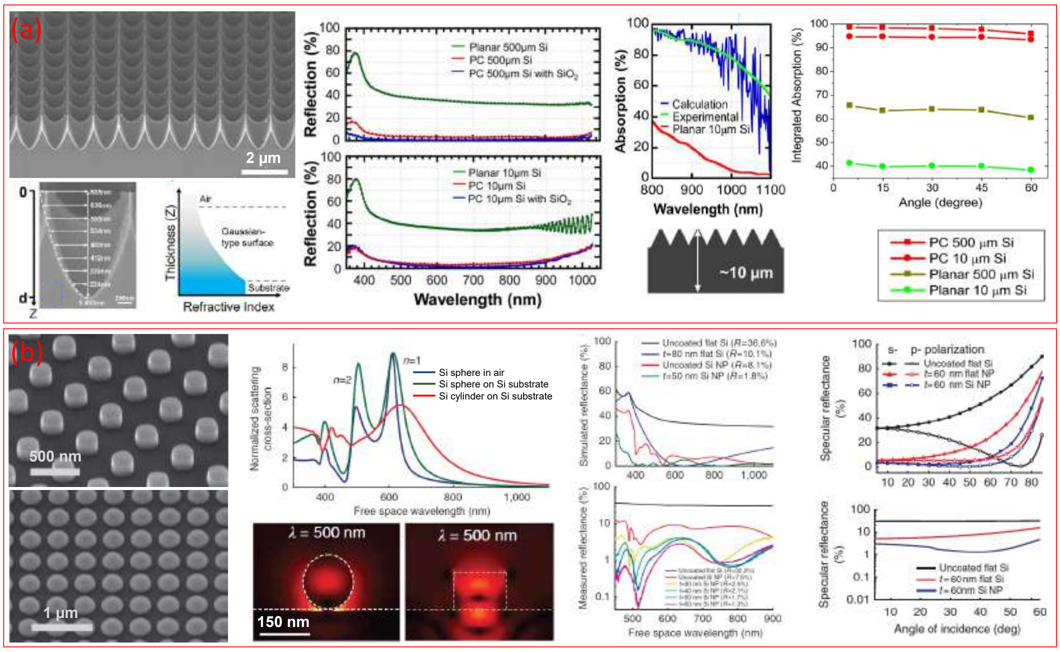

Figure 1.12: Resonant light trapping anti-reflective surfaces reported in literature. (a) Teepee-like photonic crystal absorber surface in Si [63]. Left panels show the scanning electron microscopy images of the structure, along with the effective refractive index profile. Reflectance spectra are provided for both thick 500 µm wafers as well as thin film 10 µm Si layers. Enhanced absorbance at the Si band gap edge is shown separately, and the cumulative absorption enhancement is maintained over a wide range of incidence angles. (b) Mie resonator array Si anti-reflecting surface [64]. Scanning electron images of the Si cylinder grating and a similar structure with a Si_3N_4 coating are given in left top and bottom panels, respectively. Scattering cross section spectral dependencies and field intensity profiles illustrate behavior of individual Mie resonators. Reflectance spectra are given for structures with and without Si_3N_4 anti-reflectance coatings. Rightmost panels show angular dependence of specular reflectance at $\lambda = 632$ nm wavelength.

their unique feature is that specific realizations of such gratings can be made to redirect incident light into diffraction orders that lie outside the escape cone of the substrate, hence, achieving light trapping of vital importance for thin-film solar cells among other applications. Such periodic structures for light capture and confinement can be fabricated on both front and back surfaces of a planar device for a substantial photogeneration rate enhancement [65, 66].

A highly refined photolithographic realization of an anti-reflective grating tailored for ultra-thin Si solar absorber is the teepee-like photonic crystal [63], summarized in Figure 1.12 (a). The structure was designed to maximize solar spectrum absorbance in thin Si films, and particularly to provide a boost in the weakly absorbing $\lambda = 800 - 1000$ nm near-IR indirect band gap edge, by making use of the parallel-to-interface refraction phenomenon exhibited by the tailored photonic crystal for light trapping [67]. Parallel-to-interface refracted modes propagate almost parallel to the substrate-air interface in a vortex-like fashion, giving rise to anomalously long optical paths and propagation durations for 13 times enhanced absorbance to occur. Furthermore, reflectance throughout the entire visible-to-near-IR spectral range was suppressed down to an average $\sim 3.4\%$ by means of the Gaussian-type gradient effective index profile of the wedge-like lattice as well as an ultra thin 60 nm SiO_2 anti-reflectance coating. Overall, the teepee-like photonic crystal structure achieves an average $\sim 94.7\%$ absorbance over an $\lambda = 400 - 1000$ nm wavelength and $0 - 60^\circ$ incidence angle range in a 10 µm thickness silicon film [63].

Another related mechanism for enhancing light coupling makes use of optical resonances supported by nanoscale dielectric particles, wires or voids with field distributions that extend and overlap with guided modes in the bulk material [68]. Such structures can be readily created in almost arbitrary arrangements by a variety of lithography methods. Hence, an anti-reflective grating structure can be comprised of individual Mie resonators, thereby significantly augmenting the number of states available for light coupling. This type of Mie resonator array anti-reflective surface was created on crystalline Si [64] and is shown in Figure 1.12 (b). Here the Mie resonators were 250 nm diameter and 150 nm height cylinders, which exhibit scattering cross-sections more than 5 times in excess of their geometrical cross-sections. This geometrical shape was chosen due to its lossy nature, meaning that electromagnetic energy can be readily transferred into the substrate (*i.e.* is over-coupled), as is visible from the spectral breadth of scattering cross-section peaks and from the field intensity profiles depicted in Figure 1.12 (b). The reflectance spectra are dominated by the sharp dip at around $\lambda = 500$ nm, a characteristic of the particle array spacing, which is attributed to a Wood's anomaly due to grating effects [69]. The Mie resonance related spectral features are likewise imprinted into the reflectance spectra as dips in the $\lambda = 700 - 800$ nm range. Like most other high performance reflectance suppression structures the Mie resonator array made use of a complimentary Si_3N_4 anti-reflectance coating to further reduce the visible wavelength reflectance from 7.5% of the optimized nanoparticle array down to an average value of 1.3%. Furthermore, $< 5\%$ specular reflectance values are maintained over a $0 - 60^\circ$ incidence angle range. Overall, while this specific example does not provide exceptional anti-reflectivity, it is highly integrated, robust and compatible with a wide array of materials and device geometries in addition to being scalable to large fabrication areas.

One of the main challenges in creating commercially viable high efficiency anti-reflective surfaces are the associated fabrication costs, which can be substantial when well defined resonant structures with rigorous translational symmetry need to be produced. Therefore, there is substantial interest nanotextured surfaces which exhibit deterministic and high performance anti-reflective and light trapping properties whilst either not requiring high precision fabrication methods or being robust against manufacturing imperfections. Conventional understanding states that periodic photonic light trapping structures should outperform their disordered counterparts, as they avoid deleterious scattering into lossy radiative modes. However, referring back to the simplest k-space example of a periodic 2D grating in Figure 1.11 (b) it is evident that only a very limited set of optical states, confined by the two light lines, serve to productively couple light into guided modes. Furthermore, their discrete nature underlies the often problematic wavelength, polarization as well as incidence angle sensitivity of reflectance suppression and light confinement. When a periodic structure posses a certain amount of disorder the individual resonances become broader and less pronounced, hence the overall performance turns more robust to properties of incident light at the cost of peak efficiency [70]. So, a small amount of disorder can be shown to slightly increase the local density of optical states as well as the coupling rate. On the other hand care must be taken, since too much disruption wipes out coherent modes and equalizes the rates of in- and out-coupling thereby negating any light trapping effects.

Ideally, a broadband, omnidirectional and polarization agnostic light coupling and trapping surface should posses a reasonably continuous Fourier spectrum which is matched to the avail-

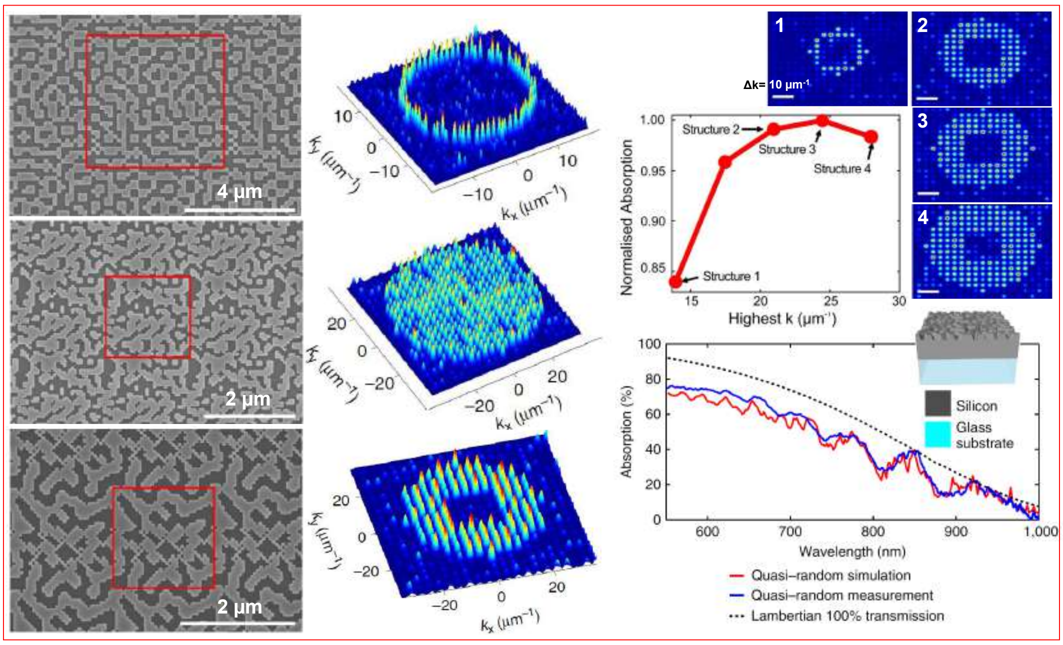

Figure 1.13: Quasi-random light coupling surfaces reported in literature [27, 71]. Left panels show scanning electron microscopy images of the 100 nm depth binary grating structures etched in Si along with their deterministic Fourier spectra. Unit cell of the structure is outlined in red. Top right panel shows simulated integrated absorbance dependence on the Fourier spectrum of the trapping surface. Bottom right panel shows comparison of experimentally measured and numerically calculated absorbance of a quasi-randomly patterned 1 µm thickness Si layer.

able guided modes corresponding to the wavelength in question. One class of nanotextured structures that allow for precisely such control of their k-space spectra are thin-film quasi-random coupling surfaces [27, 71], illustrated in Figure 1.13. Their patterns are devised by running an automated binary search algorithm against a desired distribution of Fourier spectral components and subsequently lithographically defined and reactive ion etched into thin-film silicon. Such structures have periods extending over several multiples of the operating wavelength, hence, allow for a broad range of deterministically placed Fourier components. Almost arbitrary k-space distributions are possible as can be seen in the left panels of Figure 1.13. However, for optical coupling and trapping spatial frequencies exhibited by the pattern should in a broad sense fall within the previously mentioned light line bounds for each of the relevant wavelengths:

$$\frac{2\pi}{\lambda} \leq k_{\parallel} \leq \frac{2\pi n}{\lambda}, \tag{1.13}$$

or, more precisely, they must match the guided modes supported by the thin-film slab waveguide [71]. Broadening the spatial spectrum beyond the optimum can be detrimental, since every additional Fourier component serves to slightly reduce the diffraction efficiency of all the others, potentially resulting in an overall decrease in performance (as can be seen in the top right panel in Figure 1.13). The design flexibility of this type of nanotextured surface makes it relevant for a multitude of optical in- and out-coupling applications. Furthermore, it is amenable for fabrication by means of nanoimprint lithography. Lastly it is an instructive model system for probing influence of structural randomness in photonic devices.

For example, different varieties of the bottom-up reactive ion etched nanotip-based gradient effective index black silicon surfaces (one example is given in Figure 1.9 (a)) exhibit slightly different light confinement properties, which in part can be explained by topology related disparities in their Fourier spectra. This in turn is linked to the correlation length separating individual structural features [72]. However, unlike in the nearly 2D case of quasi-random coupling surfaces, analysis of mode coupling *via* 3D black silicon textures have to also take into consideration different propagation lengths along the nanotips and the resulting variations in scattering probability.

The light coupling and trapping methods that rely on resonant effects or mode engineering tailored for thin-film applications are frequently benchmarked against well established, far less technologically demanding, but often no less efficient random scattering textures. While such statistical ray trapping structures are not suitable for applications involving thin-films, they afford comparatively cost-effective reflectance suppression and light trapping performance when applied onto wafer substrates above 50 µm thickness.

1.1.5 Textured ray trapping surfaces

All methods of reflectance suppression outlined hitherto rely on surface textures with features that in size do not markedly exceed, and are often far below, the wavelength in at least one dimension. As a result such surfaces require a wave-optics-based treatment to adequately describe their operation. However, microscale textures operating well within the ray optics regime can also be made to exhibit light trapping by harnessing Fresnel reflections instead of suppressing them. This can be done through a combination of maximizing the number of bounces a reflected incident light ray undergoes before escaping, and through forcing refracted light to propagate at angles outside the loss cone of the material. While not the most high performing of solutions, textured ray trapping surfaces can be fabricated with relative ease, can be combined to boost performance of other anti-reflectance mechanisms, and, since they are not reliant on wavelength-scale effects, are inherently broadband. Two major types of ray trapping schemes, namely random statistical (Figure 1.14 (a)) and regular geometric (Figure 1.14 (b)), are applicable to microtextured reflectance suppression surfaces, therefore, warrant some discussion.

Statistical ray trapping represents an important principle, which is generally applicable to all surfaces that exhibit some degree of randomness in the way they refract or scatter light [73]. It relies on the density of states in a given optical medium being proportional to its electric susceptibility, *i.e.* to n^2, and some randomization mechanism to ensure their equal occupancy. In this scheme, ideally, propagation of any ray coupled into the substrate should immediately loose all correlation with its initial angle of external incidence. Therefore, a Lambertian scattering surface is most well suited for statistical ray trapping. However, even when the texture is relatively ordered and randomization does not occur at first refraction, it can subsequently come into play during the multiple internal reflections or as a result of averaging over both the surface area and the angle of incidence. So, in most realistic ray optics situations there exists a strong bias towards angular randomization of light propagation [73].

The main result of statistical ray trapping [73] can be obtained considering a perfect randomizing surface subjected to I_{inc} incident radiation power per unit area dA, directed at an angle φ to its surface normal, as sketched in Figure 1.15. Conversely, it is assumed that this randomizing surface produces a uniform and isotropic internal brightness per solid angle of B within the substrate. Of course, at oblique incidence angles θ, internal intensity on the area

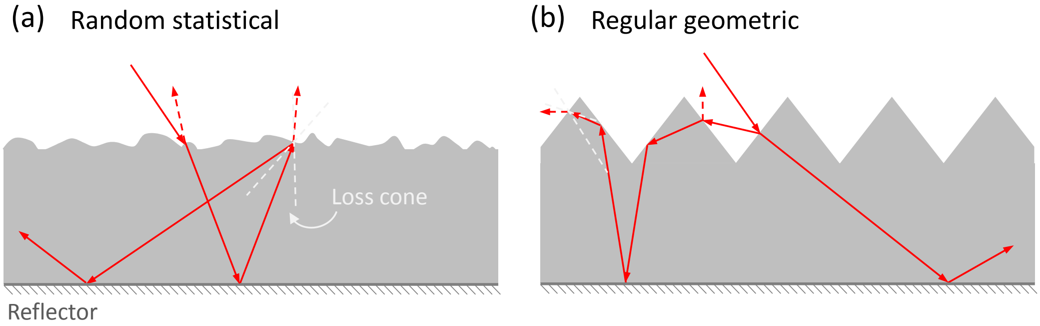

Figure 1.14: Examples of light trapping methods in the ray optics limit. (a) A textured surface which randomizes the propagation directions of refracted light. (b) A deterministically patterned surface which traps light through maximizing the number of bounces rays undergo during reflection and controlling propagation within the substrate to ensure total internal reflection outside the escape cone. In both cases mirrored back-sides serves to double the effective optical path.

element dA will be reduced to $B\cos\theta$. Furthermore, bottom substrate surface is assumed to be perfectly reflective, hence, ruling out transmittance losses through it and effectively doubling the total internal intensity I_{int} expressed as:

$$I_{int} = 2\times 2\pi \int_0^{\pi/2} B\cos\theta\sin\theta d\theta = 2\pi B. \tag{1.14}$$

Total internal reflection precludes the out-coupling of rays which fall outside the narrow loss cone defined by the critical angle $\theta_c = \arcsin(n^{-1})$, therefore only intensity I_{esc}, which amounts to merely a fraction of the total I_{int}, can escape:

$$I_{esc} = 2\pi \int_0^{\theta_c} T_{esc}(\theta)B\cos\theta\sin\theta d\theta = I_{int}\frac{\bar{T}_{esc}}{n^2}, \tag{1.15}$$

where the angle-dependent out-coupling transmittance factor $T_{esc}(\theta)$ was substituted to the weighted-average out-coupling transmittance factor $\bar{T}_{esc}$. Under equilibrium conditions this escaping radiation must be continuously replenished by light incident on the substrate as a

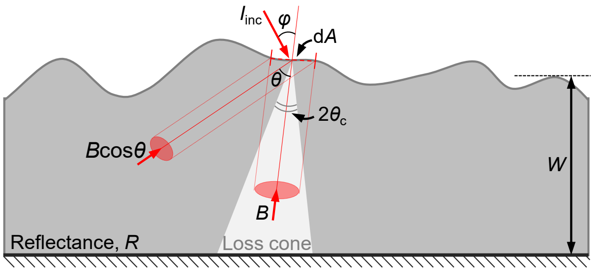

Figure 1.15: Sketch outlining the notations used in the derivation of the Yablonovitch limit of statistical ray optics [73, 74]. According to the principle of detailed balance out-coupled radiation has to be replenished by in-coupled light.

result of the principle of detailed balance:

$$T_{inc}(\varphi)I_{inc} = I_{int}\frac{\bar{T}_{esc}}{n^2} \quad \longrightarrow \quad I_{int} = 2n^2 \times \frac{T_{inc}(\varphi)}{\bar{T}_{esc}} \times I_{inc}. \tag{1.16}$$

Here $T_{inc}(\varphi)$ is the transmittance factor into the substrate, and in most cases time-reversal symmetry ensures that $T_{inc}(\varphi)/\bar{T}_{esc} \simeq 1$, with the exception of certain angularly selective light trapping geometries. Equation 1.16 illustrates the first key result of statistical ray optics - that, in the presence of a perfect scattering surface and a lossless rear reflector, light intensity in a substrate will be enhanced by a factor of $2n^2$. Conversely, in the worst case scenario of a perfectly transmitting rear surface, the internal intensity enhancement factor would be reduced to n^2.

One further effect resulting from randomization of light propagation is the increase in the average optical path. As can be seen in Figure 1.15, a ray propagating through the substrate at an oblique angle θ would be expected to traverse a distance of $W/\cos\theta$, where W is the average substrate thickness. Therefore, the average path length can be expressed as [74]:

$$\int_0^{\pi/2} (W/\cos\theta)\cos\theta\sin\theta d\theta \bigg/ \int_0^{\pi/2} \cos\theta\sin\theta d\theta = 2W. \tag{1.17}$$

Taken in aggregate the results of intensity and optical path enhancement give rise to an overall absorbance enhancement ranging from $4n^2$ to $2n^2$ (with and without a rear reflector respectively) in the presence of a random scattering texture. This enhancement is commonly referred to as the Lambertian or Yablonovitch limit [73]. The result is valid when substrates are fairly thick, preferably $W \gg \lambda/2n$, so that the optical mode density can be considered continuous. Applicability of the concept becomes limited for thin-film structures that have to be treated using wave optics. In such a case new methods of light confinement become possible [75], as noted in Section 1.1.4.

Some of the earliest realizations of a randomizing textured surface operating in the ray optics limit involved alkaline or acidic wet-etching of silicon [76]. Monocrystalline Si is etched preferentially along the $\langle 100 \rangle$ orientation, leaving behind square-based pyramids roughly 10 μm in height, delimited by (111) crystallographic planes. Some of the more widely used etching agents are KOH and NaOH [74, 77], and, in cases were metal contamination needs to be avoided, tetramethylammonium hydroxide (TMAH) [78] with iso-2-propyl alcohol added as a complexing agent in most cases. A typical random microscale pyramid textured Si surface along with representative reflectance spectra is shown in Figure 1.16 (a). Reflectance suppression exhibited by micro-pyramidal textures on silicon surfaces is fairly minor, as reflectance values generally remain within the 10% to 20% range. However, the requisite SiN passivation layer can provide an additional anti-reflectance mechanism, which yields below 3% averaged reflectance in the visible-to-near-IR spectral range through the use of two fairly affordable and scalable techniques [78].

A slightly superior light trapping geometry is the inverted pyramid structure that can be obtained by means of alkaline etching through a lithographically defined mask [79]. Likewise, random arrangements of inverted pyramids can be created using a maskless metal assisted etching process [80], which was shown to have superior anti-reflectance to similar arrangements of convex pyramids, as outlined in Figure 1.16 (b). Differences in light trapping performance between different textures operating in the geometric optics limit have been elucidated through ray tracing simulations [81]. Thereby it was shown that randomly arranged pyramid textures tend to outperform their regular counterparts [74]. Since random textures can

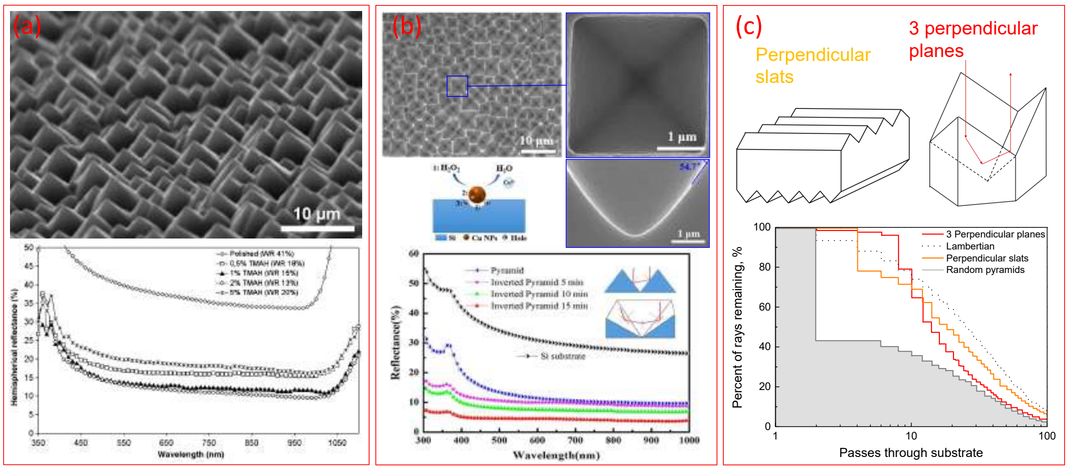

Figure 1.16: Textured ray trapping surfaces reported in literature [74, 78, 80, 81]. (a) Random microscale pyramid texture prepared by means of wet chemical etching in an aqueous TMAH solution with iso-2-propyl alcohol as a complexing agent [78]. Hemispherical reflectance between 10% to 20% was achieved in the visible spectral region. (b) Random inverted pyramid surface prepared by Cu nanoparticle-catalyzed etching in a HF/H_2O_2/H_2O etching bath [80]. Reflectance suppression of a concave pyramid texture was shown to surpass that of a convex pyramid surface. (c) Proposed examples of deterministic light trapping geometries, namely, perpendicular slats [74] and three perpendicular planes [81]. Simulated ray retention histograms show the expected light trapping performance benchmarked against a random pyramid texture and a Lambertian scatterer.

be treated as a weighted average of possible regular geometric layouts, their high performance implies the existence of certain deterministic arrangements which are better still.

In contrast to random statistical surfaces, regular geometric ray trapping structures are devised through rigorous ray tracing simulations which seek to maximize the optical path within a substrate. Two examples are the "perpendicular slat", and the "three perpendicular plane" arrangements sketched in Figure 1.16 (c), along with histograms of the percentage of incident rays remaining trapped as the number of passes through substrates increase [74, 81]. The perpendicular slat geometry relies on the double bounce of light on the top surface to cut down on losses upon initial reflection [74]. Furthermore, the orthogonal internal reflection at the opposite grating helps prevent rays from escaping the substrate after the first internal reflection through a slat face opposite to the one light was coupled through, which is so detrimental to the performance of pyramidal textures.

The three perpendicular plane geometry is a further improvement as it ensures three light bonces at the front surface. Furthermore, the planes are positioned favorably for total internal reflection to occur and only requires the texturing of a single substrate face. While light trapping performance of regular geometric textures can, for several initial passes, exceed the Yablonovitch limit, fabrication difficulties and costs prevented their wider adoption. Particularly, since much more simple pyramid-based structures when combined with a Lambertian back-reflector can match or even exceed their performance [81].

Although geometrical ray trapping methods can offer only modest reflectance suppression in the 10% range and the difficulty of their fabrication can vary widely, they are inherently broadband and readily compatible with other aforementioned anti-reflectance methods.

1.2 Fabrication and properties of black silicon

The term black silicon encompasses a wide range of different nanoscale surface textures that all share a dark appearance owing to their exceptional anti-reflectance exhibited throughout the visible spectral range [82]. In addition to the evident photon harvesting enhancement applications in solar cells [9, 52, 72] and photodetectors [83, 84], black silicon finds wide-ranging uses in fields as disparate as photoelectrochemical water splitting [85], surface-enhanced spectroscopy [86, 87], lithium-ion battery anodes [88], drug delivery [89–91], water repelling [92] and bactericidal surfaces [56], as well as biocompatible functional materials for implants [93]. Fabrication methods for black silicon are also numerous, with electrochemical etching [45, 94], metal-assisted chemical etching [50, 95], reactive ion etching [54, 96–98] and laser nanostructuring [99, 100] being the most prevalent examples, most of which possess a high degree of affordability, process parallelism and scalability.

This work is aimed at both experimental and numerical investigation of photonic effects exhibited by black silicon, and in particular how nanoscale morphology relates to light-matter interaction and anti-reflectance. Methods of controlling the reflectance suppression bandwidth are given particular attention. Reactive ion etching was used for preparing the black silicon surfaces for the vast majority of experiments described herein. Similarly, finite-difference time-domain simulations were the primary method of probing the relationship between geometrical properties and optical performance. As an initial point of reference, a description of the fabrication protocol, characterization results and numerical simulation findings of basic planar black silicon is outlined next.

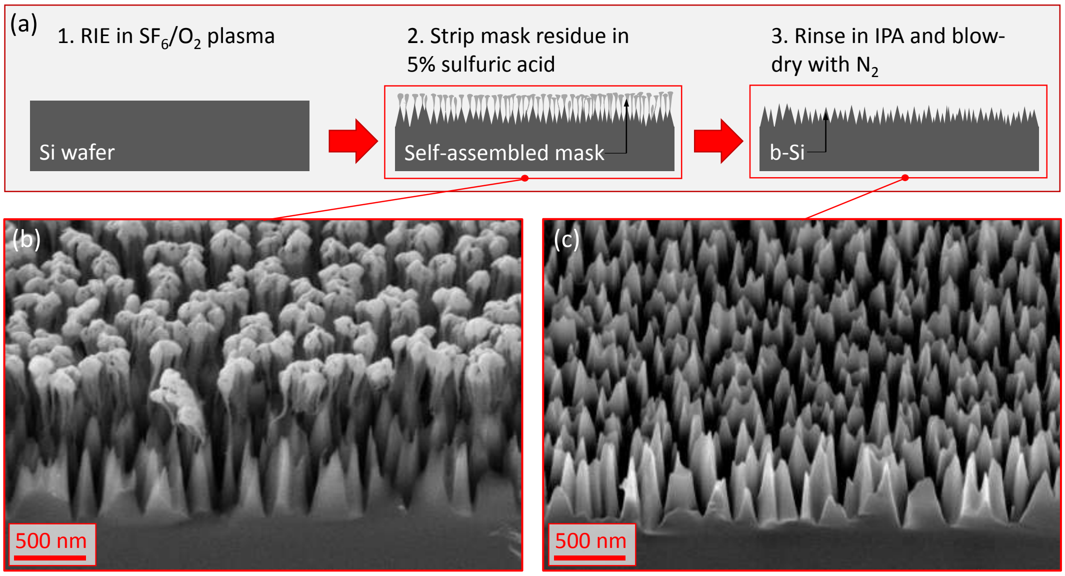

Figure 1.17: Fabrication process of black silicon used in this work. (a) Sketch outlining the main fabrication steps, namely, reactive ion etching in a SF_6/O_2 gas mixture plasma and chemical cleaning in dilute sulfuric acid to strip residues of the self-organized mask. Isometric view scanning electron microscopy images of (b) black silicon spikes immediately after 15 minutes of reactive ion etching and (c) final result after chemical cleaning and removal of the residual mask.

1.2.1 Reactive ion etching of silicon

Creation of black silicon during reactive ion etching is a spontaneous mask-free process which, despite being random, produces arrays of densely packed subwavelength scale spikes with a high degree of uniformity and reproducibility. This method has numerous advantages, such as etching not being dependent on the crystallographic orientation or doping of the substrate, morphology of the resultant surface being controllable through adjustments to process parameters, as well as its inherent compatibility with conventional micro-fabrication methods. Reactive ion etching is predominantly used for directional lithographic pattern transfer in microelectronic and micro-photonic fabrication, where black silicon (also called "grass") appears as a result of sub-optimal process conditions [97]. Chef drawbacks of this nanotexturing method are its limited scalability due to the need to use vacuum equipment, as well as substantial surface damage of the substrate as a result of ion bombardment, which often necessitates remedial etching or annealing steps [82].

In this back silicon fabrication process, reactive gasses are activated in a low pressure radio frequency plasma chamber, impinge onto a Si substrate end erode it, creating both volatile and nonvolatile reaction products. Explicitly, nanoscale spikes are created at conditions where a particular balance between chemical etching/physical sputtering and passivation *via* nonvolatile reaction products is maintained. Various different process conditions, applied using disparate halide-based plasma gas chemistry compositions, have been demonstrated to yield black silicon textured surfaces [82]. In large part this is due to differences between etching setups, like the types of electrode configurations and reactor geometries used. This particular work employed a SAMCO RIE-101iPH inductively coupled plasma reactive ion etching tool. The simple two step process is schematically outlined in Figure 1.17 (a). A gas mixture of SF_2/O_2 was injected at corresponding flow rates of 35/45 SCCM resulting in a reaction chamber pressure of 1 Pa. Inductively coupled plasma power was maintained at 150 W and the reactive ion etching bias power was set at 15 W.

Figure 1.17 (b) depicts a scanning electron microscopy image of the resultant black silicon surface immediately following the reactive ion plasma treatment. The nanoscale tips of individual pillars are decorated by plumes of residual self-masking material, which underlies their spontaneous formation. Plasma agitation causes the cracking of SF_6 and O_2 gas molecules and the creation of F^- and O^- radicals [97]. These, in turn, chemically react with silicon, where F^- gives rise to etching by creating volatile SiF_4, and O^- engages in a competing reaction that creates the nonvolatile, hence, passivating silicon-oxyfluoride ($SiF_y + xO^- \rightarrow SiO_xF_y$). On the other hand, the protective SiO_xF_y is concurrently removed either chemically, through reactions with SF_x which give rise to the volatile SO_xF_y, or through physical ion sputtering. The passivation layer is rapidly stripped from horizontal trench regions by direct ion bombardment, however on the pillar sidewalls it remains in large part protected from such erosion. The etch recipe used in this work allows the desorbed nonvolatile reaction products to precipitate from the gas phase onto residual islands of native SiO_2 or contaminant particulates incident from the reactor chamber, thereby spontaneously forming the aforementioned micromasking layer. This is indicative of the heating up of the Si substrate, as SiO_xF_y is known to desorb at elevated temperatures. The plume-like islands serve as a continually replenishing protective mask, forcing the reactive ion flux to etch interconnected trenches around them which give rise to spike-like features associated with black silicon [72].

Flowing the reactive ion treatment residual mask material was removed by wet-etching in a 5% aqueous sulfuric acid solution for 5 minutes. As can be seen in Figure 1.17 (c), exposure to diluted mineral acid fully removes the micromasking layer and has a negligible effect on

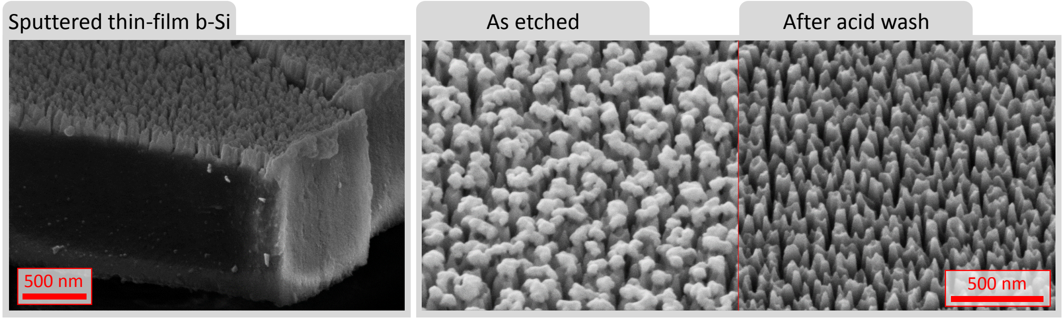

Figure 1.18: Cross-section view of flexible black silicon prepared by reactive ion etching a thin-film of Si is shown in the left panel. Silicon was deposited on a heat resistant kapton film using magnetron sputtering. Right panels show closeup scanning electron microscopy images of the black silicon immediately following dry etching as well as the final nanotextured surface after an acid cleaning step.

the morphology of the spikes. Furthermore, the entire cleaning process can be expedited by agitating the etching solution in an ultrasonic bath. Following the acid etch, nanotextured black silicon wafers are rinsed first in deionized water and then in iso-2-propyl alcohol. Lastly, the wafers are blow-dried using nitrogen gas. Overall, the present fabrication process was extraordinarily reproducible, however, considerations such as batch-to-batch variability can pose quite severe process optimization challenges when different reactive ion etching tools with correspondingly disparate etching recipes are employed [101].

As mentioned previously, reactive ion etching of black silicon has the advantage of performing equivalently for all crystallographic orientations of the substrate. This is equally applicable to the fabrication protocol used in this work. More importantly, it can be used to process amorphous silicon films, as shown in Figure 1.18. Here, 2 µm-thick layer of silicon was first deposited on flexible kapton films using radio frequency magnetron sputtering. Since kapton possesses strong heat and chemical resistance it can easily withstand both, reactive ion etching and the subsequent acid cleaning. The resultant flexible black silicon film exhibited a similar morphology to what was obtained for a crystalline substrate. Such composite materials can be used to create thin absorbers that can conformally overlay complex curved geometry surfaces.

In summary, creation of black silicon occurs when competing processes of etching by F^- are balanced by O^- radical induced passivation. Aspect ratio of resultant spikes can be slightly adjusted by varying the SF_6/O_2 ratio. A relative increase in the SF_6 flow rate enhances the chemical aspect of the process, decreases effects of passivation, and makes the etch profile more isotropic. Conversely, more O_2 increases the rate of passivation which blocks the chemical etching mechanism. Furthermore, oxygen at the same time enhances the DC self-bias of the substrate, which in turn provides stronger acceleration for incoming ions thereby making the etching more physical, hence, anisotropic [97]. Therefore, an increase in oxygen flow rate is generally associated with an aspect ratio increase of the black silicon spikes, whereas SF_6 can have the opposite effect of under-etching the masking microstructures and making the texture more sparse and shallow. Apart from that, the main adjustable process parameter is etching time, which alters the scale of the nanotexture without changing the aspect ratio of individual spikes, as will be discussed in Section 1.3.

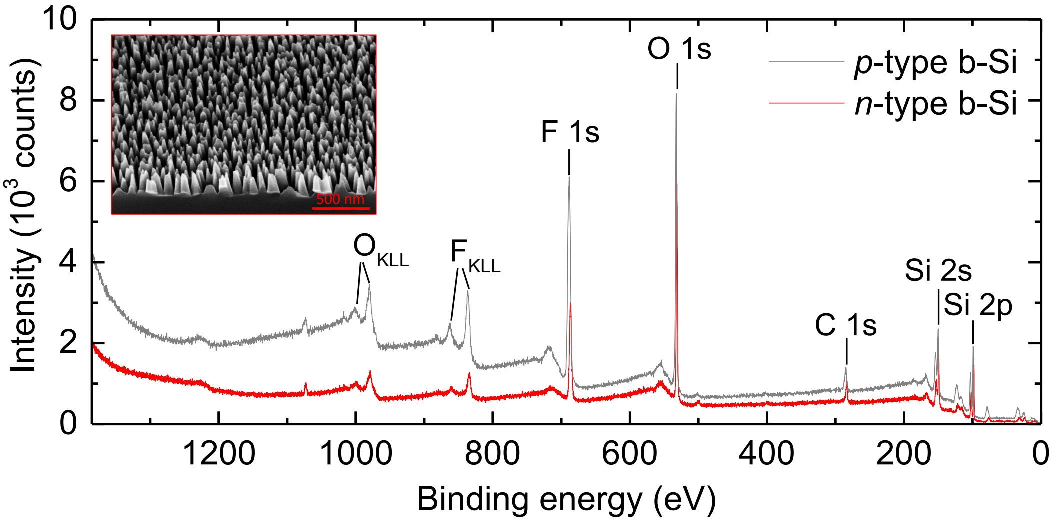

Figure 1.19: Wide-scan X-ray photoelectron spectra of black silicon surfaces prepared on p-type and n-type Si substrates. Etching process related oxygen and fluorine peaks are particularly prominent. Inset shows a scanning electron image of black silicon, tilted at a 45° angle.

1.2.2 Black silicon surface characterization

Probing the properties of fabricated black silicon involves determining the resultant chemical surface composition, investigating the anti-reflectance exhibited by the nanotexture, as well as visualizing its morphology and analyzing how it relates to overall performance.

Surface chemical characterization was performed using x-ray photoelectron spectroscopy at the Soft X-ray Spectroscopy beamline at the Australian synchrotron. The resultant photoelectron spectra for black silicon surfaces prepared on both boron-doped as well as phosphorus-doped silicon substrates are depicted in Figure 1.19. The main spectral components are associated with fluorine, oxygen and silicon, as well as a small contribution from adventitious carbon. The O 1s peak is centered at a binding energy of 532.5 eV, which is typically assigned to the Si–O_2 bond. Fluorine 1s peak is located at a binding energy of 688 eV, which was previously reported to be associated with the presence of SiO_xF_y depositions [102]. Lastly, the two Si 2p peaks can be assigned to Si–Si (99 eV) and Si–O/Si–F (103 eV) bonds. Despite the use of SF_6 no sulfur related spectral signatures have been detected. Hence, it can be concluded that, apart from a layer of native oxide, the black silicon surface has some residual SiO_xF_y compounds overlaying its texture. These compounds could potentially be removed by using more aggressive wet etch cleaning solutions.

Hemispherical UV-to-near-IR reflectance spectra of black silicon were measured using a LAMBDA 1050 spectrophotometer (Perkin-Elmer Inc.) equipped with a 150 mm integrating sphere attachment. Light is incident at an 8° angle to the sample surface normal, therefore specular reflectance could be excluded at will through a appropriately aligned port. Thereby specular and diffuse contributions to the total reflectance could be estimated separately. Figure 1.20 depicts the reflectance spectra of 500 microm-thick black silicon wafer, fabricated over 15 minutes of reactive ion etching, as well as that of an equivalent flat single side polished silicon wafer for reference.

As was the case for a silicon-air interface mentioned in Section 1.1.1, reflectance of

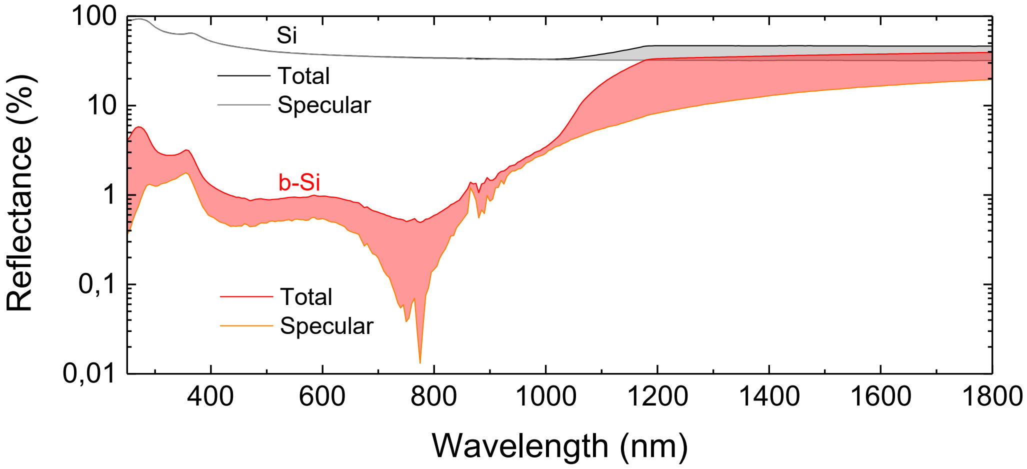

Figure 1.20: Reflectance spectra of Si wafers with and without a black silicon surface layer reactive ion etched for 15 minutes (200 nm average height of nanospikes). Total hemispherical and specular reflectance spectra are plotted separately. The shaded region corresponds to the intensity fraction reflected diffusely.

visible light from a single side polished Si wafer falls within the 35–55% range. At near-IR, where photon energy starts to fall short of the indirect band gap of silicon, reflectance is further increased by an additional 10% due to the diffuse reflectance contribution from the opposing wafer face. Nanotextured black silicon, on the other hand, exhibits a total hemispherical reflectance of 0.5–2% throughout the visible range. Most of the reflectance at visible wavelengths is diffuse in nature, since the specular portion is diminished particularly strongly by the anti-reflective texture and becomes almost undetectable at the onset of near-IR. Further towards the infrared spectral domain specular reflectance starts to gradually increase in a linear manner. This is similar to the anti-reflectance performance deterioration of gradient effective refractive index layers, discussed in Section 1.1.3, observed when wavelengths start to markedly exceed the film thickness in Figure 1.7 (b). The black silicon reflectance spectrum provided in Figure 1.20 corresponds to a texture where average spike height is around 200 nm, therefore it is unsurprising that performance would gradually diminish at near-IR. Of further note is that at wavelengths where Si becomes transparent, black silicon exhibits a sharp and broadband increase of diffuse reflectance from the unpolished back-surface, apparent in the flat wafer spectrum. However, there is an overall decrease in reflected radiation. Therefore, the nanotextured surface, in addition to reflectance suppression, exhibits a light trapping mechanism.

The tapered and densely packed black silicon spikes create a gradient effective refractive index layer and underlie much of the observed anti-reflectance. However, in addition to the shape of individual structures, their arrangement likewise plays an important role in reflectance suppression. A top-down view scanning electron microscopy image of black silicon is shown in Figure 1.21 (a). The spatial arrangement of spikes has a distinct affinity with the binary quasi-random light coupling surfaces [27, 71] described in Section 1.1.4 and depicted in Figure 1.13. The topology of a black silicon surface is aperiodic, however, the self-organized mechanism of its creation ensures that the distribution of relevant spatial parameters is narrow enough to correspond to a sufficiently well defined scattering behavior. On the other hand, the morphological variance, hence the span of available spatial frequencies, is sufficiently large,

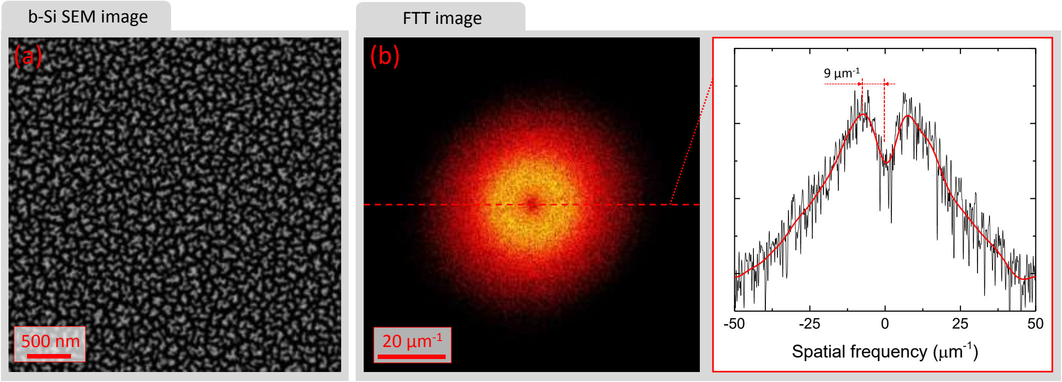

Figure 1.21: 2D spatial component analysis of black silicon with 200 nm average spike height. (a) Top-down scanning electron microscopy image of the nanoscale spike array. (b) Logarithmic scale spatial frequency spectrum of black silicon, obtained by performing a 2D fast Fourier transform of the image in panel (a). The rightmost panel shows a 1D cross-section of the Fourier spectrum.

so that broadband diffraction into quasi-guided modes is possible. Of course, a large number of spatial frequencies split the overall diffraction efficiency between themselves, therefore, for quasi-random light trapping structures there exists a trade-off between coupling efficiency and bandwidth.

The fast Fourier transform plot of a 200 nm spike-height black silicon surface image along with its horizontal cross-section is given in Figure 1.21 (b). The spatial frequencies form a prominently ring-like Fourier spectrum. These frequencies act as grating vectors mediating the coupling of light form air into the substrate. Therefore, according to Equation 1.13, to be effective at optoelectronically relevant Si absorbance wavelengths, the spatial Fourier spectrum of black silicon should roughly span from 5 μm^{-1} to 55 μm^{-1} [71]. Black silicon with 200 nm spike height exhibits strongest Fourier components in the range 4 μm^{-1} to 25 μm^{-1} and the peak spatial frequency is at 9 μm^{-1}. Incidentally, this range of spatial components are well matched to the red part of the visible spectrum, where the indirect band gap absorption in Si becomes weak. This also correlates with the strong suppression of specular reflectance at $\lambda \sim 780$ nm observed in Figure 1.20.

1.2.3 Numerical simulation for black silicon photonics

Farfield optical characterization nanotextures yields their cumulative properties most relevant for practical applicability. On the other hand, insights for predictive design of surface morphology obtained by such means can be sparse, especially when potentially relevant effects of the fabrication methods used, *i.e.* surface damage or chemical contamination, are not known. Numerical simulations represent an important complimentary method for investigating the performance and behavior of nanotextured surfaces arising solely as a result of their morphology. Furthermore, simulations can yield information on light-mater interactions at nanoscale structural features that is not readily obtainable by direct experimental methods.

In this work black silicon photonic properties were investigated using a commercially available finite-difference time-domain solver for Maxwell's equations "FDTD Solutions" (Lumerical Solutions Inc). This method is rigorous, inherently broadband and compatible with complex 3D topologies, therefore it is particularly well suited for simulating optical behavior

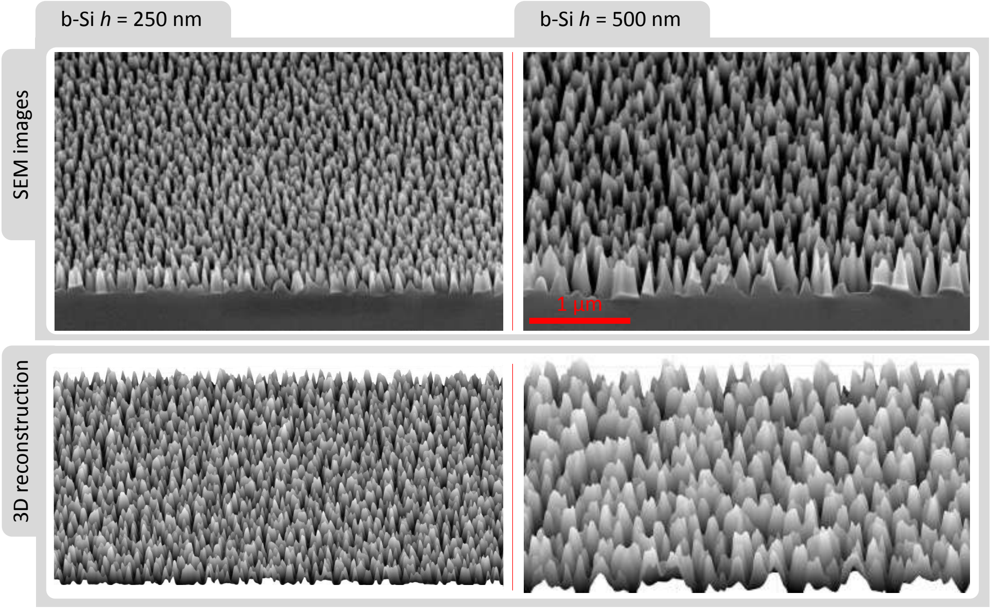

Figure 1.22: Isometric view comparisons between scanning electron microscopy images (top) and digital 3D models (bottom) of black silicon. Left and right panels respectively show results for black silicon with 250 nm and 500 nm average height spikes.

nanotextured surfaces. On the other hand, FDTD techniques are computationally demanding and were run on the SwinSTAR supercomputer at Swinburne University of Technology.

The first prerequisite for conducting numerical investigation of black silicon involved establishing an adequate 3D model of its surface geometry. The spikes which constitute a black silicon layer are prominently irregular in size, shape as well as arrangement. As a result such a surface cannot be easily modeled using a predefined set of rules and assumptions. Therefore, direct reconstruction from top-down scanning electron microscopy image data was used as the best method to create high-fidelity digital representations of 4×4 µm^2 black silicon surface area segments.

Isometric view comparisons between scanning electron micrographs and digital reconstructions of black silicon are shown in Figure 1.22. Here, high resolution top-down images acquired using a back-scattered electron detector were processed using a custom Matlab script. The grey-scale image pixel values approximately correspond to topological feature height, therefore, by rescaling those values to experimentally obtained spike heights a good first approximation of the texture can be obtained. Next step involves fine-tuning the tapered shape of spikes to be in close accordance with what was observed by electron microscopy. This was done by iteratively selecting and applying a set of Gaussian image filters.

As mentioned previously, due to the nanoscale dimensions of the black silicon spikes, a fairly fine discretization mesh has to be employed, with individual Yee cells being below $\lambda_{min}/(10 \cdot n)$ in size, where λ_{min} is the smallest wavelength used in a simulation. Furthermore, since black silicon is inherently disordered and irregular, a rather large surface area, at the very least bigger than the longest wavelength λ_{min}, needs to be modeled to get adequately representative behavior of a nanotexture. In the following simulations either periodic or perfectly matched layer boundary conditions and a broadband linearly polarized plane wave excitation source was used. Refractive index values for Si were obtained from the literature [103].

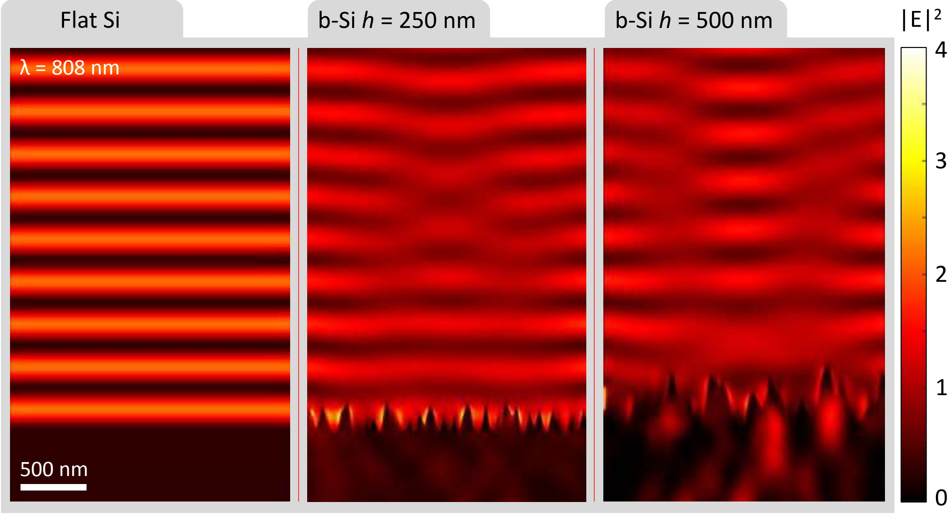

Figure 1.23: FDTD simulated electric field intensity profiles of $\lambda = 808$ nm light incident on black silicon surfaces with 250 nm and 500 nm average height spikes as well as on a flat silicon substrate for reference. Electric field intensity scale bar is the same for all of the panels.

A unique advantage afforded by solving Maxwell's equations using finite-difference time-domain methods is that electromagnetic fields can be visualized at each cell of a simulation. As a result nanoscale near field effects can be elucidated in ways that experimental methods are not easily capable of. Figure 1.23 gives examples of light-matter interaction with two different black silicon textures (introduced in Figure 1.22) as well as a flat Si substrate for reference. Here, simulation results corresponding to a $\lambda = 808$ nm excitation wavelength are shown, which corresponds to intermediate absorption in Si and therefore allows better visualization of in-coupled radiation.

The most noticeable effect that black silicon spikes exert on a plane wavefront is localization of electric field in trenches between the subwavelength features. Stronger light confinement is observed for the topology comprised of 250 nm spikes due to the presence of smaller and more numerous gaps. Electric field intensity enhancements up to a factor of 4 at the most active sites are predicted. These leaky Mie-like resonances are directly linked to the scattering behavior of the surface, with smaller inter-spike spacings providing larger k-vectors for coupling light into the substrate. Scattering behavior becomes evident when considering the intensity distribution of electromagnetic radiation propagating within the underlying Si substrate. In particular, light in-coupled *via* the 250 nm height nanotexture tends to propagate at higher angles with respect to the surface normal than its 500 nm height counterpart. Such behavior is, therefore, indicative of better light trapping performance, as it is closer to the Lambertian ideal. Lastly, the diminished overall intensity of electric fields present in the ambient medium above black silicon, as compared to flat Si, is characteristic of an anti-reflective surface and distortion of the coherent wavefront means that there is a substantive contribution of diffuse reflectance.

In the next section work on black silicon is presented in which near field localization of light in the immediate vicinity of the texture is used to enhance the laser trapping efficiency of microscale polystyrene beads. Numerical simulations in finite-difference time-domain proved particularly expedient in this case for identifying the operative mechanism underlying the phenomenon.

1.2.4 Optical trapping enhancement on black silicon

As was demonstrated in the pioneering works on optical manipulation [104, 105], tightly focused light beams can be used to establish gradient force traps for dielectric particles ranging in size from tens-of-microns down to the nanoscale. Such optical traps [106] have since been used to capture and manipulate objects as diverse as neutral atoms [107], cells [108], viruses and bacteria [109], metal nanoparticles [110] and quantum dots [111] just to name a select few [112].

In simple terms, optical trapping proceeds when a particle is polarized in an inhomogeneous electric field and experiences a force along the field gradient, which is of a magnitude sufficient to counterbalance the radiation pressure due to light scattering as well as fluctuations due to stochastic Brownian motion. However, since polarizability of a particle scales with its volume according to the Clausius-Mossotti relationship given in Equation 1.8, trapping of subwavelength particles can require prohibitively high beam intensities to establish a potential well deep enough to overwhelm disruptive Brownian motion. Furthermore, smaller particles experience diminished viscous drag that would otherwise assist in damping stochastic perturbations. Yet, most of the trapping objects relevant to nanotechnology fall squarely into this subwavelength range, therefore, numerous techniques have been devised to enhance trapping performance well below the diffraction limit [112].

One of the more prominent approaches involves the use of either lithographically defined [114–116] or quasi-random [117, 118] nanostructured plasmonic optical trapping substrates to concentrate incoming light into evanescent optical hot spots, unbeholden to conventional diffraction limitations. Nanoscale plasmonic modes enhance local field intensities and the associated gradients by up to 3 orders of magnitude, thereby allowing trapping to proceed at substantially lower incident laser intensities [116]. In addition, plasmonic structures can be engineered in a way that exploits their interaction with the trapping particle so as to create

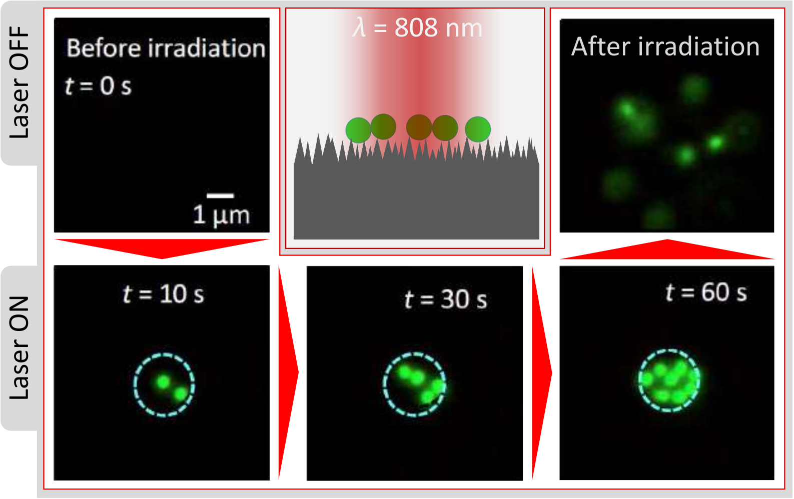

Figure 1.24: Fluorescence imaging micrographs of $d = 500$ nm diameter polystyrene beads, trapped on black silicon using continuous wave $\lambda = 808$ nm laser spot, outlined by the dashed line. The three lower panels illustrate the gradual accumulation of beads in the trapping region. Inset shows a cross section sketch of the trapping process [113]. Optical trapping experiments were performed at Osaka City University by the research group under supervision of Prof. Yasuyuki Tsuboi.

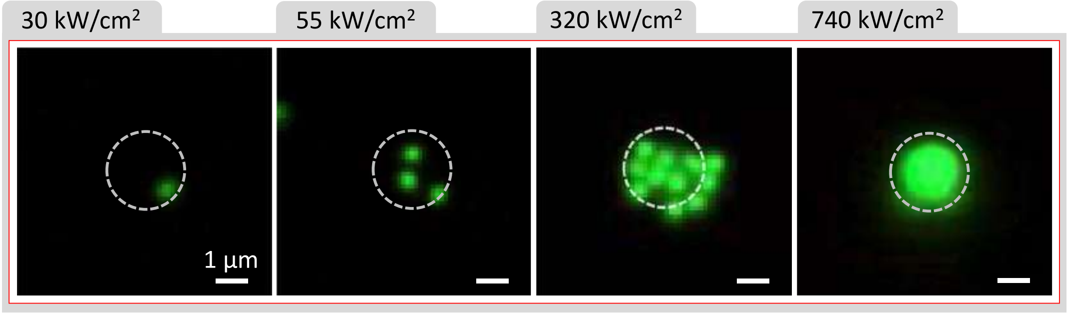

Figure 1.25: Laser intensity dependent trapping visualized *via* fluorescence imaging micrographs of $d = 500$ nm diameter polystyrene beads dispersed in water and trapped on black silicon using continuous wave $\lambda = 808$ nm laser spot, outlined by the dashed line [113]. Optical trapping experiments were performed at Osaka City University by the research group under supervision of Prof. Yasuyuki Tsuboi.

a real-time force feedback counteracting Brownian perturbations, known as self-induced back-action (SIBA) [119, 120].

In this work, conducted in collaboration with the research group headed by Prof. Yasuyuki Tsuboi at Osaka City University, black silicon was demonstrated to operate as an efficient metal-free optical trapping substrate [113]. The key advantage of this non-plasmonic approach is that it avoids most of the local heat generation issues that arise as a result of optical damping in metals [121]. While generally increases in temperature as a result of plasmonic effects are modest, they can give rise to significant thermal gradients on the order of $\nabla T \approx 1$ Kµm^{-1} [113]. Such thermal variance results in thermophoresis as well as convective flows that complicate the behavior of particles and reduce the trap stiffness so that it is effective only in a narrow range of incident laser intensities. A further advantage of metal-free black silicon is that its self-organized fabrication procedure is much simpler and scalable than the lithographic techniques required for the preparation of most plasmonic optical trapping surfaces.

Micrographs in Figure 1.24 outline the optical trapping temporal evolution of fluorescent $d = 500$ nm diameter polystyrene beads on 250 nm average spike height black silicon. The beads were suspended in an aqueous medium and, in this case, a continuous wave $\lambda = 808$ nm laser intensity of 320 kWcm^{-2} was maintained throughout the experiment. This value is significantly below the estimated intensity threshold of $I > 1000$ kWcm^{-2} for conventional optical trapping of particles at that size range [122]. As can be seen in the bottom panels of Figure 1.24, there is a steady increase in the number of polystyrene beads as they are sequentially captured on the laser illuminated 2D surface region 3 µm in diameter. After the laser was switched off the beads were released from the trap and rapidly dispersed by Brownian motion. When black silicon was substituted by either flat polished silicon or a silica glass substrate no appreciable optical trapping was observed at equivalent laser intensities.

Illumination intensity dependence of $d = 500$ nm diameter polystyrene bead trapping behavior on black silicon is illustrated in Figure 1.25. First beads are captured at the intensity threshold value of 30 kWcm^{-2}. As laser fluence is raised up to 740 kWcm^{-2} (which was the maximum output for the laser source used) the number of trapped polystyrene beads likewise increased, which indicates a deepening of the trapping potential. In this sense operation of the black silicon trapping surface is in sharp contrast to that exhibited by plasmonic structures, such as gold nanopyramidal-dimer arrays [122]. There, trapping intensity threshold values

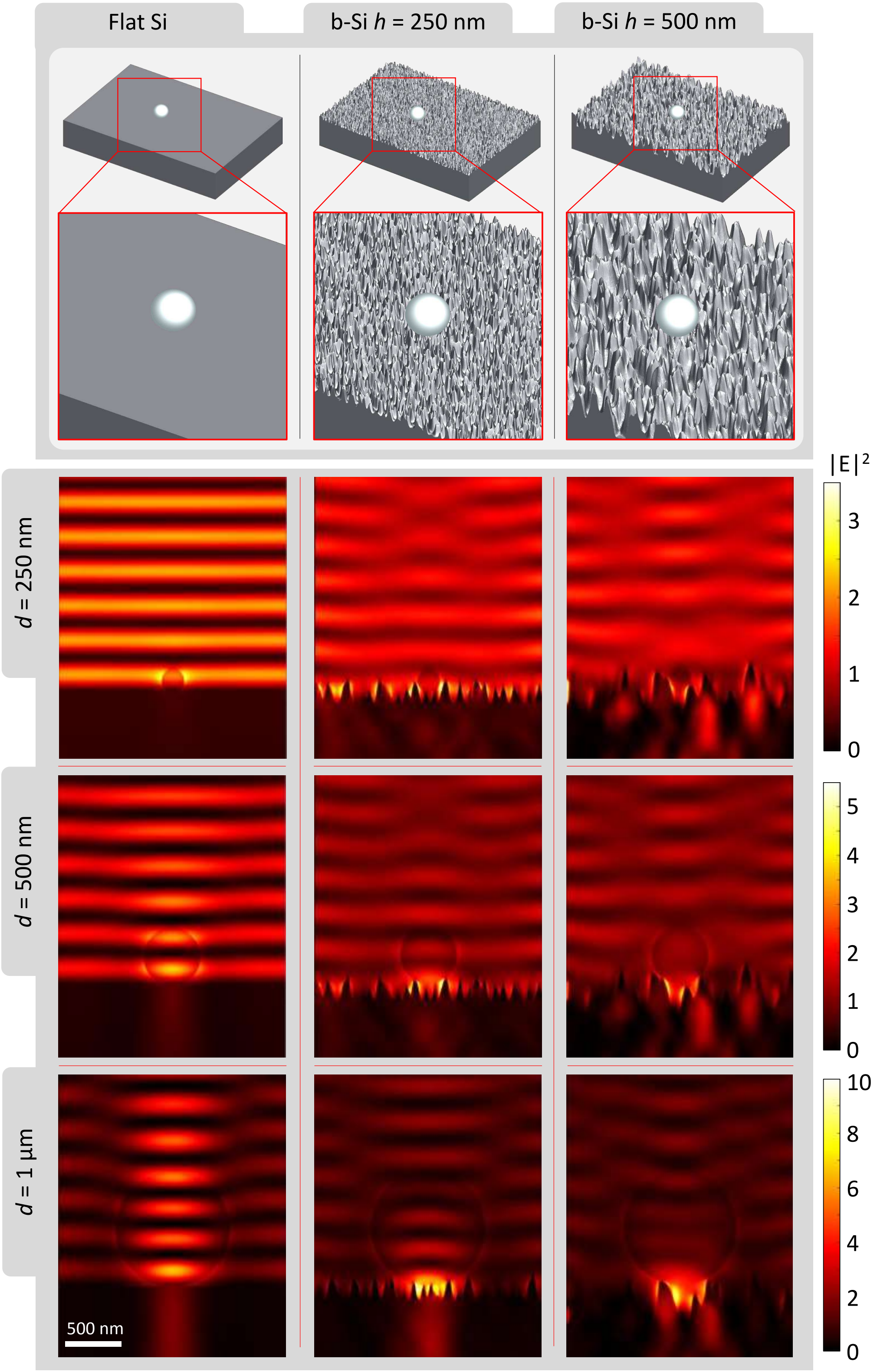

Figure 1.26: FDTD simulation results illustrating optical field intensity profiles around different diameter dielectric particles situated on black silicon surfaces with average spike heights of 250 nm and 500 nm, as well as flat polished silicon for reference. Top panels show 3D renderings of the simulation geometries used.

were significantly lower, at around $I = 1$ kWcm^{-2}, however, trap stability is already lost at $I \geq 5$ kWcm^{-2} as a result of thermal effects such as Marangoni convection and thermophoresis. Therefore, optical trapping substrates based on nanotextured black silicon surfaces fulfill a unique complimentary role in facilitating particle capture and binding at high irradiation powers with negligible thermal disturbance effects.

Further insights into the operational principle of optical trapping enhancement on black silicon can be gleamed from FDTD simulations. Figure 1.26 shows optical field intensity profile simulation results of a dielectric particle situated on black silicon surfaces with average spike heights of 250 nm and 500 nm, as well as flat polished silicon for reference. Substrate interactions with three different diameter particles, namely 250 nm, 500 nm and 1 µm, were tested. Ambient refractive index was chosen to match that of water ($n = 1.33$) and the simulation region was terminated using perfectly matched layer boundary conditions. Plane wave $\lambda = 808$ nm illumination in accordance with the experimental setup was assumed. This highly simplified simulation neglects to account for focusing, as well as nonlinear effects and the influence of aberrations - all of which can have a substantial influence on experimental trapping behavior. Despite this, numerical results uncover important qualitative features of light interaction with dielectric beads on black silicon.

The most obvious finding observable in Figure 1.26 is that the electric field intensity localized in the trenches between black silicon spikes (shown in Figure 1.23) is locally augmented by the prescience of a dielectric bead. Such pockets of enhanced intensity optical fields provide the gradient forces necessary to stably pin particles to black silicon surfaces. This interplay between the particle and the substrate is analogous to SIBA trapping enhancement observed on certain plasmonic structures [123]. Local field enhancement at the point-of-contact between black silicon and a particle becomes especially pronounced for larger beads that operate in the ray-optics regime and act as microscale ball lenses, as can be seen for the 1 µm diameter particle case. Nonetheless, the effect is appreciable even for beads 250 nm in diameter, well below the near-IR wavelength scale used for optical trapping. The field intensity enhancements on black silicon predicted by simulations generally do not exceed a factor of 10, roughly one or two orders of magnitude lower than would be typically observed in proximity of plasmonic structures [116], which accounts for the higher trapping threshold fluence observed experimentally.

Anti-reflectance of black silicon is likewise clearly demonstrated by way of light forward-scattered into the bulk material in Figure 1.26, especially in contrast to the flat polished silicon substrate case. Lower reflectance would be expected to contribute to a reduction of detrimental radiation pressure from the back-scattered wavefront. Overall, a fine texture of 250 nm average height silicon spikes appears to yield higher intensity hot-spots than the more coarse 500 nm height counterpart due to tighter electromagnetic confinement in smaller gaps. Of course, the contribution to trapping enhancement may not be entirely optical in nature, as, in addition to gradient field forces, pining of particles on the black silicon spikes may also contribute to damping of Brownian perturbations.

The aforementioned finding that trapping on black silicon proceeds regardless if a particle is subwavelength on the scale of individual spikes or if it is substantially larger presents an intriguing peculiarity. As can be seen in the $d = 250$ nm and $d = 500$ nm diameter sections of Figure 1.26, small particles are incapable of appreciably distorting the incident wavefront, hence, have to rely on mutual polarization effects in the proximity of Si spikes to produce enhanced optical field regions. Conversely, larger $d = 1$ µm beads introduce an additional focused light component that further boosts optical field intensity at the particle/black silicon interface.

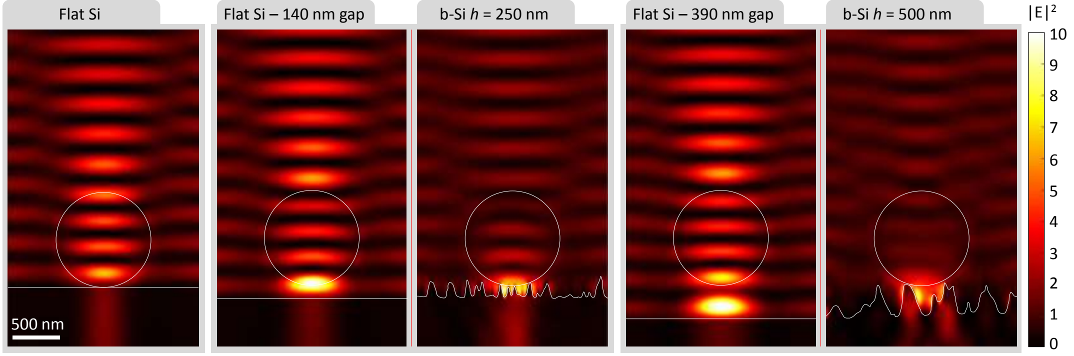

Figure 1.27: FDTD simulation results of a $d = 1$ µm diameter dielectric bead suspended in different configurations over flat polished as well as black silicon substrates under $\lambda = 808$ nm plane wave illumination. From left to right: bead in immediate contact with flat Si, bead suspended 140 nm above flat Si and at the same position in contact with 250 nm average height black silicon, bead suspended 390 nm above flat Si and at the same position in contact with 500 nm average height black silicon.

Simulation results outlined in Figure 1.27 aim to illustrate the optical field enhancement contribution arising as a consequence of focusing by the dielectric bead with dimensions at the onset of the geometrical optics regime. It is evident that in this case black silicon spikes act as a spacer of intermediate effective refractive index in which a high intensity focal spot, external to both the particle and the substrate, can be established. This high field intensity region polarizes both the substrate and the particle, thereby providing the gradient force necessary to induce trapping with properties akin to SIBA. Furthermore, black silicon aids in coupling light into the bulk substrate thereby substantially reducing repulsive radiation pressure due to reflected waves.

A standout property of black silicon when used as a surface for optical capture and manipulation of particles is the extraordinary stiffness of the attainable trapping potentials. Comparison between trapping behavior of fluorescent $d = 500$ nm polystyrene beads on a plasmonic gold nanopyramidal-dimer array substrate [122] and on 250 nm average height black silicon is given in Figure 1.28. As mentioned previously, plasmonic optical traps operate at low threshold laser fluences, however are also highly susceptible to heating related effects due to the lossy nature of metals at optical frequencies. Therefore, it is not surprising that substantial fluctuations of captured polystyrene beads are visible in the leftmost panel of Figure 1.28. This is indicative of the trapping force being able to override Brownian motion by only a slight margin. It was demonstrated that an irradiation fluence of $I = 5$ kWcm^{-2} on a plasmonic optical trapping substrate can produce local temperature increases on the order of 10 K, which gives rise to enormous temperature gradients [124]. As a result the binding electromagnetic gradient force is to a substantial extent canceled out, and even completely overridden at higher laser intensities, by the repulsive thermophoretic force.

Metal-free nanotextured black silicon requires approximately one order of magnitude higher irradiation powers to accomplish trapping than is typically necessary for metallic substrates due to lower attainable electromagnetic enhancement values close to dielectric structures. However, unlike its plasmonic counterpart, black silicon is not prone to heating when illuminated with $\lambda = 808$ nm radiation not strongly absorbed in Si. The estimated local temperature change ΔT, hence the thermal gradient ∇T, was approximately zero up to an

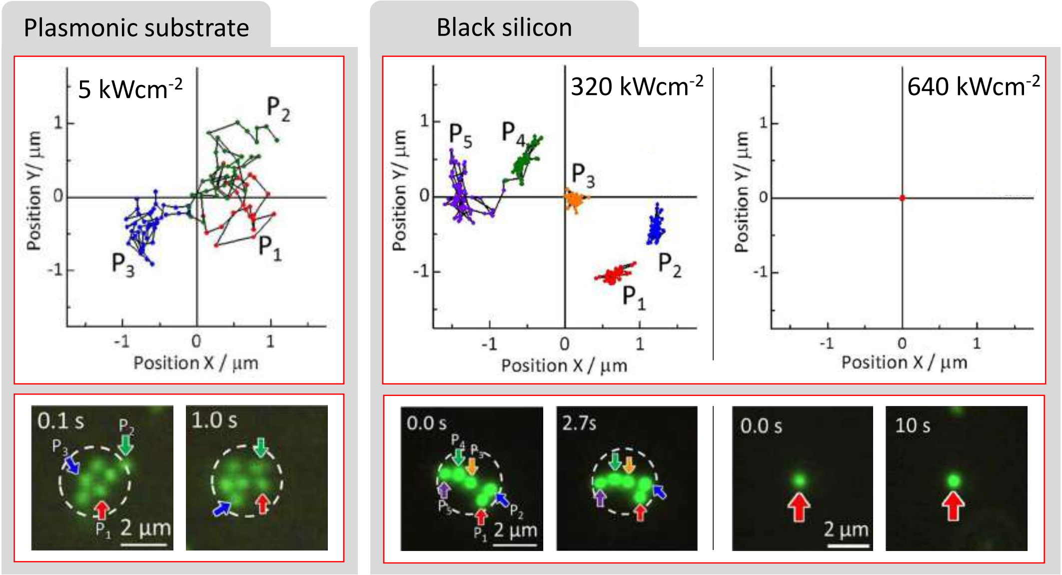

Figure 1.28: Trajectories of $d = 500$ nm diameter fluorescent polystyrene beads captured on a plasmonic substrate [122] as well as black silicon at laser fluence values corresponding to 2D ($I = 1$ kWcm^{-2}) and 1D ($I = 1$ kWcm^{-2}) trapping [113]. Positions were recorded at 33 ms increments. Micrographs in lower panels show the initial and final configurations of polystyrene beads for each experiment. Optical trapping work was performed at Osaka City University by the research group under supervision of Prof. Yasuyuki Tsuboi.

irradiation fluence of $I = 740$ kWcm^{-2} [113]. Therefore, as is evident from Figure 1.28, optical binding on black silicon is free from detrimental thermal effects and only becomes tighter with increasing irradiation fluence. 2D trapping of particles on black silicon at $I = 320$ kWcm^{-2} irradiation fluence is noticeably tighter than that observed on a gold nanopyramidal-dimer array substrate. Furthermore, as fluence further is scaled up to $I = 640$ kWcm^{-2}, polystyrene particles are effectively immobilized resulting in a 1D trapping situation.

To summarize in brief, black silicon substrates provide a new method for enhancing optical trapping through multiple light scattering and SIBA-like effects in an operation regime complimentary to most plasmonic approaches. While it exhibits weaker optical field gradients than metal based structures, black silicon is inherently broadband, performs tighter trapping due to absence of detrimental thermal gradients, and binding potentials scale up to high incident intensities thereby allowing switching between 2D and 1D trapping modes. In addition, single-step self-organized fabrication of black silicon is substantially more scalable and affordable than the vast majority of plasmonic substrates. Hence, black silicon is a promising platform for probing nonlinear effects in optical trapping.

Unlike in most solar energy harvesting applications, this new way of utilizing black silicon in optical trapping relies on operational wavelengths being close to or within the transparency window of Si. As in this case, numerous problems in sensing, broadband reflectance suppression and black body emission can benefit from nanotextures compatible with longer wavelength radiation. Therefore, the next section describes work aimed at extending the anti-reflective behavior of black silicon to the infrared spectral range.

1.3 Extending anti-reflectance to IR

The infrared spectral range is of extensive utility in fields as wide ranging as biomedical sensing, manufacturing process control, consumer grade optoelectronics, optical communications, astronomy, as well as numerous applications in defense [125]. As shown in Figure 1.10 silicon exhibits a modest degree of indirect band gap absorbance at the onset of near-IR, typically defined as spanning the 750 nm to 1.4 µm wavelength range. This IR spectral segment, in addition to a multitude of more esoteric uses, is widely exploited in optical communications, image intensifiers, and light detection and ranging (LIDAR) [126]. LIDAR in particular is experiencing burgeoning growth with the advent of machine vision, where boosting photon detection efficiency by way of reflectance suppression and light trapping translates in both more rapid and longer range mapping at the same eye-safe levels of IR laser radiation intensity [127].

At the lower frequency short-wavelength IR and mid-IR ranges, silicon exhibits only minor doping-dependent free carrier absorbance [128], hence, can only function as a passive optical element. Nevertheless, numerous free-space applications for these types of radiation exist and can benefit from minimizing reflective losses. For instance, short-wavelength IR is used for covert illumination and night vision purposes, whereas mid-IR coincides with the atmospheric window for remote sensing the vibrational spectra of various molecular species [129] and also where most thermally guided infrared homing solutions operate.

In this section work which aims to extend the anti-reflectance of black silicon towards the infrared spectral range is presented. First, the effects of the scale of nanotextured surface morphology on the optical behavior of black silicon are investigated. Further enhancements in anti-reflective bandwidth were attained using a two-step hierarchical texturing processes, and the resulting black silicon was investigated both experimentally and numerically.

1.3.1 Relationship between morphology and optical properties of black silicon

In addition to anti-reflectance, surface morphology of black silicon gives rise to a multitude of disparate properties, such as hydrophobicity [130, 131] and bactericidal behavior [56], absent in plain crystalline Si, thus hinting at their topology-related origin. Hence, considerable effort has been put in optimizing the black silicon morphology for applications that diverge widely from aforementioned radiation harvesting enhancement primarily discussed here. Works on tailoring black silicon for uses in microfluidic systems [132], surface-enhanced Raman scattering [133] and mass spectroscopy [134] substrates represent only a few notable examples.

Investigations into the influence black silicon morphology exerts over its optical properties such as solar energy harvesting efficiency have been far more numerous, however, mainly focused on the crystalline Si absorbance region [72, 135, 136]. Texturing of silicon performed by different methods, like laser nanostructuring, electrochemical etching or reactive ion etching, can yield drastically distinct morphologies whilst exhibiting similar optical performance [82]. This in turn makes any general conclusions about mechanisms underlying black silicon anti-reflectance somewhat tenuous. Even when only considering reactive ion etching, the fabrication method used in this work, strong variations in resultant surfaces can be obtained when disparate process gas mixtures, pressures, substrate temperatures [135], plasma source powers, and also when different reactor models are used.

In this work, conducted in collaboration with the research group headed by Prof. Junko Morikawa at Tokyo Institute of Technology, the effect of Si texture scale on black silicon optical properties was investigated [137]. For this a reactive ion etching regime was set up so that larger silicon spikes could be created as the process duration was increased whilst preserving the self-affinity of all the resultant surfaces, *i.e.* maintaining approximately the same fill factor and aspect ratio values between different samples. As a result reflectance suppression and light trapping effects related to both texture depth and inter-spike spacing (often referred to as correlation length) could be probed. This investigation was an experimental extension of numerical work reported in the literature [135]. Thereby it was determined that the biggest influence of correlation length on black silicon reflectance is exerted at the near-to-mid-IR spectral bands.

Black silicon samples used in this work were prepared on single side polished (100) crystallographic orientation Si wafers using the reactive ion etching process described in Section 1.2.1. Select scanning electron microscope images of the resultant surface textures are displayed in Figure 1.29 (a). Since the etching was set up to operate in a stable over-passivation regime, with an abundant volume of spontaneous mask material (illustrated in Figure 1.17), only the process duration had to be changed to obtain structures at different scales. Initially, height of silicon spikes increases approximately linearly with etch time, as depth of trenches between the features became deeper and wider. The texture likewise turned appropriately sparser due to spontaneous removal of weakly adhering segments of the masking material. However, as can be inferred from Figure 1.29 (b), for etching durations in excess of 90 minutes the process becomes self-limiting. This is due to etching rates for trenches above 1.2 µm in depth being lower than erosion rates for the mask. Thereby a stable equilibrium is reached as a constant spike-height texture is transferred ever deeper into the wafer. After reactive ion etching residual mask material is stripped in a 5% aqueous sulfuric acid solution and blow-dried using nitrogen gas.

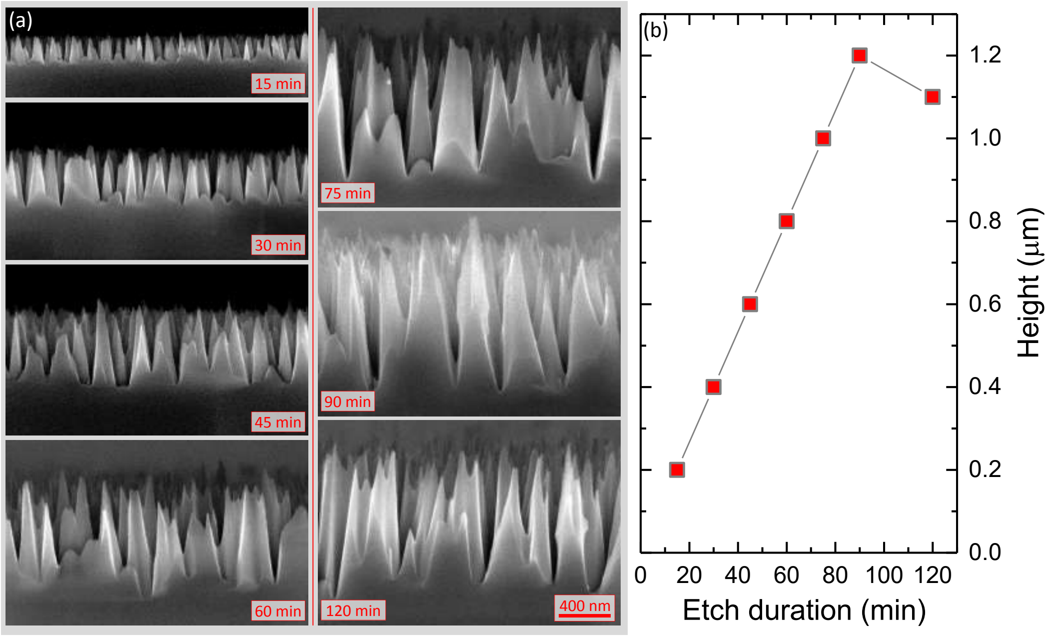

Figure 1.29: Black silicon surface textures prepared at varying size-scales. (a) Side-view scanning electron micrographs of black silicon after different reactive ion etch durations. Scale bar is the same for all images. (b) The average height of black silicon spikes plotted against the reactive ion etching duration.

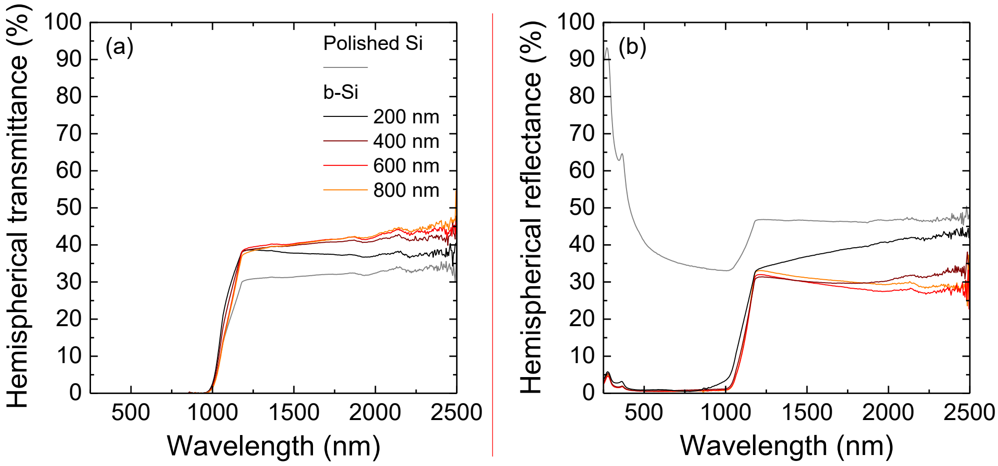

Figure 1.30: Total hemispherical UV-to-near-IR (a) transmittance and (b) reflectance spectra of black silicon with different texture scales, here distinguished by the average height of spikes. Samples were prepared on single side polished Si wafers, whose transmittance and reflectance spectra are also shown for reference.

Initial optical characterization of the different texture scale black silicon substrates was performed in a 150 mm integrating sphere using a LAMBDA 1050 UV/Vis/NIR spectrometer (Perkin-Elmer Inc.). In this hemispherical setup the total reflectance and transmittance values, encompassing both coherent and scattered radiation, can be determined. Transmittance spectra of black silicon samples with average spike heights ranging from 200 nm to 800 nm exhibit the same general behavior and are shown in Figure 1.30 (a). The 500 µm-thick substrate is opaque to radiation with energy in excess of the indirect band gap of Si, therefore no transmittance is observed up to $\lambda \approx 1000$ nm. In the near-IR, however, transmittance reaches 30% for untextured Si and above 40% for black silicon. Furthermore, surfaces textured with larger spikes tend to transmit a slightly higher fraction of energy than the 200 nm average height black silicon sample, especially at longer wavelengths.

Total hemispherical reflectance spectra of all black silicon samples under consideration are displayed in Figure 1.30 (b) and show that surface texturing reduces reflectance to levels below 1 % throughout the Si absorbance region. The 600 nm average spike height sample exhibited strongest and most consistent anti-reflectance among them. At wavelengths above $\lambda \approx 1000$ nm reflectance from the opposite unpolished wafer surface comes into play, hence, only a moderate 20% reduction in reflected radiation compared to untextured Si is observed. Again, the 200 nm average height black silicon sample provides the weakest reflectance suppression at near-IR among the textured surfaces, and approaches the value of flat Si when wavelengths are increased further. As the average spike height is increased reflectance suppression at near-IR tends to reach a limit of around 30%. Lastly, the simultaneous redshifts in both reflectance and transmittance spectral edges for black silicon with deeper texturing hint at an absorbance enhancing light trapping contribution.

Further information on the nature of light interaction with black silicon can be gleaned from the spectral dependence of specular and diffuse reflectance contributions, plotted separately in Figure 1.31. The diffusely reflected radiation portion could be measured by placing samples with their surface normal at a slight 8° angle to the incident light. In this geometry the specularly reflected part could be allowed to leave the integration sphere through an

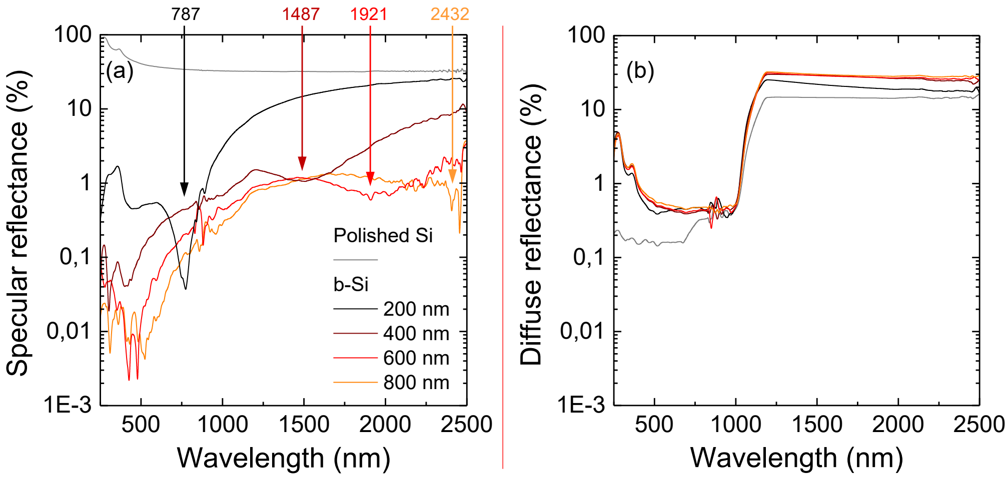

Figure 1.31: (a) Specular and (b) diffuse reflectance spectra of black silicon with different texture scales, here distinguished by the average height of spikes. Samples were prepared on single side polished Si wafers, whose specular and diffuse reflectance spectra are also shown for reference. Arrows denote local minima of specular reflectance. Both types of reflectance for each surface combine to yield the total hemispherical reflectance shown in Figure 1.30 (b).

appropriately placed exit port. On the other hand, specular reflectance could subsequently be estimated from the total hemispherical reflectance by subtracting the scattered portion. Adequacy of the method was verified by conducting said measurements on a flat single side polished silicon wafer. As can be seen from the corresponding curves in Figure 1.31, specular reflectance from the polished front-side of the wafer could be separated from the diffuse part scattered by the microtextured rear-side.

Differences in anti-reflectance of black silicon with different texture scales become particularly apparent when considering specularly reflected radiation at the near-IR, shown in Figure 1.31 (a). The fine 200 nm average height texture exhibits acceptable performance in the visible light region, however, anti-reflectance degrades rapidly for radiation with higher wavelengths. This is expected to occur in large part due to the thickness of the gradient effective refractive index layer, established by this black silicon sample, being insufficient to provide efficient impedance matching for IR radiation. Specular reflectance is gradually eliminated when the average size of texture features is increased. Conversely, as the near-IR specular reflectance decreases, the diffuse portion asymptotically climbs to a limit just above 30%. However, this is not related to higher scattering in the black silicon texture. Rather, the presence of a limit hints at this being merely the result of a larger part of the incident energy reaching the back surface to experience Fresnel-type reflection.

Reflectance at near-IR could not resolve differences in performance between black silicon textures with 600 nm and 800 nm average spike heights. Therefore, measurements at mid-IR wavelengths became necessary and were conducted using a Spectrum Spotlight 300 Fourier transform IR imaging spectrometer (Perkin-Elmer Inc.). The system uses a $NA = 0.5$ Cassegrain-type magnifying mirror system with an 17° to 30° off-axis acceptance angle range, therefore, only specular reflectance could be measured. Yet, despite using different spectrometers and acquisition methods, remarkable consistency between mid-IR reflectance in Figure 1.32 and near-IR results in Figure 1.31 (a) was maintained at the switch-over wavelength of $\lambda = 2500$ nm.

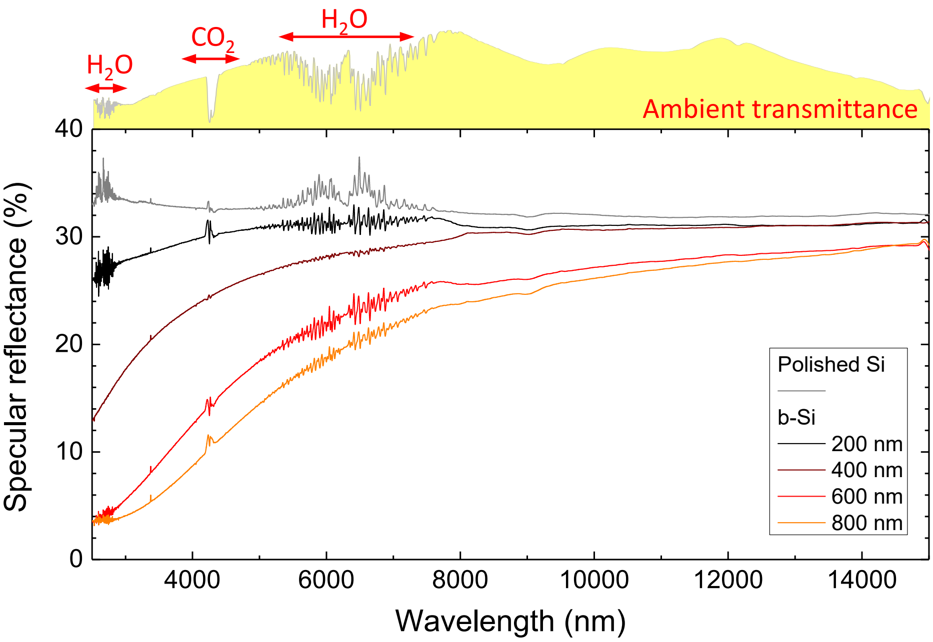

Figure 1.32: Infrared specular reflectance spectra of black silicon with different texture scales, here distinguished by the average height of spikes [137]. An IR reflectance spectrum of single side polished Si wafer is shown for reference. Ambient air transmittance is shown at the top of the plot to illustrate absorbance features responsible for the noise. Mid-IR spectroscopy experiments were performed at Tokyo Institute of Technology by the research group under supervision of Prof. Junko Morikawa.

Mid-IR specular reflectance curves of black silicon with different texture scales, shown in Figure 1.32 illustrate, how black silicon reflectance can be tuned form $\sim 35\%$, typical for flat Si, down to 4% throughout the near and short-wavelength IR spectral regions. Therefore, the nanotextures investigated in this work can be tailored to provide anti-reflectance at atmospheric infrared transmittance windows up to $\lambda \approx 5$ µm, relevant for remote spectroscopic sensing. However, towards long-wavelength IR region specular reflectance suppression loses its efficacy even for the largest scale black silicon textures due to insufficient depth of the gradient effective index layer. Even larger scale or, preferably, higher aspect ratio silicon texturing would be necessary for uses at these low optical frequencies. Fabrication of high aspect ratio black silicon has been demonstrated using electron cyclotron resonance plasma sources [54] as well as cryogenic substrate cooling [135].

Evidently the gradient effective refractive index layer established by silicon spikes represents the primary anti-reflectance mechanism in all black silicon samples discussed here. However, the presence of local minima in the specular reflectance spectra of Figure 1.31 (a) that scale with the sizes of structural components indicate the prescience of an additional effect. An obvious candidate to account for this contribution would be scattering by quasi-random Mie-like subwavelength resonators [64] (akin to those shown in Figure 1.12 (b)), since the spikes constituting black silicon fall within the scaled wavelength ($\sim \lambda/n_{\mathrm{Si}}$) size range. Furthermore, top-down views of black silicon surfaces, shown in top panels of Figure 1.33, also share similarities with the deterministic spatial spectrum light coupling structures [27] depicted in Figure 1.13. Indeed, the spatial spectra of black silicon, shown in the bottom

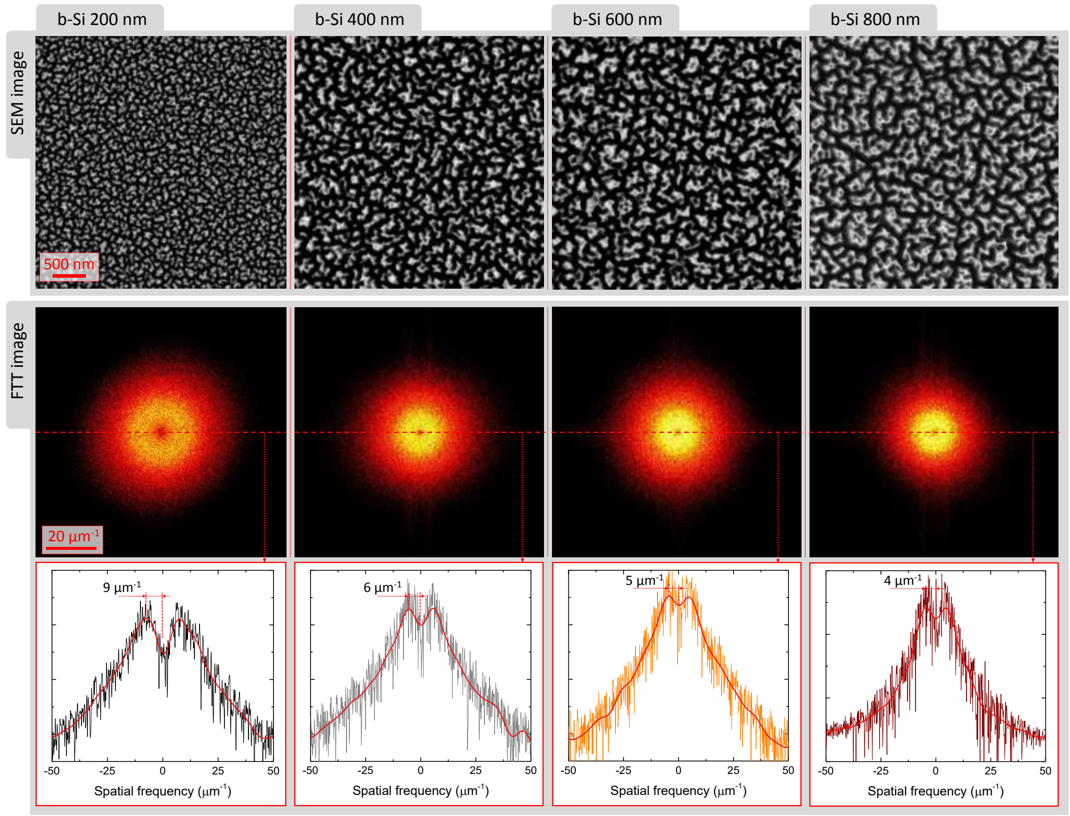

Figure 1.33: 2D spatial component analysis of black silicon with with different texture scales. Upper row panels show the top-down scanning electron microscopy images of the corresponding surfaces. Middle row panels show the logarithmic scale spatial frequency spectra of black silicon, obtained by performing a 2D fast Fourier transform of respective images. The bottom row panels show horizontal cross-sections of the Fourier spectra.

panel rows of Figure 1.33, closely resemble that of the aforementioned coupling surfaces. For larger scale textures intensity of the ring-like Fourier spectrum shrinks toward lower spatial frequencies. This would result in better *k*-vector matching at IR wavelengths, as was observed experimentally. Of course, black silicon is ultimately a 3D surface, and the qualitative nature of such 2D image analysis is incapable of producing a quantitative match with experimental results. However, this example is instructive how correlation length between texture features can be used to further boost reflectance suppression and induce light trapping through large angle scattering in a particular spectral region.

In summary, this work showed how the scale of a black silicon surface texture relates to its reflectance, which mechanisms dominate, and how alterations of morphology can be utilized to improve radiation coupling efficiency at infrared wavelengths. Larger texture scales would be expected to perform better at IR at the cost of lower efficiency at visible wavelengths. Conversely, higher aspect ratio structural features would provide more broadband anti-reflectance without this trade-off, however, such surfaces are not as robust and require more demanding fabrication methods. Therefore, next sections describe efforts to further extend reflectance suppression bandwidth by developing hierarchical micro/nano-textures, realized by combining two simple texturing steps.

1.3.2 Hierarchically nanostructured optical surfaces

The task of ensuring truly broadband reflectance suppression, spanning throughout the visible as well as most of the infrared spectral region, limits the use of certain radiation coupling techniques. Out of the four main approaches for establishing anti-reflectance illustrated in Figure 1.3 the two resonant methods, namely anti-reflective coatings and gratings, can at best be used as auxiliary mechanisms due to being effective in only a limited wavelength range. Furthermore, as mentioned in Section 1.1.5, textured light trapping surfaces provide only moderate reduction in wasted optical energy, since they rely on coupling light over a limited number of inherently lossy Fresnel reflections. Hence, gradient effective refractive index layers comprised of fine texturing over a long optical path theoretically would seem to be the best candidate to realize high efficiency broadband anti-reflectance.

In practice, however, gradient effective refractive index textured surfaces have numerous drawbacks. First of all, fine textures give rise to large surface areas, which in turn mean excessive rates of carrier recombination at defect states, and therefore have limited suitability for optoelectronic uses [72]. Next, high aspect ratio structural features tend to lack the robustness necessary for practical applications. Lastly, their preparation often requires high performance fabrication tools [54] and specialized processes [138].

An alternative approach to address the conflicting demands placed on broadband anti-reflective surfaces involves hierarchical superimposition of disparate yet complimentary light coupling surfaces at different scale sizes [139, 140]. The individual constituents of such compound textures can either become active at different spectral regions or cumulatively augment each other. Of course, the most refined realizations of cascading nanotextures can be encountered in the biological realm, where due to inherent robustness they often don externally facing surfaces. More notable examples are anti-reflective moth eyes [10], velvet black snake scales [141], and hydrophobic lotus leaves [5], which have inspired a great number of artificial biomimetic counterparts [7, 142]. The simplest and most scalable techniques to create hierarchical surface textures involve combining wet etching, plasma etching, nanoimprint lithography or laser processing, and have been demonstrated on polymers [7], semiconductors [143, 144] and metals [145]. The chief advantage of this approach, namely the ability to independently tailor the processes at each fabrication stage for optimal combined performance, is yet to be utilized to its fullest extent however.

In this work, conducted in collaboration with the research group headed by Assoc. Prof. Yoshiaki Nishijima at Yokohama National University, hierarchical anti-reflective Si surfaces created by combining wet etched micro-pyramid texturing with a black silicon superstructure were investigated [146]. The main focus of this study was to increase the reflectance suppression bandwidth without compromising the overall performance. Furthermore, textures with a wavelength-scale black silicon superstructure were benchmarked against those with extremely high aspect ratio Si nanowires, which approximate a high optical thickness gradient effective refractive index layer. Reflectance suppression was similar in both cases [146], therefore to maintain continuity only black silicon related work will be discussed in detail here. Experimental results bolstered by numerical simulations showed that hierarchical surface texturing can reduce broadband specular reflectance by up to two orders of magnitude whilst completely altering the method of light trapping within the substrate.

Fabrication of hierarchical anti-reflective surfaces used in this work is relatively straightforward and merely requires the sequential application of the respective techniques for creating individual basic textures. In this case it involves combining alkaline wet etching of micro-pyramids with subsequent dry etching of black silicon. A simplified sketch and scanning

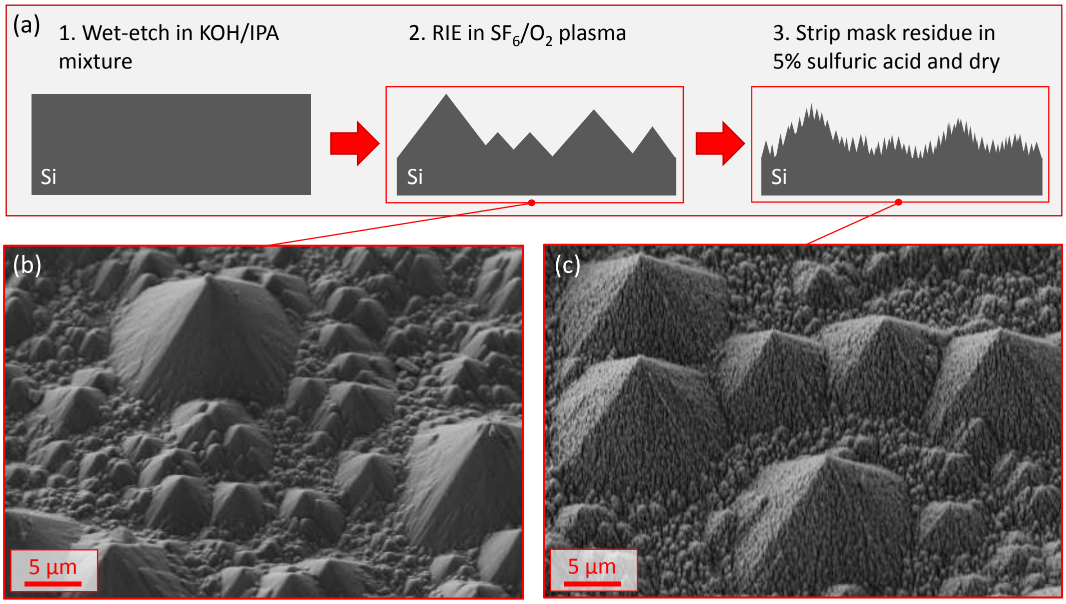

Figure 1.34: Fabrication process of a hierarchical anti-reflective surface with a black silicon superstructure. (a) Sketch outlining the main fabrication steps which involve wet etching in a 0.5 M NaOH solution to establish the microscale texture and subsequent reactive ion etching to create nanoscale spikes as outlined in Figure 1.17. Scanning electron microscopy images of (b) wet etched Si micro-pyramids and (c) final hierarchical texture with superimposed black silicon.

electron microscopy images illustrating the process are given in Figure 1.34, where differences between the scale of the two constituent textures become apparent. Fabrication of micro-pyramid coated substrates was done by immersing 3″ diameter (100) crystallographic orientation Si wafers in a commercially available NaOH based etching solution Pure Etch T501S (Hayashi Pure Chemical Ind Ltd.), which was diluted down to a concentration of 0.5 M (12% by weight). Etching was conducted over a duration anywhere from 10 minutes up to 72 hours, depending on the desired scale of pyramids. Shorter processes at an elevated temperature of 80 °C yielded a random arrangement of pyramids ranging from 2 µm to 10 µm in height, whereas longer more gradual etches at room temperature produced substantially larger 10 µm to 40 µm height variance surface features.

Nanoscale black silicon texturing was conducted using the reactive ion etching process described in Section 1.2.1 without any noteworthy modifications. Therefore, black silicon average spike heights can also be controlled by changing the treatment duration, as shown in Figure 1.35. Hierarchical textures of silicon spikes ranging anywhere from 200 nm to 1.2 µm in height, overlaying randomly arranged pyramids up to 20 µm in height could be obtained. However, an important consideration when creating the superstructure is that excessive reactive ion etching durations tend to erode the finer microscale pyramid features, planarizing significant parts of the surface and thereby detrimentally affecting reflectance suppression in the infrared spectral region. For this reason the underlying micro-texture should be sufficiently pronounced, preferably comprised of 10 µm average height pyramids, to allow for consumption of an approximately 3 µm thickness Si layer without marked topological deterioration.

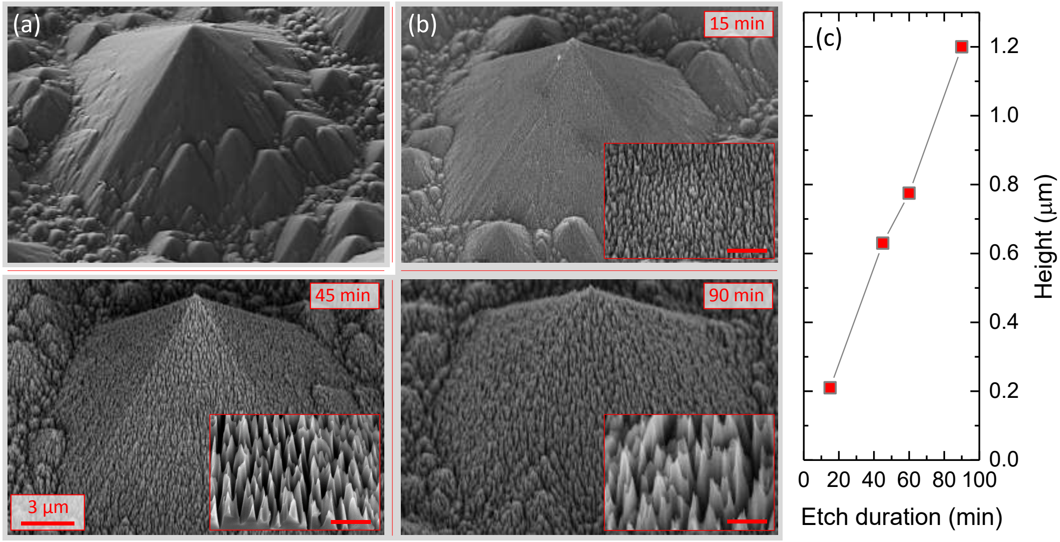

Figure 1.35: Hierarchical surface textures of different size scale black silicon etched into micro-pyramids. (a) Isometric-view scanning electron micrographs of micro-pyramids as created by wet etching, and (b) cascading micro/nano-textures after different reactive ion etch durations along with insets showing close-up view of nanoscale features. The 3 µm scale bar is applicable to all 4 main images. Scale bars in the insets correspond to 500 nm. (c) The average height of black silicon spikes etched into pyramids plotted against the reactive ion etching duration.

The general reflectance behavior of each constituent texture can be inferred from the size scale of its features. Microscale pyramids, for instance, are large enough to fall squarely in the geometric optics operational regime, therefore, should provide modest anti-reflectance over a broad spectral range. Black silicon morphology, on the other hand, is within the wave optics range for visible and near-IR, and is subwavelength at radiation frequencies below that. Optical thickness of the effective refractive index gradient established by the nanoscale spikes is likewise only sufficient for coupling radiation with wavelengths below mid-IR. As a result a sharp drop-off in black silicon anti-reflectance can be expected for lower frequency radiation.

The specular reflectance spectra for the basic textures, shown in Figure 1.36, appear to coincide with these predictions. In the Si absorbance wavelength range black silicon exhibits severely diminished reflectance, consistently below 1%. As expected, micro pyramids reflect around 5% of incoming radiation, hence, performance is fairly unremarkable as far as reflectance minimum values are concerned. On the other hand, in the infrared region, where Si is transparent, anti-reflectance of micro-pyramid decorated surfaces is much more consistent and extends to the lowest optical frequencies. Conversely, reflectance suppression of black silicon rapidly degrades towards the infrared range due to factors outlined in Section 1.3.1. Specular reflectance of the hierarchical composite structure appears to largely combine the advantages of both individual methods, *i.e.* exhibits the strong anti-reflectance typical for black silicon in the Si absorbance region whilst simultaneously suppressing reflectance throughout the infrared spectral range down to several percent, almost an order of magnitude below that of the micro-pyramid texture alone.

The spectra shown in Figure 1.36 account only for radiation reflected in a narrow cone around the angle of reflection, therefore, approximately represent specular reflectance. How-

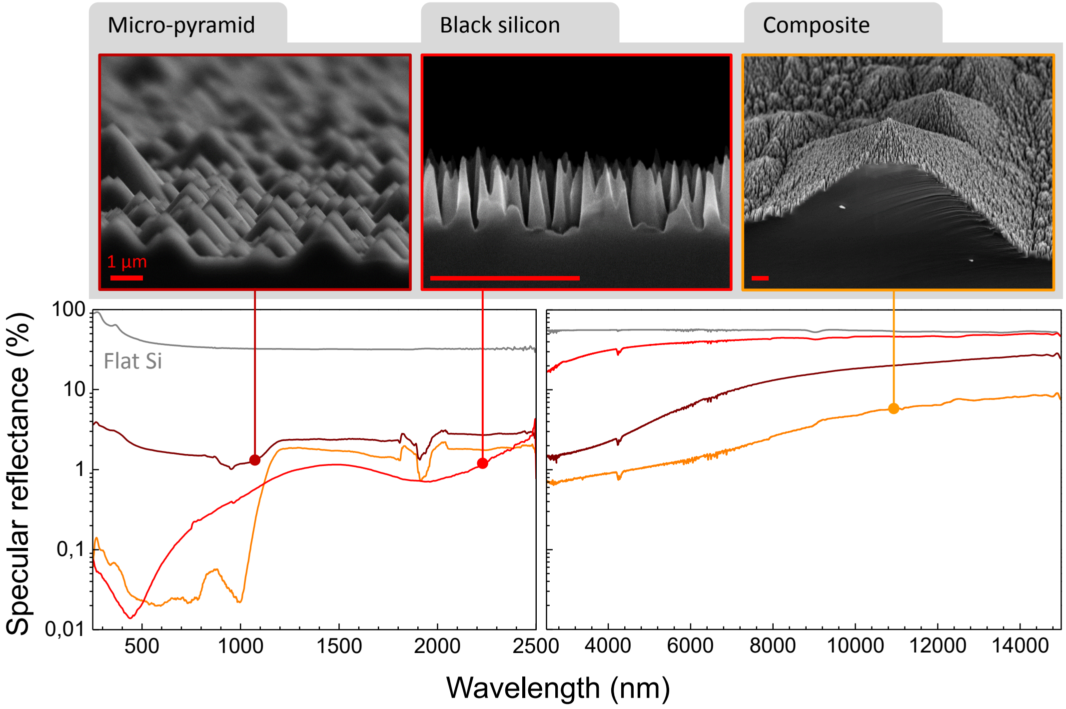

Figure 1.36: Single-etch-step and dual-scale textured silicon anti-reflective surfaces: alkaline wet etched micro-pyramids, reactive ion etched black silicon, and their hierarchical composite. Top panels show side view scanning electron microscopy images of the textures. Scale bar for each image represents 1 µm. Lower panels show the visible-to-far-IR specular reflectance spectra for each of the surface textures [146]. Infrared spectroscopy experiments were performed at Yokohama National University by the research group under supervision of Assoc. Prof. Yoshiaki Nishijima.

ever, owing to discontinuities in surface morphology a considerable portion of radiation can also be scattered out of the collection optics acceptance range. This energy would be reflected diffusely and is not accounted for in Figure 1.36. The same considerations hold if transmittance was to be measured. Directly transmitted light rays will propagate according to the law of refraction, whereas diffusely transmitted, *i.e.* scattered, light can exit the sample at a wide range of angles within the loss cone. Therefore, to more fully characterize light interaction with the different textured surfaces it becomes necessary to investigate their scattering behavior.

To this end spectroscopic measurements were conducted with the goal of determining how intensity of incoming radiation is distributed among various mechanisms of reflectance, transmittance and extinction. Results of these experiments for the constituent micro-pyramid, black silicon and their hierarchical composite surfaces, as well as for polished Si for reference, are depicted in Figure 1.37. Each of the panels is separated into two parts, namely the UV-to-near-IR and mid-IR regions, due to the different setups used for acquisition of spectra. On the higher frequency end, reflectance and transmittance spectra of textured silicon wafers were acquired using a 150 mm integrating sphere mounted in a LAMBDA 1050 UV/Vis/NIR spectrometer (Perkin-Elmer Inc.). The detectors could register hemispherically scattered radiation with wavelengths ranging from 250 nm to 2.5 µm. The specular portions of UV-to-near-IR reflectance were separated *via* an exit port. Direct transmittance was measured using $NA = 0.3$ collection optics, however this results in a narrow angle scattered portion of light being misinterpreted as direct transmittance, therefore in the legend of Figure 1.37 the more adequate term "narrow angle reflectance/transmittance" is used. On the other hand, mid-IR spectroscopic measurements from $\lambda = 2500$ nm onward were performed using a FT-IR-4000 Fourier transform IR $NA = 0.5$ imaging system (JASCO Inc.) without an integrating sphere attachment. Therefore, scattered radiation could not be detected at longer wavelengths and is not shown.

At wavelengths below $\lambda = 1.1$ µm Si is opaque, hence, extinction is overwhelmingly due to strong absorbance therein. So, if a beam is somehow coupled into the substrate its energy will be taken up by the electron system of Si and thereby extinguished. In this spectral range, comparison between panels (a) and (b) of Figure 1.37, which respectively correspond to a single side polished Si wafer and a wafer with both sides covered by micro-pyramids, is particularly illustrative of the scattering-related effects brought on by microtexturing. For a flat Si surface the main source of optical loss is due to the initial specular reflectance at the front face, and only at the onset of the Si transparency window an additional diffuse reflectance component from the rough rear-side appears. On the other hand, the micro-pyramid textured surface is highly disruptive to the incident wavefront and as a result reflectance is almost entirely diffuse. Therefore, when scattering is taken into consideration, such microscale

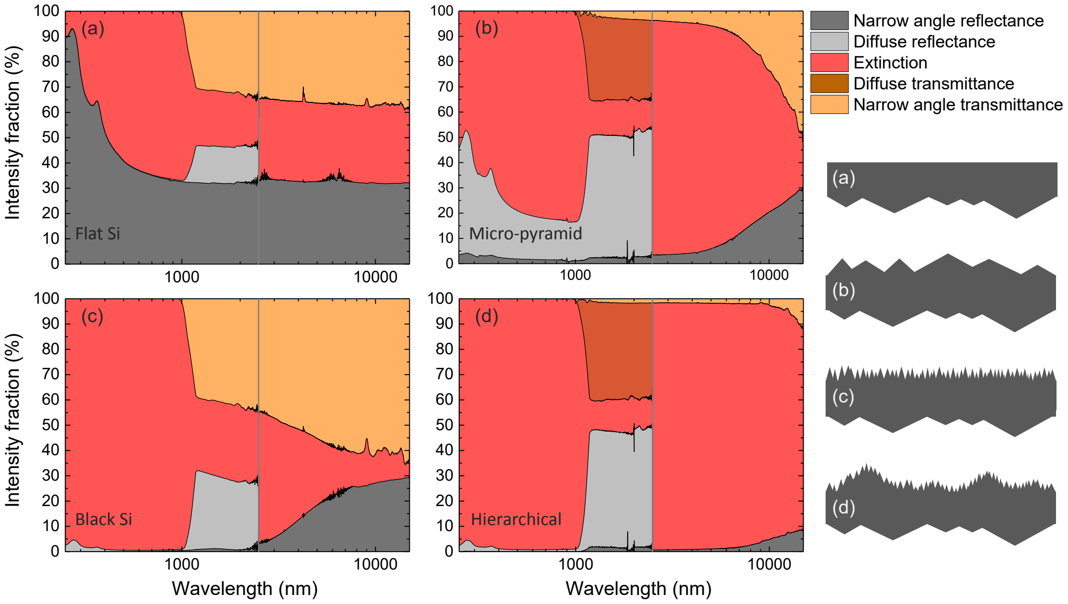

Figure 1.37: Experimentally measured spectra of intensity fractions corresponding to radiation reflected and transmitted either specularly of diffusely by Si wafers with different textures [146]. The residual portion marked in red represents the intensity fraction that is either absorbed or scattered outside of the detection optics acceptance range. Diffusely reflected and transmitted intensity portions in the mid-IR range are unavailable due to numerical aperture limitations in the Fourier transform IR imaging system used in this work. Sketches illustrate Si wafer topologies corresponding to each of the panels. Infrared spectroscopy part of experimental work was performed at Yokohama National University by the research group under supervision of Assoc. Prof. Yoshiaki Nishijima.

surface topologies reduce reflectance related losses only by a factor of two. Transmittance of the two samples, given in Figure 1.37 (a) and (b) at IR wavelengths, follows the same pattern observed for reflectance, *i.e.* for a polished wafer it is mainly direct, whereas in the double side microtextured case it is for the most part diffuse. The substantially lower scattering observed in samples with single-side micro-texturing is because the loss cone, strictly tied to the surface normal, can take a wide range of orientations when both sides of a Si surface are randomly faceted. In this way such a double-side textured surface is reminiscent of a Lambertian reflector, as was discussed in Section 1.1.5.

The phenomena underlying the exceptionally low reflectance off a single-etch-step black silicon wafer were described in Section 1.3.1 and for conciseness will not be reiterated in detail here. In the most general terms, low reflectance at visible wavelengths is a result of the gradient effective refractive index effect, and is additionally extended towards near-IR due to resonant quasi-random forward-scattering [27, 71]. However, mid-IR wavelengths are well beyond the size-scale of the nanotexture and reflectance suppression rapidly deteriorates. As is evident in Figure 1.37 (c), virtually all reflectance in the visible-to-near-IR range is diffuse, therefore, includes a minuscule contribution from the front-side nanotexture and a much more substantial portion back-scatted at the rough rear-side in the transparency band of Si. On the other hand, reflectance of the micro-pyramid/black silicon hierarchical composite, shown in Figure 1.37 (d), shares properties with each of its constituents. Anti-reflectance at the visible range matches that of flat black silicon, whereas at near-IR significant back-scattering, akin to that observed for micro-pyramids, is present. Compared to black silicon, diffuse reflectance at near-IR is almost doubled and the intensity part associated with extinction is decreased by a factor of three. This indicates that the guided mode light trapping mechanism exhibited by flat black silicon in hierarchical textures is substituted for statistical ray trapping.

The mostly direct near-IR transmittance of black silicon becomes diffuse when texturing is hierarchical, likely due to the same statistical mechanism underlying the behavior of double-side micro-textured surfaces. Of further note is that total transmittance of hierarchically textured surfaces is higher than merely micro-textured ones, as can be seen in panels (b) and (d) of Figure 1.37. This indicates that while micro-textured and hierarchical surfaces have similar values of total reflectance at near-IR, anti-reflectance at the front-surface is superior at the latter.

Experimental reflectance and transmittance spectroscopy results hint at the strong anti-reflectance of hierarchically textured black silicon/micro-pyramid surfaces. However, at wavelengths where Si is transparent it was not possible to separate the diffuse reflectance contributions of the two opposing wafer surfaces. This, in principle, could be deduced experimentally by preparing and investigating textured samples with flat, scattering and mirrored rear-sides. Nevertheless, numerical simulations can also help in elucidating this point, with the added benefit of the results being strictly topology related and unaffected by structural changes in materials induced by different fabrication techniques. For these reasons FDTD simulations were performed on representative segments of textured surfaces to isolate their single-interface reflectance and transmittance behavior.

Optical simulations on large fully 3D segments of each texture spanning over 10×7 μm^2 areas were performed using the "FDTD Solutions" software package (Lumerical Solutions Inc). The extent of simulated volume, combined with the need not to compromise resolution of nanoscale features, necessitated enormous computational power. Therefore, calculations were performed on the swinSTAR supercomputer at Swinburne University of Technology. A model of a micro-pyramid textured surface was rendered by scripted semi-random placement of pyramids on a predefined plane. Parameters of the individual pyramids were determined by

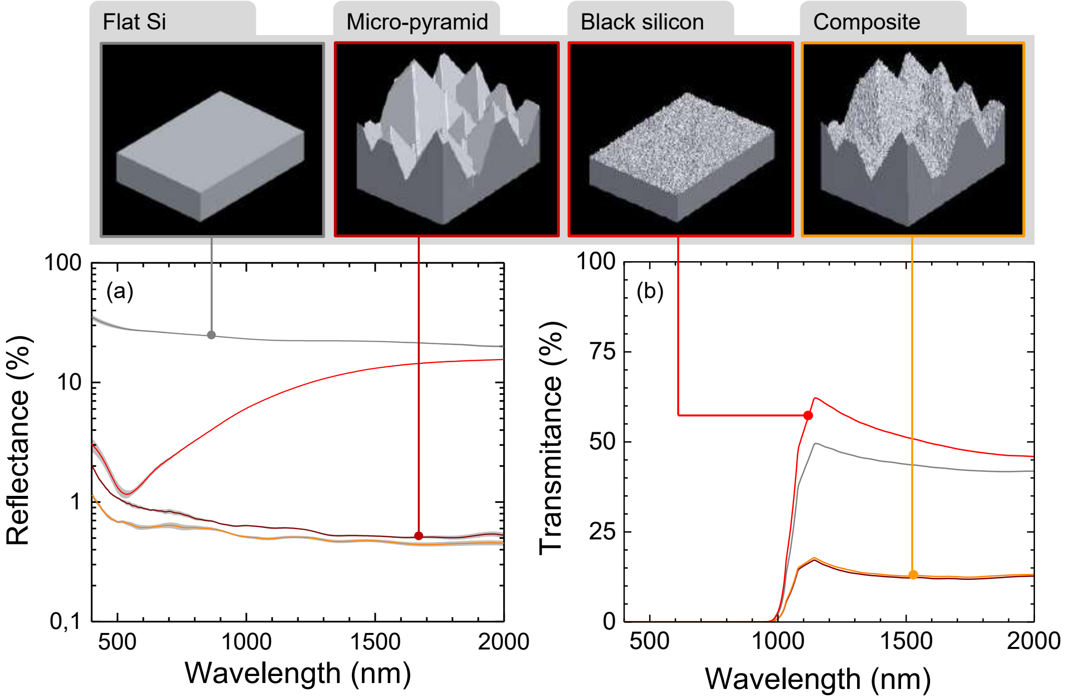

Figure 1.38: FDTD simulated spectra of single interface (a) reflectance and (b) transmittance of the basic micro-pyramid and black silicon textures, their hierarchical composite, as well as flat Si for reference. Top panels illustrate the respective 3D renderings on which calculations were conducted. Simulations were performed using the swinSTAR supercomputer at Swinburne University of Technology.

scanning electron microscopy inspection of NaOH-etched Si surfaces, and only their height was allowed to change during the generation process, assuming a normal distribution. Black silicon nanotextured surface model was created directly from a scanning electron microscopy image, according to the procedure described in Section 1.2.3, and additively superimposed onto either a flat plane or the micro-pyramid texture. Images of the 3D models used in FDTD simulations are depicted in the top panels of Figure 1.38. The simulation volume was terminated using perfectly matched boundary conditions and a broadband linearly polarized plane wave source was used for excitation. Simulations were performed for two orthogonal light polarizations and the results were subsequently averaged to obtain the unpolarized response. Transmittance spectra were acquired at a 2.5 μm depth beneath the surface texture and subsequently recalculated using the Beer-Lambert law to add an additional 500 μm optical path through a Si wafer [41].

Simulated reflectance and transmittance spectra, shown in Figure 1.38 panels (a) and (b) respectively, fall broadly in line with experimental observations for black silicon. However, simulations coincide only with the specular intensity portions of the experimental results, especially when microtexturing is involved. As a result of this one major discrepancy anti-reflectance of the micro-pyramid and hierarchical surfaces is is overestimated. Furthermore, their transmittance is likewise much lower than expected. So, it can be deduced that the calculated reflectance is low not due to efficient light coupling, but because of obtuse scattering in parallel to the surface, hence, outside of the detection region. Therefore, while the attainable simulation volume was insufficient for achieving parity with experiment, numerical findings corroborate the significance of in plane scattering effects in both micro-textured and hierarchical anti-reflective surfaces.

This work demonstrates how superimposition of different surface textures results in cumulative optical behavior. Here hierarchical application of anti-reflective black silicon onto a statistical ray trapping micro-pyramid texture almost completely suppressed the originally diffuse reflectance at the Si absorbance range. This additional anti-reflectance did not affect the Lambertian scattering properties of the alkaline-etched surface. It implies that such a composite texture would increase the mean average path of rays coupled into the substrate, as well as boast superior bandwidth and ominidirectionality compared to flat black silicon. However, drawbacks such as loss of ability to couple guided modes also have to be considered. Furthermore, etching hierarchical textures up to 20 µm in height necessitates chemical consumption of a substantial volume of material. As a result such textures would not be compatible with most thin-film solar cell technologies, however, can be applicable a coupling surface for harnessing radiation at the infrared.

While the hierarchical nanotextured surfaces described here exhibit excellent anti-reflectance at infrared wavelengths, radiation is eventually scattered out of the material as silicon is transparent in this range. This ties into a general problem that the ability to couple optical energy into a surface is moot if there exists no viable mechanism for its uptake and gainful exploitation. So, the next section describes methods of imparting absorbance to black silicon based substrates in order to harness infrared energy.

1.4 Black silicon absorbance enhancement

Multi-crystalline and mono-crystalline silicon based photovoltaic devices presently represent an overwhelming market share among all direct solar energy harvesting solutions [147]. This is hardly surprising, considering that silicon is second only to gallium arsenide in terms of single-junction solar cell efficiency, all the while benefiting from decreased costs associated with having well established manufacturing processes and an abundant supply of raw materials. Current state of the art realizations of single-junction silicon solar cells exhibit a photoconversion efficiency in excess of 26% [148]. However, this is relatively close to the fundamental detailed balance limit [149] which for Si equals approximately 32%, and would remain below 34% even in the hypothetical case of an optimal 1.34 eV band gap semiconductor single-junction cell.

Implications of such a limit for an ideal Si-based solar cell are illustrated in Figure 1.39, where a standard air mass 1.5 solar irradiance spectrum [150] is separated into portions accessible for standard photovoltaic conversion and those which cannot be gainfully harnessed. Thermal losses at the short wavelength edge arise due to thermalization of the excess kinetic energy imparted to an electron by photons above the band gap, whereas infrared transmittance losses represent radiation incapable of initiating interband transitions in Si. In order to further improve solar energy harvesting efficiency numerous approaches to increase the absorption and effective usage of solar energy [151], such as multijunction, up- and down-conversion cells as well as concentrator-based setups, are being vigorously pursued.

A different semiconductor based method for generating electrical power, with an efficiency at least in theory capped at the much more lenient Carnot thermodynamic limit, is thermoelectric conversion. It relies on the Seebeck effect at the junction of oppositely doped semiconductor materials across which a thermal gradient is established. However, said thermoelectric materials must simultaneously exhibit high electric conductivity σ, low thermal conductivity κ and a high Seebeck coefficient S, which together with the operating temperature T denote the figure of merit parameter $ZT = (S^2\sigma/\kappa)T$ [152]. Presently bismuth chalcogenide ceramics, such as Bi_2Te_3 and Bi_2Se_3 based systems, represent some of the higher performing

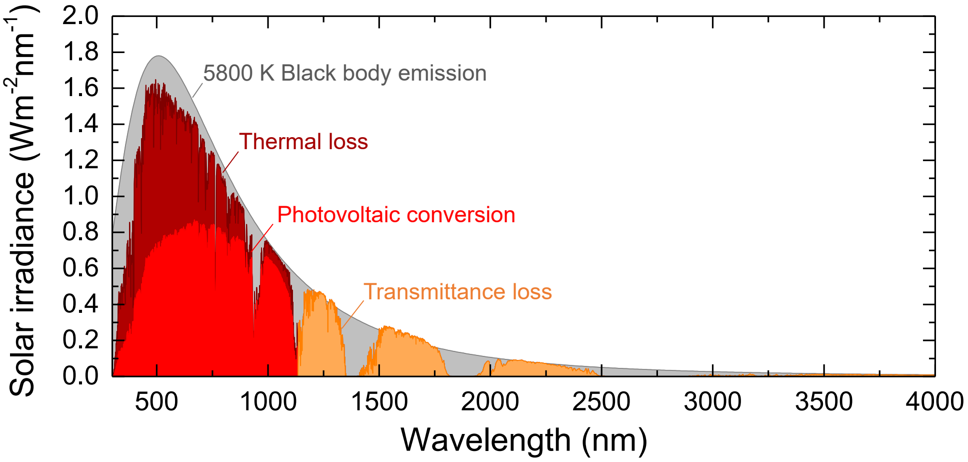

Figure 1.39: Air mass 1.5 solar radiation energy spectrum [150], approximated by a 5800 K temperature black body. Energy absorbed by a Si solar cell operating at the detailed balance limit is highlighted in red. Remaining energy is lost due to carrier thermalization and sub-band gap transmittance.

thermoelectric materials under ambient conditions, with a a figure of merit up to $ZT \approx 1.4$ at room temperature [152]. Advances in material engineering resulted in figure of merit values reaching and even exceeding $ZT \approx 2$, albeit at temperatures in excess of 700 K [153]. However, materials with $ZT \geq 4$ are necessary for thermoelectric generation efficiency to approach that attainable by photovoltaic solar cells, whereas edging towards the Carnot limit would require a ZT close to infinity. Present thermophotovoltaic conversion efficiencies are at or below 10% as a result, hence, cannot directly compete with photovoltaics [151, 154, 155].

Despite the aforementioned issues thermoelectric converters have certain noteworthy advantages. First of all, unlike other energy conversion systems, thermoelectric devices tend to preserve efficiency when scaled down therefore are well suited for miniaturization. Also, thermoelectric devices effectively can be considered as heat engine without moving parts and exhibit remarkable reliability as a result. It is not surprising, therefore, that thermoelectric generators were used to power the Viking and Pioneer deep space missions [156]. More recently thermoelectric converters have found prominent use in the reclamation of energy dissipated by industrial processes and vehicles, where up to 60% of primary energy is given off as waste heat [157].

The present section describes work related to thermoelectric solar energy harvesting using black silicon as an absorber platform. Methods of inducing the absorption of sub-band gap photons in black silicon are given particular attention. Two prototype device realizations are discussed, namely, a purely thermoelectric solar radiation harvester, and a hybrid device which aims to combine photovoltaic generation in a Si solar cell with simultaneous thermoelectric conversion of infrared radiation as well as waste heat.

1.4.1 Plasmonic nanoparticle augmented black silicon absorber

In the preceding Section 1.3 it was shown how nanotexturing can facilitate anti-reflectance over bandwidths well in excess of the absorbance wavelength range of silicon. Therefore, the problem of coupling radiation past the material interface in such a case ceases to be primary and methods of taking up the energy have to be sought out. Moderate augmentations of infrared absorbance in silicon have been demonstrated either through increasing the free carrier absorption through heavy doping [158], or through introduction of deep energy levels associated with sulfur impurity defects [159, 160]. However, such silicon modifications have limited applicability since they strongly and for the most part detrimentally impact the electronic properties of the semiconductor.

A different method for both enhancing radiation coupling and absorbance, which does not rely on direct modifications of the active material, involves the use of plasmonic nanoparticles. The localized surface plasmon-polariton response is inherently broadband and can be widely tuned by changing their shape and size. When placed in the immediate vicinity of a high refractive index dielectric substrate resonant metal nanoparticles tend to preferentially scatter radiation into the material. Furthermore, hot-spots of highly concentrated optical field are established and aid in increasing local rates of absorbance [161]. These mechanisms have been successfully employed in enhancing the short-circuit current performance of certain moderate conversion efficiency thin film solar cells [162, 163]. However, due to the lossy nature of metals at optical frequencies a substantial portion of energy is dissipated as heat by the localized surface plasmon excitations, hence, in cells aiming for a high efficiency, nanoscale metal textures are mainly used as back-reflectors [164–166]. On the other hand, unlike in the photovoltaic case, heat produced by optically excited nanoparticles would not be a detriment in a system that generates power thermoelectrically.

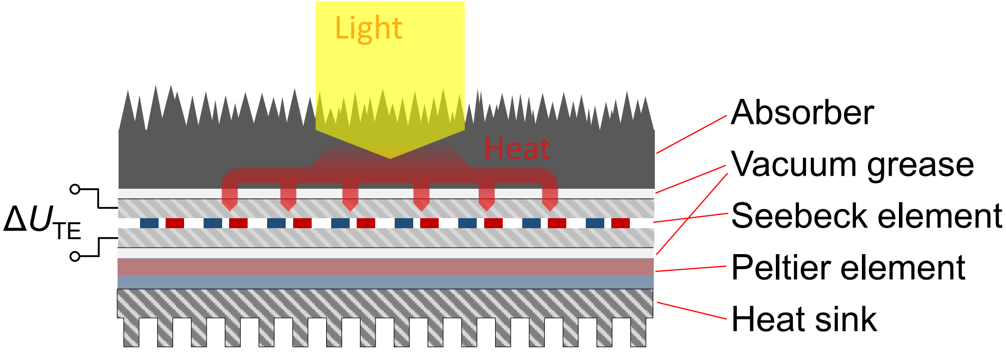

Figure 1.40: Sketch illustrating the composition of the thermophotovoltaic converter device with a black silicon based absorber used in this work [167]. Heat from the absorber is converted into electric power using a Seebeck element. Device was assembled at Yokohama National University by the research group under supervision of Assoc. Prof. Yoshiaki Nishijima.

In this work, conducted in collaboration with the research group headed by Assoc. Prof. Yoshiaki Nishijima at Yokohama National University, black silicon is used as a solar absorber platform for a Seebeck effect-based thermoelectric solar energy harvester [167]. Gold nanoparticles were deposited onto black silicon to further enhance solar-to-thermal energy conversion yield and increase the device efficiency. Furthermore, finite-difference time-domain simulations were conducted in order to elucidate the effect of plasmonic excitations on light-mater interaction and localization at the nanotextured absorber surface.

A schematic of the prototype thermophotovoltaic converter device is provided in Figure 1.40. Here electromotive force, denoted as ΔU_{TE}, is generated by a commercially available Bi-Te based thermoelectric module TEP1-1264-1.5 (Thermonamic Electronics Corp., Ltd.) with a maximum heat-to-electrical power conversion efficiency of 6% [167]. A transverse thermal gradient was established by using an illuminated black silicon based solar absorber at the hot side, and attaching either a Peltier element or a metal heat sink at the cold side of the device. Photoexcitation of the absorber is transformed into heat through various thermalization processes which is in turn conducted towards the Seebeck element. Thermally conductive contacts for both sides of the module were ensured through the application of vacuum grease X-23-7877 (Shin-Etsu Chemical Co., Ltd.). The optional Peltier element between the cold side of the thermoelectric module and the heat sink is used for experimental measurements of the thermal gradient during calibration. By using a second Peltier element in place of the absorber a thermoelectric conversion coefficient value of 28 $\mathrm{mV\,K^{-1}}$ was determined. Two test illumination source types were used - monochromatic 532 nm wavelength laser light, as well as a broadband metal halide lamp, which roughly approximates the solar power spectrum at the visible range [167].

Solar radiation absorbers were fabricated by nanotexturing 500 µm thickness p-type Si wafer surfaces by means of the reactive ion etching process described in Section 1.2.1. Black silicon with 250 nm average height spikes was obtained after 15 minutes of treatment. Further plasmonic absorbance enhancement effects were investigated by drop casting various concentrations of iso-2-propyl alcohol dispersions of different commercially available colloidal gold nanoparticle solutions (Tanaka Co. Ltd) onto black silicon. Average nanoparticle diameters ranged from 15 nm, for which absorption is expected to be the dominant light extinction contribution, up to 100 nm where scattering component is more strongly pronounced.

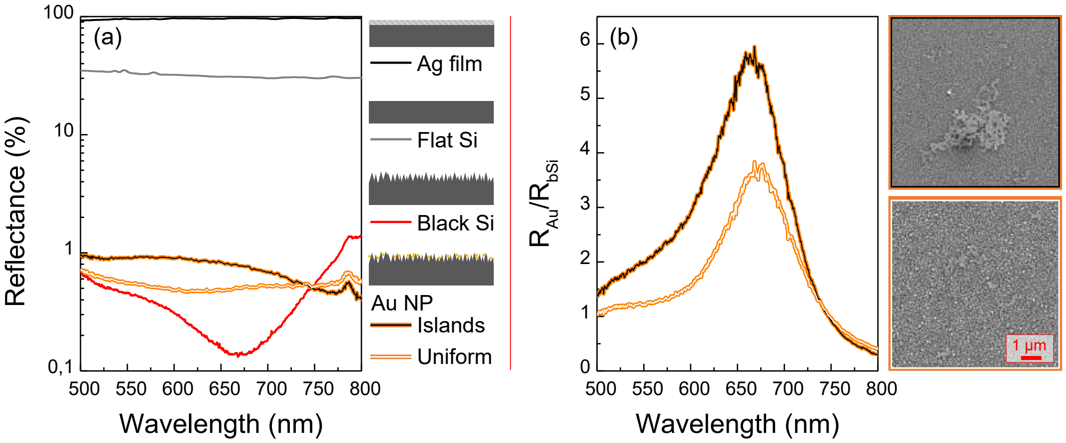

Figure 1.41: (a) Specular reflectance spectra of black silicon absorbers with and without 50 nm diameter Au nanoparticle coatings, as well as of flat Si and Ag mirror reference surfaces. Depending on concentration Au nanoparticle distribution can either be uniform, or aggregated into islands. (b) Nanoparticle decorated absorber reflectance spectra normalized to the reflectance of plain black silicon [167]. Scanning electron microscope images illustrate aggregated (top) and optimal (bottom) black silicon surface coverage by Au nanoparticles. Reflectance measurements were performed at Yokohama National University by the research group under supervision of Assoc. Prof. Yoshiaki Nishijima.

Specular reflectance spectra of the black silicon derived absorbers, along with flat and 2 µm thickness Ag film coated Si reference surfaces, are given in Figure 1.41 (a). The silver film is, obviously, highly reflective, with up to 98% of incident energy redirected to the detector, and in this work it represents the non-absorbing case. On the other hand a flat polished silicon wafer exhibits the expected ∼ 35% Fresnel reflectance and exemplifies the baseline non-textured air-Si interface. In line with results given in prior sections, nanotextured black silicon is highly anti-reflective, hence specularly reflected energy amounts to no more than 1% throughout the visible spectral region. However, with the application of 50 nm diameter Au nanoparticles the observed reflectance is slightly increased, which can be attributed to Mie scattering as a result of the plasmonic excitations.

Figure 1.41 (a) also shows the reflectance of two distinct gold nanoparticle decorated black silicon absorbers, prepared using different concentration colloidal particle suspensions. Scanning electron microscopy inspection of the resultant surfaces, illustrated on the left side of Figure 1.41 (b), show that applying particle suspensions with concentrations close to the optimal surface coverage 7.2×10^8 particles/cm^{-2} produces a uniform distribution, whereas densities in excess of that result in agglomerated gold micro-island formation. These in turn give rise to additional reflectance which can be expected to negatively affect absorber performance. The plasmonic mechanisms underlying nanoparticle contribution to the overall optical behavior of the composite absorbers become apparent when their reflectance spectra are normalized to that of plain black silicon, with the result shown in Figure 1.41 (b). The black silicon-normalized reflectance spectra are reminiscent of the extinction exhibited by spherical gold nanoparticles, however, show substantial redshifts from the ∼ 530 nm resonance position expected when their diameters are 50 nm. Such a resonance shift can be attributed to hybridized collective resonant modes of nanoparticle assemblies [168] or to mirror charge

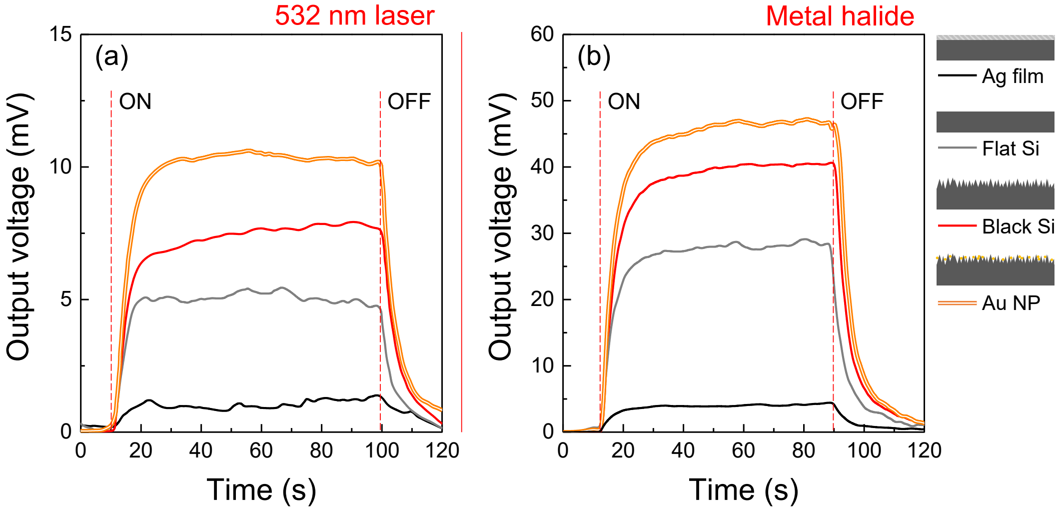

Figure 1.42: Thermoelectric module voltage output when different absorbers are used as the hot contact under (a) monochromatic 532 nm wavelength laser, and (b) broadband metal halide lamp illumination [167]. Note the different voltage axes scales of the two panels. Thermoelectric power generation experiments were performed at Yokohama National University by the research group under supervision of Assoc. Prof. Yoshiaki Nishijima.

interactions due to high refractive index silicon proximity [169]. The latter mechanism in particular is in good accordance with the observation that uniform nanoparticle coverage results in a somewhat stronger redshift, since interaction with the silicon substrate would be more pronounced is such a case.

Thermophotovoltaic response of the prototype device equipped with different absorbers and under different illumination conditions is illustrated in Figure 1.42. The overall trend in voltage response is the same for 532 nm wavelength laser as well as for broadband metal halide illumination, shown in panels (a) and (b) respectively, just with a different overall magnitude of the effect owing to variance in source powers. Regardless of the choice of absorber a linear relationship between incident luminous power and thermogeneration voltage is observed, however, the conversion efficiency slope is predictably absorber-dependent. Evidently the highly reflective silver mirror surface prevents substantial buildup of a heat gradient, estimated to be below 0.2 K in this case, and results in low thermoelectric conversion efficiency. Silicon, on the other hand, is expected to absorb around 65% of visible wavelength radiation, and provides a decent baseline efficacy.

Anti-reflective black silicon nanotexturing results in an increase of the thermoelectric output voltage by roughly 50%, all of which can be accounted for by the almost total elimination of reflection losses at the silicon-air interface. Application of a uniform Au nanoparticle coating gives rise to voltage output increase by up to an additional 50%, on top of the prior gains due to reflectance suppression of black silicon. While the absolute increase of output voltage due to Au nanoparticle augmentation was similar regardless if absorbers were exposed a lamp or a laser, the relative increase in the broadband case is half of that observed for monochromatic illumination. This likely relates to the limited bandwidth of plasmonic effects being better matched to the 532 nm wavelength.

More detailed results of plasmonic thermoelectric conversion efficiency enhancement dependence on the size and density of Au nanoparticles overlaying the black silicon texture is

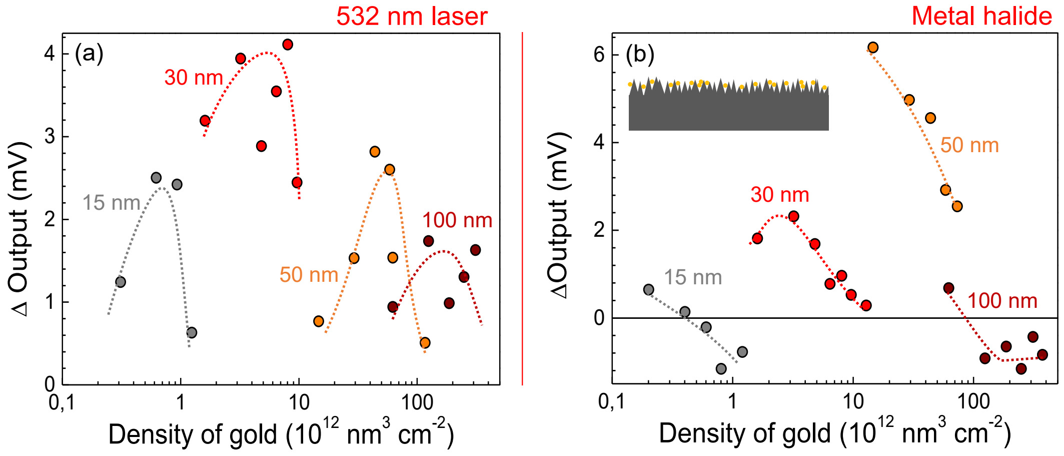

Figure 1.43: Thermoelectric voltage output increase under (a) monochromatic 532 nm wavelength laser, and (b) broadband metal halide lamp illumination, plotted against density of gold deposited onto black silicon *via* colloidal Au nanoparticles of different diameters [167]. Thermoelectric power generation experiments were performed at Yokohama National University by the research group under supervision of Assoc. Prof. Yoshiaki Nishijima.

illustrated in Figure 1.43. Here, increases in thermoelectric voltage output above the value obtained using a plain black silicon absorber are plotted against the estimated volume of gold overlaying the surface. In the case of monochromatic 532 nm laser illumination, shown in Figure 1.43 (a), a sharp critical thermoelectric voltage dependence on gold density is observed regardless of the nanoparticle diameter. The initial rise in voltage output with increased particle concentrations can be attributed to enhanced plasmonic absorbance. On the other hand, the subsequent drop-off can be explained as resulting from the redshift of plasmonic peak out of the 532 nm laser wavelength due to particle aggregation, and in part by an overall increase in diffuse reflectance. Best thermophotovoltaic conversion results are observed when 30 nm diameter gold nanoparticles are used, likely due to their localized surface plasmon resonances having the best overlap with the laser wavelength.

Plasmonic enhancement of thermoelectric conversion efficiency under metal halide lamp illumination, shown in Figure 1.43 (b), exhibits a more complex dependence on both particle size and gold coverage. First of all, either insufficient or excessive amounts of gold result in negligible and even negative changes in output voltage. Next, when illumination is broadband 50 nm diameter nanoparticles offer the highest enhancement, likely due to the plasmonic peak shifting towards the near-infrared, as shown in Figure 1.41 (b), where optical absorbance in silicon starts to diminish. Lastly, the acute gold density dependence observed for each nanoparticle size under monochromatic illumination is substantially less pronounced in the broadband case.

While experimental results clearly show improvements in plasmonically enhanced absorber performance, any understanding as to the underlying optical effects operating at the nanoscale can be only conjectured from them. Numerical simulations can help in remedying this gap in knowledge by providing somewhat indirect, however, very intuitive visualizations of light-matter interaction with the various nanotextures. To this end calculations were performed on the swinSTAR supercomputer at Swinburne University of Technology using the "FDTD Solutions" software package (Lumerical Solutions Inc). 3D renderings of the basic ~ 250 nm average spike height black silicon texture were prepared based on scanning electron microscopy images using methods described in Section 1.2.3. Stochastic 50 nm diameter gold nanoparticle application onto black silicon was simulated through their random initial placement, followed by a scripted dynamical overlap detection mechanism. A plane wave broadband visible-to-near-IR wavelength source was used for excitation of the 1.5 μm^2 surface area segment. The simulation area was laterally terminated using periodic boundary conditions and transversely by perfectly matched layers. Calculations were performed for two orthogonal polarizations of incident radiation, and their results were subsequently averaged and normalized to the 1.5 air mass solar radiation spectrum [150].

Visualizations of the black silicon surfaces with and without nanoparticle decoration are provided in Figure 1.44, along with FDTD simulation results of absorbance rates and electric field intensity distributions. Solar radiation absorbance rates are substantially increased above that of a flat wafer by black silicon nanotexturing, with roughly 80% of visible wavelength photons absorbed in the spiky upper layer. Also, light is scattered by the irregular surface and forms up to 4 times increased field intensity pockets in between nanotexture features. In the plasmonically augmented case metallic nanoparticles exhibit an up to two orders of magnitude higher absorbance per unit volume than that of silicon, and, furthermore, create absorbance hot-spots at their point of contact with the semiconductor. This can be traced back to the strong electric field enhancement in the vicinity of Au due to excitation of localized

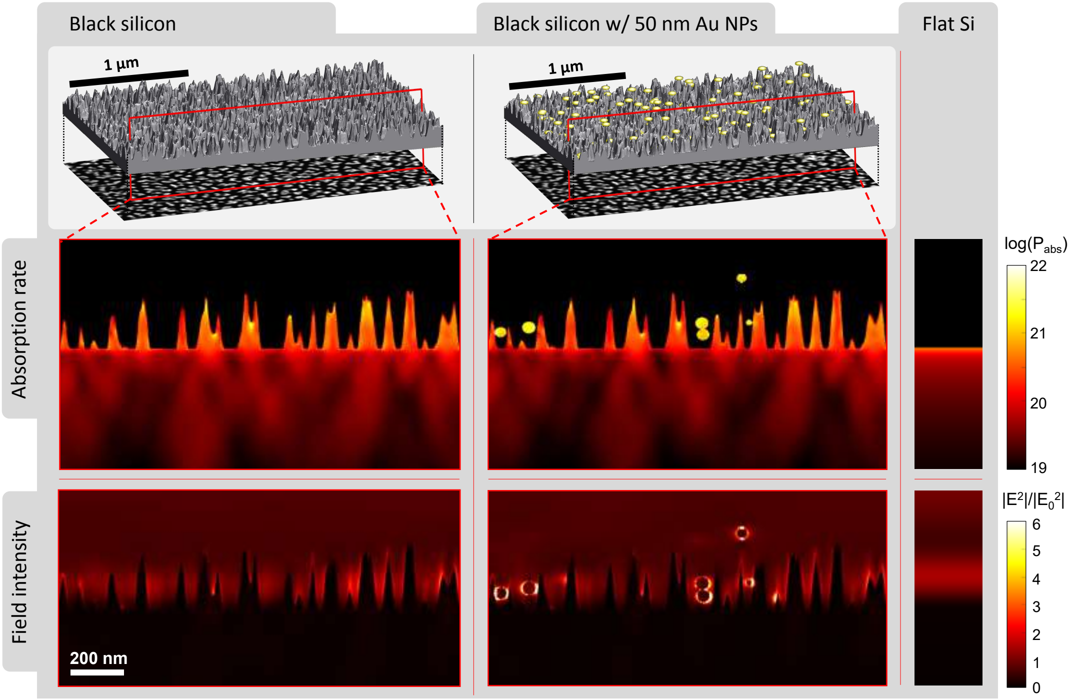

Figure 1.44: FDTD simulations of broadband solar radiation interaction with plain and 50 nm diameter Au nanoparticle decorated black silicon absorber surfaces. Top panels show the 3D renderings used in the calculation. Middle and bottom row panels respectively show cross-section plots of absorbance rate (logarithmic scale) and relative optical field intensity (linear scale), both integrated over the 1.5 air mass solar spectrum. Equivalent results for a flat silicon surface are given for reference. Simulations were performed using the swinSTAR supercomputer at Swinburne University of Technology.

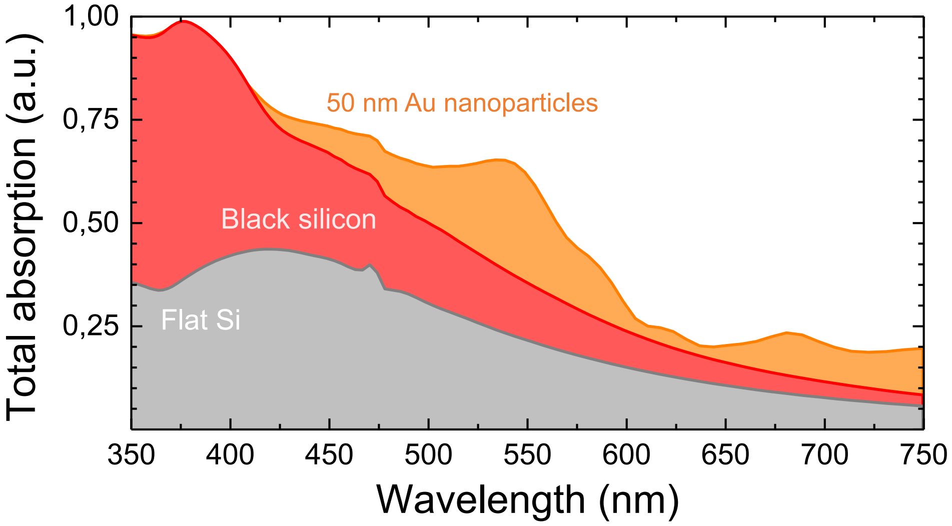

Figure 1.45: FDTD simulated solar radiation absorption, calculated up to a 5 μm depth under the surfaces of flat silicon, black silicon and 50 nm Au nanoparticle decorated black silicon. Simulations were performed using the swinSTAR supercomputer at Swinburne University of Technology.

surface plasmons, visible in the lower left panel of Figure 1.44.

Calculated visible wavelength absorbance spectra obtained by spatial integration over the simulation volume, given in Figure 1.45, illustrate the additive nature of nanotexturing and plasmonic augmentation to the overall increase in luminous energy uptake. Here the unexpected absorption drop-off at longer wavelengths is a result of the limited integration depth, extending only 5 μm below the surface. Evidently, semiconductor nanotexturing provides an improvement through broadband light coupling into silicon, whereas gold nanoparticles absorb and dissipate optical energy as heat at the expected ~ 530 nm wavelength as well as at near-IR, where Si absorption is weak. Therefore, it can be deduced that application of plasmonic nanoparticles can be expected to increase the amount of heat generated, provided that metal coverage is low enough as to not substantially interfere with reflectance suppression. Of course, such purely photonic simulations cannot provide information on heat generation and flow underlying thermoelectric energy conversion, however, such results can be used as stationary initial conditions for follow-up heat transport simulations.

To summarize, this work shows how black silicon can be applied as an affordable high efficiency absorber to uses in thermoelectric power conversion. Since in this case heat generation is of primary concern, absorption enhancement methods such as nanoparticle coating, which would be untenable in photovoltaic situations, can be readily harnessed and yielded an up to 50% improvement in output voltage. While the efficiency of the prototype device shown here is below 2%, further improvements could be obtained to gainfully convert up to 6% of incident luminous energy by using solar concentrator schemes to increase the overall operating temperature, and encapsulation in a vacuum to prevent convective losses [155]. Ultimately, however, regardless of absorber efficacy, performance of such a device will be limited for the foreseeable future by the lack of high figure of merit thermoelectric materials. Therefore, presently thermoelectric conversion can, at best, be used to compliment other more productive solar energy harvesting approaches.

1.4.2 Hybrid photo-voltaic/thermal conversion cell

Presently, the vast majority of photovoltaic methods of solar-to-electric energy conversion rely on the optical absorbance of silicon. It generally exhibits acceptable rates of photon uptake in the visible optical region, and remains reasonably adequate well into the near-IR, even if considerable optical thicknesses are needed to compensate for its indirect band gap at that range. However, as was shown in Figure 1.39, the fraction of luminous power converted to electric energy sharply drops to either side of the 1.12 eV ($\lambda \approx 1100$ nm) band gap due to either thermalization or transmittance losses. Yet, while no single semiconductor material can effectively harness the broadband solar spectrum, conventional detailed balance limitations can be sidestepped by spectrally selective combination of different conversion materials and systems.

Multijunction solar cells, composed through sequential stacking of different semiconductor *p*-*n* junctions by band gap, represent some of the earliest and currently most successful attempts at efficiency enhancement [151]. Still, using presently available materials and practicable numbers of junctions a substantial energy loss is incurred through device heating and residual infrared wavelength transmittance. The mostly thermal nature of the two aforementioned effects implies that a thermoelectric approach for converting this wasted energy into electric power would be the obvious choice. Hence, it is unsurprising that in recent years several attempts in augmenting energy output of dye sensitized [170, 171] or perovskite solar cells [172] using infrared absorbers and thermoelectric converters have been reported.

In this work, conducted in collaboration with the research group headed by Assoc. Prof. Yoshiaki Nishijima at Yokohama National University, a prototype hybrid photovoltaic and thermoelectric device, capable of utilizing the entire solar spectrum, was created and tested [173]. A black silicon based solar cell was used as the first stage solar-to-electrical power converter. Any residual transmitted infrared radiation was taken up by a GeSn alloy rear-side absorber and converted into thermal energy which, along with waste heat from the silicon solar cell, was used to drive a Seebeck element. Absorbance behavior of the constituent device layers was illustrated by means of finite-difference time-domain simulations.

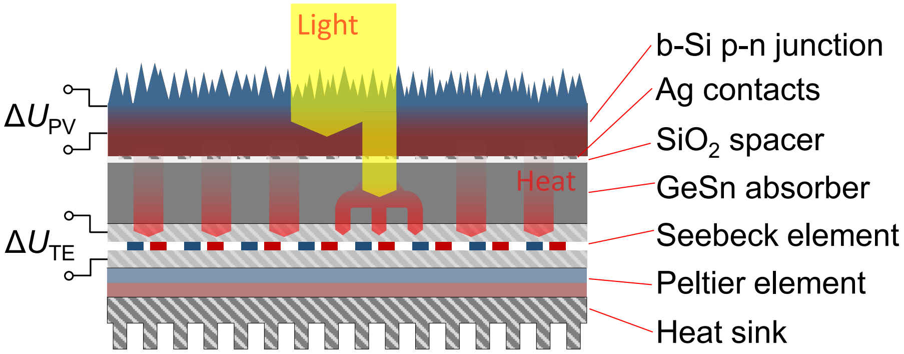

Figure 1.46: Sketch illustrating the hybrid device which, by combining photovoltaic and thermophotovoltaic electric energy generation, harnesses the entire breadth of the solar radiation spectrum [173]. Photovoltaic charge separation is done at a *p*-*n* junction realized in a black silicon wafer, whereas radiation transmitted through Si and patterned Ag electrodes is captured in a GeSn alloy absorber, used as the hot contact for a thermoelectric Seebeck element. Device was assembled at Yokohama National University by the research group under supervision of Assoc. Prof. Yoshiaki Nishijima.

The hybrid solar radiation energy harvesting device prototype is schematically illustrated in Figure 1.46. A simple realization of a black silicon solar cell comprises the upper section of the device and is directly exposed to incident radiation. Anti-reflective nanotexturing of a *p*-type silicon wafer top surface was performed using the reactive ion etching process described in Section 1.2.1. The *p-n* junction for photogenerated charge separation was formed using a dopant diffusion process. To that end a phosphorus based doping agent EPLUS SC-909 (Tokyo Ohka Kogyo Co., Ltd.) was spin-coated onto the intrinsically boron-doped black silicon surface at 3500 rpm for 20 seconds. Diffusion was conducted by way of a two-step annealing process - initially 60 s at 200 °C followed by a longer 10 minute duration heat treatment at a 950 °C temperature. After the anneal, oxidized surface layers were stripped by etching in a 1% aqueous HF solution for 15 minutes and patterned Ag electrodes were thermally evaporated on both sides of the wafer.

Subsequent fabrication steps involved creation of an infrared radiation absorption module on the photovoltaic cell rear-side to capture any luminous energy transmitted through Si and convert it into heat. Leakage current related deterioration of solar cell electrical properties due to absorber deposition was avoided by overlaying rear-side patterned Ag contacts with an insulating 100 nm thickness SiO_2 layer. A GeSn alloy, with an approximately 4:1 atomic ratio composition, was chosen as the infrared absorber material [174]. The 4 μm thickness GeSn film was coated onto the SiO_2 spacer layer by thermal evaporation of a germanium and tin mixture placed in the same crucible source. Resultant hybrid structure was mounted onto a Bi-Te based commercially available Seebeck element TEP1-1264-1.5 (Thermonamic Electronics Corp., Ltd.), same type that was used in creating the device described in Section 1.4.1. Thermal contact with the GeSn alloy film was mediated using vacuum grease X-23-7877 (Shin-Etsu Chemical Co., Ltd.). Thermal energy due to infrared radiation absorbed in GeSn, as well as waste heat from the photovoltaic cell itself, is converted into electrical power by the thermoelectric module, thereby boosting the total efficiency of the system. Lastly, the optional Peltier element, sandwiched between the cold contact of the Seebeck element and a metal heat sink, was used for temperature stabilization during characterization measurements.

Initial characterization of the composite full solar spectrum absorber was conducted on its simplified realization, fabricated on a flat crystalline Si surface by evaporating a 4 μm thick GeSn film which was subsequently overlaid with a 1 μm layer of silicon *via* magnetron sputtering. The deposited top amorphous silicon layer was then nanotextured using reactive ion etching to obtain a gradient effective refractive index anti-reflective surface. An isometric scanning electron image of the resultant absorber stack is shown in Figure 1.47 (a), whereas the atomic composition of layers has been evaluated using energy-dispersive X-ray spectroscopy (EDS) and is visualized in Figure 1.47 (b). Evidently, despite part of the Si material being consumed during reactive ion texturing, the top layer is comprised of silicon, geared towards visible-to-near-IR radiation coupling and absorption.

Conversely, the underlying GeSn alloy was chosen due to its silicon-complimentary near-to-mid-IR absorbance properties. Constituent components Ge and Sn exhibit band gaps of 0.67 eV and 0 eV respectively, whereas their solid solution $Ge_{0.85}Sn_{0.15}$ is intermediate, with a band gap somewhere between 0.2 eV and 0.4 eV [174]. EDS data shows that alloy film composition shifts from an initial $Ge_{0.65}Sn_{0.35}$ to $Ge_{0.93}Sn_{0.07}$ throughout the layer thickness. This results from the rapid evaporation of Sn, which has both a lower melting point and a lower vapor pressure than Ge for a given temperature, and its gradual removal from the predominantly Ge containing crucible over the course of the deposition. Hence, the GeSn absorber is expected to exhibit a progressively decreasing band gap, which aids in creating more evenly distributed absorbance induced heating throughout the film volume, thereby

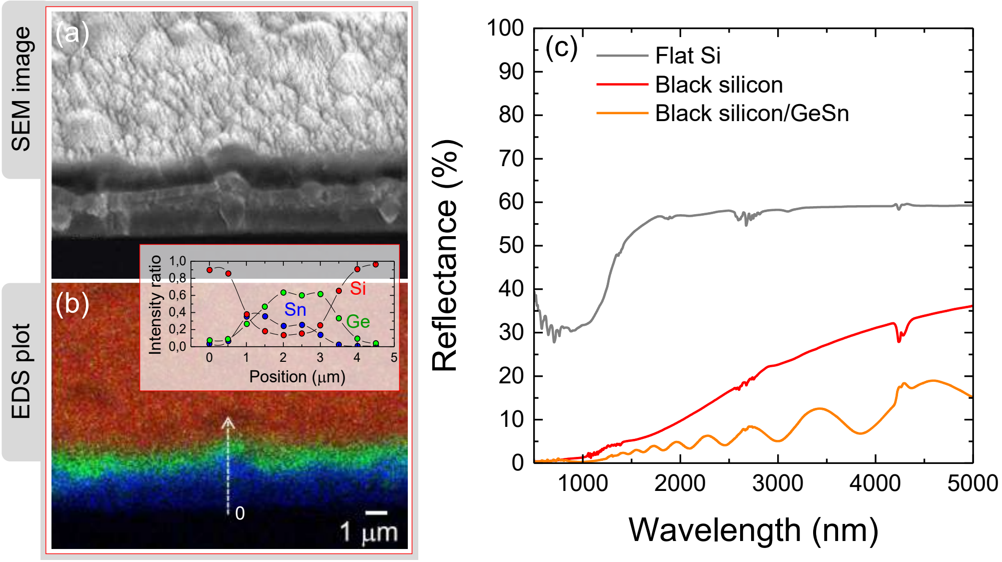

Figure 1.47: (a) Scanning electron microscopy image of a thin-film solar spectrum absorber comprised of a 1 µm thick black silicon top layer and 4 µm of GeSn alloy underneath, deposited onto flat Si [173]. (b) Energy-dispersive X-ray spectroscopy representation of image (a). Elemental composition along the layer thickness is given in the inset. (c) Broadband specular reflectance spectra of black silicon with a GeSn absorber layer, plain black silicon as well as flat Si wafer for reference. All characterization was performed at Yokohama National University by the research group under supervision of Assoc. Prof. Yoshiaki Nishijima.

helping avoid heat leakage to overlaying silicon.

Specular reflectance spectra of the black silicon and GeSn alloy composite absorber is given in Figure 1.47 (c), along with that of typical plain black silicon and a flat Si wafer for reference. Predictably, addition of a narrow band gap absorber results in a substantial decrease in reflected infrared radiation, achieved without compromising anti-reflectance at visible wavelengths. Indeed, visible wavelength reflectance suppression of the composite absorber remains equivalent to that of a black silicon wafer surface. The peculiar reflectance oscillations exhibited by the composite absorber at infrared wavelengths are most likely due to multiple reflections from air/Si and Si/GeSn interfaces. Therefore, it can be concluded that optical losses stem mainly from infrared radiation which falls within the Si band gap and fails to couple into the GeSn film, where it could potentially be absorbed.

Further investigation on how the constituent black silicon and GaSn alloy layers contribute to the overall absorber optical behavior was conducted by means of FDTD simulations. For this purpose the swinSTAR supercomputer was used to run calculations in a commercially available "FDTD Solutions" software environment (Lumerical Solutions Inc). Surface topology of the black silicon nanotexture was again rendered according the method described in Section 1.2.3, and complex permitivity values reported in the literature were used in defining silicon [41] and GeSn alloy [174] optical properties. For simplicity, composition of the infrared absorber film was considered uniform and defined as $Ge_{0.85}Sn_{0.15}$ throughout, based on the average determined by EDS in Figure 1.47 (b). The simulation region spanned an 2.5×2.5 µm^2 area segment and in the lateral directions was truncated assuming periodic repetition, whereas longitudinally it was terminated using perfectly matched layer boundary conditions. A linearly polarized plane wave broadband light source was used to probe the absorber segments.

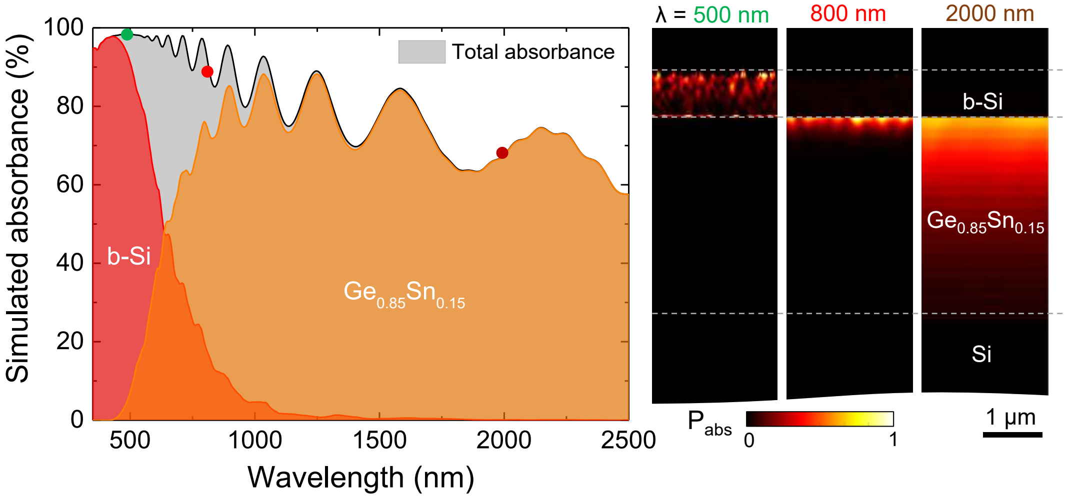

Figure 1.48: FDTD simulation results for the black silicon and GeSn alloy layered absorber shown in Figure 1.47. Left panel depicts the simulated absorbance spectrum of the composite absorber, with contributions due to 1 μm thickness black silicon and 4 μm thickness $Ge_{0.85}Sn_{0.15}$ films plotted separately. Right panels show spatial distributions of absorbance at three select wavelengths. Simulations were performed using the swinSTAR supercomputer at Swinburne University of Technology.

Figure 1.48 depicts the FDTD simulation results of optical absorbance in a thin-film black silicon with a GeSn underlayer, defined according to electron microscopy images in Figure 1.47. As can be seen in the left panel, visible wavelength absorbance occurs in silicon, whereas the vast majority of infrared radiation gets taken up by the GeSn alloy. Overall the simulated absorbance spectral dependence closely matches the experimental reflectance shown in Figure 1.47 (c), and even exhibits the same interference derived oscillations. Thereby numerical investigation corroborates that optical losses are for the most part due to reflectance at the Si/GeSn interface.

Spatial distribution of absorbance rates throughout the thickness of the black silicon/GeSn alloy stack are shown in the right panel of Figure 1.48 for 500 nm, 800 nm and 2000 nm wavelengths. Evidently, the 1 μm thickness top black silicon layer is mostly adequate in absorbing visible wavelength radiation, as is exemplified by the $\lambda = 500$ nm plot. Similarly, near-IR photons, with energies well below the band gap of Si, are absorbed by the 4 μm GeSn film, so that barely any radiation with wavelengths at or below $\lambda = 2000$ nm gets transmitted to the underlying Si wafer. However, at the onset of near-IR where photon energy is still sufficient for induction of interband transitions in Si, most radiation is transmitted through the thin top black silicon layer and absorbed in GeSn, as illustrated by the intermediate $\lambda = 800$ nm plot. So, in a solar power harvesting device this energy would be converted to electrical power not photovoltaically, but by means of the much less efficient thermoelectric process, driven by heat generated *via* electron thermalization. Therefore, to obtain higher solar-to-electrical power conversion efficiencies, the simplified stack design in Figures 1.47 and 1.48 has to be modified so that absorbance in silicon is maximized.

In the absence of selective light trapping mechanisms capable of confining radiation with wavelengths below $\lambda \sim 1100$ nm in Si, the most straightforward way of maximizing the solar energy fraction available for photovoltaic conversion is by increasing the optical thickness

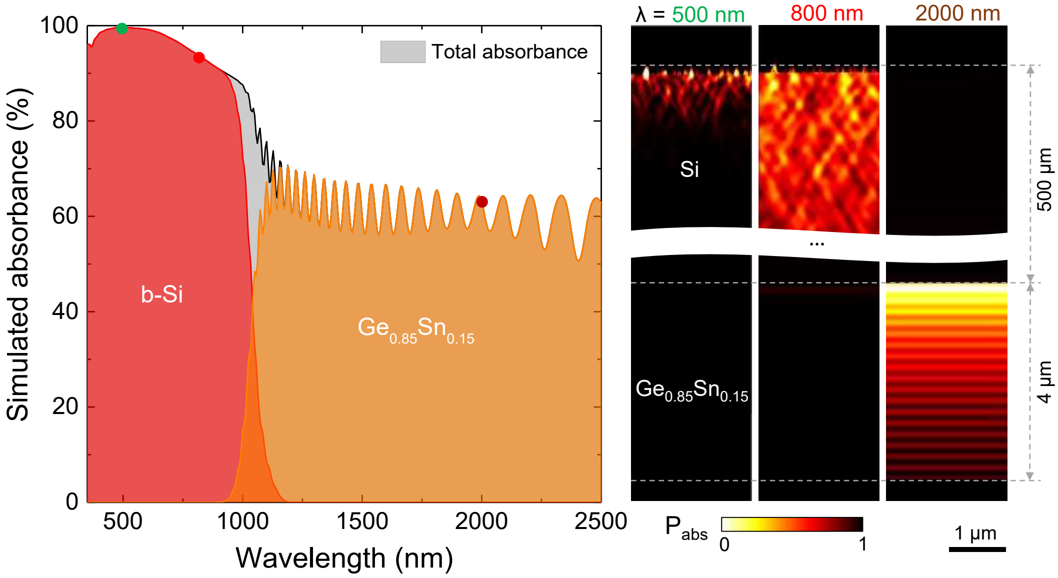

Figure 1.49: FDTD simulation results for the hybrid photovoltaic/thermovoltaic solar cell structure. Left panel shows the simulated absorbance spectrum of the hybrid solar cell, with contributions due to the 500 µm thickness black silicon wafer and a rear-side 4 µm thickness $Ge_{0.85}Sn_{0.15}$ absorber film plotted separately. Right panels show spatial absorbance distributions of top black silicon layer and bottom $Ge_{0.85}Sn_{0.15}$ at three select wavelengths. Simulations were performed using the swinSTAR supercomputer at Swinburne University of Technology.

of silicon. As was previously shown in Figure 1.10, an at least 100 µm optical path length is needed to take up most of the near-IR photons capable of inducing phonon-assisted band gap transitions in silicon. In light of this it becomes obvious why the hybrid photo-voltaic/thermal conversion cell prototype, sketched in Figure 1.46 and described in prior paragraphs, was created using a 500 µm thickness silicon wafer.

Photonic FDTD simulation results for the black silicon and GeSn alloy absorber stack used for creating the hybrid photo-voltaic/thermal solar cell are shown in Figure 1.46. In this case simulations were conducted separately for the two opposing black silicon and GeSn surface segments, and an estimation of their mutual interaction through the 500 µm wafer was obtained by applying the Beer-Lambert law. As can be seen from the absorbance spectrum in the left panel of Figure 1.46, a substantially larger fraction of the incident energy is taken up by silicon compared to the case in Figure 1.48. On the other hand, the overall simulated reflectance at infrared wavelengths noticeably increased, likely due to the presence of interfaces with a low refractive index SiO_2 electric insulation spacer, sandwiched between silicon and GeSn. The free spectral range of reflectance oscillations is likewise consistent with multiple reflections in the 100 nm thickness SiO_2 film. Spatial distributions of absorbed optical power, given in the right panel of Figure 1.49, illustrate how photon uptake shifts from the black silicon surface for $\lambda = 500$ nm wavelengths, to being distributed over bulk Si when $\lambda = 800$ nm. Finally, only radiation that falls within the band gap of Si reaches and is absorbed by the GeSn layer.

Figure 1.50 summarizes experimental performance results of the prototype hybrid solar energy harvesting device when it is exposed to $E_e = 72.8\ \mathrm{mW/cm^2}$ total irradiance of combined halogen and metal halide light source illumination, which loosely approximates the solar

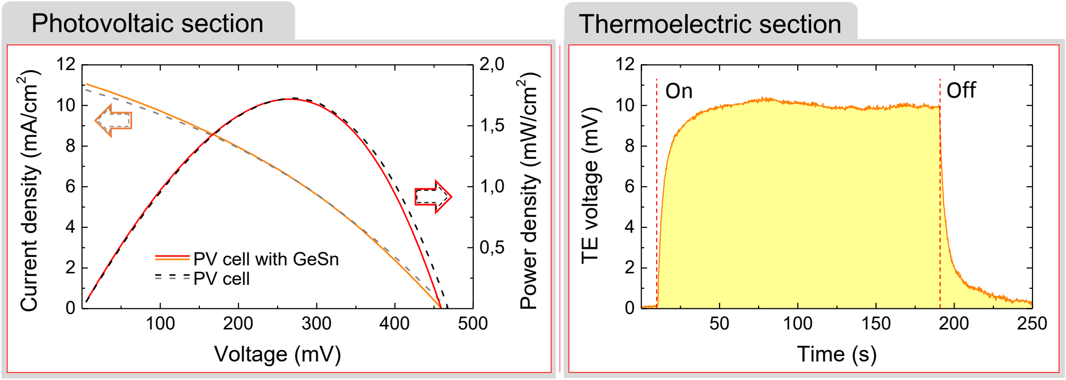

Figure 1.50: Photovoltaic and thermoelectric output of the different hybrid solar cell segments [173]. Separate current-voltage and power curves are given in the left panel for equivalent photovoltaic cells with and without a deposited GeSn alloy absorber. Right panel shows thermoelectric voltage output transients after light is switched on and then off. Incident illumination irradiance is $E_e = 72.8\ \mathrm{mW/cm^2}$. The hybrid solar cell device was assembled an characterized at Yokohama National University by the research group under supervision of Assoc. Prof. Yoshiaki Nishijima.

spectrum [173]. Photovoltaic and thermoelectric sections are able to work separately and, as can be seen from the current-voltage and power curves, the 100 nm thickness SiO_2 insulator spacer is adequate for preventing the GeSn alloy infrared absorber film from interfering with silicon solar cell operation. Under the aforementioned irradiance conditions the photovolataic section yielded an open circuit voltage of $U_{OC} = 0.46$ V, a short circuit current density of $I_{SC} = 11.06\ \mathrm{mA/cm^2}$ and a maximum power $P_{max} = 1.72\ \mathrm{mW/cm^2}$, which corresponds to a fill factor $FF = 0.34$, hence, an admittedly very modest photovoltaic conversion efficiency of 2.4%. Also, thermoelectric conversion gave rise to an additional $U_{TE} = 10.6$ mV voltage, a current density of $I_{TE} = 12.2\ \mathrm{mA/cm^2}$ and a maximum power $P_{max} = 0.129\ \mathrm{mW/cm^2}$, thereby augmenting the overall conversion efficiency of the device by a further 0.2%.

This first proof-of-concept demonstration was only able to achieve a total optical-to-electrical power conversion efficiency of 2.6%, however, through further optimization of dopant diffusion protocols and by passivating the anti-reflective nanotexture substantial improvements would surely be achieved. Furthermore, operation under concentrated illumination would benefit from thermal energy recovery to a much larger extent, and the Seebeck element could potentially contribute to junction cooling. The key finding in this work, however, is that infrared radiation transmitted through silicon can be harvested without compromising photovoltaic generation efficiency. Gains due to thermal energy uptake reported here are small due to the presently limited effectiveness of available thermoelectric materials. Still, harvesting the infrared part of the solar spectrum and recovery of waste heat would prove worthwhile if better thermoelectrical conversion methods were to emerge.

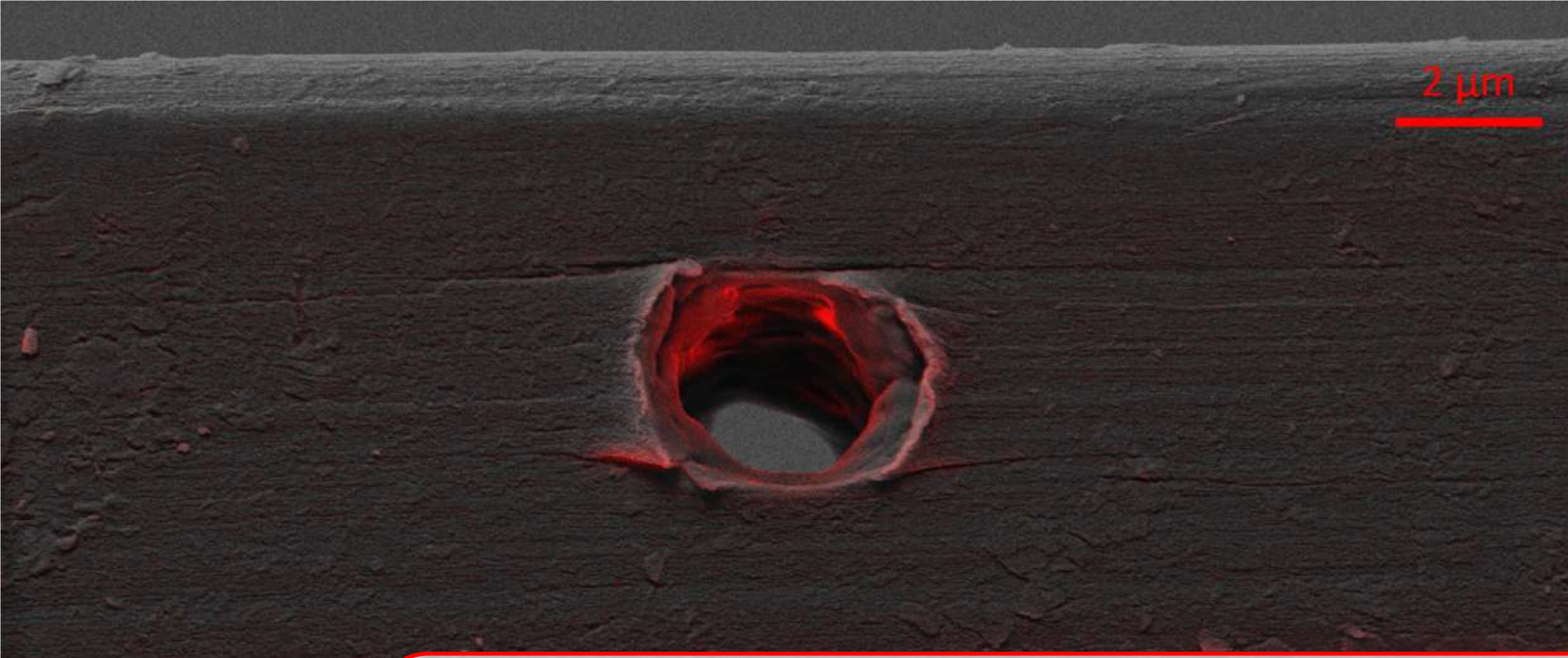

2. Optical biomaterials

The practically inexhaustible variety of forms and functions exhibited in the biological realm has been a longstanding source of inspiration for human technological achievement, and is presently termed biomimetics [175]. Natural biodiversity becomes even more fascinating considering that it is all, for the most part, comprised of a very limited range of amino acids and monosaccharide units. Indeed, much like phenotypes of biological systems are subject to natural selection, so too must the presently ubiquitous biochemical machinery have been selected as the most adaptable, energetically affordable and versatile, since it evidently out-competed all of its alternatives.

It is unsurprising then, that emulation of DNA and protein based self-assembly fabrication methods is of immense interest as both a fundamental problem and a challenge to create technology that blends seamlessly with human physiology. While full bottom-up nanoscale control is still out of reach, use of present top down fabrication techniques is necessitated by an immediate demand for flexible and biocompatible biomedical diagnostic devices. For such applications photonic approaches, due to their high-sensitivity, low-power consumption and unintrusiveness, are particularly well suited. Similarly, the search for a favorable biopolymer platform has found much merit in silk fibroin [176], which, in addition to optical transparency, exhibits mechanical properties and water solubility that can be manipulated *via* their secondary protein structure. Of course, control over light propagation often calls for subwavelength-scale precision in defining functional components, which only a select few techniques, laser processing and electron beam lithography being among them, can provide.

This chapter focuses on the optical properties biopolymer materials, the natural nanotextures they comprise, as well as methods of applying them in the technological domain for creation of functional photonic structures. It begins with a brief outline illustrating select examples of evolutionarily optimized nanotexturing, which leads into a detailed description of original research performed on structural and optical characterization of multifunctional cicada wings. Further on, a concise description on the use of biopolymers for photonic device fabrication is provided, with a particular emphasis on silk fibroin protein-based platforms. Subsequent original research centers on the broadband electromagnetic radiation response of natural silk fibers (pictured in the title figure with a hole shot through it by a laser), as well as on nanopatterning silk biopolymer films using laser and electron beam lithographies.

2.1 Applications of nanotextures in nature

Genesis of the Earth's biosphere has been traced back 4.28 billion years, and is now understood as having arisen virtually instantaneously after the planet was formed 4.54 billion years ago [177]. Over the vast geological timescales since its humble beginnings, life has flourished through ruthless competition for maximum fitness at every level – from single biomolecules, cells, organisms and up to entire ecosystems – which gave rise to the presently ubiquitous state of the biological realm. The complexity of processes underlying life and that of the emergent organisms themselves is so great, however, that only in the last decades have human tools and methods achieved the sophistication required to investigate them at a fundamental level. Resultant findings revealed not only curious realizations of phenotypic adaptation in specific organisms, but also convergently evolved recurring design approaches from disparate lineages, hinting at optimal solutions to certain functional requirements or, at the very least, shared developmental constraints [178].

Even when vast swaths of important discoveries in the fields of biochemistry and pharmacology are disregarded, the amount of intriguing findings relating to biomimetics is still remarkable [179]. For instance, materials science has only recently been able to devise a spinning process that produces protein fibers approaching the strength of spider dragline silk, which, despite being a polypeptide, exhibits mechanical properties rivaling that of toughest synthetic fibers [180]. Resilin is another protein-based biopolymer, similar and often superior to high resilience rubber compounds, that, due to its low stiffness and high strain, can reversibly stretch to three times its original length and thus store tensile energy instrumental in enabling flight and jumping capabilities of insects [181]. Similarly, the methods by which marine sponges mineralize complex rigid silica glass architectures at ambient temperatures using organic filament templates [182], or how cephalopods can rapidly and extensively manipulate their skin papilla to form millimeter-scale 3D shapes and textures for the purposes of camouflage [183] are presently under intense investigation. Engineering-focused fields have also found much to imitate in the natural world, such as how the aligned microscale riblet structures covering the skin of sharks, known to reduce drag in the turbulent-flow regime [184], have inspired coatings and fabrics that improve aerodynamic or hydrodynamic performance of aircraft and Olympic swimmers, respectively. Another example is how development of hook and loop fasteners, better known under the brand name "Velcro", has been sparked by the microscopic hook system that burdock plant seeds use to attach themselves to animal fur for dispersal. Furthermore, reversible dry adhesion exhibited by the leg attachment pads of insects and certain lizards, such as geckos [185, 186], allow for locomotion over vertical surfaces, and has been subject to numerous attempts at imitation.

From a nanotechnology point of view, the amount of functional texturing adaptations of biological surfaces, of primary interest here, is likewise so vast and varied that any attempt at a comprehensive overview would end up being anything but concise. In general, nanotextures in nature fulfill a broad range of specific purposes and their combinations which include: optical functions like anti-reflectance, crypsis, signaling, thermoregulation; mechanical roles such as attaining specific tribological performance or exerting control over wettability by water and oil; as well as providing anti-biofouling or bactericidal activity. One way to illustrate the remarkable degree of functional optimization attainable by evolutionary processes is to note that each of the anti-reflectance mechanisms, discussed in Section 1.1 of the preceding chapter, can be found in the natural world, as illustrated in Figure 2.1.

Multilayer stacks are among the most prevalent of photonic structures employed by various organisms, however, due to their light incidence angle-dependent performance, are rarely used as a main mechanism for reflectance suppression. Instead, they are most often utilized to enhance the efficacy of other anti-reflectance mechanisms, to attain optical contrast filtering as exhibited by the eyes of a horsefly [193], as well as to produce iridescent colors [194], presumably, for camouflage or sexual signaling purposes. When it comes to the latter pair of functions, exoskeletons of *Coleoptera* beetles offer a particularly wide range of multilayer reflector application examples [187], one of which is summarized in Figure 2.1 (a). Here, the striking coloration of the *Cicindela scutellaris* insect carapace is achieved by light interference

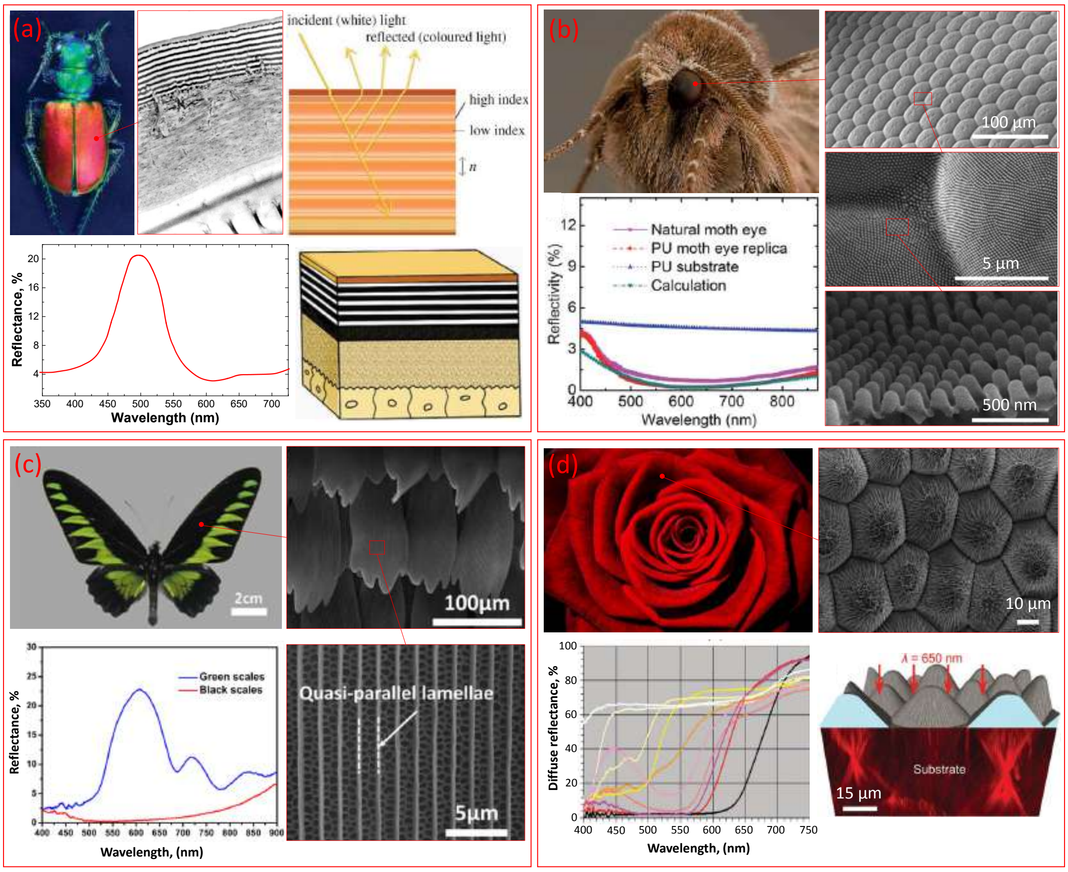

Figure 2.1: Select examples of reflectance control mechanisms employed by biological organisms. (a) Multilayer reflector on the exoskeleton of a *Cicindela scutellaris* beetle [187]. Clockwise shown are: cross-section electron micrograph, optical schematic, a sketch of exocuticular reflector physiology, and a normal incidence reflectance spectrum [188]. (b) Anti-reflective gradient effective refractive index layer-endowed compound eyes of an *Attacus atlas* moth [189]. Images on the right side show the papilla array nanotexture. Spectra in the lower-left corner show reflectances of the moth eyes as well as their poly(urethane) replicas. (c) Anti-reflective grating-like light trapping structures on the wing scales of a *Trogonoptera brookiana* butterfly [190]. Scanning electron images of black scales and their surface nanostructures are shown on the right. Lower-left depicts a reflectance spectra comparison between black and green wing regions. (d) Geometrical ray trapping texture of a rose petal surface [191]. Top-down scanning electron microscopy image and a 3D visualization of light propagation beneath the microtexture are given on the right. Lower-left panel plots the diffuse spectra of roses with colors represented by a corresponding curve [192].

from parallel alternating refractive index layers of non-chitinous epicuticle laminated with ultra-thin layers of melanin, and spectrally manifests as a prominent reflectance peak in a viewing angle determined wavelength region.

However, when maximal anti-reflectance of natural surfaces is the primary concern, gradient effective refractive index layer nanotextures tend to be preferable, with the most well known example being the eyes of night-active moths [189], illustrated in Figure 2.1 (b). As revealed by scanning electron microscopy imaging, each of the microscale ommatidia making up the compound eye of the insect is covered by a closely-packed array of subwavelength scale tapered pillars, which collectively serve to couple incident light into the vision organ. This fulfills a dual purpose of increasing the photosensitivity in a dim environment as well as drastically suppressing reflections that could render the insect visible to potential predators [10]. A different method, geared towards augmenting the fraction of light absorbed by pigmentation, is exploited by certain species of butterfly, where deep black coloration of wing surfaces is attained by way of a light trapping mechanism akin to that of anti-reflective gratings [190, 195]. Figure 2.1 (c) shows scanning electron microscopy images of scales covering the black regions of a *Trogonoptera brookiana* butterfly wing and their submicron scale surface texture features, which share more than a passing resemblance to anti-reflective photonic structures depicted in Figure 1.12 (a) and discussed in Section 1.1.4. Reflectance below 3% throughout the visible wavelength region is in part related to absorption by melanin pigments, however, immersion in index matching bromophorm fluid and the resultant elimination of nanostructure related effects reveals, that up to 40% of the nearly total extinction is attributable to light trapping [196]. The primary purpose of deep black sections of wing surfaces is likely to enhance the perceived brilliance of adjacent brightly colored patches, and a similar strategy is employed not only by different butterflies, but also by certain bird of paradise species [197].

Lastly, the diffuse reflectance produced by microscale texturation of geometric ray trapping surfaces is made extensive use of in the realm of flowering plants. This mechanism is exemplified by rose petals, depicted in Figure 2.1 (d), where convexly shaped epidermal cells not only aid in reducing the overall surface reflectance and increasing the saturation of pigment absorbance-derived colors, but also ensure a high degree of omnidirectionality in both the uptake and scattering of incident radiation. This, in turn, helps to produce a uniform color perception regardless of variations in viewing angles.

Illumination and viewing direction independent optical appearance is particularly critical for patterns employed for camouflage by way of cryptic coloration. While diffuse scattering of bright colors is relatively straightforward to achieve by way of a microscale rough surface and appropriate pigmentation, creation of an omnidirectional deep black perception demands an additional optical impedance matching mechanism. Hence, it is unsurprising that even hierarchically nanostructured optical surfaces, discussed in Section 1.3.2, are well represented in the biological realm. Figure 2.2 illustrates the background matching exhibited by a *Bitis rhinoceros* snake, which serves to obscure the animal from both its prey and predators. This pattern is created as a mosaic of variable color scales, differentiated by both pigment content as well as their surface texture. Black scales have particularly pronounced microscale protrusions up to 30 μm in height, which are, in turn, decorated by a fine layer of 600 nm height nanoscale ridges [141] that establish a gradual effective refractive index transition. Conversely, pale scales have a rather subdued microtexture, in which protrusions rarely possess heights above 10 μm, and barely show any significant nanoscale roughness. Reflectance spectra of the different coloration scales quantitatively highlight the clear disparity between their optical behavior, as black areas on average absorb close to 90% of visible radiation, whereas for those with a pale appearance this number is only around 75%. In addition, application of a 15 nm

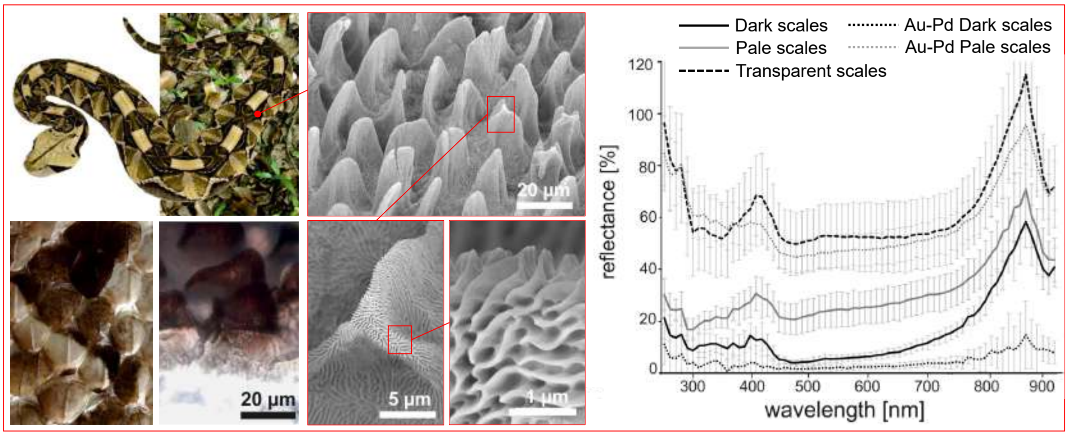

Figure 2.2: Hierarchical anti-reflective velvet black scales of a *Bitis rhinoceros* snake [141]. Lower-left panels respectively provide a close-up photograph of scale patterns and a cross-section optical microscopy image of their wrinkled surface topology. Scanning electron microscopy images in the middle reveal the multiscale cascading hierarchical micro/nano-texture, particularly prominent on black scales. Plot on the right provides the reflectance spectra of scales with three different colorations, as well as those of their 15 nm Au-Pd metal-coated counterparts.

thickness Au-Pd alloy layer results in further exaggeration of this disparity, thereby illustrating the nanotexturation induced differences in optical performance.

Among the relatively ubiquitous general reflectance modification nanotexturing strategies employed by a multitude of plants and animals there is a select subset that have developed exceptionally elaborate and advanced optical behaviors. Structural coloration, exhibited by some insects and bird feathers, is, perhaps, the most well known example of sophisticated manipulation of light. It harnesses complex ordered subwavelength structures to induce interference effects that give rise to a partial photonic band gap for radiation at specific frequencies and propagation directions. As photons with wavelengths that fall within the band gap have no modes available for coupling within the photonic structure, they are re-radiated back into free space, resulting in a very intense and well spectrally defined iridescent reflectance. This purely physical mechanism is far superior to pigment-derived coloration as far as brightness and visibility, especially in low-light conditions, is concerned, and is highly beneficial for the sexual signaling purposes of an animal. Notable examples of photonic crystal-like structure realizations in nature are the iridescent feathers of a peacock [201], as well as the diamond lattice opal arrangements that give the weevil beetle its striking and nearly viewing angle independent coloration [202].

However, the photonics employed by butterflies to endow their wings with highly varied iridescent coloration patterns [203] has been subject to particularly numerous studies [198, 204] and attempts at imitation [199]. Figure 2.3 (a) depicts the visual appearance, composition and nanoscale morphology of *Morpho didius* butterfly wings. Much like in the case outlined in Figure 2.1 (c), the wing is covered by two types of microstructure layers – almost transparent cover scales and iridescent cyan-blue ground scales, the latter of which are dominant in establishing the structural color of the surface. Close-up scanning electron microscopy images reveal the presence of a submicron period grating pattern of ridges extending lengthwise along the scale, where, furthermore, each ridge is comprised of a nanoscale stack of lamellae. Hence, the surface of every scale effectively behaves as a superposition of a grating and a multilayer reflector, which concurrently enforce interference conditions for incident light that give rise to a partial photonic band gap responsible for structural coloration of the wing, that, for the specific 3D geometry exhibited by *Morpho didius*, manifests as a distinct spectral reflectance peak in the blue wavelength region.

A different example of an intricate optical response is provided by the *Chrysina gloriosa* beetle [200] shown in Figure 2.3 (b), which selectively reflects left circularly polarized green light, however, appears dark brown when observed in only right circularly polarized illumination. The surface of its exoskeleton is decorated by a mosaic of mainly hexagonal cusps, each of which appears to have a chiral molecular structure akin to the long-range order exhibited by certain cholesteric liquid crystals and illustrated in the upper-right corner of the figure. The main purpose of such polarization-specific reflectance is likely to draw the attention of members of the same species, as scarabs as well as other insects have been shown to posses the ability to detect polarized light at different wavelength ranges, whilst avoiding notice by predators [187].

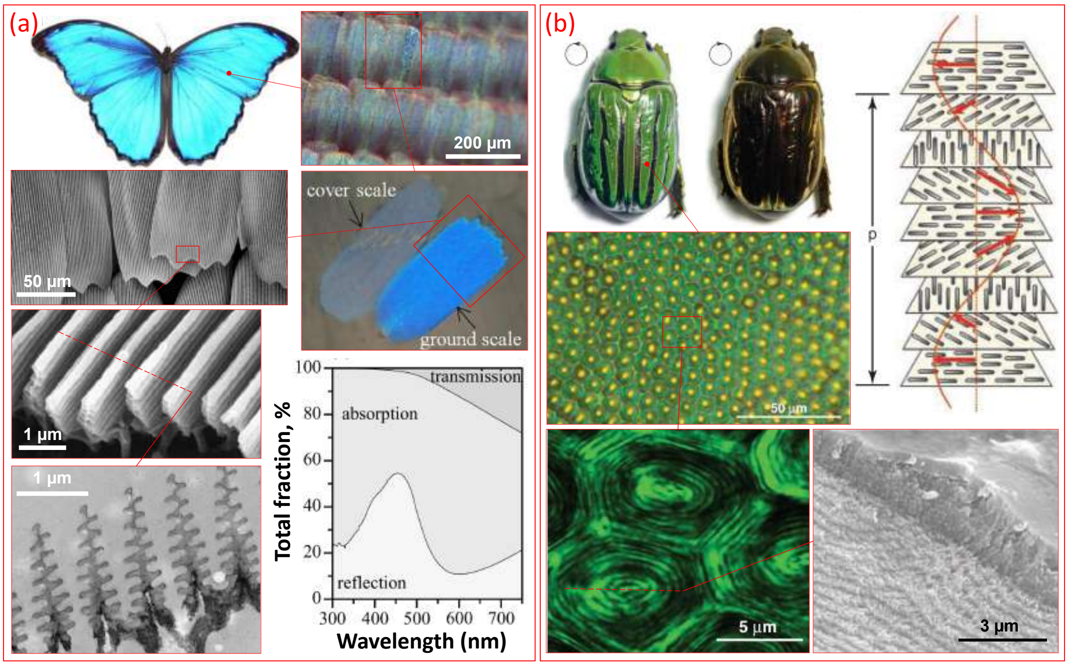

Figure 2.3: Advanced photonic functions in biological surfaces. (a) Structural coloration of *Morpho didius* butterfly wings with a partial photonic band gap [198, 199]. Close-up optical image on the top left shows the iridescent coloration exhibited by the wing pattern, comprised by two types of scales depicted below. Left side of the panel provide scanning electron microscopy images of ground scales, and reveal the grating-like ridges which, in turn, are comprised of multiple stacked lamellae. Spectra on the lower-right plot the fraction of light reflected, absorbed and transmitted by the wing. (b) Selective left circularly polarized light reflectance of a *Chrysina gloriosa* beetle carapace [200]. Optical and scanning electron microscopy images of the exoskeleton surface show that it is comprised as a mosaic of ~ 10 μm diameter conical cells. Scanning confocal fluorescence microscopy reveals the chirality exhibited by each feature, analogous to that of a cholesteric liquid crystal the structure of which is sketched in the top-right corner.

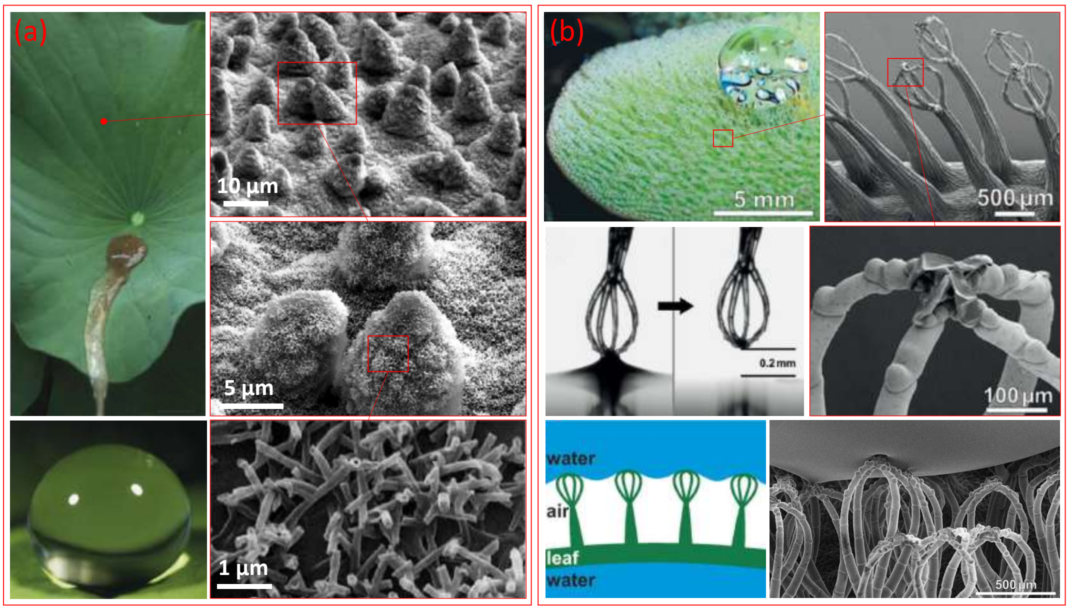

Figure 2.4: Water-manipulating surface texturing of plants. (a) Superhydrophobic and self-cleaning surfaces of *Nelumbo nucifera* lotus leaves [205]. Photographs on the left show how water removes contaminant particles without wetting the leaf, as well as a close-up view of a water droplet on the superhydrophobic surface. Scanning electron images on the right depict the hierarchical texture, comprised of microscale cell papilla protrusions and an overlayer of nanoscale wax tubules. (b) Superhydrophobic surfaces with hydrophilic pins on a *Salvinia molesta* floating water fern [206]. Scanning electron images on the right show millimeter-scale whiskers, coated by water-replant wax crystals everywhere except for the hydrophilic terminal end, that pin a water droplet. The primary function of the surface is trapping and long-term retention of air in case of water submergence.

Generally, functional behavior of surface textures is predicated on their constituent structural features having dimensions on a scale particularly suited to either individually or collectively interact with some physical phenomenon. In the case of nano/micro-textures their components tend to exhibit sizes close to those of relevant radiation wavelengths, hence, well suited to produce scattering and interference underlying many different optical phenomena. However, there is a wide range of other effects that depend on the presence of similar textural features, among the most important of which in nature is control over how a surface interacts with water, since at microscopic sizes and below surface tension forces start to exceed those exerted by gravity. Specifically, hydrophobicity in the Cassie–Baxter state [207] hinges on liquid-air interface tension bridging asperities between texture features, thus making wetting down the rest of the substrate energetically unfavorable. This keeps a droplet suspended and mobile above a surface and enables important functions such as self-cleaning. However, the liquid-air interface holding water above the rough solid can be maintained only up to a pressure that is inversely proportional to the characteristic size of structural features [208].

The quintessential example of a natural hydrophobic self-cleaning interface – and one which inspired a great multitude of artificial coatings, textiles and surfaces – is the lotus leaf [205] depicted in Figure 2.4 (a). Scanning electron micrographs of the leaf reveal a composite texture, made up of microscale convex epidermal cell protrusions that are thoroughly

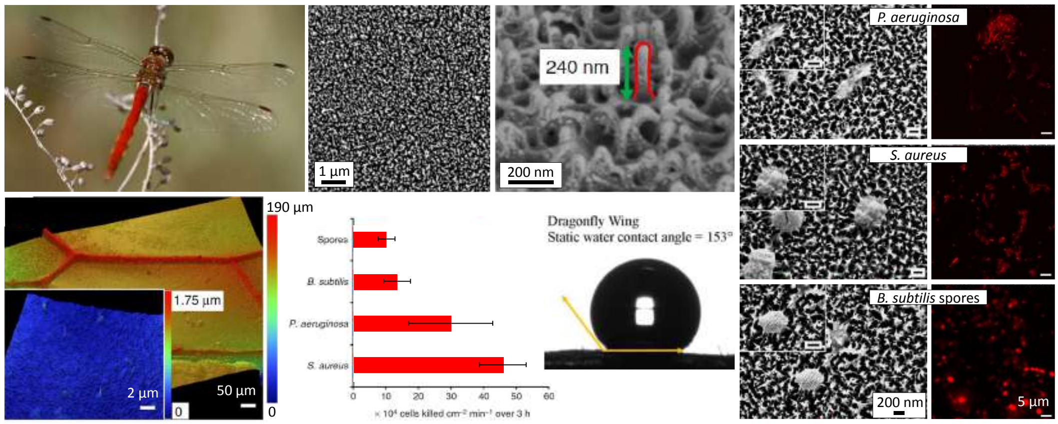

Figure 2.5: Bactericidal wing surfaces of a *Diplacodes bipunctata* dragonfly [56]. Lower-left optical profilometry image reveals the microscale topology of the wing, where a higher-resolution rendering of the epicuticle is given as an inset. Scanning electron microscopy images of the nanotexture at different magnifications are provided in the upper-middle panels. Pathogen interaction with the surface is outlined on the right by means of electron and confocal laser scanning images. In the latter case dead cells appear red and living ones, if there were any, would be green. Bactericidal efficiency histogram and superhydrophobic behavior of dragonfly wings are shown in two lower middle panels.

decorated by an inherently water repellent mesh of nanoscale tubular wax crystallites. The resulting hierarchical roughness is able to maximize the water-air interface all the while keeping solid-water interaction at a minimum, which gives rise to the superhydrophobicity of lotus leaves, as characterized by their 160° water contact angle and a 4° hysteresis [205]. Furthermore, nanoscale roughness limits the adhesion strength of contaminant particles on the plants surface, and the weak van der Waals forces responsible for their surface attachment are easily overwhelmed by capillary force interaction between a particle and a rolling water droplet. This imbalance of interaction strengths underlies the self-cleaning behavior, illustrated by the effortless removal of dirt by water in Figure 2.4 (a), that *Nelumbo nucifera* lotus is particularly well known for.

A different ingenious example of how plants leverage water surface tension forces to their own benefit is given by the floating water fern *Salvinia molesta* [206], depicted in Figure 2.4 (b). Its surface is covered by complex multicellular whiskers approximately 2 mm in length, each of which is terminated by four connected hairs which give rise to an egg-beater-like structure. Most of the plant's surface is covered by water repellent wax crystals similar to those observed on a lotus leaf, however, quite unlike in the lotus case, the very tip of the whisker is made up of four dead cells that are quite hydrophillic, hence, easily wetted by water, as shown in the middle-left photograph of Figure 2.4 (b). The primary function of high water affinity patches is to pin and stabilize the liquid-air interface, which is then kept suspended on the long whisker structures and wielded as a barrier that prevents further wetting of the plant, thereby ensuring the retention of survival-critical air for an extended period of time even in case of total submergence and perturbation by turbulent flows.

Anti-biofouling behavior, *i.e.* the ability to prevent accumulation of microorganisms on a wetted surface, is an advantageous feature of numerous nanotextured surfaces and tends to be related to their hydrophobicity and general self-cleaning functionalities. Certain natural interfaces endowed with closely-spaced high-aspect-ratio protrusions can, however, go one step further by being lethal to a wide range of pathogens. One example of just such a bactericidal surface, summarized in Figure 2.5, is the wing of a *Diplacodes bipunctata* dragonfly. The nanotexture, comprised of semi-stochastically arranged 240 nm average height pillars spaced approximately 200 nm apart, was demonstrated to be disruptive to membranes of prokaryotes such as Gram-negative *P. aeruginosa*, Gram-positive *S. aureus*, as well as to both the vegetative cells and spores of *B. subtilis*, leading to their mechanical rupture. Such a passive defense mechanism against infestation by pathogens can be assumed to be of substantial importance to the dragonfly, as its wide-spanning non-foldable wings are too large to be cleaned manually by the insect. It is noteworthy that the effect appears to be purely mechanical, as similar feature morphology black silicon wafers exhibited comparable bactericidal activity, and even drastic changes to surface chemistry performed by sputtering gold did not inhibit cell death [56].

All the examples outlined in this section offer only a brief and incomplete overview of the vast rage of morphological and functional diversity possessed by nanotextures in the biological realm. Furthermore, while here only the principal known purpose of each realization was highlighted, in many cases evolutionary pressures result in a given surface exhibiting a combination of behaviors. For instance, the hydrodynamic drag-reducing skin of a shark is also anti-biofouling [209], structurally colored butterfly wings [210] as well as diffusely reflecting rose petals [211] can be superhydrophobic, and bactericidal dragonfly wings are simultaneously anti-reflective [212], just to name a few examples. Such multipurpose realizations are undoubtedly expedient for an organism, however, can be difficult to untangle in biomimetics, as it is not evident how much one property of a nanotexture has been compromised from its potential optimal realization by adaptations to different selection pressures. To illustrate this point it is worthwhile to have an in depth look at the breadth of characteristics that a single nanotextured bio-surface can exhibit.

2.2 Multifunctional nanotextured cicada wings

As mentioned in the prior section, rarely, if ever, are natural nanotextures restricted to fulfilling a singular function. Selection pressures acting on an organism will, at a bare minimum, tend to ensure that in addition to their primary purpose functional surfaces will possess additional mechanisms of preserving their own integrity, for example, by way of removing pathogens and contaminants.

Nanotexture patterns overlaying the wings of insects in the cicadoidea family provide an example particularly multifaceted in its functionality, and one that has provided much inspiration for biomimetic design approaches [56, 213, 214]. Among the most prominent properties exhibited by such surfaces is their superhydrophobicity, critical in maintaining flight capability upon contact with water [215]. This is achieved by leveraging texturation as well as due to the presence of a water-repellent wax coating [216]. Hydrophobicity, in turn, enables the self-cleaning of wing surfaces, which is instrumental in maintaining all other functionalities provided by the nanotexture through removal of various contaminant particles and substances. Methods of self-cleaning include the familiar lotus effect, which involves impacting or rolling water droplets [5], as well as the self-propelled jumping condensate mechanism, that harnesses atmospheric humidity [217]. Such passive ways of ridding surfaces of excess water and contaminants are especially important for larger cicada species, which have extremities too short to extend over the entirety of their wings. Furthermore, cicada wing nanotextures exhibit a high level of bactericidal activity by way of mechanical rupturing of cell membranes on nanopillar features, particularly effective against Gram-negative bacteria [4, 218]. Lastly, but no less notably, cicada wings are anti-reflective [219], since the tightly-packed subwavelength conical bumps establish a gradient effective index layer akin to that overlaying the eyes of night-active moths [10].

In this work, conducted in collaboration with with the research group headed by Prof. Junko Morikawa at Tokyo Institute of Technology, nanotextured cicada wings were probed for their heat and light transmission properties [220]. The macroscale and microscale morphology of the forewings are described first, followed by spectroscopic characterization of their chemical makeup. Next, contact as well as non-contact thermal diffusivity measurement schemes are employed to deduce both the lateral and transverse heat transport behavior at various positions on the wing. Lastly, reflectance suppression behavior by the surface nanotexture is investigated by means of FDTD simulations and the most important operative mechanisms are discussed.

2.2.1 Morphology and structural properties

Despite drawing considerable interest due to its unique nanotexturation, cicada wings first and foremost are highly specialized and sophisticated flight organs. As a result they have to be sufficiently robust to support loads far in excess of the animal's bodyweight, whilst being lightweight and resilient themselves. These requirements necessitate the incorporation of chitin, which is polysaccharide-based high molecular weight biopolymer with a high degree of crystallinity owing to the prevalence of hydrogen bonding.

The left side of Figure 2.6 depicts a photograph of a *Cyclochila australasiae* forewing, comprised of a transparent membrane suspended on and supported by an interlinked system of veins. In addition to mechanical support, major veins are connected to the open circulatory system of an insect and contain hemolymph fluid, trachea tubes as well as nerve strands. Cicada wings are notably large, which makes them practicable for use as nanotexture replication templates [214], as well as easy to handle during other types of experimental work. However,

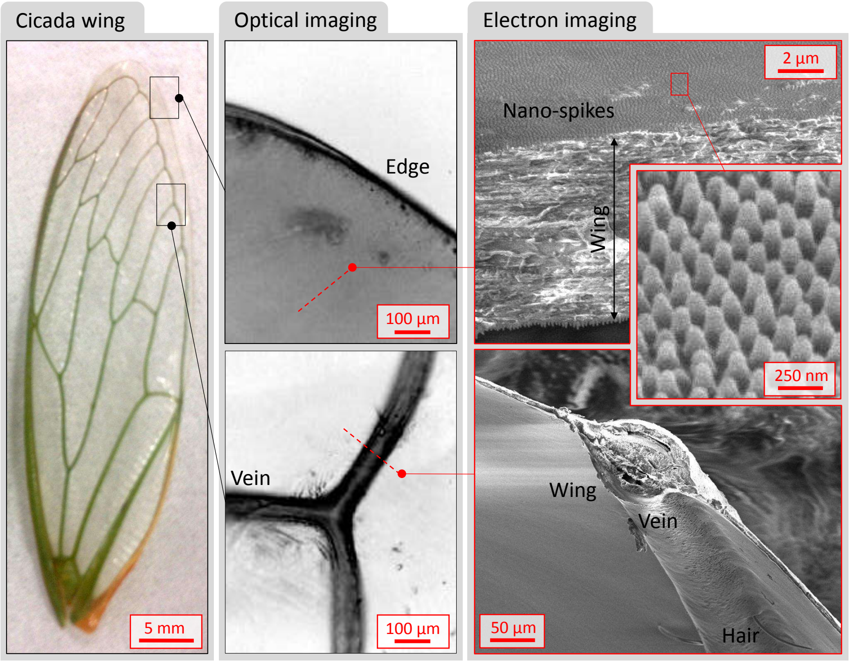

Figure 2.6: Morphology of a cicada (*Cyclochila australasiae*) wing, shown in the left panel photograph [220]. Optical microscopy images of highlighted edge and vein segments of the wing are shown in the two middle panels. Scanning electron microscopy images of representative cross-sections of wing membrane as well as that of a vein are depicted on the right.

most of the interesting complexity is uncovered only in higher magnification optical or scanning electron microscopy images. For instance, approximately 4 µm diameter single socketed hairs protrude at somewhat irregular positions along the vein and are used by the insect as mechanoreceptors [221]. Cross-section images acquired using scanning electron microscopy and shown on the right side of Figure 2.6 reveal, that both sides of the wing membrane are coated by pillar-like protrusions, quasi-regularly arranged with an average spacing of $p = 170 \pm 15$ nm. As can be seen in the high magnification inset image, individual pillars have a rounded-tip cone shape, their average height is $h = 240 \pm 30$ nm, whereas the diameters at tip and base are respectively $r_t = 70 \pm 10$ nm and $r_b = 200 \pm 20$ nm.

The wing surface is comprised of upper and lower cuticle layers, which are tightly joined in the membrane regions, however, remain separate wherever veins are situated. As a result membrane thickness can range between 4 µm and 6 µm, whereas vein cross-sectional diameters are in the 60–150 µm range. Furthermore, the vein enveloping cuticle is notably thicker and exhibits a color akin to that of the insect's exoskeleton. This is attributable to sclerotization by which chitin is hardened into a rigid cross-linked biocomposite material.

Variations in the structural composition of a cicada wing can be readily discerned *via* mid-infrared absorbance mapping, which enables spatially resolved fingerprinting of compounds by their various molecular bond vibrations. Spectral acquisitions were performed in transmission mode using a Spectrum Spotlight 300 Fourier transform IR imaging spectrometer (Perkin-Elmer Inc.), equipped with a 6.25 µm pixel size linear mercury cadmium telluride detector array. The mid-infrared absorbance spectral plot of a cicada wing, given at the top of Figure 2.7, exhibits signatures broadly consistent with those reported in the literature as characteristic of α-chitin [222]. The most prominent high frequency features in the 3600 cm^{-1} to 3000 cm^{-1} amide A band range are attributable to stretching vibrations of OH and NH groups at approximately 3479 cm^{-1} and 3290 cm^{-1} wavenumbers respectively. However, the overlapping peaks possess a complex broadened shape, owing to the variety of possible bond arrangements in the elaborate macromolecular network.

The next two pairs of spectral peaks around 2900 cm^{-1} are related to symmetric as well as antisymmetric C–H stretching in CH_3 and CH_2 groups. The CH_2 associated features, namely $\nu^{as}_{\mathrm{CH}_2}$ at 2920 cm^{-1} and $\nu^{s}_{\mathrm{CH}_2}$ at 2850 cm^{-1}, have considerably higher intensities relative to their CH_3 counterparts than would be expected for pure α-chitin. This additional absorbance contribution has been attributed to long-chain hydrocarbons comprising a thin-film lipid-based waxy surface coating, which is important in rendering cicada wings hydrophobic [216].

Most descriptive parts of the cicada wing mid-IR absorbance spectrum are situated at wavenumbers above 1750 cm^{-1}, where the prominent amide bands provide information on the secondary structure of proteins and polypeptides. For example, the C=O stretching vibration related amide I peak, centered at 1649 cm^{-1}, is actually comprised of two signatures discernible at 1657 cm^{-1} and 1635 cm^{-1}, which arise due to differences in hydrogen bond configuration. In α-chitin the higher energy 1657 cm^{-1} mode corresponds to the conventional $\mathrm{C{=}O}\cdots\mathrm{H{-}N}$ hydrogen bonding, whereas in the 1635 cm^{-1} case an additional bond with the $-CH_2OH$ side chain group is established [222]. Such interchain bonds are instrumental in

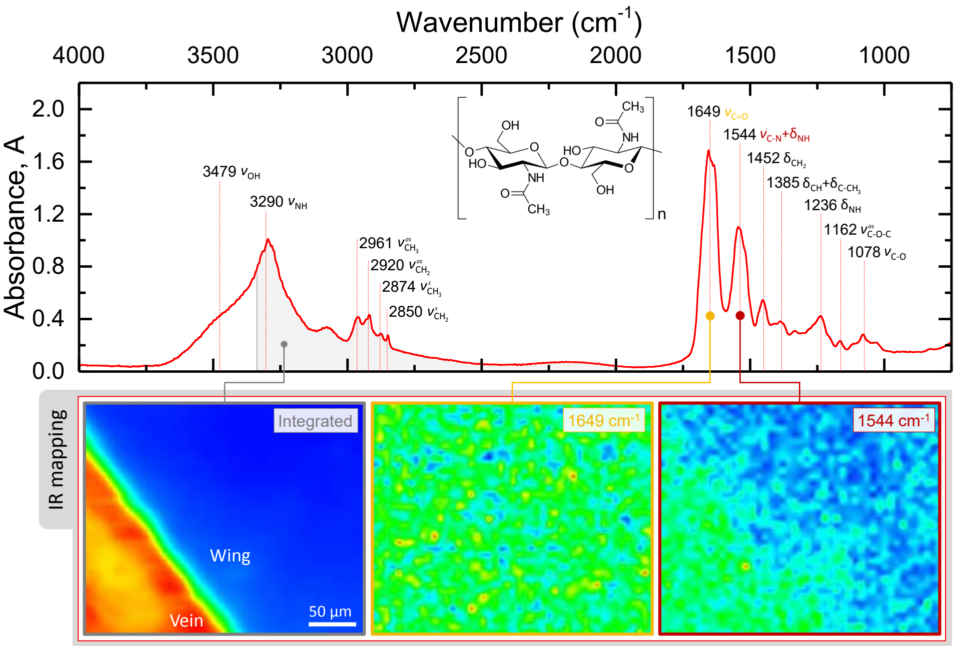

Figure 2.7: Infrared spectroscopy of a cicada wing segment [220]. Plot in top panel shows a typical mid-IR spectrum of the wing membrane, where the most prominent spectral signatures can be attributed to the presence of chitin polysaccharides (molecular structure given as an inset) and cuticular waxes. Infrared absorbance maps – respectively corresponding to the spectral intensity integrated over the 3300 cm^{-1} to 2000 cm^{-1} range, amide I band at 1649 cm^{-1} and amide II band at 1544 cm^{-1} – are given in the three bottom panels. Mid-IR spectroscopy experiments were performed at Tokyo Institute of Technology by the research group under supervision of Prof. Junko Morikawa.

endowing chitin with its chemical and mechanical stability. Coupled C–N stretching and N–H bending vibrations, manifesting as the amide II band at 1544 cm^{-1}, is also notably strong, however, its constituent components are not as readily distinguishable.

Spatial infrared absorbance mapping images, shown in the bottom panels of Figure 2.7, illustrate the intensity distributions of the aforementioned most prominent spectral features over an extended wing surface area. The leftmost absorbance map was obtained by integrating over the 3300 cm^{-1} to 2000 cm^{-1} wavenumber range wherein the wing is relatively transparent. It primarily provides information about the sample thickness and allows for a clear distinction between the thin membrane and vein regions, where cuticle is particularly bulky. However, even within the vein some transmittance variability exists, as the tubular central cavity of the vein gives rise to considerably less absorbance than the side walls. The main structural difference between membrane and vein cuticle compositions is revealed by comparing the absorbance maps corresponding to amide I and amide II signatures. Respectively, here the C=O stretching vibration attributed 1649 cm^{-1} mode intensity is uniform over the wing segment, whereas the C-N and N-H related feature is notably more prevalent in the vein region. This disparity is the result of the chemical agents, such as arterenone, used by the insect to induce cross-linking and hardening of chitin by way of sclerotization [223].

The CH_2 and CH_3 group bending vibration mode related peaks for a cicada wing, respectively at 1452 cm^{-1} and 1385 cm^{-1}, are considerably broadened and blueshifted compared to those observed in pure chitin [224]. This is likely due to infrared absorbance contributions from the wax coating overlaying the surface. Other strong spectral features include the N–H bending related peak at 1236 cm^{-1}, the antisymmetric ring-confined C–O–C bond stretching mode at 1162 cm^{-1}, as well as the C–O stretch vibration at 1078 cm^{-1}. Overall, infrared spectral characterization shows that the α-chitin comprising cicada wing membranes derives its robustness in large part from the hydrogen bonding performed by the side-chains of the polysaccharide based polymer.

Numerous different biopolymer materials with outstanding mechanical strength and elasticity share structural similarities with chitin in that they are organized as a mesh of crystallized regions interlinked by amorphous polymer chains, as is the case for fibroin comprising silk. For dragline silk of spiders in particular this composite makeup had been reported as giving rise to a controversially high thermal conductivity of the strands, on par with that of metals [225]. For fibroin-based materials these results were subsequently shown to be overestimated by approximately two orders of magnitude [226, 227], and this work yields further verification by probing the thermal diffusivity of chitin, which shares similarities to the structure of silk, however is comprised of different biopolymers. Furthermore, insects in the cicadoidea family are known to perform both passive [228] as well as active evaporative cooling by consuming sap and secreting water [229], which in turn indicates that these animals are subject to thermal management related selection pressures.

In this work thermal diffusivity of a cicada wing was measured by means of complimentary contact as well as non-contact methods, that, respectively, yield information on heat transfer across the membrane thickness and along its surface. Lateral thermal diffusivity $\alpha_{\|}$ was measured using a temperature wave method, in which localized sample heating is induced remotely *via* continuous wave $\lambda = 630$ nm laser illumination [230]. Conversely, a bolometric thermal camera enabled the spatially resolved imaging of over the 7 to 14 μm wavelength thermal radiation emitted by the sample as heat spreads from the laser spot. An example of a thermal image acquired during laser illumination is depicted in the top-left panel of Figure 2.8, were the beam is focused on one of the veins comprising the wing support frame. Evidently, temperature of the thin membrane becomes noticeably elevated once stationary state is reached, however, veins themselves remain considerably cooler owing to the high thermal conduction afforded by their considerable bulk volume and interconnectedness.

The temporal component, necessary to deduce the characteristic parameters of a transient process that is heat transport, is introduced by pulsed modulation of the laser beam at some low frequency which the thermal imaging camera can readily follow. Bolometer camera images are then analyzed by performing a fast Fourier transform operation, and the resultant plots of amplitude and phase distribution are shown on the right side of Figure 2.8, where red cross hairs correspond to the laser heating spot. Fourier transform amplitude image provides a contour plot proportional to the radiant exitance of the wing surface, defined according to the Stefan–Boltzmann law of gray body emission $j = \varepsilon\sigma T^4$. However, radiant exitance j does not allow for unambiguous determination of surface temperature T, as, in addition to the Stefan–Boltzmann constant σ, it also depends on emissivity ε, which, in turn, is contingent on a multitude of factors that include surface texture. The Fourier transform phase plot, on the other hand, is related solely to temporal lag in response to laser modulation, hence is directly tied to thermal diffusivity $\alpha_{\parallel}$ as $\Delta\theta(x)/\Delta x = \sqrt{\omega/2\alpha_{\parallel}} + c$ [230], where x is the coordinate, $\theta(x)$ in the phase, ω is the cyclic frequency of modulation, and c is a measurement setup dependent constant.

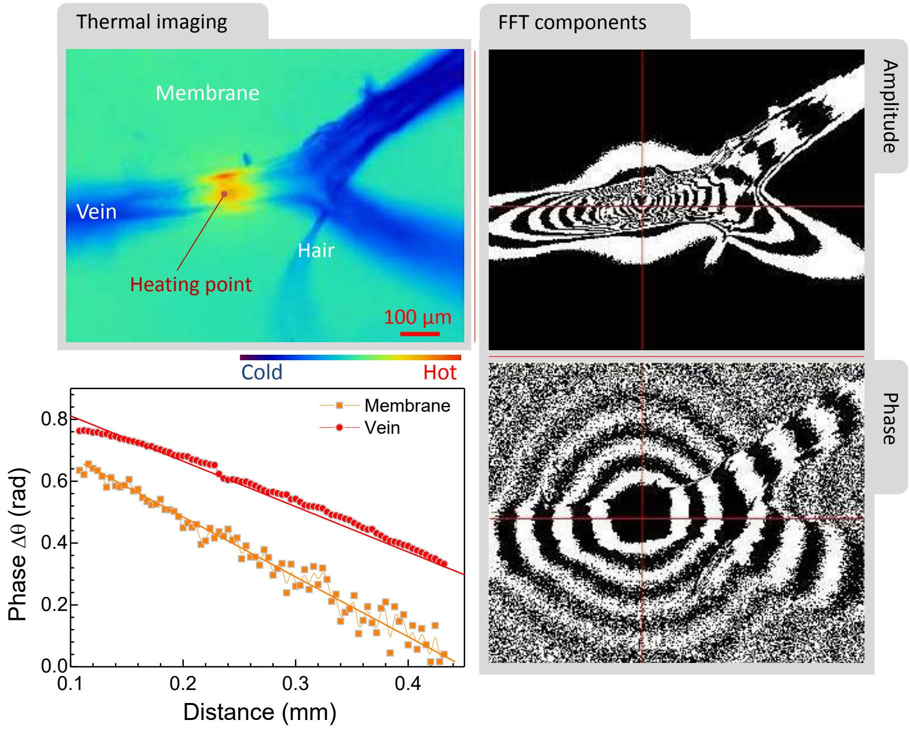

Figure 2.8: Non-contact measurements of lateral thermal diffusivity along cicada wing surfaces [220]. Thermal image acquired during pulsed laser excitation is shown top-left. Fast Fourier transform amplitude and phase plots for the image, which respectively reveal the thermal radiant exitance and diffusivity, are shown on the right. Lower-left panel plots the fast Fourier transform phase dependence on distance from the heating spot for both vein and membrane surfaces, and its slope is related to thermal diffusivity $\alpha_{\parallel}$. Measurements of thermal diffusivity were performed at Tokyo Institute of Technology by the research group under supervision of Prof. Junko Morikawa.

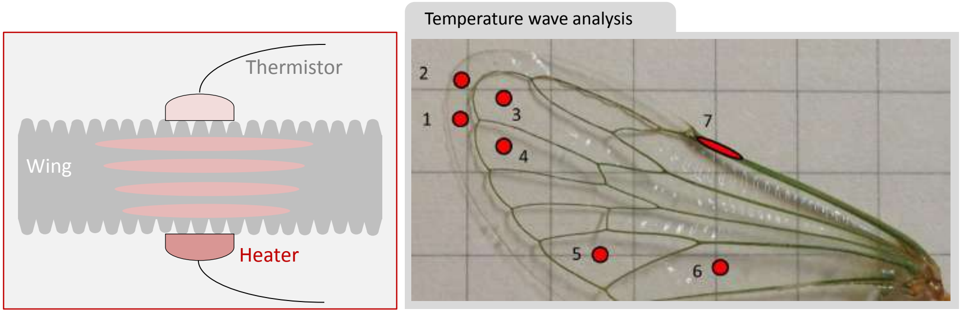

Figure 2.9: Contact measurements of transverse thermal diffusivity across a cicada wing [220]. Sketch on the left illustrates the temperature wave measurement method. Right panel shows a photograph of the wing with different measurement positions highlighted in red. Average transverse thermal diffusivity of the membrane was $\alpha_{\perp}^{m} = (0.71 \pm 0.15) \times 10^{-7}$ m^{2}s^{-1} (points 1–6), and that for a vein was $\alpha_{\perp}^{v} = (2.11 \pm 0.15) \times 10^{-7}$ m^{2}s^{-1} (point 7). Measurements of thermal diffusivity were performed at Tokyo Institute of Technology by the research group under supervision of Prof. Junko Morikawa.

As can be deduced from fast Fourier component image plots, the isothermal regions on the vein are considerably more widely spaced than those on the thin nanotextured membrane, which is indicative of much more rapid heat transport. Indeed, phase gradient plots of thermal waves measured on membrane and vein surfaces, depicted in the lower-left part of Figure 2.8, yield the corresponding thermal diffusivity parameters $\alpha_{\parallel}^{m} = (3.6 \pm 0.2) \times 10^{-7}$ m^{2}s^{-1} and $\alpha_{\parallel}^{v} = (6.7 \pm 0.2) \times 10^{-7}$ m^{2}s^{-1}. These values are considerably lower than the thermal diffusivity of air, which is $\alpha_{\parallel}^{m} = (3.6 \pm 0.2) \times 10^{5}$ m^{2}s^{-1}, hence, a competing heat transport channel along the nanotextured wing interface *via* air becomes viable. Therefore, thermal diffusivity values determined by means of non-contact thermal wave methods can be substantially higher that what is inherently exhibited by the biopolymer.

A much more direct, contact-based thermal wave analysis method [231], sketched on the left side of Figure 2.9, enables the determination of transverse thermal diffusivity $\alpha_{\perp}$ across the wing thickness, that is related to innate properties of the cuticle. To this end a measurement system, comprised of a 250×150 μm^2 surface area resistive heater, a counterposing thermistor as well as a function synthesizer for modulation and a lock-in amplifier for signal detection (ai-Phase Co., Ltd.), was employed. Oscillating output of the heater gives rise to wavelike heat flow, hence temperature, within the sample bulk, which is then picked up by the synchronized thermistor. Thermal diffusivity can then be recovered from both the thermal wave attenuation as well as the phase lag. Furthermore, an inductive coil can be used for simultaneous determination of the sample thickness, which for cicada wing membranes corresponded to 5 ± 1 μm, in good agreement with values obtained by scanning electron microscopy.

Transverse thermal diffusivity values attained by the contact-based thermal wave analysis method were $\alpha_{\perp}^{m} = (0.71 \pm 0.15) \times 10^{-7}$ m^{2}s^{-1} for the wing membrane and $\alpha_{\perp}^{v} = (2.11 \pm 0.15) \times 10^{-7}$ m^{2}s^{-1} for the supporting veins. In both cases transverse thermal diffusivity values were several times lower than in the lateral case. This discrepancy is in large part explained by elimination of the air contribution to heat transport, however, can also in part be attributed to heterogeneities in the interface between the two cuticle layers comprising the membrane. Here the measurements were performed at multiple locations of the wing and acquisitions were repeated several times at each site to enable adequate averaging of results.

This procedure proved to be necessary, since differences in the volume of air trapped within the nanotexture as well as in the amount of wax coating for each of the opposing surfaces can give rise to disparate probe contact conditions.

When taken together thermal transport measurement results indicate that chitin-based biopolymers exhibit thermal diffusivity values in line with those of silk fibroin [226] as well as of synthetic polymer materials [231]. Therefore, these findings contribute to clarifying controversial reports of extraordinarily rapid thermal transport in biopolymers. Similarly, while cicadas employ strategies for thermal management and may passively use the nanotextured high surface area of their wings to give off heat into its environment, neither the morphology nor the structural composition of these flying organs appear to be endowed with special temperature control capabilities in the same way that they are geared for reflectance suppression.

2.2.2 Anti-reflective optical behavior

Wing nanotexturation is a mainstay property exhibited by a wide range of different insect species such as dragonflies, moths, flies and butterflies among many others [232], which, much like for the aforementioned cicada, appear to be geared towards attaining hydrophobicity along with some type of optical reflectance modification behavior. However, even when functionalities seem to converge nanotextures can posses notably different morphologies.

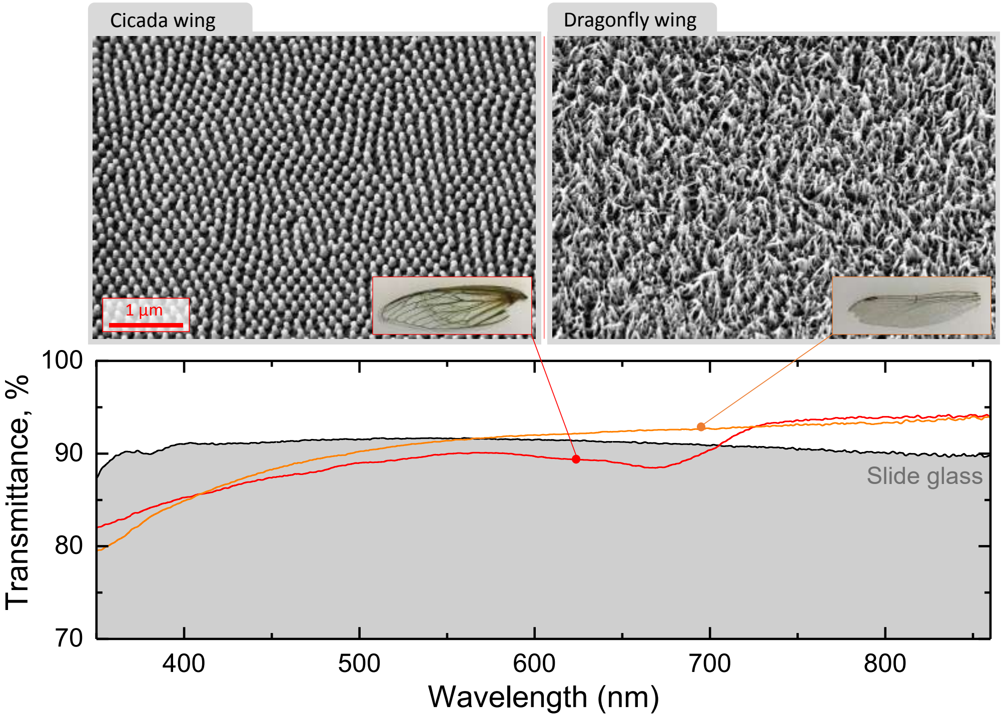

Figure 2.10: Scanning electron microscopy images of nanotextured cicada and dragonfly wing surfaces are shown in the top panels. Insets illustrate the visual appearance of respective insect wings. The 1 µm scale bar is applicable to both images. Plot at the bottom depicts the hemispherical transmittance spectra of cicada and dragonfly wings at normal incidence in the visible wavelength region. Transmittance through a 1 mm thickness slide glass is also displayed for comparison.

A case-in-point example of such a situation is given in Figure 2.10, where isometric scanning electron microscopy images of dragonfly and cicada wing membranes are contrasted. Evidently the nanotexturing approaches employed by the two insects are clearly distinct, since in the cicada case the surface is comprised of a somewhat regular pattern of conical pillars, whereas dragonfly wings are covered by a much more random mesh of delicate wire-like features. Yet, despite these obvious differences in topology, both surfaces have been shown to be hydrophobic as well as highly bactericidal [218, 233]. Furthermore, the total hemispherical transmittance behavior of both of these membranes in the visible wavelength range is roughly equivalent, as can be observed in the bottom plot of Figure 2.10.

In both cases, despite veination rendering notable fractions of surface areas opaque, cicada and dragonfly wings end up transmitting between 80% and 90% of incident visible wavelength light. This is in large part the result of anti-reflectance afforded by subwavelength features comprising their surface topology. Evidently, nanotextures employed by the insects possess a gradual transition of material density from air to the bulk cuticle, which is known to produce an effective refractive index gradient, as discussed in Section 1.1.3. Dragonfly wings achieve this by a randomly meshing nanoscale fibers, thereby giving rise to a morphology akin to that of chemically etched porous silicon [45]. Cicada wings, on the other hand, exhibit a notable degree of order, and mirror the appearance of subwavelength anti-reflective gratings [26] as well as, to a slightly lesser extent, black silicon surfaces, described in Sections 1.1.4 and 1.2.1 respectively.

One intriguing difference between transmittances of the two insect wings is the notable dip situated around the $\lambda \approx 670$ nm spectral region exhibited only in the cicada case. Similar behavior was observed for different texture scale black silicon samples, described in Section 1.3.1, where it was attributed to quasi-deterministic forward-scattering of light into substrate-guided modes as the spatial frequency spectrum of the texture gets imprinted into the incident optical field. Figure 2.11 (a) shows a top-down scanning electron microscopy image of a cicada wing, where each conical component appears as a bright dot. It is clear that, while rigorous translation symmetry is not maintained, the nanotexture exhibits a degree of short-range order substantial enough to act as a disordered two-dimensional grating. The fast

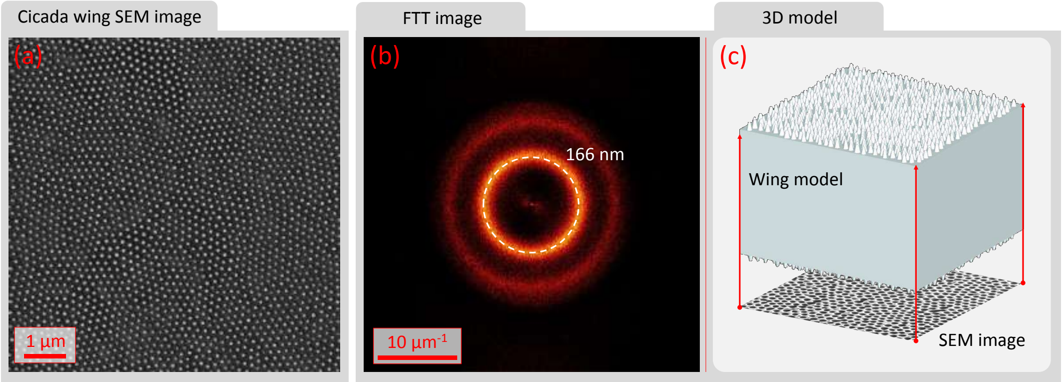

Figure 2.11: Cicada wing FDTD optical simulation setup. (a) Top-down scanning electron microscopy image of the nanotextured cicada wing surface. (b) Logarithmic scale spatial frequency spectrum of a cicada wing pattern, obtained by performing a 2D fast Fourier transform of the image in panel (a). (c) Isometric view of the wing segment 3D model, constructed based on a scanning electron microscopy image and used for FDTD simulations.

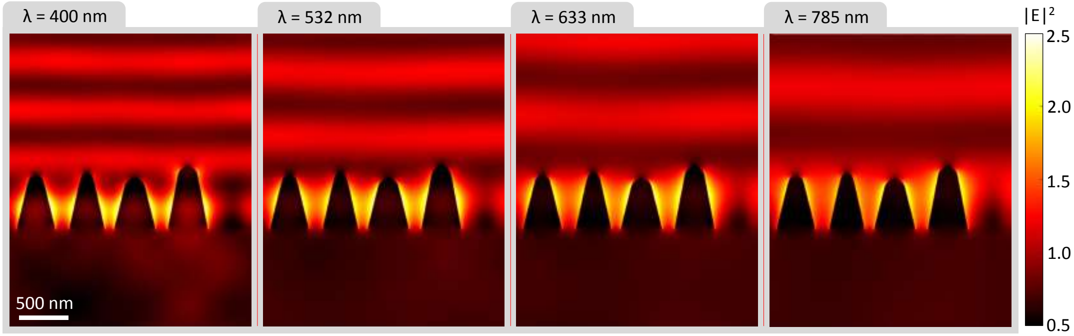

Figure 2.12: FDTD simulated electric field intensity profiles for light of various wavelengths incident on a nanotextured cicada wing surface. Electric field intensity as well as length scale bars are the same for all of the panels.

Fourier transform plot of the corresponding image is depicted in Figure 2.11 (b), where the principal spatial frequency components are distributed in a well defined ring that is characteristic of a 166 nm pillar spacing. Ring-like 2D surface Fourier component spectra are indicative of correlations between nearest-neighbor feature placement in the absence of any long-range order, as is also the case for similarly anti-reflective glasswing butterfly wings [234], as well as for black silicon illustrated in Figure 1.33 of Section 1.3.1. Therefore, it is feasible to infer that the dip observed in transmittance of cicada wings is due to light diffracted by nanopillar features into the total internal reflection angle range of the 5 μm thickness membrane bulk, since similar behavior was observed for polymer replicas of such nanotextured surfaces [214].

Further investigation of light interaction with cicada wing nanotextures was conducted *via* finite-difference time-domain simulations. Here, numerical work was performed using the commercially available Maxwell's equation solver "FDTD Solutions" (Lumerical Solutions Inc.), largely in accordance with the process previously described in Section 1.2.3. Initial preparation involved the definition of a realistic 3D model of the wing surface based on its scanning electron microscopy images. First, positions of nanopillars irregularly arranged on a wing segment were extracted from the aforementioned micrographs. At each of these coordinates a pillar with randomized parameters, following normal distributions likewise deduced from imaging results, was generated. The resultant 3D rendering of a double-sided cicada wing membrane segment is shown in Figure 2.11 (c). It was assumed that the refractive index of constituent materials is uniform throughout the structure and equal to $n = 1.55$, which is in good agreement with values reported for chitin and keratin [235]. Furthermore, dispersion effects as well as absorbance losses were considered negligible.

Calculations were performed on 3×3 μm^2 area segments of both the cicada wing model as well as of an equivalent flat surface for reference. Simulation region was laterally terminated using Bloch periodic boundary conditions, whereas surface-parallel limits were established by way of perfectly matched layer absorbers. Solar illumination conditions were approximated by conducting all simulations in compliments of two, with orthogonal polarizations of incident broadband plane-wave light, which when averaged yield the unpolarized response. Similarly, to account for the wide range of illumination configurations an insect is bound to experience in nature, the angle of incidence was varied from 0° to 75° with respect to the membrane surface normal in one hundred increments.

Figure 2.12 visualizes the interaction between optical fields of different wavelengths and the nanopillar-covered wing membrane topology. Again, notable similarities with near-field

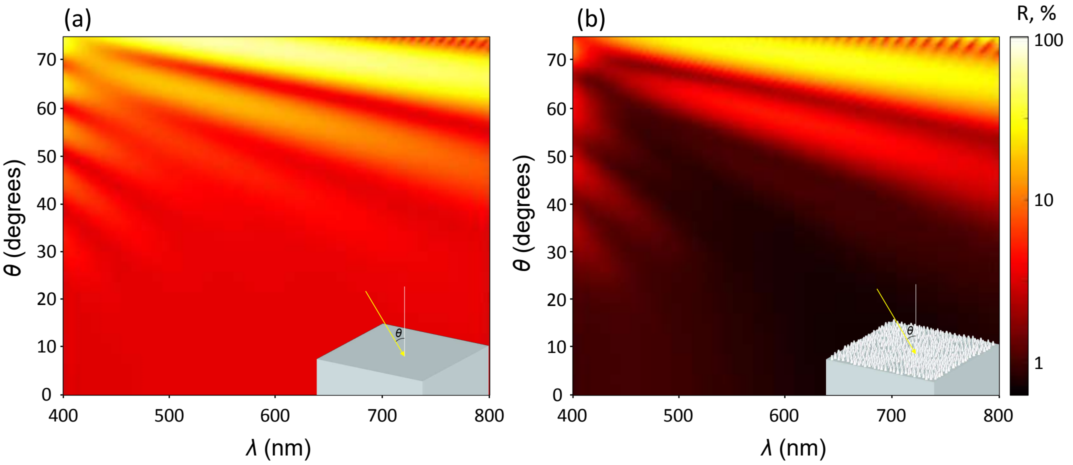

Figure 2.13: FDTD simulated angle dependent variations of unpolarized visible light reflectance spectra from (a) flat and (b) cicada nanopillar pattern covered 3×3 μm^2 surface area segments. Insets illustrate the respective 3D surface models employed in the calculations. Simulations were performed using the swinSTAR supercomputer at Swinburne University of Technology.

behavior of black silicon surfaces, illustrated by FDTD simulated electric field intensity profiles in Figure 1.23, can be observed. Here, electromagnetic energy is also localized in the gaps between the pillars, although attainable intensity values are lower due to smaller refractive index values of biopolymer materials. However, the dielectric nanofeatures are polarized by the incident fields and support Mie-like modes, which are expected to aid in coupling light into the underlying substrate bulk. This effect is clearly visible in the $\lambda = 400$ nm case, wherein coupled light is deflected substantially from the surface normal, and appears more subdued at higher wavelengths. Lastly, some distortion in the wavefront of initially plane wave illumination is discernible, which indicates some back-scattering contribution due to the disordered surface texture. On the whole, however, the fraction of light reflected from the pillar-covered surface is dramatically reduced.

The omnidirectionality of cicada wing reflectance suppression was probed by running angle of incidence dependent reflectance simulation sweeps on the model texture, as well as on a planar interface for comparison. However, FDTD broadband spectral calculations using light injected at an angle within periodically bounded simulation regions can be problematic, since the propagation vector becomes frequency dependent [236]. Here this issue was circumvented by interpolating the results from one hundred broadband simulations onto a common wavelength and plane wave source angle grid. The resulting 2D plots of reflectance dependence on wavelength and incidence angle of light are given in Figure 2.13 for (a) flat interface and (b) cicada wing texture respectively. Clearly, surface texturation diminishes the amount of reflected light by at least one order of magnitude throughout most of the visible spectral region at moderately oblique angles of incidence. Even at large incidence angles, where Fresnel reflectance is particularly strong, the amount of light not coupled into the substrate is reduced by at least a factor of four. These results demonstrate the broadband and omnidirectional efficacy of the gradient effective refractive index layer established by conical subwavelength pillars overlaying cicada wing membranes. Hence, such a surface is likely an integral component in optical camouflage strategies employed by the insect.

The aforementioned similarities between cicada wing nanotextures and black silicon, described in Section 1.2.1, is in large part due to equivalent methods of optical impedance matching in both of these surfaces. The chief operative mechanisms of cicada wings and black silicon rely on the gradient refractive index as well as on anti-reflective grating effects working in unison. Choice of substrate material in this case makes light coupling efficiency into high refractive index Si considerably more challenging than into a less optically dense biopolymer. Overall, the sharp spikes separated by narrow trenches at the base comprising black silicon provide a more gradual effective refractive index transition from air to substrate than the somewhat rounded pillars comprising a cicada wing surface, rendering black silicon superior based on this primary aspect. On the other hand, the higher local order exhibited by the cicada wing texture results in a narrower range of spatial frequency components, which would translate to a higher efficiency and more spectrally localized subwavelength grating reflectance suppression mechanism than in the quasi-random broadband black silicon case. Overall, black silicon appears to possess the superior anti-reflectance topology, however, cicada wing surfaces have many additional beneficial factors such as flexibility, hydrophobicity and robustness.

In summary, cicada wing membranes are complex evolutionarily optimized flight organ tissues as well as, owing to their anti-reflective nanotextures, photonic devices of notable efficiency. In addition, their surfaces perform other important functionalities, ranging from liquid repellence and self-cleaning to bactericidal activity. While the chitin comprising it does not possess any extraordinary thermal management capability, being more in line with other biopolymers and plastics, it is nevertheless robust, flexible, biocompatible and optically transparent, which all are properties in high demand for applications related to ever increasing integration between technology and the human body.

2.3 Key advances in biopolymer based photonics

Human healthcare is among the most powerful drivers of technological advancement, to which physical sciences have been able to contribute heavily by devising new functional materials and harnessing various physical phenomena for therapeutic or sensing purposes. In particular, probing the complex variety of biochemical processes in living organisms with high sensitivity and specificity is a critical prerequisite for the timeliness and adequacy of any medical intervention. These demands, in turn, have given rise to a push for ever more close interfacing of medical devices and human physiology, with the ultimate goal being implantable biosensors capable of providing real time diagnostic information.

However, any object to be introduced into the human body has to fulfill a stringent set of biocompatibility demands [237], meaning that materials should not induce inflammation or a foreign body response, and cannot contain residues of cytotoxic compounds. Furthermore, a device should be mechanically robust, however, sufficiently flexible and stretchable so that natural movements can be accommodated. In addition, controllable biodegradability is likewise a desirable trait, as it allows to forgo follow-up procedures to retrieve a device once it has outlived its usefulness. Examples of implantable materials include select synthetic polymers [238], such as poly(lactic acid) and poly(ethylene-glycol) or hydrogels akin to poly(vinyl-alcohol), each of which have hydrolytically degradable chemical bonds in their macromolecular backbone.

On the other hand, naturally-sourced biomaterials like chitin-derived chitosan amino-polysaccharide [240] and silk fibroin protein [241] are degraded metabolically, by way of lysozyme and proteolytic enzymes respectively [238]. As such biopolymers are made up of constituents ubiquitous in the human body, they are generally not subject to adverse immune system responses. Hence, biological materials have found frequent use as platforms for fabricating various field effect transistor-based [242, 243] or electrochemical [244] biosensors, implantable transient devices [245] and electronic skin surfaces [11]. While in electronic

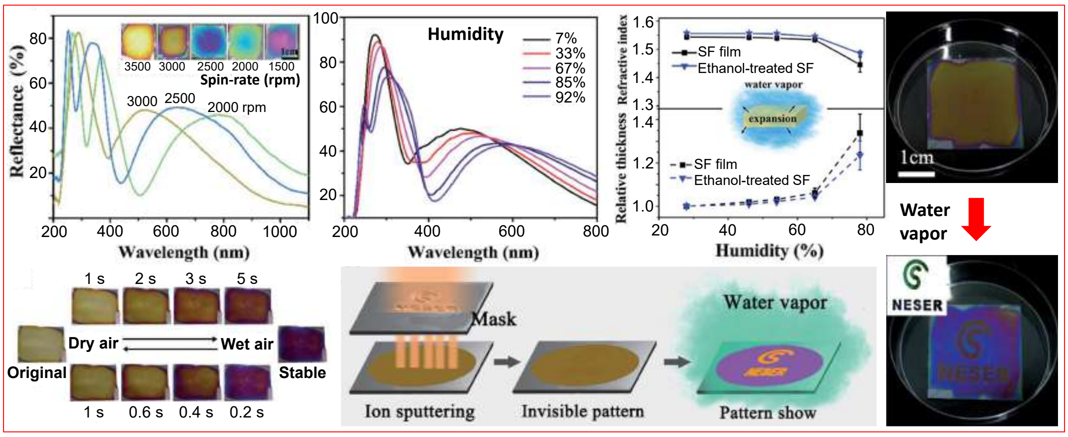

Figure 2.14: A rudimentary humidity sensor based on color changing of a silk fibroin film [239]. Plots at the top show silk film reflectance spectra variations depending on their thickness and ambient humidity. Layer thickness and refractive index depends on the humidity of the surrounding atmosphere regardless of silk crystallinity, as shown in the plot top-right. Pictures bottom-left depict reversible film iridescence color changes due to water vapor exposure. Gold sputtering can be used to modify the fibroin films to suppress humidity induced color changes, as shown on the right.

sensors insulating biopolymers tend to fulfill the role of a biocompatible and biodegradable passive substrate, biomedical optics [246] relies on their transparency as well as surface smoothness to avoid excessive optical losses, and makes full use of their notably high $n > 1.44$ refractive index values throughout the visible-to-near-IR wavelength range [247, 248], that enable light guiding in most human tissues.

While chitin is ubiquitous in nature – integral in producing many of the photonic structures described in Section 2.1, and is the major constituent of the cicada wing described previously – its technologically relevant deacetylated derivative chitosan, frequently used for scaffolds in tissue engineering [249] and electronic sensor substrates [250], is somewhat less popular for fabrication of biopolymer optics. Protein-based silk fibroin, on the other hand, is among the most widely used, as, in addition to all the aforementioned positive features, this biopolymer excels over available alternatives largely due to its excellent elasticity and all-water processing [176]. The simplest silk-based photonic device can be prepared by merely spin-coating its aqueous solution onto a planar substrate to form a submicron fibroin film, that can act as a basic interferometer where signal readout is performed with the naked eye based on iridescent colors observed under white light illumination. In damp environments silk fibroin tends to be infiltrated by water and undergo substantial yet reversible swelling, which, in turn, changes the color appearance of the film that acts as a rudimentary humidity sensor that can also be employed as an anti-counterfeit measure [239], shown in Figure 2.14.

Much more elaborate optical behaviors can be realized on a silk fibroin platform by performing microscale or nanoscale structuring, as illustrated by examples given in Figure 2.15. For instance, silk fibroin waveguides for transmitting visible or near-IR radiation can be created by way of printing of a 28% aqueous regenerated silk fibroin solution onto a planar silica substrate by extruding through a 5 μm diameter tapered microcapillary nozzle into a methanol-rich coagulation reservoir, wherein silk undergoes crystallization [251]. Representative pictures of resultant structures are provided in Figure 2.15 (a), where top-down images reveal the uniformity and smooth side-wall surface of the waveguides, whereas the cleaved cross-section view shows the trapezoid transverse profile formed due to the silk solution wetting the substrate. For $\lambda = 633$ nm light the refractive index of printed silk was determined to be around $n = 1.54$, *i.e.* slightly above that of the borosilicate glass substrate, which was sufficient to guide this light with propagation losses of around 0.25 dBcm^{-1} [251].

Silk fibroin has also been demonstrated as amenable to creation of photonic structures with subwavelength feature sizes by using soft lithography methods, such as the one summarized in Figure 2.15 (b). In this case a regenerated fibroin solution was spread over a polydimethylsiloxane mold of various holographic or diffraction gratings with groove densities ranging from 600 to 3600 per millimeter [176, 252]. The film is then left to dry for solvent removal, upon which the fibroin layer is separated from the mold and hardened in water vapor for up to 36 hours. Similar methods have been shown to yield a variety of structures, ranging from microscale 2D microprism array reflectors [255] to nanoscale planar diffractive patterns containing features as small as 100 nm with 30 nm separation [256]. What promotes such structures from being generic refractive index sensors [257] to full fledged biochemical detection devices, however, is the ability of silk fibroin to accommodate biological dopants such as enzymes and proteins in a state that maintains their functionality [258]. In Figure 2.15 (b) the spectral response of a silk grating transducer is modified by hemoglobin inclusion, which in turn undergoes a reversible change, observable in its absorbance spectrum, depending on whether it is immersed in an oxygenated or a deoxygenated solution [252]. Furthermore, viability other active molecules, such as horseradish peroxidase enzyme for peroxide detection, or an organic pH indicator phenol red has also been demonstrated [252].

A somewhat related silk templating method can also be employed to create more elaborate 3D inverse opal photonic crystals, illustrated in Figure 2.15 (c). In this case the master is comprised of an opal structure, made up of monodisperse polymethylmetacrilate nanospheres self-assembled on a silicon wafer surface [253]. The air gaps in this photonic crystal where then infiltrated with a 8% by weight optical grade solution of regenerated silk fibroin. Once dry the resultant film was detached from the Si wafer and immersed in acetone to dissolve the template nanospheres. What remains is a *fcc* fibroin scaffold lattice that exhibits structural coloration as a result of its partial photonic band gap, evident in the image given top-left in

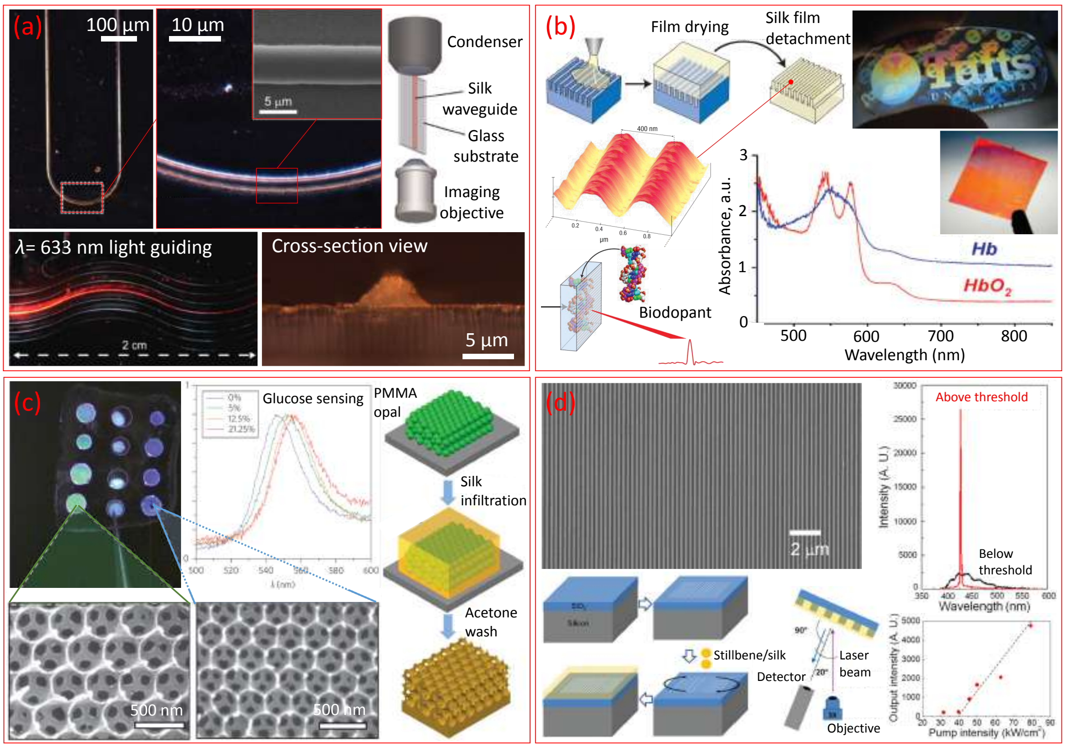

Figure 2.15: Silk photonic devices operating in the visible wavelength range. (a) Ink-printed fibroin waveguides [251]. Top-down images of the waveguides patterned on a silica substrate are on the left, whereas a cross-section view is displayed on the lower-right. (b) Functionalized silk diffraction grating sensors [176]. Sketch at the top illustrates the soft lithography fibroin templating process of a 2400 groove per millimeter grating, visualized close-up by way of atomic force microscopy, along with a picture of a silk-imprinted white-light hologram. Silk can be functionalized using bioactive molecules, as shown bottom-left. Graph on lower-right plots the spectral response of a hemoglobin-doped silk grating, pictured in the inset, in the presence as well as absence of O_2 [252]. (c) Silk inverse opal 3D photonic crystals [253]. Image on the upper-left shows the structural colors exhibited by different period photonic structures, respectively visualized by scanning electron microscopy. A simplified sketch of the fabrication process is on the right. Spectral response was shown to be sensitive to the aqueous concentration of glucose. (d) Blue lasing in stilbene-doped silk fibroin distributed feedback Bragg grating [254]. Scanning electron microscopy image of the grating, as well as its preparation and investigation setup sketches, are given on the left. Spectral and excitation characteristics of the resulting laser are plotted on the right.

Figure 2.15 (c). Not constrained exclusively to silk, this technique has been used to produce similar structures in a chitosan biopolymer as well [259]. The spectral response of a silk inverse opal can be controlled by using different diameter polymethylmetacrilate spheres during fabrication, but also by subsequent exposure to water vapor or UV radiation, which compresses the lattice blueshifting its spectral response, or by infiltrating its cavities with an appropriate refractive index solvent, resulting in a redshift [260]. Much like in the case of a grating, silk inverse opal photonic crystals can be used for refractive index sensing, as demonstrated by way of optical glucose detection demonstrated in Figure 2.15 (c), or, when doped with strongly absorbing gold nanoparticles, can also be employed as a biodegradable optical implant for photothermal therapy applications [253].

Furthermore, silk fibroin, much like certain other biomaterials, is not restricted for use in production of passive optical components either, as it has been demonstrated under suitable dye doping and optical pumping to act as an optical gain medium [254, 261, 262]. One of the realizations of lasing, using a stilbene azo-dye doped silk one-dimensional distributed feedback Bragg grating platform, is summarized in Figure 2.15 (d). Here, again, a templating approach was used, in which second order Bragg gratings with periods in the vicinity of 270 nm were etched into a silica film that acted as a master onto which the doped regenerated silk fibroin solution was subsequently spin coated [254]. When excited by a $\lambda = 355$ nm laser, the silk-embedded dye molecules start to exhibit stimulated emission once pumping power exceeds the fairly low threshold of 45 kWcm^{-2}, and produce a sharp spectral peak at around 430 nm, set by the refractive index-adjusted Bragg grating periodicity.

While the aforementioned biocompatible silk-based photonic device examples were designed to operate mainly at visible wavelengths, notable complementary data, particularly relevant for biochemical sensing related applications, can be gleamed at other spectral regions. The terahertz range is particularly rich in biomedical information, as many of the DNA and protein intra/intermolecular vibration modes have energies which correspond to those electromagnetic frequencies [265, 266]. Recent advances in submillimeter wavelength metamaterials have attained substantial enhancements in both local terahertz field intensity as well as spatial selectivity [267, 268], hence, biocompatible realizations of equivalent devices will be needed to fully utilize the unique biosensing properties of this spectral region *in vivo*.

This motivation has led to the first large-area realization of planar split-ring resonator array terahertz frequency range metamaterials on a free-standing flexible fibroin substrate [269]. The microscale metal structures were created by physical vapor deposition of gold through a shadow mask pattern, thereby avoiding any use of potentially toxic photoresists or solvent chemicals. The top section of Figure 2.16 (a) provides an optical image of such a biocompatible metamaterial that, unlike its solid-state counterparts, can be conformally applied to any number of curved surfaces. In the present example various types of metal antenna structures on silk have been used as sensors for the quality control of food [263]. As the impedance of an antenna is dependent on the dielectric environment, any resonance response will be affected by factors such as moisture, gas emission, and salt content of various perishable goods in its immediate vicinity. Substantial terahertz spectroscopic signal enhancement can be observed when metamaterial antennas are applied onto the surface of an egg, however, the same principle is applicable at other electromagnetic radiation wavelengths, such as the microwave or radio frequency ranges. Figure 2.16 (a) gives further examples of how silk-patterned planar gold antennas, akin to radio-frequency identification tags, can be used to monitor the ripening process of fruit or bacterial fouling of cheese products. Also, spoilage of milk was observable using a 1.5 GHz resonant antenna, which operates in the minimum electromagnetic energy absorbance region for the product. In all these cases silk fulfills the role of a flexible, adhesive, biodegradable, biocompatible and edible substrate. Furthermore, fibroin biopolymers, despite being polypeptides with a complex range of secondary structures, appear to be reasonably well suited due to their semi-transparency in the 0.15-to-1.5 THz frequency range [269].

However, submillimeter wavelength radiation absorbance losses in silk are approximately 30 times above those in polyethylene [270], commonly used for producing terahertz radiation guiding fibers. One way of producing a medium suitable for transmitting radiation over extended distances in biocompatible, yet somewhat dissipative, fibroin is to create a foam-like porous material, in which most of the submillimeter radiation propagates in a highly transmittive dry gas. Such a silk foam waveguide [264] was prepared and characterized as part of the work summarized in Figure 2.16 (b). Here, the foam waveguide was created by pouring an 8% aqueous solution of fibroin into a 5 mm diameter mold vessel and subsequently removing all water by way of lyophilisation. Optical images and scanning electron micrographs of the resulting material reveal that it is constituted as a radial arrangement of microscale thickness fibroin flakes, where air makes up approximately 94% of the foam volume. Terahertz radiation propagation trough silk foam structures was investigated using time-domain spectroscopy over a series of cutback measurement iterations [270] and yielded a bulk refractive index value

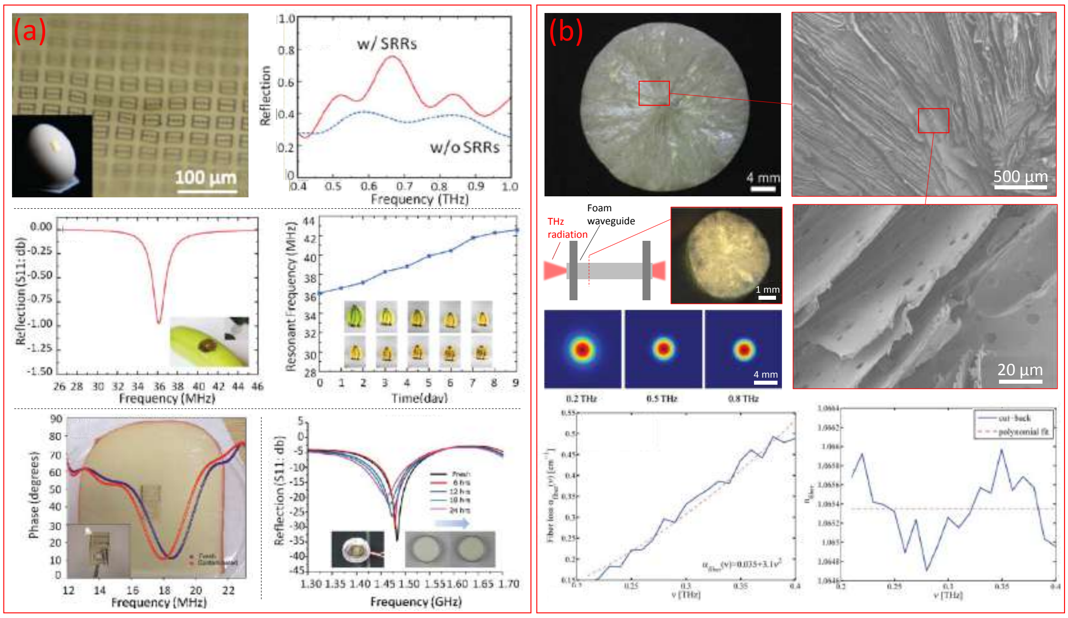

Figure 2.16: Silk at or below the terahertz radiation frequency region. (a) Metallic antennas on flexible silk for food quality control [263]. Top panels depict split-ring resonators (SSR) applied on an egg as well as associated terahertz reflectance spectra. Middle panels show the spectrum of a silk-printed radio frequency antenna applied onto a banana, as well as its resonance shift occurring over the course of ripening. Antenna impedance phase angle spectral dependence for cheese with and without bacterial contamination, and resonance shift of a microwave resonator during milk spoilage are plotted bottom left and right respectively. (b) Fibroin foam terahertz waveguides [264]. Top of the panel depicts the 94% air fraction silk foam, as well as close-up images of its microstructure. A cross-section view of a 5 mm diameter waveguide and its simulated fundamental HE_{11} mode intensity distributions at different frequencies are provided middle-left. Plots at the bottom show experimental spectra of waveguide absorption losses and modal effective refractive index.

of $n_{\text{foam}} \approx 1.0594$ and an extinction coefficient which scales quadratically with frequency as $\alpha_{\text{foam}}[\text{dBcm}^{-1}] \approx 0.78 + 36.9 \cdot (\nu[\text{THz}])$. Hence, foam fibers attain an approximately one order of magnitude reduction in absorbance compared to bulk silk, and can exhibit propagation loss as low as 3.5 dBcm^{-1} in the 0.2-to-0.5 THz electromagnetic radiation frequency region.

Biologically derived polymers such as the chitosan and cellulose polysaccharides, as well as proteins like silk are generally robust, flexible, biocompatible and biodegradable insulating dielectrics. However, as illustrated by the wealth of different functionalities described here, silk fibroin tends to stand out as a platform for a wide range of photonic applications. The main advantages of silk are its high optical transparency and, more importantly, high water solubility in its regenerated amorphous state, which makes fibroin inherently compatible with a multitude of established nanofabrication approaches. Similarly, this protein can exhibit a number of different secondary structures with diverging physical properties, which endows it with considerable versatility, but makes it a complex material to understand and control. Yet, the technologically relevant intricacies of fibroin behavior can be illustrated and untangled most readily by investigating its primary evolutionarily derived state – the natural silk fiber.

2.4 Optical properties of silk

Silks are a class of fibrous protein-based biopolymers independently yet convergently evolved by the larvae of certain insects such as moths, as well as by arthropods, most notably spiders [271, 272]. Structures constructed from these materials fulfill critical functions related to prey capture, protection, reproduction and dispersal among may others, therefore it is within expectation that silk, as result of being subjected to stringent natural selection pressures, possesses extraordinary tensile strength and elasticity on par with that of the most robust of artificial fibers [273–275]. Furthermore, as a result of the high degree of crystallinity and hydrophobicity exhibited by much of the protein, natural silks possess notable chemical stability, as they are insoluble in water, most organic solvents, as well as dilute alkali and acidic solutions [276].

Initial adoption of silk for human use was related to its optical transparency which, when coupled with the triangular prism-like cross-section profiles as well as the smooth surfaces of individual fibers spun by the domesticated *Bombyx mori* silkworm, results in the lustrous appearance of fabrics they comprise. Furthermore, silk does not illicit a strong immunological response from the human body, and was therefore frequently used for wound sutures and dressings [277]. It is unsurprising then, that even the most contemporary complex biotechnological applications of fibroin-based polymers [278] hinge on those very same favorable optical characteristics [176, 252] as well as on their biocompatibility [279, 280] and controllable biodegradability [241].

The aforementioned exceptional properties of silk become all the more remarkable considering that it is predominantly constituted of only several different non-vital amino acids – mostly glycine, alanine and serine – arranged in recurrent motifs that comprise macromolecular fibroin protein constructions of up to 350 kD in total mean molecular weight. Furthermore, its synthesis in the familiar fibrillar form is conducted under ambient physiological conditions and using aqueous non-toxic chemistry, which, despite appearing facile in natural organisms, has proved challenging to replicate artificially [180]. Most of the mechanical and chemical resilience of silk fibers is a result of the hierarchical supramolecular structure of the biopolymer, stabilized *via* extensive hydrogen bonding that gives rise to complex secondary protein structures. In particular, rigid β-sheet nanoscrystals, interlinked by extensible semiamorphous random coil regions, form a sophisticated network for efficient load distribution [281], which, despite relying on one of the weakest molecular bond types, yields tensile fiber strengths close to those of steel. So, while the extraordinary technological versatility of fibroin allows for it to be prepared for human uses as hydrogels, planar films, conformal coatings as well as porous or solid 3D matrices [282], the natural fiber state of this biopolymer is particularly relevant, since it possesses the full evolutionarily self-optimized complexity that needs to be unraveled to emulate the control over composite material properties demonstrated in nature.

To this end spectroscopic methods are among the most sensitive for probing various possible dipolar excitations inherent to a complex molecular network. These include electronic transitions between different molecular orbitals at UV or visible frequencies, vibrations of specific bonding configurations in the infrared, as well as collective oscillations of large supramolecular elements observable towards the submillimeter wavelength range. Indeed, all this spectral information should be viewed as complimentary in deducing the properties of molecular composites. For example, different forms of silk, despite having virtually identical amino acid compositions, can possess radically disparate secondary molecular structure derived properties, such as water solubility or mechanical strength. Conversely, broadband spectroscopic characterization reveals the possible utility as well as limitations of a composite material in a given radiation wavelength region, thereby identifying key parameters relevant for their diverse possible photonic applications.

In this work, conducted in collaboration with with the group headed by Prof. Junko Morikawa at Tokyo Institute of Technology, researchers overseen by Assoc. Prof. Jingliang Li at Deakin University, as well as with the team supervised by Assoc. Prof. Jeffrey Davis at Swinburne University of Technology, electromagnetic radiation absorbance properties of natural silk fibers were probed over an unprecedentedly broad span of wavelengths, ranging from ultraviolet all the way to the terahertz region [283]. First, electronic excitations of the fibroin amino acid constituents are investigated by means of photoluminescence as well as visible wavelength spectroscopies. The infrared spectral region, in turn, yields the fingerprinting information related to bond vibrations, and also offers insight relating to their conformations in the complex macromolecular network that is silk. Furthermore, diffraction-limited imaging at mid-infrared wavelengths allows for resolutions sufficient for spatially mapping the structure of a single microscale silk fiber [284]. Lastly, terahertz frequency radiation absorbance spectroscopy methods are shown to uncover long-range collective vibrational motion related spectral peaks. Sensitivity to subtle conformational variations in silk was tested by performing all measurements on natural fibers spun by domesticated *Bombyx mori* and wild *Antheraea pernyi* silkworms, and, wherever informative, by giving equivalent spectroscopic information for water-soluble reconstituted fibroin devoid of an appreciable presence of β-sheet secondary structures.

2.4.1 Ultraviolet-to-near-infrared range

Silk fiber samples spectroscopically investigated here primarily come from two organisms – the domesticated mulberry silkmoth *Bombyx mori*, and the wild Chinese tussah silkmoth *Antheraea pernyi*. For at least five millenia the familiar *B. mori* species has been selectively bred for the transparency and texture of the threads they spin, hence, it is the chief source of commercial silk fabric available worldwide. Likewise, the optical clarity of domesticated silkworm sourced biopolymers make them particularly applicable for use in photonics. On the other hand, *A. pernyi* silkworms exist in the wild and, unlike their human dependent counterparts, survive the most extreme temperature variations among all silkmoth pulpa [285]. While historically the degree of *A. pernyi* cultivation in the textile industry was much more limited, this silk has recently attracted considerable attention due to its similarity in protein structure to the much more mechanically robust spider dragline fibers [286], as well as due to its facilitation of cell adhesion [287].

B. mori cocoons used for sample preparation originate from a silkworm rearing house in the Jiangsu province of China. On the other hand, wild *A. pernyi* silkworm cocoons were obtained from Liaoning province of China. Natural silk threads are comprised of two fibroin-based fibers encased in a glue-like protective sericin coating. In totality a silkworm cocoon is comprised of roughly $20-30\%$ sericin and $70-80\%$ fibroin proteins, along with trace amounts of carbohydrates and waxes [288]. While sericin has numerous uses of its own [289], it has to be washed out to unravel fibroin based fibers from the cocoons. This procedure, called degumming, was done by immersing raw cocoons in a 0.5% aqueous Na_2CO_3 solution heated to a 98°C temperature. The process was repeated three times, with each stage having a duration of 60 and 30 minutes for *A. pernyi* and *B. mori* cocoons respectively [290, 291]. Lastly, the degummed silk fibers were thoroughly rinsed in 60 °C temperature deionised water and dried in air.

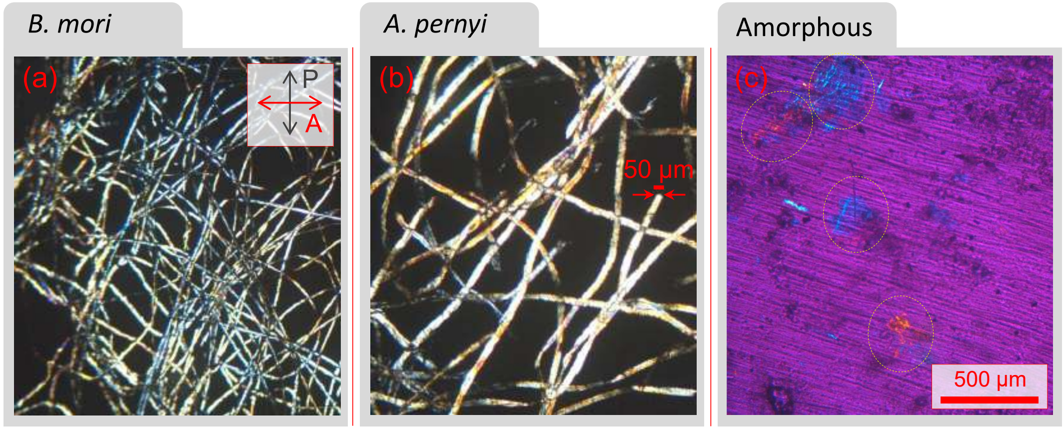

Figure 2.17: Cross-polarized optical microscopy images of silk [283]. Degummed silk fibers spun by (a) *B. mori* and (b) *A. pernyi* moths. (c) Amorphous *B. mori* silk fibroin, compressed in a KBr powder pellet. Regions rich with amorphous fibroin are highlighted by yellow circles. Images were acquired at Tokyo Institute of Technology by the research group under supervision of Prof. Junko Morikawa.

Cross-polarized optical microscopy images of the resultant birefringent fibers are provided in Figure 2.17, where panel (a) shows *B. mori* and (b) depicts *A. pernyi* cocoon-extracted strands. Morphologically *B. mori* silk is comprised of fine 10 μm diameter fibers, substantially thinner than in the *A. pernyi* case were 50 μm widths are quite common. Shapes of these two types of fibers differ notably as well, since *B. mori* derived strands have rounded-tip triangle shaped cross-sections, whereas those spun by *A. pernyi* larva exhibit an elongated wedge-like appearance [292]. Of primary interest here, however, are the structural differences in the composition of silk created by the two different species of organism. In both cases the biopolymer materials are made up of the same amino acids, such as the main constituents alanine (Ala) and glycine (Gly) as well as some contributions from serine (Ser) and tyrosine (Tyr). However, the relative quantity of the main ingredients is different for the two fibroin types, as *B. mori* case can be considered glycine rich, with an Ala/Gly molar percentage ratio of 30%/43%, while in *A. pernyi* silk alanine is more prevalent at 49%/28% [293]. Furthermore, the primary structures of the two fibroin protein compounds are also fairly distinct. In particular, *B. mori* β-sheets are in large part made up of repetitive alternating (Gly-Ala)$_n$ motifs [294], whereas in *A. pernyi* case those two amino acids are mostly kept in separate large poly-alanine blocks and glycine rich regions [293, 295] in a way that mirrors spider dragline silks [286].

Amino acids constituting silk fibroin exhibit strong electronic absorbance in the ultraviolet wavelength region, and in this work have been probed by means of photoluminescence excitation spectroscopy. Measurements were conducted by placing a small number of fibers in a quartz cuvette, which was then mounted into a LS-55 fluorescence spectrometer (Perkin-Elmer Inc.). The photoluminescence excitation spectra, shown as 2D plots Figure 2.18, were obtained by sequentially acquiring spectra of emitted light whilst exposing the fibers to monochromatic incident radiation with gradually shifting wavelengths. The prominent straight bright lines, numbered in Figure 2.18 (b), are diffraction artifacts and provide no spectroscopic information. Similarly, the emission bands observable between higher order diffraction signatures are merely replicas of the true fluorescence bands situated between the

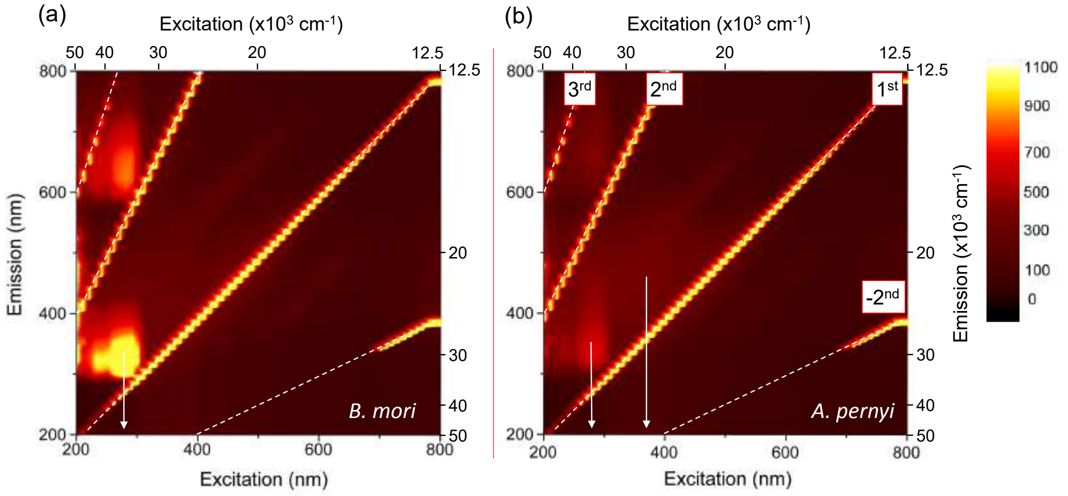

Figure 2.18: Photoluminescence excitation spectra of degummed (a) *B. mori* and (b) *A. pernyi* silkworm-spun fibers. Arrows mark notable fluorescence bands observed at 280 nm and 380 nm excitation. High intensity linear features, numbered in panel (b), are diffraction related artifacts. Only the signatures located between the 1st and 2nd order diffraction artifacts correspond to unique spectroscopic information.

1st and 2nd order diffraction artifacts. The difference in emission band intensities between *B. mori* and *A. pernyi* fibers is mainly due to disparities in sampled volumes.

The primary building blocks of fibroin – alanine, glycine and serine – absorb in the ultraviolet spectral region at wavelengths below 210 nm [296], which was just out of reach for full acquisition by the present experimental apparatus. However, strong fluorescence signatures, emitting at roughly 340 nm and observable at the very onset of the excitation axis for both *B. mori* and *A. pernyi* fibroin samples, can be tentatively assigned to these amino acids. Still, even with full spectral information of UV absorbance at wavelengths below 200 nm, due to the immense variety and abundance of peptide bonds in biopolymers as well as overlapping absorption of other materials, analytical work conducted in this spectral region is wrought with considerable challenges.

On the other hand, protein absorbance at mid-UV frequencies is typically related to the presence of aromatic amino acids such as tyrosine, phenylalanine, tryptophan and histidine, hence can be understood much more readily. The most prominent fluorescence bands exhibited by *B. mori* as well as *A. pernyi* silks are induced by 230 nm and 280 nm excitation wavelengths, and manifest as emission situated at 340 nm. In the particular case of fibroin these signatures are assignable to $\pi \longrightarrow \pi^*$ transitions in tyrosine [297, 298], which makes up approximately 5% of domestic and 4% of wild silk molar composition [293]. Weak fluorescence signatures observable in the 215-to-235 nm excitation wavelength region can be attributed to sericin residues [299].

The single major qualitative difference between the photoluminescence excitation spectra of *B. mori* and *A. pernyi* fibroins is the additional broad indistinct fluorescence band at approximately 450 nm, induced by 380 nm radiation, which is observable for wild silks but is absent for domesticated ones. Similar spectral signatures at ~ 345 nm have been reported for sericin solutions extracted from *A. pernyi* silks, where sericin samples obtained from strands spun by different silkworm species exhibited notable variations in their UV spectral

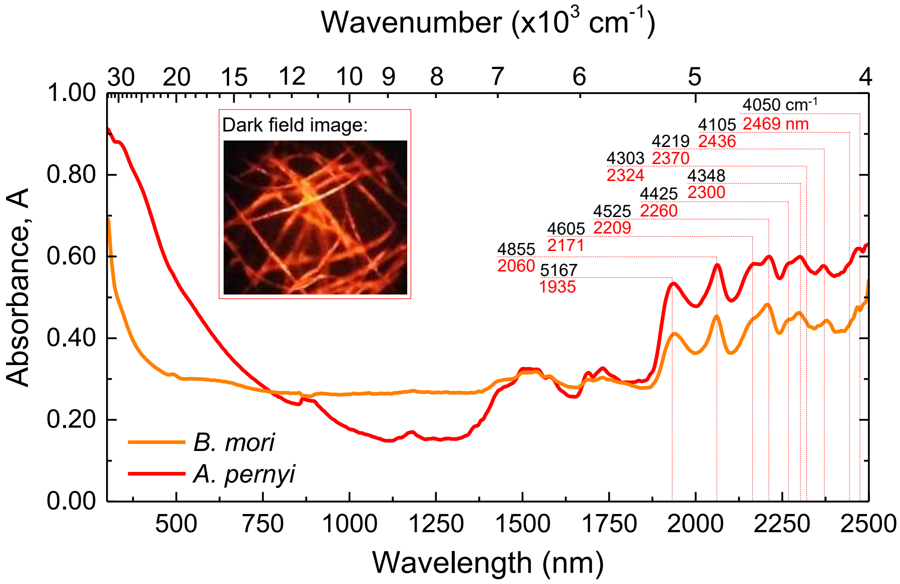

Figure 2.19: Absorbance of degummed *B. mori* and *A. pernyi* silk fibers in the UV-to-near-IR wavelength region. Highlighted spectral features correspond to main overtone vibrational modes. Inset shows a dark-field optical microscopy image of *A. pernyi* silk fibers.

responses [297]. Furthermore, visible brown pigmentation of certain wild silks has also been hypothesized as resulting from 460 nm wavelength absorbing chromophores created through UV photo-oxidation of tyrosine, which may play a part in UV protection provided by a silk cocoon to the insect in its vulnerable pupal stage [297].

Fibroin biopolymers possess a low molar absorptivity throughout the visible spectral region and at the onset of the near-IR, as photon energies there are too low to induce electronic transitions in the constituent peptides, however, above those necessary to be in resonance with molecular bond vibrations. Spectral characterization of *B. mori* and *A. pernyi* silk fibers at these wavelengths was performed using a LAMBDA 1050 spectrophotometer (Perkin-Elmer Inc.), equipped with a 150 mm diameter integrating sphere attachment which allowed to minimize the influence of elastic scattering in the stochastic fiber mesh. Absorbance spectra were deduced from full hemispherical transmittance and reflectance measurement results and are depicted in Figure 2.19.

The near ultraviolet portion of silk spectral response captures the tail-end of peptide absorbance, which for *B. mori* silk all but vanishes at the onset of the visible wavelength region. In the *A. pernyi* case, on the other hand, this decrease is much more gradual, extending all the way to the red portion of the visible spectral range and resulting in the silk having a yellowish tint. Fibroin can be ruled out as the source of this coloration, since both types of fibers are made up of the same amino acids. In addition to the previously mentioned photodecomposition related tanning mechanism, the most likely explanation for the coloration of wild silk is that fibers are coated with carotenoid-containing excretory liquids of the silkworm during spinning [300, 301]. These pigments cannot be synthesized by animals and must originate from plants the larva consume. Furthermore, diet-derived chromophores tend to be localized in the outer sericin layer [302], which explains the aforementioned spectroscopic variability of sericin originating from different silkworm species [297], as they tend to feed on different plants.

When external sources of pigmentation are accounted for fibroin based biopolymers are virtually transparent, and most of the optical losses exhibited by *B. mori* silk in the 400 nm to 1800 nm wavelength region are a result of scattering that the integration sphere setup fails to capture. Hence, it is unsurprising that natural spider dragline silk strands have been shown to act as reasonably efficient optical fibers with an attenuation coefficient of 10.4 dBcm^{-1} for 800 nm radiation [303]. Similar results, only with with slightly higher propagation losses of 28 dBcm^{-1}, have also been demonstrated for *B. mori* silk strands [304]. However, as mentioned in Section 2.3, regenerated silk fibroin can be used to make planar optical fibers which, as a result of single-mode operation optimized geometry and avoidance of scattering defects commonly present on natural fibers, exhibit optical losses below 0.1 dBcm^{-1}, in line with those typical for polymethylmetacrilate waveguides [251].

In the short-wavelength infrared spectral range above 1400 nm first vibrational peaks begin to appear, and are related to high energy combination overtone modes of the various peptide chemical bonds [305]. To keep with the usual conventions of vibrational spectroscopy the peak assignments discussed further on will be done in wavenumber units of spatial frequency $\tilde{\nu}$, related to the wavelength as $\tilde{\nu}\left[\mathrm{cm}^{-1}\right] = 10^7/\lambda\,[\mathrm{nm}]$. The indistinct complex arrangement of features up until 5200 cm^{-1} is generally attributable to the first and second overtones of various hydrogen bond vibrations, which, while lacking in specificity, illustrates the complex variety exhibited by the secondary structure of fibroin in natural silk fibers.

Covalent bond related vibrational peaks are much more pronounced and readily distinguishable however, and are highlighted by red lines in Figure 2.19. The first prominent spectral signature, situated at 5167 cm^{-1}, is reported as arising due to the combined stretching and bending vibrations of O–H bonds [305]. The wavenumber region spanning roughly from 4900 cm^{-1} to 4500 cm^{-1} is associated with combined vibrations of the different amide bands discussed further on in Section 2.4.2, such as Amide A and Amide II at 4855 cm^{-1} related to random coil as well as α-helix secondary structures [305, 306], Amide B and Amide II at 4605 cm^{-1}, and Amide A and Amide III at 4525 cm^{-1} which pertains to both the strength and prevalence of hydrogen bonds as well as to the amount of β-sheets in a biopolymer [306]. The latter mode is particularly informative as it exhibits the one evident difference in relative peak intensity between the absorbance spectra of *B. mori* and *A. pernyi* silks. It is more pronounced in the domesticated silk sample, which corroborates its higher β-sheet content.

The remaining simultaneous excitation modes are related to various motions of aliphatic C–H bonds, starting with a group of four possible $\nu_{\mathrm{CH}}/\delta_{\mathrm{CH}}$ vibration symmetry combinations, where 4425 cm^{-1} corresponds to an antisymmetric/antisymmetric, 4348 cm^{-1} to a symmetric/antisymmetric, 4303 cm^{-1} to an antisymmetric/symmetric, and 4250 cm^{-1} to a symmetric/symmetric configuration [305]. Similarly, the next pair of peaks at 4170 cm^{-1} and 4050 cm^{-1} are attributable to a combination of C–H bond stretching and rocking motions in their respective antisymmetric $\nu^{as}_{\mathrm{CH}}/r_{\mathrm{CH}}$ and symmetric $\nu^{s}_{\mathrm{CH}}/r_{\mathrm{CH}}$ varieties. Lastly, the bands at 4105 cm^{-1} and 4010 cm^{-1} are, correspondingly, assigned to skeletal C–H vibration combinations with ν^{as}_{CH} and ν^{s}_{CH} [305].

The main advantage of silk fibroin in the visible and near-IR spectral ranges is the distinct lack of spectroscopically observable activity at those wavelengths. Therefore, such biopolymers can be readily used as biocompatible, conformable and robust passive dielectric media for numerous photonic devices and applications. Short-wavelength IR radiation, on the other hand, can induce a multitude of complex molecular vibration combinations or overtones in the peptide network. Therefore, photonic utility of silk at these wavelengths appears unlikely. Furthermore, while this segment of the infrared spectrum can provide a lot of information about the secondary structure of protein-based materials, combination spectral peaks generally have lower intensities than their fundamental counterparts and a diminished specificity, hence, short-wavelength IR spectroscopy is rarely used for characterization of silk. On the other hand, the mid-IR region hosts many of the prominent fundamental vibrational bands of fibroin as well as other amino acid based materials and is for that reason discussed in the next section.

2.4.2 Silk at mid-infrared

Among all the spectral regions used to probe fibroin as well as other protein based materials, mid-IR, spanning form 4000 cm^{-1} to 400 cm^{-1} (or 2.5 µm to 25 µm in wavelength units) is arguably the most expedient and definitely the most widely used. This is unsurprising given the multitude of fundamental vibrational bands resonant at these radiation frequencies and the wealth of information about silks that can be deduced from them, which includes the secondary structure and the crystallinity degree of their constituent proteins [307, 308] as well as the presence of non-organic compounds like water [309] or calcium oxalate [310]. Furthermore, mid-infrared spectroscopy was shown to be capable of sufficient specificity to discriminate and classify silk samples based on evolutionary relatedness of silkworm species they were derived from [311].

The infrared radiation absorbance spectral measurements were performed using a Fourier-transform IR spectrometer ALPHA (Bruker Corp.), operated in an attenuated total reflectance configuration through a diamond widow. In this case optical excitation is evanescent, hence, requires little in terms of sample preparation and is particularly convenient when dealing with rough and deformable solids such as natural silk fibers. On the other hand, evanescent infrared radiation can only penetrate less than a few micrometers into the sample, so only the surface region of a fiber can be effectively sampled.

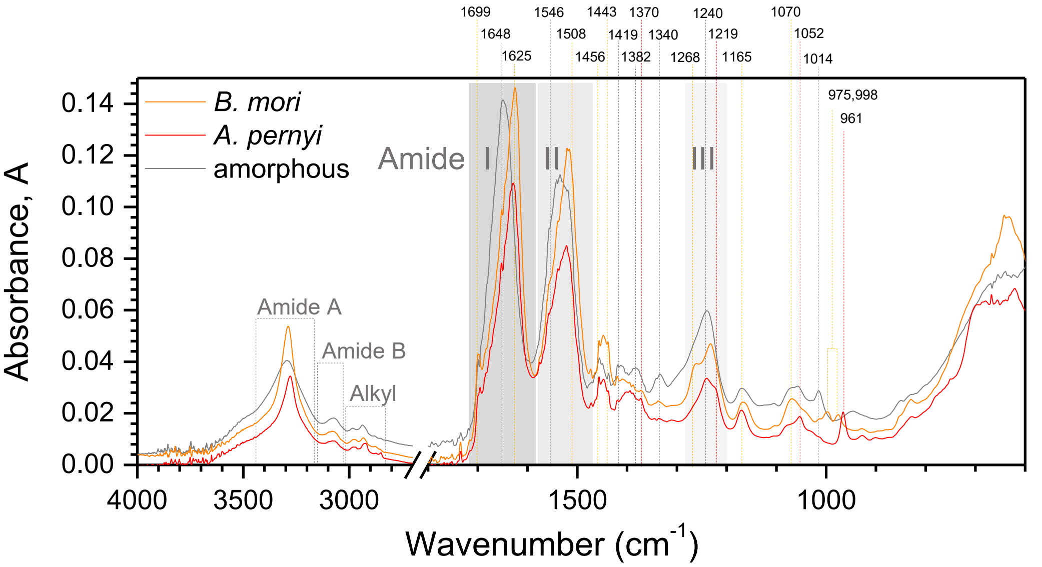

Figure 2.20: Attenuated total reflectance-derived absorbance of degummed *B. mori* and *A. pernyi* silk fibers, as well as that of amorphous *B. mori* fibroin, in the mid-IR wavelength region [283]. Main peaks in each spectrum are indicated by color-matching dashed lines. Mid-IR spectroscopy experiments were performed at Tokyo Institute of Technology by the research group under supervision of Prof. Junko Morikawa.

Figure 2.20 depicts the mid-infrared attenuated total reflectance-derived absorbance spectra of natural fibroin-based biopolymers in the form of *B. mori* and *A. pernyi* silk fibers, which were stripped of their sericin coatings by means of a degumming process described in Section 2.4.1. In addition, spectra of β-sheet rich, high-crystallinity, hence water insoluble, fibers are compared to those of mostly amorphous and water soluble regenerated silk fibroin, which in large part exhibits a random coil secondary structure. Amorphous regenerated silk fibroin used here was extracted from degummed *B. mori* silk fibers by dissolving them in a 65 °C temperature ternary 1:8:2 molar ratio mixture of $CaCl_2$, water and ethanol. Salt-containing solvent systems are known to disrupt the hydrogen bonds that maintain the secondary structures of fibroin, particularly the β-sheets crucial for stabilization of silk, without inducing chemical degradation of the protein [312]. The solution was subsequently dialysed against ultra-pure water using 14 kDa molecular weight cut-off cellulose tubing (Sigma-Aldrich Inc.) at room temperature for 4 days. The last step of the procedure involved the regeneration of silk fibroin by lyophilizing the dialysed solution [313]. Amorphous fibroin samples were prepared for spectroscopic investigation by pulverizing and mixing them with KBr powder, and subsequently pressing it into a 100 µm thickness IR transparent pellet, the surface of which is depicted in the cross-polarized optical microscopy image of Figure 2.17 (c).

The highest wavenumber mid-IR absorbance peaks prominent in all the spectra of Figure 2.20 and centered around 3300 cm^{-1} are attributable to the amide A band, which mainly corresponds to N–H vibrations. This mode, due to being confined exclusively in the NH group, is not particularly sensitive to the conformation of the peptide backbone, however, its spectral position is highly dependent on hydrogen bonding [314]. Here the first major difference between crystalline silk and amorphous regenerated fibroin mid-IR absorbance becomes evident, as the amide A bands of fibers exhibit sharp peaks attributable to the β-sheet structure. Conversely, amorphous fibroin has a much broader spectral signature, indicative of stochastic hydrogen bonding in the random coil network. The amide B band at around 3100 cm^{-1} is much weaker than its higher energy counterpart and is typically understood as either a Fermi resonance between the fundamental N-H vibrations and the first amide II band overtone [314] or as arising due to intramolecularly hydrogen bonded NH groups [315]. The group of mid-IR vibrational modes in the 3000 cm^{-1} to 2800 cm^{-1} wavenumber range is attributable to C–H bond vibrations. Here a striking difference between domestic and wild silk samples is that in both natural as well as regenerated *B. mori* fibroin only the $\nu^{as}_{\text{CH}_3}$ at 2961 cm^{-1} and $\nu^{s}_{\text{CH}_3}$ at 2874 cm^{-1} vibrations are pronounced. Natural *A. pernyi* silk fibers, on the other hand, have noticeable $\nu^{as}_{\text{CH}_2}$ at 2920 cm^{-1} and $\nu^{s}_{\text{CH}_2}$ at 2850 cm^{-1} modes as well, which is likely due to the presence of chromophores that give the silk its yellow appearance.

Below 1700 cm^{-1} wavenumbers the highest intensity peaks in the spectra of silk fibroin biopolymers are the three amide bands, highlighted in Figure 2.20, where each of them has a complex spectral composition due to conformational variations of the protein [316]. For instance, the amide I signature is attributable to C=O stretching with minor contributions from the out-of-phase C–N stretch, the C–C–N deformation and the N-H in-plane bending vibrations [314]. Generally hydrogen bonding, in which C=O groups readily partake, lowers the frequency of stretching vibrations, therefore, amide peaks of β-sheet rich crystalline fibers are redshifted with respect to their amorphous fibroin counterpart. Specifically, amide I band spectral peaks appearing at 1648 cm^{-1} are associated with the presence of irregular random coil and extended chain structures, whereas 1625 cm^{-1} is attributed to β-sheets [316]. Other notable but less prominent features are turns and bends of the peptide backbone at 1699 cm^{-1}, α-helix in the 1664–1658 cm^{-1} range, and β-turns in the 1654–1647 cm^{-1} region [317].

The amide II band mainly results from out-of-phase combined N–H bending and C–N stretching vibrations, with additional minor contributions from C–C and N–C stretching [314]. It is likewise strongly affected by the secondary structure of the protein, and is not particularly sensitive to side-chain conformation. The major constituents of the Amide II band of silk fibroin are the random coil associated feature at 1546 cm^{-1} and β-sheet related 1508 cm^{-1} shoulder, visible in the fiber samples from *A. pernyi*, but particularly strongly represented in the *B. mori* derived crystalline silk.

Next assembly of peaks approximately in the 1500–1440 cm^{-1} wavenumber range are associated with antisymmetric C–H bending vibrations of CH_3 groups in various conformation state polypeptides [318]. While the line at 1456 cm^{-1} is related to generic $\delta^{as}_{CH_3}$ vibrations in alanine and valine, the shoulder at 1443 cm^{-1} corresponds to these same vibrations in β-sheets of both poly-alanine $(Ala)_n$ and Ala-Gly_n [311]. Its intensity is related to the β-sheet content of a biopolymer and, evidently, the degree of crystallinity is highest in *B. mori* silks, followed by *A. pernyi* fibers, and lowest in regenerated fibroin. Similarly, the symmetric counterparts of the aforementioned polypeptide C–H bending vibrations are located in the 1420–1300 cm^{-1} region [318], the most interesting of which is the one at 1340 cm^{-1}, attributable to α-helical structures [316] strongly represented in *B. mori* regenerated fibroin spectra.

Origins of the amide III band, ranging from 1300 cm^{-1} to 1200 cm^{-1} wavenumber values, are similar to those of the aforementioned amide II signature, the main difference being that N–H bending and C–N stretching vibrations are combined in-phase with each other [314]. However, interpretation of this spectral region is complicated by its dependence on arrangements of both the peptide backbone and its side chains. The band is constituted by signatures related to all the typical secondary structures of silk fibroin [319], such as β-turns at 1308 cm^{-1}, α-helix at 1268 cm^{-1}, random coils at 1240 cm^{-1}, and β-sheets at 1219 cm^{-1} [311]. Amorphous regenerated silk fibroin is particularly spectrally dissimilar to the crystalline fiber samples in this region, as its amide III band is broad and indistinct in a way that is expected for disordered polymer networks. Furthermore, *B. mori* silk fibers, again, appear to have a notably more significant β-sheet contribution to its spectral response than in the case of wild silk.

The first peak just beyond the amide III band, centered around 1165 cm^{-1}, is related to ν_{NC_α} vibrations (where C_α is the carbon atom to which the side chain is attached), and commonly observed in spectra of all silks. However, this line tends to be broader for silks sourced from domesticated silkworm varieties, and even more so for amorphous regenerated fibroin, indicating a larger variety of conformations [311]. Further on, the ν_{CC} skeletal vibration region is where large differences between spectra of different primary structure fibroin samples start to appear [311], as it is sensitive to interruptions of the usual Ala and Gly based patterns by different amino acids. For the samples under investigation here this range hosts two notable peaks, namely the β-sheet related band at 1070 cm^{-1} and the α-coil and metastable β-turn associated signature at 1052 cm^{-1} [316]. Lastly, the tail end of mid-IR spectral region enables the distinction between $(\text{Ala-Gly})_n$ recurring sequence based *B. mori*, and $(Ala)_n$ heavy *A. pernyi* fibroin secondary structures. For example, the feature at 1014 cm^{-1} corresponds to random coil (Ala-Gly) sequences with frequent interruptions by tyrosine or valine [316], and, unsurprisingly, it is primarily observable in the spectrum of amorphous regenerated *B. mori* silk fibroin. Furthermore, differences in the primary structure of β-sheets also become spectrally distinguishable in this wavenumber range, where a doublet at 998 cm^{-1} and 975 cm^{-1} corresponds to $(\text{Ala-Gly})_n$, and a single peak at 961 cm^{-1} is attributable to $(Ala)_n$ amino acid compositions [311, 316].

Despite the obvious convenience of attenuated total reflectance measurements, evanescent excitation extends only over the surface layers of a microscale natural silk fiber. Furthermore, similar spectroscopic investigation performed in transmittance mode yielded broader amide bands, indicating some variance in fibroin conformations throughout the filament volume resulting from the drawing process [284]. This, in turn, raises the question of how secondary structures associated with silk are distributed within a single fiber.

Gaining access to the internal composition of a heterogeneous biopolymer object in the mid-IR spectral region necessitates the restriction of sampled volume either through the use of an optical coherence tomography technique [320], or by preparing thin cross-sections of the sample which are then probed by conventional microspectroscopy methods. However, since individual silk fibers can have thicknesses below 10 µm, highest attainable IR mapping resolutions are crucial for spatial discrimination between different regions in a fiber, hence, the latter more invasive sample preparation method was chosen for this work. It involved embedding pre-aligned single silk strands in a block of epoxy resin jER 828 (Mitsubishi Chemical Co., Ltd.), which, following its solidification, was cut into 1 µm to 5 µm thickness slices using a RV-240 microtome (Yamato Khoki Industrial Co., Ltd.). Both lateral as well as transverse *A. pernyi* and *B. mori* epoxy-embedded silk fiber cross-section slices were prepared, and their cross-polarized optical microscopy images are shown in the leftmost panel of Figure 2.21.

Spectral mapping was performed at the Australian Synchrotron Infrared Microspectroscopy Beamline using a Hyperion 2000 infrared microscope coupled to a Vertex V80v Fourier-transform infrared spectrometer (Bruker Corp.), equipped with a liquid nitrogen-cooled narrow-band mercury cadmium telluride detector. Two types of collection methods

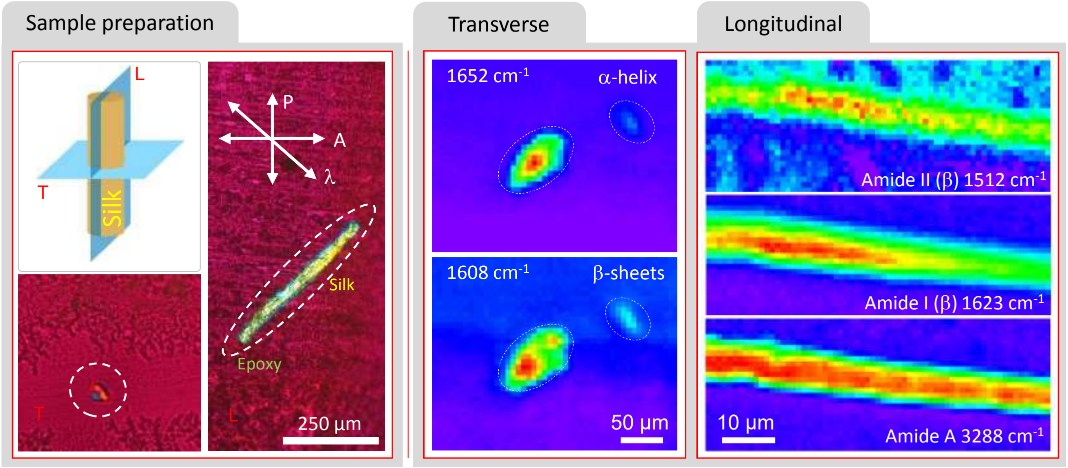

Figure 2.21: Mid-IR absorbance mapping of microtomed silk fiber cross-sections [284]. Leftmost panels show a sketch of naming conventions as well as cross-polarized optical microscopy images of transverse and longitudinal slices of silk fibers embedded in epoxy. Middle panel depicts IR transmittance maps of transverse *A. pernyi* silk fiber slices at wavenumbers associated with α-coil and β-sheet spectral signatures. Rightmost panel shows IR attenuated total reflectance maps of longitudinal *B. mori* silk fiber slices in wavelength regions related to different amide bands. Microtomed silk fiber cross-section samples were prepared at Tokyo Institute of Technology by the research group under supervision of Prof. Junko Morikawa. Mid-IR absorbance mapping experiments were performed at the Australian Synchrotron Infrared Microspectroscopy Beamline.

were used for acquiring spatially resolved spectra – by way of far-field transmittance using a $NA = 0.5$ 36× magnification Cassegrainian objective lens, and through a $n = 4$ refractive index 100 μm diameter facet germanium attenuated total reflectance element coupled to a $NA = 2.6$ solid immersion lens. The far-field transmittance method can ensure a 6.25 μm resolution, which, as shown in the middle panel of Figure 2.21, is sufficient to spectrally map 50 μm thickness *A. pernyi* fibers. However, it proved to be wholly inadequate for investigating much finer *B. mori* silks, which necessitated the approximately 1.9 μm spatial resolution in the amide band region that a full contact Ge solid immersion lens is capable of achieving [321], as demonstrated in the rightmost panel of Figure 2.21.

Transverse spectral maps of an *A. pernyi* silk fiber, representing the 1652 cm^{-1} α-helix and β-sheet 1608 cm^{-1} fibroin conformations, show that both of these crystalline phases are are preferentially located towards the middle of the filament, forming its robust core. Similar distribution of β-sheet associated spectral signatures in the amide I and amide II bands at 1623 cm^{-1} and 1512 cm^{-1} respective wavenumbers are observed in longitudinal cross-sections of *B. mori* fibers as well. Conversely, the generic secondary structure insensitive amide A 3288 cm^{-1} band spectral plots are distributed more broadly across the fiber, showing that hydrogen bonding is prevalent throughout the macromolecular network. This internal structure likely is a result of the shear stress and dehydration during pulling out of the fiber from its initially liquid crystalline state [180], which also gives rise to preferential alignment of β-sheets parallel to the fiber axis [284, 308].

Mid-infrared spectroscopy is eminently useful in characterizing the composition and conformation states of biopolymers in general and, by extension, fibroin-based silks and their complex hierarchical secondary structures. The vast body of work reported in the literature [311, 322] likewise helps to contextualize and verify the present broadband absorbance study of natural silk fibers. Furthermore, infrared radiation wavelengths at spectroscopically relevant amide bands are just small enough to allow for probing the spatial variance of peptide conformations within a single silk fiber. However, spectral signatures of domesticated *B. mori* and wild *A. pernyi* silks with different primary structures of fibroin become strongly divergent only at the skeletal ν_{CC} vibration range. Hence, lower energy collective oscillations of the macromolecular network can be expected to provide additional insight into the higher order structure of natural silk and are therefore described next.

2.4.3 Far-infrared and terahertz spectroscopy

The spectral region spanning approximately from around 600 cm^{-1} to 10 cm^{-1} in wavenumber units, which correspond to the $\lambda = 15$–1000 μm range that encompasses $\lambda = 0.1$–1 mm terahertz wavelengths, is associated with long-range macromolecular motions strongly affected by changes in both the primary and secondary structures of polymer chains. An illustrative example of this type of absorbance is that observed in long alkane chain saturated fatty acids [323] as well as paraffin [324], whose longitudinal accordion mode vibration frequencies redshift with chain length l as $\tilde{\nu} = \sqrt{\frac{E}{\rho}}/(2lc)$, where ρ is the mass density, E is the Young's modulus, and c is the speed of light. Similarly, spectral signatures of first order alkane crystal solid-solid transitions into rotator phases [325] just below melting point, where despite the presence of crystalline order low energy molecular rotations become possible, are also observable in the far-IR [326].

Various ordering configurations and molecular interactions underlying the properties of more complex and biomedically relevant protein and peptide based materials likewise yield useful information in the far-infrared wavelength range [327]. For instance, protein fibril

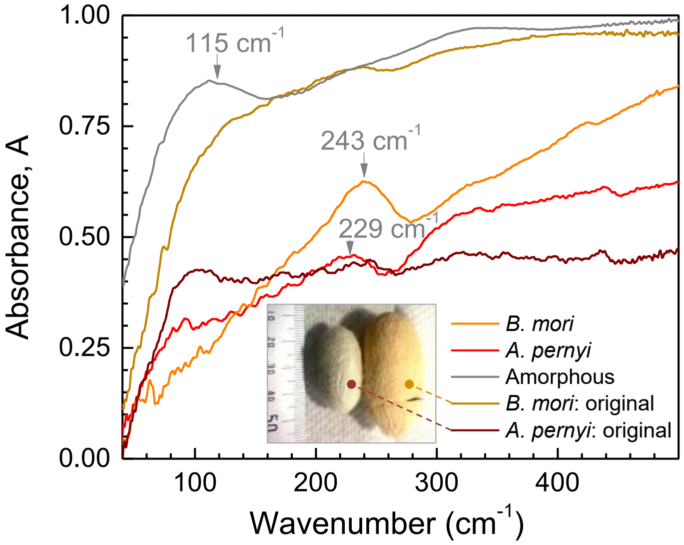

Figure 2.22: Far-IR absorbance spectra of amorphous *B. mori* fibroin, degummed *B. mori* and *A. pernyi* silk fibers, as well as that of corresponding sericin-rich cocoon segments, shown in the inset photograph. Far-IR absorbance spectroscopy experiments were performed at the Australian Synchrotron THz/Far-IR Beamline.

formation, notably present in the *amyloidose* class of degenerative diseases with Alzheimer's and type-II diabetes counted among them, can be monitored in the terahertz spectral region [328]. More in line with the present study, the multitude of fibroin protein secondary structure components that make up the molecular 3D network of natural silk fibers – notably amorphous random coils, crystalline α-helices and β-sheets, as well as metastable β-turns – are responsible for their extraordinary properties and provide an informative model system to further the understanding of complex polypeptide behavior. Conversely, functionality of biopolymer-based long-wavelength radiation photonic components, such as silk foam terahertz waveguides [264], critically depends on control over long-range vibrations occurring on supramolecular scales.

Far-infrared characterization of degummed natural *B. mori* and *A. pernyi* silk fibers, as well as of amorphous regenerated fibroin sourced from domesticated silkworm cocoons, was conducted at the Australian Synchrotron THz/Far-IR Beamline. Measurements were performed in a transmittance configuration over the 60–600 cm^{-1} wavenumber region using a high resolution IFS 125HR Fourier-transform infrared spectrometer (Bruker Corp.), equipped with a Si bolometer radiation detector. A high signal-to-noise ratio was ensured by averaging each spectrum over 100 individual acquisitions, and sample heterogeneity related effects were minimized by using a large 3 mm diameter collimated beam. For low temperature measurements biopolymer samples were mounted in a liquid nitrogen cryostat and controllably cooled down to 78 K.

Overview spectra of far-IR synchrotron radiation absorbance in different forms of silk are shown in Figure 2.22. Each natural *B. mori* and *A. pernyi* degummed fiber spectrum exhibits one signature absorbance band at 243 cm^{-1} and 229 cm^{-1} wavenumbers respectively. Conversely, the amorphous regenerated *B. mori* silk fibroin has a much broader shoulder at around 115 cm^{-1} and is generally more absorptive throughout the probed wavelength range. For comparison, spectra of *B. mori* and *A. pernyi* silkworm cocoon shells, where fibroin based

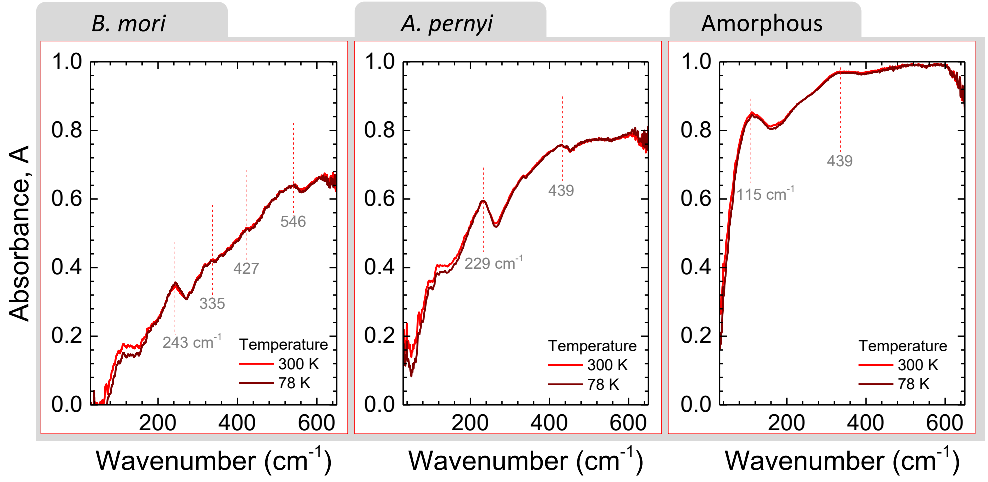

Figure 2.23: Temperature dependent variations between far-IR absorbance spectra of *B. mori* and *A. pernyi* silk fibers, as well as that of amorphous *B. mori* fibroin. Far-IR absorbance spectroscopy experiments were performed at the Australian Synchrotron THz/Far-IR Beamline.

strands are glued together by sericin gum, are also plotted and appear as combinations of crystalline fiber and amorphous protein spectral responses.

The prominent absorbance peaks situated in the 229–250 cm^{-1} spectral region appear exclusively for the crystalline and water insoluble fibroin fibers, which suggests them being associated with the presence of β-sheets. However, peaks located in the vicinity of 240 cm^{-1} wavenumbers are known to arise due to water-related absorption. More specifically, at room temperature intermolecular hydrogen bond stretching tends to produce a broad spectral feature at around 200 cm^{-1}, and librational molecular motions manifest as a peak at 700 cm^{-1} [329, 330]. As mentioned previously, silk fiber spinning, as well as fibroin regeneration, is performed from an aqueous chemistry, therefore, the spectral analysis of silk fibroin necessitates the ruling out of any possible residual water content related contributions.

One way of revealing the presence of water involves lowering the sample temperature below that of ice formation, upon which a spectrally narrow crystalline H_2O associated peak at around 230 cm^{-1} is expected to emerge [331, 332]. To this end, the different fibroin biopolymer samples were cooled down to liquid nitrogen temperatures and their far-IR absorbances were measured. Figure 2.23 provides the comparison of *B. mori* and *A. pernyi* silk fiber as well as amorphous fibroin spectra acquired at room temperature *versus* those obtained from the same samples at 78 K, which in wavenumbers corresponds to a thermal energy of 53.5 cm^{-1}. However, not a trace of an ice related band could be observed. Indeed, the spectra acquired at drastically different temperatures exhibit hardly any differences at all, save for a slight narrowing of absorbance bands, most readily observed in the *A. pernyi* case. In light of these results residual water can be ruled out as the underlying cause of the observed absorbance features, likely intrinsic to structural components of the crystalline silk fibers and for amorphous fibroin respectively.

Heat exposure offers an alternative way of both verifying the potential effects of water content and, more importantly, inducing structural changes in amorphous fibroin biopolymer domains whilst barely affecting the crystalline ones [333]. Here, degummed *B. mori* and *A. pernyi* spun fibers as well as amorphous regenerated *B. mori* silk fibroin were subjected to various durations of ambient atmosphere hot-plate annealing at 250 °C, which represents the

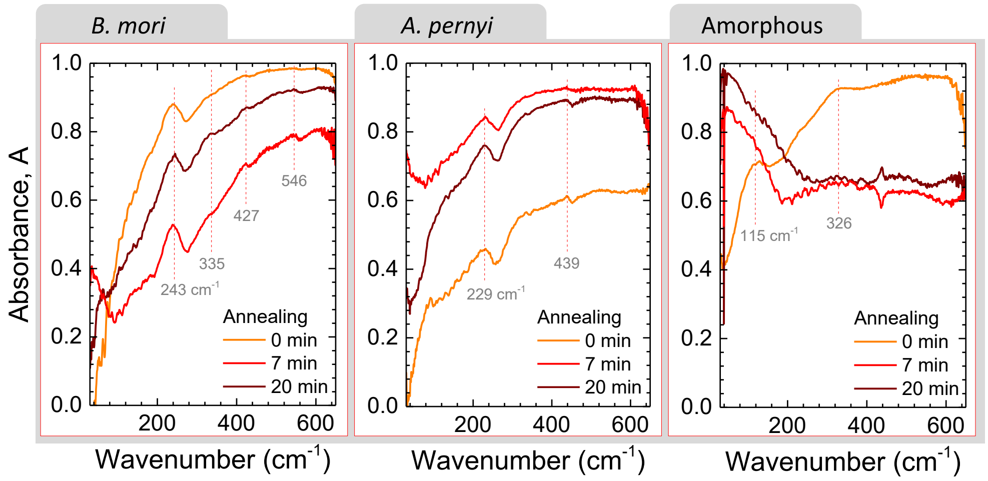

Figure 2.24: Annealing duration dependent variations between far-IR absorbance spectra of *B. mori* and *A. pernyi* silk fibers, as well as that of amorphous *B. mori* fibroin. Dashed red lines indicate the most notable spectral features. Annealing was performed on a 250 °C temperature hot-plate under ambient atmosphere conditions. Far-IR absorbance spectroscopy experiments were conducted at the Australian Synchrotron THz/Far-IR Beamline.

onset of thermal degradation [334]. The process resulted in silks exhibiting a notably darker coloration, consistent with oxidation occurring at high temperatures. The corresponding far-IR absorbance spectra of fibroin-based materials subjected to different durations of heat-treatment are provided in Figure 2.24. While the nondescript background absorbance appears to change substantially with heat exposure, the respective minor peaks as well as the major spectral signatures at 243 ± 15 cm^{-1} and 229 ± 15 cm^{-1} wavenumbers for β-sheet crystalline secondary structure rich *B. mori* and *A. pernyi* silk fibers appear unaffected. Conversely, spectra of amorphous *B. mori* fibroin are strongly altered by heat treatment, as it caused a significant reduction in absorbance throughout most of the shorter wavelength region, a suppression of the 115 ± 15 cm^{-1} band, as well as the appearance of a multitude of low intensity minor spectral peaks.

The observed spectral response to heat treatment is consistent with β-sheets, integral to fibers but virtually absent from regenerated fibroin, exhibiting a higher resilience to thermal decomposition than amorphous random coil secondary structures. Furthermore, elevated temperatures are known to even induce increases in both number and size of β-sheet sections at the expense of metastable secondary fibroin structures, which connect crystalline and amorphous regions [334]. Of further interest is the opposite thermally induced changes in the absorbance backgrounds of *B. mori* and *A. pernyi* silk fibers. Differences in heat treatment response between these silks are not exclusively spectroscopic either, as *A. pernyi* fibers contract at high temperatures much more than their *B. mori* derived counterparts [333]. This behavior is explained as arising from the stabilizing and order inducing effects that a higher β-sheet content in domesticated silks has on the polymer. With the growth of β-sheets metastable secondary structures adjacent to them extend farther into the biopolymer network thereby increasing the degree of order it exhibits. On the other hand, *A. pernyi* fibers are reported as having a much lower content of ordered metastable phases [333], therefore, thermal decomposition of the amorphous regions can be conjectured to increase disorder in the protein, leading to a higher generic far-IR absorbance.

Assignments of specific far-IR absorbance peaks in natural fibers can be problematic due to the wide range of conformations their constituent proteins exhibit. However, the quartet of spectral signatures visible in *B. mori* fiber spectra at approximately 243 cm^{-1}, 335 cm^{-1}, 427 cm^{-1}, and 546 cm^{-1} wavenumber values provide a reasonably close mach to those detected in β-sheet rich *B. mori* fibroin films at 250 cm^{-1}, 328 cm^{-1}, 427 cm^{-1}, and 553 cm^{-1} [335]. *A. pernyi* silk, on the other hand, exhibits only two notable peaks – at 229 cm^{-1} and 439 cm^{-1} – which are very close to 240 cm^{-1} and 432 cm^{-1} bands observed in a stretched β-form of poly-L-alanine [335]. The peak at 546 cm^{-1} is of particular interest, as it appears in (Ala-Gly)$_n$ copolymer spectra, but not for either poly-alanine or poly-glycine. The conspicuous absence of an equivalent peak in far-IR spectra of *A. pernyi* fibers, where β-sheets are comprised of segregated alanine and glycine rich regions, lends further credence to the respective assignments. Lastly, amorphous regenerated *B. mori* silk fibroin spectra have a shoulder at 115 cm^{-1} as well as a broad peak at 326 cm^{-1}, consistent with the α-helix secondary structure of (Ala-Gly)$_n$ [335]. Furthermore, the reported far-IR absorbance of fibroin samples, extracted from silkworm glands that correspond to different stages of the spinning process, showed a progressive decrease in the intensity of a peak centered around $\sim$ 120 cm^{-1} together with a simultaneous increase of a feature at approximately $\sim$ 250 cm^{-1} [336]. This behavior was respectively related to a diminished content of α-helix and random coil structures and a greater amount of β-sheets formed over the course of silk creation.

Radiation in the far-end of the submillimeter wavelength region is resonant with collective motions of entire segments of a protein chain comprised of hundreds of molecular bonds. While the vast range of possible configurations present in a natural biomaterial rarely yields specific spectral signatures, the density of delocalized vibrational modes can nevertheless be uncovered and denotes the conformational flexibility of a given polymer network [337]. Due to its superior signal-to-noise ratio in the 8–80 cm^{-1} spectral region, time-domain spectroscopy [338] was used to probe *B. mori* and *A. pernyi* silk fibers at the long-wavelength edge of far-IR.

Intense single-cycle 1 ps terahertz impulses used for time-domain spectroscopy were generated *via* optical rectification of amplified femtosecond laser pulses in a 0.6% MgO doped $LiNbO_3$ crystal [338]. The resultant submillimeter wavelength radiation was focused onto the fiber mesh samples using an off-axis $f = 100$ mm focal length parabolic mirror. Two more identical optical elements were used for collecting the transmitted beam fraction for detection in a 500 µm thickness ZnTe crystal by means of electro-optical sampling [339]. Temporally resolved optical fields, transmitted through either the silks or an ambient air reference, were subsequently Fourier-transformed to yield amplitude and phase values in the frequency domain. The amplitude magnitudes can be used to calculate the absorbance A, whereas phase, provided sample thickness is known, can be related to the refractive index n. However, for the stochastic silk fiber mesh samples investigated here, optical path could not be known, hence, only absorbance was obtained.

Figure 2.25 shows the time-domain spectroscopy derived terahertz absorbance of *B. mori* and *A. pernyi* silk fibers. The error bars are standard deviation values corresponding to an average of 50 alternating sample and reference signal acquisitions. The intensity of both spectra increases towards higher wavenumbers, as large-scale motions responsible for low-frequency modes are much less prevalent than the more energetic fluctuations in smaller protein chain segments [337]. *A. pernyi* silk biopolymer structure appears to possess more conformational freedom and flexibility than the *B. mori* counterpart, as can be deduced from higher absorbance values related to a larger overall density of collective vibration states [336].

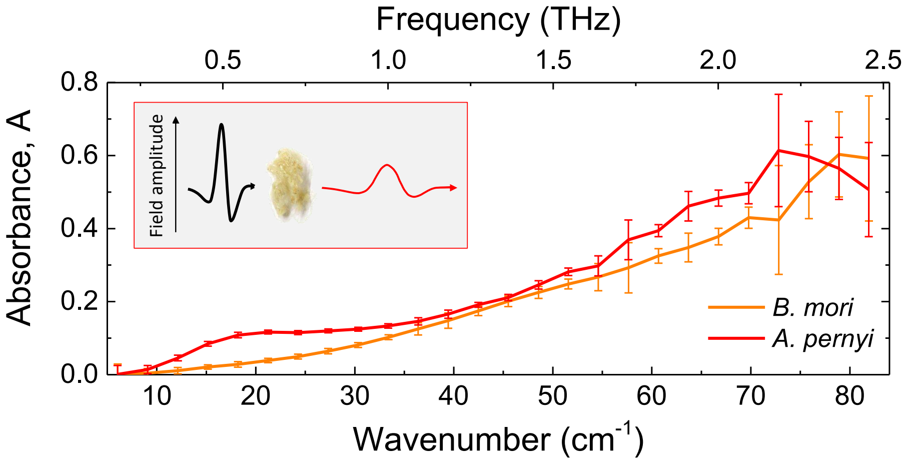

Figure 2.25: Terahertz radiation absorbance spectra of *B. mori* and *A. pernyi* silk fibers, acquired by means of the time-domain spectroscopy method [283]. Terahertz spectroscopy measurements were performed by the research group under supervision of Assoc. Prof. Jeffrey Davis.

This is, again, consistent with the lower amount of β-sheet secondary structures in *A. pernyi* fibers [291], in which the polymeric network is notably less rigid and long-range interactions are further facilitated by hydrogen bond interlinked segments.

Furthermore, prominent peaks, situated around 20 cm^{-1} and 67 cm^{-1} wavenumbers, are observable in the *A. pernyi* fiber spectra, with no equivalent signatures present in the *B. mori* case. The relatively narrow width of the band at 20 cm^{-1} would suggest its origins being collective vibrations of some structure with a high degree of order. The uninterrupted $(\mathrm{Ala})_n$ or $(\mathrm{Gly})_n$ rich regions in the β-sheets of *A. pernyi* silk fibroin are the likely cause, as it is one of the major differences between the wild and domesticated silks investigated here. Conversely, the broad *A. pernyi* spectral feature at 67 cm^{-1} is most probably related to vibrations of amorphous biopolymer regions, mediated by $\mathrm{O{-}H}\cdots\mathrm{O}$ hydrogen bonds in a similar way to that observed for water, where a 70 cm^{-1} band was attributed to a third- or fourth-neighbor response in the molecular network [340].

Silk, as a result of being a hierarchical composite material, exhibits an equally complex optical behavior. The strong electronic and vibrational absorbance bands present in, respectively, ultraviolet and near-to-mid-infrared spectral regions are mainly useful for structural analysis, hence, the applicability of silk biopolymers in those spectral regions is scant. On the other hand, silk absorbance of far-IR wavelengths is more subdued and manifests as spectral signatures with low specificity, however, high sensitivity to secondary structures comprising the protein network. Furthermore, the potential of controlling fibroin optical response in the far-IR range through alterations to its secondary structures holds promise for realization of both active and passive devices operating in the submillimeter wavelength range. Lastly, the transparency of fibroin-related compounds throughout the visible spectral range, when combined with their mechanical flexibility, biocompatibility and biodegradability, makes silk an attractive photonic platform for biomedical uses. However, operation of photonic devices is predicated on relevant wavelength scale functional elements, whose creation, in turn, necessitates high resolution fabrication methods for fibroin-based material patterning, some of which are described in the next section.

2.5 Silk as a platform for microscale fabrication

Creation of biocompatible optical interfaces and devices necessitates the use of fabrication methods which, in addition to preferably possessing subwavelength scale resolutions, use materials that do not illicit inflammatory or foreign body responses *in vivo* and that do not involve toxic chemicals [237, 238]. Among possible candidates regenerated silk fibroin biopolymers not only possess the requisite physiological compatibility [282], but can also be used to prepare planar films with high transparency and low surface roughness [252]. This, in turn, means that silk is available in a state that simultaneously exhibits low optical absorbance and scattering losses in the visible wavelength region, as well as is compatible with a wide range of contemporary lithographic approaches, which makes it a practicable photonic platform with considerable biomedical appeal.

Numerous direct and indirect approaches to patterning of planar biopolymer films have been mentioned in Section 2.3. Indirect methods involve the use of a pre-fabricated master which is then transferred into the biomaterial by applying it as a full-contact mold for inverse opal templating [253], soft [252, 255] as well as nanoimprint [341] lithography. Conversely, pattern generation can be performed by way of a photolithographic mask transfer process [342], which, however, typically requires doping the biopolymer with potentially toxic photoinitiator compounds. Direct writing techniques, on the other hand, while being more costly and slow due to reliance on serial patterning, do not require templates and are therefore more versatile. Notable examples include biopolymer processing by means of direct ink writing [251], laser polymerization [343], focused ion beam milling [344], and electron beam lithography [345].

This section presents work geared towards the development of both positive and negative tone silk fibroin resist materials for biocompatible laser and electron beam lithography purposes. First, feasibility of silk film patterning using femtosecond laser irradiation without photoinitiator doping is tested. Furthermore, regenerated silk fibroin is used as a high resolution electron beam lithography resist. In both of these cases one of the key properties of silk fibroin, namely its primary and secondary protein structure dependent water solubility, is exploited to pattern and develop optical-scale biopolymer structures on a planar substrate.

2.5.1 Laser patterning on silk fibroin films

Among all subwavelength resolution serial processing direct write methods, laser micromachining is, arguably, the most rapid and readily scalable towards industrial levels of throughput [346]. Furthermore, it is not restricted to planar geometries and can be used to print complex 3D objects by means of laser photopolymerization [347, 348]. In particular, even at optical frequencies, use of tightly focused ultra-short sub-picosecond laser pulses allows for induction of nonlinear processes that result in modification or ablation of materials that is confined to volumes notably smaller than the diffraction limit.

Laser fabrication of both 2D and 3D protein based structures has drawn considerable interest since it was shown to be capable of producing biocompatible functional surfaces [349], optical elements [350] as well as artificial scaffolds for cells [351]. As silk fibroin stands out among biomaterials due to its favorable mechanical and optical properties as well as readily achievable chemical functionalization [252], it has likewise been the subject of 3D photopolymerization experiments, which yielded submicron resolution fibroin structures as well as noble metal/biopolymer composite patterns [343]. However, in most cases light induced polymerization of silk was demonstrated to proceed only when doped with photoinitiator chromophores such as methylene blue, which was revealed to be severely toxic to the human central nervous system [352].

In this work, conducted in collaboration with the research group under supervision by Assoc. Prof. Jingliang Li at Deakin University, methods of silk fibroin film femtosecond pulse laser processing without the use of photoinitiators were investigated [353]. Printing of silk residue negative tone patterns from an amorphous fibroin layer were demonstrated at the onset of underlying glass surface damage. Conversely, β-sheet rich crystallized fibroin films were laser ablated to create positive tone resist patterns.

The amorphous regenerated fibroin samples used for creating silk thin-films on various substrates were prepared using the method outlined in Section 2.4.2. Briefly, fibroin was extracted from degummed *B. mori* silk fibers by dissolving them in a 65 °C temperature mixture $CaCl_2$, water and ethanol, prepared with a molar ratio of 1:8:2, respectively. Dialysis of the resultant solution was performed over 4 days against ultra-pure water by using 14 kDa molecular weight cut-off cellulose tubing (Sigma-Aldrich Inc.). The dialysed solution was subsequently lyophilized to recover silk fibroin in a foam-like water-soluble state [313].

Sketch in Figure 2.26 gives a general outline of the steps involved in preparing and processing thin fibroin films using laser irradiation, discussed here, and electron beams, described further on. Planar substrates, such as Si wafers, glass slides, or CaF_2 windows for IR spectroscopy measurements, were cleaned by way of sonication in acetone and isopropanol organic solvents. Thin-film application was performed by spin-coating a 10% aqueous silk fibroin solution on the substrate over a two stage process that involved a 10 s spreading step at 500 rpm, followed by a 40 s spin cycle at 3000 rpm. The films were then dried on a 90 °C temperature hot-plate for 1 min, and the process resulted in an overall silk fibroin film thickness of 250 ± 20 nm. In their initial state the silk layers are amorphous, hence, water-soluble, so, would be expected to operate as negative tone resists, where only structurally modified regions of the film would continue to remain on the substrate surface after aqueous development. Positive tone resist behavior can be induced by crystallizing the fibroin film into its water-insoluble form by way of β-sheet creation. This was done by soaking substrates with amorphous silk films in a 1 : 1 by volume methanol and ethanol mixture for 10 min and then performing a high humidity anneal on the samples in a convection oven at a 80 °C temperature over a 2 h duration.

Laser processing was performed using a $\lambda = 1030$ nm wavelength and 230 fs pulse duration PHAROS Yb:KGW laser system (Light Conversion, Ltd.) operating at a 100 kHz frequency. The near-IR wavelength beam, incident on the silk fibroin films, was focused

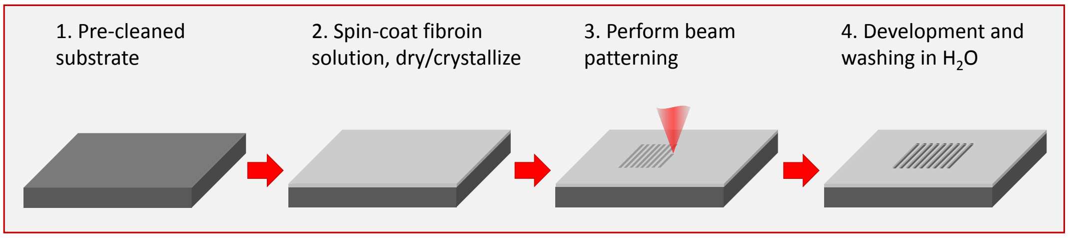

Figure 2.26: Sketch of a generic process for patterning silk fibroin thin-films. A planar substrate is spin-coated with an ≈ 5% aqueous regenerated silk fibroin solution and then dried. Initial film operates as a negative tone resist. Positive tone performance is obtained by rendering the film water-insoluble *via* dipping in a 1 : 1 ethanol and methanol mixture and annealing in water vapor. Patterning is done using scanning laser or electron beams. Resist development is performed in water.

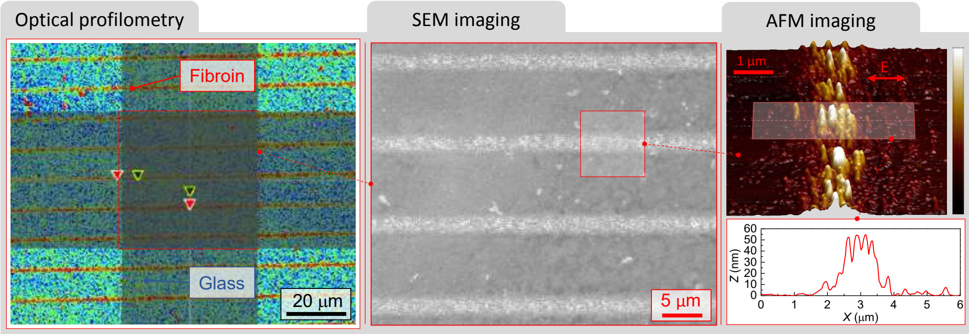

Figure 2.27: Imaging of a 10 µm period grating, created on a silica cover slip by $E_\mathrm{p} = 20$ nJ pulse energy laser writing on a 250 nm thickness amorphous silk fibroin film and subsequently developing in water. Leftmost wide-view image was acquired using optical profilometry [353]. Middle panel shows an electron microscopy image of the lines. Rightmost panel provides a close-up atomic force microscopy 3D rendering of a line segment. Its bottom section gives a cross-section plot of the ripple pattern, averaged over the marked region.

using either a $NA = 0.26$ or $NA = 0.5$ numerical aperture infinity corrected long working distance objective (Mitutoyo Corporation). Submicron precision lithographic positioning of the substrates was ensured by using an air-bearing x-y moving stage (Aerotech Inc.). Laser writing was performed at a scanning rate of 1 $\mathrm{mm\,s^{-1}}$, or 100 highly overlapping pulses per 1 µm. Surface damage of an underlying borosilicate glass substrate was identified at a pulse energy of $E_\mathrm{th} = 15.7$ nJ, which for a $NA = 0.26$ objective translates into a fluence of $F_\mathrm{th} = E_\mathrm{th}/(\pi w_0^2) \approx 86$ $\mathrm{mJcm^{-2}}$ and a corresponding irradiance of $I_\mathrm{th} = E_\mathrm{th}/(\pi w_0^2 t_\mathrm{p}) \approx$ 0.37 $\mathrm{TWcm^{-2}}$, where t_p is the duration of a single pulse, and $w_0 = 0.61\lambda/NA \approx 2.4$ µm is the beam waist radius. These values are well below the single pulse surface damage threshold of borosilicate glass.

Figure 2.27 depicts various images of 10 µm period grating patterns, laser-scribed into amorphous silk fibroin films coated on a glass substrate and developed in water. Since the initial state of the biopolymer used here was soluble in aqueous media, it operates as a negative tone resist, meaning that fibroin is washed away from all areas except for the laser processed regions. However, these lines start to appear only when single pulse energies $E_\mathrm{p} \geqslant 0.95 \times E_\mathrm{th}$, *i.e.* at the onset or above surface damage threshold, are used. The optical profilometry image in the left panel of Figure 2.27, acquired using a ContourGT optical microscope (Bruker Corp.), shows, that $E_\mathrm{p} = 20$ nJ pulse energy laser exposure results in the development of approximately 3 µm full-width half-maximum lines, each of which has an estimated height of 20 nm. Higher magnification scanning electron microscopy imaging, shown in the middle panel of the same figure, reveals that there indeed is some residual biopolymer material around the laser irradiated areas, as evidenced *via* chemical composition contrast afforded by the back-scattered electron detector. In addition, the lines exhibit a fine structure that is aligned at almost right angles to the polarization of incident radiation. Further detail can be gleaned from contact mode atomic force microscopy visualizations obtained using a Dimension iCon instrument (Bruker Corp.). The isometric rendering of a laser patterned line segment, depicted in the rightmost panel of Figure 2.27, reveals the presence of self-organized ripple structures [354, 355], which is indicative of the onset of glass substrate ablation. Furthermore, patterned lines have heights of around 45 nm, as evidenced by the plot in the bottom part of the same panel.

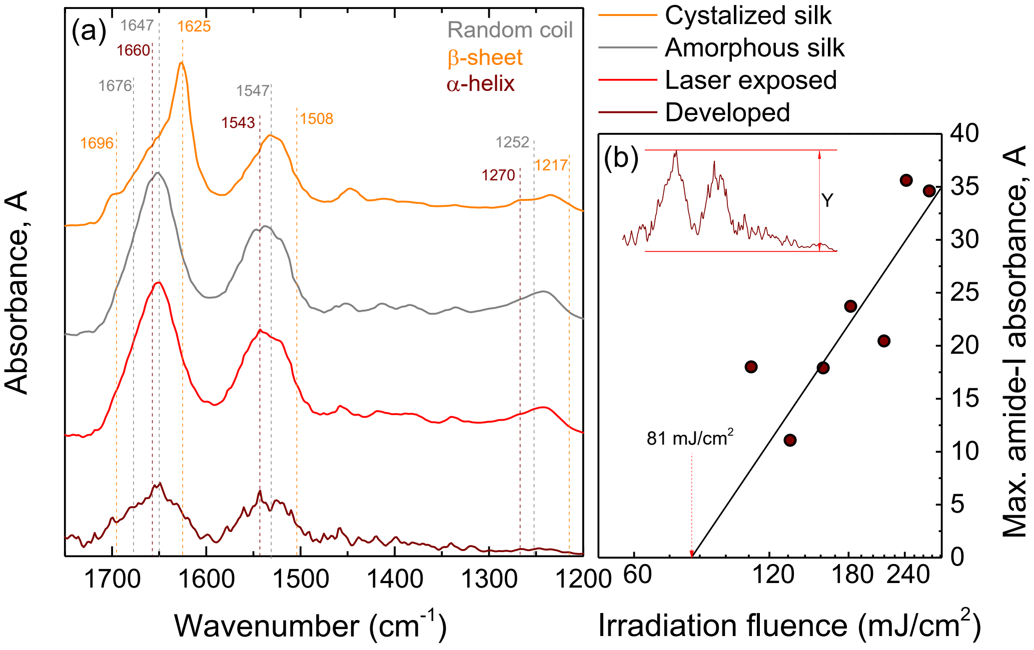

Figure 2.28: (a) Fourier-transform infrared absorbance in the amide spectral region for fibroin films, from top-to-bottom, crystallized by dipping in an ethanol/methanol mixture and annealing in water vapors, in a water-soluble as-spin-coated state, after laser beam exposure, and laser-exposed after development in water. Colors of spectral peak assignment wavenumbers correspond to specific secondary structures of silk. (b) Irradiation fluence dependence of the amide I band intensity exhibited by the laser-exposed and water-developed fibroin films.

Based solely on imaging and topology mapping data the nature of laser inscribed patterns remains somewhat ambiguous. More direct information on the chemical composition and conformation states of silk fibroin residue after water development can be obtained by means of Fourier-transform infrared spectroscopy in the amide band region. To this end spectra of laser patterned and reference films of silk fibroin were acquired in transmittance mode using a Hyperion 2000 infrared microscope which was coupled to a Vertex70 IR spectrometer (Bruker Corp.). Sample preparation for spectroscopy work involved spin-coating of silk fibroin films on IR transparent $\mathrm{CaCl_2}$ crystalline windows, and laser exposing $500 \times 500\ \mu\mathrm{m}^2$ area grating patterns using different irradiation fluence values.

Typical Fourier-transform infrared absorbance spectra of thin silk fibroin films in various states of processing are given in Figure 2.28 (a). Here the main amide band peaks generally mirror the vibration mode assignments to protein secondary structures described in Section 2.4.2 for natural silk fibers. For instance, the methanol/ethanol mixture treated and water vapor annealed crystalline silk fibroin films exhibit prominent β-sheet related signatures at around 1625 cm^{-1}, 1508 cm^{-1} and 1217 cm^{-1} as well as the β-turn associated shoulder at 1696 cm^{-1} [356]. On the other hand, regardless if it was laser exposed or not, the water soluble amorphous fibroin film in its negative resist state is mainly dominated by random coil protein conformation related bands at 1647 cm^{-1}, 1547 cm^{-1} and 1252 cm^{-1} [311], with an additional indistinct feature at around 1676 cm^{-1} typically assigned to the turns and bends of a chaotic polypeptide chain [356].

Water development of fibroin films with laser inscribed grating patterns removes all amorphous silk from unexposed regions, leading to an overall factor of 4 decrease in amide band absorbance, with increased irradiation fluencies giving rise to higher intensity residual peaks. Furthermore, notable alterations in spectral response are likewise evident and mostly involve the reduced prevalence of random coil associated features, whereas α-helix and β-sheet crystalline conformations are more resilient, hence, more strongly represented in the spectra, resulting in the broadened appearance of peaks. The features centered around 1660 cm^{-1} and 1543 cm^{-1} are at positions typically assigned to α-helices, however, their uncharacteristically narrow lineshapes prevent definite assignment. Lastly, numerous sharp spectral signatures appeared throughout the amide band region, and likely are indicative of laser induced stochastic bond breaking or the presence of water residues from the development process.

Figure 2.28 (b) shows the irradiation fluence response of the amide I band intensity, which exhibits a logarithmic scaling behavior. Mid-IR amide absorbance becomes measurable only at irradiation fluences above the borosilicate glass substrate surface damage threshold of $F_{\mathrm{th}} \approx 86$ mJcm^{-2}. This, in turn, implies that laser induced structural modification of a substrate is instrumental in rendering amorphous silk fibroin water insoluble. Furthermore, when these films are laser exposed not in an isolated line grating pattern, but in an overlapping raster-scan fashion over an area, virtually all biopolymer gets ablated and hardly any amide band absorbance can be detected spectroscopically. Hence, fibroin sintering on a planar substrate occurs not exclusively at the incident spot, but around the laser exposed region. Taken together these findings indicate that amorphous fibroin is rendered water insoluble as a result of interaction with energetic electrons, ejected as a result of avalanche ionization effects at the onset of as well as during structural modification of a dielectric material by high repetition rate sub-band gap $\lambda = 1030$ nm wavelength ultrashort pulse laser irradiation. In further support, similar amorphous fibroin transition from a water soluble to an insoluble state was reported for electron beam exposed thin-films of silk, where random coil structures were reported to either fold into α-helices or become intermolecularly crosslinked by way of water radiolysis [345].

Laser patterning of water soluble regenerated silk fibroin thin-films without photoinitiator doping appears to be an inherently inefficient and destructive process, as it relies on energetic particles liberated from the underlying substrate during its breakdown to induce the requisite chemical changes in random coil secondary structures of the protein. On the other hand, light induced chemical modification of crystalline fibroin films, used here for positive tone resist film creation, would involve the selective decomposition of hydrophobic β-sheet regions which hold the entire biopolymer together and ensure its hydrophobicity. However, β-sheets are the most resilient secondary structures of silk and during thermal decomposition tend to undergo carbonization into a graphite-like compound [334]. Furthermore nanosecond pulse duration direct UV photon absorbance possesses a notable heating component and has been shown to more likely result in formation of silk foams [357]. Hence, as the thermal modification route appears unfeasible, positive tone patterns on a crystallized water insoluble fibroin film can most readily be achieved *via* its localized removal by near-IR femtosecond laser ablation.

Figure 2.29 depicts the optical profilometry height maps and corresponding cross-section plots of 10 μm period gratings, created by laser ablation of a crystallized 250 ± 20 nm thickness silk fibroin film, before and after washing them in water. Here, again, laser exposure was performed using a $NA = 0.26$ objective at a scanning rate which resulted in 100 $E_{\mathrm{p}} = 22$ nJ strongly overlapping pulses per 1 μm. The resulting lines exhibited widths of around 3.5 μm,

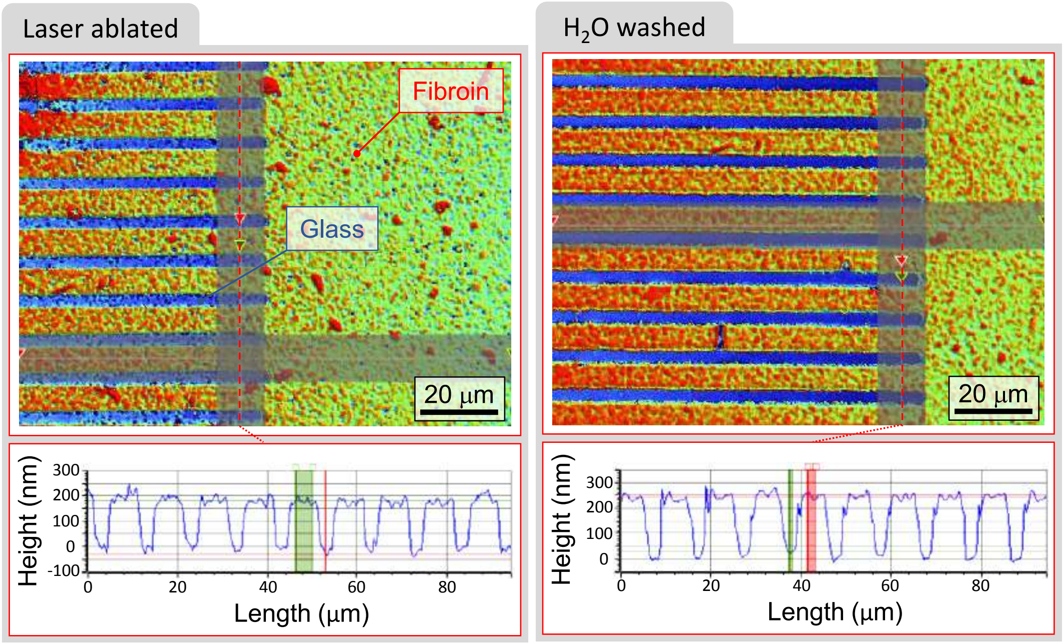

Figure 2.29: Optical profilometry images of 10 µm period gratings laser ablated into a crystallized fibroin film coated on a silica cover slip [353]. Top-down views and lateral cross-section plots of surface height data immediately after laser processing and after an additional water washing step are depicted in left and right panels respectively.

i.e. slightly higher than the beam spot size, and had notably vertical ridges. One drawback of using crystallized fibroin films is that their surfaces tend to exhibit submicron scale roughness as a result of the water vapor treatment, which is far above the 5 nm root mean square values observed for amorphous layers. This general unevenness of the surface is, presumably, the due to β-sheet crystals and is the major reason for defects in laser-inscribed patterns. Nevertheless, it is clear that femtosecond laser ablation can remove β-sheet rich fibroin sections with high precision and without notably affecting the surrounding regions of the film. The latter point is further evidenced by the lack of changes in the pattern geometry following a water washing step, which only served to remove any fibroin residue from the ablated areas without notably increasing their overall depth. Lastly, Fourier-transform infrared absorbance spectroscopy in the amide band region failed to uncover any qualitative spectral differences between as prepared and laser processed crystalline fibroin films.

Overall, femtosecond pulse duration laser patterning of silk fibroin films without photoinitiators is readily realized in their positive tone crystalline state, by causing ablation through the use of near-infrared radiation, far from direct absorbance in either the biopolymer or the substrate. On the other hand, writing structures in water soluble amorphous fibroin films would only become possible during the dielectric breakdown of the substrate at the onset of its ablation, which also resulted in simultaneous formation of ripple patterns. Hence, selective direct removal of β-sheet rich films appears to be the most straightforward method of preparing water insoluble fibroin biopolymer patterns using laser lithography. Of further interest is that electron irradiation has been demonstrated to induce structural changes in fibroin that change its solubility, therefore, warrants further investigation.

2.5.2 Silk-based resists for electron beam lithography

Resolution attainable by serial patterning lithography approaches is ultimately bounded by the smallest spatial dimensions that mater modification by a given energy delivery method can be confined to. For techniques directly involving propagating photons such constraints are related to the diffraction limit, which, for radiation at or around the visible spectral region, prevents reliable maskless definition of structures below approximately 100 nm, *i.e.* notably smaller then the wavelength [358]. On the other hand, mass-endowed particles like electrons or ions have de Broglie wavelengths in the picometer range, and, furthermore, carry a charge, which makes them susceptible to manipulation and focusing by tailored electric or magnetic fields. In this case the major limitation for attainable resolution is the mutual scattering of such particles, which, nevertheless, allows for focusing to spot-sizes below 10 nm, making electron or ion beam-based techniques capable of true nanoscale patterning [359, 360].

Electron beam lithography, despite being relatively expensive and slow, remains the premier fabrication method for the prototyping of nanophotonic and nanoelectronic devices, as well as for creating template patterns for other parallel processing manufacturing techniques such as nanoimprint or UV lithography. While the small mass of electrons renders kinetic energy transfer into the patterned substrate material inefficient for direct writing, it can create high resolution patterns in certain polymer based resist materials by locally changing their solubility [361]. However, processing of most synthetic resists involves fairly noxious chemicals, residues of which can result in devices prepared this way not being suitable for biointegration. Conversely, all-water processing of biocompatible resist materials not only avoids cytotoxicity issues but also allows for incorporation and stabilization of functional biomolecules [362, 363], thereby creating a new class of bioactive nanoscale patterns and devices [345, 364, 365]. Hence, it comes as no surprise that development of nontoxic water chemistry based electron beam lithography resists comprised of biocompatible materials has drawn considerable interest. Notable examples of such realizations include resist films prepared from synthetic poly(acrylic acid) [366] and trehalose glycopolymer [367] as well as natural materials, namely, egg white [368] and, of primary interest here, silk fibroin [345].

In this work, conducted in collaboration with the research group headed by by Prof. Junko Morikawa at Tokyo Institute of Technology as well as researchers overseen by Assoc. Prof. Jingliang Li at Deakin University, regenerated silk fibroin thin-films were used as both positive and negative tone electron beam lithography resists [369]. Here the secondary protein structure dependent water solubility of silk, and is modification by incident energetic electrons, was integral in defining the requisite patterns through, respectively, either degradation of β-sheets in crystalline films, or cross-linking the peptide network in amorphous fibroin exposed to high electron irradiation doses.

Silk-based electron beam lithography resist preparation was performed according to the process described in the previous Section 2.5.1. In this case, however, a 5% by weight aqueous solution of regenerated silk fibroin was used, which, when applied *via* a two stage spin-coating process consisting of a 10 s spreading step at 500 rpm and a 40 s spin cycle at 4000 rpm, resulted in a 100 ± 10 nm film thickness. Choice of underlying substrate was motivated by demands of specific characterization techniques, where gold mirrors and CaF_2 windows were required for mid-IR spectroscopy work in reflectance and transmittance modes respectively, whereas silicon wafers were sufficient for atomic force microscopy mapping. Again, as-spin-coated amorphous fibroin layers were used as negative tone resists, whereas positive tone performance was imparted by crystallizing the films through dipping in a 1 : 1 by volume methanol/ethanol mixture and subjecting the substrates to water vapor annealing.

Preliminary spectroscopic investigation of the electron beam induced changes in a β-sheet rich positive silk resist was done by performing a low resolution $D_e = 3000$ µCcm^{-2} cumulative dose exposure in a pattern generator equipped tabletop scanning electron microscopy tool. A $I_e = 500$ pA current electron beam, accelerated to a 20 keV energy, was used to generate a coarse 100 µm period 0.5 duty cycle grating pattern. This was well within the 6.25 µm mapping resolution of the infrared microscope that was coupled to a Spectrum Spotlight 300 Fourier transform IR imaging spectrometer (Perkin-Elmer Inc.), employed for acquisition of spatially resolved absorbance data for specific vibrational modes.

Plot on the right side of Figure 2.30 depicts the amide I, amide II and amide III band infrared absorbance spectral region of silk fibroin electron beam resist films at three different stages of processing. As the various silk protein-related band assignments have been discussed at some length in Sections 2.4.2 and 2.5.1 they will not be reiterated in detail here. Information most relevant for present purposes is provided by the amide I band, which corresponds to C=O stretching and additional contributions from the out-of-phase C–N stretch, the C–C–N deformation and the N-H in-plane bending vibrations – all heavily affected by their hydrogen bonding state [314]. One evident difference between amorphous and crystalline fibroin films is the β-sheet band at 1619 cm^{-1}, prominent in the latter case and used for spatial mapping of electron-exposed positive resist films before and after development, as shown in left panels of Figure 2.30. Electron irradiation of crystallized films all but wipes out the low-energy end of the amide I band, related to hydrogen-bonded segments of the peptide network. The resultant

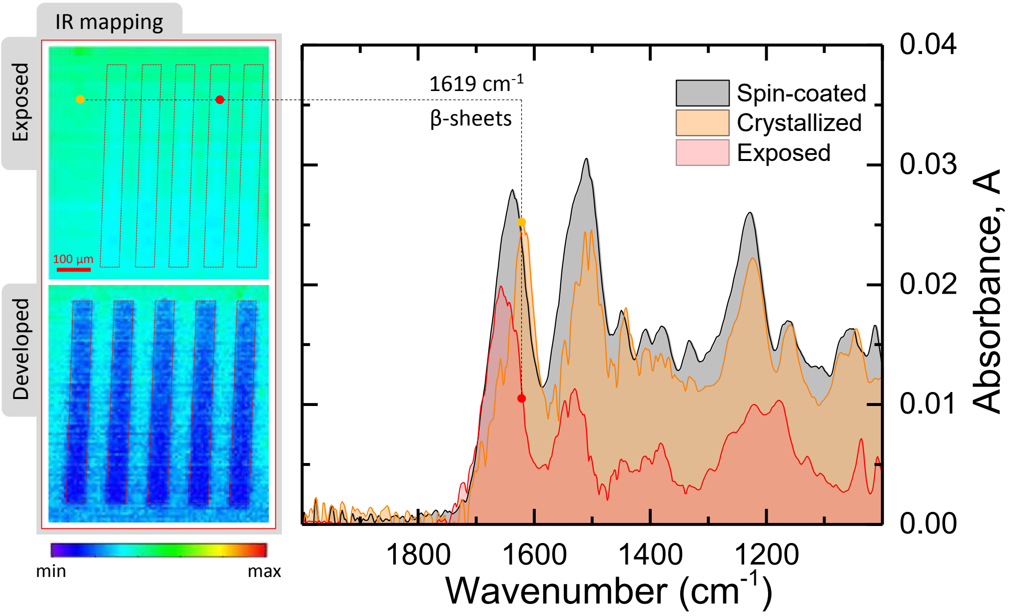

Figure 2.30: Mid-infrared absorbance spectroscopy and mapping of amorphous, crystallized and electron beam exposed silk fibroin films [369]. Left panels show absorbance maps at the 1619 cm^{-1} β-sheet related spectral signature respectively for an electron beam exposed and subsequently water-developed 100 µm period grating. Fourier-transform infrared spectra of amorphous regenerated silk fibroin, β-sheet rich crystallized, and electron beam exposed crystalline fibroin films are plotted on the left. Mid-IR spectroscopy experiments were performed at Tokyo Institute of Technology by the research group under supervision of Prof. Junko Morikawa.

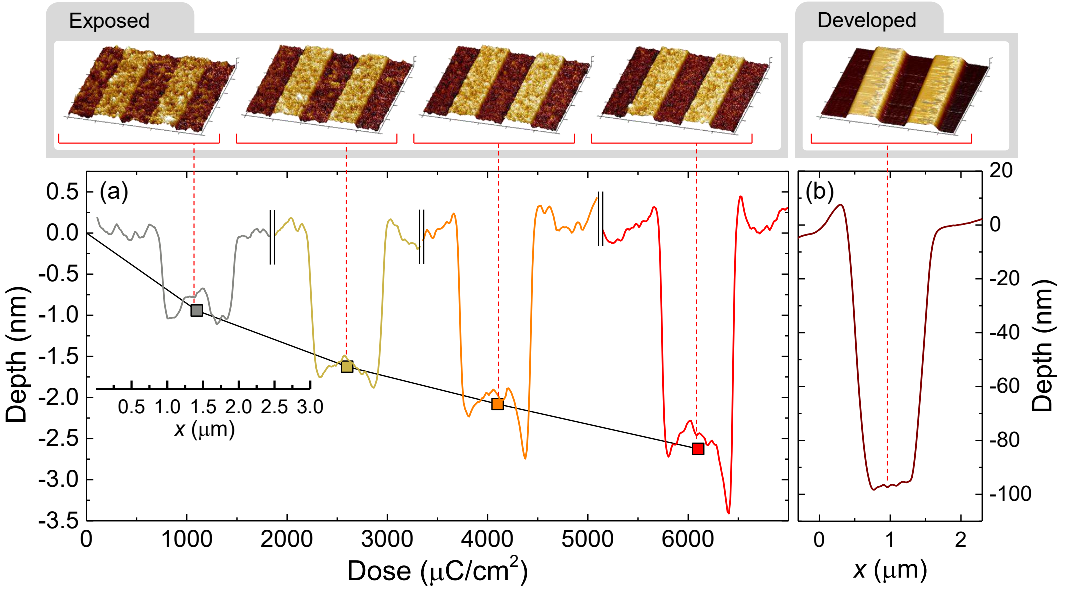

Figure 2.31: Atomic force microscopy investigation of 2 μm period gratings, patterned on positive tone silk fibroin-based resist films using electron beam lithography. (a) Plot of electron dose dependent height decrease of the 100 nm initial thickness crystalline fibroin film. Insets show cross-section height plots of electron-exposed areas. (b) Atomic force microscopy height plot of a 1 μm width electron beam exposed line after development in water. Images at the top show renderings of corresponding surface segments, where electron exposed areas are colored dark brown.

changes in secondary structure provide sufficient spectroscopic contrast to distinguish electron beam exposed sample sections from pristine resist covering the surrounding area.

After development in water the electron irradiated regions are washed out down to the underlying substrate and no significant fibroin mid-IR absorbance can be detected. These results unambiguously demonstrate that electron beam solubilization of crystalline fibroin films proceeds by way of β-sheet disruption. The effect of incident electrons likely mimics the way salt ion containing solvents are used to break down natural silk fibers by screening and disrupting the hydrogen bonds that hold β-sheets, and by extension the whole biopolymer, together [312]. On the other hand, a more conventional method of positive tone resist exposure, in which electrons break bonds of high molecular weight polymers into much smaller, hence, soluble segments [361], is also expected to be important and act in parallel [345].

More rigorous investigation of electron dose-dependent behavior of crystalline silk fibroin films was performed by creating finer 2 μm period 0.5 duty cycle grating patterns, each spanning over a 500×500 μm^2 substrate area. The positive resist was exposed using a EBPG5000plusES high-resolution electron beam lithography tool (Raith GmbH), operating at 100 kV acceleration and 20 nA current output, with doses ranging from 600 μCcm^{-2} to 6000 μCcm^{-2}. Resulting patterns were mapped using a Dimension iCon atomic force microscope (Bruker Corp.) with a contact mode Si cantilever.

Figure 2.31 (a) illustrates the electron irradiation dose dependent contraction of positive tone resist silk fibroin films. Here, the change in film thickness is fairly small, on the scale of a few nanometers, even for the highest 6000 μCcm^{-2} exposure doses. Atomic force microscopy likewise reveals the moderate 5 nm scale surface roughness of crystalline silk fibroin films.

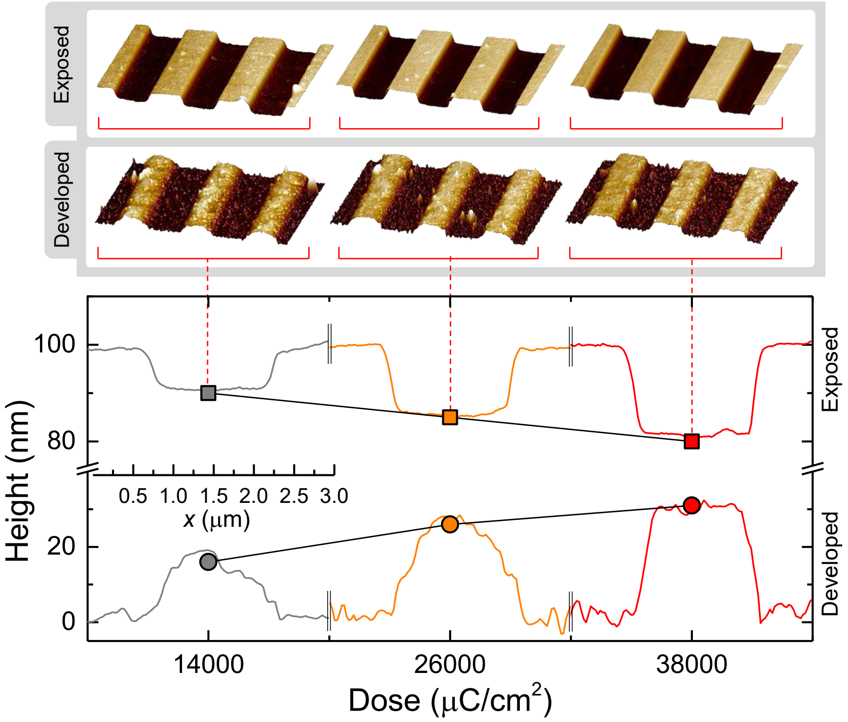

Figure 2.32: Atomic force microscopy of 2 μm period gratings, patterned on negative tone amorphous silk fibroin-based resist films using electron beam lithography. Top panels show isometric renderings of gratings after exposure and after development in water. Irradiated areas appear compressed after exposure, but remain as fibroin patterns on the substrate after development. Bottom plots depict the electron dose dependencies of the patterned line heights before and after development. Inset curves are the atomic force microscopy derived height profiles of corresponding gratings.

Ultimately, the optimal exposure dose for 100 keV electron energy beams was found to be around 4000 μCcm^{-2}, and a topology visualization as well as a transverse cross-section plot of a corresponding grating pattern after water development is provided in Figure 2.31 (b). Full removal of silk material from the exposed areas was readily achieved, giving rise to a high fidelity 100 nm height fibroin grating pattern. However, the main disadvantage of this silk biopolymer-based resist is its relatively low sensitivity compared to, say, ZEP or PMMA, which require 10 and 4 times lower electron doses respectively.

Negative tone electron beam resists, based on amorphous silk fibroin, require even higher exposure doses, which in this experiment ranged from 8000 μCcm^{-2} to 38000 μCcm^{-2}, however, values as high as 75000 μCcm^{-2} have been reported [345], which is roughly 20 times above what is required for the already quite insensitive inorganic HSQ [370]. Figure 2.32 depicts isometric renderings and cross-section height plots of focused electron beam irradiated as well as subsequently developed negative tone silk-based resist films. Decrease in thickness of the electron exposed random coil dominated amorphous fibroin film approximately continues the trend observed for positive tone resist in Figure 2.31. However, since electron beam exposure durations in this case are much longer, so are the observed degrees of contraction, which in the highest 38000 μCcm^{-2} dose case amounts to a full 20% of the initially 100 nm thickness film.

Development in water leaves behind a bottom fraction of the fibroin film in the electron beam patterned areas, with the overall thickness of the residual layer being positively correlated to the exposure dose. Still, even at the largest tested doses, only approximately 30 nm height grating features are established. So, it appears that silk polymerization occurs not throughout the fibroin film thickness, but primarily in the immediate vicinity of the substrate. Furthermore, even the unexposed areas remain covered by a substantial amount of nanoscale silk particles. Taken together both of these findings indicate that the amorphous fibroin film is rendered insoluble in water through polypeptide chain covalent cross-linking, induced by electron radiation-generated free radicals [371]. Substrate proximity is important in this case due to the abundance of electrons back-scattered from it, which, as a result of having an overall lower energy than those in the incident beam, are more likely to interact with the biopolymer. Similar behavior can likewise be observed in polymer-based positive tone resists like PMMA [372] and ZEP [373] that, when exposed to high electron doses, likewise cross-link to become resistant to most solvents and etchants, effectively behaving as a negative tone resist for specific development conditions.

In summary, silk fibroin films can be processed to act as both positive and negative tone biocompatible water chemistry based resists for laser or electron beam lithography purposes. Of course, negative tone performance of amorphous silk without cross-linking agents is somewhat lacking, as it is in large part a result of substrate breakdown during laser processing or requires impracticably large exposure doses when used for electron beam lithography. On the other hand, positive tone crystalline fibroin notably versatile and can be readily patterned either by means of laser ablation, or by using moderate degrees of electron irradiation to induce β-sheet breakdown. Furthermore, positive tone patterning avoids direct modification of relevant biopolymer regions, thereby minimizing potential adverse effects to any biofunctional dopants incorporated into the resist layer. Hence, nanopatterning of silk films, endowed with favorable optical and mechanical properties as well as high biocompatibility, fills a unique niche in the field of nanotechnology involving the creation of implantable photonic devices for *in vivo* use.

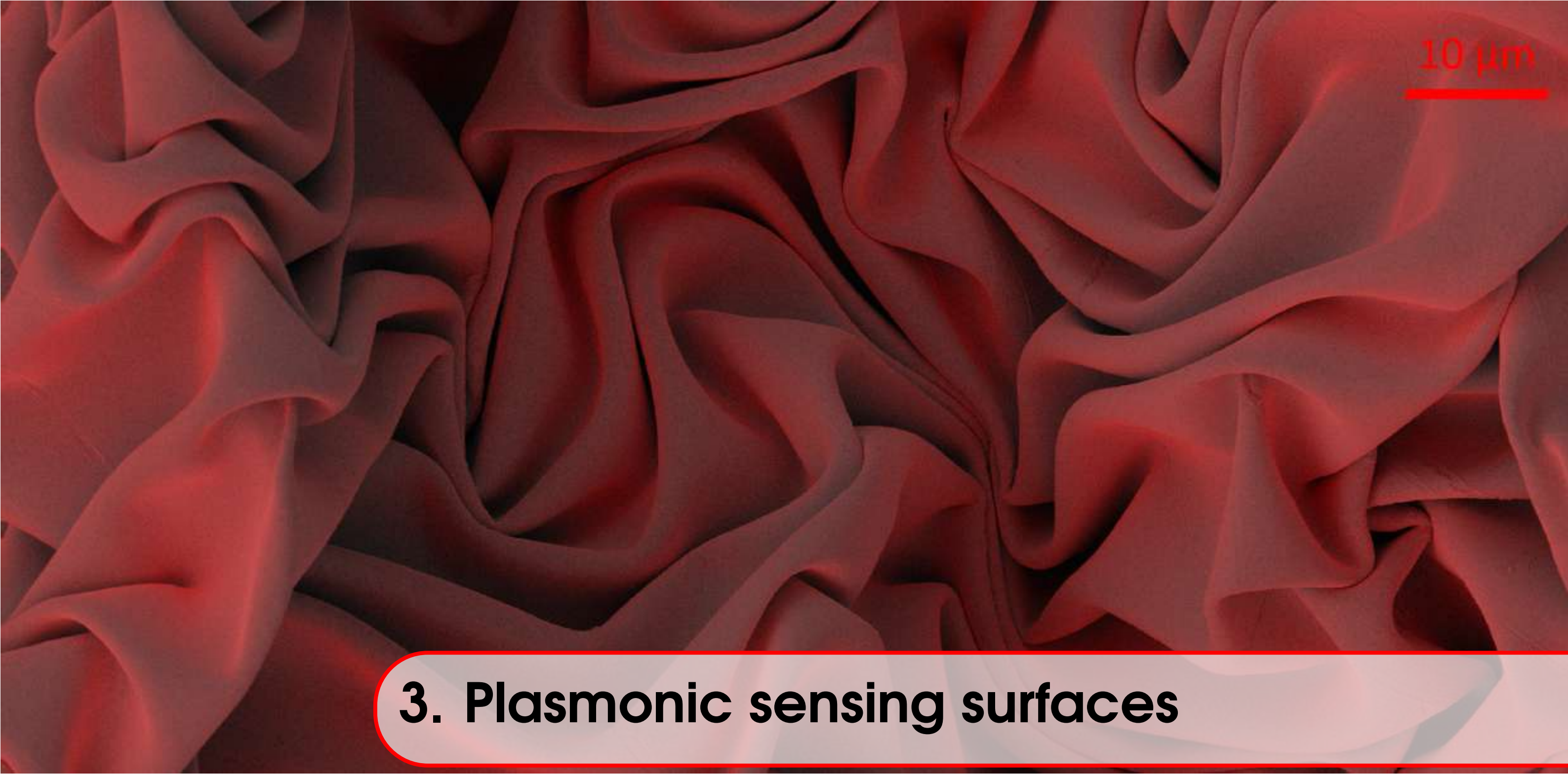

3. Plasmonic sensing surfaces

Optical detection and monitoring of various chemical compounds is of profound importance in fields as diverse as medical diagnostics, forensics, security, and environmental pollutant detection, among many others. Regardless of the particular realization, maximizing the effect an analyte species exerts on a radiation field lies at the core of optical molecular sensing. One straightforward method of achieving this involves spatial confinement of optical energy at or around the volume of analytic interest, and to this end enhanced near fields arising from optically driven subwavelength collective charge density oscillations at metal interfaces, known as surface plasmon-polaritons, presently remain unmatched. Plasmonic enhancement underlies many analytical methods such as localized or propagating surface plasmon resonance sensors, surface-enhanced infrared absorption and metal enhanced fluorescence. However, the genesis of all these techniques can be traced back to an observation that Raman scattering signals are significantly enhanced for molecules adsorbed onto roughened silver electrodes [374], which was later explained [375, 376] and came to be known as surface-enhanced Raman scattering (SERS). Here nanotexturing is instrumental in facilitating the coupling of optical energy into plasmonic oscillations, as well as in enabling its localization within nanoscale gaps and crevices, called hot spots. This enhancement turned out to be such, that the notoriously weak Raman effect could be used for detecting single molecules [377]. Still, over the 40 years since its discovery, adoption of SERS remains limited in large part due to the difficulties associated with the creation of effective yet affordable nanostructured plasmonic platforms.

This chapter focuses on noble metal coated nanotextured surfaces suitable for use as SERS substrates. The first sections lay out the main principles of SERS, which represent the intersection of plasmonics and Raman scattering. The original research contributions described here center on fabrication as well as characterization of highly effective SERS substrates made by means of ever more simple and scalable approaches. All of the methods involve plasmonic metal deposition onto different nanotextured surface templates, such as silicon nanopillars made *via* block copolymer directed self-assembly lithography, chemically textured copper oxide flakes, and thermally shrunk polystyrene wrinkles (pictured in the title figure). Since bottom-up nanotexturing methods often give rise to a certain degree of randomness in the resulting topology, effort is made in quantifying the stochastic SERS performance on such surfaces.

3.1 Basics of surface-enhanced Raman scattering

This section provides an overview of the key concepts of Raman scattering and plasmonics that, acting in unison, give rise to the SERS effect [378]. Particular attention is given to the mechanisms of Raman signal enhancement and their quantification. Furthermore, the role of nanostructuring in coupling and concentrating optical energy into subwavelength plasmonic modes, instrumental in producing the aforementioned enhancement, is likewise discussed.

3.1.1 Enhancement mechanisms in SERS

The Raman effect is a type of inelastic scattering where the vibrational oscillations of the bonds in a molecule modulate and thereby get imprinted onto an incident higher frequency optical field [379]. Spectrally this manifests as a set of satellite peaks to either side of the central carrier frequency, in a way akin to amplitude modulated signal mixing. Therefore, Raman spectroscopy can probe the structural information inherent in vibration modes, characteristic of a given molecular species, at optical frequencies instead of the infrared, where photon energies are on par with vibrational level spacings. The Raman effect is of profound utility for molecular sensing due to the abundance of both high intensity coherent radiation sources as well as of sensitive detectors operating at optical frequencies. In addition, Raman spectroscopy can extract molecular structure information at a high spatial resolution as a result of the substantially lower diffraction limit at visible wavelengths.

However, Raman scattering is an extraordinarily weak effect, with differential cross sections at around 10^{-27} cm^{2}sr^{-1} for dye molecules with conjugate systems and at an even more modest 10^{-30} cm^{2}sr^{-1} for other more conventional non-resonant compounds [380]. For comparison, such values are approximately 13 orders of magnitude below the fluorescence cross sections of dyes used in single-molecule experiments [381]. In light of this the aforementioned first observations of a Raman signal from pyridine molecules adsorbed onto a textured silver electrode [374] seemed extremely disproportionate (*i.e.* by roughly $10^5 - 10^6$ orders of magnitude) to what would be expected due to an increase in probed substrate surface area alone, hence, gave rise to the term surface-enhanced Raman scattering (SERS). The phenomenon was soon shown to stem from a general plasmonic enhancement due to optical properties of the substrate [376, 382], or from a more analyte-specific chemical enhancement as a result of molecule-substrate interactions [375, 383, 384]. These mechanisms were subsequently determined to be both fairly independent in their causes and multiplicative in their effects [385]. Further investigations culminated in the demonstration of single-molecule sensitivity Raman scattering results, which initially relied on statistical analysis of signal intensity fluctuations and were somewhat ambiguous [386, 387], however, were later confirmed using more rigorous bianalyte [388] or isotopologue [389] approaches.

A simplified illustration of the processes that give rise to SERS is provided in Figure 3.1. The three main elements inherent to SERS are: local enhancement of electromagnetic field intensity available for analyte excitation, Raman transitions which may or may not be altered in symmetry and magnitude by surface proximity, and electromagnetic enhancement of scattered radiation which includes the spectrally imprinted Raman signal. Each of these phenomena can to some degree contribute to SERS, however, most of the enhancement associated with SERS is electromagnetic. It relies upon evanescent optical energy concentration in the vicinity of high polarizability material interfaces and structures, especially those with large intrinsic or transient free carrier concentrations and low damping. Furthermore, emitted Raman scattering radiation power can also be enhanced *via* a reciprocal mechanism in which diploar oscillations of a molecule drive resonant emission from those same structures.

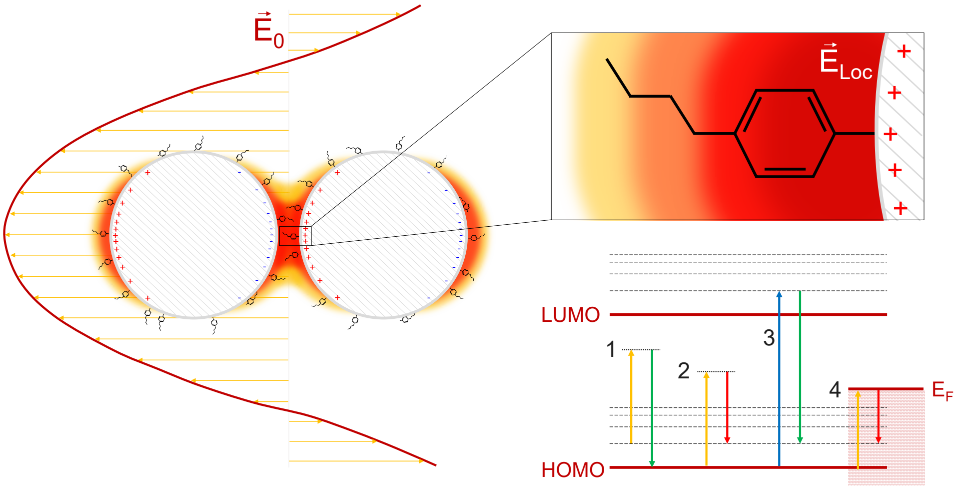

Figure 3.1: Sketch outlining the main elements of SERS. A high polarizability structure, in this case a dimer of plasmonic nanoparticles, acts as an antenna which collects the energy of an incident optical field and confines it into a localized high intensity mode, where certain surface-adsorbed analyte molecules are situated. The plasmonic antenna also serves to enhance the Raman scattered radiation. Schematic in the lower left of the figure provides a simplified representation of (1) anti-Stokes, (2) Stokes, (3) resonant and (4) charge-transfer surface-enhanced Raman scattering transitions.

Electromagnetic enhancement is general in the sense that it depends mainly on physical properties of the enhancing surface and its interaction with incident radiation, therefore acts irrespective of the particular analyte species being probed. Here, for the sake of specificity, a simple case of molecules adsorbed onto a subwavelength metal nanoparticle dimer, excited by monochromatic illumination of frequency ω_0, is considered. Conceptually, the plasmonic platform acts as a resonant antenna that collects electromagnetic energy from its extended spatial vicinity and concentrates it in nanoscale regions called "hot-spots", which in the present example would be the near field dipolar mode regions and, especially, the inter-particle gap. Any molecule with a Raman polarizability tensor $\hat{\alpha}_R(\omega_\mathrm{R},\omega_0)$ situated in a hot-spot site at position $\mathbf{r}_\mathrm{m}$ is exposed to local electric field strengths $\mathbf{E}_\mathrm{Loc}(\mathbf{r}_\mathrm{m},\omega_0)$ several orders of magnitude above that exhibited by incident radiation $\mathbf{E}_0(\mathbf{r}_\mathrm{m},\omega_0)$. This augmented local field induces a proportionately enhanced oscillating molecular dipole $\mathbf{p}_\mathrm{R}(\mathbf{r}_\mathrm{m},\omega_\mathrm{R}) = \hat{\alpha}_R(\omega_\mathrm{R},\omega_0)\mathbf{E}_\mathrm{Loc}(\mathbf{r}_\mathrm{m},\omega_0)$. Since radiation power emitted by a dipole in free space P_0 is proportional to $|\mathbf{p}_\mathrm{R}(\mathbf{r}_\mathrm{m},\omega_\mathrm{R})|^2$, this mechanism can be phenomenologically quantified as the local field intensity enhancement factor $M_\mathrm{Loc}(\mathbf{r}_\mathrm{m},\omega_0)$ [382, 390]:

$$M_\mathrm{Loc}(\mathbf{r}_\mathrm{m},\omega_0) = \frac{|\mathbf{E}_\mathrm{Loc}(\mathbf{r}_\mathrm{m},\omega_0)|^2}{|\mathbf{E}_0(\mathbf{r}_\mathrm{m},\omega_0)|^2}. \tag{3.1}$$

However, in SERS the Raman dipole does not emit into free space, and its radiation pattern $\mathrm{d}P_\mathrm{Rad}/\mathrm{d}\Omega$ as well as power P_Rad can be drastically altered by the proximity of a polarizable substrate. In keeping with the previously outlined concept, electromagnetic radiation put out by the molecule at Raman frequency ω_R drives the resonant emission of the plasmonic antenna, thereby leading to an additional source of electromagnetic enhancement by way of modified spontaneous emission [391]. An alternative way of describing this phenomenon states that proximity of the SERS substrate increases the local density of optical states that the Raman dipole can radiatively couple to. The SERS signal contribution resulting from this effect is described by the radiation enhancement factor $M_{\mathrm{Rad}}(\mathbf{r}_{\mathrm{m}}, \omega_{\mathrm{R}})$, and most often expressed trough the following approximation [390]:

$$M_{\mathrm{Rad}}(\mathbf{r}_{\mathrm{m}}, \omega_0) = \frac{P_{\mathrm{Rad}}}{P_0} \approx \frac{|\mathbf{E}_{\mathrm{Loc}}(\mathbf{r}_{\mathrm{m}}, \omega_{\mathrm{R}})|^2}{|\mathbf{E}_0(\mathbf{r}_{\mathrm{m}}, \omega_{\mathrm{R}})|^2} = M_{\mathrm{Loc}}(\mathbf{r}_{\mathrm{m}}, \omega_{\mathrm{R}}). \tag{3.2}$$

Here, by applying the optical reciprocity theorem [392], the task of finding the power radiated by a dipole towards a given direction was substituted by a much simpler problem of determining the electric field induced at the dipole site under plane wave excitation, incident form the aforementioned direction. As a result radiation enhancement can be approximately represented by the local field enhancement factor at the Raman-shifted frequency ω_{R}. However, when using this simplification care must be taken to consider that radiation enhancement factors determined thereby are valid only for a small solid angle range $\Delta\Omega$ in a particular direction. Since radiation patterns of plasmonic antennas are likely to be at least somewhat anisotropic, a more rigorous treatment of SERS would involve spatial averaging of the radiation enhancement factors over some specific solid angle range characteristic of the collection optics in a given Raman spectroscopy setup.

When taken together, the field intensity enhancement factor, related to excitation of an analyte, and the radiation enhancement factor, associated with emission of Raman signal, act multiplicatively and give rise to the total electromagnetic enhancement factor $EF_{\mathrm{EM}}(\mathbf{r}_{\mathrm{m}}, \omega_0, \omega_{\mathrm{R}})$:

$$\begin{aligned} EF_{\mathrm{EM}}(\mathbf{r}_{\mathrm{m}}, \omega_0, \omega_{\mathrm{R}}) = M_{\mathrm{Loc}}(\mathbf{r}_{\mathrm{m}}, \omega_0) M_{\mathrm{Rad}}(\mathbf{r}_{\mathrm{m}}, \omega_{\mathrm{R}}) &\approx \frac{|\mathbf{E}_{\mathrm{Loc}}(\mathbf{r}_{\mathrm{m}}, \omega_0)|^2}{|\mathbf{E}_0(\mathbf{r}_{\mathrm{m}}, \omega_0)|^2} \cdot \frac{|\mathbf{E}_{\mathrm{Loc}}(\mathbf{r}_{\mathrm{m}}, \omega_{\mathrm{R}})|^2}{|\mathbf{E}_0(\mathbf{r}_{\mathrm{m}}, \omega_{\mathrm{R}})|^2} \\ &\approx \frac{|\mathbf{E}_{\mathrm{Loc}}(\mathbf{r}_{\mathrm{m}}, \omega_0)|^4}{|\mathbf{E}_0(\mathbf{r}_{\mathrm{m}}, \omega_0)|^4}. \end{aligned} \tag{3.3}$$

Here, the position-specificity of the total electromagnetic enhancement factor is inherited from constituent field and radiation enhancement contributions. Local field enhancement can vary dramatically between any two positions due to the evanescent nature and non-uniform spatial profile of plasmonic modes. As a result only analytes adsorbed in the immediate 10 nm vicinity of, or covalently bonded to, the SERS substrate at a hot-spot site will experience exceptional field intensities [393, 394]. In addition, molecular orientation with respect to the polarization of local electric field can have a marked effect on rates of a given Raman transition through surface selection rules [395–398]. On the other hand, radiation enhancement is strongly dependent on emitting dipole orientation relative to the plasmonic surface, with most intense far field radiation typically produced at orthogonal configurations [399]. Due to the aforementioned factors a large variability of the spectroscopic signal is fairly typical for SERS, even between any two sequential acquisitions, due to the stochastic nature of analyte molecule motion and their interactions with enhancing surfaces.

Similarly, the local field intensities of modes supported by a SERS substrate are frequency dependent, and, in general, would be expected to differ at spectral positions ω_0 and ω_{R}. For example, a decrease in the SERS signal for strongly Raman-shifted energetic vibrational modes is commonly observed [385], since electromagnetic enhancement relies on resonance effects, which have finite bandwidths by definition. However, in most cases Raman shifts are fairly narrow and plasmon resonance bands are sufficiently broad for the $|E_{\mathrm{Loc}}|^4$ approximation to be justified and to yield SERS electromagnetic enhancement factor estimates generally within one order of magnitude accuracy. Such a sharp dependence on electric field intensity

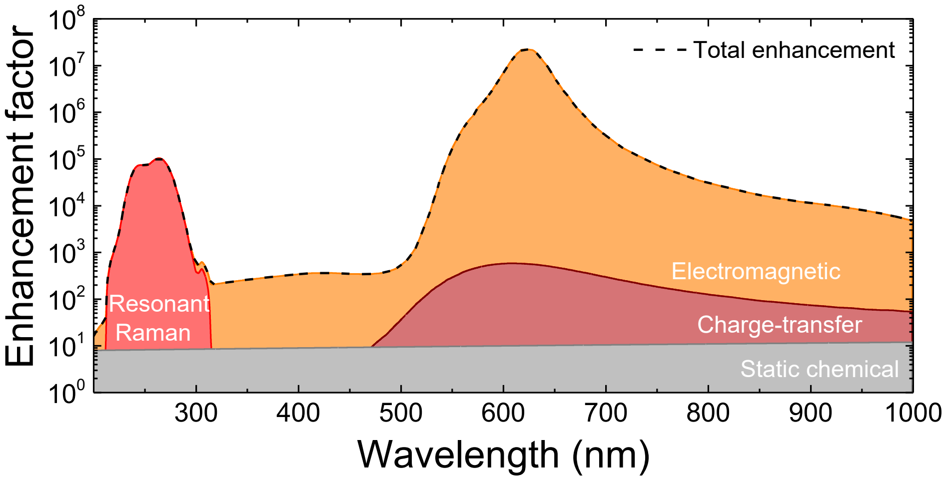

Figure 3.2: Hypothetical example of the spectral dependence of SERS, represented as a rough approximation of guanine [401] molecules adsorbed on a Au nanoparticle dimer suspended in water [390]. A metal-analyte complex is presumed to be formed, giving rise to both static chemical as well as charge-transfer enhancements. Molecular electron systems are resonant at UV wavelengths. Electromagnetic enhancement contribution is the dominant mechanism in the visible spectral region.

in spatially confined hot-spot modes has been reported to result in electromagnetic SERS enhancements from 10^4 up to the order of 10^8 [399, 400], which goes most of the way in pushing SERS towards the single-molecule sensitivity threshold.

Chemical enhancement is, in contrast, highly dependent on local electronic structures of both the analyte and of the substrate it interacts with as each of their wavefunctions start to overlap [402–404]. The term represents a class of short range first adsorbant layer effects that can be phenomenologically accounted for through modifications to the Raman polarizability tensors $\hat{\alpha}_R(\omega_\mathrm{R},\omega_0)$ specific to every mode of interest. Research of chemical enhancement in SERS has been wrought with considerable difficulty, as its influence is comparatively weaker than, hence easily drowned out by, electromagnetic enhancement contributions. Furthermore, experimental results are particular to electronic structures of probed analyte molecules, and as a result do not easily lend themselves to the drawing of general conclusions.

However, while short-range electronic phenomena in SERS seem marginal when compared with electromagnetic ones in terms of raw enhancement, they can substantially influence the types and relative intensities of transitions observable in spectra of physisorbed or chemisorbed analytes [384], for example, through mode-specific molecular resonance effects [405] or symmetry-derived rules of selection [395, 406, 407]. Therefore, investigation into chemical enhancement phenomena have been spurred on by the need to understand its implications on SERS applied as either an analytic technique or as a method to probe molecule-metal interactions in more fundamental research [408]. Through a combination of new unified theoretical models [409–411], time-dependent density functional theory simulations [412, 413], and rigorous experimental work on structural variants of certain model molecules [414, 415] significant advances towards a complete SERS framework have been made. The most pertinent electronic effects in chemical enhancement are understood as an additive combination of non-resonant changes in the molecular polarizability, enhancements from molecular excitation resonances, and charge-transfer resonances. A simple hypothetical illustration of the spectral behavior as well as relative magnitude of different chemical enhancement mechanisms, along with the electromagnetic contribution, is given in Figure 3.2.

Non-resonant changes in the molecular polarizability are related to alterations induced in the electronic structure and in the vibrational modes of an analyte through interactions with a metal surface. The resultant molecule-metal complex can exhibit increased Raman cross-sections, particularly for aromatic compounds which readily establish π-backbonding *via* sharing or transfer of charge to a metal [416]. As this phenomenon manifests through modifications of the molecular ground state it is also referred to as the static chemical enhancement, or simply CHEM for short. Non-resonant chemical enhancement is characteristically independent on excitation wavelength, since the Raman scattering processes itself proceeds in a conventional fashion *via* virtual energy levels, as sketched in the lower-left segment of Figure 3.1. Overall, the effect is generally quite modest and produces Raman signal enhancements between 10^0 and 10^2 hence, due to experimental difficulties, its investigation tends to heavily rely on time-dependent density functional theory simulations.

For example, computational investigation of pyridine weakly bound to Ag_{20} clusters uncovered the occurrence of charge transfer form the analyte towards the metal, thereby inducing a change in static polarizability and resulting in non-resonant Raman enhancement by a factor anywhere from 4 to 8, depending on adsorption site geometry [416, 417]. Similar work done on benzenethiol, much more strongly chemisorbed to Ag clusters, indicates higher enhancements for modes in close proximity to the binding site, as well as a dependence of relative peak intensity of different modes on molecular orientation and symmetry with respect to the metal cluster [412]. Subsequent findings using various analytes showed how the magnitude of non-resonant chemical enhancement scales in proportion to ω_X^4/ω_e^4, where ω_X represents the the lowest (HOMO-LUMO) excitation energy of the free molecule and ω_e is the lowest charge transfer excitation energy of the metal-molecule complex [415, 416]. Likewise, experimental results on structural derivatives of a model dye compound found correlations between the presence of stronger electron donating groups spliced onto a molecule and high static enhancements [414].

Enhancements from molecular excitation resonances arise when Raman scattering proceeds *via* electronic levels of a given analyte instead of the usual virtual states, therefore do not strictly result from surface interaction effects. This mechanism, called surface-enhanced resonance Raman scattering (SERRS), is analogous to the resonant Raman scattering observed for free molecules in that vibrational modes are populated *via* Franck–Condon activity when excited electronic states exhibit appreciable potential energy surface shifts with respect to the ground state [385, 418]. As a result Raman bands associated with molecular vibrations related to resonant electronic transitions are enhanced preferentially and tend to dominate the spectra [405, 419]. Of course, laser photon energies used for Raman excitation need to match said transitions, hence, resonant enhancement is characteristically wavelength dependent [405, 420]. The influence of a plasmonic surface, distinguishing SERRS from its bulk resonant Raman scattering counterpart, manifests through shifting and broadening of electronic states, which in turn may aid in matching the incident photon energy with the relevant transition [419]. More importantly, metal proximity provides non-radiative mechanisms for quenching fluorescence that otherwise often overwhelms the Raman signal [405]. Also, since Raman scattering benefits from electromagnetic enhancements to both absorbance and emission, whereas only the former contribution is operative for fluorescence, SERS related signal increase tends to outpace concurrent photonic effects [420, 421]. In contrast to other chemical enhancement mechanisms, SERS signal increases due to resonant molecular excitation can be substantial, with factors in the range 10^3 to 10^6 reported [422, 423].

Resonant chemical enhancement is particularly straightforward to harness for polarizable π-electron system-containing analytes, which have electronic transitions coincident with wavelengths of plasmons supported by gold or silver based SERS substrates. Therefore, it is unsurprising that a notable majority of early single-molecule SERS experiments have been reported on various chromophores [424], with rhodamine 6G being most prevalent [387]. Raman reporters or labels used for functionalization in biochemical sensing likewise are often derived from dyes or even fluorophores to make full use of resonant chemical enhancement [425]. Furthermore, in addition to the sheer increase in signal, SERRS can also provide increased specificity, as vibrational modes related to chromophore groups become readily apparent in otherwise broad and indistinct spectra of complex large molecules. Notable examples of such preferential resonant enhancement include SERRS observations of heme group related modes in myoglobin [426], as well as other chromophore containing proteins such as cytochrome *c* [427, 428]. In general, however, label-free Raman sensing of most organic compounds is wrought with challenges [429], as it cannot rely on the presence of chromophores absorbing at visible-to-near-IR wavelengths, typically associated with SERS. In light of this, considerable effort has been put into devising UV resonant plasmonic SERS platforms, which are most often based on Al [430–432] although more exotic metals such as rhodium and ruthenium have also been tried [433]. The reasoning is that UV wavelengths are where many clinically relevant proteins as well as DNA bases are resonant, hence, are able to exhibit concurrent electromagnetic and chemical enhancement whilst bypassing fluorescent background related issues [434].

Charge-transfer enhancement, abbreviated as CT, is conceptually similar to the aforementioned SERRS mechanism, the main difference being that transitions are not confined to the electronic system of a given analyte but occur *via* new excitation states established when a metal-molecule complex is created [403, 435]. The mechanism derives its name from the proposed resonant excitation processes, where an electron is promoted from the Fermi level of the metal E_F to a charge transfer level E_{CT} of the metal-molecule complex, or, conversely, from the HOMO of said complex to E_F of the metal [423], sketched by transition 4 in Figure 3.1. As the Fermi level of most metals is typically situated approximately midway between HOMO and LUMO states, charge-transfer excitation energies can be expected to be roughly half that of the UV resonant organic compounds, hence, accessible at visible wavelengths [385]. Most compelling evidence in favor of this explanation is provided by electrochemical cell SERS experiments, where E_F of the metal, and by extension the CT resonance wavelength condition, could be varied through application of an electrode potential [436, 437]. The observable amount of dynamic charge-transfer related Raman scattering cross-section enhancement is particular to different analyte and metal surface electronic structure combinations and, therefore, is difficult to generalize. However, most claims of CT enhancement in SERS fall in the range between 10^1 and 10^3, making it an effect intermediate in magnitude between static and resonant chemical enhancement contributions [438, 439].

Theoretical work using time-dependent density functional theory simulations [384, 422] has done much in elucidating processes related to formation of molecule and metal cluster complexes, such as excitation profiles of CT states [440, 441], conformation and symmetry effects [412, 442], or influence of binding site type [417], just to name a select few. Illustrative examples of charge-transfer enhancement in action come as a result of SERS investigation on DNA bases, where existence of CT bands in adsorbate-metal complexes was shown both experimentally and numerically. There, influence of CT enhancement in SERS was subsequently suppressed through atomic-layer deposition of an ultrathin 1 nm Al_2O_3 insulating layer, preventing analyte molecules from exchanging charge carriers with the underlying

Ag substrate [401]. A different approach, which used molecular interparticle junctions, experimentally revealed charge-transfer enhancement dependence on molecule orientation with respect to a metal surface as well as its coverage [443]. Furthermore, while chemical effects are largely secondary to electromagnetic ones on Au or Ag platforms, SERS observed at visible wavelengths for adsorbants on semiconductors is predominately assigned to charge-transfer chemical enhancement since plasmonic effects for such substrates would be expected only in the IR spectral range [439].

Quantification of all such disparate and potentially additive electromagnetic and chemical enhancement contributions has been a longstanding issue, particularly when performance comparisons between different SERS substrates have to be made. The aforementioned Raman polarizability tensor altering chemical mechanisms can be simultaneously active for various molecule-substrate combinations in ways that are neither known in advance nor can be easily untangled experimentally. Even the largely analyte independent electromagnetic enhancement is extremely spatially nonuniform and, furthermore, can introduce its own dependencies on excitation wavelength or polarization, as well as on the collection geometry used in a given Raman spectroscopy setup. The complex multivariate nature of SERS makes accounting for these factors exceedingly difficult or even impossible, therefore, all definitions used for experimental determination of enhancement factors involve simplifying assumptions that either make them approximate or limit their applicability only to certain situations. Two of the most useful among such definitions are the single molecule enhancement factor (EF_{SM}) and the substrate specific enhancement factor (EF_{SS}) [390, 399].

Single molecule enhancement factor is generally understood as the increase in signal at certain localized positions on a given SERS substrate relative to the conventional Raman scattering case. In practice those positions of particular interest correspond to hot-spots with highest intensity optical fields, therefore, EF_{SM} is typically treated as the maximum enhancement factor a molecule is likely to experience, and expressed as:

$$EF_{\mathrm{SM}} = \frac{I_{\mathrm{SERS}}^{\mathrm{SM}}}{\langle I_{\mathrm{RS}}^{\mathrm{SM}} \rangle} = \frac{\mathrm{d}\sigma_{\mathrm{SERS}}/\mathrm{d}\Omega}{\mathrm{d}\sigma_{\mathrm{RS}}/\mathrm{d}\Omega}. \tag{3.4}$$

Here, $I_{\mathrm{SERS}}^{\mathrm{SM}}$ represents the SERS intensity of a single molecule, whereas $\langle I_{\mathrm{RS}}^{\mathrm{SM}} \rangle$ is the average Raman signal intensity in the absence of surface enhancement. Conversely, EF_{SM} can also be expressed as the ratio of differential scattering cross-sections in SERS ($\mathrm{d}\sigma_{\mathrm{SERS}}/\mathrm{d}\Omega$) and non-SERS ($\mathrm{d}\sigma_{\mathrm{RS}}/\mathrm{d}\Omega$) cases. This notation is most often in use when single-molecule SERS experiments are discussed, since only the most active of hot-spots are relevant in producing the necessary amounts of enhancement.

Substrate specific enhancement factor, on the other hand, incorporates the nonuniformity of SERS by denoting the average Raman enhancement a molecule adsorbed on a surface is subjected to. It is usually defined as:

$$EF_{\mathrm{SS}} = \frac{I_{\mathrm{SERS}}/N_{\mathrm{Surf}}}{I_{\mathrm{RS}}/N_{\mathrm{Vol}}}, \tag{3.5}$$

where I_{SERS} and I_{RS} are the Raman intensities in SERS and non-SERS cases, normalized to the number of molecules N_{Surf} and N_{Vol} adsorbed onto a SERS substrate or located in the excitation volume, respectively. Here an implicit assumption is that the number of molecules overlaying the SERS substrate N_{Surf} amount to no more than a single monolayer, as any additional analyte layers would be subjected to an ever decreasing enhancement due to the strong distance dependence of SERS as well as increased damping of plasmonic resonances, hence, EF_{SS} would appear concentration-dependent. On top of that, high intensity localized electromagnetic fields cause heating [444] or laser induced analyte decomposition [445], and can be strongly catalytic for certain chemical reactions, which transform the original analyte compounds into a different molecular species altogether [446]. So, while the surface specific enhancement factor is most informative when SERS is used as an analytic technique or when different substrates are compared, it still appears dependent on numerous extrinsic measurement condition related factors.

Regardless which metric is chosen to quantify SERS enhancement, the expectation of linear response in relation to the incident field power is another assumption which, at high laser intensities, may not be justified due to photobleaching [399, 447, 448] or thermal [449, 450] effects. Hence, information related to Raman measurements, such as laser power and acquisition time can be important in characterizing substrate performance. Furthermore, erroneous estimates of analyte surface coverage or unaccounted-for chemical enhancement contributions may give rise to substantial errors in SERS substrate enhancement factor calculations. Still, even when enhancement factor estimations are rigorous, measurement protocols tailored to maximize the efficacy of SERS can vary dramatically between different substrate and analyte combinations, therefore, in many situations such comparisons cannot be done based on any single figure of merit.

The complex interplay of effects underpinning SERS demands input form multiple disciplines in order to further the understanding as well as practical applicability of this unique spectroscopic technique. Major contributions provided by optics and nanotechnology are related to devising efficient and affordable solutions for concentrating light in nanoscale hot-spots and thereby maximizing the attainable electromagnetic enhancement. The vast majority of SERS substrates, and definitely the highest performing among them, are based on coupling light into sub-diffraction plasmonic modes, which are in large part defined by nanoscale surface geometry.

3.1.2 Plasmons at planar metal interfaces

The primary function of plasmonic substrates in enabling electromagnetic enhancement crucial to SERS is related to their subwavelength confinement of optical energy. Of course, other platforms capable of supporting high intensity electromagnetic modes can also be used to increase Raman scattering yields [451], as has been demonstrated through numerous realizations of SERS in dielectric cavities [439, 452]. Under suitable laser excitation SERS has been observed on inorganic semiconductor-based platforms such as TiO_2 [453], Si [454], Cu_2O [455] and even organic DFH-4T [456] among others. However, none of the alternatives can match the nanoscale local field intensities produced in the immediate vicinity of subwavelength metal objects when sheer magnitude of enhancement at visible wavelengths is required. Therefore, most of the truly high performing SERS realizations rely on plasmonic coinage metals such as Ag, Au and, to a lesser extent, Cu.

The optical properties of metals arise due to the large abundance of electrons only weakly interacting with a bulk metal ion lattice background, and are well approximated by the Drude model for a free-electron gas [390]. Of course, in real metals electromagnetic energy would be dissipated through scattering losses, and, furthermore, a portion of said energy would be consumed through induction of bound electron interband transitions. Like is the case for all materials, the influence of electric field on a metal is characterized by its frequency ω dependent complex permittivity $\varepsilon(\omega) = \varepsilon'(\omega) + i\varepsilon''(\omega)$, which, using the Drude model and

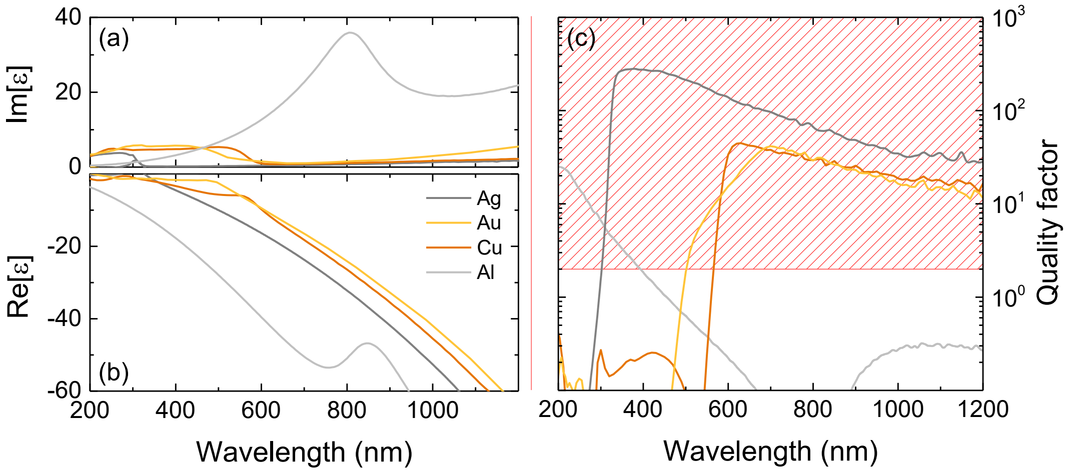

Figure 3.3: Imaginary (a) and real (b) parts of the complex relative permittivity of Ag, Au, Cu and Al metals in the UV-to-near-IR spectral range [458, 459]. (c) Approximate quality factor spectra for each of the metals, calculated using Equation 3.8 and related to optical losses due to damping. Values in the shaded region above quality factor 2 are indicative of potential utility to plasmonics.

phenomenologically accounting for interband transitions, can be expressed as [457]:

$$\varepsilon(\omega) = \varepsilon_\infty + \sum \frac{N_b e^2}{m_b^* \varepsilon_0} \cdot \frac{1}{\omega^2 - \omega_b^2 + i\gamma\omega} - \frac{\omega_p^2}{\omega^2 + i\gamma\omega}. \tag{3.6}$$

Here the last term represents the Drude contribution, where charge carriers are not subject to a restoring force. The damping rate is given by γ, whereas $\omega_p = \sqrt{Ne^2/m^*\varepsilon_0}$ is called the plasma frequency, represents the innate collective oscillation frequency of free electrons, and depends on their density N, effective mass m^* as well as on elementary charge e and vacuum permittivity ε_0 constants. The middle term, on the other hand, takes into consideration the presence of bound electrons of density N_b and effective mass m_b^*, which are described as a set of Lorentz oscillators with resonant frequencies ω_b. Lastly, the first term ε_∞ is a constant offset that includes the combined contributions of all higher energy interband transitions not explicitly incorporated into the second term.

Panels (a) and (b) in Figure 3.3 respectively depict the experimentally determined wavelength dependencies of imaginary and real parts of the complex permittivity for silver, gold, copper and aluminum [458, 459]. The imaginary part of the permittivity is indicative of detrimental absorbance related losses, and tends to be lower for shorter wavelength electromagnetic radiation. However, interband transitions, which substantially increase optical loss, become accessible at wavelengths below $\lambda \approx 600$ nm for Au as well as Cu, and in the UV spectral region for Ag, thereby reversing the trend. In contrast, interband transitions in Aluminum occur in near-IR at around $\lambda \approx 825$ nm wavelengths, and absorbance losses steadily decrease towards the UV range.

The real part of the complex permittivity, on the other hand, follows a ω^{-2} dependence in accordance with the Drude model, thereby becoming negative in sign below ω_p and progressively larger in magnitude as wavelengths of electromagnetic radiation increase. The negative sign of ε' is related to the phase delay in the motion of electrons with respect to external electric field intensity, which underlies the screening effects preventing penetration of electromagnetic radiation into the metal bulk. Similarly, large absolute values of ε' are indicative of nearly total reflectance exhibited by metals, as is evident from the Fresnel formulas given in Equation 1.1.

If a p-polarized electric field is incident onto a planar interface of two materials, one of which is characterized by a complex permittivity $\varepsilon_1(\omega)$, whereas the other is a lossless dielectric with a real $\varepsilon_2(\omega)$, Maxwell's equations with boundary conditions ensuring field continuity at the interface yield the following dispersion relations [457]:

$$k_x^2 = \frac{\varepsilon_1 \cdot \varepsilon_2}{\varepsilon_1 + \varepsilon_2} \frac{\omega^2}{c^2}, \qquad k_{j,z}^2 = \frac{\varepsilon_j}{\varepsilon_1 + \varepsilon_2} \frac{\omega^2}{c^2}, \quad j = 1,2. \tag{3.7}$$

Wave vector component k_x corresponds to in-plane propagation along the interface, whereas $k_{1,z}$ and $k_{2,z}$ denote out-of-plane waves propagating into each of the ε_1 and ε_2 permittivity materials. A particularly interesting situation is observed when $\varepsilon_1(\omega) + \varepsilon_2(\omega) < 0$, which results in imaginary $k_{1,z}(\omega)$ and $k_{2,z}(\omega)$ wave vectors. This means that an electromagnetic wave is evanescent in both of the transverse directions, giving rise to modes bound at the interface. Furthermore, k_x remains real if the condition $\varepsilon_1(\omega) \cdot \varepsilon_2(\omega) < 0$ is fulfilled. Hence, if one of the media has a negative real permittivity, which is larger in absolute value than that of the more conventional dielectric, a propagating surface wave can be created. Evidently, the coinage metals represented in Figure 3.3 (b) can fulfill the aforementioned conditions not only for interfaces with air but also with most other dielectrics. These surface waves, which in essence represent electromagnetic fields coupled to collective metal surface charge density oscillations, are called surface plasmon-polaritons (SPPs).

However, the negative sign and sufficient magnitude of $\varepsilon'(\omega)$ is a necessary but not a sufficient condition for a metal to be viable for plasmonic field intensity enhancement applications. In the absence of an out-coupling mechanism SPPs are non-radiative, hence, get dissipated through optical losses in the metal. Therefore, for substantial optical energy buildup to occur the imaginary part of metal permittivity should be sufficiently small so as not to introduce overwhelming damping. One way of characterizing the lossiness of metal nanostructures involves using a quality factor parameter defined as [460]:

$$Q = \frac{\omega \cdot \mathrm{d}\varepsilon'(\omega)/\mathrm{d}\omega}{2(\varepsilon''(\omega))^2}. \tag{3.8}$$

Quality factor dependencies on wavelength for silver, gold, copper and aluminum are plotted in Figure 3.3 (c). Metals tend to become suitable for plasmonics when $Q > 2$, and perform well for wavelengths where $Q \geq 10$ [390]. Evidently, silver is the superior plasmonic platform when surface oxidation is not considered, followed by gold with its many additional merits including chemical inertness, and then by the fairly reactive copper. The falloff in quality factor at shorter wavelengths is due to the onset of interband transitions. Lastly, aluminum becomes viable only in the UV spectral region.

Coupling energy from the incident optical field into SPPs is not a trivial process, since both energy and momentum conservation must be assured, hence, only a circumscribed set of modes is permissible. Examples of dispersion relations, linking in-plane propagation wave vectors k_x and frequency values ω according to Equation 3.7, are given in Figure 3.4 for planar interfaces of air ($\varepsilon_2 = 1$) with idealized lossless Drude metal in panel (a) as well as with silver (b) and gold (c).

The fundamental SPP coupling processes are most readily apparent in the Drude metal case, where three distinct regimes can be distinguished. The states belonging to the highest energy branch, starting just above the plasma frequency ω_p, are called Brewster's modes and correspond to the situation where $\varepsilon_1(\omega) > 0$. This means that the metal behaves like a dielectric, all wave vectors k_x, $k_{1,z}$, $k_{2,z}$ are real, and no surface confinement of optical energy occurs. The next section of the dispersion relation just below ω_p corresponds to the case where $0 < \varepsilon_1(\omega) + \varepsilon_2 < \varepsilon_2$, hence $k_{1,z}$, $k_{2,z}$ are real and k_x is imaginary, therefore localized and highly broadened radiative surface modes are supported. The lower frequency branch corresponds to the aforementioned case where $\varepsilon_1(\omega) + \varepsilon_2 < 0$, and describes propagating surface plasmon-polaritons most relevant to optical energy confinement. This curve has an upper frequency limit $\omega_p\sqrt{1+\varepsilon_2}$, which in an ideal metal no propagating SPP can exceed. Furthermore, the entire propagating surface plasmon-polariton branch is below the light line $\omega = ck_x$, meaning that radiative coupling is impossible and optical energy is trapped at the interface.

Dispersion relations of air interfaces with more realistic silver and gold metal surfaces, which have non-negligible imaginary permittivity values, exhibit marked deviations from the idealized case. Silver, represented in Figure 3.4 (b), while in principle preserving most characteristics of a Drude metal, instead of the divergence between non-radiative SPP and radiative Brewster's states possesses a continuous transition, called back-bending [461]. This effect imposes a maximum value on attainable values of k_x, that would not be observed in the absence of losses. In addition, truly localized surface states cease to exist, and instead

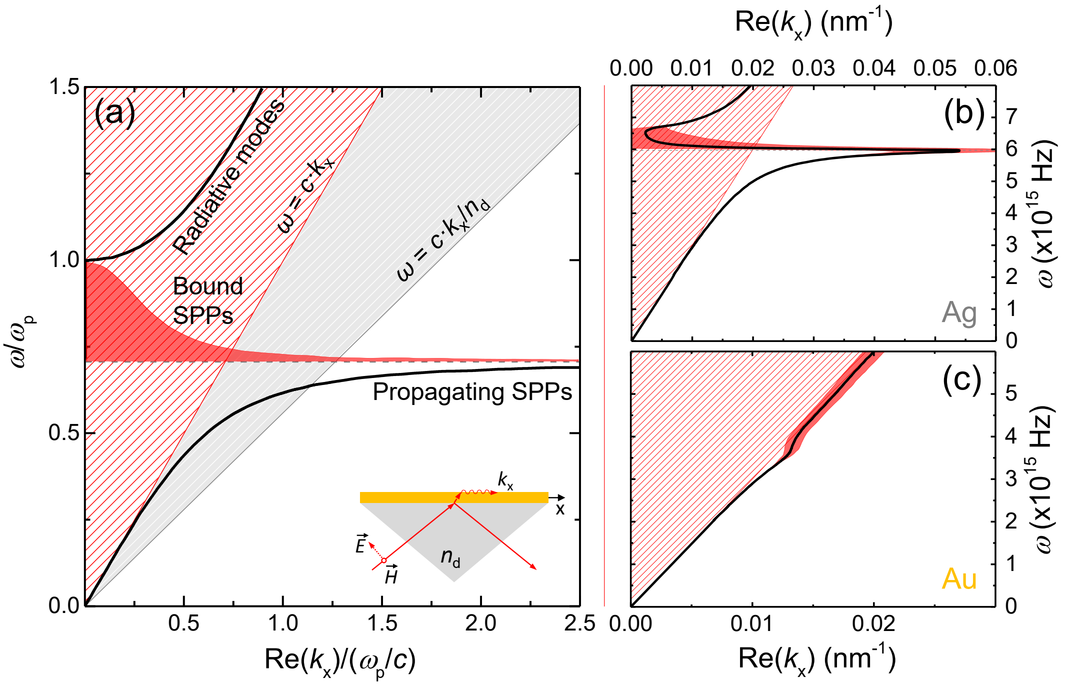

Figure 3.4: (a) Hypothetical dispersion relationship $\omega(k_x)$ of surface plasmon modes supported at a lossless Drude metal/air interface. Dispersion relationships for Ag and Au, which include damping losses, are given in panels (b) and (c) respectively. Figures are adapted from the literature [390]. Red-shaded areas represent dispersion relationships of photons in air at all possible angles of incidence. The gray-shaded area corresponds to dispersion relationships of photons in a higher refractive index n_d dielectric, used in Kretschmann or Otto evanescent SPP coupling schemes, the former of which is depicted in the inset.

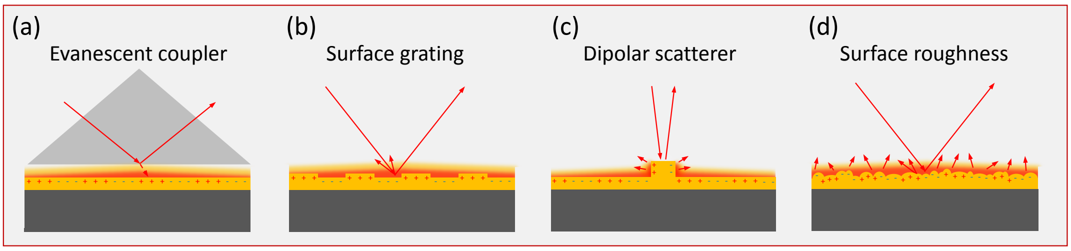

Figure 3.5: Sketches of surface plasmon-polariton excitation methods: (a) evanescent coupling from attenuated total reflectance in a prism, (b) k-vector matching *via* a periodic surface grating, (c) coupling from the near field of an excited defect, (d) scattering from random surface roughness.

become pseudo-propagating. In the case of gold, shown in Figure 3.4 (b), the propagating SPP dispersion curve is reminiscent of the ideal metal case only when $\lambda > 600$ nm. However, the presence of interband transitions at higher frequencies completely transforms the coupling behavior and the prior distinctions between different types of modes loose their meaning. Due to being strongly damped the higher energy plasmonic modes at a gold/air surface can best be described as lossy and somewhat localized [390].

In all cases, however, surface plasmon-polaritons at a single planar metal/dielectric interface possess k_x wave vector values above those of photons propagating in the dielectric even at grazing angles of incidence. Therefore, a photon can neither directly excite nor escape from a SPP mode in the absence of some coupling mechanism to ensure conservation of momentum. One way of achieving this involves the use of evanescent coupling from a higher refractive index medium in a total internal reflectance scheme trough either a wavelength-scale dielectric gap in the Otto configuration [462] (illustrated in Figure 3.5 (a)), or through the approximately 50 nm thickness metal film itself in the Kretschmann configuration [463] (sketched as an inset in Figure 3.4 (a)). Regardless of the particular realization, the light-line of a higher refractive index dielectric will encompass some portion of the propagating SPP dispersion curve, as shown in Figure 3.4 (a), so that by tuning the internal reflection angle both momentum and energy conservation conditions for exciting surface plasmon-polaritons can be met. The translational invariance of the planar metal surface means that said momentum conservation requirements are very strict, which in turn manifests as an acute sensitivity to parameters such as angle of incidence, wavelength as well as ambient refractive index. When critical coupling is achieved a sharp dip in total internal reflectance of the prism can be readily observed and exploited in SPP refractive index sensors for the detection of sub-monolayer molecular adsorbate on a plasmonic metal film [464].

However, attenuated total reflection SPP excitation schemes are bulky and not readily compatible with most SERS measurement setups, although some specialized realizations combining the Kretschmann configuration with a microscope to collect Raman scattered radiation have been demonstrated [465, 466]. Still, the electromagnetic enhancement component introduced by SPPs on planar surfaces, while not particularly large, is highly uniform, reproducible and simple to control, therefore, suitable for the investigation of chemical enhancement contributions in particular [467].

Alternative ways to bridge the momentum disparity between propagating photons and SPP modes involve making use of subwavelength-scale surface texturing. The method shown in Figure 3.5 (b) uses a periodic structure formed in the metal surface and designed in such a way that integer multiples of its grating vector $\mathbf{G} = 2\pi/d$ enable coupling light into SPPs for specific wavelength and incidence angle combinations. If the grating is shallow enough not to significantly perturb the surface modes, SPP resonance coupling conditions tend to preserve their sharpness. A different approach, sketched in Figure 3.5 (c), relies on some type of a subwavelength scale surface discontinuity or defect to act as a secondary localized near field emitter, which, due to its immediate vicinity to the metal film, possesses an exceptionally broad angular spectrum that overlaps with SPP states. Lastly, random roughness of plasmonic metal films can also aid in SPP excitation, and is represented by Figure 3.5 (d). In this case the surface can be interpreted as a stochastic superposition of all possible grating vectors $\mathbf{G}$, hence, momentum conservation can be assured at random. However, coupling efficiency for rough surfaces is low and, due to translational invariance no longer being in effect, does not exhibit spectrally sharp resonant features. Yet, beneficial effects of plasmonic substrate roughness have been an important aspect in SERS form its earliest realizations [376], and is often harnessed to both facilitate plasmon excitation and to host high intensity hot-spots in various substrate geometries [468, 469].

Electromagnetic enhancement in SERS requires high intensity local fields in the vicinity of relevant analytes. Suitably, propagating SPP modes are confined in one dimension at the metal/dielectric interface and decay exponentially with distance from it. For example, when a silver/air planar interface is excited with $\lambda = 633$ nm illumination the intensity falloff occurs over characteristic lengths of $1/k_{1,z} = 23$ nm and $1/k_{2,z} = 421$ nm for each of the respective media [457]. This in turn gives rise to an estimated maximum local field intensity enhancement $M_{\mathrm{Loc}} = |E_{\mathrm{Loc}}/E_{\mathrm{Inc}}|^2 \approx 256$ [390]. However, for high performing SERS realizations more substantial local field intensity enhancements in excess of $M_{\mathrm{Loc}} = 1000$, attainable trough optical field localization in two or three dimensions, is preferred.

3.1.3 Nanoplasmonics for electromagnetic enhancement

When light interacts with a metal object smaller then the wavelength, electric field oscillations drive collective motion of the entire electron system of the particle and it effectively becomes a bounded cavity. In such a case surface-plasmon polariton propagation is not possible, therefore, momentum conservation no longer applies and modes appear as distinct resonant states characterized by frequency ω_{R}. Due to their fully confined nature such excitations are called localized surface plasmons (LSP), and a simple example of a LSP is sketched in Figure 3.6 (a). For spherical objects with radii $a \ll \lambda$ the electrostatic approximation can be used to attain expressions of electric field values inside $\mathbf{E}_{\mathrm{In}}$ and outside $\mathbf{E}_{\mathrm{Out}}$ the metal sphere with permittivity $\varepsilon_1(\omega)$ surrounded by a uniform dielectric medium ε_2, in relation to the incident electric field strength $\mathbf{E}_0$ [470]:

$$\mathbf{E}_{\mathrm{In}} = \mathbf{E}_0 - \frac{\varepsilon_1(\omega) - \varepsilon_2}{\varepsilon_1(\omega) + 2\varepsilon_2}\mathbf{E}_0, \tag{3.9}$$

$$\mathbf{E}_{\mathrm{Out}} = \mathbf{E}_0 + \frac{a^3}{r^3}\frac{\varepsilon_1(\omega) - \varepsilon_2}{\varepsilon_1(\omega) + 2\varepsilon_2}\left((\mathbf{E}_0 \cdot \hat{\mathbf{r}})\hat{\mathbf{r}} - \mathbf{E}_0\right). \tag{3.10}$$

Main result immediately evident from Equation 3.9 is that the electric field $\mathbf{E}_{\mathrm{In}}$ inside the small metal particle is uniform, parallel to, and essentially comprised of the incident electric field augmented by the polarization induced in the metal. This is not surprising, since, when using the electrostatic approximation, particle size is implicitly assumed to be lower than the skin depth of the metal. Electric fields established around the sphere are much more relevant

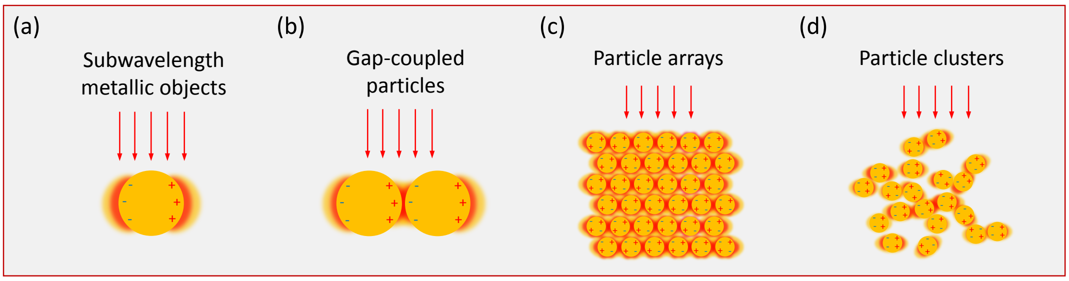

Figure 3.6: Examples of localized surface plasmon modes attainable for different particle arrangements: (a) localized dipolar surface plasmon mode of a single spherical nanoparticle, (b) gap-plasmon resonances of a nanopsphere dimer, (c) lattice plasmons supported by a translationally symmetric array of coupled nanoparticles, (d) Inhomogeneous stochastic localization pattern of plasmons supported in a disordered nanoparticle cluster.

for SERS and other types of LSP sensing, and are approximated by Equation 3.10. Here, $\mathbf{E}_{\mathrm{In}}$ is made up of the incident field and the electrostatic field of a dipole, induced through displacement of charges bounded by the nanoparticle. As a result, when distance r form the particle increases, electric field strength drops off rapidly according to r^{-3}, which relates to substantial optical energy confinement, hence, local field intensity enhancement, crucial for SERS. Indeed, characteristic length scales of LSP electromagnetic field intensity decay are estimated to be more than 10 times smaller than that of SPR [471]. Dipolar excitations are inherently radiative, therefore, the spherical LSP cavity will dissipate its electromagnetic energy not only *via* the usual absorbance in the metal, but also by readily scattering it into the far field, which underlies the radiation enhancement mechanism in SERS.

The recurring factor $\beta = (\varepsilon_1(\omega) - \varepsilon_2)/(\varepsilon_1(\omega) + 2\varepsilon_2)$ denotes a non-dimensional expression of polarizability in the special case of a spherical particle. Electric field strength, given by Equations 3.9 and 3.10, is maximized when the denominator of said polarizability vanishes at a resonance frequency ω_{R}, where $\varepsilon_1'(\omega_{\mathrm{R}}) = -2\varepsilon_2$. This condition represents the case when electron oscillations, which are subject to a restoring force at particle boundaries, are precisely $\pi/2$ out of phase with the incident field. Since $\varepsilon_1(\omega)$ is complex its imaginary component partly accounts for damping and broadening of the resonance, particularly when it coincides with interband transitions as is often the case for gold nanoparticles. In situations where nanoscale objects deviate from spherical symmetry, expressions of non-dimensional polarizability β can be strongly altered as well, since boundary-imposed restoring forces will manifest differently with respect to frequency or polarization of electromagnetic radiation. Therefore, resonant optical response of a nanoparticle is as much dependent on its shape as on the permittivity values $\varepsilon_1(\omega)$ and ε_2, and is more precisely described by the full Mie theory [472].

The dipolar LSPs, described up to this point, are typically the lowest energy state excitations, encountered for small nanoparticles roughly ranging between 10 nm and 100 nm in diameter. For larger particles ($a > 50$ nm for Ag), or at relatively lower excitation wavelengths where electric field oscillates within the object volume, higher order multipolar modes can be induced, which have lower radiant power than the dipolar plasmons, hence are not as suitable for providing enhancement of Stokes-shifted emission. Conversely if particles are small ($a < 10$ nm for Ag), optical energy will be confined much more strongly giving rise to higher local field enhancements. However, if the plasmonic cavity becomes substantially narrower

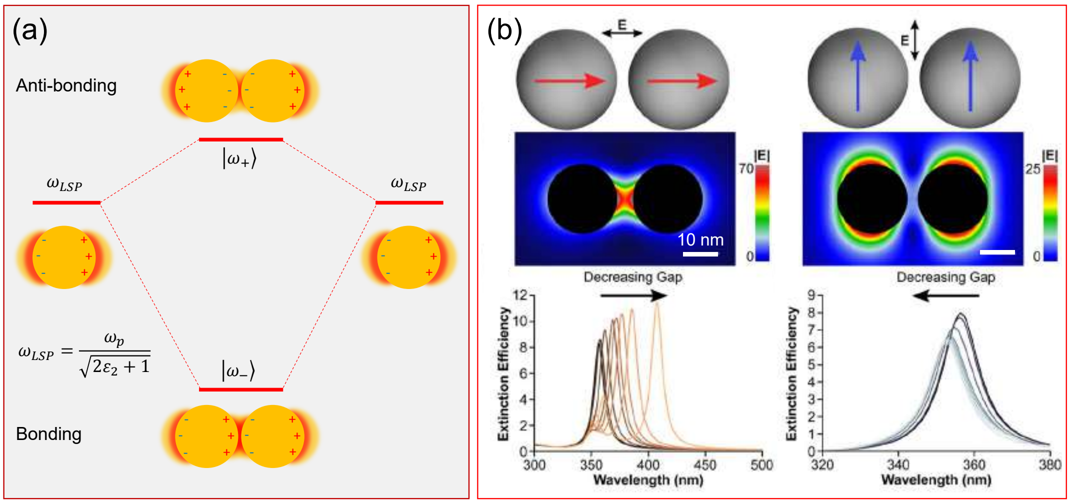

Figure 3.7: (a) Energy level diagram depicting the plasmonic hybridization of metal nanospheres when a gap-separated dimer is formed, giving rise to bonding $|\omega_-\rangle$ and anti-bonding $|\omega_+\rangle$ type new plasmonic states. (b) Optical behavior of the low energy mode $|\omega_-\rangle$ of an Ag dimer, representing in-phase oscillations of the constituent LSPs, contrasting the field intensity profiles and extinction spectra for excitation electric field polarizations along and across the dimer axis respectively [474]. Changes in gap width give rise to extinction peak shifts.

than the mean free path of an electron, absorbance losses due to charge carrier scattering at interfaces start to dominate, reducing both the quality factor of the resonance as well as the intensity of re-radiated field. Therefore, an optimal nanoparticle size, which balances dipolar mode intensity against the dissipation losses, can be set as the most well suited for particular material combinations and specific SERS uses [473]. Typically, local field intensity enhancements of the order $M_{\mathrm{Loc}}^{\mathrm{Ag}} \approx 1000$ and $M_{\mathrm{Loc}}^{\mathrm{Au}} \approx 50$ are estimated for silver and gold spheres at their respective resonances, the wavelength and magnitude of which is dependent on the dielectric environment [390]. This would result in moderate SERS performance, especially for Ag, however, further gains in electromagnetic enhancement can be obtained through mutual interactions between LSPs.

If two resonant cavities come in close enough proximity, so that the excitation of one begins to induce oscillations in another, they exhibit an optical response that is, in essence, collective and can be substantially altered from the initial LSP states. An illustrative way to describe this process involves the concept of hybridization [475]. The coupled LSP system most prevalent in SERS applications is the gap-separated nanosphere dimer, sketched in Figure 3.6 (b), which is the optical frequency equivalent of a dipole antenna [476]. Interference of the individual nanoparticle plasmonic excitations produces new states, corresponding to in-phase symmetric and opposite-phase anti-symmetric superpositions of the constituent oscillations [477], as shown in Figure 3.7 (a).

Typically, highest electromagnetic enhancement in the optimal spectral region is provided by the most redshifted bonding-type mode, illustrated in Figure 3.7 (b) for two orthogonal excitation field polarizations. When incident field polarization is perpendicular to the dimer axis, local field enhancement is effectively the same as for an isolated nanoparticle. On the other hand, when incident electric field polarization coincides with the dimer axis, and the inter-particle spacing becomes smaller than $\lambda/2\pi$, *i.e.* the phase lag between them is negligible, a gap mode of extraordinary local field intensity can be established. If the dimer separation is decreased further, resonant energy tends to redshift and field enhancement starts to escalate, much more rapidly than would be expected for two interacting dipoles, due to hybridization with higher multipole states [477]. Estimations of electromagnetic enhancement factors for a dimer with a 1 nm gap can reach values $EF_{\mathrm{EM}} \sim 10^{11}$, which are suitable for routine detection of single molecule SERS [400, 478, 479]. Furthermore, the mode redshift due to hybridization is serendipitous to gold nanoparticles, as it relocates the resonance state out of the spectral range where interband transitions result in dissipation losses. This causes the performance of gold dimers to become comparable to those of silver [390]. However, quantum tunneling through the gap serves to diminish attainable local field enhancement values when inter-particle distances are reduced below 0.5 nm [480].

New qualitatively different plasmonic modes can emerge when near field coupling and hybridization occurs in larger ensembles of LSPs, as illustrated in Figure 3.6 for ordered array or disordered cluster arrangements in panels (c) and (d) respectively. While the underlying interactions based on mutual mode interference are, in principle, the same as those giving rise to energy states of a nanosphere dimer, the variations in arrangement symmetry can yield a wide range of different behaviors.

Periodic placement of LSP supporting metal structures, in addition to the aforementioned near field static dipolar coupling, enables coherent and constructive far field radiative dipolar interparticle interactions. For small particles long range LSP interactions can be estimated using the coupled dipole approximation [483], however, larger metal objects supporting multipolar plasmon modes give rise to additional out-of-plane effects which can be described only by more rigorous approaches [484, 485]. In the simplest dipolar case interference of light multiply scattered from nearby nanoparticles gives rise to delocalized collective lattice plasmon modes at wavelengths where the Bragg condition is satisfied [474, 486]. Conversely, a significant suppression of the radiative portion of LSP damping occurs when said interference is destructive, leading to particularly sharp resonant lineshapes spectrally situated where grating modes turn from evanescent to propagating.

Figure 3.8 (a) gives a case in point example of a 2D periodic gold nanodisk LSP array with diffractive coupling [481]. When the lattice period is selected so that the Bragg wavelength is redshifted with respect to the LSP two resonant modes appear. The first one, at shorter wavelengths, resembles a localized surface plasmon resonance of an isolated particle, is spectrally broad and spatially confined in the vicinity of the disk, hence, more prone to damping losses. On the other hand, the lower frequency lattice plasmon mode is delocalized and possesses a Fano-like narrow lineshape. Furthermore, it closely follows the $(0, \pm 1)$ Rayleigh anomaly, which is indicative of grazing wave propagation.

For SERS in particular this yields electromagnetic enhancement factors above those of isolated LSPs, since roughly up to one order of magnitude higher buildup of local electric field intensity can be achieved [487]. Although the narrow-band nature of lattice plasmons makes simultaneous enhancement of excitation and Stokes-shifted radiation difficult to achieve, they have been harnessed in IR and Raman spectroscopy as an effective antenna for enhancing either the former [488] or the latter [489].

Random or aperiodic placement of mutually coupled LSPs produces a situation in sharp contrast to the aforementioned long-range ordered case, and aims to leverage the principles underlying the broader field of disordered photonics [490–492]. In an irregular near field coupled system, akin to the random particle cluster sketched in Figure 3.6 (d), plasmonic hybridization interactions give rise to a multitude of stochastic eigenstates, each of which

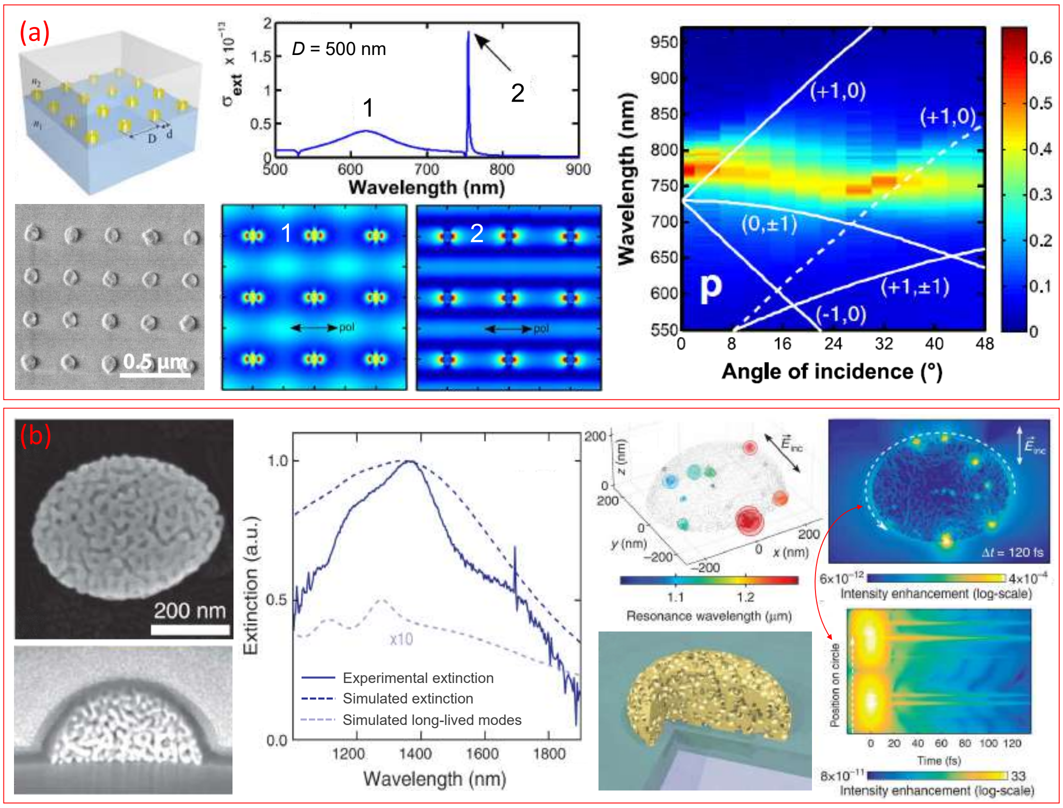

Figure 3.8: Coupled LSP ensemble structures reported in literature. (a) Gold nanodisk arrays patterned on a dielectric [481]. A sketch and a scanning electron image of structures, simulated extinction spectra of a $D = 500$ nm period array with field intensity profiles for (1) localized and (2) delocalized grating plasmon modes, and experimental dispersion for *p*-polarized light. White lines represent Rayleigh anomalies. (b) Gold nanosponge structure prepared by dealloying [482]. Top-down and cross-section scanning electron images, simulated and experimental extinction spectra, and FDTD visualization of wavelength, intensity and temporal decay of localized modes.

can exhibit highly variable resonant frequencies, intensities, luminosities, spatial positions and localization lengths [493]. Therefore, instead of putting effort into establishing and maintaining strictly defined states, the plasmonic excitation is allowed to select the best one from a wide range of semi-random spatially and spectrally distributed resonators.

A particularly intriguing property of aperiodic LSP structures is the inhomogeneous localization of plasmons, where even a slight change in excitation frequency or polarization can yield drastically different field distributions. These come as a result of the deterministically chaotic scattering and interference interactions between the individual resonators, giving rise to the plasmon equivalent of a laser speckle pattern, that is, however, unbeholden to conventional diffraction limits due to being a mater-coupled wave. In self-affine LSP configurations in particular the resulting modes can be anything between collective radiative oscillations spanning the entire structure, to extraordinarily intense hot-spots almost totally confined at the smallest nanoscale features [494–496], or, potentially, even Anderson localized dark modes that can only be excited from the near field [497, 498]. In the context of SERS of highest importance is the subset of modes with highest spatial localization, hence, highest local field enhancements, which also preferably are somewhat luminous or, at the very least, are coupled to radiant dipolar excitations [499]. Out of all aperiodic geometries self-affine and fractal-like textures and structures, due to their scale invariance symmetry, are uniquely effective at channeling electromagnetic radiation into ever smaller length scales [494].

A notable example illustrating the properties of disordered plasmonic systems is given by sponge-like nanoporous gold particles, shown in Figure 3.8 (b), prepared by solid-state dewetting and subsequent dealloying [481]. The broad extinction spectrum peak centered at around $\lambda = 1.3$ µm is due to dipolar Mie scattering of the bulk spheroid, whereas several additional asymmetric Fano-like resonances are usually observed superimposed onto it, however, their lineshape and spectral position can vary substantially between different nanosponges. FDTD simulations allow the assignment of these modes to strongly localized stochastic hot-spots supported by the random porous nanostructure. The spatial positions of confined excitations occur at different sites when different excitation wavelengths are used, and, furthermore, boast longer lifetimes, presumably due to partial suppression of radiative damping. Conceptually the gold nanosponge can be described as a random cluster of nanoscale resonators coupled to the overall diploar mode of the spheroid which is itself radiatively coupled to the far field.

Extraordinary field enhancements exhibited by inhomogeneously localized plasmon modes have been observed and made use of for SERS in a multitude of self-affine stochastic geometries, such as rough metal films [500–502] and colloidal nanoparticle clusters [386, 503, 504], which were counted among the first effective SERS substrates [505]. Important later findings elucidated the stochastic distribution of SERS hot-spots on a self-affine Ag film coated onto self-assembled dielectric nanosphere arrays, showing that their enhancement factor distributions scale according to a power law, where 63 out of 10^6 molecules, situated at $EF_{\mathrm{EM}} > 10^9$ sites, account for 24% of the total Raman scattering signal [506]. Furthermore, metal surface roughness is known to improve the performance of other more deterministically created nanotextured sensing surfaces [469, 507], since additional high intensity hot-spots are sure to arise at stochastic spatial and spectral regions which support highest localization eigenstates.

On the other hand, in disordered systems high intensity nanoscale localized hot-spots with substantial SERS enhancement will amount to only a small fraction of the entire surface and be at *a priori* unknown locations both spatially as well as spectrally, hence, lack the reproducibility crucial for many research applications. However, spatial SERS averaging over a sufficiently large substrate area can, in large part, ameliorate reproducibility issues whilst still making use of the broadband behavior of disordered sensing surfaces. Furthermore, such plasmonic substrates do not require complex imaging or excitation optics, and therefore are compatible with simple handheld Raman spectrometers. This, in addition to their relative ease of preparation, makes stochastic nanotextured metal surfaces an affordable platform to conduct routine SERS experiments in the field.

3.2 SERS substrates for analytical sensing

Due to its sensitivity, specificity and minimal invasiveness SERS is steadily making headway towards ever more wide ranging applications in fields of chemical detection [508], medical diagnostics [509], forensic science [510], cultural heritage preservation [511, 512], food safety [513] and defense [514]. However, processes giving rise to surface enhancement of Raman signal, such as analyte adsorption or electromagnetic energy localization in a hot-spot, are at least partially stochastic and only limited control is attainable due to their nanoscale nature. Lack of reproducibility has, therefore, been the main problem plaguing SERS and limiting its widespread adoption.

Among the most prevalent substrates for analytical SERS are silver and gold colloids [515], with most substantive enhancements exhibited at nanoparticle dimers and aggregates [516]. Rational design approaches, such as DNA-directed self assembly or DNA origami [517], led to new controlled ways of organizing particle aggregation into said dimers [478, 518] as well as more complex antenna arrangements [519] with well defined nanometer-sized gap widths, that can readily ensure single-molecule sensitivity. Erratic analyte-metal interaction or chemical alterations can also cause Raman signal fluctuations, which shell-isolated nanoparticle-enhanced Raman spectroscopy, abbreviated as SHINERS, was developed to prevent [520, 521]. It chooses to forgo chemical enhancement and fluorescence quenching of the metal in favor of increased reproducibility and robustness by isolating the plasmonic platform from direct contact with the probed materials *via* atomic layer deposition of approximately 1 nm thickness dielectric layers. However, despite advances in colloidal metal particle synthesis [522] their polidispersity and batch variability, in addition to the strong polarization dependence of plasmonic excitation on nanoparticle assemblies, still presents obstacles for attaining consistency in SERS performance [510].

Lithographically prepared plasmonic metal patterns, with well defined subwavelength-scale features as well as particular rotational and translational symmetries, present an alternative approach to attaining a consistent SERS response. For substantial electromagnetic Raman signal enhancement to occur $d < 10$ nm size gaps have to be established, which implies the necessity of using high resolution electron or ion beam lithography nanofabrication methods. Indeed, effective SERS substrates, such as multiscale coupled directional emission nanoantennas [523, 524], bowtie structures [525], fractal patterns [526], and nanoparticle [480, 527] or nanohole [528] arrays, have been demonstrated. Furthermore, significant fundamental findings, like the interrogation of distance dependencies in SERS enhancement [480], or determining the influence of pattern randomization [529] were enabled by these techniques. However, the serial and slow manner of charged particle beam patterning renders such methods prohibitively expensive and lacking in scalability necessary for any practical application apart from basic research.

Controllable nanotextured SERS substrates far more affordable for routine analytical sensing can be prepared using higher throughput parallel patterning techniques based on, for example, optical, nanoimprint or nanosphere lithography. While the aforementioned techniques lack the resolution requisite for direct nanoscale control, augmenting them with other approaches can give rise to high-intensity hot-spots. For instance, combining optical lithography with atomic layer deposition of conformal thin films and subsequent etching steps resulted in sub-10 nm size SERS active vertical gaps being formed [530]. Simple injection molded microtextured polymer substrates, sputtered with an overlaying rough Ag film, gave rise to reproducible Raman enhancement over large areas [531]. Also, self-assembled nanosphere lithography, due to its relative simplicity and flexibility, is among the more widely used SERS substrate fabrication techniques, and can be tailored to produce either strongly enhancing 3D metal film-over-nanosphere textures [532–534], or controlled planar periodic triangle patterns if nanosphere lift-off is performed [535].

In this work, conducted in collaboration with the research group headed by Dr. Sivashankar Krishnamoorthy at Luxembourg Institute of Science and Technology, close-packed periodic gold nanopillar array substrates for substantial and reproducible Raman enhancement are investigated [536]. Initial template texture with well defined feature positions and sizes is prepared using a scalable and cost effective self-assembly based copolymer soft-lithography method, and a plasmonic metal superstructure is sputtered subsequently. While fabrication and SERS performance characterization is described in some depth, here particular focus is given to FDTD simulation derived insights into influence of feature shape and metal film thickness effects on attainable electromagnetic enhancement.

3.2.1 Fabrication and characterization of gold nanopillar arrays

Discrete and ordered nanoparticle arrays are among the more reproducible SERS substrates, as they limit the randomness-driven inhomogeneous localization that often arises on continuous roughened or self-affine metal surfaces. An additional advantage of deterministic textures is their potential for pattern tunability and predictive rational design by way of controlled fabrication and numerical simulations, both of which are typically impossible for more stochastic SERS substrates. However, electromagnetic enhancements sufficient for analytical SERS applications can be attained when optical fields are confined in metal gap regions below 10 nm in size, which only a few cost-effective patterning techniques can provide.

Notable bottom-up methods of creating nanoparticle arrays for SERS include the aforementioned nanosphere lithography [535], which often faces issues when homogeneous close-packed structures with resolutions below 100 nm are sought. Anodized alumina template directed nanoparticle or nanowire growth can routinely produce sub-25 nm gaps [537], however, collapse and bundling during template removal can negatively affect uniformity. Lastly, block copolymer lithography [538, 539] represents a broad family of molecular self-assembly based patterning techniques, which, due to the wealth of adjustable parameters of the underlying chemistry, can yield a diverse range of nanoscale patterns over wafer-sized areas.

In this work sub-50 nm spatial resolution plasmonic nanopillar textures for SERS were prepared by means of a copolymer lithography variant, which harnesses the self-assembly of spherical reverse micelles into close-packed 2D dot array soft-mask patterns [536, 540]. This lithography method is inherently simple, produces uniform patterns with a high degree of local order, can be readily applied at a wafer-scale, and exhibits a fair amount of tunability over shape, size as well as spacing of constituent features. A schematic outline of the process used for creating gold nanopillar array SERS substrates is given in Figure 3.9.

Reverse micelles are formed by dissolving the amphiphilic copolymer polystyrene-*block*-poly(2-vinylpyridine), abbreviated as PS-*b*-P2VP (57000-*b*-57000 $\mathrm{g\,mol^{-1}}$), in a nonpolar *m*-xylene solvent to a concentration of 0.5% by weight. This gives rise to aggregation in which hydrophilic groups face away from the solvent, whereas hydrophobic ones extend towards it. Soft polymeric nanoparticles are formed as a result, and their size is limited to approximately 60 nm in diameter by energetically unfavorable electrostatic interactions between tightly-packed polar hydrophilic copolymer segments. Standard deviation of micelle diameter can be as low as 5.5%, as has been shown by dynamic light scattering measurements [540]. The solution was then spin-coated at 5000 rpm and at 45% relative ambient humidity onto a 4" Si wafer, which was thermally oxidized beforehand to have a 25 nm SiO_2 top layer. Micelles are thereby deposited as nanoscale hemispheres, arranged in a close-packed quasi-hexagonal pattern with an approximately 114 nm period. Changes in the concentration of PS-*b*-P2VP allows for the control over the periodicity of micelle arrangement, however, excessively dilute solutions result in patchy coverage, and high concentrations give rise to multilayers, therefore, tunability range is limited to a roughly 20 nm interval [540].

Lithographic mask transfer was performed over three sequential dry etching steps. First, the micelle layer was treated with O_2 plasma to remove the organic material between individual polymer nanoparticles. Next, the polymer pattern was transferred through the 25 nm thickness SiO_2 by means of a C_4F_8/CH_4 plasma reactive ion etching, thereby exchanging the fragile soft lithography layer for an inorganic hard-mask. Finally, silicon etching was conducted using a Cl_2 plasma, resulting in a quasi-periodic array of Si pillars, akin to those shown in the inset of Figure 3.9. The aforementioned 114 nm micelle periodicity was carried over onto the final texture, whereas individual pillars had an average height of 120 nm, apex widths $\sim$ 55 nm, and a positively tapered profile.

Plasmonic activity was subsequently imparted by magnetron sputtering the 3D Si pillar array template with gold layers of thicknesses ranging from 10 nm to 120 nm using an Explorer thin film deposition system (Denton Vacuum LLC). As can be observed in scanning electron microscopy images of gold covered Si nanopillars displayed in Figure 3.10, sputtering induces preferential metal deposition on top of the bumps, which brings about the formation of a gold pillar superstructure up to 280 nm in total height. Furthermore, sidewall coating also increases in thickness for higher deposited Au volumes, albeit at a significantly lower rate. This results in a gradual decrease of inter-pillar spacing, which would be expected to give rise to stronger electromagnetic field confinement in plasmonic gap modes.

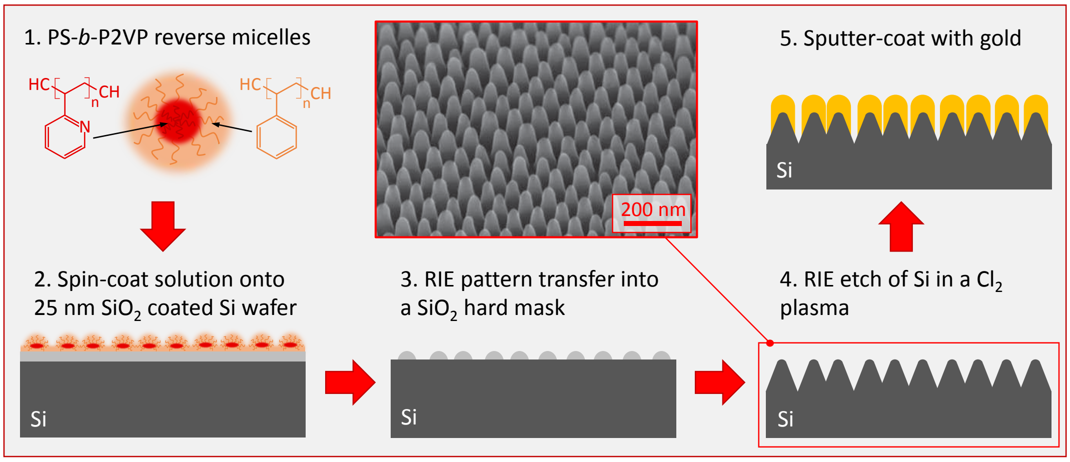

Figure 3.9: Sketch outlining the fabrication process of gold nanopillar arrays used in this work [536, 540]. Reverse micelles are prepared out of amphiphilic polystyrene-*block*-poly(2-vinylpyridine) co-polymer in a nonpolar solvent and spin-coated onto a thermally oxidized Si wafer. Micelle pattern is transferred down to the SiO_2 hard mask using reactive ion etching in a C_4F_8/CH_4 plasma. Subsequently, etching of Si pillars was performed in a Cl_2 plasma. A scanning electron image of the resulting nanotexture is provided in the inset. To impart plasmonic activity the surface was sputtered with gold. Substrate fabrication process was developed and performed at Luxembourg Institute of Science and Technology by the research group under supervision of Dr. Sivashankar Krishnamoorthy.

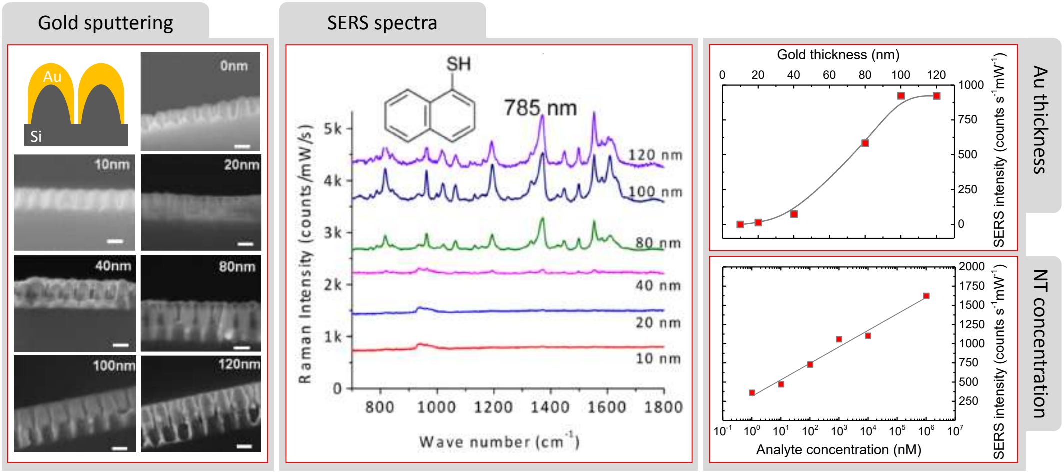

Figure 3.10: SERS performance of gold nanopillar array substrates [536]. Leftmost panel shows the side-view scanning electron microscopy images of nanopillars prepared by sputtering different amounts of gold. Raman spectra of 1-naphthalene thiol are given for substrates with different Au layer thicknesses. Top-right panel provides an intensity dependence of the 1372 cm^{-1} peak on Au thickness. Concentration dependence of the SERS signal is shown bottom-right. SERS performance characterization was performed at Luxembourg Institute of Science and Technology by the research group under supervision of Dr. Sivashankar Krishnamoorthy.

SERS performance of the plasmonic nanopillar array nanotextured surfaces, prepared with varying thicknesses of overlaying metal, was probed by using 1-naphthalene thiol as a non-resonant reporter molecule, which forms covalent bonds with gold. Prior to spectral measurements the substrates were exposed to the analyte in a *n*-hexane solution for 20 hours, after which they were rinsed in pure solvent and blow-dried using nitrogen. The spectra, shown in the middle panel of Figure 3.10, were acquired by means of a LabRAM Raman microscope (Horiba, Ltd.) equipped with a $\lambda = 785$ nm laser, a Peltier cooled CCD detector, and a $NA = 0.55$ objective. Acquisition was performed at 6.5 mW laser power over a 10 s accumulation time interval.

Evidently, Raman signal intensity becomes progressively higher with increasing amounts of deposited gold. The top-right panel of Figure 3.10 shows the dependence of 1372 cm^{-1} 1-naphthalene thiol ring stretching mode Raman peak intensity on volume of gold on a substrate. Signal starts to rapidly increase when Au thickness begins to exceed 40 nm, likely due to formation of increasingly narrow inter-pillar gaps, which facilitate the formation of localized hot-spots. On the other hand, SERS performance saturates for gold thicknesses above 100 nm, presumably since at such thicknesses gaps at the base of the pillar close, therefore, instead of an isolated pillar array, the structure becomes a pattern of crevices in a metal layer, with a morphology that does not markedly change with additional conformal deposition of metal. In all SERS measurements for a given substrate, standard deviations of spectral intensity between acquisitions at different locations was found not to exceed $SD = 10\%$.

The nanopilar array substrates with the largest volume of deposited gold, amounting to a 120 nm equivalent planar thickness, were chosen to investigate the Raman signal intensity dependence on analyte concentration. Samples were exposed to 1-naphthalene thiol concentrations ranging from 1 mM down to 1 nM using the aforementioned incubation procedure. The concentration dependence of the 1372 cm^{-1} Raman peak intensity is shown in the bottom-right panel of Figure 3.10. This logarithmic dependence yielded an estimated lowest detection limit value of 0.46 nM, or 74 parts-per-billion, which is below monolayer surface coverage. Here the lowest detection limit is defined as $3 \cdot SD/b$, where $SD = 10\%$ is the standard deviation mentioned previously, and b is the concentration dependence slope of Raman signal intensity.

The combined properties of nanoscale resolution and wafer-scale uniformity result in gold nanopillar arrays simultaneously providing strong SERS enhancement as well as good spatial uniformity. However, experimental Raman signal intensity measurement results follow a complex dependence on the thickness of deposited gold, which is explained in a rather speculative fashion. This aspect of light interaction with the plasmonic surface and the influence of metal coating topology on hot-spot formation can be further elucidated by means of finite-difference time-domain simulations.

3.2.2 Numerical investigation of field enhancement at nanopillars

One of the advantages provided by the high degree of order and controlability exhibited by self-assembled copolymer reverse micelle lithography is that rational design approaches based on predictive numerical simulations are relatively straightforward. Here, plasmonic nanoscale light confinement around the gold nanopillar array structures, instrumental to providing electromagnetic enhancement is SERS, was simulated using a commercially available Maxwell's equation solver "FDTD solutions" (Lumerical Solutions Inc).

3D renderings approximating the various gold sputtered Si nanopillar array textures were defined based on side-view scanning electron microscopy images shown in Figure 3.10. Corresponding cross-sections along the x-y plane, illustrating the models assumed for different amounts of deposited gold, are given in the top-row panel of Figure 3.11. The underlying Si texture is maintained the same for all model iterations, with a 114 nm period hexagonal lattice arrangement of 120 nm height rounded pillars. On the other hand, the gold thickness is gradually changed from 0 nm to 140 nm, so that metal buildup would occur preferentially towards feature tips. Conversely, sidewall coating thickness is increased more slowly, therefore, the 20 nm Si pillar spacing at base is fully covered by gold only when overlaying metal shell is 80 nm tall. Simulations were conducted using a uniform 1 nm step size mesh, spanning one period of the texture. Boundary conditions were periodic in both lateral directions, whereas perfectly matched layers were used to establish simulation region limits parallel to the surface. Excitation was simulated by way of a broadband visible-to-near-IR total-field scattered-field plane wave source, incident at a normal angle to the substrate. Calculations were performed for two orthogonal light polarizations, the results of which were subsequently averaged to give an unpolarized response.

Lower panels of Figure 3.11 show the logarithmic scale local field intensity distributions established around the metallized nanotexture for a $\lambda = 785$ nm incident wavelength, which corresponds to laser excitation used in the experimental Raman spectroscopy work outlined in Figure 3.10. Initial Si pillar template structures hardly exhibit any local field intensity enhancement, apart from some minor polarization related optical energy confinement at the semiconductor interface. Deposition of a gold shell substantially increases the observed electric field intensities due to optical energy confinement in surface plasmon polariton modes. While for thin metal shells this enhancement is fairly low, it continues to increase linearly up to a gold thickness of 60 nm, most likely due to the decreased influence of absorbance losses in silicon for bulkier coatings.

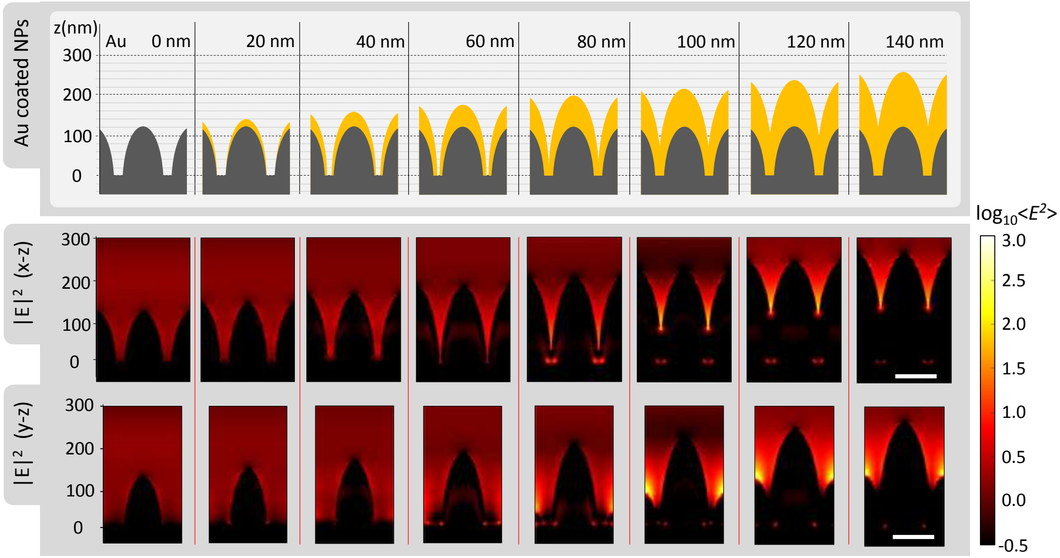

Figure 3.11: FDTD simulations of Si nanopillar arrays coated with different amounts of gold. The top row provides cross-section refractive index plots illustrating the different assumed metal deposition profiles. Logarithmic scale near field electric field intensity profiles for $\lambda = 785$ nm excitation in the x-z and x-z planes are shown in the two lower rows. Scale bar corresponds to 100 nm.

As the metal shells of neighboring structures start to encroach on each other, and the interpillar distance drops below 10 nm, gap modes start to dominate the field profile, as can be seen in the electric field intensity plots of Figure 3.11 when gold thickness is 80 nm and above. Further increase in metal thickness results in closing of the gap and hot-spot intensity saturates, since no other substantial changes in texture topology are produced by conformal coating. Strongest field localization is observed in the trenches that form at the mid-point between two neighboring pillars, particularly when incident light polarization is oriented perpendicular to such features. The anti-wedge site at the very bottom of the trench is host to a charge pileup that is associated with near-singular behavior [541], where local field intensity enhancements of up to $M_{\text{Loc}} = 400$ can be observed. However, while FDTD simulations are very informative for understanding the general behavior of a plasmonic system, this technique cannot be relied upon to give accurate estimates of enhancement factor values at several nanometer scale metal gaps. This is in part because maximum observable optical field intensity values tend to sale with fineness of the digitization mesh, but also, more importantly, due to disregard for non-local phenomena, which become relevant at such distances from a conductor surface and tend to limit attainable enhancements [542, 543].

Figure 3.12 (a) shows the complex spectral dependencies of the highest intensity gap modes for substrates with different gold shell thicknesses. It is evident how, when gold coatings of neighboring pillars start to overlap, the spectra transform from being reminiscent of a gap-separated dimer with blueshifted anti-bonding and redshifted bonding modes [474] and where charge neutrality must be maintained for each individual pillar, into a qualitatively different situation of touching particles that each can have a net charge, hence, the mode landscape changes drastically [541]. For example, once electric contact is established for gold thicknesses above 80 nm, a completely new lowest energy dipolar mode corresponding to

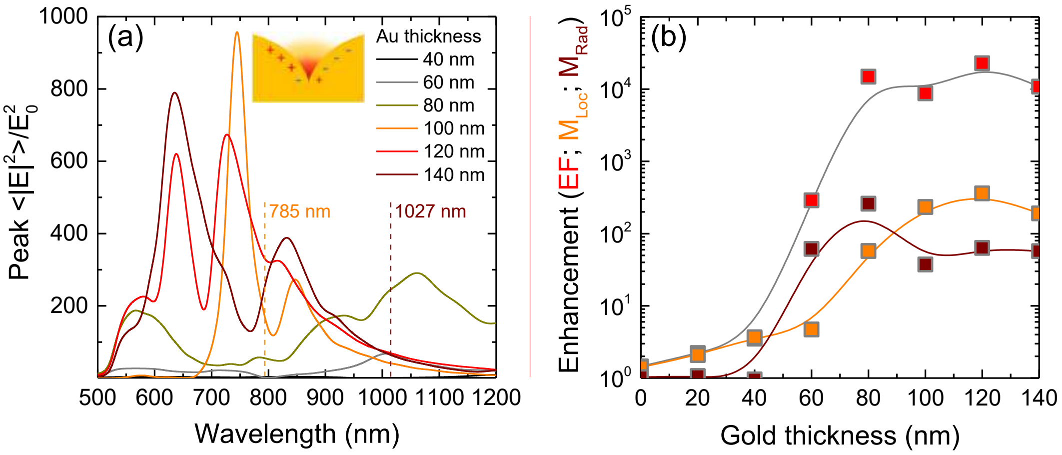

Figure 3.12: (a) FDTD simulated spectral dependencies of electric field intensity at most active hot-spot sites for different thickness gold coated nanopillar arrays. The two verticals at $\lambda = 785$ nm and $\lambda = 1027$ nm respectively correspond to the laser excitation and Stokes-shifted 3000 cm^{-1} C-H stretching mode Raman peak wavelengths. Inset shows the charge distribution of the relevant mode. (b) Simulated gold thickness dependence of local field enhancement M_{Loc} at excitation wavelength, radiative enhancement M_{Rad} at Stokes-shifted wavelength, and enhancement factor $EF = M_{\mathrm{Loc}} \cdot M_{\mathrm{Rad}}$.

the entire aggregate becomes allowed, however, it is shifted far towards the IR spectral range and out of the simulated wavelength region. Instead, a complex multitude of higher order modes, that the lowest energy excitations of the initial dimer transition into, begin to dominate the visible spectral region and tend to blueshift with increasing shell overlap. The multiple peaks observed in the 600 nm to 900 nm wavelength range all correspond to the plasmon excitation shown in the inset of Figure 3.12 (a), but are split due to hybridization as a result of the hexagonal lattice arrangement.

According to Equation 3.3, attainable field enhancement EF can be approximately estimated as the product of local field enhancements at laser excitation and Raman-shifted emission wavelengths. Figure 3.12 (b) depicts the gold layer thickness dependencies of both of these parameters, deduced from panel (a). Here the $\lambda = 785$ nm excitation laser wavelength and the C-H stretching Raman mode, Stokes-shifted by 3000 cm^{-1} to the $\lambda = 1027$ nm spectral position, were chosen as an illustrative example. It is evident, that the estimated enhancement factor EF closely follows the equivalent experimental SERS intensity data shown in the top-right panel of Figure 3.10, which gives credence to the numerically simulated model. Furthermore, FDTD simulations show that better SERS performance at $\lambda = 785$ nm excitation wavelengths could be obtained if texture period was to be increased, since this would likely result in a redshift of the relevant plasmonic modes.

Overall, this work demonstrates how gold nanopillar array SERS substrates, prepared by way of reverse micelle soft lithography on Si, provide strong and consistent Raman signal enhancement, well suited for routine analytic work. Their controlled topology enables the use of rational design and predictive numerical modeling. However, even self-assembly based lithographic fabrication procedures are inherently costly and require stringent process control. Therefore, next sections describe substantially more simple, affordable and, potentially, disposable SERS substrates for sensitive detection suitable for applications in the field.

3.3 Towards affordable SERS spectroscopy

Health care providers, law enforcement, and environmental protection agencies represent only a few of the numerous stakeholders driving analytical sensing methods, SERS being one of them, from the confines of a laboratory ever closer to being applicable in the field or for point-of-care testing. The wealth of information provided by vibrational spectra of molecular compounds gives Raman spectroscopy the specificity that only few single techniques can match, hence, there has been no shortage of effort in devising portable SERS systems [544] and a number of such devices are commercially available. For tasks such as pollution monitoring [545] or enforcement of narcotics restrictions [546] sensing in the field represents both a simplification and an increase in cost-effectiveness over having to rely on a central lab model. The immediacy of other concerns, such as detection of explosives [547], nerve gasses [548] or biological agents [549–551], however, makes on-site detection indispensable.

One of the more pressing issues hampering the broader adoption of SERS is the lack of effective and reproducible yet still affordable enhancing substrates. The complexity of instrumentation and processes involved in lithographic definition of exact nanoscale plasmonic structures makes them prohibitively expensive for routine use. However, much like strict control over the roughened silver electrode surface topology was not required for first observations of SERS [374], so was it not necessary for the examples of portable Raman sensing given in this section, where colloids as well as planar template substrates with metal either sputtered or chemically deposited on them were used. Indeed, in most cases a disordered photonics based approach [492] can yield a substantial number of active hot-spots by way of inhomogeneous localization [493, 495], discussed in Section 3.1.3. Furthermore, provided that a sufficiently large surface area is sampled and averaging is used, good reproducibility, suitable for early detection in the field, can be attained.

Planar SERS substrates are particularly convenient in portable applications due to their ease of handling. While the materials and techniques involved in the fabrication of such semi-random surfaces can differ greatly, there is, generally, some resemblance between the final metal topologies of the highest-performing examples. Most notably recurrent is the usually exaggerated nanoscale metal surface roughness, and its self-affinity with larger plasmonic wavelength scale surface features. Unsurprisingly, there is a large and rapidly increasing number of metal-coated nanotextured surface types suitable for SERS enhancement. Among them metal films over nanospheres [532, 552], mainly abbreviated as AgFON due to silver being most often used as the metal, are arguably the most popular. The self-affinity exhibited between the packed nanospheres and the nanoscale roughness of the deposited metal film ensures effective inhomogeneous coupling between incident light and stochastic high intensity hot-spots [494]. While originally AgFON fabrication was, in essence, lithographic, realizations by way of much simpler drop coating were shown to be similarly effective [553]. Furthermore, application of a metal nanoparticle superstructure resulted in an additional two order of magnitude increase in SERS enhancement [554], thereby demonstrating the important role stochastic roughness plays in plasmonic energy confinement.

However, similar textures can be readily prepared by much more direct maskless methods. For example, femtosecond laser patterning of semiconductor wafers gives rise to nanoscale ripple textures, which, when sputtered with plasmonic metals, provide substantial SERS enhancement [555] that was harnessed for sensing vapors of explosive materials [556] as well as for statistically quantified detection of biomarkers associated with early stages of Alzheimer's disease [557]. Parallel processing techniques, such as reactive ion etching in the spontaneous self-masking regime of operation, can likewise produce template structures for high performance SERS, as was shown for black silicon [86, 87, 548]. In this case, sputtering results in preferential metal deposition on the Si tips, thereby creating a rough pattern of overlapping plasmonic particles. Even less technologically demanding methods for simple SERS substrate preparation involve the use of oblique angle deposition to create a film of discontinuous metal islands [558], which can be applied even on tips of optical fibers [559].

Wafer-based methods for generating SERS templates subsume into themselves the cost of the underlying substrate, which, in cases where silicon [86] or sapphire [555] is used, can be substantial. Furthermore, physical methods of texturing, such as laser patterning or plasma etching in a vacuum chamber may have limited scalability, which is likewise negatively related to cost. On the other hand, chemical synthesis or etching-out of nanotextures is among the most affordable methods of generating a diverse range of self-assembled templates. Subsequent plasmonic metal deposition with thicknesses in excess of 100 nm serves to optically isolate the underlying template, rendering all of its properties apart from the initial subwavelength topology largely irrelevant to SERS. Provided appropriate nanoscale surface roughness for stochastic hot-spot localization is induced, such sensing surfaces can exhibit performances suitable for detecting sub-monolayer quantities of analyte molecules, which when creating deterministic structures would necessitate the use of elaborate lithography to match.

Notable examples of such self-assembled random templates include hydrothermally prepared leaf-like nanostructures of bohemite, generated by simply boiling a glass slide with a pre-deposited 20 nm thickness aluminum layer in water [560]. When coated with gold the substrate becomes SERS active and, despite its random nature, exhibits Raman signal variations below 11.5%. Furthermore, the nanotextured coating is optically transparent, hence, back-side Raman excitation can be readily applied. Converesly, physical vapor deposition of α,ω-diperfluorohexylquaterthiophene (DFH-4T) nanostructured high electron mobility π-conjugated organic semiconductor layers offers an alternative method of attaining highly active SERS substrates [456]. These templates innately provide up to a factor of 2×10^3 charge-transfer chemical enhancement, however, when a gold coating is applied electromagnetic enhancements up to 10^{10} in magnitude have been reported.

In this work, conducted in collaboration with the research group headed by Prof. Junko Morikawa at Tokyo Institute of Technology, highly enhancing copper(II) oxide semiconductor nanotextured template based SERS substrates, prepared by affordable and scalable wet chemical etching of Cu foils and their subsequent magnetron sputtering with gold, are investigated [561]. First, the facile fabrication and relevant physical properties of the random flake-like CuO template surface are described as a prelude to the subsequent SERS characterization of its metal coated plasmonic counterpart. Lastly, insights in quantifying the degree of randomness in SERS enhancement and the spatial distribution of hot-spot sites by means of Raman mapping are outlined.

3.3.1 Cupric oxide nanotextured surface templates

Copper(II) oxide, also called cupric oxide and abbreviated as CuO, is a p-type semiconductor with a multitude of fairly unique properties, in large part determined by its controllable nanoscale morphology [562]. For example, the high catalytic activity of CuO finds use in gas sensing [563] and electrochemical water splitting [564]. Furthermore, depending on the synthesis method, the band gap of cupric oxide can range anywhere from 1.2 eV to 2.1 eV, making CuO an attractive low-cost material for solar cells [565, 566] and photodetectors [567, 568]. Nanotextured cupric oxide surfaces due to their high surface areas are applicable as electrodes in lithium ion batteries [569, 570] as well as in supercapacitors [571, 572].

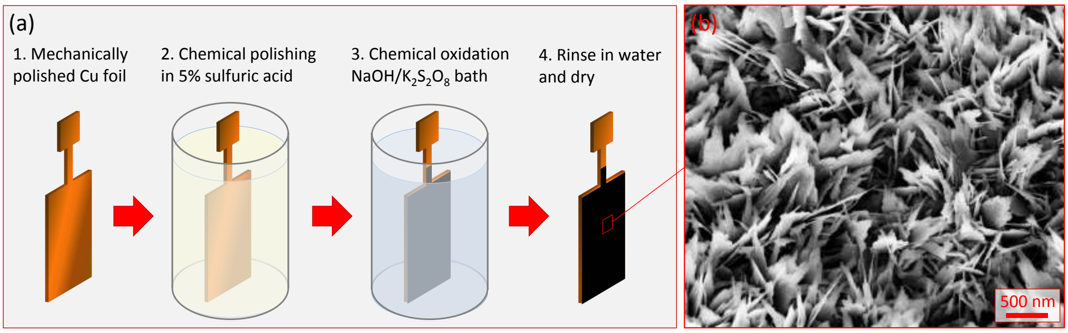

Figure 3.13: Fabrication process of a nanotextured CuO surface [573]. (a) Sketch illustrating the main steps in the procedure that uses mechanically polished copper foil as the substrate. The metal is chemically cleaned in 5% sulfuric acid and oxidized in an aqueous solution of NaOH (1.25 M) and $K_2S_2O_8$ (66 mM) at a 65 °C temperature for 5 minutes. Lastly, the foil is rinsed in water and dried. (b) Scanning electron microscopy image of the resultant CuO surface.

Here, however, CuO is used as a nanotextured template for creating random plasmonic surfaces for SERS enhancement, with highly affordable and scalable method of its fabrication being the most important merit. Figure 3.13 (a) outlines the main steps involved in preparing CuO coated substrates by way of simple chemical oxidation in an alkaline persulfate solution [573]. In this work 0.2 mm thickness copper foil was used as the starting material, however, this technique can be used on any smooth metallic Cu substrate and even electrochemically deposited copper films can be similarly processed. For best results vienna lime powder is used to mechanically polish and degrease the Cu surface before performing chemical polishing in a 5% by volume aqueous dilution of sulfuric acid for 5 minutes. After a brief rinse in deionized water, texturation of copper is performed by way of chemical oxidation in an aqueous solution of NaOH (1.25 M) and $K_2S_2O_8$ (66 mM) at a 65 °C temperature for 5 minutes. Processed Cu foil is then again rinsed in water and annealed at 250 °C in ambient atmosphere for 1 hour in order to dehydrate the oxide film and to promote its further crystallization.

A scanning electron microscopy image of the resultant CuO nanotextured surface coating is presented in Figure 3.13 (b). It is comprised of numerous flat, approximately 30 nm thickness and up to 1 µm lateral span flakes, which are arranged semi-randomly in a way that resembles a grass-like pattern. Evidently, the texture exhibits an extraordinarily expansive surface area, which was previously estimated based on its electrochemical activity to be anywhere between 200 and 300 times larger than an equivalent planar surface [574]. The wet chemical process allows for a certain degree of control over the final morphology of the surface, for example, an increased amount of $K_2S_2O_8$ oxidant results in a larger number of bulky dandelion-like CuO flake aggregates [575]. On the other hand, variations in the alkaline solution concentration and composition have been shown to give rise to radically different textures altogether [576].

Composition, purity and chemical bonding nature of the nanotextured metal oxide surfaces was verified by way of X-ray photoelectron spectroscopy (XPS) measurements conducted at the Australian Synchrotron. A wide-scan XPS plot of a nanotextured CuO surface, acquired using Al K_α radiation, is shown in Figure 3.14 (a). Observable spectral contributions are related to the presence of copper, oxygen and carbon. The Auger electron lines O_{KLL} and

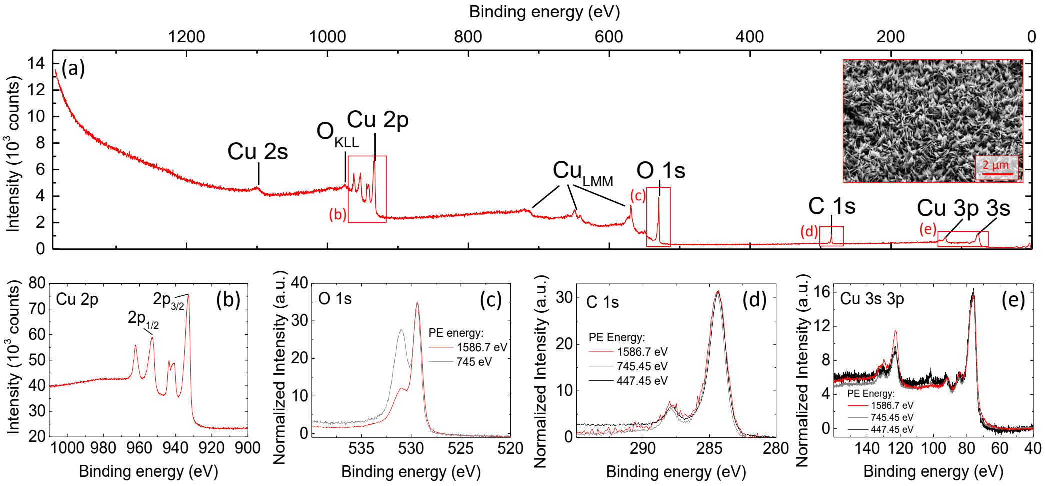

Figure 3.14: X-ray photoelectron spectra of CuO chemically nanotextured layers. (a) Wide-scan photoelectron binding energy spectrum of CuO. High resolution spectra of main spectral peaks, marked with red boxes, are plotted in panels (b) for Cu 2p, (c) for O 1s, (d) for C 1s, and (e) for Cu 3s as well as Cu 3p. Inset shows a scanning electron microscopy image of the CuO surface. X-ray photoelectron spectroscopy was performed by Dr. Bruce C. C. Cowie at the Soft X-ray beamline at the Australian Synchrotron.

Cu_{LMM} were identified by the lack of changes in their kinetic energy when incident photon energy was increased by 100 eV, which for conventional photoelectron peaks gives rise to a commensurate blueshift.

The high resolution XPS spectrum of the Cu 2p, shown in Figure 3.14 (b), exhibits four features, which include two main signatures, namely the Cu $2p_{1/2}$ attributed line with a binding energy of 953 eV and the Cu $2p_{3/2}$ peak at 933 eV, along with two additional shakeup satellites at 962 eV and 942 eV respectively. The fact that Cu $2p_{1/2}$ and Cu $2p_{3/2}$ lines are separated by a 20 eV gap, and that shakeup satellites are shifted by 9 eV from the main peaks is strongly indicative of high purity CuO [577]. Figure 3.14 (c) depicts XPS spectra around the location of the O 1s line, acquired using two different incident X-ray photon energies. Here, two features are visible — a sharp line at 529.3 eV typically assigned to metal-bound oxygen, and a broader less distinct band at 531.1 eV. The nature of the latter peak can be elucidated by lowering the photon energy of the synchrotron source, thereby limiting the kinetic energy available to photoelectrons, hence, decreasing the CuO sample depth from which they can be liberated. A lowering of X-ray energy down to 745 eV results in the 531.1 eV line increasing in relative intensity, therefore, it is most likely due to adventitious oxygen overlaying the nanotextured surface.

In addition, a weak signature related to C 1s, likely related to either adventitious carbon or residual polishing materials, was observed and is depicted in Figure 3.14 (d). Lastly, Figure 3.14 (e) shows a high resolution plot of the Cu 3s and Cu 3p peaks, which are in positions consistent with cupric oxide. Taken in totality the XPS results point toward the nanotextured surface being comprised of high purity CuO with no heterogeneity throughout the sampled depth except for a minor presence of adventitious carbon and oxygen. Furthermore, no signatures of cuprous oxide Cu_2O could be detected, which shows the high degree of consistency exhibited by the chemical oxidation process.

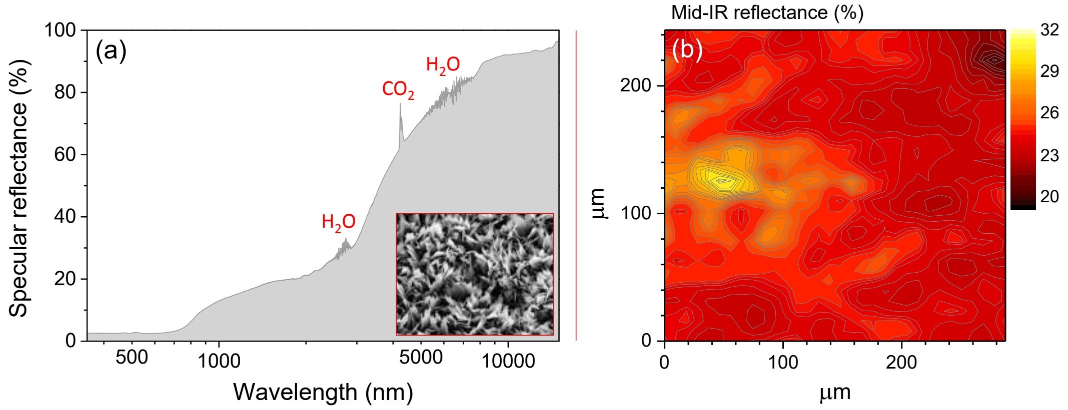

Figure 3.15: (a) Visible-to-mid-IR reflectance spectrum of a CuO nanotextured surface. Red text indicates the atmospheric absorption artifacts related to the presence of H_2O and CO_2. Inset depicts a scanning electron microscopy image of the CuO surface. (b) Mid-IR reflectance map of an extended CuO surface area, performed at a 6.25 µm spatial resolution [561]. Mid-IR portion of the reflectance experiments was performed at Tokyo Institute of Technology by the research group under supervision of Prof. Junko Morikawa.

Visually the chemically nanotextured copper based surfaces have a black color and exhibit a velour-like matte appearance. The broadband CuO specular reflectance spectrum, encompassing wavelengths ranging from visible to mid-IR, is provided in Figure 3.15 (a). Measurements up to $\lambda = 2.5$ µm wavelengths were conducted using a LAMBDA 1050 spectrophotometer (Perkin-Elmer Inc.) equipped with a 150 mm integrating sphere attachment, whereas longer wavelength spectra were acquired using a Spectrum Spotlight 300 Fourier transform IR imaging spectrometer (Perkin-Elmer Inc.). The flake-like surface coatings exhibit low reflectance throughout the visible spectral region, despite cupric oxide having a fairly high refractive index of $n = 2.63$. This is likely due to the effective refractive index gradient established by the progressive increase in CuO density towards the bottom of the textured layer. However, full hemispherical reflectance measurements show that roughly two thirds of the light impinging on CuO substrates is scattered diffusely, hence, in total approximately 8% of visible radiation fails to be absorbed in the semiconductor.

At near-IR wavelengths photons begin to fall short of the $E_g \approx 1.45$ eV indirect CuO band gap, which is in part effected by the nanoscale morphology of the layer [578]. As a result the reflectance begins to increase gradually at first, and much more rapidly throughout the mid-IR range, where radiation starts to permeate the nanotextured layer and interaction with, and therefore reflection from, the underlying Cu metal becomes possible. The H_2O and CO_2 related lines are due to absorbance in the ambient atmosphere and are not related to the samples under study.

Microscale surface uniformity was probed by performing 6.25 µm spatial resolution CuO reflectance mapping over an extended surface area at the onset of mid-IR, the results of which are plotted in Figure 3.15 (b). Appreciable variance in reflectance of $R = 26 \pm 6\%$ was observed and is most likely the result of a confluence of two factors, namely the roughness of the initial copper substrate surface, and the occasional presence of dandelion-like CuO flake aggregates. Greater uniformity can be attained by preparing CuO nanotextured coatings on copper layers electroplated onto planar substrates, instead of using the much less topologically stringent flexible metal foils.

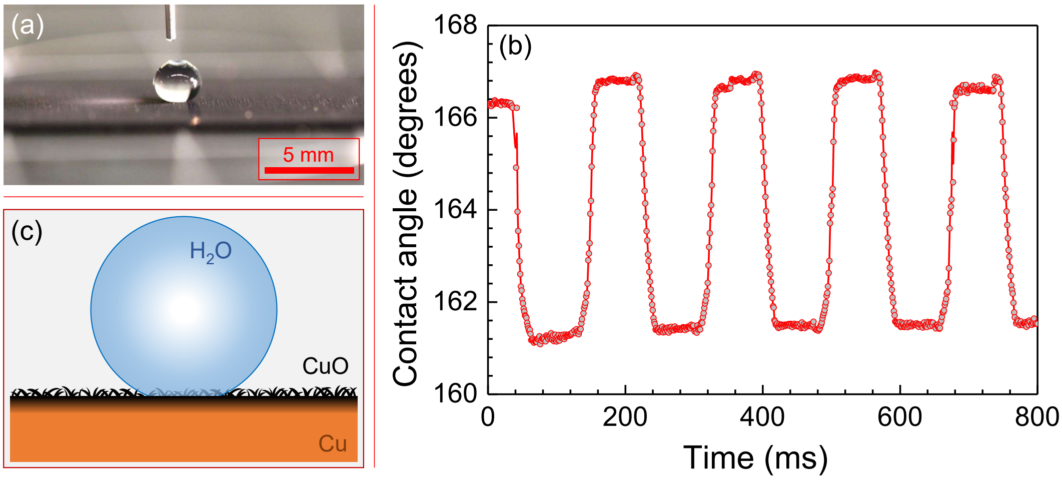

Figure 3.16: Hydrophobicity measurements conducted on CuO-on-Cu layers treated with 1h,1h,2h,2h-perfluorodecyltrichlorosilane (PFTS). (a) Close-up photograph of a water droplet on PFTS treated CuO. (b) Measurement results showing an average contact angle of 160° with 5° hysteresis. (c) Sketch illustrating pinning of a water droplet by flakes of the nanotextured CuO. Hydrophobization treatment and contact angle measurements were performed at RMIT university by Dr. Florian Lapierre.

An important property shared between many different nanotextured surfaces is that they tend to readily exhibit superhydrophobicity, meaning that water contact angle with the surface is in excess of 150°. Indeed, nanoscale or microscale roughness is one of the two prerequisites — in addition to low adhesion forces between the liquid and the substrate materials — necessary to produce fluid repellent and self-cleaning surfaces of broad utility to a diverse range of fields [579]. Even in chemical sensing *via* SERS, hydrophobic interactions can be used to localize analyte molecules from large drops of highly dilute solutions down to micron sized regions as the weakly surface-pinned liquid recedes during evaporation of the solvent [580].

In order to determine the wettability properties of nanotextured CuO layers, measurements of water contact angle, illustrative of the equilibrium state, and its hysteresis, which quantifies by how much the contact angle can be changed without the drop moving, were performed. The as-prepared cupric oxide coating does not exhibit any intrinsic hydrophobic properties, possessing a contact angle of only 3° with an extremely large hysteresis, likely due to strong water adhesion to CuO. However, surface tension at the water-substrate interface can be altered through chemical functionalization without markedly influencing the nanoscale morphology of the texture. Here this was done by exposing the CuO covered copper substrates to vapors of Teflon-like fluoropolymer 1h,1h,2h,2h-perfluorodecyltrichlorosilane (PFTS) in a desiccator in order to create a self-assembled monolayer of the innately hydrophobic material [581]. As can be seen in the photograph provided in Figure 3.16 (a), after the PFTS treatment nanotextured CuO layers became superhydrophobic with an average water contact angle of $160° \pm 2°$.

On the other hand, when the droplet was perturbed substantive contact angle hysteresis, amounting to $5° \pm 1°$, could be observed, as plotted in Figure 3.16 (b). This shows that the droplet is at least partially pinned on the sharp flake-like CuO surface features, meaning that the surface is not fully in the Cassie-Baxter state, where a fluid is suspended by surface tension on the tips of the texture [207], but approaches the Wenzel situation, where full interfacial contact between liquid and the substrate is maintained [582], as sketched in Figure 3.16 (c).

In general, hydrophobized CuO surfaces, onto which metalization is applied selectively to create microscale SERS active plasmonic regions, can offer enhanced sensitivity through the localization of a dilute analyte from an evaporating drop of solvent [580]. However, in essence nanotextured cupric oxide is merely a cost-effective stochastic template with useful self-affine morphological properties onto which SERS active noble metals are deposited. Only then CuO becomes a plasmonic sensing surface that enables substantial enhancement of the Raman signal.

3.3.2 Gold sputtered CuO as a SERS substrate

The as-prepared semiconducting CuO nanotextured coatings were converted into stochastic plasmonic surfaces *via* magnetron sputtering of overlaying gold shells using a AXXIS physical vapor deposition system (Kurt J. Lesker). The degree of metalization was varied by changing the sputtering duration so that Au layers ranging from 25 nm to 250 nm in thicknesses would be produced on an equivalent flat surface.

Figure 3.17 depicts the scanning electron microscopy images of CuO nanotextured substrates coated by varying amounts of gold. It is readily apparent that metal forms a conformal shell around the template features, thereby giving rise to a complex random metallic scaffold. Furthermore, as a result of the high surface area of the CuO texture, the actual thickness of the Au coating is substantially lower than what would be deposited on a flat film. For instance, deposition of a 150 nm gold overlayer increases the thickness of CuO flakes from an initial $d \approx 30$ nm to approximately $d \approx 65$ nm. When metal thicknesses are below 50 nm surface features remain smooth, but at higher Au volumes nanoscale roughness in the form of metal bumps starts to develop, and at 150 nm and above gold crystalites with noticeable facets become apparent. Here gold was chosen due to its chemical inertness and respectable plasmonic performance second only to silver, however, similar conformal coatings have been obtained for aluminum as well as palladium, showing the versatility of the template sputtering approach.

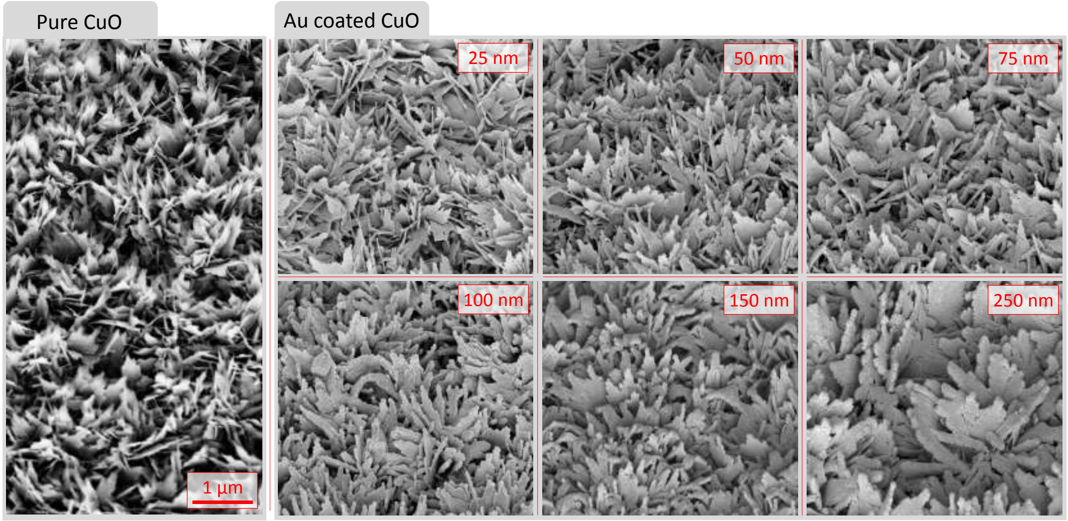

Figure 3.17: Scanning electron microscopy images of chemically nanotextured CuO on copper foil surfaces before and after conformal magnetron sputtering with gold, taken at a 45° tilt. Length values given in the different panels correspond to gold thicknesses that would be obtained if the surface was flat.

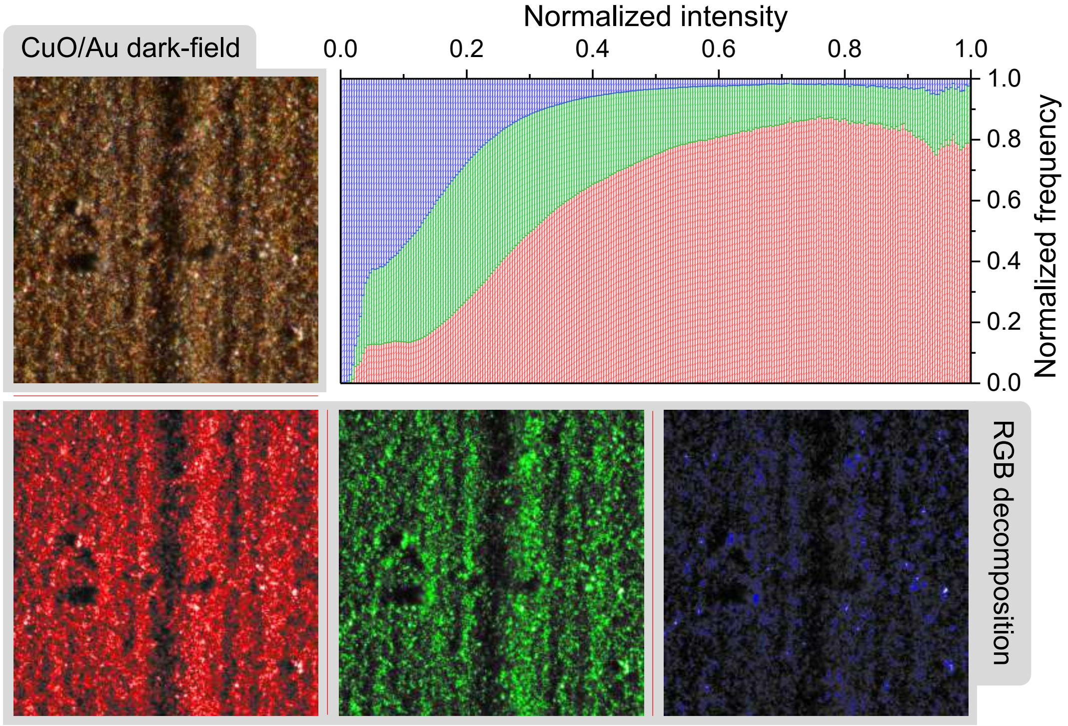

Figure 3.18: Dark-field optical microscopy imaging of nanotextured CuO surfaces coated with a 150 nm thickness gold layer. Scattered light speckle pattern at substrate surface is given in the top-left panel, with decomposited RGB color channel images of this micrograph given in panels at the bottom. Normalized color channel histograms comparing relative red, green and blue component intensities are given in the top-right plot.

Upon visual inspection the gold coated CuO template nanotextures appear in a matte brown color, becoming progressively more yellow as the metal thickness is increased. As an example, top-left panel of Figure 3.18 shows the dark-field micrograph image of cupric oxide coated by 150 nm of nominal gold thickness. Strong scattering behavior is readily apparent, with complex random speckle patterns spread somewhat uniformly over the entire surface area. Separated color channels of the image are depicted in the bottom row of Figure 3.18 and indicate that scattering is primarily dominant in the red part of the visible spectrum, followed in prevalence by green and blue contributions in that order. Quantification of white light scattering expressed through normalized intensity histograms show that the vast majority of pixels registering a high intensity are red, therefore, strongest plasmonic activity, hence biggest SERS enhancement, can be expected at wavelengths above $\lambda \sim 630$ nm.

More rigorous spectral information can be deduced from UV-to-near-IR hemispherical reflectance spectra of gold coated CuO substrates, provided in Figure 3.19 (a) where they are contrasted to that of unmetallized semiconductor surfaces. It is evident that at wavelengths $\lambda <$ 500 nm, exceeding the CuO band gap, substrates retain most of their anti-reflectance despite deposition of a substantial amount of Au. This is likely to result due to interband transition related absorbance in gold, further aided by light trapping in the complex nanotextured metal network. Au sputtered substrate reflectance starts to gradually increase towards the red portion of the visible spectrum, which can be attributed to stochastic plasmonic modes, in addition to not being strongly absorbed in gold, no longer being able to induce interband transitions

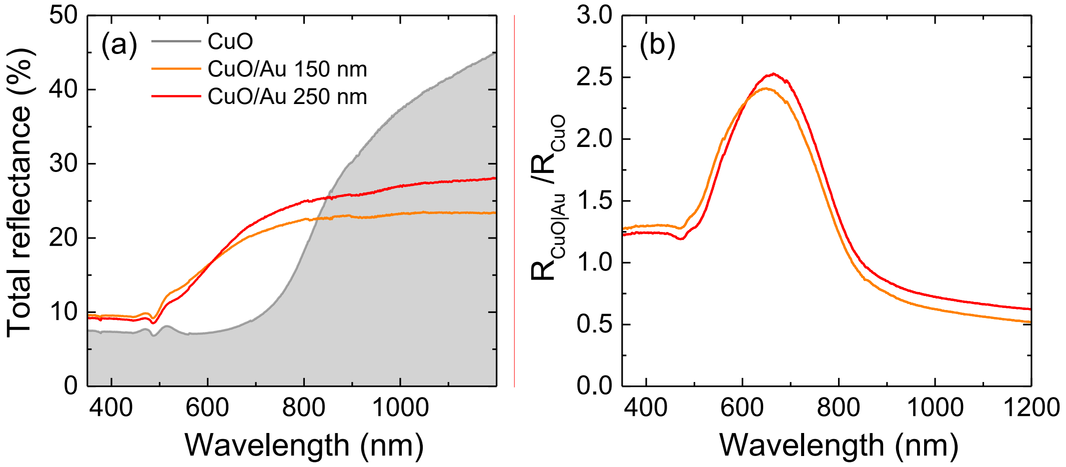

Figure 3.19: (a) Total hemispherical reflectance spectra of CuO nanotextured surfaces sputtered with 150 nm and 250 nm thickness Au layers, as well as of uncoated CuO for reference. (b) Gold coated CuO plasmonic surface reflectance spectra normalized to the reflectance of plain cupric oxide.

in the underlying CuO, hence overall experiencing less damping. Lastly, at near-IR, metal coated surface reflectance saturates at approximately $R \sim 25\%$, less than the $R_{\mathrm{CuO}} \approx 45\%$ for nanotextured cupric oxide, and far below the $R_{\mathrm{Au}} \approx 95\%$ expected for a flat gold film, pointing to efficient coupling into various plasmonic modes at least part of which are non-radiative.

Figure 3.19 (b) shows each of the total reflectance spectra of 150 nm and 250 nm gold sputtered cupric oxide surfaces normalized to that of pure nanotextured CuO. The most evident observation is that plasmonic activity tends to redshift with increasing amounts of sputtered Au, which can be explained by increases in the size of particles comprising the rough metal superstructure overlaying CuO flakes as a shell. Furthermore, more deposited metal results in higher observed reflectance, likely related to relatively higher radiative scattering contribution to extinction exhibited by larger nanoscale metal features. Therefore, dark-field imaging as well as optical spectroscopy findings indicate that random plasmonic sensing surfaces comprised of CuO with thick gold shells can be expected to provide best SERS performance, particularly at $\lambda > 600$ nm wavelengths.

Investigation of surface enhancement of Raman signal was conducted using an inVia Raman microscope (Renishaw plc.), equipped with 633 nm and 785 nm continuous wave excitation lasers. Initial characterization was performed using the $\lambda = 785$ nm laser with an incident power of $P = 690$ µW, focused by an 50× magnification $NA = 0.75$ objective down to a 20×2 µm^2 line to obtain spatial averaging over an extended area of the random substrate. Benzenethiol was chosen as the reporter analyte, as it is non-resonant at excitation wavelengths under consideration, and readily forms covalent bonds with gold surfaces thereby creating monolayer molecular films. Nanotextured CuO surfaces, prepared on thin sheets of copper and sputtered with different amounts of Au, were immersed in a 10 mM ethanol solution of benzenethiol for 30 min, after which the substrates were rinsed in pure ethanol to remove residual non-chemisorbed molecules and blow-dried using N_2 gas.

SERS spectra of benzenethiol acquired on CuO-based sensing surfaces, prepared by sputtering different amounts of gold, are depicted in Figure 3.20 (a). In general, cupric oxide produces a notable fluorescent background during Raman scattering measurements,

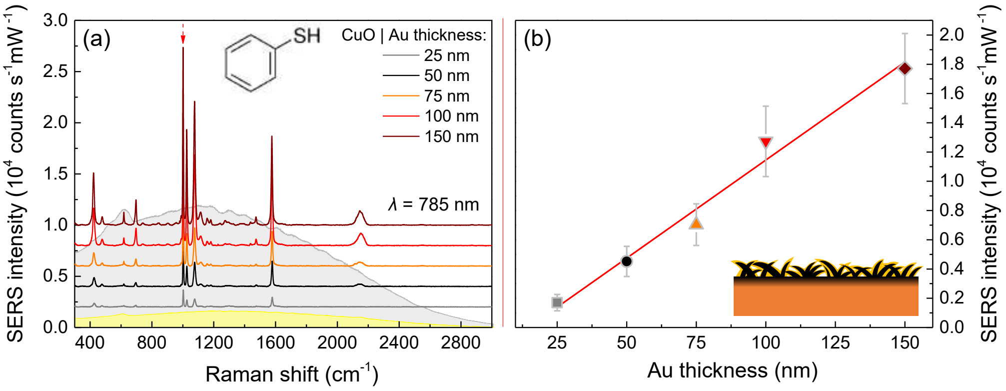

Figure 3.20: SERS performance of gold sputtered nanotextured cupric oxide. (a) Raman spectra of benzenethiol measured on CuO with various gold coating thicknesses. Excitation laser wavelength was $\lambda = 785$ nm, and spectra are offset for clarity. Curves in the background show the fluorescent background of CuO with Au coating in yellow, and without in gray. (b) Intensity dependence of the 1001 cm^{-1} benzenethiol peak, marked by the arrow in panel (a), on thickness of sputtered gold. Sketch in inset illustrates the conformal gold coating of CuO flakes.

here plotted by the gray curve, however, the quenching effect of metallization reduces it by approximately a factor of eight, as plotted in yellow. Beneznetiol spectra shown in all figures are displayed with their fluorescent backgrounds subtracted according to an automated adaptive-weight penalized least squares fitting method [583].

The most prominent gold-chemisorbed benzenethiol spectral peaks are the in-plane benzene ring-breathing mode at 1000 cm^{-1}, the in-plane C–H bend at 1026 cm^{-1}, and the coupled in-plane ring-breathing and C–S bond stretching modes at 1075 cm^{-1} [584]. Other strong signatures are the coupled C–S stretching and ring in-plane deformation modes at 422 cm^{-1}, benzene ring in-plane deformations at 618 cm^{-1} and 697 cm^{-1}, as well as the C–C symmetric stretching vibration at 1576 cm^{-1} [585]. The broad peak at approximately 2150 cm^{-1} is not assignable to any known vibration of metal-bound benzenethiol, and is likely due to residual contamination by adventitious carbon. Notably absent in the spectra is the usually very strong S–H stretching band expected at 2567 cm^{-1}, which is due to the dissociative adsorption of benzenethiol on gold [586], indicating that the analyte is bonded as a monolayer overlaying the substrate.

Figure 3.20 (b) follows the changes in SERS intensity of the most pronounced 1000 cm^{-1} in-plane benzene ring-breathing mode measured on CuO nanotextured surfaces sputtered with different nominal gold thicknesses. Evidently, the intensity enhancement of this peak, as that of all the other modes not shown in the plot, increases linearly with larger amounts of overlaying gold. Similar linear scaling has been observed on other metal sputtered random template-based substrates, such as black silicon [86] or laser-inscribed ripple surfaces [555, 556]. Substrate specific enhancement factor values were estimated, assuming single monolayer benzenethiol coverage [587] over the electrochemically estimated large accessible surface area [574], to range likewise linearly from $EF_{SS} = 7 \times 10^5$ for 25 nm nominal gold thickness, to $EF_{SS} = 7 \times 10^6$ when 150 nm of Au was deposited. Furthermore, despite their stochastic makeup, Au coated CuO nanotextures produce highly reproducible Raman signal enhancements with standard deviations $SD = 10\%$, on par with that of much more rigorous and costly plasmonic substrates, when line scan averaging is employed.

The SERS signal augmentation, observed as the thickness of Au shell overlaying the CuO texture is increased, follows a simple linear trend, however, the reasons underlying it can potentially be assigned to any of the numerous variances between the different plasmonic substrates. One important factor is the decrease in absorbance losses as metal thickness grows beyond the mean free path of an electron in gold. In addition, as can be observed in the up-close scanning electron microscopy images of CuO flakes coated with different amounts of gold shown in the top row of Figure 3.21, another important change is the escalation of metal roughness as a result of prolonged sputtering. When nominal gold deposition thicknesses start to exceed 100 nm, surfaces begin to appear as a tightly-packed array of overlapping nanoparticles, with many of them exhibiting distinct crystal-like facets.

Groves and crevices that separate the nanoscale metal surface roughness features can be host to high intensity anti-wedge type plasmonic modes [541], previously mentioned in Section 3.2.2 as underlying SERS enhancement of gold nanopillar arrays. FDTD simulations depicted in the bottom row of Figure 3.21 provide a qualitative illustration of how an increase in curvature radii of gold roughness features can result in augmented local field intensity enhancements under $\lambda = 785$ nm excitation. Furthermore, in much more realistic and complex self-affine metal surfaces, as those of gold coated CuO flakes, stochastic inhmogenious mode localization can give rise to chaotic collective plasmonic eigenstates, with SERS enhancements that at certain specific positions can far exceed the $EF \sim 10^6$ predicted by the simple visualizations of Figure 3.21.

In essence gold sputtered nanotextured cupric oxide template surfaces provide a complex metallic network, with at least three identifiable hierarchical factors contributing to their efficacy in coupling optical energy into plasmonic hot-spots. First of all, the random distribution of slanted flake-like features give rise to anti-reflectance of the metal surface through geometrical light trapping within the texture, which multiplies the probability for air-propagating modes to couple into plasmonic ones. Next, individual flakes can be host to radiative dipolar excitations, therefore acting like large antennas for concentrating light from an extended spatial region into plasmons, or for coupling it out into the far field for detection. Lastly, the nanoscale roughness enables extreme optical energy localization in various gap and anti-wedge hot-spot sites, where most of the SERS presumably occurs. In particular,

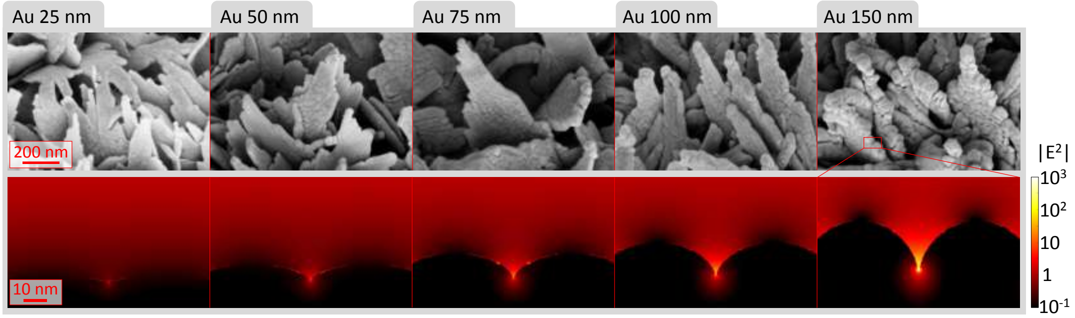

Figure 3.21: Changes in cupric oxide nanotextured surface roughness with increasing thickness of sputtered gold. Top row panels show close-up scanning electron microscopy images of Au coated CuO flakes, which illustrate how size of spontaneously formed particles scales with the volume of deposited metal. Bottom row panels depict qualitative FDTD simulations on how intensity of hot-spots changes with increasing curvature radii of surface-bound gold nanoparticles.

the interplay between the two last factors make gold sputtered CuO disordered plasmonic textures at least conceptually similar to the sponge-like nanoporous gold particles described in Figure 3.8 (b) of Section 3.1.3.

The nanoscale plasmonic confinement, which occurs at various random rough surface feature sites, appears to play a particularly critical role in enabling SERS on various stochastic metal textures. However, too often differences in metal surface roughness between substrates are overlooked, whereas excessive attention is paid to the morphology of the template itself. Therefore, further understanding of the mechanisms underlying random plasmonic sensing surface performance can be gained by altering the way metal coating proceeds through control over the surface chemistry of the template.

3.3.3 Effect of metal roughness on Raman signal enhancement

From the earliest days following the discovery of SERS, metal surface roughness was found to be an important component in its facilitation [588]. Early controversies were related to what type of roughness – whether atomic scale manifesting *via* chemical effects [589, 590] or plasmonic scale through electromagnetic interactions [591] – was required to attain Raman signal enhancement. Ultimately, 20 nm to 100 nm scale features were determined to be the dominant ones due to their enablement of plasmonic mode coupling [376] and inhomogeneous hot-spot localization [496]. However, reported observations of single-atom picocavities at low temperature SERS have rekindled interest in mesoscopic scale electromagnetic enhancement effects [592].

Changes in surface roughness of a sputtered or thermally evaporated metal film can be induced through control over process parameters, such as deposition rate [593] or the temperature of the substrate [594]. Homologous temperature T_h, defined as the ratio between the temperature of the substrate T and the melting temperature of the metal T_m, is an instructive empirical parameter for identifying the thermally activated processes dominant during deposition. For instance, at high T_h adatom mobility is high, hence, bulk diffusion is dominant, and coating is relatively insensitive to most other parameters as a result of ergodicity. At intermediate substrate temperatures surface diffusion becomes the limiting factor, and at even lower $T_\mathrm{h} \sim 0.3$, which is approximately the deposition regime used in this work that corresponds to room temperature, diffusion becomes suppressed to a sufficient degree that shadowing effects due to surface morphology and process chamber geometry become important. In the latter two regimes in particular, metal coating of dissimilar materials tends to produce films with divergent morphologies as a result of the disparate activation energies for adatom surface diffusion on substrates of different structural composition [595].

However, in this work metalization had to be performed on delicate nanoscale CuO template textures, which most substrate temperature control reliant methods of affecting Au layer growth behavior were expected to alter in unpredictable ways. In this work, therefore, surface chemistry modification was the method of choice for modifying gold deposition conditions, and thereby the resultant metal layer morphology. Here, for example, CuO template changes which result in a decrease of the surface mobility of adatoms would be equivalent to a commensurate decrease in the temperature of an unmodified substrate. To the aforementioned ends, nanotextured CuO surfaces were conformally coated with a 2 nm thick layer of Al_2O_3 by way of the plasma-assisted atomic layer deposition (ALD) technique [596]. The procedure was performed at a minimally elevated temperature of 120° with trimethylaluminum $Al(CH_3)_3$ and oxygen O_2 precursor plasmas using the Fiji F200 ALD system (Veeco Instruments Inc.) at the Melbourne Centre for Nanofabrication.

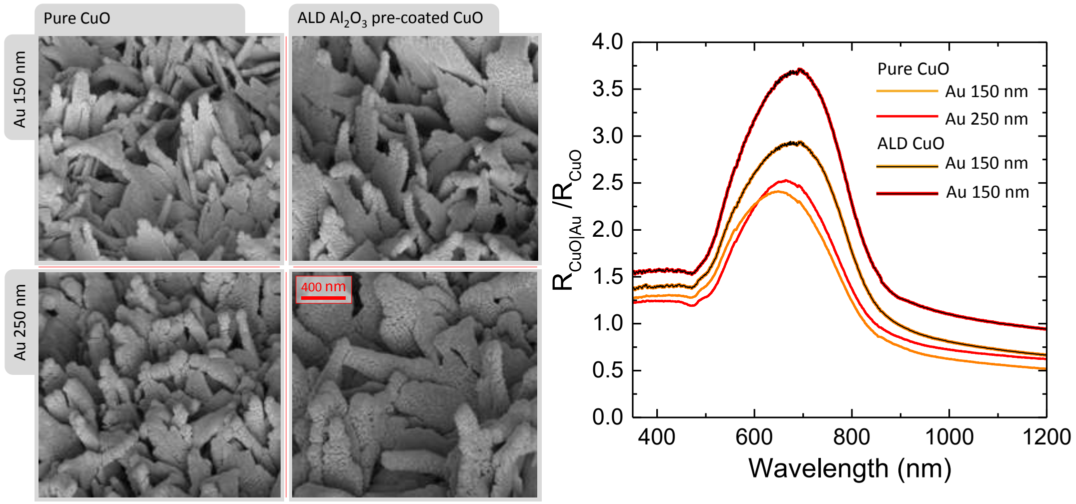

Figure 3.22: Morphological and optical differences between Au films deposited on pure and Al_2O_3 atomic layer deposition coated CuO flakes. Left panels provide scanning electron microscopy image comparisons between gold layers with 150 nm and 250 nm nominal thicknesses, whereas plots on the right show corresponding plasmonic surface reflectance spectra normalized to that of corresponding pure and Al_2O_3 pre-coated CuO.

Both ALD treated and unmodified CuO nanotextured templates were then concurrently magnetron sputtered with 150 nm and 250 nm nominal thickness gold layers by using a AXXIS physical vapor deposition system (Kurt J. Lesker). Scanning electron microscopy images of the resultant nano-rough Au coated cupric oxide flakes are given in the left part of Figure 3.22. The most evident disparity between metal films deposited on the two different surface chemistry textures is that Al_2O_3 coating gives rise to much more pronounced roughness, with a vast number of randomly arranged fine bump-like surface features. Pure CuO, on the other hand, gets coated with larger faceted gold nanocrystallites packed in a more planar fashion. Such differences are likely due to small metal nanoparticles being readily stabilized on numerous defects in the 2 nm $Al(CH_3)_3$ layer, induced by frustration due to lattice mismatch with the underlying CuO. Such behavior was observed for 2.2 nm diameter catalytic Au nanoparticles on nanotextured alumina, which resisted aggregation even after annealing at a 900 °C temperature [597].

Morphological variations in nanoscale metal roughness have a noticeable effect on Au coated CuO substrate visual appearance. For instance, gold coated CuO substrates with Al_2O_3 ALD films appear in a much brighter yellow color than samples prepared without a dielectric spacer. The right panel of Figure 3.22 compares the total hemispherical reflectance spectra of 150 nm and 250 nm gold sputtered cupric oxide textures with different surface chemistries, normalized to that of unmetallized samples. The rougher textures with alumina underlayers exhibit consistently higher scattering than equivalent metal thickness coated pure CuO throughout the visible and near-IR spectral ranges. It can be expected that the larger number of dipolar mode supporting nanoparticles would result in a more substantive fraction of radiative plasmon dissipation.

Changes in plasmonic behavior are related to differences in Raman signal enhancement, as can be seen from benzenethiol SERS spectra acquired on gold coated cupric oxide nanotextured surfaces with and without an Al_2O_3 spacer, respectively shown in panels (a) and (b) of

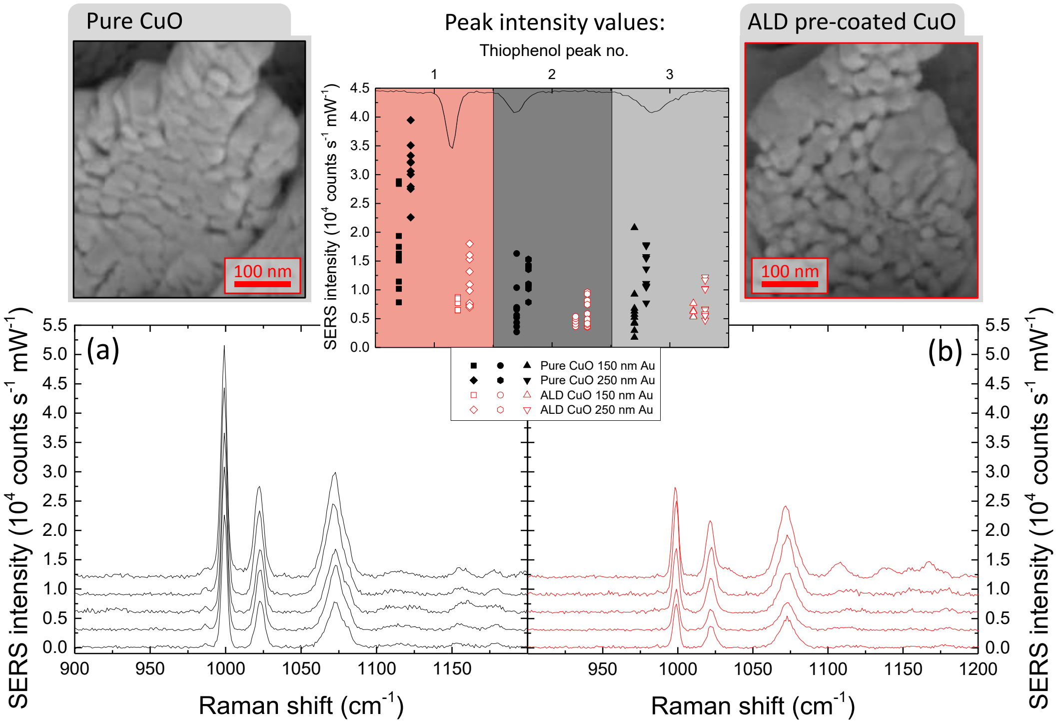

Figure 3.23: SERS spectra of benzenethiol, acquired on (a) pure CuO and (b) Al_2O_3 pre-coated CuO nanotextured films, overlaid with 150 nm and 250 nm Au thicknesses. Representative scanning electron microscopy images are shown as corresponding insets. Top-middle panel summarizes the benzenethiol main peak intensity values obtained by measuring at different locations of the various substrates.

Figure 3.23. Furthermore, a sampling of the three main analyte peak intensities at different positions of the various substrates is provided in the central panel. Based on these results it is clear that stronger plasmonic scattering activity does not necessitate superior SERS performance, as the rougher alumina overlaying gold nanotexture consistently produces roughly 60% weaker signals, especially when 250 nm nominal gold thicknesses are considered. Indeed, the coarse crystalline texture overlaying pure CuO flakes likely more preferentially localizes high intensity hot-spot modes in the narrower inter-grain crevices, rather than dissipating optical energy radiatively into free space. Here, $\lambda = 633$ nm wavelength single diffraction limited spot excitation was used, therefore peak intensity variance for different acquisitions is appreciably larger than in the spatially averaged case previously displayed in Figure 3.20 (b).

Another intriguing observation is that on gold coated pure CuO the in-plane benzene ring-breathing modes at 1000 cm^{-1} have a higher intensity in relation to the other two vibration peaks — namely the in-plane C–H bend at 1026 cm^{-1}, and the coupled in-plane ring-breathing/C–S bond stretching modes at 1075 cm^{-1} — however, on alumina pre-coated substrates this peculiarity is absent. Typically, such changes in spectra of chemisorbed benzenethiol are related to differences in average orientation of the benzene ring with respect to the metal surface [598]. Accordingly, the relative intensities of the three main analyte peaks observed on pure CuO metallized templates are consistent with benzene rings being tilted slightly more towards the gold surface, hence the preferential electromagnetic enhancement of their in-plane modes. On the other hand, benzenethiol Raman spectra on rough substrates

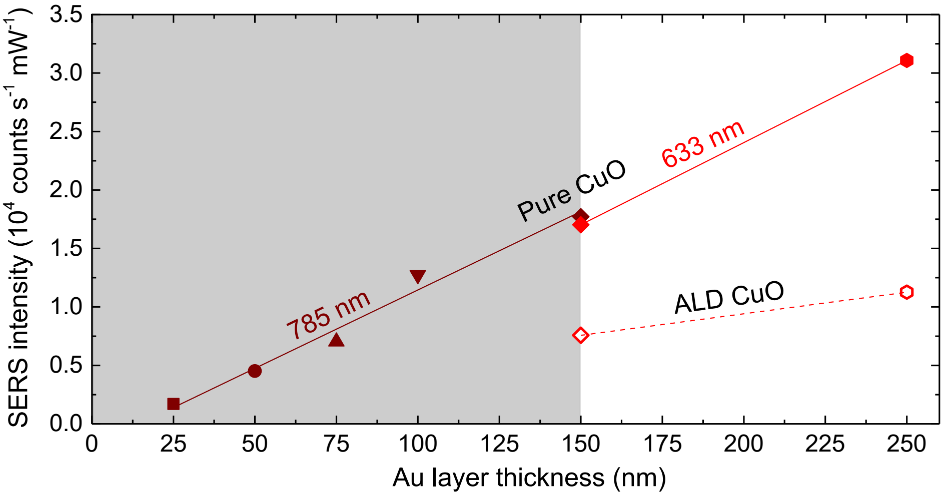

Figure 3.24: SERS intensity dependencies of the 1001 cm^{-1} benzenethiol peak, summarizing measurements conducted on substrates with different gold layer morphologies and thicknesses, acquired using $\lambda = 633$ nm as well as $\lambda = 785$ nm wavelength excitation lasers.

with alumina spacers are consistent with more vertical molecular alignment of the analyte monolayer. Therefore, differences in metal morphology, and specifically the degree of crystallinity on substrates without surface chemistry modifying spacer layers can be expected to modify the spectral signature of benzenethiol [599].

The gold shell thickness dependent 1000 cm^{-1} benzenethiol peak SERS intensity results on substrates prepared by magnetron over-sputtering of CuO nanotextured templates are summarized in Figure 3.24. Upon normalization of incident optical excitation energy flux a remarkable continuity between measurement results obtained using 785 nm and 633 nm wavelength excitation lasers was obtained, which is indicative of the inherently broadband nature of this type of disordered plasmonic surface. Furthermore, linear intensity scaling persists even for highest 250 nm Au thicknesses without an appreciable onset of saturation. Lastly, SERS enhancement is highest when overlaying metal roughness is managed so that the constituent particle size is large enough not to induce detrimental dissipation *via* absorbance, and so that the arrangement of said particles favors creation of localized plasmonic hot-spots over radiative far field scattering.

Overall, gold coated nanotextured CuO template surfaces are high-performing and cost effective SERS substrates with a self-affine morphology for effective optical energy localization and a favorable surface composition for Au nanoparticle generation. However, their inherent randomness can give rise to substantial signal variance, which, unless spatially averaged Raman signal acquisition is employed, is detrimental to analytic reproducibility. Therefore, uncovering the reasons behind SERS variance on CuO based substrates is a prerequisite for further optimization of their features.

3.3.4 Spatial probing of stochastic SERS performance

Variance in the attainable Raman signal has been a longstanding issue hampering the broad acceptance of SERS as an analytic technique for routine quantitative sensing. Reasons behind such stochastic output are related to the complex chain of events required for surface enhancement to proceed. In the simplest case, incident light has to be coupled and confined in a nanoscale localized hot-spot site, which, by definition, will result in a spatially inhomogeneous optical energy distribution. Then, a molecule has to find its way within a few nanometers of said region, where its probability of excitation is highly dependent on position, orientation as well as its mode of adsorption. Lastly, the Stokes-shifted radiation has to posses a coupling channel out of the molecular near field into the numerical aperture of the collection optics. In light of this it is unsurprising that Raman enhancement factors tend to follow a long-tail probability distribution [600], where a basis point fraction of highest intensity hot-spots can dominate the overall SERS signal, whereas 61% of analytes towards the bottom of the intensity curve can cumulatively be responsible for only 4% of it [506].

Substantial effort has been put into limiting possible sources of SERS signal variance through rigorous lithographic definition of plasmonic patterns, geared towards constraining the randomness of the enhancing substrate performance [601]. However, despite all these efforts, mechanisms such as plasmons inhomogeneously localized due to metal surface roughness, subtle photo-thermally induced changes in structure topology, or stochastic analyte diffusion give rise to a 10% standard deviation of the SERS signal [601]. Furthermore, such deterministic setups by laboriously and at great cost striving for consistency tend to seek the exclusion of all extremities in Raman enhancement, stochastic high intensity hot-spots being among the unwanted effects.

The self-affine gold coated CuO nanotextured template-based substrates considered in this work, however, provide a completely contrary approach towards robust SERS performance. Here, the fine nanotextured topology results in near-effortless creation of a huge density of potential hot-spot sites. Consistency, then, can be achieved through area averaging, as was demonstrated in Figure 3.20 (b) of Section 3.3.2, where by simultaneous sampling of a $20 \times 2\ \mu\text{m}^2$ line a 10% standard deviation in the signal was likewise achieved. Such SERS substrates, in addition to low fabrication costs and not being reliant on precise microscopic positioning to a specific measurement site, are set up to benefit from rare stochastic high intensity hot-spot sites and the general asymmetry of the long-tail enhancement factor distribution [506]. Still, it is not readily evident what amount of randomness can be practically averaged out, or which among the vast number of stochastic surface morphologies are best suited for both strong and consistent enhancement.

The first step in in understanding the Raman enhancement behavior of gold coated CuO substrates involved visualizing the surface distribution of hot-spot sites by means of Raman mapping. An inVia Raman microscope (Renishaw plc.) equipped with a high speed encoded stage capable of down to 100 nm step size movement was again used for performing spectral measurements. Excitation was conducted using continuous wave 633 nm laser excitation, which is the lowest wavelength where gold still has sufficiently low plasmon damping, focused close to the diffraction limit in air through a $NA = 0.85$ objective. Nanotextured 250 nm nominal gold thickness coated CuO, chosen as the test substrate due to its high enhancement, prior to measurements was functionalized *via* immersion in a 10 mM ethanolic benzenethiol solution. Mapping was done by way of raster-scanning the substrate during sequential spot-by-spot acquisitions with a 0.2 s dwell duration. The spectra of each individual pixel were then subjected to fluorescence background subtraction, and Lorenzian peak fitting in accordance with typical benzenethiol signatures was performed.

Figure 3.25 outlines the results of initial SERS mapping tests, all done on the same $20 \times 20\ \mu\text{m}^2$ substrate area segment, however, measured using different stage step sizes Δx. The scanning electron microscopy image on the top-left illustrates the general scale of the Au/CuO texture in relation to the mapping region. A representative benzenethiol Raman spectrum from a strongly enhancing pixel is given in the top-right plot, and all of the SERS

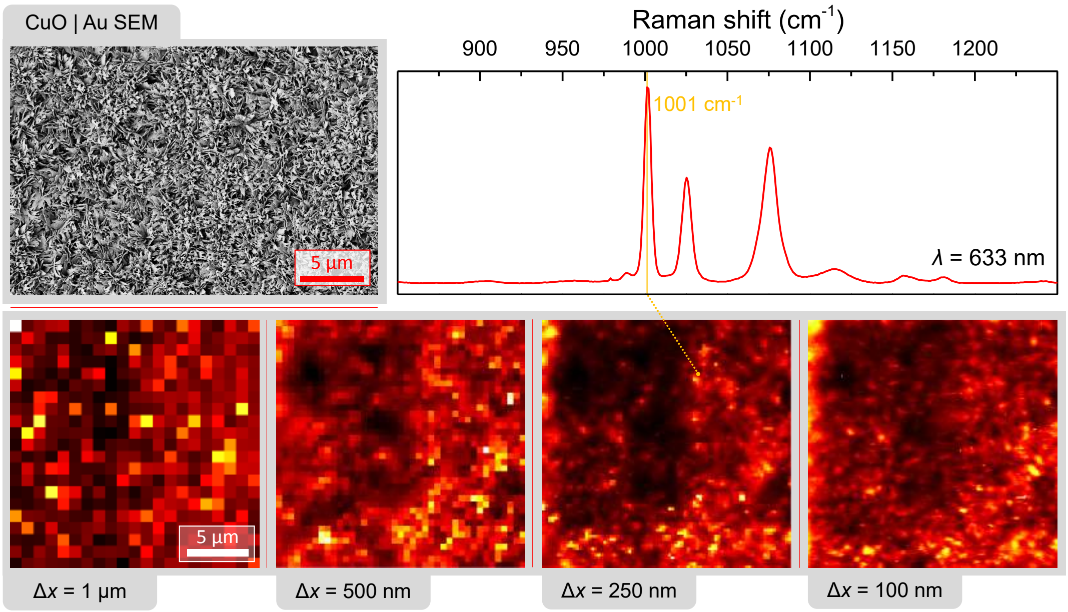

Figure 3.25: SERS mapping experiments on a Au coated CuO nanotextured surface. Top-left panel shows a scanning electron microscopy image of a representative surface segment of CuO coated with a 250 nm nominal thickness of gold. A representative single-shot acquisition spectrum of benzenethiol is given top-right. SERS maps of the 1001 cm^{-1} peak intensity, acquired using different microscope stage step sizes, are given in the four bottom panels.

maps were obtained using the fitted intensity of the most prominent 1001 cm^{-1} in-plane ring-breathing vibrational mode. The leftmost spectral map was conducted using a fairly large $\Delta x = 1$ µm step, which means that laser spots have almost no overlap. This type of mapping is suitable for performing statistical analysis of enhancement due to the individual measurements being independent, however, it hardly provides sufficient resolution to relate SERS with nanotexture topology. Finer $\Delta x = 500$ nm steps start to exhibit some overlap, but the resultant mapping plot yields substantially more spatial detail. Lastly, the SERS imaging spatial resolution saturates at $\Delta x = 250$ nm, whereas the highly over-sampled $\Delta x = 100$ nm case does not uncover much additional detail but increases image quality by boosting the attainable signal to noise ratio.

It is important to note that progressive laser exposures of the mapping area result in a diminishing SERS signal intensity, most likely due to photoinduced decomposition of the analyte. These very same processes occur during over-sampled mapping acquisitions, leading to a decrease in the average spectral output. Photodecomposition during spectroscopic mapping can be recognized when the first line of pixels exhibits a much larger intensity than all the subsequent ones. So, while in this work over-sampled images are used to visualize the hot-spot distribution, care must be taken not to rely on such data to make quantitative substrate performance estimates, as highest intensity enhancement sites are eliminated from the sample through photobeaching. On the other hand, this information can subsequently be recovered by simultaneously monitoring Raman bands related to resultant photoproducts [506].

The mostly stochastic nature of SERS enhancement is readily visible in the highest resolution Raman mapping images of Figure 3.25. This behavior is likely a result of chaotic inhomogeneous localization of plasmon modes, and is also observed in SERS maps of random silver island films [602] as well as more deterministic nanosphere lithography-based substrates [603]. Furthermore, the spatial variance of SERS possesses lengthscales close to the spacings between individual CuO flakes. Also of note is that, despite evident photobleaching and signal decrease, the overall distribution of hot spot sites is preserved over sequential mapping exposures. In light of this, experiments for attaining direct comparisons between the morphology of nanotextured plasmonic surfaces and SERS output were conducted.

Figure 3.26 outlines the approach used for accurately defining a substrate region for subsequent scanning electron as well as Raman microscopy imaging. A set of 100×100 µm^2 size marking frames were created at arbitrary locations on the gold coated surfaces *via* laser ablation using a PHAROS femtosecond laser (Light Conversion, Ltd.). Submicron positional accuracy was ensured by the high precision air-bearing x-y positioning stage (Aerotech Inc.). While only the central 20×20 µm^2 area was of experimental interest, the marking frame was kept much larger to prevent ablation debris from reaching and contaminating the central region. The markers were then used for alignment using scanning electron microscope and Raman microscope stages, and the respective images of a representative segment of an Au coated CuO substrate are shown in middle and rightmost panels of Figure 3.26.

Two somewhat disparate substrate surface segments can be identified by comparing the secondary electron and Raman scanning images, where their approximate boundary is indicated by a yellow-dashed curve. It is evident that the right side of the surface region exhibits a finer texture, which gives rise to abundant hot-spot sites. The left side, on the other hand, is comprised of larger Au coated CuO flakes and appears far less efficient. However, in addition to differences in plasmonic behavior, such spatial SERS disparities can arise due to height variations of the substrate, supported on a coarse Cu foil, which would result in the texture moving out of the high-*NA* lens shallow depth of focus. Hence, these results point towards finer textures exhibiting more consistent enhancements, but not definitively, as larger focal spots used in more realistic sensing setups might not be susceptible to such issues. Therefore, while it might not be necessary for adequate SERS substrate performance, high resolution Raman mapping investigations would benefit from minimization of surface

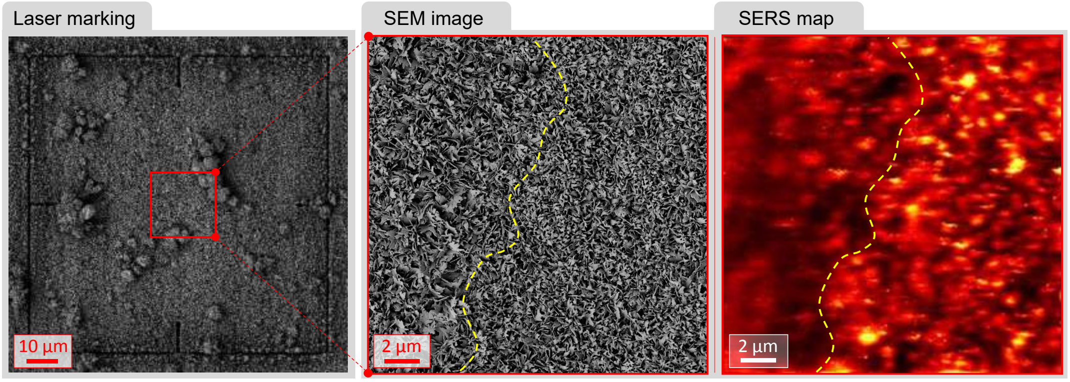

Figure 3.26: Illustration of the marking scheme used to investigate the relationship between nanotextured plasmonic surface morphology and SERS signal intensity. Leftmost panel shows the 100×100 µm^2 marking frame created by means of laser ablation. These markers were used for alignment to acquire the scanning electron image displayed in the middle panel, and the coincident 1001 cm^{-1} benzenethiol peak SERS intensity mapping plot on the right. Yellow curve separates two surface regions with different morphology.

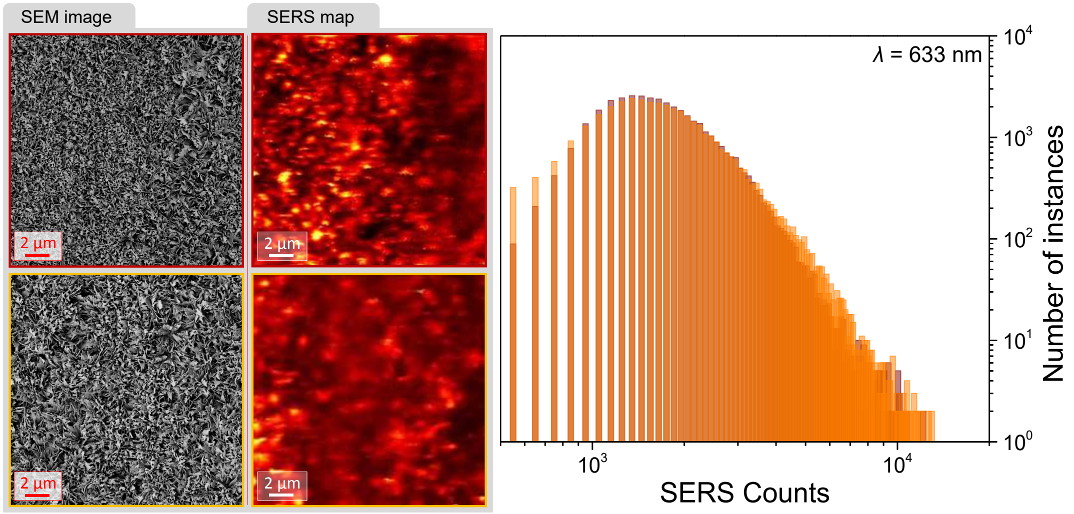

Figure 3.27: Comparison of stochastic distribution of SERS active hot-spots on different areas of CuO template-based nanotextured surfaces coated with 250 nm of Au. Left panels show scanning electron microscopy images and their corresponding benzenethiol 1001 cm^{-1} in-plane ring-breathing Raman peak intensity mapping plots. Plot on the right depicts the overlapping histograms corresponding to each of the spectroscopic maps.

unevenness, for example, by creating the nanotextured surfaces from Cu films electroplated onto planar wafers.

Despite the variances observed within the hot-spot distribution of a single 20×20 μm^2 substrate region, distinct 250 nm nominal thickness gold coated CuO surface segments can exhibit similar performance when taken as a whole. This is illustrated in Figure 3.27, where scanning electron microscopy and Raman mapping images are provided for two completely different SERS substrate areas. While the bottom row of images represent a noticeably coarser nanotexture and its SERS enhancement appears to be less consistent, Raman signal intensity histograms, plotted on the right side of Figure 3.27, show remarkable overlap, with deviations mainly becoming pronounced in the long-tail region of the distribution. This is a strong indication that spatial averaging can mitigate many of the irreproducibility issues related to stochastic SERS substrates, provided the hot-spot density is sufficiently high. Still more conclusive results could be obtained by performing similar mapping with a larger step size to avoid laser spot overlap and excessive photobleaching.

In summary, this work shows how noble metal coated CuO nanotextured surfaces can be used as cost effective and high-performing SERS substrates for molecular sensing applications in the field. Furthermore, when area averaging is performed over a sufficiently large number of hot-spot sites such surfaces can match the Raman signal reproducibility exhibited by much more elaborate and costly deterministic plasmonic platforms. In contrast to strictly defined lithographic patterns, self-affine stochastic textures can leverage the asymmetric distribution of hot-spot intensities, and are readily compatible for use in portable Raman spectroscopy setups without any precise positioning capabilities. While less technologically demanding fabrication methods help in broadening the possible range of SERS applications without marked deterioration of attainable performance, the question of how much further simplification is feasible arises. The next section, therefore, addresses one of easiest the ways of preparing platforms for SERS.

3.4 Facile Raman enhancement platforms

An important indicator of the maturity of a given technology is its accommodation for simple on-demand preparation of requisite components. In the context of SERS substrate fabrication this would mean that platforms with high Raman enhancement can be attained without either resorting to costly and complex machinery or using hazardous chemicals. Indeed, the common features shared between the different approaches for creating stochastic SERS substrates, namely an abundance of nanoscale hot-spots for optical field confinement and self-affine features for coupling efficacy, are not inherently prescriptive of any particular method of implementation. Therefore, with the gradually broadening overall adoption of SERS there has been a considerable number of attempts to apply said principles by means of extremely low cost methods, which, in tandem with advances in smartphone technology, could spread molecular sensing from specialized applications into the ubiquity of everyday use.

Among the most exhaustively investigated and popular facile SERS platforms are paper-based substrates, prepared by growing or depositing noble metal nanoparticles onto a hierarchical cellulose fiber mesh scaffold [604–606]. It uses abundant, readily disposable and biodegradable porous filter sheets or even plain office paper [607], which is then metallized by, among other methods, soaking [608], *in-situ* growth [609], inkjet printing [610], and even just by writing with a pen [611]. In addition to its low cost and simplicity, paper is flexible hence can be used for swabbing surfaces [605] and exhibits capillary force induced wicking, applicable for analyte pre-concentration [546] as well as for compatibility with affordable paper-based microfluidic platforms [612, 613]. However, issues related to residual unquenched paper fluorescence and notable signal variability between acquisitions are counted among the disadvantages of paper-based SERS platforms [614]. Furthermore, in contrast to planar substrates, the porous 3D scaffold can absorb a substantial fraction of analyte in its inner volume, where no metal nanoparticles are located, hence no plasmonic enhancement can proceed, thereby detrimentally increasing attainable detection thresholds.

Plastic or polymeric materials represent a different yet similarly cost-effective platform for producing plasmonic substrates [615]. The electrospinning method, for instance, can produce submicron width-scale polymer fiber meshes, which, much like cellulose scaffolds, can subsequently be impregnated with noble metal nanoparticles [616, 617]. Planar realizations include flexible polydimethylsiloxane based SERS substrates where plasmonic enhancement is introduced by coating the surface using oblique angle physical vapor deposition [618] as well as *via* chemical or electrostatic [619] nanoparticle attachment. Furthermore, a wide range of plastics such as polyethylene sheets can be used as substrates for screen printing nanoparticle-containing inks [620]. Much like for other template-based SERS substrates, metal coatings mostly quench or outright block any polymer-related background effects, as well as prevent texture degradation due to laser heating [621].

In this work, conducted in collaboration with with the research group headed by Prof. Junko Morikawa at Tokyo Institute of Technology as well as with the team supervised by Prof. Elena Ivanova at Swinburne University of Technology, extraordinarily facile wrinkled nanotextures of metal-coated consumer-grade polystyrene are probed for their notable surface properties [622] as well as their SERS performance [623]. First, after a brief overview of the chemical makeup of polystyrene, the creation of wrinkled surface patterns due to buckling of a mismatched skin layer under compressive strain during thermally induced shrinkage is described. Optical properties of wrinkled gold films at both visible and infrared spectral regions are outlined next, and, lastly, Raman enhancement measurement results are presented and most relevant mechanisms of plasmonic enhancement are discussed.

3.4.1 Thermal rescaling of polystyrene sheets

Induction of instabilities on soft matter surfaces is among the most readily affordable routes to the attainment of complex nanotextured interfaces. It is unsurprising then, that wrinkling is one of the most general and pervasive realizations of such phenomena in nature [624, 625], where it generally results from the buckling of a stiff surface layer during contraction of a more complaint underlying substrate. However, only with the advent of nanotechnology has it drawn substantial interest for applications related to surface patterning [626–628], stretchable electronics [629], microfluidics [630], texturing of 2D materials [631] and thin-film metrology [632].

Artificial realizations of self-organized wrinkle-textured surfaces tend to rely on polymeric substrates, such as polystyrene, polydimethylsiloxane or polyolefins among others, in large part due to relative ease of inducing strain in such materials as well as due to their ubiquity and low cost. In this work a particularly cost-effective type of pre-stretched polymer, in the form of commercially available 0.4 mm thickness flat 36.4×25.7 cm^2 area "PLA Plate" sheets (Tamiya Inc.), was used. Figure 3.29 (a) shows the high-resolution X-ray photoelectron spectrum of such a plastic in the vicinity of the carbon C 1s signature, acquired using a Thermo Scientific K-alpha spectrometer with a 1486.6 eV monochromatic X-ray source. The prominent peaks associated with C–C and $\pi - \pi^*$ bonding are strongly indicative of polystyrene. However, notably intense contributions from C–O and C=O chemical states were observed and could be due to contamination by adventitious carbon or the presence of plastifier compounds.

Similarly, a mid-IR absorbance spectrum of the polymer sheet is shown as the red curve in Figure 3.28 (b), measured using an attenuated total reflection Fourier transform spectrometer ALPHA (Bruker Corp.), equipped with a diamond internal reflection element. The spectrum is fully consistent with that of polystyrene [633], where the peaks at 3082 cm^{-1}, 3059 cm^{-1} and 3025 cm^{-1} are attributable to various aromatic C–H bond stretch vibrations. Similarly, the 2921 cm^{-1} and 2849 cm^{-1} bands are related to, correspondingly, asymmetric and symmetric

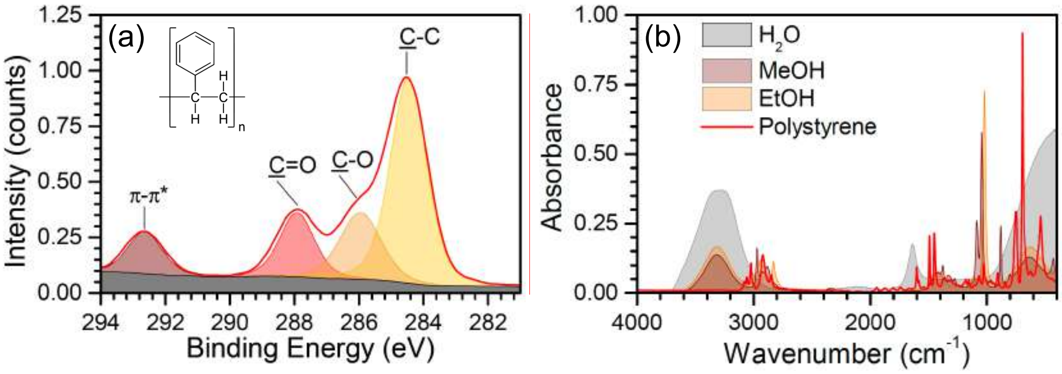

Figure 3.28: Structural characterization of polystyrene, used for subsequent nanotexturing. (a) X-ray photoelectron spectrum of polystyrene sheets in the carbon C 1s range [622]. Shaded curves are fit components to various probable bonding states of carbon. X-ray photoelectron spectroscopy was performed by the research group under supervision of Prof. Elena Ivanova. (b) Mid-infrared absorbance spectrum of polystyrene, along with that of various solvents commonly used for SERS analysis [623]. Mid-IR spectroscopy experiments were performed at Tokyo Institute of Technology by the research group under supervision of Prof. Junko Morikawa.

methylene –CH_2 group stretching modes. Other prominent spectral signatures, situated at 1601 cm^{-1} and 1583 cm^{-1}, as well as the tandem at 1492 cm^{-1} and 1451 cm^{-1} are due to C–C stretches as a result of in-plane aromatic ring breathing. The notably intense 1068 cm^{-1} and 1028 cm^{-1} bands are attributed to benzene ring C–H bond bending. Lastly, the two most pronounced peaks at 750 cm^{-1} as well as 694 cm^{-1} are assigned to out-of-plane C–H bond bending vibration modes. Therefore, any carbonyl or ether related groups, observed using X-ray photoelectron spectroscopy, are attributable solely to surface contamination.

As mentioned previously, the polystyrene sheets are fabricated in a bi-axially pre-stressed metastable state, and tend to laterally shrink when heated above the glass transition temperature of approximately 110 °C. Over the course of thermal rescaling the in-plane dimensions of the plastic substrates decrease to 50% of their initial value, whereas transverse thickness swells by 400% in accordance to volume conservation. However, if a thin interfacial layer of such a sheet is modified, so that it does not undergo thermal contraction along with the underlying bulk material, it will tend to maintain the original surface area. Furthermore, the compressive strain induced in the surface layer by the shrinking substrate is relieved through hierarchical buckling and wrinkle creation.

A schematic illustration of the exceptionally facile thermal nanotexturing process used in this work is provided in Figure 3.30 (a). The commercially available polystyrene sheets can be used as received, and any further cleaning steps in iso-2-propyl alcohol are purely optional. Surface modification to increase its stiffness can be performed in a number of different ways, including metal deposition [623], laser irradiation [634] as well as plasma treatment [635].

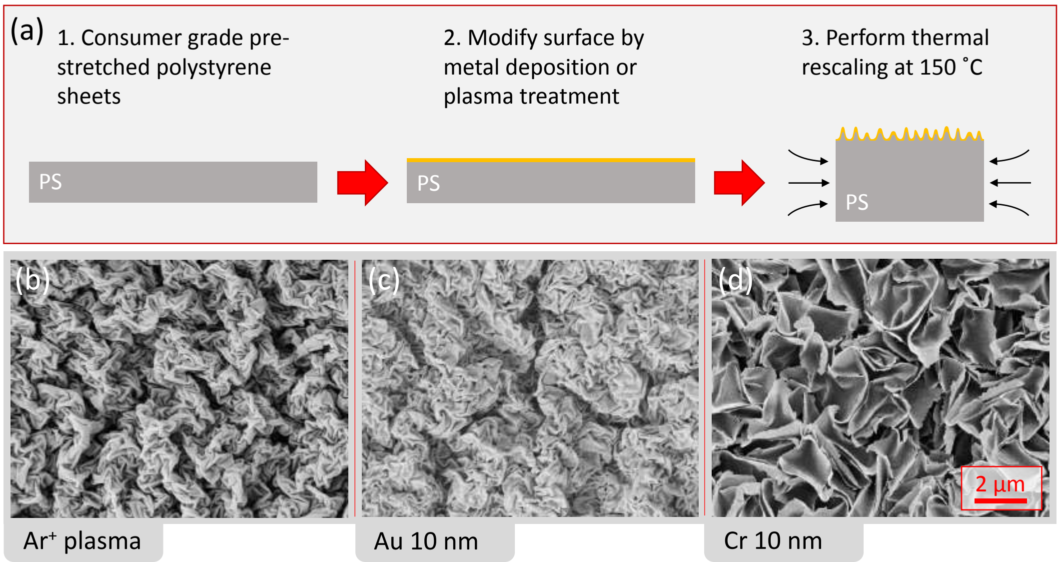

Figure 3.29: Process for polystyrene surface nanotexturing *via* thermal shrinkage. (a) Sketch illustrating the main steps in the procedure that uses pre-stretched polystyrene sheets. The nanoscale surface layer stiffness is modified either through metal deposition or chemical treatment. The plastic is then heated above the glass transition temperature, during which it biaxially shrinks to span half of its initial lateral dimensions. Compressive strain causes the wrinkling of the treated surface. Lower panels show scanning electron images of textures obtained through various surface modification methods, such as hardening through Ar^+ plasma treatment (b), as well as deposition of either ductile Au (c) or brittle Cr (d).

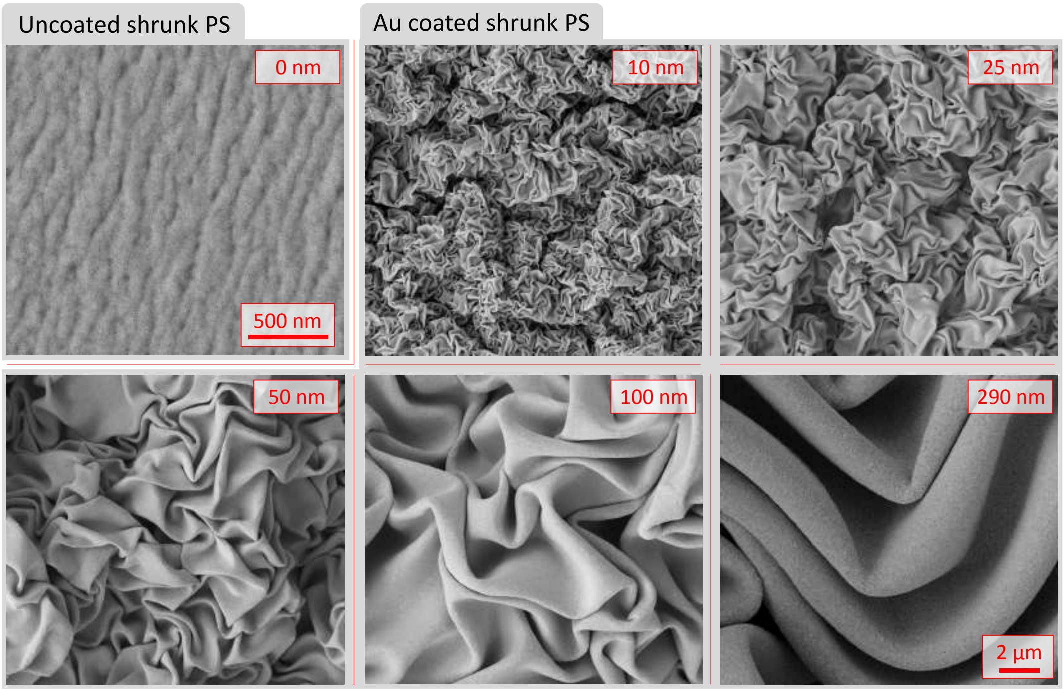

Figure 3.30: Scanning electron microscopy images of thermally rescaled polystyrene surfaces. Surface topology obtained without any modification is compared to texturing arising due to compression strain acting upon gold layers deposited with thicknesses ranging from 10 nm to 290 nm. All metal-coated substrate images use the same 2 µm scale bar.

Lastly, thermal shrinkage is allowed to proceed in a convection oven at 150 °C until an equilibrium state is reached, which produces the desired wrinkled surface. Interestingly, as can be inferred from the scanning electron microscopy images in Figures 3.29 (b) and (c), regardless if polystyrene surface modification is performed by means of Ar^+ plasma exposure in a reactive ion etching tool, which results in cross-linking of polymer chains in the top layer of the substrate, or by depositing a film of gold or other reasonably malleable metal, the resulting wrinkle patterns tend to appear quite similar. Conversely, when the surface film is brittle, as is the case for 10 nm thickness thermally evaporated chromium, the resultant nanotexture will be comprised of randomly aligned metal flakes, depicted in Figure 3.29 (d).

Among the most intriguing properties of mechanical instability-induced texturation is that the characteristic surface wrinkle wavelengths λ_s are deterministic, and depend linearly on the skin layer thickness h, as well as non-linearly on the ratio of Young's modulli E_s and E_b of surface and bulk materials respectively, as [624]:

$$\lambda_s = 2\pi h \sqrt[3]{E_s/E_b}. \tag{3.11}$$

To illustrate, Figure 3.30 shows the wrinkle patterns produced when pre-stretched polystyrene sheets are thermally rescaled with different thicknesses of overlaying gold. Here metallization was performed by means of magnetron sputtering using an AXXIS physical vapor deposition system (Kurt J. Lesker). When no surface modification is performed prior to shrinkage the resultant rescaled surface remains mostly flat apart for some indistinct nanoscale ripple patterns, depicted in the close-up scanning electron microscopy image on the top-left of Figure 3.30.

The stiffer metal layer, however, is compressed by the shrinking substrate, which causes partial delamination and the dissipation of strain through plastic deformation of the initially planar film into complex topologies, comprised of folds and creases. In addition, said topologies possess a degree of self-affinity, were a cascading hierarchy of buckled features is formed [627]. This arises naturally out of the wrinkling mechanics, where lowest wavelength buckles, set by the stiffness of the metal layer, are formed first and proceed to grow in amplitude, thereby creating a new effective skin layer. As shrinkage of the underlying substrate continues to run its course, compressive stress required for further growth of initial wrinkle amplitude starts to exceed that of creating a new generation of buckles of the deformed effective metal skin. This process can be repeated over successive generations until the substrate bulk reaches equilibrium. Lastly, while the deposited thickness of Au profoundly affects the average wavelength attributable to surface features, all of the textures exhibit a strong scale invariance, where higher metal film thickness surfaces tend to resemble magnified versions of finer thin metal wrinkle patterns.

Such complex hierarchical surface topologies can exhibit many of the behaviors typically associated with other micro/nano-textured interfaces, such as hydrophilicity or hydrophobicity [636], as well as reduced biofouling through suppressed bacterial attachment [622]. Topologically controllable thermal diffusivity α, however, is a property fairly unique to wrinkled metal film textures, interesting from both a fundamental and an application oriented perspective. This parameter is defined as $\alpha = k/(\rho c_p)$, where k is the thermal conductivity, ρ stands for mass density, and c_p represents the specific heat capacity at constant pressure. Thermal diffusivity characterizes the temporal spread rate of heat, described by the temperature T, according to the diffusion equation $\partial T/\partial t = \alpha \nabla^2 T$.

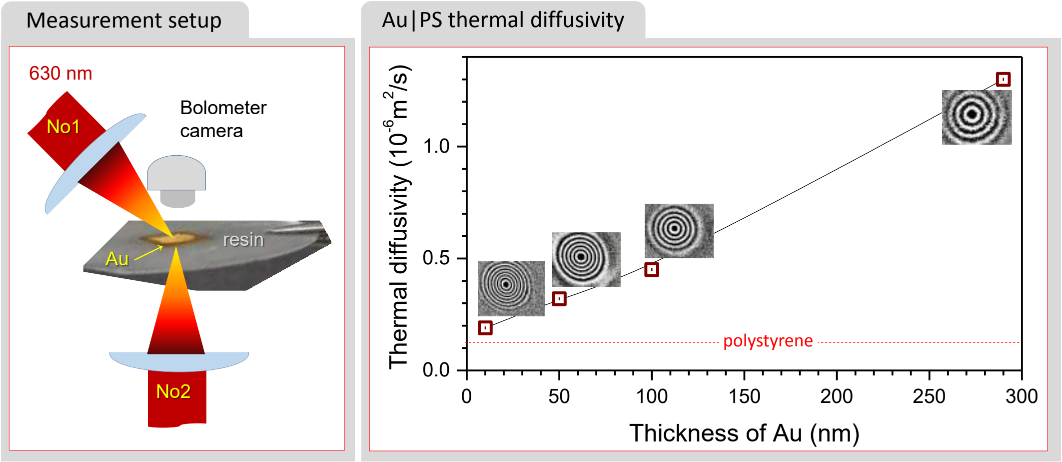

Figure 3.31: Non-contact measurements of thermal diffusivity of wrinkled gold surfaces [623]. Sketch on the left illustrates the measurement setup, wherein 1 Hz modulated $\lambda = 630$ nm laser illumination is focused onto the sample either from the top-side or from the bottom, respectively through ports No 1 or No 2. A bolometer camera is used to image the laser heating spot, and the spreading thermal wave is visualized by performing a fast Fourier transform. Thermal diffusivity dependence on wrinkled gold surface thickness is plotted on the right. Insets show the fast Fourier phase images of thermal waves spreading over corresponding textured surfaces. Measurements of thermal diffusivity were performed at Tokyo Institute of Technology by the research group under supervision of Prof. Junko Morikawa.

Here, thermal diffusivity of rescaled Au coated polystyrene was measured using the non-contact temperature wave method [623], previously described in Section 2.2.1 and schematically outlined in the left panel of Figure 3.31, which combines continuous wave $\lambda = 630$ nm laser spot heating with micro-bolometric imaging over the 7 to 14 µm spectral range. Laser illumination is focused onto a diffraction-limited interface region, and its intensity is modulated at a $\omega = 1$ Hz frequency, which provides the carrier signal for subsequent fast Fourier transform bolometric image analysis. The amplitude of resultant spatial harmonic plots is related to surface radiant exitance, whereas the fast Fourier transform phase images, depicted as insets on the right panel of Figure 3.31, illustrate the thermal wave spread. This process is directly related to thermal conductivity exhibited by the surface, and the slope of the phase plots is inversely dependent on thermal diffusivity α as $\Delta\theta(x)/\Delta x = \sqrt{\omega/2\alpha} + c$ [230], where c is a measurement setup contingent constant. Either oblique front-side or perpendicular back-side texture illumination modes can be used, with the latter method providing a superior signal-to-noise ratio. However, strong scattering in the polystyrene substrate bulk prevents diffraction-limited laser focusing onto, and localized heating of, the wrinkled metal texture rear-side. To mitigate this effect the shrunken plastic substrates were partially embedded in a protective epoxy resin and mechanically polished down to a 100 µm total thickness, which eliminated most of the detrimental scattering.

The planar counterparts of materials constituting the wrinkled metallic nanotextures possess severely disparate thermal diffusivities, with polystyrene being the most insulating at $\alpha_{\mathrm{PS}} = 1.06 \times 10^{-7}$ m^{2}s^{-1} [637], followed by air $\alpha_{\mathrm{Air}} \sim 1.9 \times 10^{-5}$ m^{2}s^{-1}, and, lastly, gold $\alpha_{\mathrm{Au}} \sim 1.27 \times 10^{-4}$ m^{2}s^{-1} providing the fastest thermal pathway. However, as is readily observed in the right plot of Figure 3.31, wrinkled gold layers of various thicknesses exhibit up to two order of magnitude reduced thermal diffusivities compared to those of their initial flat state. While thermal diffusivities of the thinnest 10 nm metal coatings are barely above that of polystyrene, for every additional 10 nm of Au the parameter increases linearly by approximately 4%. Such a change manifests as an ever more rapid thermal spread, visualized by larger fringe spacings in micro-bolometer image fast Fourier transform phase plots, illustrated by the aforementioned insets in the right panel of Figure 3.31.

This scaling behavior with increasing metal thickness can be understood by considering that in a textured material heat can be transported not only through thermal conductance in gold and, to a much lesser extent, polystyrene, but also *via* convective flow in air pockets trapped between morphological features. In order for thermal energy transfer through air to become viable, however, gaps between wrinkle ridges have to be at least $\alpha_{\mathrm{Au}}/\alpha_{\mathrm{Air}} \simeq 6.7$ times smaller than the conductivity path through the hierarchically buckled surface of a given thickness metal. This condition can be readily achieved by way of the diminished thermal conductivity of thinner gold layers on one end, and through the coincident decrease in average wrinkle wavelength, hence, expected air gap width. Therefore, thermal diffusivity can be tuned from the value of either the underlying substrate or air, depending on which is higher, to that of flat Au.

Controllable heat diffusion enables the management and investigation of locally induced thermal gradients underlying thermophoresis, also known as the Soret effect [450], which represents a long-standing issue affecting SERS, among other spectroscopic analytical measurement techniques performed in solution. Ultimately, the self-affine hierarchical surface topologies of wrinkled metal films are conceptually similar to previously described self-affine nanotextured SERS substrates, however, accurate performance estimates of these facile platforms can be obtained only through experimental measurements of their optical and Raman enhancement behavior.

3.4.2 SERS on thermally shrunk Au coated plastic

Changes in the optical properties of a metal surface, induced by self-organized wrinkling processes of a pre-stretched thermoplastic, have been shown to enhance fluorescence emission of adsorbed molecules [638], as well as to drastically improve the SERS performance of nanoporous gold films prepared by dealloying [639]. Conversely, applying a silver layer onto a pre-wrinkled spin-coated polystyrene thin-film provided an eightfold increase in Raman signal over that acquired on an equivalent thickness of planar Ag [640]. In all cases the augmentation of surface-enhanced processes has been attributed to stochastic plasmon confinement in nanoscale gaps between the multitude of folds and crevices in the wrinkled metal film. In this work, however, altering the amount of deposited gold enabled tuning the characteristic lengthscale of the wrinkled metal textures, which in turn allows to estimate the effect of their morphology on SERS signal.

As is evident from the dark-field optical microscopy images of different Au thickness coated rescaled polystyrene substrate surfaces given in Figure 3.32, the first readily appreciable change induced by wrinkling is the increase in the prevalence of light scattering as a result of the disordered texture. Indeed, the initially mirror-like gold films are turned matte by the thermal shrinkage of the underlying plastic. This is attributable to diffuse reflectance as a result of the quasi-random surface topology being imprinted onto the wavefront of incident light during reflection at the metal interface. Hemispherical reflectance measurements, performed using a LAMBDA 1050 spectrophotometer (Perkin-Elmer Inc.) equipped with a 150 mm diameter integrating sphere, likewise showed that, for Au thicknesses of 50 nm and above, texturing does not noticeably change the absolute amount of reflected light, but merely turns the reflectance diffuse. Furthermore, the 50 nm and 100 nm thickness rough gold films exhibit numerous random speckle patterns, which tend to cluster in the vicinity of the wrinkle crests. This behavior becomes less prominent on the 290 nm thickness film, which has buckles marginally distinguishable with the naked eye, hence, are not in the size-range optimal for induction of random interference of scattered light.

The 10 nm gold thickness texture with smallest characteristic wrinkle wavelengths exhibits a notably different behavior due to its subwavelength morphological feature size and partial transparency of the metal coating. Here, scattering is considerably weaker and mostly relegated to the red portion of the visible wavelength region, likely due to the anti-reflectance exhibited by the nanotexture. Much of the incident radiation is either coupled into the substrate or outright absorbed by the gold film as a result, leading to a dark brown appearance of the substrate.

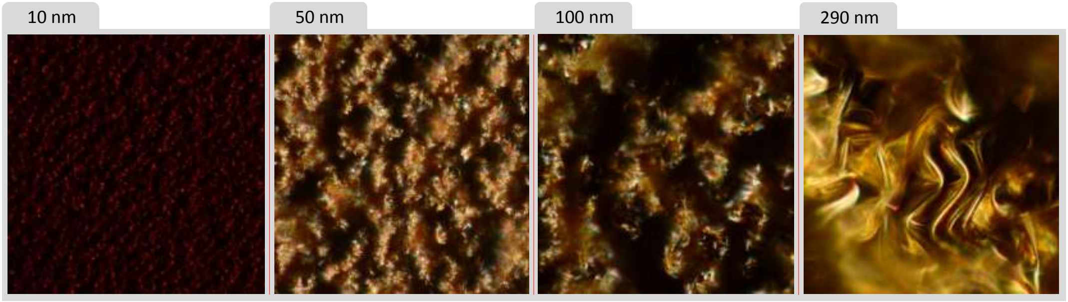

Figure 3.32: Dark-field optical microscopy images of wrinkled Au films on thermally shrunk polystyrene, prepared using different gold deposition thicknesses. Speckle patterns on 50 nm and 100 nm thickness films are indicative of strong plasmonic scattering activity.

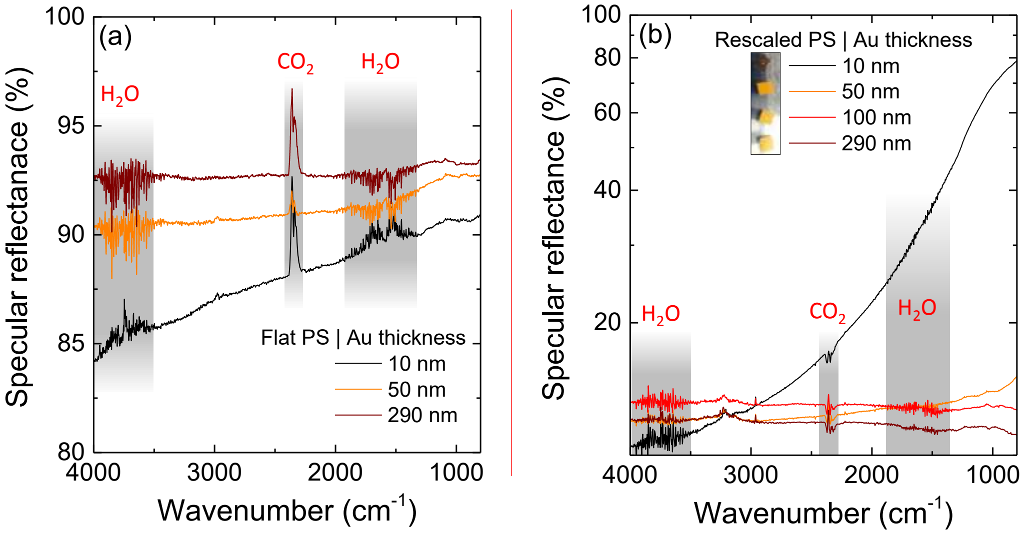

Figure 3.33: Mid-infrared specular reflectance spectra of different thickness gold layers deposited on pre-stretched polystyrene (a) before and (b) after thermal shrinkage [623]. Inset in panel (b) shows respective photographs of 5×5 mm^2 sized substrate pieces. Note the different scales used on ordinate axes for the two plots. Mid-IR spectroscopy experiments were performed at Tokyo Institute of Technology by the research group under supervision of Prof. Junko Morikawa.

Figures 3.33 (a) and (b) show the mid-infrared specular reflectance spectra of gold films magnetron-sputtered on polystyrene sheets respectively prior to thermal rescaling and after the process has run its course. Here, measurements were conducted using a Spectrum Spotlight 300 Fourier transform IR imaging spectrometer (Perkin-Elmer Inc.), equipped with a limited acceptance angle $NA = 0.5$ Cassegrain-type magnifying mirror system. Marked spectral regions correspond to atmospheric absorbance bands due to the presence of H_2O and CO_2. The as-deposited flat gold films exhibit the high degree of specular reflectance typical for most bulk metals, with 290 nm thickness layers being the most mirror-like. On the other hand, in the 10 nm Au case reflectivity falls off towards the near-IR range due the onset of transmittance as the skin-depth starts to exceed the metal thickness.

Wrinkled gold layers on thermally rescaled polystyrene sheets demonstrate a contrasting behavior, where, according to Figure 3.33 (b), specular reflectance drops well below 10% for Au film thicknesses at or above 50 nm. This is attributable to diffuse scattering from the quasi-random surface texture, in line with what was observed at the visible spectral range. However, the lowest 10 nm thickness wrinkled gold layer again shows notably distinct behavior, where strong specular reflectance is reconstituted towards the far-IR, likely due to all hierarchically self-similar generations of the texture becoming subwavelength in this spectral region. Hints as to the onset of such a regime are discernible also at the lowest wavenumber portion of the 50 nm gold thickness substrate. As described in the previous section, other randomly nanotextured plasmonic surfaces used for SERS likewise tend to exhibit substantial broadband scattering of electromagnetic radiation. Hence, such reflectance behavior is a strong, albeit not definite, indication of a high potential for attaining substantial Raman signal intensity enhancement.

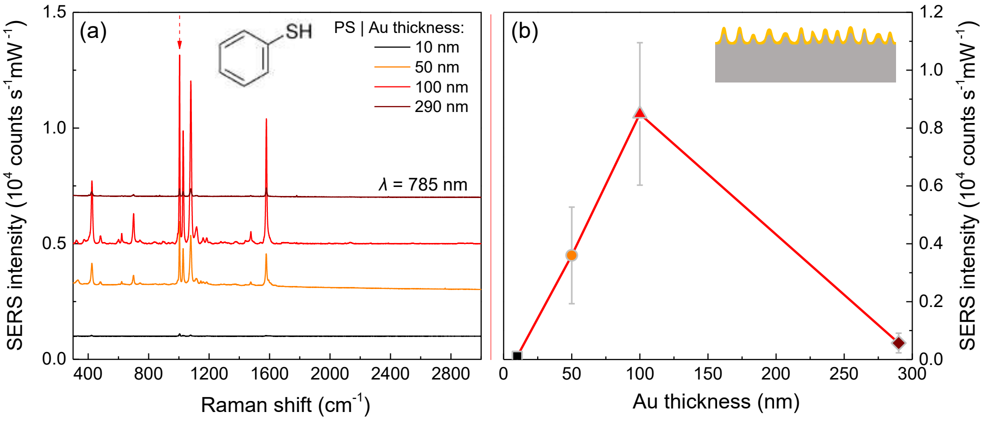

Figure 3.34: SERS performance of wrinkled gold films prepared on thermally rescaled polystyrene sheets. (a) Raman spectra of benzenethiol measured on wrinkled Au with various layer thicknesses. Excitation laser wavelength was $\lambda = 785$ nm, and spectra are offset for clarity. (b) Intensity dependence of the 1001 cm^{-1} benzenethiol peak, marked by the arrow in panel (a), on thickness of the initial gold film. Gray error bars represent the standard deviation between different measurement positions. Sketch in the inset illustrates the textured metal surface.

SERS performance of thermally shrunk Au coated plastic substrates was, again, probed using benzenethiol as a reporter molecule, applied by way of the protocol previously described in Section 3.3.2. Spectral acquisitions were performed with an inVia Raman microscope (Renishaw plc.) using 785 nm continuous wave laser excitation and a $NA = 0.75$ objective in 20×2 $\mu\mathrm{m}^2$ line-focus mode. Representative SERS spectra of benzenethiol measured on different thickness buckled Au films, which according to Figure 3.30 exhibit disparate average surface wrinkle wavelengths, are shown in Figure 3.34 (a). Here, as is commonly observed on other stochastic noble metal sputtered template SERS substrates, Raman scattering peaks tend to initially scale linearly in intensity with increasing amounts of gold overlaying the textured substrate.

Figure 3.34 (b) outlines these changes in both average SERS signal as well as its point-to-point standard deviations for the most prominent 1001 cm^{-1} in-plane benzene ring breathing vibrational mode. Despite possessing a fine subwavelength nanotexture, 10 nm thickness gold wrinkles appear to be insufficient to establish notable Raman enhancement. This is likely in part due to strong plasmonic damping, as a result of dissipative electron scattering at layer interfaces, as well as due to optical energy loss by way of transmittance through the thin Au film. The optically opaque 50 nm thickness wrinkled gold substrate performs much better, however, is unmistakably surpassed by the sample with 100 nm of deposited Au.

All of the aforementioned substrates notably exhibited a similar $\sim 30\%$ signal variability between different acquisitions, which, while sub-optimal for analytic applications, could be mitigated by spatial averaging schemes. Much of this point-to-point variance can be attributed to the microscale topological unevenness of the hierarchically wrinkled surface, which complicates the consistency of both excitation as well as scattered radiation collection. Indeed, the 290 nm wrinkled Au layer represents an extreme case, where even the smallest wrinkle generations comprising the texture are so far beyond the submicron lengthscales associated with optical and plasmonic processes, that they become hardly distinguishable from planar gold, hence the low SERS efficacy.

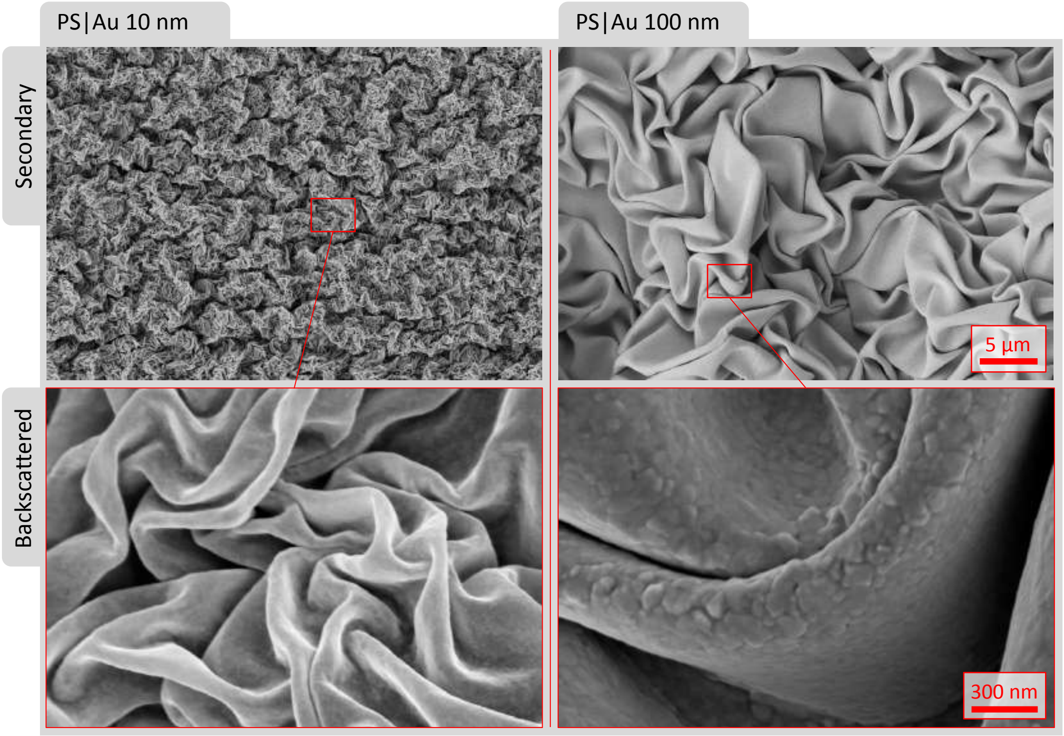

Figure 3.35: Wide-field as well as close-up scanning electron microscopy images, respectively acquired using secondary and backscattered electron detectors, of wrinkled 10 nm and 100 nm thickness gold films on polystyrene. Both morphological surface roughness as well as numerous nanoscale gaps in the strained thick metal film can host high intensity SERS hot-spots.

However, while on average the SERS enhancement demonstrated by the large scale 290 nm Au wrinkles only marginally exceeded that of the lowest thickness gold film, it exhibited a huge variance in signal output. Some rare outlier points near the crests of the microscale wrinkle pattern provided enhancements far above what was observable on any of the less metal-loaded substrates. This behavior, in turn, raises questions as to what is actually required to facilitate hot-spot formation. Purely from the morphology point of view surface topologies with smallest wrinkles packed in the densest fashion, akin to those on 10 nm thick Au films, maximize the number of possible nanoscale gaps per unit surface area, and, therefore, would be expected to yield the best SERS performance. Conversely, thick gold layers have large wrinkles tens of microns in size and mostly produce gaps that are on length scales far beyond those relevant for near-field plasmonic proceses.

On the other hand, from a structural point of view more bulky gold layers, at least 40 nm in thickness, would be preferable, since only then does the effective medium approach, which plasmonics is based on, become valid and dissipation losses due to electron scattering at metal interfaces are sufficiently low. Furthermore, thicker gold coatings have larger Au grain sizes, as can be seen for the 100 nm substrate in Figure 3.35, whereas 10 nm layers are just above the percolation threshold and appear fairly smooth. Metal surface roughness has been shown to enable stochastic inhomogeneous localization of extraordinarily intense plasmon modes [501], and can be invoked here to describe the rare occurrences of high Raman enhancement on otherwise unremarkable thick metal wrinkles.

In the case of thermally rescaled gold-coated surfaces it appears both aspects – sufficient Au grain size and nanoscale roughness, as well as small and densely packed wrinkles for field enhancing gap formation – are necessary for adequate SERS substrate performance. Hence, only 50 nm and 100 nm Au thickness wrinkles offer both significant as well as reasonably consistent Raman enhancement as a result of both morphological and structural factors being able to contribute towards hot-spot formation. The substrate specific enhancement factor for the highest performing 100 nm gold thickness case was estimated at around $EF_{\mathrm{SS}} = 3 \times 10^6$, which, despite its simplicity, is not far behind many considerably more complex and technologically demanding quasi-random SERS platforms. On the other hand, surface thermal diffusivity is smaller for more finely wrinkled films with lower metal thicknesses. Hence, the limited nanotextured surface parameter region optimal for SERS is somewhat limiting to the range of thermal conductance values attainable by tuning the wrinkled surface morphology. However, it might nevertheless be possible to extend the range in which both parameter sets can be controlled independently by further conformal sputtering of additional metal onto pre-wrinkled substrates, which would help to both increase plasmonic propagation efficiency as well as thermal conductivity.

To summarize, thermally rescaled gold coated polystyrene represents an extraordinarily facile and highly effective SERS platform, with its main disadvantage being a considerable point-to-point variability of the signal. Plasmonic enhancement exhibited by buckled metal films, like for most other stochastic Raman enhancement substrates, relies on hierarchical transfer of optical energy from free space into ever more confined plasmonic modes, and *vice versa*. Here, micron and submicron scale wrinkles and creases can provide discontinuities required for the coupling of surface plasmon-polaritons, which can then be inhomogeneously localized in random anti-wedge and gap modes at nanoscale metal roughness sites. The primary application of such a plasmonic sensing surface would be in enabling cost-effective molecular detection by way of enhanced fluorescence emission or Raman scattering. However, wrinkled metal films possesses numerous unique properties such as the ability to deterministically and drastically change the scale of surface topology, control their thermal diffusivity, as well as to accurately determine the surface area, which make this platform relevant even for fundamental investigations related to plasmon-enhanced spectroscopy.

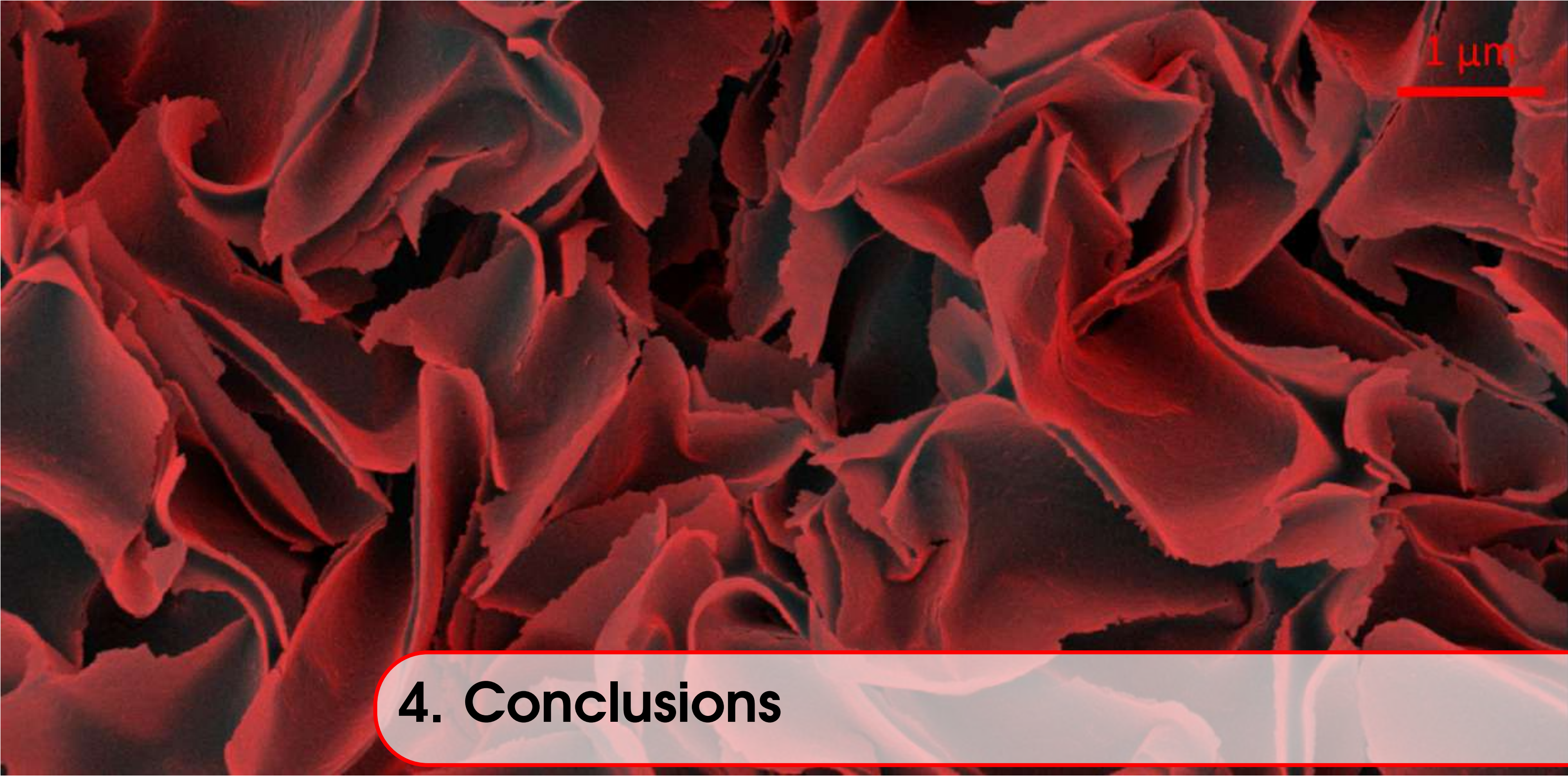

4. Conclusions

This work is centered around development of methods and techniques for the creation of effective and cost-efficient nanotextured surfaces exhibiting a range of optical functionalities related to control over the interaction between radiation and matter, and in particular for luminous energy harvesting as well as optical sensing. Its three main prongs are: tailored anti-reflectance realized on a black silicon platform, understanding the optically relevant nanoscale composition of silk fibroin biopolymers and honing of techniques for their top-down patterning, and creating ever more affordable disordered plasmonic substrates for surface-enhanced Raman sensing. The major findings of this project are summarized as follows.

- Black silicon is a high-performance anti-reflective nanotextured surface comprised of a densely-packed quasi-random arrangement of tapered subwavelength spikes. Furthermore, it is created using a cost-effective mask-free reactive ion etching process. Similar textures are employed by certain natural organisms to reduce reflectance or increase light collection efficiency, as exemplified by moth eye and cicada wing surfaces. Anti-reflectance of black silicon is primarily predicated on it operating as a gradient effective refractive index layer, however, can be further augmented and extended towards the infrared spectral region by altering the constituent arrangement of spikes or by using hierarchical texturation approaches. When infrared wavelength anti-reflectance is combined with methods to induce additional absorbance in this spectral range, black silicon becomes an effective absorber for thermoelectric power generation approaches.
    1. Total hemispherical reflectance of black silicon with different scale nanotextures, comprised of spikes with heights ranging from 200 nm to 800 nm, exhibits values below 1 % throughout the Si absorbance spectral region. While the gradient effective refractive index layer, established by silicon spikes, represents its main anti-reflectance mechanism, the presence of local minima in the specular reflectance spectra that scale with the sizes of structural components are indicative of an additional trapping mechanism due to quasi-deterministic forward-scattering of light into substrate-guided modes as the spatial frequency spectrum of the texture gets imprinted into the incident optical field [137].

2. A notable majority of the optical properties exhibited by black silicon are mirrored by the anti-reflective nanotextures of cicada wings. Similarities include the overall subwavelength surface topology, gradient effective refractive index layer-based anti-reflectance, principal spatial frequency components that cause light trapping *via* diffraction into the total internal reflection angle range of the substrate, and near field intensity distribution of the incident optical field. Cicada wing reflectance suppression is highly omnidirectional, as verified by FDTD calculations. Wing surface texturation diminishes the amount of reflected light throughout most of the visible spectral region by factors ranging from 10 at normal illumination, to 4 at a large oblique 75° angle of incidence [220].

3. Black silicon represents a new method for enhancing optical trapping through local field enhancement at the point-of-contact between its texture and a dielectric particle, as was deduced based on FDTD simulations. When using a $\lambda = 808$ nm wavelength laser, submicron polystyrene beads were trapped at irradiation powers ranging from 30 $\mathrm{kWcm^{-2}}$ to 740 $\mathrm{kWcm^{-2}}$, limited by the maximum output of the light source. This trapping regime is complimentary to plasmonic approaches, and, while it exhibits weaker optical field gradients than metal structures, black silicon is inherently broadband, performs tighter trapping due to absence of detrimental thermal gradients, and binding potentials scale up to high incident intensities thereby allowing switching between 2D and 1D trapping modes [113].

4. Hierarchical superimposition of different scale surface textures results in a cumulative optical behavior. When anti-reflective black silicon is applied onto a statistical ray trapping micro-pyramid texture the originally diffuse reflectance at the Si absorbance range is almost completely suppressed. Experimental results bolstered by numerical simulations showed that hierarchical surface texturing can reduce broadband specular reflectance by up to two orders of magnitude well into the mid-infrared region whilst completely altering the method of light trapping within the substrate from slab-guided to statistical [146].

5. Black silicon can be applied to uses in Seebeck element-based photothermoelectric power conversion as an affordable high efficiency luminous energy absorber. FDTD simulations revealed that roughly 80% of visible wavelength photons are absorbed in the spiky nanotexture. Gold nanoparticles were deposited onto black silicon to further enhance solar-to-thermal energy conversion yield by an additional 50%. In the plasmonically augmented case metallic nanoparticles exhibit an up to two orders of magnitude higher absorbance per unit volume than that of silicon. Efficiency of the prototype device was around 2%, mainly due to limitations related to low thermoelectric conversion yield in the Seebeck element [167].

6. A prototype hybrid solar energy harvesting device, comprised of a photovoltaic top section made up of a black silicon wafer, and an electrically insulated thermoelectric bottom section comprised of a GeSn alloy infrared absorber film and a Seebeck element, is proposed. The prototype device had a modest photovoltaic conversion efficiency of 2.4%, which was increased by a further 8% by the thermoelectric section, utilizing waste heat and infrared radiation not absorbed in Si. The total optical-to-electrical power conversion efficiency of this not optimized first realization was 2.6% [173].

- Natural silk fibers derive their remarkable toughness and chemical resilience from the elaborate hierarchical network of different protein secondary structures, mainly random coils, α-helices, and β-sheets. Such a complex composition of covalent and hydrogen bonds inevitably results in a wealth of interactions with electromagnetic radiation over a wide spectral range, which presents both difficulties as well as opportunities for both their spectroscopic investigation, as well as utilization for creating various photonic devices on a silk fibroin platform. Similarly, applications of silk in nanofabrication for the most part harness the inherent natural properties of this protein, and, in particular, how β-sheets stabilize the biopolymer and render it water insoluble. Hence, in order to create nanoscale functional components using silk it is of prime importance to find methods to accurately recognize as well as to exert precise local modification of such secondary structures of fibroin.

    7. Probing of the electromagnetic radiation absorbance properties of natural silk fibers over an extraordinarily broad spectral range, from ultraviolet all the way to the terahertz region, allowed for comprehensive characterization of fibroin behavior at all levels of its hierarchical composition. In particular, terahertz frequency radiation absorbance spectroscopy identified long-range collective vibrational motion-related spectral peaks at around 20 cm^{-1} and 240 cm^{-1} wavenumbers, which were sensitive to subtle primary and secondary protein structure variations between fibers spun by different *Bombyx mori* and *Antheraea pernyi* silkworm species [283].

    8. Femtosecond laser patterning of silk fibroin films without photoinitiators is possible by ablation of their positive tone water insoluble β-sheet rich state, using infrared radiation that is not directly absorbed in either the substrate or silk. Laser polymerization of water soluble amorphous fibroin films only becomes observable at the onset of substrate ablation, and likely proceeds as a result of irradiation by energetic electrons liberated during avalanche breakdown of the dielectric [353].

    9. Regenerated silk fibroin films can be processed to act as both positive as well as negative tone biocompatible water chemistry based high resolution electron beam lithography resists. The optimal exposure dose for crystallized fibroin-based positive resists using 100 keV electron energy beams was approximately 4000 μCcm^{-2}, as it was found to be sufficient to induce β-sheet breakdown. Exposure doses required for negative tone amorphous fibroin layers are impractically large however, and at 38000 μCcm^{-2} managed to cross-link only the bottom 20% of the initially 100 nm thickness film. This shows that substrate back-scattered electrons are instrumental in inducing polymerization of silk [369].

- Plasmonic noble metal coated nanotextures can be used as highly effective yet affordable sensing substrates for surface-enhanced Raman scattering. Such disordered plasmonic systems make use of inhomogeneous localization of optical energy at certain high intensity hot-spot sites, behaving as a matter-coupled wave equivalent of a laser speckle pattern. This stochastic behavior is inherently broadband, however, exhibits a somewhat lower degree of signal reproducibility that can be mitigated by way of area averaging. Three different realizations of SERS substrates, each with varying degrees of inherent disorder and ever lower fabrication complexity, are proposed.

10. Reproducible Raman signal enhancement, showing a $SD = 10\%$ standard deviation variance without area averaging, has been realized using ordered gold nanopillar array SERS substrates, prepared on a silicon wafer by means of reverse micelle soft-lithography and gold sputtering. The detection limit value for 1-naphthalene thiol was 0.46 nM, or 74 parts-per-billion, which is below monolayer surface coverage. FDTD simulations allowed to relate the metal layer thickness-dependent nanotexture surface topology to SERS enhancement, and showed that highest intensity surface plasmon-polariton modes are localized in the trenches between gold pillars [536]

11. Nanotextured copper(II) oxide semiconductor template-based gold sputtered SERS substrates represent an effective, scalable and affordable stochastic plasmonic platform for SERS detection. Signal enhancement factors for benzenethiol were shown to scale approximately linearly with increasing amounts of deposited gold, and reached $EF_{\mathrm{SS}} = 1.1 \times 10^7$ for 250 nm gold thicknesses. Furthermore, while these stochastic metal nanotextures exhibit considerable spatial variability in SERS intensity, line-scan area averaging schemes can ensure a $SD = 10\%$ standard deviation, on par with that of much more elaborate and costly lithographically defined plasmonic geometries [561].

12. Thermally rescaled gold coated polystyrene is an exceptionally simple, yet notably effective self-affine SERS platform, which has demonstrated benzenethiol spectroscopic signal enhancement factors of approximately $EF_{\mathrm{SS}} = 3 \times 10^6$ in the optimal case when surface wrinkles are comprised of 100 nm thickness gold. Its main disadvantage, however, is a considerable point-to-point variability in performance that can amount to $SD = 30\%$ standard deviations of the signal. An additional beneficial feature of the wrinkled metal texture surface is the ability to estimate and predictably control its thermal diffusivity by changing the layer thickness [623].

These conclusion statements are validated and further elaborated on in the correspondingly cited peer-reviewed papers published as part of this PhD project, all of which are summarized in the Appendix "Publications during this PhD project".

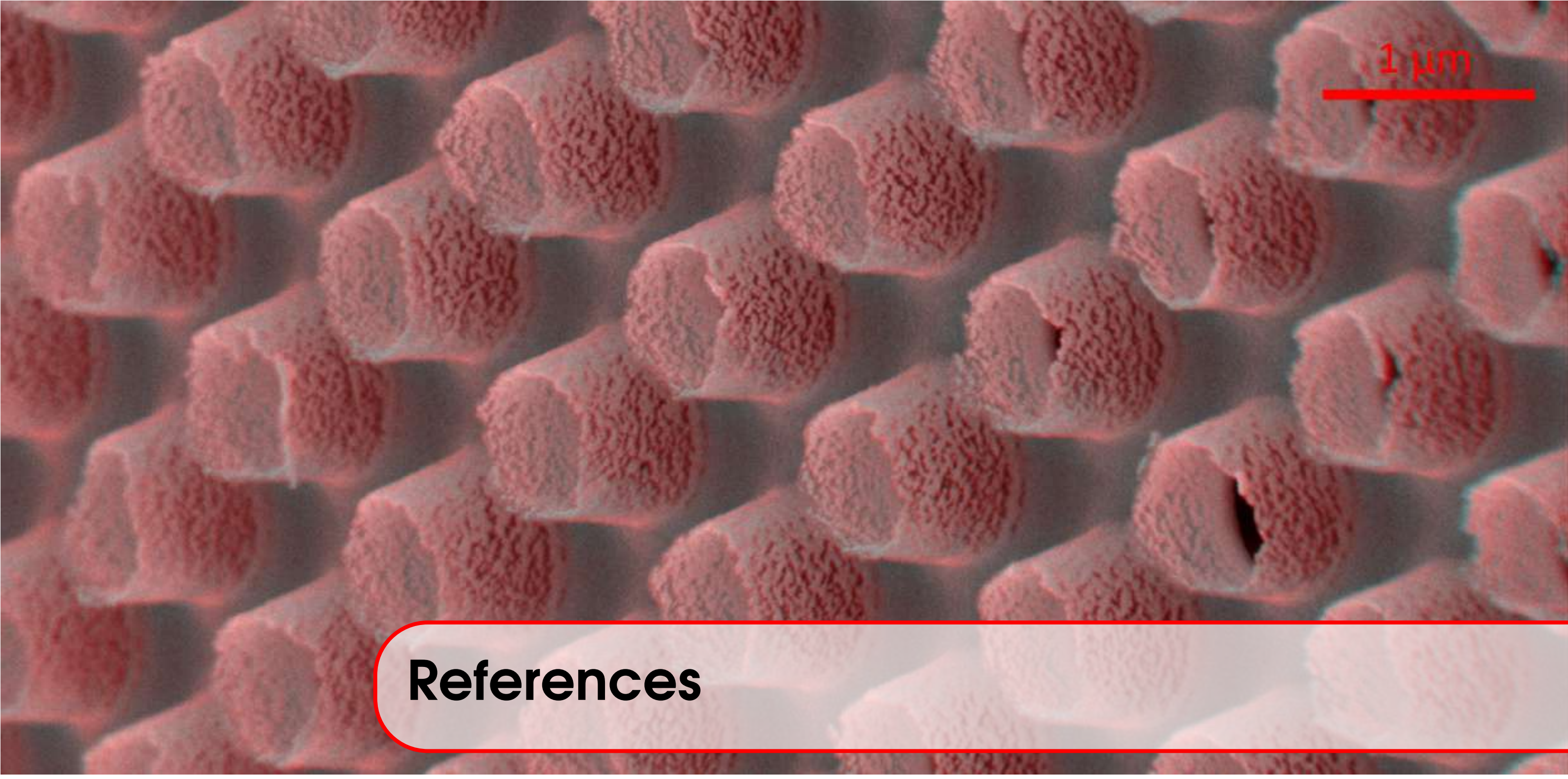

References

[1] G. A. Niklasson, C. G. Granqvist, and O. Hunderi. Effective medium models for the optical properties of inhomogeneous materials. *Appl. Opt.*, 20(1):26–30, 1981.

[2] M. Haruta, T. Kobayashi, H. Sano, and N. Yamada. Novel gold catalysts for the oxidation of carbon monoxide at a temperature far below 0 °C. *Chem. Lett.*, 16(2): 405–408, 1987.

[3] R. M. Rioux, H. Song, J. D. Hoefelmeyer, P. Yang, and G. A. Somorjai. High-surface-area catalyst design: Synthesis, characterization, and reaction studies of platinum nanoparticles in mesoporous SBA-15 silica. *J. Phys. Chem. B*, 109(6):2192–2202, 2005.

[4] S. Pogodin, J. Hasan, V. A. Baulin, H. K. Webb, V. K. Truong, T. H. Phong Nguyen, V. Boshkovikj, C. J. Fluke, G. S. Watson, J. A. Watson, R. J. Crawford, and E. P. Ivanova. Biophysical model of bacterial cell interactions with nanopatterned cicada wing surfaces. *Biophys. J.*, 104(4):835–840, 2013.

[5] T. Darmanin and F. Guittard. Superhydrophobic and superoleophobic properties in nature. *Mater. Today*, 18(5):273–285, 2015.

[6] H. Ghiradella. Light and color on the wing: Structural colors in butterflies and moths. *Appl. Opt.*, 30(24):3492–3500, 1991.

[7] H. K. Raut, S. S. Dinachali, Y. C. Loke, R. Ganesan, K. K. Ansah-Antwi, A Góra, E. H. Khoo, V. A. Ganesh, M. S. M. Saifullah, and S. Ramakrishna. Multiscale ommatidial arrays with broadband and omnidirectional antireflection and antifogging properties by sacrificial layer mediated nanoimprinting. *ACS Nano*, 9(2):1305–1314, 2015.

[8] H. Kasugai, Y. Miyake, A. Honshio, S. Mishima, T. Kawashima, K. Iida, M. Iwaya, S. Kamiyama, H. Amano, I. Akasaki, H. Kinoshita, and H. Shiomi. High-efficiency nitride-based light-emitting diodes with moth-eye structure. *Jpn. J. Appl. Phys.*, 44(10): 7414–7417, 2005.

[9] H. Savin, P. Repo, G. von Gastrow, P. Ortega, E. Calle, M. Garín, and R. Alcubilla. Black silicon solar cells with interdigitated back-contacts achieve 22.1% efficiency.

Nat. Nanotechnol., 10:624–628, 2015.

[10] C. G. Bernhard. Structural and functional adaptation in a visual system. *Endeavour*, 16 (98):79–84, 1967.

[11] M. L. Hammock, A. Chortos, B. C.-K. Tee, J. B.-H. Tok, and Z. Bao. 25th anniversary article: The evolution of electronic skin (e-skin): A brief history, design considerations, and recent progress. *Adv. Mater.*, 25(42):5997–6038, 2013.

[12] C. Pang, J. H. Koo, A. Nguyen, J. M. Caves, M.-G. Kim, A. Chortos, K. Kim, P. J. Wang, J. B.-H. Tok, and Z. Bao. Highly skin-conformal microhairy sensor for pulse signal amplification. *Adv. Mater.*, 27(4):634–640, 2015.

[13] D.-H. Kim, J. Viventi, J. J. Amsden, J. Xiao, L. Vigeland, Y.-S. Kim, J. A. Blanco, B. Panilaitis, E. S. Frechette, D. Contreras, D. L. Kaplan, F. G. Omenetto, Y. Huang, K.-C. Hwang, M. R. Zakin, B. Litt, and J. A. Rogers. Dissolvable films of silk fibroin for ultrathin conformal bio-integrated electronics. *Nat. Mater.*, 9:511–517, 2010.

[14] T.-I Kim, J. G. McCall, Y. H. Jung, X. Huang, E. R. Siuda, Y. Li, J. Song, Y. M. Song, H. A. Pao, R.-H. Kim, C. Lu, S. D. Lee, I.-S. Song, G. Shin, R. Al-Hasani, S. Kim, M. P. Tan, Y. Huang, F. G. Omenetto, J. A. Rogers, and M. R. Bruchas. Injectable, cellular-scale optoelectronics with applications for wireless optogenetics. *Science*, 340 (6129):211–216, 2013.

[15] S. Keten, Z. Xu, B. Ihle, and M. J. Buehler. Nanoconfinement controls stiffness, strength and mechanical toughness of β-sheet crystals in silk. *Nat. Mater.*, 9:359–367, 2010.

[16] J. N. Anker, W. Paige Hall, O. Lyandres, N. C. Shah, J. Zhao, and R. P. Van Duyne. Biosensing with plasmonic nanosensors. *Nat. Mater.*, 7:442–453, 2008.

[17] H. H. Nguyen, J. Park, S. Kang, and M. Kim. Surface plasmon resonance: A versatile technique for biosensor applications. *Sensors*, 15(5):10481–10510, 2015.

[18] M. Fleischmann and P. J. Hendra and. A. J. McQuillan. Raman spectra of pyridine adsorbed at a silver electrode. *Chem. Phys. Lett.*, 26(2):163–166, 1974.

[19] S. Schlücker. Surface-enhanced raman spectroscopy: Concepts and chemical applications. *Angew. Chem. Int. Ed.*, 53(19):4756–4795, 2014.

[20] A. Hartstein, J. R. Kirtley, and J. C. Tsang. Enhancement of the infrared absorption from molecular monolayers with thin metal overlayers. *Phys. Rev. Lett.*, 45(3):201–204, 1980.

[21] K. Ataka and J. Heberle. Biochemical applications of surface-enhanced infrared absorption spectroscopy. *Anal. Bioanal. Chem.*, 388(1):47–54, 2007.

[22] L. Rayleigh. On reflection of vibrations at the confines of two media between which the transition is gradual. *Proc. Lond. Math. Soc.*, 1(1):51–56, 1879.

[23] R. P. Feynman, R. B. Leighton, and M. Sands. *Mainly mechanics, radiation, and heat*, volume 1 of *The Feynman Lectures on Physics*. Addison-Wesley Pub. Co., Reading, Mass., USA, 1964.

[24] E. Hecht. *Optics*. Addison-Wesley Pub. Co., London, UK, 4th edition, 2002.

[25] H. K. Raut, V. A. Ganesh, A. S. Nair, and S. Ramakrishna. Anti-reflective coatings: A critical, in-depth review. *Energy Environ. Sci.*, 4(10):3779–3804, 2011.

[26] R. Brunner, O. Sandfuchs, C. Pacholski, C. Morhard, and J. Spatz. Lessons from nature: Biomimetic subwavelength structures for high-performance optics. *Laser Photon. Rev.*, 6(5):641–659, 2012.

[27] E. R. Martins, J. Li, YK. Liu, V. Depauw, Z. Chen, J. Zhou, and T. F. Krauss. Deterministic quasi-random nanostructures for photon control. *Nat. Commun.*, 4:2665, 2013.

[28] H. Angus Macleod. *Thin-Film Optical Filters*. Series in Optics and Optoelectronics. CRC Press, Boca Raton, FL, USA, 4th edition, 2010.

[29] I. G. Kavakli and K. Kantarli. Single and double-layer antireflection coatings on silicon. *Turk. J. Phys.*, 26:349–354, 2002.

[30] S. Chattopadhyay, Y. F. Huang, Y. J. Jen, A. Ganguly, K. H. Chen, and L. C. Chen. Anti-reflecting and photonic nanostructures. *Mater. Sci. Eng. R-Rep*, 69(1–3):1–35, 2010.

[31] D. N. Wright, E. S. Marstein, and A. Holt. Double layer anti-reflective coatings for silicon solar cells. In *Conference Record of the Thirty-first IEEE Photovoltaic Specialists Conference*, pages 1237–1240, 2005.

[32] S. Duttagupta, F. Ma, B. Hoex, T. Mueller, and A. G. Aberle. Optimised antireflection coatings using silicon nitride on textured silicon surfaces based on measurements and multidimensional modelling. *Energy Procedia*, 15:78–83, 2012.

[33] B. Sopori. Silicon nitride processing for control of optical and electronic properties of silicon solar cells. *J. Electron. Mater.*, 32(10):1034–1042, 2003.

[34] J.-Q. Xi, J. K. Kim, and E. F. Schubert. Silica nanorod-array films with very low refractive indices. *Nano Lett.*, 5(7):1385–1387, 2005.

[35] J.-Q. Xi, M. F. Schubert, J. K. Kim, E. F. Schubert, M. Chen, S.-Y. Lin, W. Liu, and J. A. Smart. Optical thin-film materials with low refractive index for broadband elimination of Fresnel reflection. *Nat. Photon.*, 1:176–179, 2007.

[36] T. C. Choy. *Effective Medium Theory: Principles and Applications*. Oxford University Press, Oxford, UK, 2nd edition, 2016.

[37] J. C. Maxwell Garnett. Colours in metal glasses and in metallic films. *Philos. Trans. R. Soc. London, Ser. A*, 203:385–420, 1904.

[38] J. C. Maxwell Garnett. Colours in metal glasses, in metallic films, and in metallic solutions. II. *Philos. Trans. R. Soc. London, Ser. A*, 205:237–288, 1906.

[39] D. A. G. Bruggeman. Berechnung verschiedener physikalischer konstanten von heterogenen substanzen. I. Dielektrizitätskonstanten und leitfähigkeiten der mischkörper aus isotropen substanzen. *Ann. Phys.*, 416(7):636–664, 1935.

[40] F. J. Milford, J. R. Reitz, and R. W. Christy. *Foundations of Electromagnetic Theory*. Addison-Wesley Pub. Co., Reading, Mass. USA, 4th edition, 2008.

[41] M. A. Green. Self-consistent optical parameters of intrinsic silicon at 300 K including temperature coefficients. *Sol. Energ. Mat. Sol. Cells*, 92(11):1305–1310, 2008.

[42] I. H. Malitson. Interspecimen comparison of the refractive index of fused silica. *J. Opt. Soc. Am.*, 55(10):1205–1209, 1965.

[43] W. H. Southwell. Gradient-index antireflection coatings. *Opt. Lett.*, 8(11):584–586, 1983.

[44] D. Poitras and J. A. Dobrowolsk. Toward perfect antireflection coatings. 2. Theory. *Appl. Opt.*, 43(6):1286–1295, 2004.

[45] C. C. Striemer and P. M. Fauchet. Dynamic etching of silicon for broadband antireflection applications. *Appl. Phys. Lett.*, 81(16):2980–2982, 2002.

[46] H.-C. Chang, K.-Y. Lai, Y.-A. Dai, H.-H. Wang, C.-A. Lin, and J.-H. He. Nanowire arrays with controlled structure profiles for maximizing optical collection efficiency. *Energy Environ. Sci.*, 4(8):2863–2869, 2011.

[47] D. Chen. Anti-reflection (AR) coatings made by sol–gel processes: A review. *Sol. Energ. Mat. Sol. Cells*, 68(3-4):313–336, 2001.

[48] S. Walheim, E. Schäffer, J. Mlynek, and U. Steiner. Nanophase-separated polymer films as high-performance antireflection coatings. *Science*, 283(5401):520–522, 1999.

[49] V. Torres-Costa and R. J. Martín-Palma. Application of nanostructured porous silicon in the field of optics. A review. *J. Mater. Sci.*, 45(11):2823–2838, 2010.

[50] Z. Huang, N. Geyer, P. Werner amd J. de Boor, and U. Gösele. Metal-assisted chemical etching of silicon: A review. *Adv. Matter.*, 23(2):285–308, 2011.

[51] K. Peng, Y. Xu, Y. Wu Y. Yan, S.-T. Lee, and J. Zhu. Aligned single-crystalline si nanowire arrays for photovoltaic applications. *Small*, 1:1062–1067, 2005.

[52] J. Oh, H.-C. Yuan, and H. M. Branz. An 18.2%-efficient black-silicon solar cell achieved through control of carrier recombination in nanostructures. *Nat. Nanotech.*, 7: 743–748, 2012.

[53] A. Barranco, A. Borras, A. R. Gonzalez-Elipe, and A. Palmero. Perspectives on oblique angle deposition of thin films: From fundamentals to devices. *ACS Nano*, 76:59–153, 2016.

[54] Y.-F. Huang, S. Chattopadhyay, Y.-J. Jen, C.-Y. Peng, T.-A. Liu, Y.-K. Hsu, C.-L. Pan, H.-C. Lo, C.-H. Hsu, Y.-H. Chang, C.-S. Lee, K.-H. Chen, and L.-C. Chen. Improved broadband and quasi-omnidirectional anti-reflection properties with biomimetic silicon nanostructures. *Nat. Nanotech.*, 2:770–774, 2007.

[55] K.-C. Park, H. J. Choi, C.-H. Chang, R. E. Cohen, G. H. McKinley, and G. Barbastathis. Nanotextured silica surfaces with robust superhydrophobicity and omnidirectional broadband supertransmissivity. *ACS Nano*, 6(5):3789–3799, 2012.

[56] E. P. Ivanova, J. Hasan, H. K. Webb, G. Gervinskas, S. Juodkazis, V. K. Truong, A. H. F. Wu, R. N. Lamb, V. A. Baulin, G. S. Watson, J. A. Watson, D. E. Mainwaring, and R. J. Crawford. Bactericidal activity of black silicon. *Nat. Commun.*, 4:2838, 2013.

[57] P. Spinelli, M. A. Verschuuren, and A. Polman. Broadband omnidirectional antireflection coating based on subwavelength surface Mie resonators. *Nat. Commun.*, 3:692, 2012.

[58] D. M. Callahan, J. N. Munday, and H. A. Atwater. Solar cell light trapping beyond the ray optic limit. *Nano Lett.*, 12(1):214–218, 2012.

[59] S. Mokkapati and K. R. Catchpole. Nanophotonic light trapping in solar cells. *J. Appl. Phys.*, 112(10):101101, 2012.

[60] A. Shah, P. Torres1, R. Tscharner, N. Wyrsch, and H. Keppner. Photovoltaic technology: The case for thin-film solar cells. *Science*, 285(5428):692–698, 1999.

[61] R. Brendel. *Thin-Film Crystalline Silicon Solar Cells: Physics and Technology*. W1LEY-VCH Verlag GmbH & Co. KGaA, Weinheim, Germany, 2003.

[62] P. Kowalczewski, A. Bozzola, M. Liscidini, and L. C. Andreani. Light trapping and electrical transport in thin-film solar cells with randomly rough textures. *J. Appl. Phys.*, 115(19):194504, 2014.

[63] P. Kuang, S. Eyderman, M.-L. Hsieh, A. Post, S. John, and S.-Y Lin. Achieving an accurate surface profile of a photonic crystal for near-unity solar absorption in a super thin-film architecture. *ACS Nano*, 10(6):6116–6124, 2016.

[64] P. Spinelli, M. A. Verschuuren, and A. Polman. Broadband omnidirectional antireflection coating based on subwavelength surface Mie resonators. *Nat. Commun.*, 3:692, 2012.

[65] L. Zeng, P. Bermel, Y. Yi, B. A. Alamariu, K. A. Broderick, J. Liu, C. Hong, X. Duan, J. Joannopoulos, and L. C. Kimerling. Demonstration of enhanced absorption in thin film Si solar cells with textured photonic crystal back reflector. *Appl. Phys. Lett*, 93 (22):221105, 2008.

[66] K. X. Wang, Z. Yu, V. Liu, Y. Cui, and S. Fan. Absorption enhancement in ultrathin crystalline silicon solar cells with antireflection and light-trapping nanocone gratings. *Nano Lett.*, 12(3):1616–1619, 2012.

[67] A. Chutinan and S. John. Light trapping and absorption optimization in certain thin-film photonic crystal architectures. *Phys. Rev. A*, 78(2):023825, 2008.

[68] M. L. Brongersma, Y. Cui, and S. Fan. Light management for photovoltaics using high-index nanostructures. *Nat. Matter.*, 13:451–460, 2014.

[69] A. Hessel and A. A. Oliner. A new theory of Wood's anomalies on optical gratings. *Appl. Opt.*, 4(10):1275–1297, 1965.

[70] A. Oskooi, P. A. Favuzzi, Y. Tanaka, H. Shigeta, Y. Kawakami, and S. Noda. Partially disordered photonic-crystal thin films for enhanced and robust photovoltaics. *Appl. Phys. Lett.*, 100(18):181110, 2012.

[71] J. Li, K. Li, C. Schuster, R. Su, X. Wang, B.-H. V. Borges, T. F. Krauss, and E. R. Martins. Spatial resolution effect of light coupling structures. *Sci. Rep.*, 5:18500, 2015.

[72] M. Otto, M. Algasinger, H. Branz, B. Gesemann, T. Gimpel, K. Füchsel, S. Kontermann T. Ksebier, S. Koynov, X. Li, V. Naumann, J. Oh, A. N. Sprafke, J. Ziegler, M. Zilk, and R. B. Wehrspohn. Black silicon photovoltaics. *Adv. Opt. Mater.*, 3(2):147–164, 2014.

[73] E. Yablonovitch. Statistical ray optics. *J. Opt. Soc. Am.*, 72(7):899–907, 1982.

[74] P. Campbell and M. A. Green. Light trapping properties of pyramidally textured surfaces. *J. Appl. Phys.*, 62(1):243–249, 1987.

[75] Z. Yu, A. Raman, and S. Fan. Fundamental limit of nanophotonic light trapping in solar cells. *Proc. Natl. Acad. Sci. U.S.A.*, 107(41):17491–17496, 2010.

[76] D. B. Lee. Anisotropic etching of silicon. *J. Appl. Phys.*, 40(11):4569–4574, 1969.

[77] D. L. King and M. E. Buck. Experimental optimization of an anisotropic etching process for random texturization of silicon solar cells. In *The Conference Record of the Twenty-Second IEEE Photovoltaic Specialists Conference - 1991*, pages 303–308 vol.1, 1991.

[78] P. Papet, O. Nichiporuk, A. Kaminski, Y.Rozier, J. Kraiem, J.-F. Lelievre, A. Chaumartin, A. Fave, and M. Lemiti. Pyramidal texturing of silicon solar cell with TMAH chemical anisotropic etching. *Sol. Energ. Mat. Sol. Cells*, 90(15):2319–2328, 2006.

[79] Y. Fan, P. Han, P. Liang, Y. Xing, Z. Ye, and S. Hu. Differences in etching characteristics of TMAH and KOH on preparing inverted pyramids for silicon solar cells. *Appl. Surf. Sci.*, 264:761–766, 2013.

[80] Y. Wang, L. Yang, Y. Liu, Z. Mei, W. Chen, J. Li, H. Liang A. Kuznetsov, and D. Xiaolong. Maskless inverted pyramid texturization of silicon. *Sci. Rep.*, 5:10843, 2015.

[81] A. W. Smith and A. Rohatgi. A new texturing geometry for producing high efficiency solar cells with no antireflection coatings. *Sol. Energ. Mat. Sol. Cells*, 29(1):51–65, 1993.

[82] X. Liu, P. R. Coxon, M. Peters, B. Hoex, J. M. Cole, and D. J. Fray. Black silicon: Fabrication methods, properties and solar energy applications. *Energy Environ. Sci.*, 7 (10):3223–3263, 2014.

[83] M. A. Juntunen, J. Heinonen, V. Vähänissi, P. Repo, D. Valluru, and H. Savin. Near-unity quantum efficiency of broadband black silicon photodiodes with an induced junction. *Nat. Photon.*, 10:777–781, 2016.

[84] M. Steglich, M. Oehme, T. Käsebier, M. Zilk, K. Kostecki, E.-B. Kley, J. Schulze, and A. Tünnermann. Ge-on-Si photodiode with black silicon boosted responsivity. *Appl. Phys. Lett.*, 102(5):051103, 2015.

[85] J. Oh, T. G. Deutsch, H.-C. Yuan, and H. M. Branz. Nanoporous black silicon photocathode for H_2 production by photoelectrochemical water splitting. *Energy Environ.*

Sci., 4(5):1690–1694, 2011.

[86] G. Gervinskas, G. Seniutinas, J. S. Hartley, S. Kandasamy, P. R. Stoddart, N. F. Fahim, and S. Juodkazis. Surface-enhanced Raman scattering sensing on black silicon. *Ann. Phys. (Berlin)*, 525(12):907–914, 2013.

[87] G. Seniutinas, G. Gervinskas, R. Verma, B. D. Gupta, F. Lapierre, P. R. Stoddart, F. Clark, S. L. McArthur, and S. Juodkazis. Versatile SERS sensing based on black silicon. *Opt. Express*, 23(5):6763–6772, 2015.

[88] M. Ge, X. Fang, J. Rong, and C. Zhou. Review of porous silicon preparation and its application for lithium-ion battery anodes. *Nanotechnology*, 24(42):1266–1277, 2013.

[89] C. Chiappini, E. De Rosa, J. O. Martinez, X. Liu, J. Steele, M. M. Stevens, and E. Tasciotti. Biodegradable silicon nanoneedles delivering nucleic acids intracellularly induce localized *in vivo* neovascularization. *Nat. Mater.*, 14:532–539, 2015.

[90] J.-H. Park, L. Gu, G. von Maltzahn, E. Ruoslahti, S. N. Bhatia, and M. J. Sailor. Biodegradable luminescent porous silicon nanoparticles for *in vivo* applications. *Nat. Mater.*, 8:331–336, 2009.

[91] E. J. Anglin, L. Cheng, W. R. Freeman, and M. J. Sailor. Porous silicon in drug delivery devices and materials. *Adv. Drug Deliv. Rev.*, 60(11):1266–1277, 2008.

[92] M. Barberoglou, V. Zorba, A. Pagozidis, C. Fotakis, and E. Stratakis. Electrowetting properties of micro/nanostructured black silicon. *Langmuir*, 26(15):13007–13014, 2010.

[93] J. O. Lee, V. Narasimhan, J. Du, B. Ndjamen, D. Sretavan, and H. Choo. Biocompatible multifunctional black-silicon for implantable intraocular sensor. *Adv. Healthcare Mat.*, 6(4):1601356, 2017.

[94] O. Bisi, S. Ossicini, and L. Pavesi. Porous silicon: A quantum sponge structure for silicon based optoelectronics. *Surf. Sci. Rep.*, 38(1-3):1–126, 2000.

[95] X. Li and P. W. Bohn. Metal-assisted chemical etching in HF/H_2O_2 produces porous silicon. *Appl. Phys. Lett.*, 77(16):2572, 2000.

[96] J. I. Gittleman, E. K. Sichel, H. W. Lehmann, and R. Widmer. Textured silicon: A selective absorber for solar thermal conversion. *Appl. Phys. Lett.*, 35(10):742–744, 1979.

[97] H. Jansen, M. de Boer, R. Legtenberg, and M. Elwenspoek. The black silicon method: A universal method for determining the parameter setting of a fluorine-based reactive ion etcher in deep silicon trench etching with profile control. *J. Micromech. Microeng.*, 5(2):115–120, 1995.

[98] C.-H. Hsu, H.-C. Lo, C.-F. Chen, C. T. Wu, J.-S. Hwang, D. Das, J. Tsai, L.-C. Chen, and K.-H. Chen. Generally applicable self-masked dry etching technique for nanotip array fabrication. *Nano Lett.*, 4(3):471–475, 2004.

[99] T.-H. Her, R. J. Finlay, C. Wu, S. Deliwala, and E. Mazur. Microstructuring of silicon with femtosecond laser pulses. *Appl. Phys. Lett.*, 73(12):1673, 1998.

[100] A. Y. Vorobyev and C. Guo. Direct femtosecond laser surface nano/microstructuring and its applications. *Laser Photon. Rev.*, 7(3):385–407, 2013.

[101] C. M. Bhadra, M. Werner, V. A. Baulin, V. K. Truong, M. Al Kobaisi, S. H. Nguyen, A. Balčytis, S. Juodkazis, J. Y. Wang, D. E. Mainwaring, R. J. Crawford, and E. P. Ivanova. Subtle variations in surface properties of black silicon surfaces influence the degree of bactericidal efficiency. *Nano-Micro Lett.*, 10(2):36, 2018.

[102] Y. Xia, B. Liu, S. Zhong, and C. Li. X-ray photoelectron spectroscopic studies of black silicon for solar cell. *J. Electron. Spectrosc. Relat. Phenom.*, 184(11–12):589–592, 2012.

[103] D. F. Edwards. Silicon (Si). In E. D. Palik, editor, *Handbook of Optical Constants of Solids*, pages 547–569. Academic Press, Burlington, Mass., USA, 1997.

[104] A. Ashkin. Acceleration and trapping of particles by radiation pressure. *Phys. Rev. Lett.*, 24(4):156–159, 1970.

[105] A. Ashkin, J. M. Dziedzic, J. E. Bjorkholm, and S. Chu. Observation of a single-beam gradient force optical trap for dielectric particles. *Opt. Lett.*, 11(5):288–290, 1986.

[106] K. C. Neuman and S. M. Block. Optical trapping. *Rev. Sci. Instrum.*, 75(9):2787–2809, 2004.

[107] W. D. Phillips. Nobel lecture: Laser cooling and trapping of neutral atoms. *Rev. Mod. Phys.*, 70(3):721–741, 1998.

[108] A. Ashkin, J. M. Dziedzic, and T. Yamane. Optical trapping and manipulation of single cells using infrared laser beams. *Nature*, 330:769–771, 1987.

[109] A. Ashkin and J. M. Dziedzic. Optical trapping and manipulation of viruses and bacteria. *Science*, 235(4795):1517–1520, 1987.

[110] K. Svoboda and S. M. Block. Optical trapping of metallic Rayleigh particles. *Opt. Lett.*, 19(13):930–932, 1994.

[111] L. Jauffred, A. C. Richardson, and L. B. Oddershede. Three-dimensional optical control of individual quantum dots. *Nano Lett.*, 8(10):3376–3380, 2008.

[112] O. M. Maragò, P. H. Jones, P. G. Gucciardi, G. Volpe, and A. C. Ferrari. Optical trapping and manipulation of nanostructures. *Nat. Nanotechnol.*, 8:807–819, 2013.

[113] T. Shoji, A. Mototsuji, A. Balčytis, D. Linklater, S. Juodkazis, and Y. Tsuboi. Optical tweezing and binding at high irradiation powers on black-Si. *Sci. Rep.*, 7:12298, 2017.

[114] A. N. Grigorenko, N. W. Roberts, M. R. Dickinson, and Y. Zhang. Nanometric optical tweezers based on nanostructured substrates. *Nat. Photon.*, 2:365–370, 2008.

[115] M. L. Juan, M. Righini, and R. Quidant. Plasmon nano-optical tweezers. *Nat. Photon.*, 5:349–356, 2011.

[116] T. Shoji and Y. Tsuboi. Plasmonic optical tweezers toward molecular manipulation: Tailoring plasmonic nanostructure, light source, and resonant trapping. *J. Phys. Chem. Lett.*, 5(17):2957–2967, 2014.

[117] D. G. Kotsifaki, M. Kandyla, and P. G. Lagoudakis. Near-field enhanced optical tweezers utilizing femtosecond-laser nanostructured substrates. *Appl. Phys. Lett.*, 107 (21):211111, 2015.

[118] D. G. Kotsifaki, M. Kandyla, and P. G. Lagoudakis. Plasmon enhanced optical tweezers with gold-coated black silicon. *Sci. Rep.*, 6:26275, 2016.

[119] M. L. Juan, R. Gordon, Y. Pang, F. Eftekhari, and R. Quidant. Self-induced back-action optical trapping of dielectric nanoparticles. *Nat. Phys.*, 5:915–919, 2009.

[120] L. Neumeier, R. Quidant, and D. E. Chang. Self-induced back-action optical trapping in nanophotonic systems. *New J. Phys.*, 17:123008, 2015.

[121] B. J. Roxworthy, A. M. Bhuiya, S. P. Vanka, and K. C. Toussaint Jr. Understanding and controlling plasmon-induced convection. *Nat. Commun.*, 5:3173, 2014.

[122] T. Shoji, M. Shibata, N. Kitamura, F. Nagasawa, M. Takase, K. Murakoshi, A. Nobuhiro, Y. Mizumoto, H. Ishihara, and Y. Tsuboi. Reversible photoinduced formation and manipulation of a two-dimensional closely packed assembly of polystyrene nanospheres on a metallic nanostructure. *J. Phys. Chem. C*, 117(6):2500–2506, 2013.

[123] P. Mestres, J. Berthelot, S. S. Aćimović, and R. Quidant. Unraveling the optomechanical nature of plasmonic trapping. *Light Sci. Appl.*, 5:e16092, 2016.

[124] M. Toshimitsu, Y. Matsumura, T. Shoji, N. Kitamura, M. Takase, K. Murakoshi, H. Yamauchi, S. Ito, H. Miyasaka, A. Nobuhiro, Y. Mizumoto, H. Ishihara, and Y. Tsuboi. Metallic-nanostructure-enhanced optical trapping of flexible polymer chains in aqueous solution as revealed by confocal fluorescence microspectroscopy. *J. Phys. Chem. C*, 116(27):14610–14618, 2012.

[125] A. R. Jha. *Infrared Technology: Applications to Electro-Optics, Photonic Devices and Sensors*. John Wiley & Sons, New York, NY, USA, 2000.

[126] B. Schwarz. LIDAR: Mapping the world in 3D. *Nat. Photon.*, 4:429–430, 2010.

[127] K. Zang, X. Jiang, Y. Huo, X. Ding, M. Morea, X. Chen, C.-Y. Lu, J. Ma, M. Zhou, Z. Xia, Z. Yu, T. I. Kamins, Q. Zhang, and J. S. Harris. Silicon single-photon avalanche diodes with nano-structured light trapping. *Nat. Commun.*, 8:628, 2017.

[128] D. K. Schroder, R. Noel Thomas, and J. C. Swartz. Free carrier absorption in silicon. *IEEE J. Solid-State Circuits*, 13(1):180–187, 1978.

[129] B. M. Walsh, H. R. Lee, and N. P. Barnes. Mid infrared lasers for remote sensing applications. *J. Lumin.*, 169(B):400–405, 2016.

[130] V. Jokinen, L. Sainiemi, and S. Franssila. Complex droplets on chemically modified silicon nanograss. *J. Mater. Chem.*, 20(18):3453–3456, 2008.

[131] Y. Li, J. Zhang, S. Zhu, H. Dong, Z. Wang, Z. Sun, J. Guo, and B. Yang. Bioinspired silicon hollow-tip arrays for high performance broadband anti-reflective and water-repellent coatings. *J. Mater. Chem.*, 19(13):1806–1810, 2009.

[132] M. Stubenrauch, M. Fischer, C. Kremin, S. Stoebenau, A. Albrecht, and O. Nagel. Black silicon - new functionalities in microsystems. *J. Micromech. Microeng.*, 16(6):

S82, 2006.

[133] Y.-L. Deng and Y.-J. Juang. Black silicon SERS substrate: Effect of surface morphology on SERS detection and application of single algal cell analysis. *Biosens. Bioelectron.*, 53:37–42, 2014.

[134] J. Gao, M. de Raad, B. P. Bowen, R. N. Zuckermann, and T. R. Northen. Application of black silicon for nanostructure-initiator mass spectrometry. *Anal. Chem.*, 88(3): 1625–1630, 2016.

[135] M. Steglich, T. Käsebier, M. Zilk, T. Pertsch, E.-B. Kley, and A. Tünnermann. The structural and optical properties of black silicon by inductively coupled plasma reactive ion etching. *J. Appl. Phys.*, 116(17):173503, 2014.

[136] Z. R. Chowdhury, J. Y. Y. Loh, Md. Nishanto Nahid Pishon, and N. P. Kherani. Black silicon morphologies using conventional RIE processing. *AIP Adv.*, 7(5):055115, 2017.

[137] A. Balčytis, M. Ryu, G. Seniutinas, Y. Nishijima, Y. Hikima, M. Zamengo, R. Petruškevičius, J. Morikawa, and S. Juodkazis. Si-based infrared optical filters. *Opt. Eng.*, 54 (12):127103, 2015.

[138] K. Richter, C. Kubasch, and J.-W. Bartha. Micro-patterned silicon surfaces for biomedical devices. *Plasma Process. Polym.*, 4(S1):S411–S415, 2007.

[139] G. Sun, T. Gao, X. Zhao, and H. Zhang. Fabrication of micro/nano dual-scale structures by improved deep reactive ion etching. *J. Micromech. Microeng.*, 20(7):075028, 2010.

[140] X. Zhang, Q. Di, F. Zhu, G. Sun, and H. Zhang. Wideband anti-reflective micro/nano dual-scale structures: Fabrication and optical properties. *Micro Nano Lett.*, 6(11): 947–950, 2011.

[141] M. Spinner, A. Kovalev, S. N. Gorb, and G. Westhoff. Snake velvet black: Hierarchical micro- and nanostructure enhances dark colouration in *Bitis rhinoceros*. *Sci. Rep.*, 3: 1846, 2013.

[142] Y. Xiu, Y. Liu, D. W. Hess, and C. P. Wong. Mechanically robust superhydrophobicity on hierarchically structured Si surfaces. *Nanotechnology*, 21(15):155705, 2010.

[143] D. Qi, N. Lu, H. Xu, B. Yang, C. Huang, M. Xu, L. Gao, Z. Wang, and L. Chi. Simple approach to wafer-scale self-cleaning antireflective silicon surfaces. *Langmuir*, 25(14): 7769–7772, 2009.

[144] K. Kim, Y. Song, and J. Oh. Nano/micro dual-textured antireflective subwavelength structures in anisotropically etched gaas. *Opt. Lett.*, 42(16):3105–3108, 2017.

[145] P. Fan, B. Bai, M. Zhong, H. Zhang, J. Long, J. Han, W. Wang, and G. Jin. General strategy toward dual-scale-controlled metallic micro–nano hybrid structures with ultralow reflectance. *ACS Nano*, 11(7):7401–7408, 2017.

[146] Y. Nishijima, R. Komatsu, S. Ota, G. Seniutinas, A. Balčytis, and S. Juodkazis. Antireflective surfaces: Cascading nano/microstructuring. *APL Photonics*, 1(7):076104, 2016.

[147] M. A. Green. Commercial progress and challenges for photovoltaics. *Nat. Energy*, 1:

15015, 2016.

[148] K. Yoshikawa, H. Kawasaki, W. Yoshida, T. Irie, K. Konishi, K. Nakano, T. Uto, D. Adachi, M. Kanematsu, H. Uzu, and K. Yamamoto. Silicon heterojunction solar cell with interdigitated back contacts for a photoconversion efficiency over 26%. *Nat. Energy*, 2:17032, 2017.

[149] W. Shockley and H. J. Queisser. Detailed balance limit of efficiency of *p-n* junction solar cells. *J. Appl. Phys.*, 32(3):510–519, 1961.

[150] ASTM G173-03(2012). Standard tables for reference solar spectral irradiances: Direct normal and hemispherical on 37° tilted surface. Standard, ASTM International, West Conshohocken, PA, USA, 2012.

[151] M. A. Green and S. P. Bremner. Energy conversion approaches and materials for high-efficiency photovoltaics. *Nat. Mater.*, 16:23–34, 2017.

[152] J. R. Sootsman, D. Y. Chung, and M. G. Kanatzidis. New and old concepts in thermoelectric materials. *Angew. Chem. Int. Ed.*, 48(46):8616–8639, 2009.

[153] X. Zhang and L.-D. Zhao. Thermoelectric materials: Energy conversion between heat and electricity. *J. Materiomics.*, 1(2):92–105, 2015.

[154] C. B. Vining. An inconvenient truth about thermoelectrics. *Nat. Mater.*, 8:83–85, 2009.

[155] D. Kraemer, B. Poude, H.-P. Feng, J. Christopher Caylor, B. Yu X. Yan, Y. Ma, X. Wang, D. Wang, A. Muto, K. McEnaney, M. Chiesa, Z. Ren, and G. Chen. High-performance flat-panel solar thermoelectric generators with high thermal concentration. *Nat. Mater.*, 10:532–538, 2011.

[156] R. R. Furlong and E. J. Wahlquist. U.S. space missions using radioisotope power systems. *Nucl. News*, 42:26–34, 1999.

[157] B. Orr, A. Akbarzadeh, M. Mochizuki, and R. Singh. A review of car waste heat recovery systems utilising thermoelectric generators and heat pipes. *Appl. Therm. Eng.*, 101:490–495, 2016.

[158] S. C. Baker-Finch, K. R. McIntosh, D. Yan, K. Chern Fong, and T. C. Kho. Near-infrared free carrier absorption in heavily doped silicon. *J. Appl. Phys.*, 116(6):063106, 2014.

[159] C. H. Crouch, J. E. Carey, M. Shen, E. Mazur, and F. Y. Génin. Infrared absorption by sulfur-doped silicon formed by femtosecond laser irradiation. *Appl. Phys. A*, 79(7): 1635–1641, 2004.

[160] T. G. Kim, J. M. Warrender, and M. J. Aziz. Strong sub-band-gap infrared absorption in silicon supersaturated with sulfur. *Appl. Phys. Lett.*, 88(24):241902, 2006.

[161] K. R. Catchpole and A. Polman. Plasmonic solar cells. *Opt. Express*, 16(26):21793–21800, 2008.

[162] S.-S. Kim, S.-I. Na, J. Jo, D.-Y. Kim, , and Y.-C. Nah. Plasmon enhanced performance of organic solar cells using electrodeposited Ag nanoparticles. *Appl. Phys. Lett.*, 93(7): 073307, 2008.

[163] X. Li, W. C. H. Choy, L. Huo, F. Xie, W. E. I. Sha, B. Ding, X. Guo, Y. Li, J. Hou, J. You, and Y. Yang. Dual plasmonic nanostructures for high performance inverted organic solar cells. *Appl. Phys. Lett.*, 24(22):3046–3052, 2012.

[164] V. E. Ferry, L. A. Sweatlock, D. Pacifici, and H. A. Atwater. Plasmonic nanostructure design for efficient light coupling into solar cells. *Appl. Phys. Lett.*, 8(12):4391–4397, 2008.

[165] V. E. Ferry, J. N. Munday, and H. A. Atwater. Design considerations for plasmonic photovoltaics. *Adv. Mater.*, 22:4794–4808, 2010.

[166] V. E. Ferry, M. A. Verschuuren, H. B. T. Li, E. Verhagen, R. J. Walters, R. E. I. Schropp, H. A. Atwater, and A. Polman. Light trapping in ultrathin plasmonic solar cells. *Opt. Express*, 18(S2):A237–A245, 2010.

[167] R. Komatsu, A. Balčytis, G. Seniutinas T. Yamamura, Y. Nishijima, and S. Juodkazis. Plasmonic photo-thermoelectric energy converter with black-Si absorber. *Sol. Energ. Mater. Sol. Cells*, 143:72–77, 2015.

[168] S. J. Barrow, A. M. Funston, D. E. Gómez, T. J. Davis, and P. Mulvaney. Surface plasmon resonances in strongly coupled gold nanosphere chains from monomer to hexamer. *Nano Lett.*, 11(10):4180–4187, 2011.

[169] K. C. Vernon, A. M. Funston, C. Novo, D. E. Gómez, P. Mulvaney, and T. J. Davis. Influence of particle-substrate interaction on localized plasmon resonances. *Nano Lett.*, 10(6):2080–2086, 2010.

[170] N. Wang, L. Han, H. He, N.-H. Park, and K. Koumoto. A novel high-performance photovoltaic–thermoelectric hybrid device. *Energy Environ. Sci.*, 4(9):3676–3679, 2011.

[171] T. Park, J. Na, B. Kim, Y. Kim, H. Shin, and E. Kim. Photothermally activated pyroelectric polymer films for harvesting of solar heat with a hybrid energy cell structure. *ACS Nano*, 9(12):11830–11839, 2015.

[172] Z. Liu, B. Sun, Y. Zhong, X. Liu, J. Han, T. Shi, Z. Tang, and G. Liao. Novel integration of carbon counter electrode based perovskite solar cell with thermoelectric generator for efficient solar energy conversion. *Nano Energy*, 38:457–466, 2017.

[173] Y. Nishijima, R. Komatsu, T. Yamamura, A. Balčytis, G. Seniutinas, and S. Juodkazis. Design concept of a hybrid photo-voltaic/thermal conversion cell for mid-infrared light energy harvester. *Opt. Mater. Express*, 7(11):3484–3493, 2015.

[174] G. He and H. A. Atwater. Interband transitions in $\mathrm{Sn}_x\mathrm{Ge}_{1-x}$ alloys. *Phys. Rev. Lett.*, 79 (10):1937–1940, 1997.

[175] C. Sanchez, H. Arribart, and M. M. Giraud Guille. Biomimetism and bioinspiration as tools for the design of innovative materials and systems. *Nat. Mater.*, 4:277–288, 2005.

[176] F. G. Omenetto and D. L. Kaplan. A new route for silk. *Nat. Photon.*, 2:641–643, 2008.

[177] M. S. Dodd, D. Papineau, T. Grenne, J. F. Slack, M. Rittner, F. Pirajno, J. O'Neil, and C. T. S. Little. Evidence for early life in Earth's oldest hydrothermal vent precipitates.

Nature, 543:60–64, 2017.

[178] D. L. Stern. The genetic causes of convergent evolution. *Nat. Rev. Genet.*, 14:87–110, 2013.

[179] B. Bhushan. Biomimetics: lessons from nature - an overview. *Philos. Trans. Royal Soc. A*, 367(1893):1445–1486, 2009.

[180] S. Ling, Z. Qin, C. Li, W. Huang, D. L. Kaplan, and M. J. Buehler. Polymorphic regenerated silk fibers assembled through bioinspired spinning. *Nat. Commun.*, 8:1387, 2017.

[181] C. M. Elvin, A. G. Carr, M. G. Huson, J. M. Maxwell, R. D. Pearson, T. Vuocolo, N. E. Liyou, D. C. C. Wong, D. J. Merritt, and N. E. Dixon. Synthesis and properties of crosslinked recombinant pro-resilin. *Nature*, 437:999–1002, 2005.

[182] V. Schoeppler, E. Reich, J. Vacelet, M. Rosenthal, A. Pacureanu, A. Rack, P. Zaslansky, E. Zolotoyabko, and I. Zlotnikov. Shaping highly regular glass architectures: A lesson from nature. *Sci. Adv.*, 3(10):eaao2047, 2017.

[183] J. H. Pikul, S. Li, H. Bai, R. T. Hanlon, I. Cohen, and R. F. Shepherd. Stretchable surfaces with programmable 3D texture morphing for synthetic camouflaging skins. *Science*, 358(6360):210–214, 2017.

[184] B. Dean and B. Bhushan. Shark-skin surfaces for fluid-drag reduction in turbulent flow: a review. *Philos. Trans. Royal Soc. A*, 368(1929):4775–4806, 2010.

[185] K. Autumn, Y. A. Liang, S. T. Hsieh, W. Zesch, W. P. Chan, T. W. Kenny, R. Fearing, and R. J. Full. Adhesive force of a single gecko foot-hair. *Nature*, 405:681–685, 2000.

[186] B. Bhushan. Adhesion of multi-level hierarchical attachment systems in gecko feet. *J. Adhes. Sci. Technol.*, 21(12-13):1213–1258, 2007.

[187] A. E. Seago, P. Brady, J.-P. Vigneron, and T. D. Schultz. Gold bugs and beyond: a review of iridescence and structural colour mechanisms in beetles (*Coleoptera*). *J. Royal Soc. Interface*, 6(Supl 2):S165–S184, 2009.

[188] T. D. Schultz and M. A. Rankin. The ultrastructure of the epicuticular interference reflectors of tiger beetles (*Cicindela*). *J. Exp. Biol.*, 117:87–110, 1985.

[189] D.-H. Ko, J. R. Tumbleston, K. J. Henderson, L. E. Euliss, J. M. DeSimone, R. Lopez, and E. T. Samulski. Biomimetic microlens array with antireflective "moth-eye" surface. *Soft Matter*, 7(14):6404–6407, 2011.

[190] Z. Han, B. Li, Z. Mu, M. Yang, S. Niu, J. Zhang, and L. Ren. An ingenious super light trapping surface templated from butterfly wing scales. *Nanoscale Res. Lett.*, 10(1):344, 2015.

[191] R. Hünig, A. Mertens, M. Stephan, A. Schulz, B. Richter, M. Hetterich, M. Powalla, U. Lemmer, A. Colsmann, and G. Gomard. Flower power: Exploiting plants' epidermal structures for enhanced light harvesting in thin-film solar cells. *Adv. Opt. Mater.*, 4(10): 1487–1493, 2016.

[192] G. Rao, J. Garofalo, and E. Lanides. Diffuse reflectance-factor measurements of rose

petals. *Color Res. Appl.*, 36(2):148–154, 2011.

[193] G. D. Bernard and W. H. Miller. Interference filters in the corneas of *Diptera*. *Invest. Ophthalmol. Vis. Sci.*, 7(4):416–434, 1968.

[194] P. Vukusic, J. R. Sambles, and C. R. Lawrence. Structural colour: Colour mixing in wing scales of a butterfly. *Nature*, 404:457, 2000.

[195] Q. Zhao, X. Guo, T. Fan, J. Ding, D. Zhang, and Q. Guo. Art of blackness in butterfly wings as natural solar collector. *Soft Matter*, 7(24):11433–11439, 2011.

[196] P. Vukusic, J. R. Sambles, and C. R. Lawrence. Structurally assisted blackness in butterfly scales. *Proc. R. Soc. Lond. B*, 271(Suppl 4):S237–S239, 2004.

[197] D. E. McCoy, T. Feo, T. A. Harvey, and R. O. Prum. Structural absorption by barbule microstructures of super black bird of paradise feathers. *Nat. Commun.*, 9:1, 2018.

[198] S. Kinoshita, S. Yoshioka, and K. Kawagoe. Mechanisms of structural colour in the *Morpho* butterfly: cooperation of regularity and irregularity in an iridescent scale. *Proc. R. Soc. Lond. B*, 269(1499):1417–1421, 2002.

[199] X. Yang, Z. Peng, H. Zuo, T. Shi, and G. Liao. Using hierarchy architecture of *Morpho* butterfly scales for chemical sensing: Experiment and modeling. *Sens. Actuators A Phys.*, 167(2):367–373, 2011.

[200] V. Sharma, M. Crne, J. O. Park, and M. Srinivasarao. Structural origin of circularly polarized iridescence in jeweled beetles. *Science*, 325(5939):449–451, 2009.

[201] J. Zi, X. Yu, Y. Li, X. Hu, C. Xu, X. Wang, X. Liu, and R. Fu. Coloration strategies in peacock feathers. *Proc. Natl. Acad. Sci. U.S.A.*, 100(22):12576–12578, 2003.

[202] J. W. Galusha, L. R. Richey, J. S. Gardner, J. N. Cha, and M. H. Bartl. Discovery of a diamond-based photonic crystal structure in beetle scales. *Phys. Rev. E*, 77(5): 050904(R), 2008.

[203] A. L. Ingram and A. R. Parker. A review of the diversity and evolution of photonic structures in butterflies, incorporating the work of John Huxley (The Natural History Museum, London from 1961 to 1990). *Philos. Trans. Royal Soc. B*, 363(1502):2465–2480, 2008.

[204] R. A. Potyrailo, H. Ghiradella, A. Vertiatchikh, K. Dovidenko, J. R. Cournoyer, and E. Olson. *Morpho* butterfly wing scales demonstrate highly selective vapour response. *Nat. Photon.*, 1:123–128, 2007.

[205] K. Koch, B. Bhushan, and W. Barthlott. Multifunctional surface structures of plants: An inspiration for biomimetics. *Prog. Mater. Sci.*, 54(2):137–178, 2009.

[206] W. Barthlott, T. Schimmel, S. Wiersch, K. Koch, M. Brede, M. Barczewski, S. Walheim, A. Weis, A. Kaltenmaier, A. Leder, and H. F. Bohn. The *Salvinia* paradox: Superhydrophobic surfaces with hydrophilic pins for air retention under water. *Adv. Mater.*, 22 (21):2325–2328, 2010.

[207] A. B. D. Cassie and S. Baxter. Wettability of porous surfaces. *Trans. Faraday Soc.*, 40: 546–551, 1944.

[208] M. Nosonovsky and B. Bhushan. Patterned nonadhesive surfaces: Superhydrophobicity and wetting regime transitions. *Langmuir*, 24(4):1525–1533, 2008.

[209] G. D. Bixler and B. Bhushan. Biofouling: lessons from nature. *Philos. Trans. Royal Soc. A*, 370(1967):2381–2417, 2012.

[210] Y. Zheng, X. Gao, and L. Jiang. Directional adhesion of superhydrophobic butterfly wings. *Soft Mater*, 3(2):178–182, 2007.

[211] B. Bhushan and M. Nosonovsky. The rose petal effect and the modes of superhydrophobicity. *Philos. Trans. Royal Soc. A*, 368(1929):4713–4728, 2010.

[212] I. R. Hooper, P. Vukusic, and R. J. Wootton. Detailed optical study of the transparent wing membranes of the dragonfly *Aeshna cyanea*. *Opt. Express*, 14(11):4891–4897, 2006.

[213] W.-L. Min, B. Jiang, and P. Jiang. Bioinspired self-cleaning antireflection coatings. *Adv. Mater.*, 20(20):3914–3918, 2011.

[214] X. Zhang, D. Ji, T. Lei, B. Zhao, K. Song, W. Hu, J.-Y. Wang, J. Pei, and Y. Wang. Integration of antireflection and light diffraction in nature: a strategy for light trapping. *J. Mater. Chem. A*, 1(36):10607–10611, 2013.

[215] M. Sun, G. S. Watson, Y. Zheng, J. A. Watson, and A. Liang. Wetting properties on nanostructured surfaces of cicada wings. *J. Exp. Biol.*, 212:3148–3155, 2009.

[216] M. J. Tobin, L. Puskar, J. Hasan, H. K. Webb, C. J. Hirschmugl, M. J. Nasse, G. Gervinskas, S. Juodkazis, G. S. Watson, J. A. Watson, R. J. Crawford, and E. P. Ivanova. High-spatial-resolution mapping of superhydrophobic cicada wing surface chemistry using infrared microspectroscopy and infrared imaging at two synchrotron beamlines. *J. Synchrotron Rad.*, 20(3):482–489, 2013.

[217] K. M. Wisdom, J. A. Watson, X. Qu, F. Liu, G. S. Watson, and C.-H. Chen. Self-cleaning of superhydrophobic surfaces by self-propelled jumping condensate. *Proc. Natl. Acad. Sci. U.S.A.*, 110(20):7992–7997, 2013.

[218] E. P. Ivanova, J. Hasan, H. K. Webb, V. K. Truong, G. S. Watson, J. A. Watson, V. A. Baulin, S. Pogodin, J. Y. Wang, M. J. Tobin, C. Löbbe, and R. J. Crawford. Natural bactericidal surfaces: Mechanical rupture of *Pseudomonas aeruginosa* cells by cicada wings. *Small*, 8(16):2489–2494, 2012.

[219] M. Sun, A. Liang, Y. Zheng, G. S. Watson, and J. A. Watson. A study of the antireflection efficiency of natural nano-arrays of varying sizes. *Bioinspir. Biomim.*, 6(2): 026003, 2011.

[220] J. Morikawa, M. Ryu, G. Seniutinas, A. Balčytis, K. Maximova, X. Wang, M. Zamengo, E. P. Ivanova, and S. Juodkazis. Nanostructured antireflective and thermoisolative cicada wings. *Langmuir*, 32(18):4698–4703, 2016.

[221] J. C. Tuthill and R. I. Wilson. Mechanosensation and adaptive motor control in insects. *Curr. Biol.*, 26(20):R1022–R1038, 2016.

[222] G. Cárdenas, G. Cabrera, E. Taboada, and S. P. Miranda. Chitin characterization by

SEM, FTIR, XRD, and ^{13}C cross polarization/mass angle spinning NMR. *J. Appl. Polym. Sci.*, 93(4):1876–1885, 2004.

[223] K. J. Kramer, M. R. Kanost, T. L. Hopkins, H. Jiang, Y. C. Zhu, R. Xu, J. L. Kerwin, and F. Turecek. Oxidative conjugation of catechols with proteins in insect skeletal systems. *Tetrahedron*, 57(2):385–392, 2001.

[224] I. F. M. Rumengan, E. Suryanto, R. Modaso, S. Wullur, T. E. Tallei, and D. Limbong. Structural characteristics of chitin and chitosan isolated from the biomass of cultivated rotifer, *Brachionus rotundiformis*. *Int. J. Fish. Aquat. Sci.*, 3(1):12–18, 2014.

[225] X. Huang, G. Liu, and X. Wang. New secrets of spider silk: Exceptionally high thermal conductivity and its abnormal change under stretching. *Adv. Mater.*, 24(11):1482–1486, 2012.

[226] R. Fuente, A. Mendioroz, and A. Salazar. Revising the exceptionally high thermal diffusivity of spider silk. *Mater. Lett.*, 114:1–3, 2014.

[227] C. Xing, T. Munro, B. White, H. Ban, C. G. Copeland, and R. V. Lewis. Thermophysical properties of the dragline silk of *Nephila clavipes* spider. *Polymer*, 55(16):4226–4231, 2014.

[228] E. C. Toolson and E. K. Toolson. Evaporative cooling and endothermy in the 13-year periodical cicada, *Magicicada tredecem*. *J. Comp. Physiol. B*, 161(1):109–115, 1991.

[229] N. F. Hadley, M. C. Quinlan, and M. L. Kennedy. Evaporative cooling in the desert cicada: Thermal efficiency and water/metabolic costs. *J. Exp. Biol.*, 159:269–283, 1991.

[230] J. Morikawa, E. Hayakawa, T. Hashimoto, R. Buividas, and S. Juodkazis. Thermal imaging of a heat transport in regions structured by femtosecond laser. *Opt. Express*, 19(21):20542–20550, 2011.

[231] J. Morikawa and T. Hashimoto. Thermal diffusivity of aromatic polyimide thin films by temperature wave analysis. *J. Appl. Phys.*, 105(11):113506, 2009.

[232] T. Wagner, C. Neinhuis, and W. Barthlott. Wettability and contaminability of insect wings as a function of their surface sculptures. *Acta Zool.*, 77(3):213–225, 1996.

[233] D. E. Mainwaring, S. H. Nguyen, H. Webb, T. Jakubov, M. Tobin, R. N. Lamb, A. H.-F. Wu, R. Marchant, R. J. Crawford, and E. P. Ivanova. The nature of inherent bactericidal activity: insights from the nanotopology of three species of dragonfly. *Nanoscale*, 8 (12):6527–6534, 2009.

[234] R. H. Siddique, G. Gomard, and H. Hölscher. The role of random nanostructures for the omnidirectional anti-reflection properties of the glasswing butterfly. *Nat. Commun.*, 6:6909, 2015.

[235] H. L. Leertouwer, B. D. Wilts, and D. G. Stavenga. Refractive index and dispersion of butterfly chitin and bird keratin measured by polarizing interference microscopy. *Opt. Express*, 19(24):24061–24066, 2011.

[236] B. Liang, M. Bai, H. Ma, N. Ou, and J. Miao. Wideband analysis of periodic structures

at oblique incidence by material independent FDTD algorithm. *IEEE Trans. Antennas Propag.*, 62(1):354–360, 2014.

[237] M. Humara, S. J. J. Kwoka, M. Choi, A. K. Yetisen, S. Cho, and S.-H. Yun. Toward biomaterial-based implantable photonic devices. *Nanophotonics*, 6(2):414–434, 2017.

[238] L. S. Naira and C. T. Laurencin. Biodegradable polymers as biomaterials. *Prog. Polym. Sci.*, 32(8-9):762–798, 2007.

[239] Q. Li, N. Qi, Y. Peng, Y. Zhang, L. Shi, X. Zhang, Y. Lai, K. Wei, I. S. Kim, and K.-Q. Zhang. Sub-micron silk fibroin film with high humidity sensibility through color changing. *RSC Adv.*, 7(29):17889–17897, 2017.

[240] S. K.Shukla, A. K. Mishra, O. A. Arotiba, and B. B. Mamba. Chitosan-based nanomaterials: A state-of-the-art review. *Int. J. Fish. Aquat. Sci.*, 59:46–58, 2013.

[241] Q. Lu, B. Zhang, M. Li, B. Zuo, D. L. Kaplan, Y. Huang, and H. Zhu. Degradation mechanism and control of silk fibroin. *Biomacromolecules*, 12(4):1080–1086, 2011.

[242] C. Zhong, Y. Deng, A. Fadavi Roudsari, A. Kapetanovic, M. P. Anantram, and M. Rolandi. A polysaccharide bioprotonic field-effect transistor. *Nat. Commun.*, 2:476, 2011.

[243] X. You and J. J. Pak. Graphene-based field effect transistor enzymatic glucose biosensor using silk protein for enzyme immobilization and device substrate. *Sens. Actuator B-Chem.*, 202:1357–1365, 2014.

[244] W. Gao, S. Emaminejad, H. Y. Y. Nyein, S. Challa, K. Chen, A. Peck, H. M. Fahad, H. Ota, H. Shiraki, D. Kiriya, D.-H. Lien, G. A. Brooks, R. W. Davis, and A. Javey. Fully integrated wearable sensor arrays for multiplexed *in situ* perspiration analysis. *Nature*, 529:509–514, 2016.

[245] S.-W. Hwang, H. Tao, D.-H. Kim, H. Cheng, J.-K. Song, E. Rill, M. A. Brenckle, B. Panilaitis, S. M. Won, Y.-S. Kim, Y. M. Song, K. J. Yu, A. Ameen, R. Li, Y. Su, M. Yang, D. L. Kaplan, M. R. Zakin, M. J. Slepian, Y. Huang, F. G. Omenetto, and J. A. Rogers. A physically transient form of silicon electronics. *Science*, 337(6102): 1640–1644, 2012.

[246] S. H. Yun and S. J. J. Kwok. Light in diagnosis, therapy and surgery. *Nat. Biomed. Eng.*, 1:0008, 2017.

[247] D. E. Azofeifa, H. J. Arguedas, and W. E. Vargas. Optical properties of chitin and chitosan biopolymers with application to structural color analysis. *Opt. Mater.*, 35(2): 175–183, 2012.

[248] G. Perotto, Y. Zhang, D. Naskar, N. Patel, D. L. Kaplan, S. C. Kundu, and F. G. Omenetto. The optical properties of regenerated silk fibroin films obtained from different sources. *Appl. Phys. Lett.*, 111(10):103702, 2017.

[249] S. V. Madihally and H. W. T. Matthew. Porous chitosan scaffolds for tissue engineering. *Biomaterials*, 20(12):1133–1142, 1999.

[250] L. Wang, D. Chen, K. Jiang, and G. Shen. New insights and perspectives into biological

materials for flexible electronics. *Chem. Soc. Rev.*, 46(22):6764–6815, 2017.

[251] S. T. Parker, P. Domachuk, J. Amsden, J. Bressner, J. A. Lewis, D. L. Kaplan, and F. G. Omenetto. Biocompatible silk printed optical waveguides. *Adv. Mater.*, 21(23): 2411–2415, 2009.

[252] B. D. Lawrence, M. Cronin-Golomb, I. Georgakoudi, D. L. Kaplan, and F. G. Omenetto. Bioactive silk protein biomaterial systems for optical devices. *Biomacromolecules*, 9 (4):1214–1220, 2008.

[253] S. Kim, A. N. Mitropoulos, J. D. Spitzberg, H. Tao, D. L. Kaplan, and F. G. Omenetto. Silk inverse opals. *Nat. Photon.*, 6:818–823, 2012.

[254] S. Toffanin, S. Kim, S. Cavallini, M. Natali, V. Benfenati, J. J. Amsden, D. L. Kaplan, R. Zamboni, M. Muccini, and F. G. Omenetto. Low-threshold blue lasing from silk fibroin thin films. *Appl. Phys. Lett.*, 101(9):091110, 2012.

[255] H. Tao, J. M. Kainerstorfer, S. M. Siebert, E. M. Pritchard, A. Sassaroli, B. J. B. Panilaitis, M. A. Brenckle, J. J. Amsden, J. Levitt S. Fantini, D. L. Kaplan, and F. G. Omenetto. Implantable, multifunctional, bioresorbable optics. *Proc. Natl. Acad. Sci. U.S.A.*, 109(48):19584–19589, 2012.

[256] H. Perry, A. Gopinath, D. L. Kaplan, L. Dal Negro, and F. G. Omenetto. Nano- and micropatterning of optically transparent, mechanically robust, biocompatible silk fibroin films. *Adv. Mater.*, 20(16):3070–3072, 2008.

[257] J. J. Amsden, H. Perry, S. V. Boriskina, A. Gopinath, D. L. Kaplan, L. Dal Negro, and F. G. Omenetto. Spectral analysis of induced color change on periodically nanopatterned silk films. *Opt. Express*, 17(23):21271–21279, 2009.

[258] S. Lu, X. Wang, Q. Lu, X. Hu, N. Uppal, F. G. Omenetto, and D. L. Kaplan. Stabilization of enzymes in silk films. *Biomacromolecules*, 10(5):1032–1042, 2009.

[259] G. Huang, Y. Yin, Z. Pan, M. Chen, L. Zhang, Y. Liu, Y. Zhang, and J. Gao. Fabrication of 3D photonic crystals from chitosan that are responsive to organic solvents. *Biomacromolecules*, 15(12):4396–4402, 2014.

[260] Y. Wang, D. Aurelio, W. Li, P. Tseng, Z. Zheng, M. Li, D. L. Kaplan, M. Liscidini, and F. G. Omenetto. Modulation of multiscale 3D lattices through conformational control: Painting silk inverse opals with water and light. *Adv. Mater.*, 29(38):1702769, 2017.

[261] R. R. da Silva, C. T. Dominguez, M. V. dos Santos, R. Barbosa-Silva, M. Cavicchioli, L. M. Christovan, L. S. A. de Melo, A. S. L. Gomes, C. B. de Araújo, and S. J. L. Ribeiro. Silk fibroin biopolymer films as efficient hosts for DFB laser operation. *J. Mater. Chem. C*, 1(43):7181–7190, 2013.

[262] J. Mysliwiec, K. Cyprych, L. Sznitko, and A. Miniewicz. Biomaterials in light amplification. *Biomacromolecules*, 19(3):033003, 2017.

[263] H. Tao, M. A. Brenckle, M. Yang, J. Zhang, M. Liu, S. M. Siebert, R. D. Averitt, M. S. Mannoor, M. C. McAlpine, J. A. Rogers, D. L. Kaplan, and F. G. Omenetto. Silk-based conformal, adhesive, edible food sensors. *Adv. Mater.*, 24(8):1067–1072, 2012.

[264] H. Guerboukha, G. Yan, O. Skorobogata, and M. Skorobogatiy. Silk foam terahertz waveguides. *J. Am. Chem. Soc.*, 2(12):1181–1192, 2014.

[265] J.-H. Son. Terahertz electromagnetic interactions with biological matter and their applications. *J. Appl. Phys.*, 105(10):102033, 2009.

[266] L. Xie, Y. Yao, and Y. Ying. The application of terahertz spectroscopy to protein detection: A review. *Appl. Spectrosc. Rev.*, 49(6):448–461, 2014.

[267] X. Hu, G. Xu, L. Wen, H. Wang, Y. Zhao, Y. Zhang, D. R. S. Cumming, and Q. Chen. Metamaterial absorber integrated microfluidic terahertz sensors. *Laser Photon. Rev.*, 10(6):962–969, 2016.

[268] D.-K. Lee, J.-H. Kang, J. Kwon, J.-S. Lee, S. Lee, D. H. Woo, J. H. Kim, C.-S. Song, Q-H. Park, and M. Seo. Nano metamaterials for ultrasensitive terahertz biosensing. *Sci. Rep.*, 7:8146, 2017.

[269] H. Tao, J. J. Amsden, A. C. Strikwerda, K. Fan, D. L. Kaplan, X. Zhang, R. D. Averitt, and F. G. Omenetto. Metamaterial silk composites at terahertz frequencies. *Adv. Mater.*, 22(32):3527–3531, 2010.

[270] R. Mendis and D. Grischkowsky. Plastic ribbon THz waveguides. *J. Appl. Phys.*, 88(7): 4449–4451, 2000.

[271] T. D. Sutherland, J. H. Young, S. Weisman, C. Y. Hayashi, and D. J. Merritt. Insect silk: One name, many materials. *Annu. Rev. Entomol.*, 55:171–188, 2010.

[272] J. Gatesy, C. Hayashi, D. Motriuk, J. Woods, and R. Lewis. Extreme diversity, conservation, and convergence of spider silk fibroin sequences. *Science*, 291(5513):2603–2605, 2001.

[273] P. M. Cunniff, S. A. Fossey, M. A. Auerbach, J. W. Song, D. L. Kaplan, W. W. Adams, R. K. Eby, D. Mahoney, and D. L. Vezie. Mechanical and thermal properties of dragline silk from the spider *Nephila clavipes*. *Polym. Adv. Technol.*, 5(8):401–410, 1994.

[274] F. Vollrath and D. P. Knight. Liquid crystalline spinning of spider silk. *Nature*, 410: 541–548, 2001.

[275] Z. Shao and F. Vollrath. Surprising strength of silkworm silk. *Nature*, 418:741, 2001.

[276] E. S. Sashina, A. M. Bochek, N. P. Novoselov, and D. A. Kirichenko. Structure and solubility of natural silk fibroin. *Russ. J. Appl. Chem.*, 79(6):869–876, 2006.

[277] R. L. Moy, A. Lee, and A. Zalka. Commonly used suture materials in skin surgery. *Am. Fam. Physician*, 44(8):2123–2128, 1991.

[278] F. G. Omenetto and D. L. Kaplan. New opportunities for an ancient material. *Science*, 329(5991):528–531, 2010.

[279] G. Li, Y. Li, G. Cher, J. He, Y. Han, X. Wang, and D. L. Kaplan. Silk-based biomaterials in biomedical textiles and fiber-based implants. *Adv. Healthc. Mater.*, 4(8):1134–1151, 2015.

[280] W. Zhang, L. Chen, J. Chen, L. Wang, X. Gui, J. Ran, G. Xu, H. Zhao, M. Zeng, J. Ji,

L. Qian, J. Zhou, H. Ouyang, and X. Zou. Silk fibroin biomaterial shows safe and effective wound healing in animal models and a randomized controlled clinical trial. *Adv. Healthc. Mater.*, 6(10):1700121, 2017.

[281] S. Keten, Z. Xu, B. Ihle, and M. J. Buehler. Nanoconfinement controls stiffness, strength and mechanical toughness of β-sheet crystals in silk. *Nat. Mater.*, 10:359–367, 2010.

[282] G. H. Altman, F. Diaz, C. Jakuba, T. Calabro, R. L. Horan, J. Chen, H. Lu, J. Richmond, and D. L. Kaplan. Silk-based biomaterials. *Biomaterials*, 24(3):401–416, 2003.

[283] A. Balčytis, M. Ryu, X. Wang, F. Novelli, G. Seniutinas, S. Du, X. Wang, J. Li, J. Davis, D. Appadoo, J. Morikawa, and S. Juodkazis. Silk: Optical properties over 12.6 octaves THz-IR-Visible-UV range. *Materials*, 10(4):356, 2017.

[284] M. Ryu, A. Balčytis, X. Wang, J. Vongsvivut, Y. Hikima, J. Li, M. J. Tobin, S. Juodkazis, and J. Morikawa. Orientational mapping augmented sub-wavelength hyper-spectral imaging of silk. *Sci. Rep.*, 7:7419, 2017.

[285] X. Jin, J. Zhang, W. Gao, and J. Li. Cocoon of the silkworm *Antheraea pernyi* as an example of a thermally insulating biological interface. *Biointerphases*, 9(3):031013, 2014.

[286] Y. Zhang, H. Yang, H. Shao, and X. Hu. *Antheraea pernyi* silk fiber: A potential resource for artificially biospinning spider dragline silk. *J. Biomed. Biotechnol.*, 2010: 683962, 2010.

[287] A. Varone, D. Knight, S. Lesage, F. Vollrath, A. M. Rajnicek, and W. Huang. The potential of *Antheraea pernyi* silk for spinal cord repair. *Sci. Rep.*, 7:13790, 2017.

[288] S. Cavallini, S. Toffanin, C. Chieco, A. Sagnella, F. Formaggio, A. Pistone, T. Posati, M. Natali, M. Caprini, V. Benfenati, N. Di Virgilio, G. Ruani, M. Muccini, R. Zamboni, and F. Rossi. Naturally functionalized silk as useful material for photonic applications. *Composites Part B*, 71:152–158, 2015.

[289] L. Lamboni, M. Gauthier, G. Yang, and Q. Wang. Silk sericin: A versatile material for tissue engineering and drug delivery. *Biotechnol. Adv.*, 33(8):1855–1867, 2015.

[290] B. Zuo, L. Leigen, and W. Zhengyu. Effect on properties of regenerated silk fibroin fiber coagulated with aqueous methanol/ethanol. *J. Appl. Polym. Sci.*, 106(1):53–59, 2007.

[291] S. Ling, Z. Qi, D. P. Knight, Y. Huang, L. Huang, H. Zhou, Z. Shao, and X. Chen. Insight into the structure of single *Antheraea pernyi* silkworm fibers using synchrotron FTIR microspectroscopy. *Biomacromolecules*, 14(1):1885–1892, 2013.

[292] C. Fu, D. Porter, X. Chen, F. Vollrath, and Z. Shao. Understanding the mechanical properties of *Antheraea Pernyi* silk – from primary structure to condensed structure of the protein. *Adv. Funct. Mater.*, 21(4):729–737, 2011.

[293] Y. Nakazawa and T. Asakura. High-resolution ^{13}C CP/MAS NMR study on structure and structural transition of *Antheraea pernyi* silk fibroin containing poly(L-alanine) and Gly-rich regions. *Macromolecules*, 35(6):2393–2400, 2002.

[294] C.-Z. Zhou, F. Confalonieri, N. Medina, Y. Zivanovic, C. Esnault, T. Yang, M. Jacquet, J. Janin, M. Duguet, R. Perasso, and Z.-G. Li. Fine organization of *Bombyx mori* fibroin heavy chain gene. *Nucleic Acids Res.*, 28(12):2413–2419, 2000.

[295] H. Sezutsu and K. Yukuhiro. Dynamic rearrangement within the *Antheraea pernyi* silk fibroin gene is associated with four types of repetitive units. *J. Mol. Evol.*, 51(4): 329–338, 2000.

[296] J. E. Noble and M. J. A. Bailey. Quantitation of protein. In R. R. Burgess and M. P. Deutscher, editors, *Guide to Protein Purification*, volume 463 of *Methods in Enzymology*, chapter 8, pages 73–95. Academic Press, 2nd edition, 2009.

[297] J. Kaur, R. Rajkhowa, T. Tsuzuki, K. Millington, J. Zhang, and X. Wang. Photoprotection by silk cocoons. *Biomacromolecules*, 14(10):3660–3667, 2013.

[298] L. H. Fornander, B. Feng, T. Beke-Somfai, and B. Nordén. UV transition moments of tyrosine. *J. Phys. Chem. B*, 118(31):9247–9257, 2014.

[299] A. Pushpa, B.V. Goutham Vishnu, and K. S. Thippa Reddy. Preparation of nano silk sericin based hydrogels from silk industry waste. *J. Environ. Res. Develop.*, 8(2): 243–253, 2013.

[300] W. Bergmann. The natural pigments of silk. *Text. Res. J.*, 9(11):397–408, 1939.

[301] P. C. J. Brunet and B. C. Coles. Tanned silks. *Proc. R. Soc. Lond. B*, 187(1087): 133–170, 1974.

[302] M. Ma, M. Hussain, S. Dong, and W. Zhou. Characterization of the pigment in naturally yellow-colored domestic silk. *Dyes Pigm.*, 124:6–11, 2016.

[303] N. Huby, V. Vié, A. Renault, S. Beaufils, T. Lefèvre, F. Paquet-Mercier, M. Pèzolet, and B. Bêche. Native spider silk as a biological optical fiber. *Appl. Phys. Lett.*, 102 (12):123702, 2013.

[304] S. Kujala, A. Mannila, L. Karvonen, K. Kieu, and Z. Sun. Natural silk as a photonics component: a study on its light guiding and nonlinear optical properties. *Sci. Rep.*, 6: 22358, 2016.

[305] C. Mo, P. Wu, X. Chen, and Z. Shao. Near-infrared characterization on the secondary structure of regenerated *Bombyx Mori* silk fibroin. *Appl. Spectrosc.*, 60(12):1438–1441, 2006.

[306] Q. Yuan, J. Yao, L. Huang, X. Chen, and Z. Shao. Correlation between structural and dynamic mechanical transitions of regenerated silk fibroin. *Polymer*, 51(26):6278–6283, 2010.

[307] E. Goormaghtigh, J.-M. Ruysschaert, and V. Raussens. Evaluation of the information content in infrared spectra for protein secondary structure determination. *Biophys. J.*, 90(8):2946–2957, 2006.

[308] M. Boulet-Audet, T. Lefèvre, T. Buffeteau, and M. Pézolet. Attenuated total reflection infrared spectroscopy: An efficient technique to quantitatively determine the orientation and conformation of proteins in single silk fibers. *Appl. Spectrosc.*, 62(9):956–962,

2008.

[309] M. Boulet-Audet, F. Vollrath, and C. Holland. Rheo-attenuated total reflectance infrared spectroscopy: a new tool to study biopolymers. *Phys. Chem. Chem. Phys.*, 13(9):3979–3984, 2011.

[310] T. Gheysens, A. Collins, S. Raina, F. Vollrath, and D. P. Knight. Demineralization enables reeling of wild silkmoth cocoons. *Biomacromolecules*, 12(6):2257–2266, 2011.

[311] M. Boulet-Audet, F. Vollrath, and C. Holland. Identification and classification of silks using infrared spectroscopy. *J. Exp. Biol.*, 218(19):3138–3149, 2015.

[312] E. J. Ambrose, C. H. Bamford, A. Elliott, and W. E. Hanby. Water-soluble silk: an α-protein. *Nature*, 167:264–265, 1951.

[313] L. Fan, H. Wang, K. Zhang, C. He, Z. Cai, and X. Mo. Regenerated silk fibroin nanofibrous matrices treated with 75% ethanol vapor for tissue-engineering applications. *J. Biomater. Sci. Polym. Ed.*, 23(1-4):497–508, 2012.

[314] A. Barth. Infrared spectroscopy of proteins. *Biochim. Biophys. Acta, Bioenerg.*, 1767 (9):1073–1101, 2007.

[315] Y. Wang, K. Murayama, Y. Myojo, R. Tsenkova, N. Hayashi, and Y. Ozaki. Two-dimensional Fourier transform near-infrared spectroscopy study of heat denaturation of ovalbumin in aqueous solutions. *J. Phys. Chem. B*, 102(34):6655–6662, 1998.

[316] P. Taddei and P. Monti. Vibrational infrared conformational studies of model peptides representing the semicrystalline domains of *Bombyx mori* silk fibroin. *Biopolymers*, 78 (5):249–258, 2005.

[317] Q. Lu, X. Hu, X. Wang, J. A. Kluge, S. Lu, P. Cebe, and D. L. Kaplan. Water-insoluble silk films with silk I structure. *Acta Biomater.*, 6(4):1380–1387, 2010.

[318] W. H. Moore and S. Krimm. Vibrational analysis of peptides, polypeptides, and proteins. II. β-poly(L-alanine) and β-poly(L-alanylglycine). *Biopolymers*, 15:2465–2483, 1976.

[319] P. Monti, P. Taddei, G. Freddi, K. Ohgo, and T. Asakura. Vibrational ^{13}C-cross-polarization/magic angle spinning NMR spectroscopic and thermal characterization of poly(alanine-glycine) as model for silk I *Bombyx mori* fibroin. *Biopolymers*, 72(5): 329–338, 2003.

[320] L. Quaroni, M. Obst, M. Nowak, and F. Zobi. Three-dimensional mid-infrared tomographic imaging of endogenous and exogenous molecules in a single intact cell with subcellular resolution. *Angew. Chem. Int. Ed.*, 54(1):318–322, 2015.

[321] J. Vongsvivut, P. Heraud, W. Zhang, J. A. Kralovec, D. McNaughton, and C. J. Barrow. Rapid determination of protein contents in microencapsulated fish oil supplements by ATR-FTIR spectroscopy and partial least square regression (PLSR) analysis. *Food Bioproc. Tech.*, 7(1):265–277, 2014.

[322] P. Papadopoulos, J. Sölter, and F. Kremer. Structure-property relationships in major ampullate spider silk as deduced from polarized FTIR spectroscopy. *Eur. Phys. J. E*, 24 (2):193–199, 2007.

[323] G. Mlnoni and G. Zerbi. End effects on longitudinal accordion modes: Fatty acids and layered systems. *J. Phys. Chem.*, 86(24):4791–4798, 1982.

[324] S. Mizushima and T. Shimanouchi. Raman frequencies of *n*-paraffin molecules. *J. Am. Chem. Soc.*, 71(4):1320–1324, 1949.

[325] J. Doucet, I. Denicolo, and A. Craievich. X-ray study of the "rotator" phase of the odd numbered paraffins $C_{17}H_{36}$, $C_{19}H_{40}$, and $C_{21}H_{44}$. *J. Chem. Phys.*, 75(3):1523–1529, 1981.

[326] J. D. Barnes and B. M. Fanconi. Raman spectroscopy, rotational isomerism, and the "rotator" phase transition in *n*-alkanes. *J. Chem. Phys.*, 56(10):5190–5192, 1972.

[327] R. J. Falconer and A. G. Markelz. Terahertz spectroscopic analysis of peptides and proteins. *J. Infrared Milli. Terahz. Waves*, 33(10):973–988, 2012.

[328] G. M. Png, R. J. Falconer, and D. Abbott. Tracking aggregation and fibrillation of globular proteins using terahertz and far-infrared spectroscopies. *IEEE Trans. Terahertz Sci. Technol.*, 6(1):45–53, 2016.

[329] H. R. Zelsmann. Temperature dependence of the optical constants for liquid H_2O and D_2O in the far IR region. *J. Mol. Struct.*, 350(2):95–114, 1995.

[330] J.-B. Brubach, A. Mermet, A. Filabozzi, A. Gerschel, and P. Roy. Signatures of the hydrogen bonding in the infrared bands of water. *J. Chem. Phys.*, 122(18):184509, 2005.

[331] C. Medcraft, D. McNaughton, C. D. Thompson, D. Appadoo, S. Bauerecker, and E. G. Robertson. Size and temperature dependence in the far-IR spectra of water ice particles. *Astrophys. J.*, 758(1):17, 2012.

[332] C. Q. Sun, X. Zhang, X. Fu, W. Zheng, J.-L Kuo, Y. Zhou, Z. Shen, and J. Zhou. Density and phonon-stiffness anomalies of water and ice in the full temperature range. *J. Phys. Chem. Lett.*, 4(19):3238–3244, 2013.

[333] M. Tsukada, G. Freddi, M. Nagura, H. Ishikawa, and N. Kasai. Structural changes of silk fibers induced by heat treatment. *J. Appl. Polym. Sci.*, 46(11):1945–1953, 1992.

[334] S. Y. Cho, Y. Soo Yun, S. Lee, D. Jang, K.-Y. Park, J. K. Kim, B. H. Kim amd K. Kang, D. L. Kaplan, and H.-J. Jin. Carbonization of a stable β-sheet-rich silk protein into a pseudographitic pyroprotein. *Nat. Commun.*, 6:7145, 2015.

[335] K. Itoh, T. Nakahara, T. Shimanouchi, M. Oya, K. Uno, and Y. Iwakura. Far-infrared spectra of polyalanines with α-helical and β-form structures. *Biopolymers*, 6(12): 1759–1766, 1968.

[336] X. Wu, X. Wu, M. Shao, and B. Yang. Structural changes of *Bombyx mori* fibroin from silk gland to fiber as evidenced by terahertz spectroscopy and other methods. *Int. J. Biol. Macromol.*, 102:1202–1210, 2017.

[337] S. E. Whitmire, D. Wolpert, A. G. Markelz, J. R. Hillebrecht, J. Galan, and R. R. Birge. Protein flexibility and conformational state: A comparison of collective vibrational modes of wild-type and D96N bacteriorhodopsin. *Biophys. J.*, 85(2):1269–1277, 2003.

[338] J. Hebling, K.-L. Yeh, M. C. Hoffmann, B. Bartal, and K. A. Nelson. Generation of high-power terahertz pulses by tilted-pulse-front excitation and their application possibilities. *J. Opt. Soc. Am. B*, 25(7):B6–B19, 2008.

[339] F. Blanchard, G. Sharma, L. Razzari, X. Ropagnol, H.-C. Bandulet, F. Vidal, R. Morandotti, J.-C. Kieffer, T. Ozaki, H. Tiedje, H. Haugen, M. Reid, and F. Hegmann. Generation of intense terahertz radiation *via* optical methods. *IEEE J. Sel. Top. Quant. Electron.*, 17(1):5–16, 2011.

[340] G. E. Walrafen. Raman spectrum of water: Transverse and longitudinal acoustic modes below 300 cm^{-1} and optic modes above $\approx$300 cm^{-1}. *J. Phys. Chem.*, 94(6):2237–2239, 1990.

[341] J. J. Amsden, P. Domachuk, A. Gopinath, R. D. White, L. Dal Negro, D. L. Kaplan, and F. G. Omenetto. Rapid nanoimprinting of silk fibroin films for biophotonic applications. *Adv. Mater.*, 22(19):1746–1749, 2010.

[342] R. K. Pal, N. E. Kurland, C. Wang, S. C. Kundu, and V. K. Yadavalli. Biopatterning of silk proteins for soft micro-optics. *ACS Appl. Mater. Interfaces*, 7(16):8809–8816, 2015.

[343] Y.-L. Sun, Q. Li, S.-M. Sun, J.-C. Huang, B.-Y. Zheng, Q.-D. Chen, Z.-Z. Shao, and H.-B. Sun. Aqueous multiphoton lithography with multifunctional silk-centred bio-resists. *Nat. Commun.*, 6:8612, 2015.

[344] A. Handelman, N. Lapshina, B. Apter, and G. Rosenman. Peptide integrated optics. *Adv. Mater.*, 30(5):1705776, 2018.

[345] S. Kim, B. Marelli, M. A. Brenckle, A. N. Mitropoulos, E.-S. Gil, K. Tsioris, H. Tao, D. L. Kaplan, and F. G. Omenetto. All-water-based electron-beam lithography using silk as a resist. *Nat. Nanotechnol.*, 9:306–310, 2014.

[346] M. Malinauskas, A. Žukauskas, S. Hasegawa, Y. Hayasaki, V. Mizeikis, R. Buividas, and S. Juodkazis. Ultrafast laser processing of materials: from science to industry. *Light Sci. Appl.*, 5:e16133, 2016.

[347] S. Maruo, O. Nakamura, and S. Kawata. Three-dimensional microfabrication with two-photon-absorbed photopolymerization. *Opt. Lett.*, 22(2):132–134, 1997.

[348] B. H. Cumpston, S. P. Ananthavel, S. Barlow, D. L. Dyer, J. E. Ehrlich, L. L. Erskine, A. A. Heikal, S. M. Kuebler, I.-Y. S. Lee, D. McCord-Maughon, J. Qin, H. Röckel, M. Rumi, X.-L. Wu, S. R. Marder, and J. W. Perry. Two-photon polymerization initiators for three-dimensional optical data storage and microfabrication. *Nature*, 398: 51–54, 1999.

[349] S. Wei, J. Liu, Y. Zhao, T. Zhang, M. Zheng, F. Jin, X. Dong, J. Xing, and X. Duan. Protein-based 3D microstructures with controllable morphology and pH-responsive properties. *ACS Appl. Mater. Interfaces*, 9(48):42247–42257, 2017.

[350] Y.-L. Sun, W.-F. Dong, L.-G. Niu, T. Jiang, D.-X. Liu, L. Zhang, Y.-S. Wang, Q.-D. Chen, D.-P. Kim, and H.-B. Sun. Protein-based soft micro-optics fabricated by femtosecond laser direct writing. *Light Sci. Appl.*, 3:e129, 2014.

[351] S. Engelhardt, E. Hoch, K. Borchers, W. Meyer, H. Krüger, G. E. M. Tovar, and A. Gillner. Fabrication of 2D protein microstructures and 3D polymer-protein hybrid microstructures by two-photon polymerization. *Biofabrication*, 3(2):025003, 2011.

[352] P. K. Gillman. CNS toxicity involving methylene blue: the exemplar for understanding and predicting drug interactions that precipitate serotonin toxicity. *J. Psychopharmacol.*, 25(3):429–436, 2011.

[353] K. Maximova, X. Wang, A. Balčytis, L. Fan, J. Li, and S. Juodkazis. Silk patterns made by direct femtosecond laser writing. *Biomicrofluidics*, 10(5):054101, 2016.

[354] M. Huang, F. Zhao, Y. Cheng, N. Xu, and Z. Xu. Origin of laser-induced near-subwavelength ripples: Interference between surface plasmons and incident laser. *J. Laser Appl.*, 3(12):4062–4070, 2009.

[355] J. Bonse, J. Krüger, S. Höhm, and A. Rosenfeld. Femtosecond laser-induced periodic surface structures. *J. Laser Appl.*, 24(4):042006, 2012.

[356] X. Hu, K. Shmelev, L. Sun, E.-S. Gil, S.-H. Park, P. Cebe, and D. L. Kaplan. Regulation of silk material structure by temperature-controlled water vapor annealing. *Biomacromolecules*, 12(5):1686–1696, 2011.

[357] S. Lazare, A. Sionkowska, M. Zaborowicz, A. Planecka, J. Lopez, M. Dijoux, C. Louména, and M.-C. Hernandez. *Bombyx mori* silk protein films microprocessing with a nanosecond ultraviolet laser and a femtosecond laser workstation: theory and experiments. *Appl. Phys. A*, 106(1):67–77, 2011.

[358] T. Ito and S. Okazaki. Pushing the limits of lithography. *Nature*, 406:1027–1031, 2000.

[359] V. R. Manfrinato, L. Zhang, D. Su, H. Duan, R. G. Hobbs, E. A. Stach, and K. K. Berggren. Resolution limits of electron-beam lithography toward the atomic scale. *Nano Lett.*, 13(4):1555–1558, 2013.

[360] Y. Chen. Nanofabrication by electron beam lithography and its applications: A review. *Microelectron. Eng.*, 135:57–72, 2015.

[361] A. S. Gangnaik, Y. M. Georgiev, and J. D. Holmes. New generation electron beam resists: A review. *Chem. Mater.*, 29(5):1898–1917, 2017.

[362] Q. Lu, X. Wang, X. Hu, P. Cebe, F. Omenetto, and D. L. Kaplan. Stabilization and release of enzymes from silk films. *Adv. Mater.*, 10(4):359–368, 2010.

[363] C. M. Kolodziej and H. D. Maynard. Electron-beam lithography for patterning biomolecules at the micron and nanometer scale. *Chem. Mater.*, 24(5):774–780, 2012.

[364] Y.-L. Sun, Z.-S. Hou, S.-M. Sun, B.-Y. Zheng, J.-F. Ku, W.-F. Dong, Q.-D. Chen, and H.-B. Sun. Protein-based three-dimensional whispering-gallery-mode micro-lasers with stimulus-responsiveness. *Sci. Rep.*, 5:12852, 2015.

[365] U. Y. Lau, S. S. Saxer, J. Lee, E. Bat, and H. D. Maynard. Direct write protein patterns for multiplexed cytokine detection from live cells using electron beam lithography. *ACS Nano*, 10(1):723–729, 2016.

[366] I. Saaem and J. Tian. e-beam nanopatterned photo-responsive bacteriorhodopsin-

containing hydrogels. *Adv. Mater.*, 19(23):4268–4271, 2007.

[367] E. Bat, J. Lee, U. Y. Lau, and H. D. Maynard. Trehalose glycopolymer resists allow direct writing of protein patterns by electron-beam lithography. *Nat. Commun.*, 6:6654, 2015.

[368] B. Jiang, J. Yang, C. Li, L. Zhang, X. Zhang, and P. Yang. Water-based photo- and electron-beam lithography using egg white as a resist. *Adv. Mater. Interfaces*, 4(7): 1601223, 2017.

[369] J. Morikawa, M. Ryu, K. Maximova, A. Balčytis, G. Seniutinas, L. Fan, V. Mizeikis, J. Li, X. Wang, M. Zamengo, X. Wang, and S. Juodkazis. Silk fibroin as a water-soluble bio-resist and its thermal properties. *RSC Adv.*, 6(14):11863–11869, 2016.

[370] A. E. Grigorescu and C. W. Hagen. Resists for sub-20-nm electron beam lithography with a focus on HSQ: state of the art. *Nanotechnology*, 20(29):292001, 2009.

[371] W. E. Hennink C. F. van Nostrum. Novel crosslinking methods to design hydrogels. *Adv. Drug Del. Rev.*, 54(1):13–36, 2002.

[372] I. Zailer, J. E. F. Frost, V. Chabasseur-Molyneux, C. J. B. Ford, and M. Pepper. Crosslinked PMMA as a high-resolution negative resist for electron beam lithography and applications for physics of low-dimensional structures. *Semicond. Sci. Technol.*, 11 (8):1235–1238, 1996.

[373] T. Gowa Oyama, H. Nakamura, A. Oshima, M. Washio, and S. Tagawa. Positive-negative dual-tone sensitivities of ZEP resist. *Appl. Phys. Express*, 7(3):036501, 2014.

[374] M. Fleischmann, P. J. Hendra, and A. J. McQuillan. Raman spectra of pyridine adsorbed at a silver electrode. *Chem. Phys. Lett.*, 26(2):163–166, 1974.

[375] D. L. Jeanmaire and R. P. Van Duyne. Surface Raman spectroelectrochemistry: Part I. heterocyclic, aromatic, and aliphatic amines adsorbed on the anodized silver electrode. *J. Electroanal. Chem.*, 84(1):1–20, 1977.

[376] M. Moskovits. Surface roughness and the enhanced intensity of Raman scattering by molecules adsorbed on metals. *J. Chem. Phys.*, 69(9):4159–4161, 1978.

[377] A. B. Zrimsek, N. L. Wong, and R. P. Van Duyne. Single molecule surface-enhanced Raman spectroscopy: A critical analysis of the bianalyte versus isotopologue proof. *J. Phys. Chem. C*, 120(9):5133–5142, 2016.

[378] A. Balčytis, Y. Nishijima, S. Krishnamoorthy, A. Kuchmizhak, P. R. Stoddart, R. Petruškevičius, and S. Juodkazis. From fundamental toward applied SERS: Shared principles and divergent approaches. *Adv. Opt. Mater.*, 6(16):1800292, 2018.

[379] C. V. Raman and K. S. Krishnan. A new type of secondary radiation. *Nature*, 121: 501–502, 1928.

[380] R. L. McCreery. Magnitude of raman scattering. In J. D. Winefordner, editor, *Raman Spectroscopy for Chemical Analysis*, volume 157 of *Chemical Analysis*, pages 15–33. John Wiley & Sons, Inc., New York, NY, USA, 2000.

[381] L. Kastrup and S. W. Hell. Absolute optical cross section of individual fluorescent

molecules. *Angew. Chem. Int. Ed.*, 43(48):6646–6649, 2004.

[382] S.-Y. Ding, E.-M. You, Z.-Q. Tian, and M. Moskovits. Electromagnetic theories of surface-enhanced Raman spectroscopy. *Chem. Soc. Rev.*, 46(13):4042–4076, 2017.

[383] M. G. Albrecht and J. A. Creighton. Anomalously intense Raman spectra of pyridine at a silver electrode. *J. Am. Chem. Soc.*, 99(15):5215–5217, 1977.

[384] L. Jensen, C. M. Aikens, and G. C. Schatz. Electronic structure methods for studying surface-enhanced Raman scattering. *Chem. Soc. Rev.*, 37(5):1061–1073, 2008.

[385] A. Campion and P. Kambhampati. Surface-enhanced Raman scattering. *Chem. Soc. Rev.*, 27(4):241–250, 1998.

[386] K. Kneipp, Y. Wang, H. Kneipp, L. T. Perelman, I. Itzkan, and R. R. Dasari amd M. S. Feld. Single molecule detection using surface-enhanced Raman scattering (SERS). *Phys. Rev. Lett.*, 78(9):1667–1670, 1997.

[387] S. Nie and S. R. Emory. Probing single molecules and single nanoparticles by surface-enhanced Raman scattering. *Science*, 275(5303):1102–1106, 1997.

[388] E. C. Le Ru, M. Meyer, and P. G. Etchegoin. Proof of single-molecule sensitivity in surface enhanced Raman scattering (SERS) by means of a two-analyte technique. *J. Phys. Chem. B*, 110(4):1944–1948, 2006.

[389] J. A. Dieringer, R. B. Lettan II, K. A. Scheidt, and R. P. Van Duyne. A frequency domain existence proof of single-molecule surface-enhanced Raman spectroscopy. *J. Am. Chem. Soc.*, 129(51):16249–16256, 2007.

[390] E. C. Le Ru and P. G. Etchegoin. *Principles of surface-enhanced Raman spectroscopy and related plasmonic effects*. Elsevier, Amsterdam, The Netherlands, 1st edition, 2009.

[391] M. Pelton. Modified spontaneous emission in nanophotonic structures. *Nat. Photon.*, 9: 427–435, 2015.

[392] L. D. Landau, J. S. Bell, M. J. Kearsley, L. P. Pitaevskii, E. M. Lifshitz, and J. B. Sykes. *Electrodynamics of continuous media*, volume 8 of *Course of Theoretical Physics*. Pergamon Press, Oxford, UK, 2nd edition, 1984.

[393] G. J. Kovacs, R. O. Loutfy, P. S. Vincett, C. Jennings, and R. Aroca. Distance dependence of SERS enhancement factor from Langmuir-Blodgett monolayers on metal island films: Evidence for the electromagnetic mechanism. *Langmuir*, 2(6):689–694, 1986.

[394] S. S. Masango, R. A. Hackler, N. Large, A.-I. Henry, M. O. McAnally, G. C. Schatz, P. C. Stair, and R. P. Van Duyne. High-resolution distance dependence study of surface-enhanced Raman scattering enabled by atomic layer deposition. *Nano Lett.*, 16(7): 4251–4259, 2016.

[395] M. Moskovits and J. S. Suh. Surface selection rules for surface-enhanced Raman spectroscopy: calculations and application to the surface-enhanced Raman spectrum of phthalazine on silver. *J. Phys. Chem.*, 88(23):5526–5530, 1984.

[396] E. C. Le Ru, M. Meyer, E. Blackie, and P. G. Etchegoin. Advanced aspects of electromagnetic SERS enhancement factors at a hot spot. *J. Raman Spectrosc.*, 39(9): 1127–1134, 2008.

[397] E. C. Le Ru, J. Grand, N. Félidj, J. Aubard, G. Lévi, A. Hohenau, J. R. Krenn, E. Blackie, and P. G. Etchegoin. Experimental verification of the SERS electromagnetic model beyond the $|E|^4$ approximation: Polarization effects. *J. Phys. Chem. C*, 112(22): 8117–8121, 2008.

[398] A. R. L. Marshall, J. Stokes, F. N. Viscomi, J. E. Proctor, J. Gierschner, J.-S. G. Bouillard, and A. M. Adawi. Determining molecular orientation via single molecule SERS in a plasmonic nano-gap. *Nanoscale*, 9(44):17415–17421, 2017.

[399] E. C. Le Ru, E. Blackie, M. Meyer, and P. G. Etchegoin. Surface enhanced Raman scattering enhancement factors: A comprehensive study. *J. Phys. Chem. C*, 111(37): 13794–13803, 2007.

[400] H. Xu, E. J. Bjerneld, M. Käll, and L. Börjesson. Spectroscopy of single hemoglobin molecules by surface enhanced Raman scattering. *Phys. Rev. Lett.*, 83(21):4357–4360, 1999.

[401] L. M. Freeman, L. Pang, and Y. Fainman. Maximizing the electromagnetic and chemical resonances of surface-enhanced Raman scattering for nucleic acids. *ACS Nano*, 8(8): 8383–8391, 2014.

[402] A. Campion, J. E. Ivanecky III, C. M. Child, and M. Foster. On the mechanism of chemical enhancement in surface-enhanced Raman scattering. *J. Am. Chem. Soc.*, 117 (47):11807–11808, 1995.

[403] P. Kambhampati, C. M. Child, M. C. Foster, and A. Campion. On the chemical mechanism of surface enhanced Raman scattering: Experiment and theory. *J. Chem. Phys.*, 108(12):5013–5026, 1998.

[404] A. Otto. The 'chemical' (electronic) contribution to surface-enhanced Raman scattering. *J. Raman Spectrosc.*, 36(6-7):497–509, 2005.

[405] G. McNay, D. Eustace, W. Ewen Smith, K. Faulds, and D. Graham. Surface-enhanced Raman scattering (SERS) and surface-enhanced resonance Raman scattering (SERRS): A review of applications. *Appl. Spectrosc.*, 65(8):825–837, 2011.

[406] G. Lu, B. Shrestha, and A. J. Haes. Importance of tilt angles of adsorbed aromatic molecules on nanoparticle rattle SERS substrates. *J. Phys. Chem. C*, 120(37):20759–20767, 2016.

[407] A. Jorio, N. S. Mueller, and S. Reich. Symmetry-derived selection rules for plasmon-enhanced Raman scattering. *Phys. Rev. B*, 95:155409, 2017.

[408] S. Dick, M. P. Konrad, W. W. Y. Lee, H. McCabe, J. N. McCracken, T. M. D. Rahman, A. Stewart, Y. Xu, and S. E. J. Bell. Surface-enhanced Raman spectroscopy as a probe of the surface chemistry of nanostructured materials. *Adv. Mater.*, 28(27):5705–5711, 2016.

[409] J. R. Lombardi and R. L. Birke. A unified approach to surface-enhanced Raman

spectroscopy. *J. Phys. Chem. C*, 112(14):5605–5617, 2008.

[410] J. R. Lombardi and R. L. Birke. The theory of surface-enhanced Raman scattering. *J. Chem. Phys.*, 136(14):144704, 2012.

[411] P. S. Londero, M. Leona, and J. R. Lombardi. Definitive evidence for linked resonances in surface-enhanced Raman scattering: Excitation profile of Cu phthalocyanine. *Appl. Phys. Lett.*, 102(11):111101, 2013.

[412] S. K. Saikin, R. Olivares-Amaya, D. Rappoport, M. Stopa, and A. Aspuru-Guzik. On the chemical bonding effects in the Raman response: Benzenethiol adsorbed on silver clusters. *Phys. Chem. Chem. Phys.*, 11(41):9401–9411, 2009.

[413] J. E. Moore, S. M. Morton, and L. Jensen. Importance of correctly describing charge-transfer excitations for understanding the chemical effect in SERS. *J. Phys. Chem. Lett.*, 3(17):2470–2475, 2012.

[414] N. Valley, N. Greeneltch, R. P. Van Duyne, and G. C. Schatz. A look at the origin and magnitude of the chemical contribution to the enhancement mechanism of surface-enhanced Raman spectroscopy (SERS): Theory and experiment. *J. Phys. Chem. Lett.*, 4(16):2599–2604, 2013.

[415] K. Kneipp. Chemical contribution to SERS enhancement: An experimental study on a series of polymethine dyes on silver nanoaggregates. *J. Phys. Chem. C*, 120(37): 21076–21081, 2016.

[416] S. M. Morton and L. Jensen. Understanding the molecule-surface chemical coupling in SERS. *J. Am. Chem. Soc.*, 131(11):4090–4098, 2009.

[417] L. Zhao, L. Jensen, and G. C. Schatz. Pyridine-Ag_{20} cluster: A model system for studying surface-enhanced Raman scattering. *J. Am. Chem. Soc.*, 128(9):2911–2919, 2006.

[418] P. Hildebrandt and M. Stockburger. Surface-enhanced resonance Raman spectroscopy of Rhodamine 6G adsorbed on colloidal silver. *J. Phys. Chem.*, 88(24):5935–5944, 1984.

[419] K. Kneipp, H. Kneipp, I. Itzkan, R. R. Dasari, and M. S. Feld. Surface-enhanced Raman scattering and biophysics. *J. Phys.: Condens. Matter.*, 14:R597–R624, 2002.

[420] S. A. Meyer, E. C. Le Ru, and P. G. Etchegoin. Quantifying resonant Raman cross sections with SERS. *J. Phys. Chem. A*, 114(17):5515–5519, 2010.

[421] P. Johansson, H. Xu, and M. Käll. Surface-enhanced Raman scattering and fluorescence near metal nanoparticles. *Phys. Rev. B*, 72:035427, 2005.

[422] S. M. Morton, D. W. Silverstein, and L. Jensen. Theoretical studies of plasmonics using electronic structure methods. *Chem. Rev.*, 111(6):3962–3994, 2011.

[423] A. Królikowska. Surface-enhanced resonance Raman scattering (SERRS) as a tool for the studies of electron transfer proteins attached to biomimetic surfaces: Case of cytochrome c. *Electrochim. Acta*, 111:952–995, 2013.

[424] N. P. W. Pieczonka and R. F. Aroca. Single molecule analysis by surfaced-enhanced

Raman scattering. *Chem. Soc. Rev.*, 37(5):946–954, 2008.

[425] S. Laing, L. E. Jamieson, K. Faulds, and D. Graham. Surface-enhanced Raman spectroscopy for *in vivo* biosensing. *Nat. Rev. Chem.*, 1:0060, 2017.

[426] A. V. Soldatova, M. Ibrahim, J. S. Olson, R. S. Czernuszewicz, and T. G. Spiro. New light on NO bonding in Fe(III) heme proteins from resonance Raman spectroscopy and DFT modeling. *J. Am. Chem. Soc.*, 132(13):4614–4625, 2010.

[427] L. A. Dick, A. J. Haes, and R. P. Van Duyne. Distance and orientation dependence of heterogeneous electron transfer: A surface-enhanced resonance Raman scattering study of cytochrome *c* bound to carboxylic acid terminated alkanethiols adsorbed on silver electrodes. *J. Phys. Chem. B*, 104(49):11752–11762, 2000.

[428] D. H. Murgida and P. Hildebrandt. Heterogeneous electron transfer of cytochrome *c* on coated silver electrodes. electric field effects on structure and redox potential. *J. Phys. Chem. B*, 105(8):1578–1586, 2001.

[429] L.-J. Xu, C. Zong, X.-S. Zheng, P. Hu, J.-M. Feng, and B. Ren. Label-free detection of native proteins by surface-enhanced Raman spectroscopy using iodide-modified nanoparticles. *Anal. Chem.*, 86(4):2238–2245, 2014.

[430] D. O. Sigle, E. Perkins, J. J. Baumberg, and S. Mahajan. Reproducible deep-UV SERRS on aluminum nanovoids. *J. Phys. Chem. Lett.*, 4(9):1449–1452, 2013.

[431] B. Sharma, M. Fernanda Cardinal, M. B. Ross, A. B. Zrimsek, S. V. Bykov, D. Punihaole, S. A. Asher, G. C. Schatz, and R. P. Van Duyne. Aluminum film-over-nanosphere substrates for deep-UV surface-enhanced resonance Raman spectroscopy. *Nano Lett.*, 16(12):7968–7973, 2016.

[432] X.-M. Li, M.-H. Bi, L. Cui, Y.-Z. Zhou, X.-W. Du, S.-Z. Qiao, and J. Yang. 3D aluminum hybrid plasmonic nanostructures with large areas of dense hot spots and long-term stability. *Adv. Funct. Mater.*, 27(10):1605703, 2017.

[433] B. Ren, X.-F. Lin, Z.-L. Yang, G.-K. Liu, R. F. Aroca, B.-W. Mao, , and Z.-Q. Tian. Surface-enhanced Raman scattering in the ultraviolet spectral region: UV-SERS on rhodium and ruthenium electrodes. *J. Am. Chem. Soc.*, 125(32):9598–9599, 2003.

[434] M. Fernanda Cardinal, E. Vander Ende, R. A. Hackler, M. O. McAnally, P. C. Stair, G. C. Schatz, and R. P. Van Duyne. Expanding applications of SERS through versatile nanomaterials engineering. *Chem. Soc. Rev.*, 46(13):3886–3903, 2017.

[435] Ph. Avouris and J. E. Demuth. Electronic excitations of benzene, pyridine, and pyrazine adsorbed on Ag(111). *J. Chem. Phys.*, 75(10):4783–4794, 1981.

[436] W. B. Cai, B. Ren, X. Q. Li, C. X. She, F. M. Liu, X. W. Cai, and Z. Q. Tian. Investigation of surface-enhanced Raman scattering from platinum electrodes using a confocal raman microscope: dependence of surface roughening pretreatment. *Surf. Sci.*, 406(1-3):9–22, 1998.

[437] T. Shegai, A. Vaskevich, I. Rubinstein, and G. Haran. Raman spectroelectrochemistry of molecules within individual electromagnetic hot spots. *J. Am. Chem. Soc.*, 131(40): 14390–14398, 2009.

[438] W.-H. Park and Z. H. Kim. Charge transfer enhancement in the SERS of a single molecule. *Nano Lett.*, 10(10):4040–4048, 2010.

[439] J. R. Lombardi and R. L. Birke. Theory of surface-enhanced Raman scattering in semiconductors. *J. Phys. Chem. C*, 118(20):11120–11130, 2014.

[440] D. Chen L. Liu, H. Ma, and W. Z. Liang. Spectral characteristics of chemical enhancement on SERS of benzene-like derivatives: Franck–Condon and Herzberg–Teller contributions. *J. Phys. Chem. C*, 119(49):27609–27619, 2015.

[441] R. L. Birke, J. R. Lombardi, W. A. Saidi, and P. Norman. Surface-enhanced Raman scattering due to charge-transfer resonances: A time-dependent density functional theory study of Ag_{13}-4-mercaptopyridine. *J. Phys. Chem. C*, 120(37):20721–20735, 2016.

[442] R. L. Birke, V. Znamenskiy, and J. R. Lombardi. A charge-transfer surface enhanced Raman scattering model from time-dependent density functional theory calculations on a Ag_{10}-pyridine complex. *J. Chem. Phys.*, 132(21):214707, 2010.

[443] E. López-Tobar, K. Hara, I. Izquierdo-Lorenzo, and S. Sanchez-Cortes. Plasmonic effects of phenylenediisocyanides linked at interparticle junctions of metal nanoparticles. *J. Phys. Chem. C*, 119(1):599–609, 2015.

[444] R. L. Aggarwal, L. W. Farrar, and S. K. Saikin. Increase of SERS signal upon heating or exposure to a high-intensity laser field: Benzenethiol on an AgFON substrate. *J. Phys. Chem. C*, 116(31):16656–16659, 2012.

[445] R. Schürmann and I. Bald. Decomposition of DNA nucleobases by laser irradiation of gold nanoparticles monitored by surface-enhanced Raman scattering. *J. Phys. Chem. C*, 120(5):3001–3009, 2016.

[446] V. Joseph, C. Engelbrekt, J. Zhang, U. Gernert, J. Ulstrup, and J. Kneipp. Characterizing the kinetics of nanoparticle-catalyzed reactions by surface-enhanced Raman scattering. *Angew. Chem. Int. Ed.*, 51(30):7592–7596, 2012.

[447] R. C. Maher, L. F. Cohen, and P. Etchegoin. Single molecule photo-bleaching observed by surface enhanced resonant Raman scattering (SERRS). *Chem. Phys. Lett.*, 352(5-6): 378–384, 2002.

[448] R. C. Maher, T. Zhang, L. F. Cohen, J. C. Gallop, F. M. Liu, and M. Green. Towards a metrological determination of the performance of SERS media. *Phys. Chem. Chem. Phys.*, 11(34):7463–7468, 2009.

[449] Y. Maruyama, M. Ishikawa, and M. Futamata. Thermal activation of blinking in SERS signal. *J. Phys. Chem. B*, 108(2):673–678, 2004.

[450] T. Kang, S. Hong, Y. Choi, and L. P. Lee. The effect of thermal gradients in SERS spectroscopy. *Small*, 6(23):2649–2652, 2010.

[451] S. A. Maier. Plasmonic field enhancement and SERS in the effective mode volume picture. *Opt. Express*, 14(5):1957–1964, 2006.

[452] I. Alessandri and J. R. Lombardi. Enhanced Raman scattering with dielectrics. *Chem.*

Rev., 116(24):14921–14981, 2016.

[453] Nicolò Bontempi, L. Carletti, C. De Angelis, and I. Alessandri. Plasmon-free SERS detection of environmental CO_2 on TiO_2 surfaces. *Nanoscale*, 8(6):3226–3231, 2016.

[454] P. A. Dmitriev, D. G. Baranov, V. A. Milichko, S. V. Makarov, I. S. Mukhin, A. K. Samusev, A. E. Krasnok, P. A. Belov, and Y. S. Kivshar. Resonant Raman scattering from silicon nanoparticles enhanced by magnetic response. *Nanoscale*, 8(18):9721–9726, 2016.

[455] L. Jiang, T. You, P. Yin, Y. Shang, D. Zhang, L. Guo, and S. Yang. Surface-enhanced Raman scattering spectra of adsorbates on Cu_2O nanospheres: charge-transfer and electromagnetic enhancement. *Nanoscale*, 5(7):2784–2789, 2013.

[456] M. Yilmaz, E. Babur, M. Ozdemir, R. L. Gieseking, Y. Dede, U. Tamer, G. C. Schatz, A. Facchetti, H. Usta, and G. Demirel. Nanostructured organic semiconductor films for molecular detection with surface-enhanced Raman spectroscopy. *Nat. Mater.*, 16: 918–924, 2017.

[457] L. Novtony and B. Hecht. *Principles of nano-optics*. Cambridge University Press, Cambridge, UK, 2st edition, 2012.

[458] P. B. Johnson and R. W. Christy. Optical constants of the noble metals. *Phys. Rev. B*, 6 (12):4370–4379, 1972.

[459] K. M. McPeak, S. V. Jayanti, S. J. P. Kress, S. Meyer, S. Iotti, A. Rossinelli, and D. J. Norris. Plasmonic films can easily be better: Rules and recipes. *ACS Photonics*, 2(3): 326–333, 2015.

[460] F. Wang and Y. R. Shen. General properties of local plasmons in metal nanostructures. *Phys. Rev. Lett.*, 97(20):206806, 2006.

[461] E. T. Arakawa, M. W. Williams, R. N. Hamm, and R. H. Ritchie. Effect of damping on surface plasmon dispersion. *Phys. Rev. Lett.*, 31(18):1127–1129, 1973.

[462] A. Otto. Excitation of nonradiative surface plasma waves in silver by the method of frustrated total reflection. *Z. Phys.*, 216(4):398–410, 1968.

[463] E. Kretschmann and H. Raether. Radiative decay of non radiative surface plasmons excited by light. *Z. Naturforsch. A*, 23(12):2135–2136, 1968.

[464] H. H. Nguyen, J. Park, S. Kang, and M. Kim. Surface plasmon resonance: A versatile technique for biosensor applications. *Sensors*, 15(5):10481–10510, 2015.

[465] B. Pettinger, A. Tadjeddine, and D. M. Kolb. Enhancement in Raman intensity by use of surface plasmons. *Chem. Phys. Lett.*, 66(3):544–548, 1979.

[466] S. A. Meyer, B. Auguié, E. C. Le Ru, and P. G. Etchegoin. Combined SPR and SERS microscopy in the Kretschmann configuration. *J. Phys. Chem. A*, 116(3):1000–1007, 2012.

[467] F. Mohaghegh, A. M. Tehrani, and A. Materny. Investigation of the chemical enhancement contribution to SERS using a Kretschmann arrangement. *J. Raman Spectrosc.*, 47 (9):1029–1035, 2016.

[468] C. Lee, C. S. Robertson, A. H. Nguyen, M. Kahraman, and S. Wachsmann-Hogiu. Thickness of a metallic film, in addition to its roughness, plays a significant role in SERS activity. *Sci. Rep.*, 5:11644, 2015.

[469] G. Macias, M. Alba, L. F. Marsal, and A. Mihi. Surface roughness boosts the SERS performance of imprinted plasmonic architectures. *J. Mater. Chem. C*, 4(18):3970–3975, 2016.

[470] J. A. Stratton. *Electromagnetic Theory*. McGraw-Hill Book Company, Inc,, New York, USA, 1st edition, 1941.

[471] A. J. Haes, S. Zou, G. C. Schatz, and R. P. Van Duyne. A nanoscale optical biosensor: The long range distance dependence of the localized surface plasmon resonance of noble metal nanoparticles. *J. Phys. Chem. B*, 108(1):109–116, 2004.

[472] G. Mie. Articles on the optical characteristics of turbid tubes, especially colloidal metal solutions. *Ann. Phys.*, 25(3):377–445, 1908.

[473] M. Moskovits. Surface-enhanced Raman spectroscopy: a brief retrospective. *J. Raman Spectrosc.*, 36(6-7):485–496, 2005.

[474] M. B. Ross, C. A. Mirkin, and G. C. Schatz. Optical properties of one-, two-, and three-dimensional arrays of plasmonic nanostructures. *J. Phys. Chem. C*, 120(2):816–830, 2016.

[475] E. Prodan, C. Radloff, N. J. Halas, and P. Nordlander. A hybridization model for the plasmon response of complex nanostructures. *Science*, 302:419–422, 2003.

[476] P. Mühlschlegel, H.-J. Eisler, O. J. F. Martin, B. Hecht, and D. W. Pohl. Resonant optical antennas. *Science*, 308(5728):1607–1609, 2005.

[477] P. Nordlander, C. Oubre, E. Prodan, K. Li, and M. I. Stockman. Plasmon hybridization in nanoparticle dimers. *Nano Lett.*, 4(5):899–903, 2004.

[478] D.-K. Lim, K.-S. Jeon, H. M. Kim, J.-M. Nam, and Y. D. Suh. Nanogap-engineerable Raman-active nanodumbbells for single-molecule detection. *Nat. Mater.*, 9:60–67, 2010.

[479] V. V. Thacker, L. O. Herrmann, D. O. Sigle, T. Zhang, T. Liedl, J. J. Baumberg, and U. F. Keyser. DNA origami based assembly of gold nanoparticle dimers for surface-enhanced Raman scattering. *Nat. Commun.*, 5:3448, 2014.

[480] W. Zhu and K. B. Crozier. Quantum mechanical limit to plasmonic enhancement as observed by surface-enhanced Raman scattering. *Nat. Commun.*, 5:5228, 2014.

[481] D. Khlopin, F. Laux, W. P. Wardley, J. Martin, G. A. Wurtz, J. Plain, N. Bonod, A. V. Zayats, W. Dickson, and D. Gérard. Lattice modes and plasmonic linewidth engineering in gold and aluminum nanoparticle arrays. *J. Opt. Soc. Am. B*, 34(3):691–700, 2017.

[482] G. Hergert, J. Vogelsang, F. Schwarz, D. Wang, H. Kollmann, P. Groß, C. Lienau, E. Runge, and P. Schaaf. Long-lived electron emission reveals localized plasmon modes in disordered nanosponge antennas. *Light Sci. Appl.*, 6:e17075, 2017.

[483] S. Zou, N. Janel, and G. C. Schatz. Silver nanoparticle array structures that produce

remarkably narrow plasmon lineshapes. *Nat. Mater.*, 120(23):10871–10875, 2004.

[484] W. Zhou and T. W. Odom. Tunable subradiant lattice plasmons by out-of-plane dipolar interactions. *Nat. Nanotechnol.*, 6:423–427, 2011.

[485] A. Yang, A. J. Hryn, M. R. Bourgeois, W.-K. Lee, J. Hu, G. C. Schatz, , and T. W. Odom. Programmable and reversible plasmon mode engineering. *Proc. Natl. Acad. Sci. U.S.A*, 113(50):14201–14206, 2016.

[486] W. Wang, M. Ramezani, A. I. Väkeväinen, P. Törmä, J. Gómez Rivas, and T. W. Odom. The rich photonic world of plasmonic nanoparticle arrays. *Mater. Today*, 21(3):303–314, 2018.

[487] S. Zou and G. C. Schatz. Silver nanoparticle array structures that produce giant enhancements in electromagnetic fields. *Chem. Phys. Lett.*, 403(1–3):62–67, 2005.

[488] R. Adato, A. A. Yanik, J. J. Amsden, D. L. Kaplan, F. G. Omenetto, M. K. Hong, S. Erramilli, and H. Altug. Ultra-sensitive vibrational spectroscopy of protein monolayers with plasmonic nanoantenna arrays. *Proc. Natl. Acad. Sci. U.S.A*, 106(46): 19227–19232, 2009.

[489] K. T. Carron, W. Fluhr, M. Meier, A. Wokaun, and H. W. Lehmann. Resonances of two-dimensional particle gratings in surface-enhanced Raman scattering. *J. Opt. Soc. Am. B*, 3(3):430–440, 1986.

[490] V. M. Shalaev (Ed.). *Optical Properties of Nanostructured Random Media*, volume 82 of *Topics in Applied Physics*. Springer-Verlag, Berlin Heidelberg, Germany, 2002.

[491] L. Dal Negro and S. V. Boriskina. Deterministic aperiodic nanostructures for photonics and plasmonics applications. *Laser Photon. Rev.*, 6(2):178–218, 2012.

[492] D. S. Wiersma. Disordered photonics. *Nat. Photon.*, 7:188–196, 2013.

[493] M. I. Stockman. Nanoplasmonics: past, present, and glimpse into future. *Opt. Express*, 19(22):22029–22106, 2011.

[494] M. I. Stockman. Inhomogeneous eigenmode localization, chaos, and correlations in large disordered clusters. *Phys. Rev. E*, 56(6):6494–6507, 1997.

[495] M. I. Stockman, S. V. Faleev, and D. J. Bergman. Localization versus delocalization of surface plasmons in nanosystems: Can one state have both characteristics? *Phys. Rev. Lett.*, 87(16):167401, 2001.

[496] V. Krachmalnicoff, E. Castanié, Y. De Wilde, and R. Carminati. Fluctuations of the local density of states probe localized surface plasmons on disordered metal films. *Phys. Rev. Lett.*, 105(18):183901, 2010.

[497] S. Grésillon, L. Aigouy, A. C. Boccara, J. C. Rivoal, X. Quelin, C. Desmarest, P. Gadenne, V. A. Shubin, A. K. Sarychev, and V. M. Shalaev. Experimental observation of localized optical excitations in random metal-dielectric films. *Phys. Rev. Lett.*, 82(22):4520–4523, 1999.

[498] S. Pandey, B. Gupta, S. Mujumdar, and A. Nahata. Direct observation of Anderson localization in plasmonic terahertz devices. *Light Sci. Appl.*, 6:e16232, 2017.

[499] M. Hentschel, M. Saliba, R. Vogelgesang, H. Giessen, A. P. Alivisatos, and N. Liu. Transition from isolated to collective modes in plasmonic oligomers. *Nano Lett.*, 10(7): 2721–2726, 2010.

[500] V. M. Shalaev, R. Botet, J. Mercer, and E. B. Stechel. Optical properties of self-affine thin films. *Phys. Rev. B*, 54(11):8235–8242, 1996.

[501] E. Y. Poliakov, V. M. Shalaev, V. A. Markel, and R. Botet. Enhanced Raman scattering from self-affine thin films. *Opt. Lett.*, 21(20):1628–1630, 1996.

[502] V. M. Shalaev and A. K. Sarychev. Nonlinear optics of random metal-dielectric films. *Phys. Rev. B*, 57(20):13265–13288, 1998.

[503] M. I. Stockman, L. N. Pandey, L. S. Muratov, and T. F. George. Giant fluctuations of local optical fields in fractal clusters. *Phys. Rev. Lett.*, 72(15):2486–2489, 1994.

[504] D. P. Tsai, J. Kovacs, Z. Wang, M. Moskovits, V. M. Shalaev, J. S. Suh, and R. Botet. Photon scanning tunneling microscopy images of optical excitations of fractal metal colloid clusters. *Phys. Rev. Lett.*, 72(26):4149–4152, 1994.

[505] M. Moskovits. Surface-enhanced spectroscopy. *Rev. Mod. Phys.*, 57(3):783–826, 1985.

[506] Y. Fang, N.-H. Seong, and D. D. Dlott. Measurement of the distribution of site enhancements in surface-enhanced Raman scattering. *Science*, 321(5887):388–392, 2008.

[507] G. Eom, H. Kim, A. Hwang, H.-Y. Son, Y. Choi, J. Moon, D. Kim, M. Lee, E.-K. Lim, J. Jeong, Y.-M. Huh, M.-K. Seo, T. Kang, and B. Kim. Nanogap-rich Au nanowire SERS sensor for ultrasensitive telomerase activity detection: Application to gastric and breast cancer tissues diagnosis. *Adv. Funct. Mater.*, 27(37):1701832, 2017.

[508] M. Procházka. *Surface-Enhanced Raman Spectroscopy - Bioanalytical, Biomolecular and Medical Applications*. Biological and Medical Physics, Biomedical Engineering. Springer International Publishing, Berlin Heidelberg, Germany, 2016.

[509] Z. A. Nima, A. Biswas, I. S. Bayer, F. D. Hardcastle, D. Perry, A. Ghosh, E. Dervishi, and A. S. Biris. Applications of surface-enhanced Raman scattering in advanced bio-medical technologies and diagnostics. *Drug Metab. Rev.*, 46(2):155–175, 2014.

[510] C. Muehlethaler, M. Leona, and J. R. Lombardi. Review of surface enhanced Raman scattering applications in forensic science. *Anal. Chem.*, 88(1):152–169, 2016.

[511] M. Leona. Microanalysis of organic pigments and glazes in polychrome works of art by surface-enhanced resonance Raman scattering. *Proc. Natl. Acad. Sci. U.S.A*, 106 (35):14757–14762, 2017.

[512] F. Pozzi and M. Leona. Surface-enhanced raman spectroscopy in art and archaeology. *J. Raman Spectrosc.*, 47(1):67–77, 2016.

[513] A. P. Craig, A. S. Franca, and J. Irudayaraj. Surface-enhanced Raman spectroscopy applied to food safety. *Annu. Rev. Food Sci. Technol.*, 4:369–380, 2016.

[514] A. Hakonena, P. O. Andersson, M. Stenbæk Schmidt, T. Rindzevicius, and M. Käll. Explosive and chemical threat detection by surface-enhanced Raman scattering: A

review. *Anal. Chim. Acta*, 893(1):1–13, 2015.

[515] P. C. Lee and D. Meisel. Adsorption and surface-enhanced Raman of dyes on silver and gold sols. *J. Phys. Chem.*, 86(17):3391–3395, 1982.

[516] J. Jiang, K. Bosnick, M. Maillard, and L. Brus. Single molecule Raman spectroscopy at the junctions of large Agnanocrystals. *J. Phys. Chem. B*, 107(37):9964–9972, 2003.

[517] F. Hong, F. Zhang, Y. Liu, and H. Yan. DNA origami: Scaffolds for creating higher order structures. *ACS Photonics*, 117(20):12584–12640, 2017.

[518] V. V. Thacker, L. O. Herrmann, D. O. Sigle, T. Zhang, T. Liedl, J. J. Baumberg, and U. F. Keyser. DNA origami based assembly of gold nanoparticle dimers for surface-enhanced Raman scattering. *Nat. Commun.*, 5:3448, 2014.

[519] C. Heck, J. Prinz, A. Dathe, V. Merk, O. Stranik, W. Fritzsche, J. Kneipp, and I. Bald. Gold nanolenses self-assembled by DNA origami. *ACS Photonics*, 4(5):1123–1130, 2017.

[520] J. F. Li, Y. F. Huang, Y. Ding, Z. L. Yang, S. B. Li, X. S. Zhou, F. R. Fan, W. Zhang, Z. Y. Zhou, D. Y. Wu, B. Ren, Z. L. Wang, and Z. Q. Tian. Shell-isolated nanoparticle-enhanced Raman spectroscopy. *Nature*, 464:392–395, 2010.

[521] J. Xu, Y.-J. Zhang, H. Yin, H.-L. Zhong, M. Su, Z.-Q. Tian, and J.-F. Li. Shell-isolated nanoparticle-enhanced Raman and fluorescence spectroscopies: Synthesis and applications. *Adv. Opt. Mater.*, 6(4):1701069, 2018.

[522] C. Ziegler and A. Eychmüller. Seeded growth synthesis of uniform gold nanoparticles with diameters of 15-300 nm. *J. Phys. Chem. C*, 115(11):4502–4506, 2011.

[523] A. Ahmed and R. Gordon. Single molecule directivity enhanced Raman scattering using nanoantennas. *Nano Lett.*, 12(5):2625–2630, 2012.

[524] W. Zhu, D. Wang, and K. B. Crozier. Direct observation of beamed Raman scattering. *Nano Lett.*, 12(12):6235–6243, 2012.

[525] J. Zhang, M. Irannejad, and B. Cui. Bowtie nanoantenna with single-digit nanometer gap for surface-enhanced Raman scattering (SERS). *Plasmonics*, 10(4):831–837, 2015.

[526] S. Cakmakyapan, N. A. Cinel, A. Ozgur Cakmak, and E. Ozbay. Validation of electromagnetic field enhancement in near-infrared through Sierpinski fractal nanoantennas. *Opt. Express*, 22(16):19504–19512, 2014.

[527] L. Petti, R. Capasso, M. Rippa, M. Pannico, P. La Manna, G. Peluso, A. Calarco, E. Bobeico, and P. Musto. A plasmonic nanostructure fabricated by electron beam lithography as a sensitive and highly homogeneous SERS substrate for bio-sensing applications. *Vib. Spectrosc.*, 82:22–30, 2016.

[528] A. Lesuffleur, L. K. S. Kumar, A. G. Brolo, K. L. Kavanagh, and R. Gordon. Apex-enhanced Raman spectroscopy using double-hole arrays in a gold film. *J. Phys. Chem. C*, 111(6):2347–2350, 2007.

[529] Y. Nishijima, J. B. Khurgin, L. Rosa, H. Fujiwara, and S. Juodkazis. Randomization of gold nano-brick arrays: a tool for SERS enhancement. *Opt. Express*, 21(11):13502–

13514, 2013.

[530] H. Im, K. C. Bantz, N. C. Lindquist, C. L. Haynes, and S.-H. Oh. Vertically oriented sub-10-nm plasmonic nanogap arrays. *Nano Lett.*, 10(6):2231–2236, 2010.

[531] A. Reyer, A. Prinz, S. Giancristofaro, J. Schneider, D. Bertoldo Menezes, G. Zickler, G. R. Bourret, and M. E. Musso. Investigation of mass-produced substrates for reproducible surface-enhanced Raman scattering measurements over large areas. *ACS Appl. Mater. Interfaces*, 9(30):25445–25454, 2017.

[532] L. A. Dick, A. D. McFarland, C. L. Haynes, and R. P. Van Duyne. Metal film over nanosphere (MFON) electrodes for surface-enhanced Raman spectroscopy (SERS): Improvements in surface nanostructure stability and suppression of irreversible loss. *J. Phys. Chem. B*, 106(4):853–860, 2002.

[533] N. G. Greeneltch, M. G. Blaber, A.-I. Henry, G. C. Schatz, and R. P. Van Duyne. Immobilized nanorod assemblies: Fabrication and understanding of large area surface-enhanced Raman spectroscopy substrates. *Anal. Chem.*, 85(4):2297–2303, 2013.

[534] H. Im, K. C. Bantz, S. H. Lee, T. W. Johnson, C. L. Haynes, and S.-H. Oh. Self-assembled plasmonic nanoring cavity arrays for SERS and LSPR biosensing. *Adv. Mater.*, 25(19):2678–2685, 2013.

[535] C. L. Haynes and R. P. Van Duyne. Nanosphere lithography: A versatile nanofabrication tool for studies of size-dependent nanoparticle optics. *J. Phys. Chem. B*, 105(24):5599–5611, 2001.

[536] S. Dinda, V. Suresh, P. Thoniyot, A. Balčytis, S. Juodkazis, and S. Krishnamoorthy. Engineering 3D nanoplasmonic assemblies for high performance spectroscopic sensing. *ACS Appl. Mater. Interfaces*, 7(50):27661–27666, 2015.

[537] H.-H. Wang, C.-Y. Liu, S.-B. Wu, N.-W. Liu, C.-Y. Peng, T.-H. Chan, C.-F. Hsu, J.-K. Wang, and Y.-L. Wang. Highly Raman-enhancing substrates based on silver nanoparticle arrays with tunable sub-10 nm gaps. *Adv. Mater.*, 18(4):491–495, 2006.

[538] M. Park, C. Harrison, P. M. Chaikin, R. A. Register, and D. H. Adamson. Block copolymer lithography: Periodic arrays of $\sim 10^{11}$ holes in 1 square centimeter. *Science*, 276(5317):1401–1404, 1997.

[539] C. M. Bates, M. J. Maher, D. W. Janes, C. J. Ellison, and C. G. Willson. Block copolymer lithography. *Macromolecules*, 47(1):2–12, 2014.

[540] S. Krishnamoorthy, K. K. Manipaddy, and F. L. Yap. Wafer-level self-organized copolymer templates for nanolithography with sub-50 nm feature and spatial resolutions. *Adv. Funct. Mater.*, 21(6):1102–1112, 2011.

[541] I. Romero, J. Aizpurua, G. W. Bryant, and F. J. García de Abajo. Plasmons in nearly touching metallic nanoparticles: singular response in the limit of touching dimers. *Opt. Express*, 14(21):9988–9999, 2006.

[542] G. Toscano, S. Raza, S. Xiao, M. Wubs, A.-P. Jauho, S. I. Bozhevolnyi, and N. A. Mortensen. Surface-enhanced Raman spectroscopy: nonlocal limitations. *Opt. Lett.*, 37(13):2538–2540, 2012.

[543] N. A. Mortensen, S. Raza, M. Wubs, T. Søndergaard, and S. I. Bozhevolnyi. A generalized non-local optical response theory for plasmonic nanostructures. *Nat. Commun.*, 5:3809, 2014.

[544] J. Zheng, S. Pang, T. P. Labuza, and L. He. Evaluation of surface-enhanced Raman scattering detection using a handheld and a bench-top Raman spectrometer: A comparative study. *Talanta*, 129:79–85, 2014.

[545] D. Li, D.-W. Li, J. S. Fossey, and Y.-T. Long. Portable surface-enhanced Raman scattering sensor for rapid detection of aniline and phenol derivatives by on-site electrostatic preconcentration. *Anal. Chem.*, 82(22):9299–9305, 2010.

[546] W. W. Yu and I. M. White. Inkjet-printed paper-based SERS dipsticks and swabs for trace chemical detection. *Analyst*, 138(4):1020–1025, 2013.

[547] N. Chen, P. Ding, Y. Shi, T. Jin, Y. Su, H. Wang, and Y. He. Portable and reliable surface-enhanced Raman scattering silicon chip for signal-on detection of trace trinitrotoluene explosive in real systems. *Anal. Chem.*, 89(9):5072–5078, 2017.

[548] A. Hakonen, T. Rindzevicius, M. Stenbæk Schmidt, P. O. Andersson, L. Juhlin, M. Svedendahl, A. Boisen, and M. Käll. Detection of nerve gases using surface-enhanced Raman scattering substrates with high droplet adhesion. *Nanoscale*, 8:1305–1308, 2016.

[549] X. Zhang, M. A. Young, O. Lyandres, and R. P. Van Duyne. Rapid detection of an anthrax biomarker by surface-enhanced Raman spectroscopy. *J. Am. Chem. Soc.*, 127 (12):4484–4489, 2005.

[550] C. Song, J. D. Driskell, R. A. Tripp, Y. Cui, and Y. Zhao. The use of a handheld Raman system for virus detection. In *Proc. SPIE 8358, Chemical, Biological, Radiological, Nuclear, and Explosives (CBRNE) Sensing XIII*, page 83580I, 2012.

[551] D. P. Cowcher, Y. Xu, and R. Goodacre. Portable, quantitative detection of *bacillus* bacterial spores using surface-enhanced Raman scattering. *Anal. Chem.*, 85(6):3297–3302, 2013.

[552] B. Sharma, R. R.Frontiera, A.-I. Henry, E. Ringe, and R. P. Van Duyne. SERS: Materials, applications, and the future. *Mater. Today*, 15(1-2):16–25, 2012.

[553] J. Stropp, G. Trachta, G. Brehm, and S. Schneider. A new version of AgFON substrates for high-throughput analytical SERS applications. *J. Raman Spectrosc.*, 34(1):26–32, 2003.

[554] J. Lee, Q. Zhang, S. Park, A. Choe, Z. Fan, and H. Ko. Particle–film plasmons on periodic silver film over nanosphere (AgFON): A hybrid plasmonic nanoarchitecture for surface-enhanced Raman spectroscopy. *ACS Appl. Mater. Interfaces*, 8(1):634–642, 2016.

[555] R. Buividas, P. R. Stoddart, and S. Juodkazis. Laser fabricated ripple substrates for surface-enhanced Raman scattering. *Ann. Phys. (Berlin)*, 524(11):L5–L10, 2012.

[556] A. Chou, E. Jaatinen, R. Buividas, G. Seniutinas, S. Juodkazis, E. L. Izake, and P. M. Fredericks. SERS substrate for detection of explosives. *Nanoscale*, 4(23):7419–7424,

2012.

[557] R. Buividas, N. Dzingelevičius, R. Kubiliūtė, P. R. Stoddart, V. K. Truong, E. P. Ivanova, and S. Juodkazis. Statistically quantified measurement of an Alzheimer's marker by surface-enhanced Raman scattering. *J. Biophotonics*, 8(7):567–574, 2015.

[558] S. Jayawardhana, L. Rosa, S. Juodkazis, and P. R. Stoddart. Additional enhancement of electric field in surface-enhanced Raman scattering due to Fresnel mechanism. *Sci. Rep.*, 3:2335, 2013.

[559] S. Jayawardhana, G. Kostovski, A. P. Mazzolini, and P. R. Stoddart. Optical fiber sensor based on oblique angle deposition. *Appl. Opt.*, 50(2):155–162, 2011.

[560] S. Yamazoe, M. Naya, M. Shiota, T. Morikawa, A. Kubo, T. Tani, T. Hishiki, T. Horiuchi, M. Suematsu, and M. Kajimura. Large-area surface-enhanced Raman spectroscopy imaging of brain ischemia by gold nanoparticles grown on random nanoarrays of transparent boehmite. *ACS Nano*, 8(6):5622–5632, 2014.

[561] A. Balčytis, M. Ryu, G. Seniutinas, J. Juodkazytė, B. C. C. Cowie, P. R. Stoddart, M. Zamengo, J. Morikawa, and S. Juodkazis. Black-CuO: surface-enhanced Raman scattering and infrared properties. *Nanoscale*, 7:18299–18304, 2015.

[562] Q. Zhang, K. Zhang, D. Xu, G. Yang, H. Huang, F. Nie, C. Liu, and S. Yang. CuO nanostructures: Synthesis, characterization, growth mechanisms, fundamental properties, and applications. *Prog. Mater. Sci.*, 60:208–337, 2014.

[563] H.-J. Kim and J.-H. Lee. Highly sensitive and selective gas sensors using p-type oxide semiconductors: Overview. *Sens. Actuator B-Chem.*, 192:607–627, 2014.

[564] H. Ahmad, S. K. Kamarudin, L. J. Minggu, and M. Kassim. Hydrogen from photocatalytic water splitting process: A review. *Renew. Sust. Energ. Rev.*, 43:599–610, 2015.

[565] C. Wadia, A. P. Alivisatos, and D. M. Kammen. Materials availability expands the opportunity for large-scale photovoltaics deployment. *Electrochim. Acta*, 43(6):2072–2077, 2009.

[566] T. K. S. Wong, S. Zhuk, S. Masudy-Panah, and G. K. Dalapati. Current status and future prospects of copper oxide heterojunction solar cells. *Materials*, 9(4):271, 2016.

[567] S. B. Wang, C. H. Hsiao, S. J. Chang, , K. T. Lam, K. H. Wen, S. C. Hung, S. J. Young, and B. R. Huang. A CuO nanowire infrared photodetector. *Sens. Actuator. A-Phys.*, 171(2):207–211, 2011.

[568] Q. Hong, Y. Cao, J. Xu, H. Lu, J. He, and J.-L. Sun. Self-powered ultrafast broadband photodetector based on p–n heterojunctions of CuO/Si nanowire array. *ACS Appl. Mater. Interfaces*, 6(23):20887–20894, 2014.

[569] B. Wang, X.-L. Wu, C.-Y. Shu, , Y.-G. Guo, and C.-R. Wang. Synthesis of CuO/graphene nanocomposite as a high-performance anode material for lithium-ion batteries. *J. Mater. Chem.*, 20:10661–10664, 2010.

[570] Y. J. Mai, X. L. Wang, J. Y. Xiang, Y. Q. Qiao, D. Zhang, C. D. Gu, and J. P. Tu.

CuO/graphene composite as anode materials for lithium-ion batteries. *Electrochim. Acta*, 56(5):2306–2311, 2011.

[571] S. E. Moosavifard, M. F. El-Kady, M. S. Rahmanifar, R. B. Kaner, and M. F. Mousavi. Designing 3D highly ordered nanoporous CuO electrodes for high-performance asymmetric supercapacitors. *ACS Appl. Mater. Interfaces*, 7(8):4851–4860, 2015.

[572] S. K. Shinde, D. P. Dubal, G. S. Ghodake, and V. J. Fulari. Hierarchical 3D-flower-like CuO nanostructure on copper foil for supercapacitors. *RSC Adv.*, 5(6):4443–4447, 2015.

[573] J. Juodkazytė, B. Šebeka, I. Savickaja, A. Jagminas, V. Jasulaitienė, A. Selskis, J. Kovger, and P. Mack. Study on copper oxide stability in photoelectrochemical cell composed of nanostructured TiO_2 and Cu_xO electrodes. *Electrochim. Acta*, 137: 363–371, 2014.

[574] J. Juodkazytė, B. Šebeka, I. Savickaja, A. Selskis, V. Jasulaitienė, and P. Kalinauskas. Evaluation of electrochemically active surface area of photosensitive copper oxide nanostructures with extremely high surface roughness. *Electrochim. Acta*, 98:109–115, 2013.

[575] X. Zhang, Y.-G. Guo, W.-M. Liu, and J.-C. Hao. CuO three-dimensional flowerlike nanostructures: Controlled synthesis and characterization. *J. Appl. Phys.*, 103(11): 114304, 2008.

[576] J. Liu, X. Huang, Y. Li, K. M. Sulieman, X. He, and F. Sun. Hierarchical nanostructures of cupric oxide on a copper substrate: controllable morphology and wettability. *J. Mater. Chem.*, 16(23):4427–4434, 2006.

[577] P. Richharia, K. L. Chopra, and M. C. Bhatnagar. Surface analysis of a black copper selective coating. *Sol. Energ. Mater.*, 23(1):93–109, 1991.

[578] M. Yang and J. He. Fine tuning of the morphology of copper oxide nanostructures and their application in ambient degradation of methylene blue. *J. Colloid Interface Sci.*, 355(1):15–22, 2011.

[579] N. J. Shirtcliffe, G. McHale, S. Atherton, and M. I. Newton. An introduction to superhydrophobicity. *Adv. Colloid Interface Sci.*, 161(1-2):124–138, 2010.

[580] F. De Angelis, F. Gentile, F. Mecarini, G. Das, M. Moretti, P. Candeloro, M. L. Coluccio, G. Cojoc, A. Accardo, C. Liberale, R. P. Zaccaria, G. Perozziello, L. Tirinato, A. Toma, G. Cuda, R. Cingolani, and E. Di Fabrizio. Breaking the diffusion limit with super-hydrophobic delivery of molecules to plasmonic nanofocusing SERS structures. *Nat. Photon.*, 5:682–687, 2011.

[581] E. Hoque, J. A. DeRose, P. Hoffmann, and H. J. Mathieu. Robust perfluorosilanized copper surfaces. *Surf. Interface Anal.*, 38(2):62–68, 2006.

[582] R. N. Wenzel. Resistance of solid surfaces to wetting by water. *Ind. Eng. Chem.*, 28(8): 988–994, 1936.

[583] P. J. Cadusch, M. M. Hlaing, S. A. Wade, S. L. McArthur, and P. R. Stoddart. Improved methods for fluorescence background subtraction from Raman spectra. *J. Raman*

Spectrosc., 44(11):1587–1595, 2013.

[584] M. A. Bryant, S. L. Joa, and J. E. Pemberton. Raman scattering from monolayer films of thiophenol and 4-mercaptopyridine at platinum surfaces. *Langmuir*, 8(3):753–756, 1992.

[585] S. Li, D. Wu, X. Xu, and R. Gu. Theoretical and experimental studies on the adsorption behavior of thiophenol on gold nanoparticles. *J. Raman Spectrosc.*, 38(11):1436–1443, 2007.

[586] T. H. Joo, M. S. Kim, and K. Kim. Surface-enhanced Raman scattering of benzenethiol in silver sol. *J. Raman Spectrosc.*, 18(1):57–60, 1987.

[587] L.-J. Wan, M. Terashima, H. Noda, and M. Osawa. Molecular orientation and ordered structure of benzenethiol adsorbed on Gold(111). *J. Phys. Chem. B*, 104(15):3563–3569, 2000.

[588] J. G. Bergman, J. P. Heritage, A.Pinczuk, J. M. Worlock, and J. H. McFee. Cyanide coverage on silver in conjunction with surface enhanced Raman scattering. *Chem. Phys. Lett.*, 68(2-3):412–415, 1979.

[589] A. Otto, J. Timper J. Billmann, and I. Pockrand. Enhanced inelastic light scattering from metal electrodes caused by adatoms. *Phys. Rev. Lett.*, 45(1):46–49, 1980.

[590] T. H. Wood. Role of atomic-scale roughness in surface-enhanced raman scattering. *Phys. Rev. B*, 24(4):2289–2291, 1981.

[591] J. E. Rowe, C. V. Shank, D. A. Zwemer, and C. A. Murray. Ultrahigh-vacuum studies of enhanced Raman scattering from pyridine on Ag surfaces. *Phys. Rev. Lett.*, 44(26): 1770–1773, 1980.

[592] F. Benz, M. K. Schmidt, A. Dreismann, R. Chikkaraddy, Y. Zhang, A. Demetriadou, C. Carnegie, H. Ohadi, B. de Nijs, R. Esteban, J. Aizpurua, and J. J. Baumberg. Single-molecule optomechanics in "picocavities". *Science*, 354(6313):726–729, 2016.

[593] Z. Rakocevic, R. Petrovic, and S. Strbac. Surface roughness of ultra-thin silver films sputter depositedon a glass. *J. Microsc.*, 232(3):595–600, 2008.

[594] J. A. Thornton. The microstructure of sputter-deposited coatings. *J. Vac. Sci. Technol. A*, 4(6):3059–3065, 1986.

[595] D. Flötotto, Z. M. Wang, L. P. H. Jeurgens, E. Bischoff, and E. J. Mittemeijer. Effect of adatom surface diffusivity on microstructure and intrinsic stress evolutions during Ag film growth. *J. Appl. Phys.*, 112(4):043503, 2012.

[596] S. M. George. Atomic layer deposition: An overview. *Chem. Rev.*, 110(1):111–131, 2010.

[597] J. Wang, A.-H. Lu, M. Li, W. Zhang, Y.-S. Chen, D.-X. Tian, and W.-C. Li. Thin porous alumina sheets as supports for stabilizing gold nanoparticles. *ACS Nano*, 7(6): 4902–4910, 2013.

[598] C. A. Szafranski, W. Tanner, P. E. Laibinis, and R. L. Garrell. Surface-enhanced Raman spectroscopy of aromatic thiols and disulfides on gold electrodes. *Langmuir*, 14(13):

3570–3579, 1998.

[599] C. E. Taylor, J. E. Pemberton, G. G. Goodman, and M. H. Schoenfisch. Surface enhancement factors for Ag and Au surfaces relative to Pt surfaces for monolayers of thiophenol. *Appl. Spectrosc.*, 53(10):1212–1221, 1999.

[600] E. J. Blackie, E. C. Le Ru, and P. G. Etchegoin. Single-molecule surface-enhanced Raman spectroscopy of nonresonant molecules. *J. Am. Chem. Soc.*, 131(40):14466–14472, 2009.

[601] N. M. B. Perney, J. J. Baumberg, M. E. Zoorob, M. D. B. Charlton, S. Mahnkopf, and C. M. Netti. Tuning localized plasmons in nanostructured substrates for surface-enhanced Raman scattering. *Opt. Express*, 14(2):847–857, 2006.

[602] R. F. Aroca and C. J. L. Constantino. Surface-enhanced Raman scattering: Imaging and mapping of Langmuir-Blodgett monolayers physically adsorbed onto silver island films. *Langmuir*, 16(12):5425–5429, 2000.

[603] C. Farcau and S. Astilean. Mapping the SERS efficiency and hot-spots localization on gold film over nanospheres substrates. *J. Phys. Chem. C*, 114(27):11717–11722, 2010.

[604] C. D. Tran. *In situ* identification of paper chromatogram spots by surface enhanced Raman scattering. *J. Chromatogr. A*, 292(2):432–438, 1984.

[605] C. H. Lee, L. Tian, and S. Singamaneni. Paper-based SERS swab for rapid trace detection on real-world surfaces. *ACS Appl. Mater. Interfaces*, 2(12):3429–3435, 2010.

[606] C. H. Lee, M. E. Hankus, L. Tian, P. M. Pellegrino, and S. Singamaneni. Highly sensitive surface enhanced Raman scattering substrates based on filter paper loaded with plasmonic nanostructures. *Anal. Chem.*, 83(23):8953–8958, 2011.

[607] M. J. Oliveira, P. Quaresma, M. P. de Almeida, A. Araújo, E. Pereira, E. Fortunato, R. Martins, R. Franco, and H. Águas. Office paper decorated with silver nanostars - an alternative cost effective platform for trace analyte detection by SERS. *Sci. Rep.*, 7: 2480, 2017.

[608] Y. H. Ngo, D. Li, G. P. Simon, and G. Garnier. Gold nanoparticle-paper as a three-dimensional surface enhanced Raman scattering substrate. *Langmuir*, 28(23):8782–8790, 2012.

[609] L. F. Sallum, F. L. F. Soares, J. A. Ardila, and R. L. Carneiro. Determination of acetylsalicylic acid in commercial tablets by SERS using silver nanoparticle-coated filter paper. *Spectrochim. Acta A*, 133:107–111, 2014.

[610] W. W. Yu and I. M. White. Inkjet printed surface enhanced Raman spectroscopy array on cellulose paper. *Anal. Chem.*, 82(23):9626–9630, 2010.

[611] L. Polavarapu, A. La Porta, S. M. Novikov, M. Coronado-Puchau, and L. M. Liz-Marzán. Pen-on-paper approach toward the design of universal surface enhanced Raman scattering substrates. *Small*, 10(15):3065–3071, 2014.

[612] X. Li, D. R. Ballerini, and W. Shen. A perspective on paper-based microfluidics: Current status and future trends. *Biomicrofluidics*, 6(1):011301, 2012.

[613] A. Saha and N. R. Jana. Paper-based microfluidic approach for surface-enhanced Raman spectroscopy and highly reproducible detection of proteins beyond picomolar concentration. *ACS Appl. Mater. Interfaces*, 7(1):996–1003, 2015.

[614] P. Joshi and V. Santhanam. Paper-based SERS active substrates on demand. *RSC Adv.*, 6(72):68545–68552, 2016.

[615] L. Polavarapua and L. M. Liz-Marzán. Towards low-cost flexible substrates for nanoplasmonic sensing. *Phys. Chem. Chem. Phys.*, 15(15):5288–5300, 2013.

[616] D. He, B. Hu, Q.-F. Yao, K. Wang, and S.-H. Yu. Large-scale synthesis of flexible free-standing SERS substrates with high sensitivity: Electrospun PVA nanofibers embedded with controlled alignment of silver nanoparticles. *ACS Nano*, 3(12):3993–4002, 2009.

[617] C.-L. Zhang, K.-P. Lv, H.-P. Cong, and S.-H. Yu. Controlled assemblies of gold nanorods in PVA nanofiber matrix as flexible free-standing SERS substrates by electrospinning. *Small*, 8(5):648–653, 2012.

[618] J. P. Singh, H. Y. Chu, J. Abell, R. A. Tripp, and Y. Zhao. Flexible and mechanical strain resistant large area SERS active substrates. *Nanoscale*, 4(11):3410–3414, 2012.

[619] G. Lu, H. Li, and H. Zhang. Nanoparticle-coated PDMS elastomers for enhancement of Raman scattering. *Chem. Commun.*, 47(30):8560–8562, 2011.

[620] W. Wu, L. Liu, Z. Dai, J. Liu, S. Yang, L. Zhou, X. Xiao, C. Jiang, and V. A. L. Roy. Low-cost, disposable, flexible and highly reproducible screen printed SERS substrates for the detection of various chemicals. *Sci. Rep.*, 5:10208, 2015.

[621] M. Geissler, K. Li, B. Cui, L. Clime, and T. Veres. Plastic substrates for surface-enhanced Raman scattering. *J. Phys. Chem. C*, 113(40):17296–17300, 2009.

[622] D. H. K. Nguyen, V. T. H. Pham, V. Khanh Truong, I. Sbarski, J. Wang, A. Balčytis, S. Juodkazis, D. E. Mainwaring, R. J. Crawford, and E. P. Ivanova. Role of topological scale in the differential fouling of *Pseudomonas aeruginosa* and *Staphylococcus aureus* bacterial cells on wrinkled gold-coated polystyrene surfaces. *Nanoscale*, 10(11):5089–5096, 2018.

[623] A. Balčytis, M. Ryu, G. Seniutinas, P. R. Stoddart, M. A. Al Mamun, J. Morikawa, and S. Juodkazis. Nano-rescaling of gold films on polystyrene: thermal management for SERS. *Nanoscale*, 9(2):690–695, 2017.

[624] E. Cerda and L. Mahadevan. Geometry and physics of wrinkling. *Phys. Rev. Lett.*, 90 (7):074302, 2003.

[625] J. Yin, Z. Cao, C. Li, I. Sheinman, and X. Chen. Stress-driven buckling patterns in spheroidal core/shell structures. *Proc. Natl. Acad. Sci. U.S.A.*, 105(49):19132–19135, 2008.

[626] N. Bowden, S. Brittain, A. G. Evans, J. W. Hutchinson, and G. M. Whitesides. Spontaneous formation of ordered structures in thin films of metals supported on an elastomeric polymer. *Nature*, 393:146–149, 1998.

[627] K. Efimenko, M. Rackaitis, E. Manias, A. Vaziri, L. Mahadevan, and J. Genzer. Nested

self-similar wrinkling patterns in skins. *Nat. Mater.*, 4:293–297, 2005.

[628] J. Genzer and J. Groenewold. Soft matter with hard skin: From skin wrinkles to templating and material characterization. *Soft Matter*, 2(4):310–323, 2006.

[629] D.-Y. Khang, J. A. Rogers, and H. H. Lee. Mechanical buckling: Mechanics, metrology, and stretchable electronics. *Adv. Funct. Mater.*, 19(10):1526–1536, 2009.

[630] C.-S. Chen, D. N. Breslauer, J. I. Luna, A. Grimes, W.-C. Chin, L. P. Lee, and M. Khine. Shrinky-dink microfluidics: 3D polystyrene chips. *Lab Chip*, 8(4):622–624, 2008.

[631] P.-Y. Chen, J. Sodhi, Y. Qiu, T. M. Valentin, R. S. Steinberg, Z. Wang, R. H. Hurt, and I. Y. Wong. Multiscale graphene topographies programmed by sequential mechanical deformation. *Adv. Mater.*, 28(18):3564–3571, 2016.

[632] J. Y. Chung, A. J. Nolte, and C. M. Stafford. Surface wrinkling: A versatile platform for measuring thin-film properties. *Adv. Mater.*, 23(3):349–368, 2011.

[633] D. Olmos, E. V. Martín, and J. González-Benito. New molecular-scale information on polystyrene dynamics in PS and PS–$BaTiO_3$ composites from FTIR spectroscopy. *Phys. Chem. Chem. Phys.*, 16(44):24339–24349, 2014.

[634] D. Yin, J. Feng, R. Ma, Y.-F. Liu, Y.-L. Zhang, X.-L. Zhang, Y.-G. Bi, Q.-D. Chen, and H.-B. Sun. Efficient and mechanically robust stretchable organic light-emitting devices by a laser-programmable buckling process. *Nat. Commun.*, 7:11573, 2016.

[635] M. D. Huntington, C. J. Engel, A. J. Hryn, and T. W. Odom. Polymer nanowrinkles with continuously tunable wavelengths. *ACS Appl. Mater. Interfaces*, 5(13):6438–6442, 2013.

[636] J. M. Nokes, H. Sharma, R. Tu, M. Y. Kim, M. Chu, A. Siddiqui, and M. Khine. Nanotextured shrink wrap superhydrophobic surfaces by argon plasma etching. *Materials*, 9(3):196, 2016.

[637] J. Morikawa, A. Orie, T. Hashimoto, and S. Juodkazis. Thermal diffusivity in femtosecond-laser-structured micro-volumes of polymers. *Appl. Phys. A*, 98:551–556, 2009.

[638] H. Sharma, M. A. Digman, N. Felsinger, E. Gratton, and M. Khine. Enhanced emission of fluorophores on shrink-induced wrinkled composite structures. *Opt. Mater. Express*, 4(4):753–763, 2014.

[639] L. Zhang, X. Lang, A. Hirata, and M. Chen. Wrinkled nanoporous gold films with ultrahigh surface-enhanced Raman scattering enhancement. *ACS Nano*, 5(6):4407–4413, 2011.

[640] H. Stenberg, A. Matikainen, S. Daniel, T. Nuutinen, P. Stenberg, S. Honkanen, T. Pakkanen, P. Vahimaa, and M. Suvanto. Self-organized polymer wrinkles: A lithography-free pathway for surface-enhanced Raman scattering (SERS) substrates. *ACS Nano*, 300(4): 386–390, 2015.

Publications during this PhD project

Publications pertaining to the thesis

1. T. Shoji, A. Mototsuji, A. Balčytis, D. Linklater, S. Juodkazis, and Y. Tsuboi. Optical tweezing and binding at high irradiation powers on black-Si. *Sci. Rep.*, 7:12298, 2017.

2. A. Balčytis, M. Ryu, G. Seniutinas, Y. Nishijima, Y. Hikima, M. Zamengo, R. Petruškevičius, J. Morikawa, and S. Juodkazis. Si-based infrared optical filters. *Opt. Eng.*, 54 (12):127103, 2015.

3. Y. Nishijima, R. Komatsu, S. Ota, G. Seniutinas, A. Balčytis, and S. Juodkazis. Anti-reflective surfaces: Cascading nano/microstructuring. *APL Photonics*, 1(7):076104, 2016.

4. R. Komatsu, A. Balčytis, G. Seniutinas T. Yamamura, Y. Nishijima, and S. Juodkazis. Plasmonic photo-thermoelectric energy converter with black-Si absorber. *Sol. Energ. Mater. Sol. Cells*, 143:72–77, 2015.

5. Y. Nishijima, R. Komatsu, T. Yamamura, A. Balčytis, G. Seniutinas, and S. Juodkazis. Design concept of a hybrid photo-voltaic/thermal conversion cell for mid-infrared light energy harvester. *Opt. Mater. Express*, 7(11):3484–3493, 2015.

6. J. Morikawa, M. Ryu, G. Seniutinas, A. Balčytis, K. Maximova, X. Wang, M. Zamengo, E. P. Ivanova, and S. Juodkazis. Nanostructured antireflective and thermoisolative cicada wings. *Langmuir*, 32(18):4698–4703, 2016.

7. A. Balčytis, M. Ryu, X. Wang, F. Novelli, G. Seniutinas, S. Du, X. Wang, J. Li, J. Davis, D. Appadoo, J. Morikawa, and S. Juodkazis. Silk: Optical properties over 12.6 octaves THz-IR-Visible-UV range. *Materials*, 10(4):356, 2017.

8. M. Ryu, A. Balčytis, X. Wang, J. Vongsvivut, Y. Hikima, J. Li, M. J. Tobin, S. Juodkazis, and J. Morikawa. Orientational mapping augmented sub-wavelength hyper-spectral imaging of silk. *Sci. Rep.*, 7:7419, 2017.

9. K. Maximova, X. Wang, A. Balčytis, L. Fan, J. Li, and S. Juodkazis. Silk patterns made by direct femtosecond laser writing. *Biomicrofluidics*, 10(5):054101, 2016.

10. J. Morikawa, M. Ryu, K. Maximova, A. Balčytis, G. Seniutinas, L. Fan, V. Mizeikis, J. Li, X. Wang, M. Zamengo, X. Wang, and S. Juodkazis. Silk fibroin as a water-soluble bio-resist and its thermal properties. *RSC Adv.*, 6(14):11863–11869, 2016.

11. S. Dinda, V. Suresh, P. Thoniyot, A. Balčytis, S. Juodkazis, and S. Krishnamoorthy. Engineering 3D nanoplasmonic assemblies for high performance spectroscopic sensing. *ACS Appl. Mater. Interfaces*, 7(50):27661–27666, 2015.

12. A. Balčytis, M. Ryu, G. Seniutinas, J. Juodkazytė, B. C. C. Cowie, P. R. Stoddart, M. Zamengo, J. Morikawa, and S. Juodkazis. Black-CuO: surface-enhanced Raman scattering and infrared properties. *Nanoscale*, 7:18299–18304, 2015.

13. D. H. K. Nguyen, V. T. H. Pham, V. Khanh Truong, I. Sbarski, J. Wang, A. Balčytis, S. Juodkazis, D. E. Mainwaring, R. J. Crawford, and E. P. Ivanova. Role of topological scale in the differential fouling of *Pseudomonas aeruginosa* and *Staphylococcus aureus* bacterial cells on wrinkled gold-coated polystyrene surfaces. *Nanoscale*, 10(11): 5089–5096, 2018.

14. A. Balčytis, M. Ryu, G. Seniutinas, P. R. Stoddart, M. A. Al Mamun, J. Morikawa, and S. Juodkazis. Nano-rescaling of gold films on polystyrene: thermal management for SERS. *Nanoscale*, 9(2):690–695, 2017.

Other publications

15. D. Urbonas, A. Balčytis, M. Gabalis, K. Vaškevičius, G. Naujokaitė, S. Juodkazis, and R. Petruškevičius. Ultra-wide free spectral range, enhanced sensitivity, and removed mode splitting SOI optical ring resonator with dispersive metal nanodisks. *Opt. Lett.*, 40(13):2977–2980, 2015.

16. G. Seniutinas, A. Balčytis, Y. Nishijima, A. Nadzeyka, S. Bauerdick, and S. Juodkazis. Ion beam lithography with gold and silicon ions. *Appl. Phys. A*, 122:383, 2016.

17. Y. Hashimoto, G. Seniutinas, A. Balčytis, S. Juodkazis, and Y. Nishijima. Au-Ag-Cu nano-alloys: tailoring of permittivity. *Sci. Rep.*, 6:25010, 2016.

18. G. Seniutinas, A. Balčytis, and S. Juodkazis. Ultraviolet-photoelectric effect for augmented contrast and resolution in electron microscopy. *APL Photonics*, 1(2): 021301, 2016.

19. F. C. P. Masim, H.-L. Liu, M. Porta, T. Yonezawa, A.Balčytis, S. Juodkazis, W.-H. Hsu, and K. Hatanaka. Enhanced photoacoustics from gold nano-colloidal suspensions under femtosecond laser excitation. *Opt. Express*, 24(13):14781–14792, 2016.

20. A. Balčytis, D. Hakobyan, M. Gabalis, A. Žukauskas, D. Urbonas, M. Malinauskas, R. Petruškevičius, E. Brasselet, and S. Juodkazis. Hybrid curved nano-structured micro-optical elements. *Opt. Express*, 24(15):16988–16998, 2016.

21. F. C. P. Masim, W.-H. Hsu, C.-H. Tsai, H.-L. Liu, M. Porta, M. T. Nguyen, T. Yonezawa, A. Balčytis, X. Wang, S. Juodkazis, and K. Hatanaka. Enhanced photoacoustics from gold nano-colloidal suspensions under femtosecond laser excitation. *Opt. Express*, 24 (15):17050–17059, 2016.

22. D. Urbonas, A. Balčytis, K. Vaškevičius, M. Gabalis, and R. Petruškevičius. Air and dielectric bands photonic crystal microringresonator for refractive index sensing. *Opt. Lett.*, 41(15):3655–3658, 2016.

23. W.-H. Hsu, F. C. P. Masim, M. Porta, M. T. Nguyen, T. Yonezawa, A. Balčytis, X. Wang, L. Rosa, S. Juodkazis, and K. Hatanaka. Femtosecond laser-induced hard X-ray generation in air from a solution flow of Au nano-sphere suspension using an automatic positioning system. *Opt. Express*, 24(18):19994–20001, 2016.

24. A. Balčytis, T. Tolenis, X. Wang, G. Seniutinas, R. Drazdys, P. R. Stoddart, and S. Juodkazis. Percolation threshold gold films on columnar coatings: characterisation for SERS applications. *Asian J. Phys.*, 25(7):871–878, 2016.

25. B. Sanchez-Padilla, A. Žukauskas, A. Aleksanyan, A. Balčytis, M. Malinauskas, S. Juodkazis, and E. Brasselet. Wrinkled axicons: shaping light from cusps. *Opt. Express*, 24 (21):24075–24082, 2016.

26. X. Wang, G. Seniutinas, A. Balčytis, I. Kašalynas, V. Jakštas, V. Janonis, R. Venckevičius, R. Buividas, D. Appadoo, G. Valušis, and S. Juodkazis. Laser structuring for control of coupling between THz light and phonon modes. *J. Laser Micro Nanoeng.*, 11(3):377–380, 2016.

27. K. Vaškevičius, M. Gabalis, D. Urbonas, A. Balčytis, R. Petruškevičius, and S. Juodkazis. Enhanced sensitivity and measurement range SOI microring resonator with integrated one-dimensional photonic crystal. *J. Opt. Soc. Am. B*, 34(4):750–755, 2017.

28. G. Seniutinas, A. Balčytis, I. Reklaitis, F. Chen, J. Davis, C. David, and S. Juodkazis. Tipping solutions: emerging 3D nano-fabrication/-imaging technologies. *Nanophotonics*, 6(5):923–941, 2017.

29. Y. Wang, T. Tran, P. Surendran, I. Herrera, A. Balčytis, D. Nissen, M. Albrecht, A. Sidorov, and P. Hannaford. Trapping ultracold atoms in a sub-micron-period triangular magnetic lattice. *Phys. Rev. A*, 96(1):013630, 2017.

30. F. C. P. Masim, W.-H. Hsu, H.-L. Liu, T. Yonezawa, A. Balčytis, S. Juodkazis, and K. Hatanaka. Photoacoustic signal enhancements from gold nano-colloidal suspensions excited by a pair of time-delayed femtosecond pulses. *Opt. Express*, 25(16):19497–19507, 2017.

31. Y. Nishijima, Y. Hashimoto, A. Balčytis, G. Seniutinas, and S. Juodkazis. Alloy materials for plasmonic refractive index sensing. *Sens. Mater.*, 29(9):1233–1239, 2017.

32. Y. Nishijima, S. Suda, G. Seniutinas, A. Balčytis, and S. Juodkazis. Plasmonic sensor: towards parts-per-billion level sensitivity. *Sens. Mater.*, 29(9):1253–1258, 2017.

33. Y. Nishijima, A. Balčytis, G. Seniutinas, S. Juodkazis, T. Arakawa, S. Okazaki, and R. Petruškevičius. Plasmonic hydrogen sensor at infrared wavelengths. *Sens. Mater.*, 29(9):1269–1274, 2017.

34. Y. Nishijima, S. Shimizu, K. Kurihara, Y. Hashimoto, H. Takahashi, A. Balčytis, G. Seniutinas, S. Okazaki, J. Juodkazytė, T. Iwasa, T. Taketsugu, Y. Tominaga, and S. Juodkazis. Optical readout of hydrogen storage in films of Au and Pd. *Opt. Express*, 25(20):24081–24092, 2017.

35. W.-H. Hsu, F. C. P. Masim, A. Balčytis, S. Juodkazis, and K. Hatanaka. Dynamic position shifts of X-ray emission from a water film induced by a pair of time-delayed femtosecond laser pulses. *Opt. Express*, 25(20):24109–24118, 2017.

36. M. Ryu, H. Kobayashi, A. Balčytis, X. Wang, J. Vongsvivut, J. Li, N. Urayama, V. Mizeikis, M. Tobin, S. Juodkazis, and J. Morikawa. Nanoscale chemical mapping of laser-solubilized silk. *Mater. Res. Express*, 4(11):115028, 2017.

37. M. Ryu, D. Linklater, W. Hart, A. Balčytis, E. Skliutas, M. Malinauskas, D. Appadoo, Y.-R. E. Tan, E. P. Ivanova, J. Morikawa, and S. Juodkazis. 3D printed polarizing grids for IR-THz synchrotron radiation. *J. Opt.*, 20(3):035101, 2018.

38. C. M. Bhadra, M. Werner, V. A. Baulin, V. K. Truong, M. Al Kobaisi, S. H. Nguyen, A. Balčytis, S. Juodkazis, J. Y. Wang, D. E. Mainwaring, R. J. Crawford, and E. P. Ivanova. Subtle variations in surface properties of black silicon surfaces influence the degree of bactericidal efficiency. *Nano-Micro Lett.*, 10(2):36, 2018.

39. A. Balčytis, M. Ryu, S. Juodkazis, and J. Morikawa. Micro-thermocouple on nano-membrane: thermometer for nanoscale measurements. *Sci. Rep.*, 8:6324, 2018.

Conferences and proceeding papers

1. Y. Nishijima, R. Komatsu, T. Yamamura, G. Seniutinas, A. Balčytis, S. Juodkazis. Photo-Thermoelectric Energy Converter with Black-Si Absorber. In *IEEE Proc. 2014 Conference on Optoelectronic and Microelectronic Materials and Devices (COMMAD)*, 14-17 December, Perth, Australia, pages 109–112, 2014.

2. G. Seniutinas, A. Balčytis, R. Tomašiūnas, R. Petruškevičius, S. Urnikaitė and V. Getautis. Photo-Switching dynamics of azo-phenylcarbazoles in polycarbonate around β transition temperature. In *IEEE Proc. 2014 16th International Conference on Transparent Optical Networks (ICTON)*, 6-10 July, Graz, Austria, pages 1–4, 2014.

3. R. Petruškevičius, D. Urbonas, M. Gabalis, K. Vaškevičius and A. Balčytis. Plasmonic and silicon-on-insulator nanostructures for optical biosensing. In *IEEE Proc. 2014 16th International Conference on Transparent Optical Networks (ICTON)*, 6-10 July, Graz, Austria, pages 1–4, 2014.

4. A. Balčytis, G. Seniutinas, D. Urbonas, M. Gabalis, K. Vaškevičius, R. Petruškevičius, G. Molis, G. Valušis, S. Juodkazis. High precision fabrication of antennas and sensors. In *Proc. SPIE 9446, Ninth International Symposium on Precision Engineering Measurement and Instrumentation*, 8-10 August, Changsha, China, page 94461G, 2015.

5. Y. Nishijima, A. Balčytis, R. Komatsu, T. Yamamura, G. Seniutinas, B. T. Wong, S. Juodkazis. Thermal to electrical energy converter based on black Si. In *Proc. SPIE 9374, Advanced Fabrication Technologies for Micro/Nano Optics and Photonics VIII*, 8-11 February, San Francisco, CA, USA, page 93740J, 2015.

6. A. Balčytis, G. Seniutinas, J. Juodkazytė, B. C. C. Cowie, F. Lapierre, S. Juodkazis. Nanotextured CuO: sensing and light harvesting platform. In *Proc. SPIE 9374, Advanced Fabrication Technologies for Micro/Nano Optics and Photonics VIII*, 8-11 February, San Francisco, CA, USA, page 93740K, 2015.

7. G. Seniutinas, G. Gervinskas, A. Balčytis, F. Clark, Y. Nishijima, A. Krotkus, G. Molis, G. Valusis, S. Juodkazis. Nanoscale precision in ion milling for optical and terahertz antennas. In *Proc. SPIE 9374, Advanced Fabrication Technologies for Micro/Nano Optics and Photonics VIII*, 8-11 February, San Francisco, CA, USA, page 93740P, 2015.

8. R. Komatsu, A. Balčytis, G. Seniutinas, Y. Nishijima, S. Juodkazis. Energy harvesting with black Si/plasmonics composite material. In *Lasers and Electro-Optics Pacific Rim (CLEO-PR), 2015 11th Conference on, Vol. 2*, 24-28 August, Busan, South Korea, pages 1-2, 2015.
9. Y. Nishijima, Y. Hashimoto, S. Gediminas, A. Balčytis and S. Juodkazis. Alloy plasmonic materials. In *Lasers and Electro-Optics Pacific Rim (CLEO-PR), 2015 11th Conference on, Vol. 1*, 24-28 August, Busan, South Korea, pages 1-2, 2015.
10. J. Getautis, A. Balčytis, R. Tomašiūnas, R. Petruškevičius, S. Urnikaitė and V. Getautis. All-optical poling kinetics of azophenylcarbazoles influenced by attached anchor. In *2015 17th International Conference on Transparent Optical Networks (ICTON)*, 5-9 July, Budapest, Hungary, pages 1-4, 2015.
11. A. Balčytis, D. Hakobyan, M. Gabalis, A. Žukauskas, D. Urbonas, M. Malinauskas, R. Petruškevičius, E. Brasselet, S. Juodkazis. 3D micro-optical elements for generation of tightly focused vortex beams. In *MATEC Web of Conferences 32, International Symposium of Optomechatronics Technology (ISOT 2015)*, 14-16 October, Neuchatel, Switzerland, page 03002, 2015.
12. A. Balčytis, J. Juodkazytė, G. Seniutinas, X. Li, G. Niaura, S. Juodkazis. Nanotextured surfaces for surface enhanced Raman spectroscopy and sensors. In *Proc. SPIE 9736, Laser-based Micro- and Nanoprocessing X*, 16-18 February, San Francisco, CA, USA, page 97360G, 2016.
13. K. Maximova, X. Wang, A. Balčytis, J. Li, S. Juodkazis. Writing of bio-compatible silk patterns: 3D laser nano-printing. In *Conference on Lasers and Electro-Optics, OSA Technical Digest*, 5–10 June, San Jose, CA, USA, page AF1J.2, 2016.
14. A. Balčytis, D. Urbonas, M. Gabalis, S. Juodkazis, R. Petruškevičius. Mode control in SOI microring resonators through sub-wavelength modifications. In *Applied Nanotechnology and Nanoscience International Conference (ANNIC 2016)*, 9-11 November, Barcelona, Spain, 2016.
15. C. Briosne-Fréjaville, A. Mau, A. Balčytis, X. Li, S. Juodkazis. Resizable nanopores. In *Applied Nanotechnology and Nanoscience International Conference (ANNIC 2016)*, 9-11 November, Barcelona, Spain, 2016.
16. A. Balčytis, D. Urbonas, M. Gabalis, S. Juodkazis, R. Petruškevičius. Sub-wavelength modifications in silicon-on-insulator microring resonators for enhanced sensing. In *IONS Conference on Optics, Atoms and Laser Applications 2016 (KOALA 2016)*, 27 November - 2 December, Melbourne, VIC, Australia, 2016.
17. A. Balčytis, C. Briosne-Fréjaville, A. Mau, X. Li, S. Juodkazis. Rescalable solid-state nanopores. In *AIP Conference Proceedings 1874, International Conference on Metamaterials and Nanophotonics (METANANO-2017)*, 18-22 September, Vladivostok, Russia, page 030002, 2016.